for G.H. Lander

AECL-8488

ATOMIC ENERGY OF CANADA LIMITED

L'ÉNERGIE ATOMIQUE DU CANADA LIMITÉE

ICANS - VII

PROCEEDINGS OF THE SEVENTH MEETING OF THE INTERNATIONAL COLLABORATION ON ADVANCED NEUTRON SOURCES

Chalk River Nuclear Laboratories
1983 September 13-16

Edited by
S.O. SCHRIBER

Chalk River Nuclear Laboratories Laboratoires nucléaires de Chalk River

Chalk River, Ontario

September 1984 septembre

Jan 14, 1985

ATOMIC ENERGY OF CANADA LIMITED

ICANS-VII

Proceedings of the Seventh Meeting
of the
International Collaboration on Advanced Neutron Sources

Chalk River Nuclear Laboratories
1983 September 13-16

Edited by

S.O. Schriber

Research Company
Chalk River Nuclear Laboratories
Chalk River, Ontario, Canada K0J 1J0

September 1984 AECL-8488

L'ENERGIE ATOMIQUE DU CANADA LIMITÉE

ICANS-VII

Débats de la septième réunion de la
Collaboration internationale
sur les sources de neutrons avancés

Laboratoires nucléaires de Chalk River
13-16 septembre 1983

Édité par S.O. Schriber

Résumé

En 1983, la réunion de la Collaboration internationale sur les sources de neutrons avancés eut lieu aux Laboratoires nucléaires de Chalk River, du 13 au 16 septembre 1983. La présente publication contient les textes des travaux présentés oralement.

Société de Recherche
Laboratoires nucléaires de Chalk River
Chalk River, Ontario, Canada K0J 1J0

Septembre 1984 AECL-8488

ATOMIC ENERGY OF CANADA LIMITED

ICANS-VII

Proceedings of the Seventh Meeting
of the
International Collaboration on Advanced Neutron Sources

Chalk River Nuclear Laboratories
1983 September 13-16

Edited by S.O. Schriber

Abstract

The 1983 Meeting of the International Collaboration on Advanced Neutron Sources was held at Chalk River Nuclear Laboratories 1983 September 13-16. This publication contains the texts of contributed papers presented orally.

Research Company
Chalk River Nuclear Laboratories
Chalk River, Ontario, Canada K0J 1J0

September 1984 AECL-8488

CONFERENCE CHAIRMAN

Bruce G. Chidley

ORGANIZING COMMITTEE

Bruce G. Chidley, Chairman
Edward A. Heighway
Thomas M. Holden
Richard T. Jones
M. Aslam Lone
Stanley O. Schriber

PROGRAM COMMITTEE

Günter S. Bauer
Jack M. Carpenter
Bruce G. Chidley
Walter E. Fischer
Thomas M. Holden, Chairman
M. Aslam Lone
Geoff Manning
Garry J. Russell
Hiroshi Sasaki
Stanley O. Schriber
George C. Stirling
Ian M. Thorson

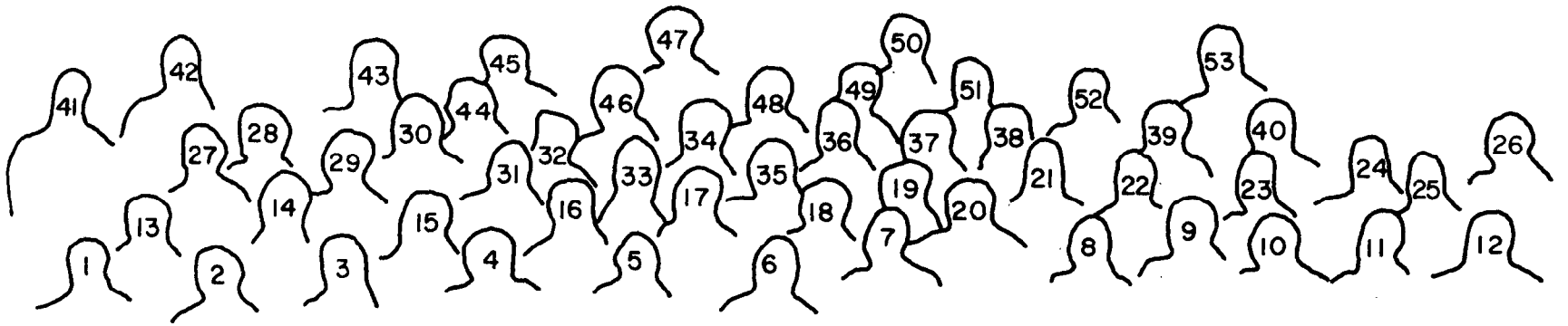

1. Lone, M.A.
2. Bohringer, D.
3. Jason, A.
4. Macek, R.J.
5. Takeda, Y.
6. Chiba, R.
7. Diplock, B.
8. Manning, G.
9. Takahashi, H.
10. Sasaki, H.
11. Kimura, M.
12. Filges, D.
13. Heighway, E.A.
14. Holden, T.M.
15. Kempson, V.
16. Woods, R.
17. Robinson, H.
18. Carne, A.
19. Schelten, J.
20. Carpenter, J.M.
21. Brockmann, H.
22. Armstrong, T.W.
23. Blackmore, E.W.
24. Egelstaff, P.A.
25. Russell, G.J.
26. Thamm, G.
27. Lawrence, G.P.
28. Robertson, J.A.L.
29. Hardekopf, R.A.
30. Clout, P.
31. Grisham, D.L.
32. Stirling, G.
33. Buyers, W.J.L.
34. Norem, J.
35. Dolling, G.
36. Jones, R.T.
37. Kustom, R.L.
38. Stechemesser, H.
39. Lohmann, W.
40. Potts, C.W.
41. Bauer, G.S.
42. Schriber, S.O.
43. Cloth, P.
44. Ormrod, J.H.
45. Atchison, F.
46. Fischer, W.E.
47. Sinclair, R.N.
48. Gilmore, J.S.
49. Rauchas, A.
50. Lander, G.H.
51. Baartmann, R.
52. Bowman, C.D.
53. Chidley, B.G.

ICANS VII

Seventh Meeting of the International Collaboration on Advanced Neutron Sources
Chalk River Nuclear Laboratories

1983 September 13-16

Editor's Note

The 1983 Meeting of the International Collaboration on Advanced Neutron Sources had 68 participants from North America, Europe and Asia. Of the 56 papers presented orally, 48 are printed in the proceedings. Although authors were given extended deadlines, for a number of reasons it was not possible to print all contributions to the meeting. Summaries of each session are not included because only three of the nine required were received.

Two contributions, one on status and one on advanced concepts, are not included in the proceedings, at the request of the authors, because excellent reviews have been published elsewhere recently. ASTOR was described in IEEE Trans. Nucl. Sci., Vol. NS-30, No. 4, August 1983, 2083 (Proceedings of the 1983 Particle Accelerator Conference) - "ASTOR, Concept of a Combined Acceleration and Storage Ring for the Production of Intense Pulsed or Continuous Beams of Neutrinos, Pions, Muons, Kaons and Neutrons" by W. Joho. ZEBRA/EMTF was described in Atomkernenergie-Kerntechnik, Vol. 44, No. 3, 177 (1984) (Proceedings of June 1983 ICENES Conference) - "An assessment of Accelerator Breeding - Economics, Developments and a Staged Program" by S.O. Schriber and Atomic Energy of Canada Limited, Report No. AECL-7840 - "Canadian Accelerator Breeder System Development" by S.O. Schriber.

I wish to thank the authors for submitting manuscripts which followed mailed instructions. This made assembly of the proceedings much easier and helped to contribute to an overall reduction in the number of pages for the proceedings. The manuscripts have been reproduced in the form supplied by the authors, so that we may present each contribution in the manner chosen by them.

The conference banquet speaker was J. Archie L. Robertson, Director of Program Planning for Atomic Energy of Canada Limited, Research Company Head Office, Ottawa, Ontario. On behalf of the attendees I would like to thank him for an entertaining and enlightening talk on research and development including the use of neutron sources.

Members of Physics Division, Public Affairs Office, General Services Division, Operations Division, and Reactor Physics Branch are thanked for their many efforts in making the conference a success.

Mrs. Margaret A. Trecartin deserves much credit for her cheerful assistance, gentle nudging on proceedings matters and preparation of material for the proceedings.

S.O. Schriber

Stanley O. Schriber.

ICANS - VII Agenda

Chalk River Nuclear Laboratories
1983 September 13-16

Monday, 1983 September 12

Evening - Program Committee Session

Tuesday, 1983 September 13

Welcome - Geoff C. Hanna, Director of Research, CRNL
Morning - Status Reports
Afternoon - Symposium on Advanced Concepts

Wednesday, 1983 September 14

Morning - Parallel Sessions - Targets/Accelerator Components and Technology
Afternoon - Science Applications of Accelerator-Based Sources

Thursday, 1983 September 15

Morning - Targets/Moderators
Afternoon - Shielding and Remote Handling

Laboratory Tours

Conference Banquet

Friday, 1983 September 16

Morning - Concepts, Materials and Performance

Summary Session and Concluding Remarks

TABLE OF CONTENTS

		Page
Session A - Chairman, G.A. Bartholomew, CRNL retired		1
	Status Reports	
A1	The SNQ Project, Status Report as of August 1983 G.S. Bauer, KfA	2
A2	Status Report on the WNR/PSR Pulsed Spallation Neutron Source at the Los Alamos National Laboratory C.D. Bowman, LANL	9
A3	Present Status of Booster Synchrotron Utilization Facility at KEK H. Sasaki, KEK	15
A4	Status Report on the SIN Neutron Source (September 1983) F. Atchison and W.E. Fischer for the Project Group, SIN	23
A5	TRIUMF Thermal Neutron Facility I.M. Thorson, J.J. Burgerjon, R.E. Blaby and T.A. Hodges, TRIUMF	31
A6	Progress on Construction and Commissioning of the Spallation Neutron Source at the Rutherford Appleton Laboratory G. Manning, RAL	34
B *X A7	Status Report and Future Plans of the Intense Pulsed Neutron Source - ANL G.H. Lander, J.M. Carpenter, R.L. Kustom and T.K. Khoe, ANL	40
Session B - Chairman, B.G. Chidley, CRNL		45
	Symposium on Advanced Concepts	
A *X B1	ASPUN, Argonne Super Intense Pulsed Spallation Neutron Source T.K. Khoe and R.L. Kustom, ANL	46
B2	Accelerator Project GEMINI for Intense Pulsed Neutron and Meson Source at KEK H. Sasaki and GEMINI Study Group, KEK	50
B3	TRIUMF Kaon Factory as a Potential Neutron Source E.W. Blackmore, TRIUMF	55

Page

Session C - Chairmen, W.E. Fischer, SIN 61
I.M. Thorson, TRIUMF

Targets I

C1 Production Rates of Spallation and Fission Products in Depleted Uranium and Natural Lead Targets Bombarded by 600 MeV and 1100 MeV Protons 62
W. Amian, N.F. Peek, D.J. Shaddan and G. Sterzenback, KfA and U of C

C2 Fertile-to-Fissile Conversion and Fission Measurements for Thorium Bombarded by 800-MeV Protons 68
J.S. Gilmore, G.J. Russell, H. Robinson and R.E. Prael, LANL

C3 Recent Target Design Calculations at KfA 78
P. Cloth, D. Filges, R.D. Neef and H. Schaal, KfA

C4 Progress in Materials Investigation for SNQ-Targets 84
P. Krautwasser and W. Lohmann, KfA

C5 Some Topics of Recent Development on Monte Carlo Computation of Target Systems in Japan 90
M. Kimura, Tohoku U

C6 Multiplying Booster Targets on the SNS 100
A. Carne, RAL

C7 Enhancement of the SNS Spallation Target by U-235 Enrichment 105
H. Brockmann and W. Scherer, KfA

C8 Target Designs for Stepwise Development of SNQ 109
H. Stechemesser and G. Thamm, KfA

C9 Heat-Up Effects of Gamma Showers on Nine Sample Materials in TRIUMF Neutron Source Geometry 118
M. Pepin, SIN

C10 SINQ Bulk Shield Analysis using the S_N-Method 122
V. Herronberger and P. Stiller, SIN

Session D - Chairmen, J.H. Ormrod, CRNL 127
C.D. Bowman, LANL

Accelerator Components and Technology

D1 Proton Storage Ring (PSR) Diagnostics and Control System 128
P. Clout, LANL

D2 PSR Beam-Pulse Formation and Control 134
R.A. Hardekopf, LANL

Page

A X D3 Preliminary Tests of a Second Harmonic RF System for the Intense Pulsed Neutron Source Synchrotron 140
J. Norem and F. Brandeberry, ANL

A X D4 Intense Pulsed Neutron Source Accelerator Status 144
C.W. Potts, F.R. Brumwell and V.F. Stipp, ANL

D5 Present Design of the Linac of the SNQ Project 148
J. Schelten and C. Zettler, KfA

B X D6 IPNS Accelerator System and Neutron Chopper Synchronization 157
A. Rauchas, G. Ostrowski, C. Pelizzari and G. Volk, ANL

D7 Development of a High Current Injector for a Spallation Neutron Source 162
B.G. Chidley, G.E. McMichael and M.R. Shubaly, CRNL

D8 Beam Loading and Beam Instabilities in High Current Accelerators 166
K.C.D. Chan and J. McKeown, CRNL

Session E - Chairman, T.M. Holden, CRNL 171

Science Applications of Accelerator-Based Sources

E1 Condensed Matter Physics with Neutrons 172
R.N. Sinclair, Harwell

E2 Nuclear and Particle Physics with High Intensity Pulsed Neutron Sources 175
T. Dombeck, LANL

C XX E3 Studies of Neutron Irradiation Effects at IPNS-REF 185
M.A. Kirk, ANL

Session F - Chairman, G.J. Russell, LANL 193

Targets II

F1 Validation of Spallation Models for Particle Production 194
D. Filges, T.W. Armstrong and P. Cloth, KfA

F2 Spallation Neutron Sources with Intermediate Energy Protons 200
M.A. Lone, CRNL

F3 HETC/KFA-1, An Updated Version of HETC for High-Energy Spallation Physics Calculations 205
T.W. Armstrong, P. Cloth, B.L. Colborn, D. Filges and G. Sterzenbach, KfA

Page

F4 Calculational Methods and High Energy Cross Sections for Spallation Source Shielding 208
T.W. Armstrong, P. Cloth, D. Filges and H. Schaal, KfA

F5 Progress Report on the SNS Target Station 214
A. Carne, RAL

F6 Thermofluid Dynamics in Liquid Targets 223
Y. Takeda, SIN

Session G - Chairman, G. Manning, RAL 229

Moderators

G1 Grooved Cold Moderator at KENS 230
Y. Ishikawa, S. Ikeda, N. Watanabe, K. Kondo, K. Inoue, Y. Kiyanagi, H. Iwasa and K. Tsuchihashi, Japan

B X G2 Measurement and Fitting of Spectrum and Pulse Shapes of a Liquid Methane Moderator at IPNS 236
J.M. Carpenter, R.A. Robinson and A.D. Taylor, ANL, LANL

G3 The Influence of Target and Reflector Coolant on the Thermal Neutron Leakage Flux from an SNQ-Type Moderator 240
G.S. Bauer, H. Conrad, K. Grünhagen, G. Milleret and H. Spitzer, KfA

Session H - Chairman, G.M. Lander, ANL 245

Shielding and Remote Handling

H1 Radiation-Resistant Beamline Components at LAMPF 246
R.J. Macek, D.L. Grisham, J.E. Lambert and R. Werbeck, LANL

H2 Remote Handling at LAMPF 252
D.L. Grisham and J.E. Lambert, LANL

H3 Operational, Handling and Safety Aspects of the SNQ Target Station 256
H. Buttgereit, H. Steckemesser, G. Thomm and J. Wolters, KfA

Session I - Chairman, G. S. Bauer, KfA 265

Concepts, Materials and Performance

I1 Beam Tube Concept for SINQ 266
F. Atchison, SIN

I2 New Directions in Neutron Diffraction 271
P.A. Egelstaff, U of Guelph

Page

I3 Irradiation Effects in Candidate Materials for the SNQ-Target Station
W. Lohmann, KfA 274

I4 Design Features and Performance of the LAMPF High Intensity Beam Area
L. Agnew, D. Grisham, R.J. Macek, W.F. Sommer and R.D. Werbeck, LANL 279

B X I5 Operating Experience with the IPNS Neutron Generating System
A.W. Schulke, D.E. Bohringer, B.S. Brown and J.M. Carpenter, ANL 285

List of Attendees 290

Author Index 291

Session A

Status Reports

Chairman - G.A. Bartholomew

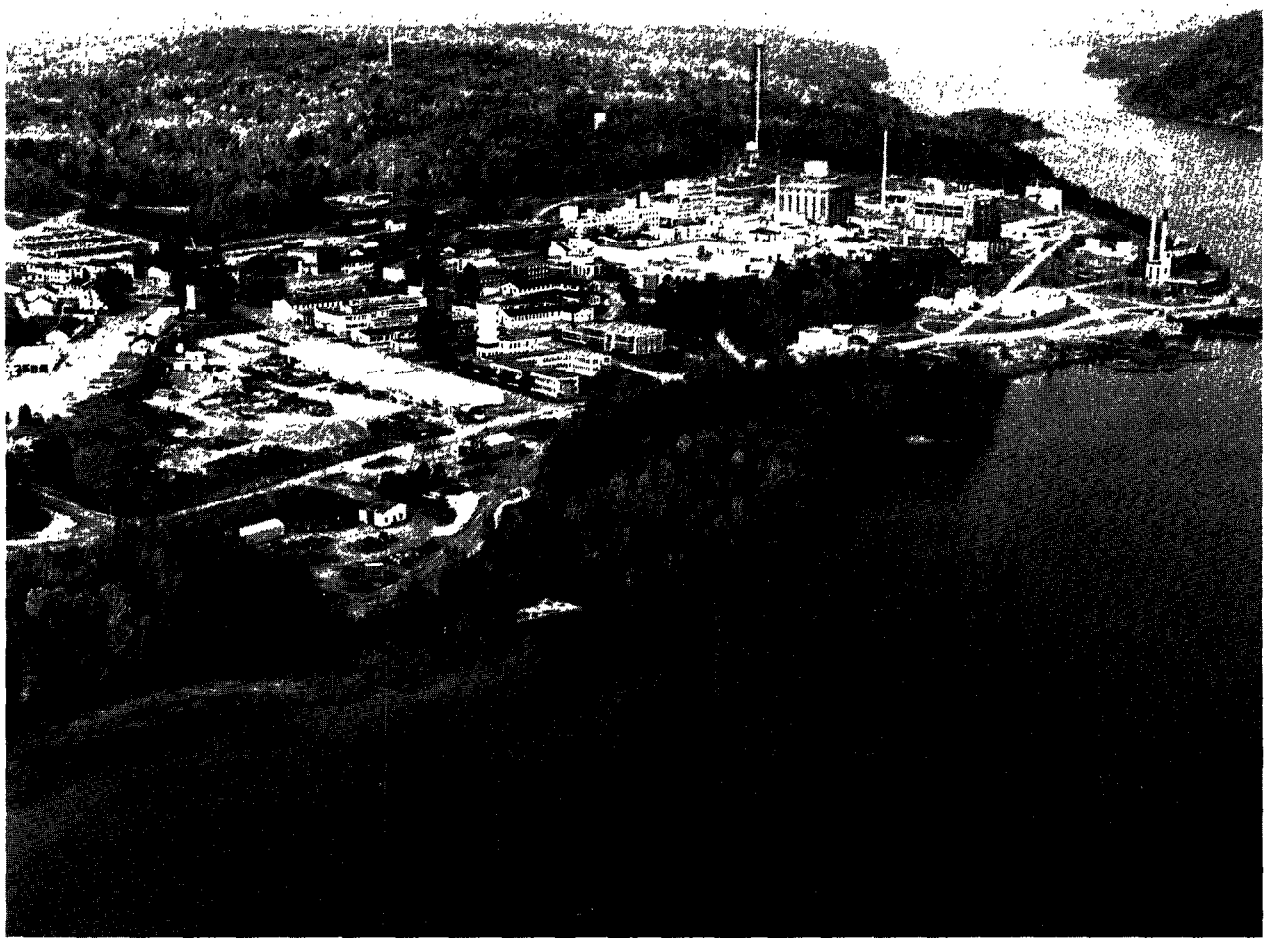

Proceedings of International Collaboration on Advanced Neutron Sources (ICANS-VII), 1983 September 13-16
Atomic Energy of Canada Limited, Report AECL-8488

The SNQ-Project

Status report as of August 1983

G. S. Bauer
Projektleitung Spallations-Neutronenquelle
KFA Jülich, D-5170 Jülich, FRG

1. Development of the SNQ-concept

The SNQ-project, with SNQ standing for the German term "Spallations-Neutronen-Quelle" (spallation neutron source) went through a fairly lengthy analysis phase during the years 1979 through 1982. During this period the goal was defined to substitute a new high flux neutron source for the slowly aging German low to medium flux research reactors, most of which were more than 20 years old and could no more be considered as meeting modern research needs in a satisfactory and economic way. A feasibility analysis was carried out jointly by the two national research centres at Karlsruhe (KfK) and at Jülich (KFA), demonstrating that with present day technology and some additional development work a spallation neutron source could be built whose effective time average thermal neutron flux is equivalent to that of an advanced thermal high flux reactor (i.e. of the order of 10^{15} $cm^{-2}s^{-1}$), but which, by virtue of a pronounced time structure and a broader range of scientific use , has a much higher performance potential. The concept included a proton linac with 5 mA time average current operating at 100 Hz repetition rate and a target station with one H_2O-moderator for thermal neutrons with good time structure and a D_2O-tank to provide good conditions for a cold neutron source and for irradiation facilities. It was described at previous ICANS-meetings and in a formal study report (Bauer et al, 1981; Vetter, 1981) as well as in several papers (e.g. Bauer and Vetter, 1983; Bauer, 1982). In order to make possible much shorter proton pulses at high intensity than can be obtained from an rf-linac, the addition of a proton pulse compressor was studied (e.g. Schaffer, 1981).

Two alternative concepts for a stepwise realization of the project were subsequently considered:

Concept 1 aimed at providing short high energy proton pulses at the earliest possible stage to establish good experimental conditions not only for neutron scattering but also for other uses of the facility such as neutrino research and μSR. For this goal a 0.5 mA time average rapid cycling synchrotron with 200 MeV injection energy which could later on be converted into a proton pulse compressor at a much higher injection energy (1100 MeV) and 5 mA time average current was studied by a joint ANL-KFA working group (1983). It was shown that, although at the limit of technical feasibility, such a machine could be built with a reasonable level of confidence but at relatively high cost. However, only a small fraction of the capital investment would be lost, if, in stage II, a high current linac was added and the synchrotron operated in a non - or only slightly - accelerating mode for pulse compression.

Concept 2 was to start with the high current linac from the very beginning but to equip it with the (costly) rf-power generation system only for some intermediate proton energy (350 MeV or above) in stage I. Stage II would then complete the linac for 1100 MeV and add a proton pulse compressor. This concept was studied by a newly established team at KFA Jülich. With respect to the original reference accelerator concept, a number of changes were made to facilitate achieving the above goal by providing added flexibility

and making the design parameters more attractive for the proposed use . **The most important change in this latter respect was the increase of the pulse current from 100 to 200 mA with a simultaneous shortening of the pulse length from 500 to 250 µs.**

A meeting of the SNQ-scientific advisory board was held in February 1983 to discuss the two concepts and to the end the analysis phase of the project by a decision, which way to follow.

Since the scientific merits of both concepts seemed to balance out in stage I, it was decided to go the apparently more direct and probably cheaper way of starting with the high current linac in stage I (concept 2).

2. The neutron source DIANE

With the new linac parameters, the design goals of the SNQ (without pulse compressor) are now as follows:

Accelerator

Time average proton current	5 mA
Pulse current	200 mA
Pulse repetition rate	100 Hz
Pulse duration	250 µs
Final proton energy	1.1 GeV

Target station DIANE

Target material	depleted U
Target coolant	H_2O
Power dissipation in target	10-12 MW
Moderators	H_2O and D_2O
Time average thermal neutron flux in moderators	$1.2 \cdot 10^{15} cm^{-2} s^{-1}$
Peak thermal neutron flux (H_2O-moderator)	$5 \cdot 10^{16} cm^{-2} s^{-1}$

It is planned to operate the target station DIANE of the SNQ as an intensity modulated source with both, high peak and high time average flux, i.e. without poisoning or decoupling the moderator. This philosophy has been discussed at various ICANS-meetings and a summary may be found in a recent paper (Bauer, 1983). Nevertheless, the changes in accelerator concept and the decision to develop a uranium target let us expect considerable improvements in the overall performance of the neutron source.

Relative to the data in the reference study, the goals in neutron flux have changed significantly:
The effective time average flux is up by almost a factor of 2, which results from the use of depleted uranium rather than lead in the target. With respect to the effective peak flux in the pulse, the increase is almost fourfold, resulting from the combined effects of the use of uranium and the shortening of the proton pulse. The effect of the duration of the proton pulse on peak flux and thermal neutron pulse shape is shown in Fig. 1.

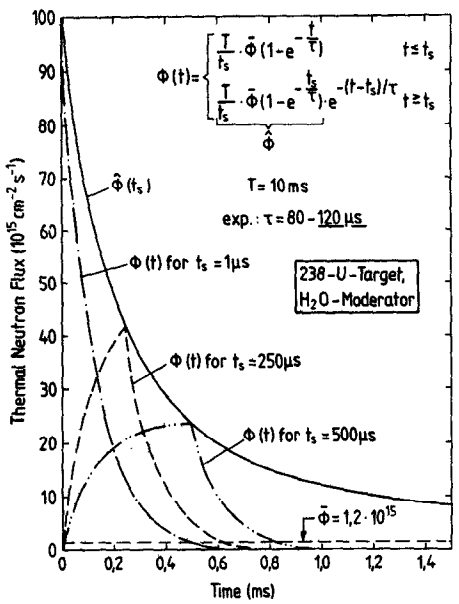

Fig. 1 Dependency of the thermal neutron peak flux in the H_2O-moderator of DIANE on the duration of the source pulse t_s at constant neutron production. Also shown is the shape of the pulses for source pulses of t_s = 1, 250 and 500 µs.

In this figure, one single decay constant τ=120 µs has been assumed as a result of experimental investigations with a fairly realistic mock-up at the SIN cyclotron as reported at the previous ICANS meeting (Bauer et al, 1983a). Earlier estimates had been based on τ=200 µs. No new data for the time constants in the D_2O have been measured. Using the ones reported at ICANS-V (Bauer et al, 1981) for a U-target (τ_1=440 µs, τ_2=5000 µs, Φ_1=97%, Φ_2=3%) we obtain the pulse shape shown in Fig. 2 for the D_2O-case in comparison to the one in the H_2O-moderator.

The peak-to-average flux ratio in the (unperturbed) D_2O-tank follows as 13.3, as compared to 7.9 which was expected for a Pb-target. This is attributed to the strong absorption of thermal neutrons by the large U-target.

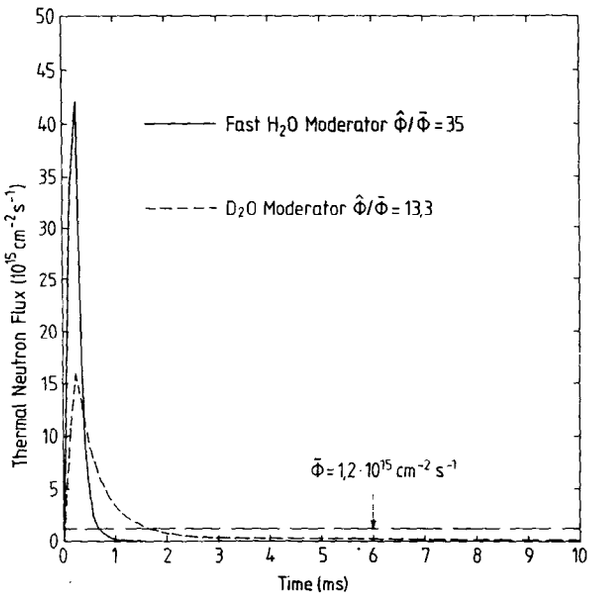

Fig. 2 Expected pulse shapes in the H_2O- and D_2O-moderators of DIANE with U-238 target.

As a result of measurements carried out at the SATURNE-accelerator in Saclay, France, with variable proton energy (Bauer et al, 1983b), we anticipate a 4.25-fold reduction in neutron flux when working with 350 MeV proton energy instead of 1100 MeV, with no changes in pulse shape or peak-to-average ratio.

3. Target related research and development work

Since this topic will be the subject of various presentations at this meeting, only a brief survey shall be given here:

The decisions to (a) start with a proton energy as low as 350 MeV and (b) develop a uranium-target were of considerable impact on the R+D-work related to the target. New calculations on production of radioactivity and heat deposition and on the resulting stress distribution had to be initiated. As will be shown in a separate paper (Filges et al, 1983) the low proton energy produces a strong peak in heat deposition at the end of the proton range. The consequences of the SNQ staging programme on the target design will be discussed by H. Stechemesser (1983). Since there are considerably more radioactive isotopes produced in a U-target than in Pb, handling and safety aspects had to be reconsidered (Thamm, 1983).

The high pulse power in the SNQ proton beam has the inevitable consequence of high heat density and hence a noticeable temperature increase during each pulse in the target. Although the number of cycles per unit time and the resulting mean operating temperature are strongly reduced by the target rotation, the effect of this thermal cycling on the structural integrity of the target material is a matter of concern. W. Lohmann (1983) is going to report on work which we have initiated to obtain more information on this problem and to develop a clad target element which can stand the thermomechanical and radiation load for at least two years of operation.

Another problem to which we devoted considerable theoretical effort was the question of appropriate target shielding and the effect of penetrations through the shield. The implementation of an appropriately coupled code system for this purpose will be discussed by Cloth et al. (1983) in this meeting.

4. The SNQ accelerator

Although a more detailed report on the new SNQ accelerator is given in a later paper at this meeting (Scholten and Zettler, 1983), it shall be described here briefly:

The concept is shown schematically in Fig. 3.

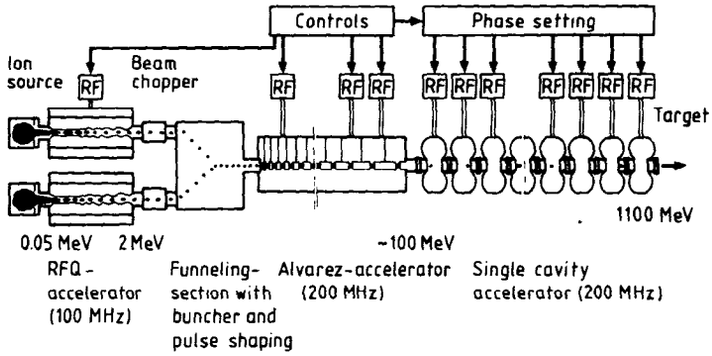

Fig. 3 Schematic illustration of the SNQ rf-accelerator.

Two ion sources operating in parallel with an extraction voltage of 50 keV inject into **two RFQ-structures** which run on 100 MHz rf-frequency with a relative phase shift of 180 degrees and accelerate the beams to an energy of 2 MeV. In a **funneling section** which includes devices for bunching and pulse shaping, the two beams are merged together according to the "zipper principle", which results in a pulse sequence of 200 MHz. This is exactly the frequency on which the subsequent **Alvarez structure** operates, which means

that each of its rf-buckets is filled for optimal accelerating efficiency. At an energy around 100 MeV the Alvarez-structure becomes rather inefficient and a different accelerating structure is used. A **single cavity structure** with a separate rf-amplifier for each cell is under study for the SNQ linac. Some reasons for this choice will be given below. It is intended to install only part of the accelerating structure initially to limit the overall cost until the first neutron producing stage can be reached and to gain experience in operating the facility at reduced power and beam energy. While incorporating essential new parts such as the low energy end and the funneling section, this allows further studies concerning the optimisation of the high energy structure (e.g. superconducting cavities).

The RFQ, which has been selected for the low energy end is generally considered a major improvement in accelerator technology. Since it uses electrostatic rather than magnetic focusing, it can handle beams of very low velocity. Due to a peculiar shaping of the edges of the four vanes which constitute the electric quadrupole, the structure is able to trap slow protons at low velocities with high efficiency, focus the beam, bunch it, and accelerate it to energies much higher than what can be achieved with dc-preacceleration at high currents. Although under development at various laboratories, this structure is still very new and no experience on its reliability and operating performance is yet available.

The funneling section, whose overall length will be about 11 m will contain beam chopping devices and several bunchers and rebunchers to maintain the micropulse structure of the beam over the whole distance. Merging of the two beams is achieved by a series of bending and septum magnets and an rf-deflector. The latter operates at 100 MHz and will give a kick in opposite directions to the microbunches arriving at 180 degrees phase intervals. So far, funneling has not been used on existing accelerators.

Alvarez accelerators of 200 MHz have been operating successfully and reliably at various laboratories over many years now and even pulse currents of 300 mA have been achieved, although for a pulse duration short enough to allow running off the stored energy in the cavities. This will not be possible in the SNQ-Alvarez. This is why well controlled distributed power feeding into the structure during the macropulses will be required, together with the usual measures to achieve a finite group (i.e. energy flow) velocity along the accelerator by two overlapping pass bands.

A single cavity structure with separate rf-feeding into each cell has been chosen for the high energy part of the accelerator for a variety of reasons:

With a coupled cavity structure, the mechanical dimensions of the cavities have to be matched to the velocity of the particles (as in the Alvarez structure). This is because a whole set of cavities is resonating with fixed rf-phase from one common feeder line. As a consequence the energy of the beam is predetermined at each point of the accelerator and no variation is possible (fixed ß-structure; ß is the ratio between the velocity of the particles and the velocity of light). Hence, if at any position the energy gain is significantly less than the design value, the beam will be out of phase with the rf in the rest of the accelerator, which means that operation cannot continue. In contrast to this, with a single cell structure (**variable ß-structure**) the relative rf-phase between cavities is controlled by electronic means and can be changed very rapidly.

With respect to the rf-supply to the accelerating gap, the optimally distributed feeding points with the single cell structure offer the important advantage that no energy flow along the accelerating structure is necessary.

The rf-amplifiers are relatively low-power units but large in number. Thus, if one or a few of them fail, the phase in the following cavities can be readjusted to the new local beam velocity and operation can continue with virtually no interruption. Suitable provisions for automatic exchange of rf-amplifiers with the accelerator in operation will be made. In order to avoid high induced voltage by the beam accross the gap of those cavities, whose rf-feeding has failed, electronic detuning of the cavity is studied. In this way it becomes possible to continue with the operation of the linac even if one or several rf-systems do not work. Rapid exchange of units and off-line repair will contribute to this.

Apart from the prospect for a high availability of the accelerator, the fact that the single cell structure can accelerate the beam with a **variable output energy** constitutes important advantages for the SNQ-accelerator:

- By reducing the voltage accross the accelerator gaps,

more economic operation of the accelerator becomes possible, although at lower output energy. Since the losses in the accelerator are proportional to the square of the electric field whereas the output energy (and the neutron production) depends linearly on it, optimization of the operating parameters is possible. This is of particular interest, if a post-accelerating proton pulse compressor (e.g. an FFAG, see below) becomes available.

- With only part of the accelerating structure installed in stage one (say for a final energy of 350 MeV at 5 mA beam current), it is still possible to produce a higher output energy at a reduced current mainly by readjusting the rf-voltage accross the accelerating gap (increasing the accelerating gradient). Since this means an increase in the losses in the cavities, the current that can be accelerated goes down, as shown in Fig. 4. Of course, as shown by the dashed curve, also the neutron yield in the target will be reduced. Nevertheless, this option is an important feature to study the next step in a staged development program at reduced intensity.

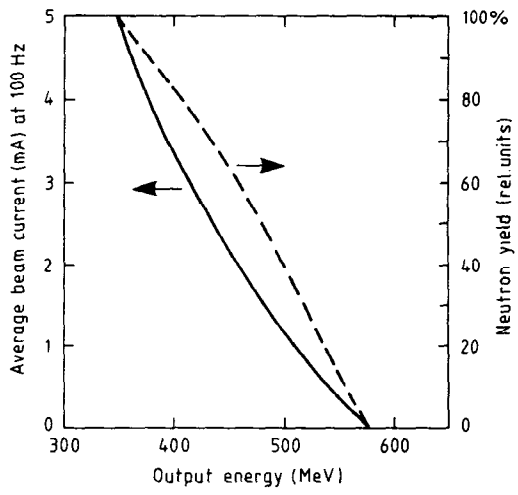

Fig. 4 Dependency of the current, that can be accelerated, on the output energy in stage I of the SNQ-accelerator. The dashed curve shows the resulting decrease of neutron yield in the target.

- Some of the non-neutron users (e.g. nuclear physics experiments, cross section measurements etc.) may want to work with an energy that is variable over a certain range. This is much more difficult with a coupled cavity structure.

- In some cases very short pulses, of the order of individual bunches, are desired for special purposes. Rather than cutting out just one bunch at a time, a method is studied to increase this intensity by time-focussing several of them by letting them pass through some low frequency (e.g. 20 MHz) cavities which are phased in such a way that the first half of the series is decelerated, the other half accelerated in proportion to their distance from the centre of the sequence. After passing a certain drift space (inactive cavities), the microbunches can thus catch up with one another and combine to one short pulse of correspondingly higher intensity, which can be further accelerated in the following cells.

Last not least, the accelerating cavities (and rf-amplifiers) can be manufactured in relatively large series rather than individually as in the case of a fixed β-structure.

Tetrodes are presently considered as the most economic solution for the rf-amplifiers, but their life time is limited and some development in the field of rf-amplifiers is highly desirable. This is also true with respect to power losses, because the largest fractional losses occur in the rf-generation system as can be seen from the diagram of anticipated power flow shown in Fig. 5.

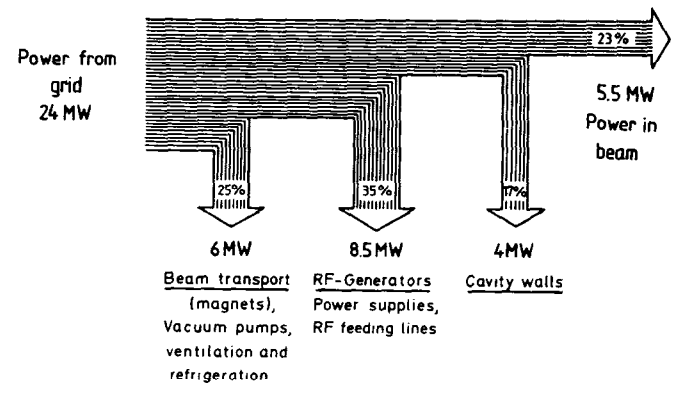

Fig. 5 Approximate energy flow scheme for the SNQ-accelerator.

5. The proton pulse compressor

While the concept of DIANE aimes at improving experimental conditions for all sorts of neutron scattering techniques over those at a high flux reactor, i.e. also for non-time of flight techniques, most other spallation neutron sources have been designed as pulsed sources, utilizing the source pulse as the first reso-

lution element in time-of-flight techniques. This has several attractive advantages, in particular if neutrons in the epithermal energy range are to be used. It is mainly for this reason, that a concept for an isochronouns compressor ring (IKOR) had been worked out in the first SNQ-study. Since the slowing-down time even to energies of several eV is of the order of several microseconds, there seemed to be little incentive to go to much less than one microsecond in the duration of the proton pulses. During the study work it became more and more obvious, however, that other scientific disciplines such as μSR and neutrino physics utilizing the beam stop neutrinos could benefit considerably from even shorter pulses. Therefore the goal was set to 200 ns for the synchrotron - which would act as proton pulse compressor later on - studied by the ANL-KFA working group (1983). This study showed, that such short pulses could probably be produced but would require a compressor ring equipped with an rf-system (which was not the case at IKOR). At a workshop held at KFA in Feb. 83 (Martin and Wüstefeld, 1983) it became obvious that the concept of a fixed field alternating gradient synchrotron which was under study at Argonne National Laboratory had a potential to serve the same purpose at probably lower cost and with added flexibility. For the SNQ-project this scheme looked particularly promising because, by going to a lower accelerating gradient in the SNQ linac, i.e. to an injection energy into the FFAG somewhere between 400 and 600 MeV, the linac can operate much more economically than at the full design gradient of 3 MeV/m. Thus, if the FFAG could be designed to handle more or less the full linac current by choosing a suitable injection energy and using it as a post-accelerator to a final energy which might even be higher than 1.1 GeV, say 1.5 to 1.6 GeV, the system looks very attractive, especially also in view of the rapidly increasing pion (and hence muon and neutrino) production rate at this energy, even if the current is reduced in such a way, that the neutron flux remains constant.

These considerations lead us to form a study group, who, as a first step, examine the possibilty of scaling the ANL - FFAG design to our parameters and determine the conditions, under which such a machine could operate. The results obtained so far seem quite encouraging. However, much more work including nonlinear calculations is needed before a technical design can be tackled.

From Fig. 1 it can be seen that even with very short source pulses, and under the assumption that a U-target can still be used, the thermal neutron peak flux can increase only by about a factor of two relative to the one for a 250 μs-pulse. At the same time it becomes slightly more difficult to phase the choppers needed for time-of-flight experiments. However, since - in contrast to choppers at pulsed sources - these choppers will not serve as time-of-flight monochromators but rather as pulse shapers for a monochromatic beam, the phasing problem is much less serious. Only the intensity of the pulse may vary slightly.

On the other hand it might become desirable to equip the SNQ-facility with a pulsed source at some date. This could either be achieved by building a second target station with poisoned and decoupled moderators or by replacing the DIANE H_2O-moderator by a differently designed one.

6. Near term outlook

With the analysis phase of the project terminated in Feb. 1983 by the decision, which staging concept to follow, the project is now in its system definition phase, in which more detailed studies of system components are carried out and preliminary designs and specifications are developed. An R+D-program is defined and preliminary manufacturing and test requirements are assessed. This phase is due to end in December 1983 at which time a report will be produced, describing a specific concept for further detailed design, preliminary specifications and preliminary schedule, resource- and management-plans. The design phase, during which the project design and specifications including manufacture, test and operating plans have to be established as well as a construction schedule with a detailed work break down structure will essentially end in spring 1985. This date was set by a recent letter from our Minister for Research and Technology which also contained the statement that the SNQ was to be part of the ministry's medium term financial planning. A final decision on the construction of the facility was announced for summer 1985. In preparation of this decision a final project plan which should also contain realistic cost estimates was requested.

References

ANL-KFA Study Group (1983)
"Conceptual Design of a Rapid Cycling Synchrotron for the KFA-Jülich Spallation Neutron Source"
report ANL-83-13, Argonne National Laboratory

Bauer, G.S. (1982)
"The General Concept for a Spallation Neutron Source in the Federal Republic of Germany"
Atomkernenergie/Kerntechnik 41 (1982), p. 234-242

Bauer, G.S. (1983)
"DIANE - A Project for a New High Performance Neutron Source in the Federal Republic of Germany"
Proc. IV Int. School on Neutron Physics, Joint Institute for Nuclear Research, Dubna 1982, D3,4-82-704
and unpublished report SNQ ØY/CV 24 08 83, KFA Jülich (revised version)

Bauer, G.S.; Conrad, H.M.; Grünhagen, K.; Spitzer, H.; Gompf, F.; Reichardt, W. and Fischer, W.E. (1983a)
"Time-Structure of Thermal Neutron Leakage from fast and slow Moderators for Spallation Neutron Sources"
Proc. ICANS-VI, report ANL-82-80, Argonne National Laboratory

Bauer, G.S.; Conrad, H.M.; Grünhagen, K.; Spitzer, H. and Milleret, G. (1983b)
"How much Thermal Neutron Flux is Gained Using; Deuterons instead of Protons?"
Proc. ICANS-VI, report ANL-82-80, Argonne National Laboratory

Bauer, G.S.; Fischer, W.E.; Gompf, F.; Küchle, M.; Reichardt, W. and Spitzer, H. (1981)
"Thermal Neutron Leakage and Time Structure Measured for Various Target-Moderator-Reflector Configurations for a Spallation Neutron Source"
Proc. ICANS-V, Jül-Conf-45, G.S. Bauer and D. Filges, eds., Kernforschungsanlage Jülich

Bauer, G.S.; Sebening, H.; Vetter, J.-E. and Willax, H. (eds.) (1981)
"Realisierungsstudie zur Spallations-Neutronenquelle, part I"
report Jül-Spez-113/KfK 3175, Jülich and Karlsruhe

Bauer, G.S. and Vetter, J.-E. (1983)
"The FRG-Project for a High-Power Spallation Neutron Source for Fundamental Research"
in "Nuclear Technologies in a Sustainable Energy System", G.S. Bauer and A. McDonald eds., IIASA - Springer, Berlin 1983

Cloth, P.; Armstrong, T.; Filges, D. and Schaal, H. (1983)
"Calculational Methods and High Energy Cross Sections for Spallation Source Shielding"
Proc. ICANS-VII, this volume

Filges, D.; Cloth, P.; Neef, R. and Schaal, H. (1983)
"Recent Target Design Calculations at KFA"
Proc. ICANS-VII, this volume

Lohmann, W. and Krautwasser, P. (1983)
"Progress in Materials Investigation for the SNQ-Target"
Proc. ICANS-VII, this volume

Martin, S. and Wüstefeld, G. (eds.)
"Informal Collection of Talks Held in the Seminar on FFAG"
unpublished report SNQ 2 MZ/BS 001

Schaffer, G. (ed.) (1981)
"IKOR - An Isochronous Pulse Compressor Ring for Proton Beams"
report Jül-Spez-114, KFA Jülich

Schelten, J. and Zettler, C.
"Present Design of the Linac of the SNQ-Project"
Proc. ICANS-VII, this volume

Stechemesser, H. and Thamm, G. (1983)
"Target Design for Stepwise Development of the SNQ"
Proc. ICANS-VII, this volume

Thamm, G.; Buttgereit, H.; Stechemesser, H. and Wolters, J. (1983)
"Operational, Handling and Safetly Aspects of the SNQ-Target Station"
Proc. ICANS-VII, this volume

Vetter, J.-E. (ed.) (1981)
"The Basic Concept of the SNQ Linear Accelerator"
report KfK 3180 B

Proceedings of International Collaboration on Advanced Neutron Sources (ICANS-VII), 1983 September 13-16
Atomic Energy of Canada Limited, Report AECL-8488

STATUS REPORT ON THE WNR/PSR PULSED SPALLATION NEUTRON SOURCE AT THE LOS ALAMOS NATIONAL LABORATORY

Charles D. Bowman
Los Alamos National Laboratory
P.O. Box 1663
Los Alamos, NM 87545

INTRODUCTION

The Los Alamos National Laboratory is constructing a high intensity spallation pulsed neutron source for neutron scattering and nuclear physics research. The facility will accept beam from the Clinton P. Anderson Meson Physics Facility (LAMPF) and accumulate it in the Proton Storage Ring (PSR) now under construction. The proton beam will then be ejected in intense bursts and transported to a neutron-production target that will be an upgrade of the existing Weapons Neutron Research (WNR) target. The initial design objective for 1986 is an average neutron production rate of 1.2×10^{16} n/s over 4π with a pulse rate of 12 pps.

Fig. 1 is our most recent drawing of the WNR/PSR facility. The principal elements for the future are identified as the beam transport channel from LAMPF(6), the Proton Storage Ring(3), and the WNR target area(1). Major changes in the facility are planned that will significantly change the appearance of the facility around the target. These are described in this report.

A neutron scattering research program was begun at the WNR in 1982 at an average source intensity of 3×10^{14} n/s. Research at the WNR will continue throughout the construction period with primary emphasis on developing new fields of research that can be studied with intense pulsed neutron sources and on construction of the new class of spectrometers required for pulsed neutron scattering research. We believe that all elements necessary to complete a world class center for pulsed neutron scattering will be in place in 1986; an unsurpassed proton source, an optimally designed neutron-producing target, new space for accommodating experiments, and an array of new spectrometers specially designed for pulsed neutron scattering research. Planning is underway for neutron intensity enhancement by as much as a factor of 10 beyond the 1986 objective.

FACILITY STATUS

The WNR facility has operated well over the past year for both neutron scattering and nuclear physics experiments. About 60% of the beam time has been devoted to the 5-μsec long pulse for the neutron scattering and about 40% to the 0.2 ns microstructure mode for nuclear physics. A summary of the operation for the most recent running period is given in Table I. During this period, the WNR operation was restricted to nights and weekends because of the construction of

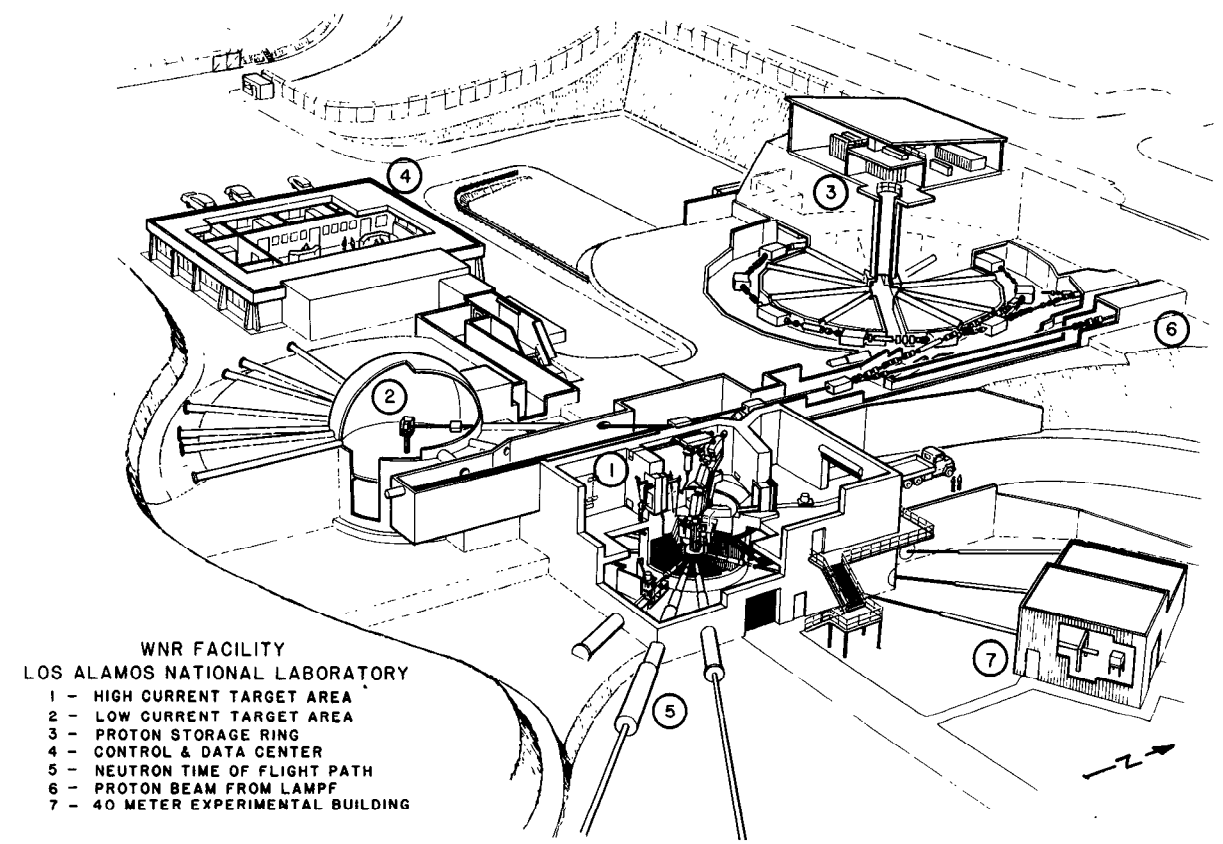

Fig. 1 Overview of the WNR/PSR Facility. With the completion of the PSR building (3), the facility presently appears very much as it is now. Major additions to the experimental area will significantly transform the appearance outside of the WNR target area (1).

Table I WNR 1982-83 Operating Summary*
(May 82-February 83)

Scheduled Operating Time	3066 Hours
Beam Available from LAMPF	2778 Hours
Beam Available for WNR Experiments	2696 Hours
Overall Availability	88%
WNR Efficiency	97%

* Daytime/Weekend-only operation due to PSR construction.

the building to house the PSR. Clearly the multiplexed magnet system, the WNR beam transport, and the target are operating excellently with only 3% down time. The construction of the building to house the PSR will be finished ahead of schedule. We received beneficial occupancy of the magnet ring hall in August.

The experimental program has been going well. Several new spectrometers operated very effectively resulting in a major improvement in research productivity. Presently operating spectrometers include a single crystal diffractometer, a constant-Q spectrometer, a beryllium difference spectrometer and an eV inelastic scattering spectrometer, the latter in collaboration with the SNS laboratory. A general purpose powder diffractometer will be brought on line in 1984.

We have begun a formal user program this year starting with two instruments--the beryllium difference spectrometer and the single crystal diffractometer. The number of instruments in the program will be increased each year. At the end of 1986, ten spectrometers should be operational and 2/3 of the neutron scattering research time will be available to outside users. Any user is eligible to apply for research time on these spectrometers. Proposals should be sent to Dr. Richard N. Silver of this laboratory. These proposals are then forwarded with comments to a joint review committee of the Los Alamos and Argonne National Laboratories, which allocates the spectrometer time among the most promising experiments. For the first running period at the WNR for the experimental program this fall, 24 proposals were received for the two spectrometers and experiental time was made available for 18 of these.

FACILITY UPGRADE PROGRAM FOR NEUTRON SCATTERING

Many changes now underway will contribute to the development of the WNR facility into an international center for neutron scattering research. These include the construction of the Proton Storage Ring, the upgrade of the target/moderator system for intense proton current and optimal neutron spectrum for several classes of experiments, a major expansion of the experimental area to allow comfortable placement of at least 15 spectrometers, a computer development program that will provide each spectrometer with a dedicated data collection system, and a formal plan for developing the spectrometer array. Each of these efforts is discussed separately below.

Proton Storage Ring

The Proton Storage Ring will enormously increase the power of the facility for both the neutron scattering and nuclear physics programs. A comparison of the two capabilities is given in Table II. Note that the pulse width will be shortened by a factor of 20 and that the intensity per burst for neutron scattering experiments will be increased by a factor of about 300. As mentioned earlier construction of the PSR is on schedule, and details are presented in a later talk in the conference by G. P. Lawrence[1]. An output current level in the long pulse mode of 20 μa is expected to be achieved at 12 pps by the fall of 1985. The full 100 μa intensity is expected in 1986 along with substantial current in 1986 in the one nanosecond mode. By 1987 full operation in both modes is expected, and work will begin on several PSR upgrade possibilities.

Additional Experimental Space

The present experimental space at the WNR is totally inadequate for the outstanding source intensity that will be available with the PSR. A plan has been proposed for an increase in space by a factor of five in order to provide ample area for a full array of spectrometers, staging area as part of the experimental floor area, quiet rooms adjacent to the floor for assessment of progress on experiments, and space for data collection systems. In all other spallation sources the beam strikes the target in a horizontal direction with limitations in spectrometer floor space associated with beam transport to the target and with target servicing facilities. It is important in our planning to take advantage of our full circle of spectrometer locations made possible by the vertically directed proton beam. Also the arrangement should allow for a number of long (∿ 200 M) drift tubes for neutron nuclear physics.

The arrangement of the area is shown in Fig. 2. The existing experimental hall will remain essentially as is except for some outfitting that will provide a better environment for experiments. Two large halls are shown on the east and west side of the present experimental area. Each hall is spanned by a 10-ton overhead crane. Space is set aside in each hall for staging area. Support space is also provided adjacent to the experiental floor. An access channel from the northeast is provided so that a forklift can be operated on the existing experimental hall floor in

Table II WNR/PSR Performance Characteristics

	WNR		PSR	
	Neutron Scattering	Nuclear Physics	Neutron Scattering	Nuclear Physics
Proton Energy (MeV)	800	800	800	800
Pulse Width (nsec)	5000	0.2	270	1
Rep Rate (pps)	120	6000	12	720
Average Current (μamps)	3	0.2	100	12
Average Neutron Rate (n/s)	4×10^{14}	1.3×10^{13}	1.2×10^{16}	1.5×10^{15}

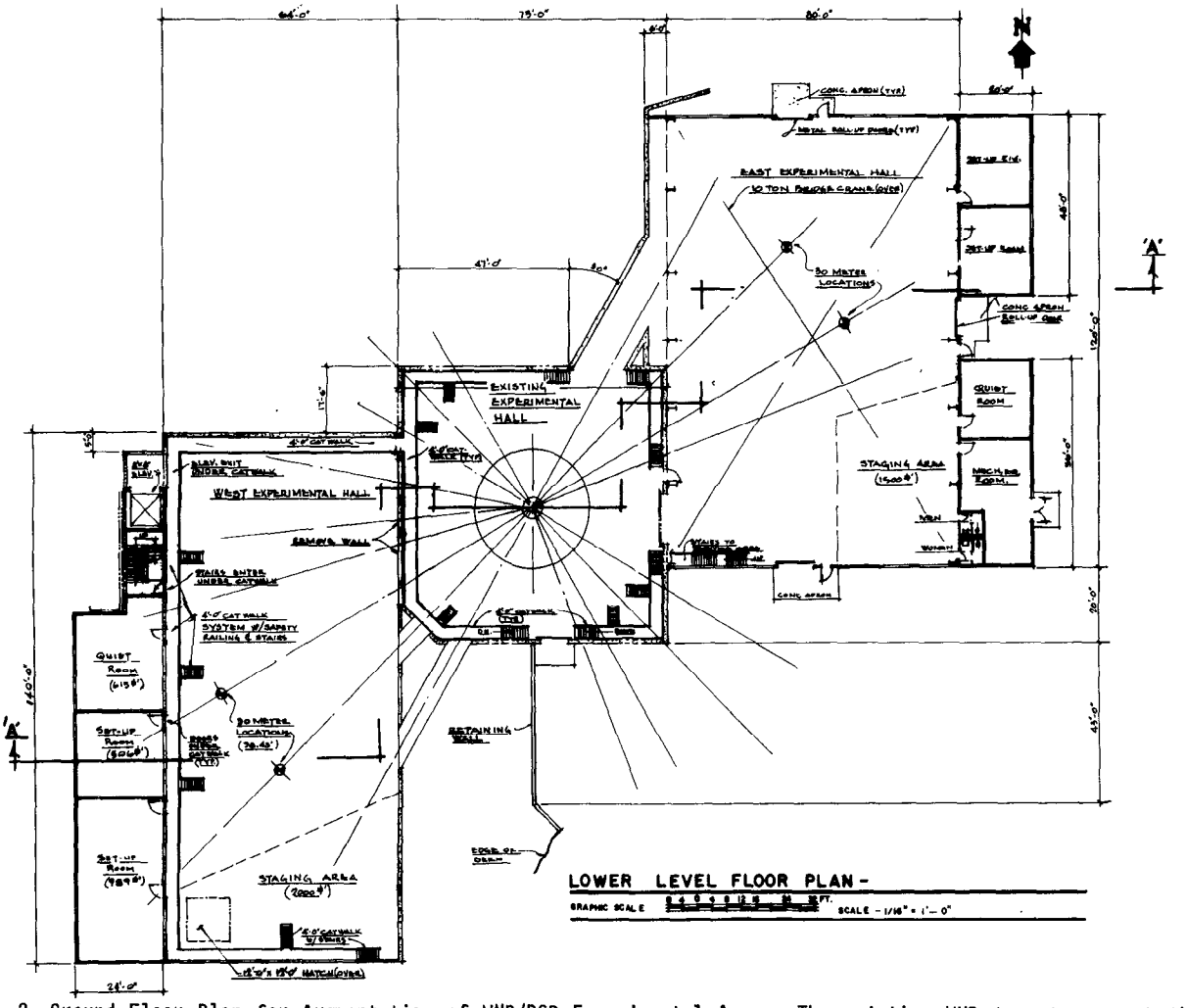

Fig. 2 Ground Floor Plan for Augmentation of WNR/PSR Experimental Area. The existing WNR target area at the center of the figure will be expanded with the addition of two large halls. New drift tubes to be drilled will increase the total for neutron scattering to 15. The four drift tubes in the southeast quadrant will be used for neutron nuclear physics research.

the north, east, and south sectors. Generally the experiments requiring the highest neutron intensity will be located in the northwest quadrant of the existing experimental hall, and the higher resolution systems and more bulky experiments in the two outer halls. Note that the low current target area identified as (2) in Fig. 1, where we now conduct moderator studies, etc., will be replaced by the west hall.

Fig. 2 shows 19 drift tubes, which are required to fully use the present and proposed experimental space. However, the biological shield was originally constructed with only 12 drift tubes. It will be necessary therefore to drill several new drift tubes through the 15-ft thick 80% iron-20% concrete shield. A new drift tube was drilled this past year to demonstrate that installing new drift tubes is practical. The four drift tubes pointing in the southeasterly direction will be devoted to long flight path nuclear physics experiments. This leaves 15 flight paths for neutron scattering research. Taking into account the possibility of two spectrometers on some of the beam lines, it is expected that space will be available for 20 or more spectrometers.

Target, Moderators, and Shielding

The intense PSR beam currents will require a complete redesign of our present target-moderator system. We must accommodate the needs of nuclear physics for 0.25 to 10,000 eV neutrons, cold moderators for both neutron scattering and nuclear physics, and tailored moderators for particular neutron scattering spectrometers. A large variety of moderators is therefore required. A target-moderator geometry under consideration now is shown in Fig. 3.

A key element of this concept is a split target arranged so that equal neutron intensity is produced in the upper and lower segment and a relatively large volume of uniform flux density is created that is relatively free of target cooling paraphenalia. Several moderator types therefore can be placed in this region to service different spectrometers. Isolation from background associated with high energy neutrons should also be optimized in this geometry. A through-tube geometry is possible, which might be valuable for some experiments. It also will be possible to use wing geometry if additional moderator types are required.

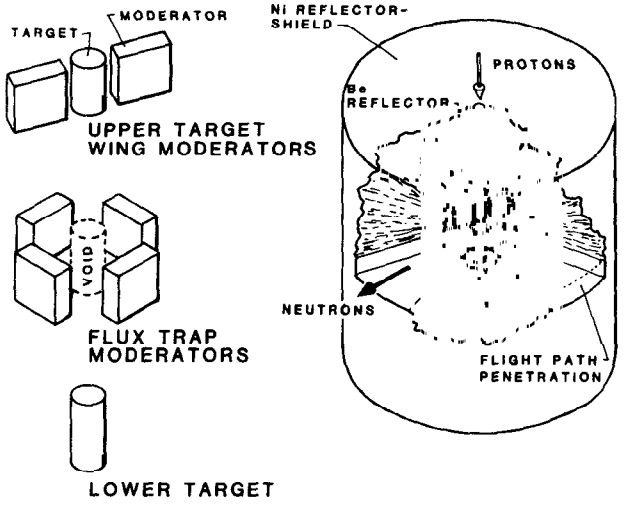

Fig. 3 Prospective WNR Target-Moderator-Reflector Assembly. The target consists of a split target surrounded by an inner Be reflector and an outer Ni reflector. The beam enters from the top. The facility can accommodate several moderators and also a through-tube flight path geometry.

The inner region of the target assembly is surrounded by a Be reflector that in turn is surrounded by a Ni annular cylinder serving as a second neutron reflector and as additional biological shielding. The complete assembly is about one meter in diameter and one meter high. We have addressed the question of broadening of the neutron pulse by the reflector. Calculations by Russell[2] show that the neutron pulse is not broadened by the reflector beyond the 270 ns width of the proton pulse from the PSR except at lower energies where moderation time in hydrogen dominates.

The clear separation between the moderator and the neutron producing target is expected to be beneficial if the facility intensity is upgraded via additional beam current, by emphasizing a ^{238}U target, or by means of a fission booster. For a possible future fission booster the reflector also could serve as a large heat sink for afterheat in case the target cooling system malfunctions. In summary this geometry allows 360° access to moderators, separates moderator and target cooling apparatus, reduces streaming of high energy background-producing neutrons down the drift tubes, creates a region of uniform flux for placement of moderators, and substantially increases the effectiveness of the biological shield. The target-moderator system is discussed in greater detail in another contribution to this meeting by Russell[2].

Spectrometer and Data Collection Development

Neutron scattering research began in 1982 with several exploratory spectrometers that performed successfully. Two of these, the filter difference spectrometer and the single crystal diffractometer were brought into operation in 1983 as fully engineered spectrometers. Adequate resources are expected to allow two additional fully engineered spectrometers to be brought on line in 1984 and 1985 and perhaps three or four in 1986. Therefore at the close of 1986 ten fully engineered spectrometers are expected to be operational. Approximately one spectrometer per year will be added after 1986. User input on the priority of instrument construction and user participation in spectrometer design and construction will be solicited for spectrometers to be installed after 1984.

The high average neutron intensity of the WNR/PSR and the low 12-hertz repetition rate will require the handling of very high instantaneous data rates from the spectrometers. A computer system to handle these rates is under construction. The system provides a data collection computer for each spectrometer and a central computer at the WNR/PSR for data reduction and analysis. A coaxial cable link to the Los Alamos National Laboratory central computing facilities was completed in 1983 that will make accessible to WNR/PSR scientists and users world forefront space in data processing and the most advanced data storage facilities.

In summary, a fully equipped world class neutron scattering facility should be operational in 1986 with 100 μa of 800-MeV average proton current at a repetition rate of 12 pps. Ten fully engineered spectrometers with a separate data collection computer for each should be operational in the newly completed and greatly enlarged experimental space. At least three separate moderators should be operational each optimized for different neutron spectral capabilities. A ^{238}U target probably also will be operational at that time. The WNR will be conducting a full experimental program throughout the '83 to '86 construction period including an active user program.

OTHER PSR-RELATED PROGRAMS

The PSR is being constructed with components that should allow rapid upgrading to 200 μa at 24 hertz; with redesign of several of the critical power components it is hoped that 400 μa will be achievable at 48 hertz. The PSR will also produce 1-nanosecond bursts at the rate of 720 hertz and at an average current of 12 μa. This latter capability is particularly powerful for MeV neutron time-of-flight experiments. Initially the PSR will run in either the long pulse or short pulse mode, but upgrading to allow multiplexing of the two modes is under consideration. The PSR has very attractive capabilities for a broad spectrum of experiments and it will be used for experiments other than neutron scattering although neutron scattering will carry the highest priority. Presently the most prominently discussed additional programs include neutron nuclear physics, neutrino research, and muon condensed matter and nuclear physics research. Such programs for spallation sources are reviewed in detail in a paper by Dombeck[3] submitted to this meeting. A brief summary of plans for the WNR/PSR is given here.

Neutron Nuclear Physics

The WNR/PSR will provide outstanding characteristics for neutron nuclear physics studies from the ultra-cold neutron energy range up to 250 MeV. This is well illustrated in Figs. 4 and 5 prepared by Auchampaugh[4] where the average neutron flux on a sample is shown as a function of neutron energy. The optimum flight path has been chosen to allow a resolution of approximately 0.1%. The pairs of numbers in parenthesis are the repetition rate and the flight path respectively. The numbers in parenthesis after the facility acronym are the pulse width. The curves for WNR show the capability with and without the PSR. The facilities referred to by acronyms are located as follows: ORELA (ORNL), Gelina (CBNM), KFK (Karlsruhe), and HELIOS (Harwell).

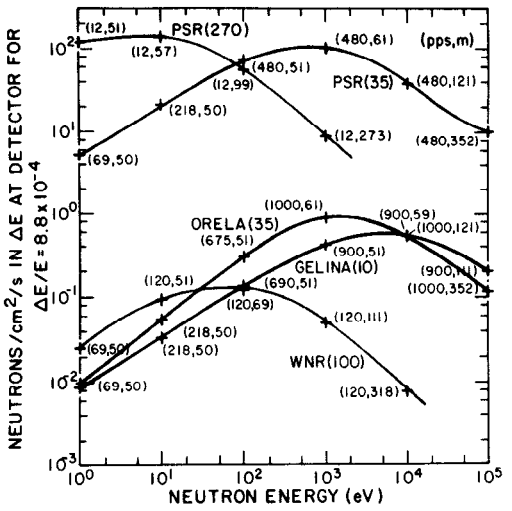

Fig. 4 Comparison of Neutron Facilities for the Low Energy Region. The two quantities in parenthesis represent pulse rate and flight path to achieve maximum neutron flux in the energy internal ΔE for the given resolution. The quantity in parenthesis by the facility name represents pulse width in nanoseconds. There are presently no plans for operating the PSR in the 35 nanosecond mode.

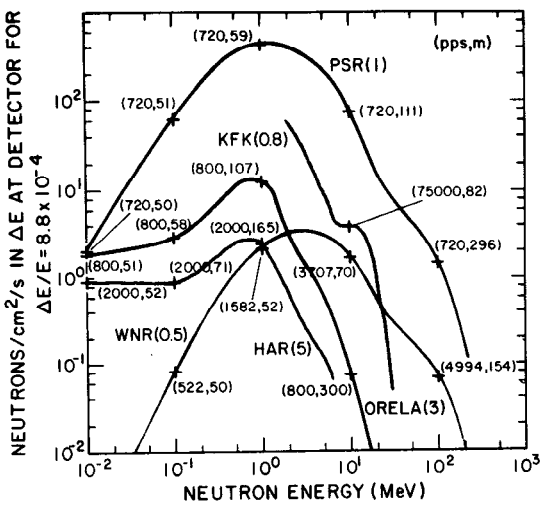

Fig. 5 Comparison of Neutron Facilities for the High Energy Region presented as in Fig. 4.

Note the enormous gain of the WNR/PSR over the WNR and the performance of the WNR/PSR relative to facilites elsewhere. Its greatest potential relative to other sources is for experiments above and below the 10-1000 keV range. At the lowest end of the range the combination of a cold moderator and a mechanical doppler system for neutron velocity reduction into the ultra-cold range (about 7 m/s) will allow collection of densities of ultra-cold neutrons that might reach 250/cm^3. A collaboration between Los Alamos National Laboratory and Argonne National Laboratory is underway to develop this for possible use in a high sensitivity attempt at measurement of a neutron electric dipole moment.

Neutron nuclear physics in the region below 1 keV has been relatively inactive in the recent years, but the factor of 1000 advantage made possible by the PSR should be a strong stimulus to this field. Studies such as doppler-free resonance neutron spectrocopy, resonance total reflection, studies with polarized beams, etc., which have not been performed thus far, should be possible. There is much in this energy range of interest at the interface of nuclear and condensed matter physics, and these two fields might well mesh here with mutual benefits to both. Since the WNR/PSR will operate 80% of the time in the long pulse mode, which is suitable for eV neutron nuclear physics, an aggressive program in this field would be possible.

For the MeV region, the WNR/PSR will be operated in the short pulse mode for approximately 20% of the time. Although this fraction is small, the very high intensity can be used to pursue experiments that cannot be done now, or experiments can be done in less time with associated increases in productivity. Experiments now underway at the WNR in fission fragment angular distribution studies and neutron-induced γ-ray emission will be greatly improved. Nuclear data measurements, particularly those of interest to the fusion programs, will be greatly facilitated by the enhanced intensity. Depending on the degree of future program development in MeV neutron nuclear physics studies, it might be appropriate to provide another target cell downstream from the PSR and WNR where such measurements could be pursued 100% of the time. Preliminary studies indicate that it should be possible to multiplex the short and long pulse modes of the PSR so that both classes or experiments could run simultaneously with separate targets.

Neutrino Physics

The attractiveness of neutrino physics using the intense proton pulses and associated low duty cycle of the PSR has been well documented[5], and facilities for a neutrino physics program are under development that would eventually use PSR beam. A neutrino experiment is being constructed at the end of the long channel that transports beam between LAMPF and the WNR. An additional beam transport line is being built into this channel that will allow LAMPF beam to be multiplexed past the PSR and the WNR and onto a target for production of muon neutrinos. The first experiments are planned for 1984. An extensive neutrino research program can be pursued for several years with the LAMPF beam while the PSR is brought on line and upgraded.

After meeting the first PSR design objectives of 100 μa in the long pulse and 12 μa in the short pulse, the long pulse capability will next be upgraded to 200 μa at which point 100 μa of beam would become available for neutrino research. Further increases in PSR current to as much as 400 μa would be allocated either to neutron scattering, to neutrino physics, or to both in accordance with relative priorities and support levels.

Muon Physics

The facilities for production of muon neutrinos for neutrino research naturally produce copious intensities of pulsed muons. A low duty cycle high intensity source of muons is highly attractive for use in condensed matter, atomic physics, and nuclear physics research. Studies by Heffner[6] indicate that muons can be collected and transported effectively from the same target used for muon neutrino production so that studies using both neutrinos and muons can be conducted simultaneously. It also appears that muon research and neutron nuclear physics research could

share the same target provided that a separate target cell for this purpose were available downstream from the WNR/PSR.

SUMMARY

Much progress has been made in WNR/PSR facility development and in planning and implementing a full research program since the last ICANS meeting. Construction of the PSR continues on schedule, a significant neutron scattering research program is under way at the WNR that can continue through the construction period, and a formal neutron scattering user program was begun this year. The problem of bothersome backgrounds at the WNR has been solved, and a versatile and effective target-moderator design has been developed. Plans are being implemented for spectrometer construction, data collection and analyses facilities, and a major augmentation in experimental space.

Other areas of research besides neutron scattering made possible by the PSR have been thoroughly examined for the purpose of strengthening the Los Alamos National Laboratory research base. Promising programs include neutron nuclear physics, neutron nuclear data, neutrino physics, and muon nuclear and condensed matter physics. It also can provide forefront capability for several branches of nuclear physics research. Development of the PSR research facilities in these directions will be pursued, with highest priority continuing for neutron scattering research.

REFERENCES

1. G. P. Lawrence, Los Alamos Proton Storage Ring, ICANS VII Proceedings, Chalk River Nuclear Laboratories, Chalk River, Ontario, Canada (1983).

2. G. J. Russell, "WNR Targets and Moderators," Ibid.

3. T. W. Dombeck, "Nuclear and Particle Physics with High Intensity Pulsed Neutron Sources," Ibid.

4. G. F. Auchampaugh, Reproduced from the paper: "Status and Comparison of New, Planned, and Upgraded Pulsed White Neutron Source Facilities Since 1970," Nuclear Cross Sections for Technology, NBS Special Publication 594, pp. 920-928 (1980).

5. G. J. Stephenson, Jr., "A National Facility to Provide a High Intensity Neutrino Source," Los Alamos National Laboratory, Los Alamos, New Mexico (1982).

6. R. H. Heffner, "Proceedings of a Workshop on Muon Science and Facilities at Los Alamos," Report LA-9582-C, Los Alamos, New Mexico, March 15-18, 1982.

Proceedings of International Collaboration on Advanced Neutron Sources (ICANS-VII), 1983 September 13-16
Atomic Energy of Canada Limited, Report AECL-8488

PRESENT STATUS OF BOOSTER SYNCHROTRON UTILIZATION FACILITY AT KEK

H. Sasaki

National Laboratory for High Energy Physics
Oho-machi, Tsukuba-gun, Ibaraki, 305, Japan

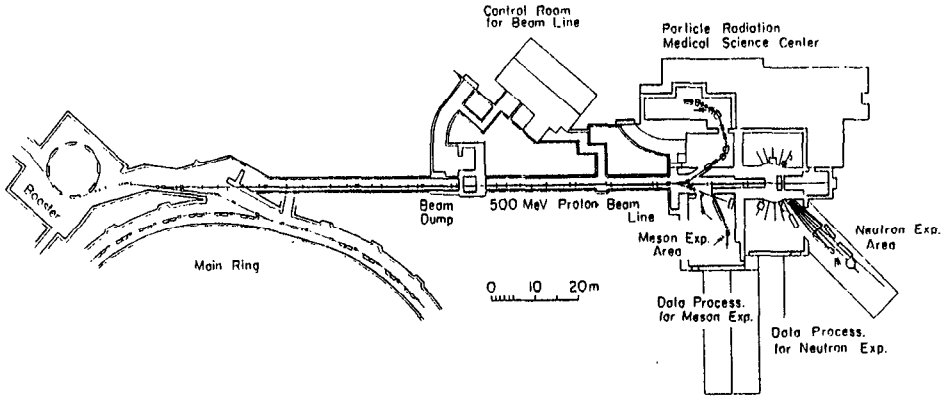

Fig. 1 Layout of Booster Synchrotron Utilization Facility

Introduction

Booster Synchrotron Utilizaton Facility BSF at KEK was established in 1978 in order to organize a neutron scattering experimental facility KENS, a pulsed muon facility BOOM and a biomedical facility PARMS. Those facilities utilize the proton beam from the 500 MeV booster for 12 GeV Proton Synchrotron. The neutron scattering experimental facility and the pulsed muon facility came into operation in the early summer of 1980, and the biomedical facility in June 1982. Figure 1 shows the layout of BSF at KEK. The 20 Hz booster synchrotron delivers about 40 beam pulses to BSF every 2.5 sec at an average beam intensity of 5 to 6 x 10^{11} protons/pulse as shown in Fig. 2. BSF has been operated for a total of 8,950 hrs and at an operating efficiency of more than 90 % since June 1980, as shown in Table 1. Most of the beam time in BSF is shared equally by the neutron scattering experiment and the pulsed muon experiment. For instance, the neutron scattering experimental facility KENS has been operated for a beam time of 1,509 hrs in the fiscal year 1982. Shortage of the beam time for the physics research program becomes more serious because BSF has started to deliver proton beams to the new biomedical facility in addition to a steady increase of the number of users in the physics research program.

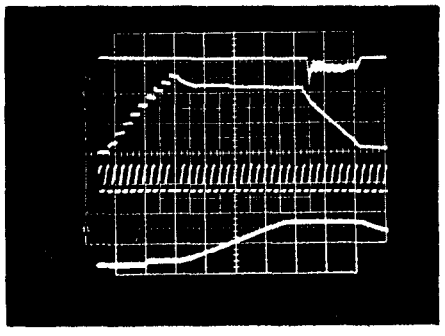

Fig. 2 Extracted 12 GeV proton beam, circulating proton beam in 12 GeV main ring synchrotron, circulating beam current in 500 MeV booster, and magnetic field of main ring synchrotron. (from upper to lower) 200 ms/div.

Table 1 BSF Operation Summary

Fiscal Year (April-March)	Accelerator Operating Time (hr)	BSF Total Operating Time (hr)	BSF Operation Efficiency (%)	Beam Time for Neutron Experiment (hr)
1980	3.533	1.628	89.9	926
1981	3.258	2.883	93.0	1,422
1982	3,652	3,219	95.0	1,509
~July 1983	1,432	1,218	95.0	516
Total	11,875	8,948	93.4	4,373

Accelerator System

Present Status

A 100 mA, 5 μsec wide proton beam is fed into the booster synchrotron from a 20 MeV injector linac at the repetition rate of 20 Hz. Figures 3(a) and (b) show the circulating proton beam at around injection and during the acceleration, respectively. In usual, the beam transmission in the booster synchrotron is some 25 %. The stability of the output beam intensity is quite satisfactory as shown in Fig. 4.

Since 1980, the booster synchrotron began to deliver the beam to BSF as well as the 12 GeV main ring synchrotron with its full capacity. Recently, therefore, the residual radioactivities at off-time of the accelerator became more serious problem to maintenance and improving works. On the other hand, there are no indications of the increase of failure hours due to the full operation of the booster synchrotron as shown in Table 2.

Conversion of Injection Scheme in Booster

The physics research programs in BSF as well as those of high energy physics in KEK demand more beam. A scheme of H^- charge-exchange injection has been considered as a powerful candidate to meet such demands. The conversion from the present multi-turn injection of proton beam to the charge-exchange injection makes possible to not only increase the

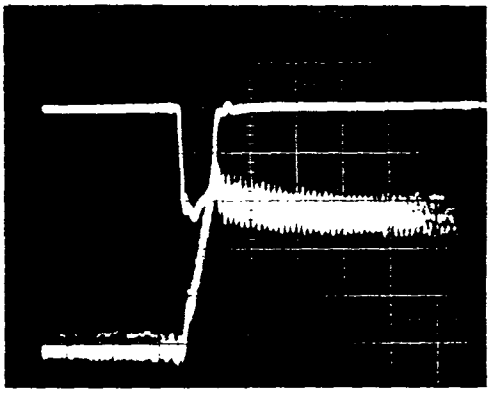

(a) 5 μsec/div.

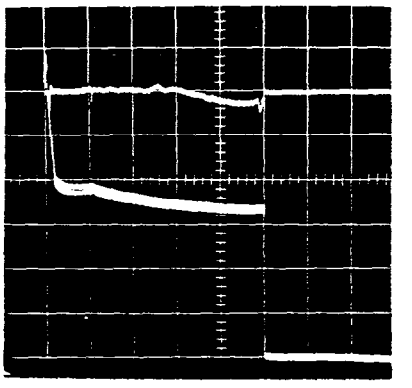

(b) 5 msec/div.

Fig. 3 (a) Injected Linac Beam: 50 mA/div.
Circulating Beam in Booster: 125 mA/div.
(b) Radial Position of Circulating Beam.
Circulating Proton Beam: 2×10^{11} protons/div.

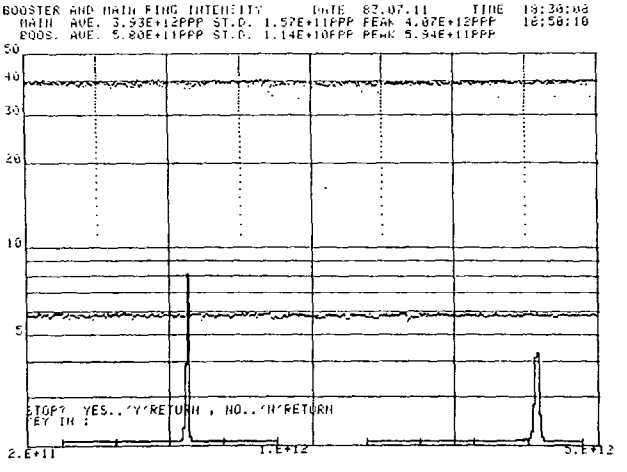

Fig. 4 Beam Intensity Fluctuation of Booster and Main Ring Synchrotron

Table 2 Failure Time of Accelerator Component (hrs)

Fiscal Year	Pre-Injector	20 MeV Linac	20 MeV Beam Line	Booster Magnet	Booster RF	Extraction & 500 MeV Beam Line
1979	14.2	23.4	17.2	4.7	17.7	41.5
1980	9.2	24.5	1.6	14.5	9.2	10.8
1981	23.1	26.8	2.1	7.9	2.0	15.2
1982	9.1	26.3	26.8	7.1	3.2	28.4

intensity of the proton beam but also to reduce considerably beam loss in the booster. In addition, an appreciable polarized proton beam would be accelerated in the synchrotron by such an injection scheme. The conversion program to the scheme of the charge-exchange injection started on 1979 together with a project of acceleration of polarized proton beam in KEK PS.

Arrangement of the H^- ion beam injection system is shown in Fig. 5. Four orbit bump magnets, each of which is 340 mm long with a useful aperture of 160 mm(H) x 40 mm(V), are excited to 0.24 T by a 7 kA, 100 μsec current pulse. Carbon foils of 30, 50 and 120 μg/cm^2 in thickness will be available for the charge stripper. Including a spare-foil mounting device with housing capacity of 40 foils, almost components of the injection system have been completed and are ready for installation.

Development of the H^- ion source started with the construction of a magnetron-type surface plasma ion source[1]. Under suitable operating conditions, more than 30 mA H^- ion beam was obtained[2]. However, it became clear that there were some technical problems on the life time of the ion source itself, stablility and control of ion beam in the source, etc. Therefore, conversion to another type of ion source has been considered. At present, a prototype of cusp or bucket H^- ion source[3] is under construction. In this type of the ion source, converter is separated from the cathode and those can be controlled independently.

The second RF cavity was introduced into the booster ring and has been examined. The RF system together with both of cavities has become more stable and reliable in its operation. This will be a powerful means of compensation for the beam loading due to the expected increased beam current in the charge-exchange injection.

Charge-exchange injection will be tested with polarized H^- and unpolarized H^- ions in this October.

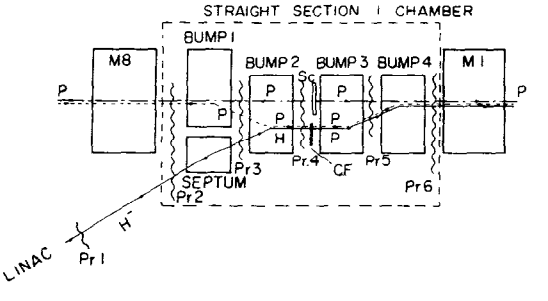

Fig. 5 Charge-exchange Injection System of Booster
H^-: Injected H^- ions.
P: Circulating proton beam.
BUMP 1 ∿ 4: Orbit bump magnet.
Pr 1 ∿ 6: Multi-wire profile monitor.
CF: Carbon foil charge stripper.
Sc: Beam scraper.

Extension of Injector Linac[4)]

If the energy of the present 20 MeV injector linac is doubled, the beam intensity of the booster synchrotron will be considerably increased in connection with the adoption of charge-exchange injection. Next year, 1984, construction of the large tunnel for an electron-positron colliding storage ring, TRISTAN, and hence shut-down of the 12 GeV proton synchrotron is scheduled. It is under planning to upgrade the linac energy in this term.

While the space for the second linac tank will be available in the present beam line to the booster without difficulty, there is no room for new high power RF source. In the present 20 MeV linac, the operating beam current is 150 mA and its beam power is 3 MW. As the excitation power of the tank is about 1 MW, the total power of 4 MW is shared by two TH516 amplifier tubes. If 30 mA H^- ion beam is assumed to be accelerated to 40 MeV, the total power including the excitation power of the tanks is 3.2 MW, which is less than that of the present operating mode with proton beam. The present two feed system for RF power, will be also adopted in the second tank. This has not only good RF characteristics for beam loading compensation but also a practical advantage. Even if one of the TH516 amplifier system is completely down, the linac will be able to run with a lower beam current.

Prameters of the second tank for the 40 MeV linac is listed in Table 3.

Table 3 Main Parameters of the Second Tank for 40 MeV Linac

Energy	20.40 - 40.48 MeV
Frequency	201.070 MHz
$\beta\lambda$	0.3060 - 0.4244 m
$\beta^2\gamma^3$	0.04491 - 0.09195
Tank Steel, copper plated	
Length	12.82 m
Inside diameter	0.90 m
Number of cells	35
Drift tube	Stainless steel, copper plated
Outer diameter	16 cm
Bore diameter	3 cm
Quadrupole magnet	permanent (ALNICO-9)
Aperture	3.4 cm
Length	16 cm
Outer diameter	13.5 cm
Field gradient	2.2 - 2.25 kG/cm
Synchronous phase	-30°
Average axial field	2.2 MV/m
Shunt impedance	74.34 - 72.51 MΩ/m
Transit time factor	0.8519 - 0.7915
Effective shunt impedance	53.95 - 45.43 MΩ/m
Excitation power	0.845 MW
Beam power (for 30 mA)	0.60 MW
Total RF power	1.445 MW
RF coupling	Loop, two feeds
Stabilizer	Post couplers
Vacuum system	
Main pump	Ion pump (1,000 ℓ/s x 8)
Auxiliary pump	Turbomolecular pump (500 ℓ/s x 2)
Temperature regulation	±0.1°C

Neutron Scattering Experimental Facility (KNES)

Numbers of neutron scattering experiments have been carried out with the 5 spectrometers of the HIT, MAX, LAM, SAN and TOP, as well as new members of machine, such as FOX (four circle single crystal diffractometer), PEN (polarized epithermal neutron spectrometer), CAT (crystal analyzer TOF spectrometer), RAT

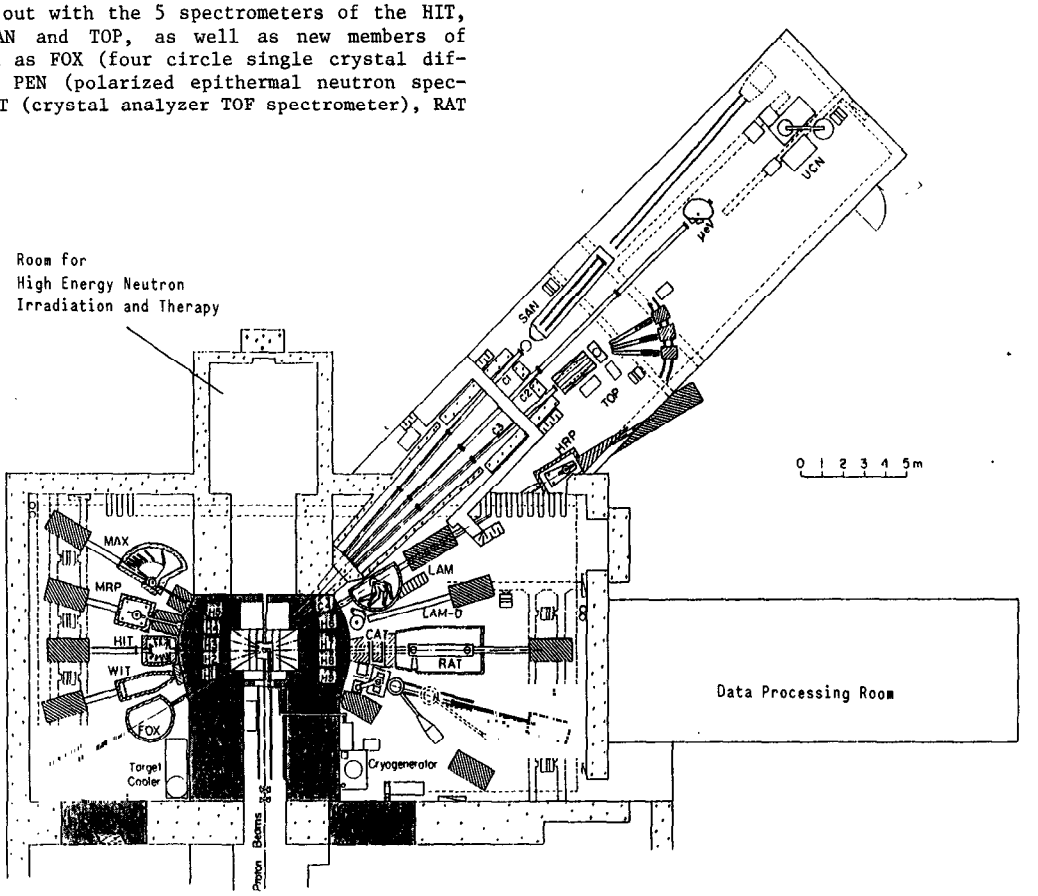

Fig. 6 Layout of the Spectrometers in KENS

(resonance detector TOF spectrometer), and LAM-D, which opened to the user community. Consequently 10 spectrometers have been operated. In fact the number of research proposal to the BSF increases steadily, but the total machine time reached the maximum and is rather decreasing recently because the beam time shared with Particle Radiation Medical Science Center is increasing. For instance, more than 100 specimens of glasses, amorphous materials and liquids have been measured with the HIT diffractometer, but several proposals are still in a waiting list.

Tow powder diffractometers HRP (high resolution powder diffractometer) and MRP (medium resolution powder deffractometer) are under construction in reply to the users' strong requests. A new high resolution quasi-elastic spectrometer LAM-80 is also under construction based on a prototype experiment already achieved. Figure 6 shows the recent layout of the spectrometers.

Neutron Source

The pulsed spallation neutron source, KENS, was operated satisfactorily throughout FY 1982. The total operation time was 1,509 hours. The second target of W installed at the beginning of this period is still in operation without any serious radiation damage. Since the first target suffered serious erosion with the condensation of NO_x gas generated by radiations, the second target is situated in a gas free environment.

As the first step of the KENS-I' project we have obtained an appreciable gain in cold neutron flux by changing a solid methane moderator with a grooved surface. After the extensive studies of both experiments at the Hokkaido linac and computer simulations at JAERI to optimize, we have installed a new grooved moderator replacing the previous flat one at the end of FY 1982. Then we confirmed the gain factor of about 1.4 which was just expected from the results of design studies. Figure 7 shows the neutron spectrum from the new grooved moderator compared to that from the previous flat one. The time structures of cold neutrons at various energies are also shown in Fig. 8, which represent an elongation of pulse width with a small preceding pulse from the teeth of the grooved surface. Pulse broadening themselves are not so serious even for the quasi-elastic spectrometer such as LAM-40 and LAM-80. Photograph of the new grooved moderator is shown in Fig. 9. Details are given in a separate article in this meeting[5].

As the second step the preparation of a depleted uranium target system is under progress. The development and fabrication of a prototype rectangular uranium target block and the fabrication of the first set of blocks (4 pieces) for KENS-I' use have already been ordered to Argonne National Laboratory. The blocks will be supplied by the end of March 1984. The target has been designed to accept an up-graded proton beam current of 10 μA.

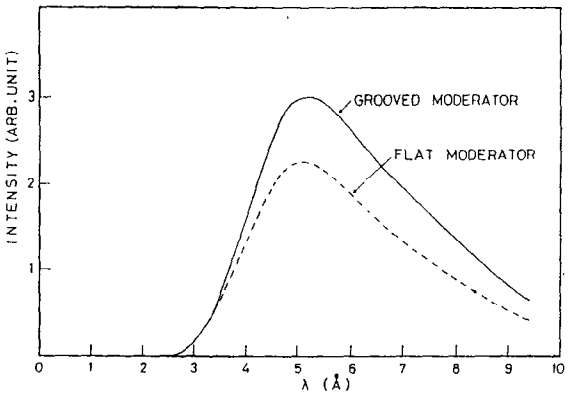

Fig. 7 Neutron Spectrum Extracted from the New KENS Grooved Solid Methane Moderator (20 K) (Solid Line). Compared dotted curve is that of the previous flat one.

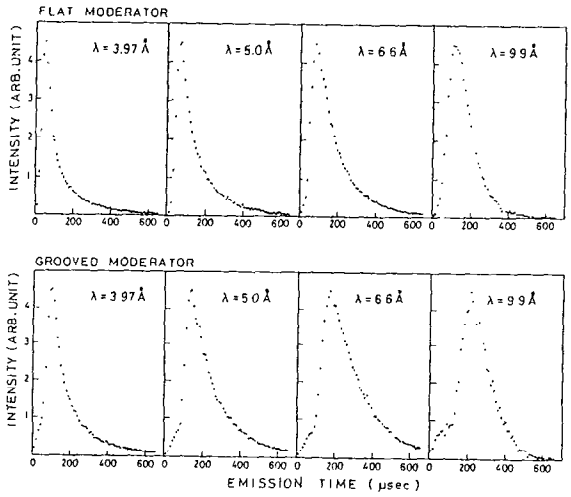

Fig. 8 Pulse Profiles in Time Scale of Cold Neutrons from Grooved and Flat Solid Methane Moderators at Various Wave Lentghes

Fig. 9 View of New KENS Crooved Moderator

Neutron Scattering Experiments

Among many experiments conducted since last ICANS meeting, several topics are selected and described very briefly in this report. The more detailed results are seen in the KENS Report IV[6].

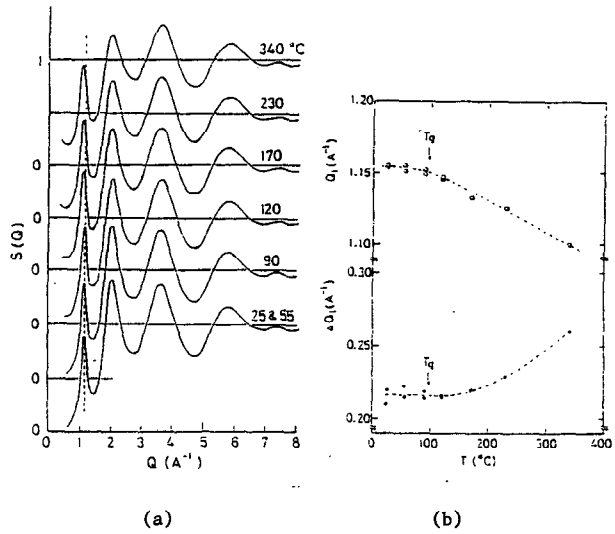

Fig. 10 (a) Temperature Variation of the Structure Factor, and
(b) the Peak Position and the Peak Width of the First Peak at Q∿1A,
in P_2Se_3 below and above the Glass Transition Temperature (100°C)

As was mentioned in the preceding section the HIT is the busiest machine in this facility. The well determined resolution components and wide range of the momentum transfer Q enable us to investigate the precise short range or partial structure factor S(Q) of the topological disordered materials. One of the remarkable examples shown here is the structural change associated with the glass transition of the P_2Se_3 glass at 100°C. As is demonstrated in Fig. 10(a), the variation of the structure factor is remarkable in the first peak near 1 A^{-1} in Q. More quantitatively the peak position and the width of the first peak in Q vary above the glass transition temperature and are frozen immediately at this transition temperature, which is shown in Fig. 10(b). The present result provides the first experimental evidence which clarifies the correlation between the glass transition temperature and the structural change at the glass transition of the glass materials.

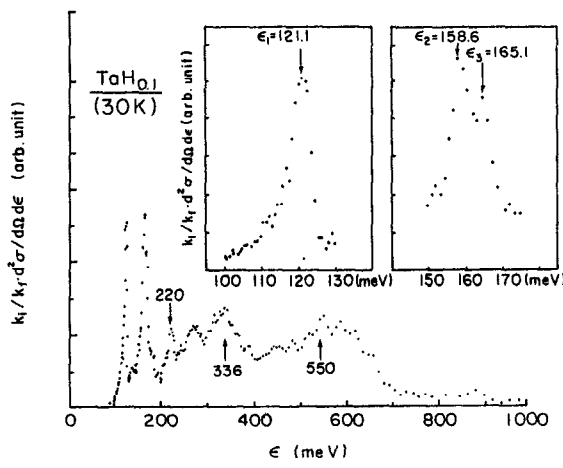

Fig. 11 Local Mode Spectrum for $TaH_{0.1}$ at 30 K. Inserted figures are those in enlarged scale near the first excited levels.

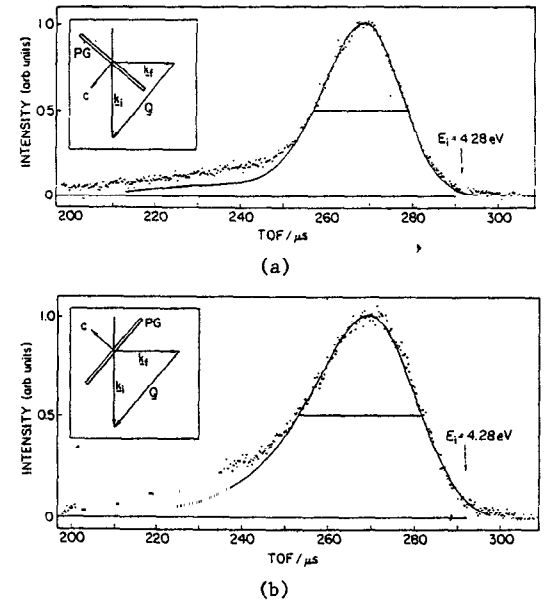

Fig. 12 High Q Scattering Spectra from Pyro-graphite for (a) Q//C and (b) Q⊥C

It has been recognized that the pulsed neutron scattering method is superior in high energy regions of sub eV or eV energy, and such experiments to demonstrate high quality investigation are performed with the RAT and CAT spectrometers. Utilizing the time focussing principle the energy resolution of the CAT reaches as small as 3 % for 1 eV energy transfer. This highest resolution spectrometer in the world is suitable to elucidate the dynamics of light elements such as H_2, Be, C, etc. embeded in the transition metals and alloys. For instance the energy splitting in the first excited energy levels of the hydrogen local modes in $TaH_{0.1}$ was well observed for the first time, which has long been considered to be degenerated (Fig. 11). The experimentally determined energy levels are also interpreted by the crystalline distortion to the orthorhombic from the cubic symmetry due to the hydrogen doping. Inelastic scattering studies at high momentum transfer Q have also been elucidated using a resonance detector technique. Numbers of technical developments have been achieved currently and a detailed line profile is able to be analyzed. Curves shown in Fig. 12 are examples looking at the scattering from the pyrolytic graphite crystal. The line widths of modes parallel and perpenticular to the C plane differ approximately by a factor of 1.5. This result is qualitatively interpreted by the fact of the mode difference of density of states of phonons.

Significant parts of activities in the neutron scattering research at KENS facility are concerned with the low energy neutron spectroscopy using the solid methane moderator. It has long been believed that the pulsed cold neutron source cannot compete with the cold neutron source at steady state reactor, and an important question has been raised whether any experiment better than those using the latter source may be performed. Several examples selected from the outcomes using the KENS cold neutron source are considered to be the answer.

Neutron quasielastic spectra of polymers, aqueous solutions, etc. have been extensively studied with the LAM-40 spectrometer. Very recently the high resolution has been attained down to less than 20 μeV with a new developed machine of LAM-80. Eventually the combination of both LAM-40 and -80 spectrometers enable us to

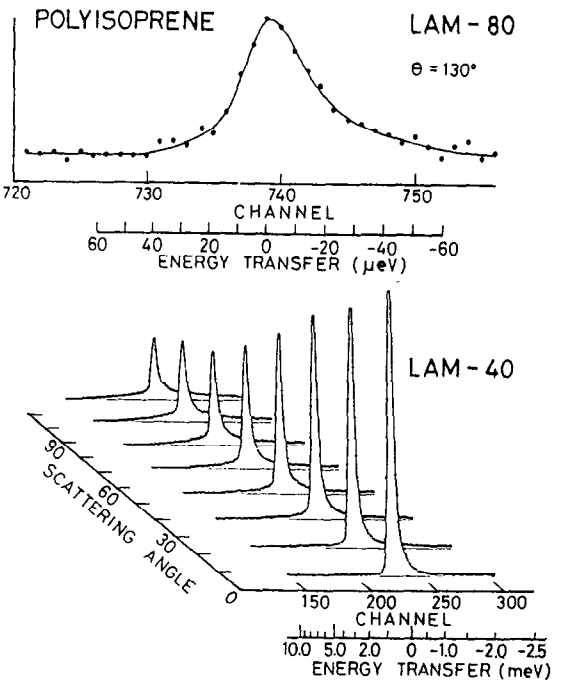

Fig. 13 Quasielastic Neutron Inelastic Spectra of Butadiene Observed by LAM-40 and LAM-80

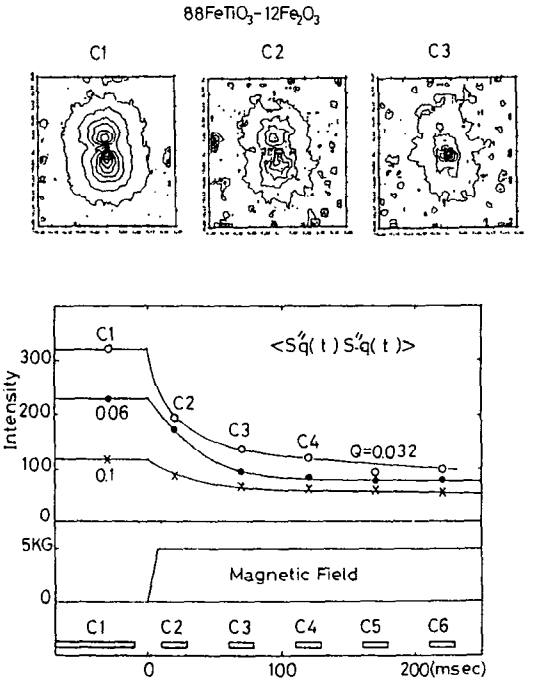

Fig. 14 Two Dimensional Display of Time Dependent Response of Magnetic Clusters in $(Fe_2O_3)_{0.12}(FeTiO_3)_{0.88}$ Spin Glass

elucidate the details of molecular or polymer diffusion processes due to the achievement of the high resolution and the wide energy transfer. A typical example obtained in this way is diffusion motions in butadiene of the commercial rubber: Looking at the quasielastic neutron spectra with the two different spectrometers as shown in Fig. 13, we are aware of existence of two types of diffusions characterized by two relevant relaxation times, τ_1 and τ_2. According to the de Gennes model, the results are interpreted as that the fast diffusion ($\tau_1 \sim 10^{-12}$ sec) corresponds to the rotational diffusion mode inside the polymer pipe due mainly to thermal fluctuations of bonding angles and that the slow motion ($\tau_2 \sim 5 \times 10^{-11}$ sec) corresponds to the jump mode along the pipe.

The small angle camera (SAN) installed at an end of the guide tube viewing the cold source contributes to many users in the research fields of polymer science, biology, metallurgy and solid state physics. The SAN has also a unique feature utilizing the full advantage of the pulse technique. Besides the coverage of the wide momentum space due to the wide band of incoming neutron wave length, the time evolution of the structure analysis can easily be performed. Consequently extensive efforts have been directed to physics of nonequilibrium state, such as problems of spinodal decomposition, spin glass transition, etc. Collecting enormous amounts of data points stored in the 2 mega bites bulk memories, time transient pictures can be taken in various time scales. As an example the response of the magnetic short range order in a spin glass material of $(FeTiO_3)_{0.88}(Fe_2O_3)_{0.12}$ to the pulsed magnetic field, which is projected on the crystalline a*c* plane, is shown in Fig. 14. These pictures depict how the magnetic clusters appearing in the zero field behave in the applied field. It seems to indicate the nonlinear growing process of such magnetic clusters. On the other hand the slower relaxation processes have been elucidated using FeCr alloys which show a well known spinodal decomposition. The successful interpretation has been obtained by a recent nonlinear theory due to the fact that we could observe the detailed time evolution of diffraction in the wide Q range.

The TOP provides polarized pulse neutrons with continuous wave length longer than 3 A. Besides the magnetic structure analysis for herimagnets with a long period, amorphous magnets, composite magnetic multilayers and fine particles, the dynamical polarization analysis is one of current topics. Wave length dependence of depolarization of transmitted polarized neutrons through a ferromagnetic thin plate was directly measured for the first time since Halpern and Holstein studied theoretically long time ago (1941). We applied this technique to the study on spin dynamics in random ferromagnets often called as spin glasses. In these materials the randomness is so strong that the ferromagnetic order may be destroyed. In other words the spin fluctuating frequency may become slow in these

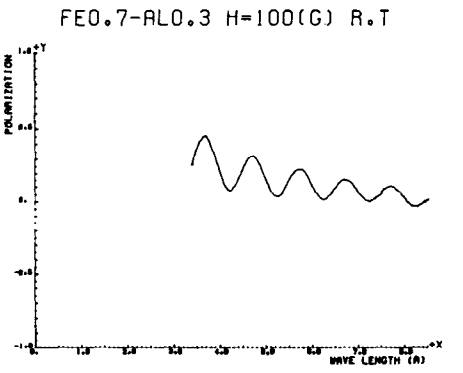

Fig. 15 Wave Length Dependence of Depolarization of Transmitted Polarized Neutrons through FeAℓ Spin Glass

materials and the neutron scattering cannot detect such low frequencies of the spin dynamical part. As is shown in Fig. 15, polarization of transmitted neutrons through a FeAℓ spin glass changes with the wave length considerably. The decrease of polarization with respect to the wave length is interpreted by introduction of the random field. If the random field is assumed to be stochastic, the neutron spins with the longer wave length spend longer time in the random field resulting more depolarization. The oscillation represents existence of a stationary field resulting the Larmor oscillation of the neutron spins.

To conclude this section we emphasize that numbers of experiments have been performed, a part of which in significant to yield scientific impacts and others are useful to develop new technique. Besides these examples just shown before, many other significant outcomes have been obtained by the MAX, PEN, FOX, LAM-D, and UCN spectrometers.

Instrumental Development

A High Resolution Powder diffractometer HRP is being installed at a position about 18 m from the cold source (downstream the LAM-40 spectrometer on the C-4 beam line). This instrument utilizes sharp pulses of thermal neutrons from the solid methane moderator at 20 K and a resolution $\Delta d/d \sim 0.002$ is expected with backward counters at $2\theta \sim 170$ deg. A Medium Resolution Powder diffractometer MRP is under construction at H-4 beam hole viewing the room temperature moderator. The instrument is designed to provide a higher counting rate but with a medium resolution $\Delta d/d = 0.007 \sim 0.02$.

Considerable progress has been achieved in the polarized epithermal neutron spectrometer PEN and an electron volt spectrometer RAT. The higher proton polarization more than 70 % has been achieved with PEN which stands far above the corresponding value of 45 % with a prototype experiment by Pre-PEN. Extensive studies on the resonance detector foil have been carried out and the best detector resolution $\Delta E_r \sim 50$ meV ($\Delta E_r/E_r = 0.75$ %) at $E_r = 6.67$ eV has been attained by an uranium foil cooled down to 25 K.

A prototype experiment for a higher resolution quasi-elastic spectrometer LAM-80 has attained higher energy resolution better than 20 μeV. The instrument utilized a similar analyzer mirror as LAM-40 but with $\theta_B \sim 80°$. LAM-80 is equipped with four analyzer mirrors at any scattering angles and being installed at the end of the C-2 guide tube.

Finally the guide tube of C-2 is extended by 6 m, and consequently the total flight path is now going to be 29 m from the source to the end of C-2 guide. Several UCN experiments and high resolution spectroscopy in the sub μeV energy region will be considered from the beginning of FY 1984.

Pulsed Muon Facility BOOM[5)]

Meson Science Laboratory was born in 1978, attached to Faculty of Science of the University of Tokyo, to conduct basic research in science using mesons, in particular, as the first step, to build a meson facility BOOM at the KEK booster synchrotron utilization facility BSF. The final goal of this experimental facility is to construct high quality pulsed muon experimental facility and to conduct research project based upon the maximum use of the time structure of the pulsed proton beam from the 500 MeV booster synchrotron. The beam has a suitable time structure of 50 nsec pulse width and 50 msec separation. Such a pulsed beam can be quite effectively coupled with the extreme experimental condition which can be realized only with a low duty factor such as a high RF field, a high power laser, etc.

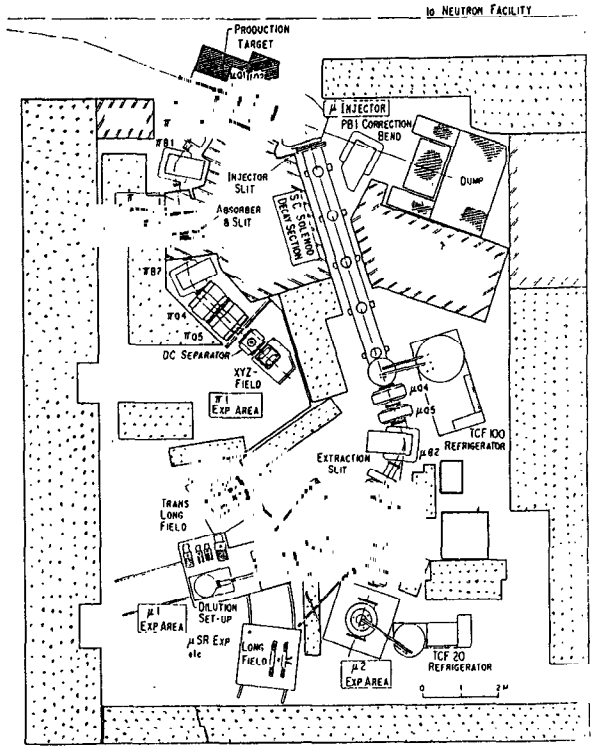

Fig. 16 Layout of Pulsed Muon Facility BOOM

Layout of the pulsed muon facility is shown in Fig. 16.

Since the first operation of the superconducting muon channel in July 1980, the superconducting solenoid and its cooling system has already marked over 7,000 hrs running time in almost maintenance-free mode. The μ1 port attached to the superconducting channel has been in use for the wide varieties of pulsed muon experiments by taking high quality backward muons. Table 4 is a summary of the muon beam properties at μ1. The μ2 muon extraction channel is used as either alternative channel for backward muons sharing beam time with μ1 port or simultaneous operational channel for forward muons. A parasite pion channel with take-off angle of 102.5° from incident proton beam is mainly used as a surface muon channel. At present, it is possible to have surface μ^+ at the π1 port with an intensity of 10^5 μ^+/sec in an area of 12 cm x 2 cm.

Almost the experiments conducted in BOOM are based on the techniques of μSR. The μSR method, utilizing asymmetric emission of $e^{\pm}$ along polarized muon spin, can be used to probe the local magnetic field and its fluctuation felt by the muon inside various condensed

Table 4 Summary of Muon Beam Properties at μ1 Port

		Case 1	Case 2
pπ	(MeV/c)	200 ± 5 %	150 ± 5 %
pμ	(MeV/c)	≃ 110	≃ 75
Stopping Range Width	(g/cm²)	3.5	2.0
Intensity	(μ^+/pulse)	35 K	28 K
	(μ^+/sec)	700 K	560 K
Polarization		80 %	80 %
Spot Area FWHM	(cm x cm)	5 x 5	5 x 5

Table 5 List of Active Experiments in BOOM (April 1982 - March 1983)

Exp. No.	Title (Abridged) Actual Subject	Beam Time (h) μ1/μ2 (BWD)	μ2 (FWD)	π1
M 1	μ-channel tuning			
	Forward μ^- tuning		168	
	Forward μ^- test		146	
M 2	π-channel tuning			
	DC separator tuning			262
	Muonium detection development			224
	Gas phase muonium formation test			77
	Pion tuning			31
M 3	Pulsed μSR developments			
	Polyacetylene test	22		138
	$REAl_2$ compound test	33		
	GaP semiconductor test	5		
M 4	Mu & μ^+ in H_2O			
	Decoupling & decoupling resonance	83		
M 5	μ^+SR on Ni			
	Critical phenomena	100	30	
M 8	Muonium in hydrocarbon			
	Decoupling & decoupling resonance	83		
	Muonium spin rotation	42		55
M10	Average polarization of ^{12}B after μ^- capture on ^{12}C			
	Testing, long-run and after-check	421		
M11	μ^+SR defects in metals			
	ZF-μSR on AlMg alloys			77
M12	Hyperfine effect in muonic atoms			
	Hyperfine capture & transition in $\mu^{-11}B$	68		
M15	Hfs resonance in muonium			
	ν_0 resonance test on Mu in SiO_2			334
M20	μ^+SR on itinerant magnetism			
	μ^+SR studies on CoS_2	52		69
M21	μ^+SR on spin glasses			
	μ^+SR on illumenite hematite & AuFe(1.0 at. %)	210		
M22	Quantum diffusion of μ^+ in Cu			
	ZF-μ^+SR on Cu from 0.09 K - 200 K	135		
M23	μ^+SR studies on dense Kondo system			
	μ^+SR on CeB_6	44		28
M24	Studies of pulsed muon & muonium spin resonance			
	Time dependent resonance on μ^+ in MnO	74		
	Resonance hunting & testing		203	
M25	μ^+SR studies on valence fluctuating system			
	μ^+SR on Sm_3Se_4	40		
M26	Chemical analysis by atomic μ^- capture			
	μ^- capture in organic compounds $C_xH_yCl_z$ & $C_xH_yS_z$	4	196	
M27	μ^+ trapping by extended defects in metals			
	μ^+SR in irradiated Al with voids			23
M28	Pulsed laser resonance spectroscopy			
	Mu reaction with NO_2 in Ar			61
M29	μ^+SR studies on magnetism with competing ordering			
	μ^+SR on $Fe_xCo_{1-x}TiO_3$			54

matters and also used to measure the μ^+ motion in metals, muonium chemical reactions, etc. In particular, with pulsed muons which have strong advantage for long time range measurement, one can now measure low frequency muon spin rotation, long $\mu^\pm$ spin relaxation, slow muonium chemical reactions, μ^+ fast diffusions, etc. Moreover, the pulsed muon beam with low duty factor can introduce the magnetic spin resonance technique, in which high RF field (closed to 100 kW peak power) is required to complete muon spin transition within muon life time.

Thus, the pulsed μSR experiments cover a wide range of research field. Active experiments in the pulsed muon facility BOOM are listed in Table 5.

Future Program

KENS-I' program of the neutron scattering facility in BSF is a project up-grading the present existing accelerator and experimental facilities in a short period. The major items of the improvement in the program are as follows.

1) Conversion of injection scheme in the booster synchrotron from the multi-turn injection of proton beam to H^- charge-exchange injection.
2) Energy-up of the 20 MeV injector linac to 40 MeV.
3) Conversion of the present tungsten target for spallation neutron production to a depleted uranium target.
4) Adoption of a grooved-surface solid methane moderator, etc.

If those are completely performed, the present neutron intensity will be increased by one order of magnitude. Some of them are already completed or under way as mentioned.

While the KENS-I' program is in progress, a long-term future program of BSF has been discussed on the basis of the encouraging results obtained by both of the neutron scattering experimental facility KENS and the pulsed muon facility BOOM in BSF. This is the construction of a more intense pulsed neutron source, KENS-II program, and the extension of the present pulsed muon facility, Super BOOM project. The central facility of this future program is an 800 MeV rapid-cycling proton synchrotron, GEMINI, which intends to deliver pulsed proton beams of 500 μA in time average. The design studies of this accelerator are in progress. Details of the design are presented in this meeting[8].

References

1) C. W. Schmidt and C. D. Curtis, IEEE Trans. Nucl. Sci., NS-26, 4120, 1979.
2) S. Fukumoto, et al., ISIAT '81, 223, 1981, and IEEE Trans. Nucl. Sci., NS-28, 2693, 1981.
3) K. N. Leung and K. W. Ehlers, Rev. Sci. Instrum., 53 803, 1982.
4) S. Fukumoto, to be submitted to ISIAT '83.
5) Y. Ishikawa, et al., presented paper to this meeting.
6) Y. Ishikawa, N. Niimura, and S. Ikeda, ed., KENS Report-IV, KEK Internal (1983).
7) Meson Science Lab., Univ. of Tokyo, UT-MSL Newsletter No. 1, 1981 and No. 2, 1982.
8) H. Sasaki, et al., presented paper to this meeting.

Proceedings of International Collaboration on Advanced Neutron Sources (ICANS-VII), 1983 September 13-16
Atomic Energy of Canada Limited, Report AECL-8488

STATUS REPORT OF THE SIN NEUTRON SOURCE (SEPTEMBER 1983)

F. Atchison and W.E. Fischer for the
Project Group
Swiss Institute for Nuclear Research
CH-5234 Villigen, Switzerland

INTRODUCTION

This report is in two parts. Part I describes the construction work for Injector II, which is scheduled for first beam tests later this year. Part II presents the status of the spallation neutron source (SINQ) which is planned to become operational after commissioning of Injector II and necessary improvements to other parts of the SIN-facility for the high currents.

PART I
THE ACCELERATOR SYSTEM AND LAYOUT OF EXPERIMENTAL FACILITIES

1. INTRODUCTION

The proposed layout of the accelerator system and experimental facilities following commissioning of Injector II are shown in Fig. 1. The site for SINQ is in the prolongation of the proton channel after the two meson targets. The guide-hall for cold neutrons is not yet included on the diagram.

At present Injector I feeds the Ring Cyclotron with a 100 to 150 μA proton beam for routine operation. During 1982 a total of $455 \cdot 10^3$ μAh were delivered on target with an average beam current of 119 μA and an availability of 92 %.

Injector II is designed to deliver a beam current of at least 1 mA and consists of an 860 keV Cockcroft-Walton pre-accelerator and an isochronous cyclotron for acceleration to 72 MeV.

2. INJECTOR II

2.1 The ion-source and pre-injector

The ion-source is of the 'multi-cusp' type: During tests, this has delivered a beam current of 40 mA, of which 40 % consisted of protons. Injector II will accept about 10 % of the current using injection without pre-bunching. A buncher could improve this ratio, but will, however, lead to a worsening of the injected beam quality.

The ion-source and acceleration tube are connected by a 60 keV beam line (ion-source extraction voltage), which contains two

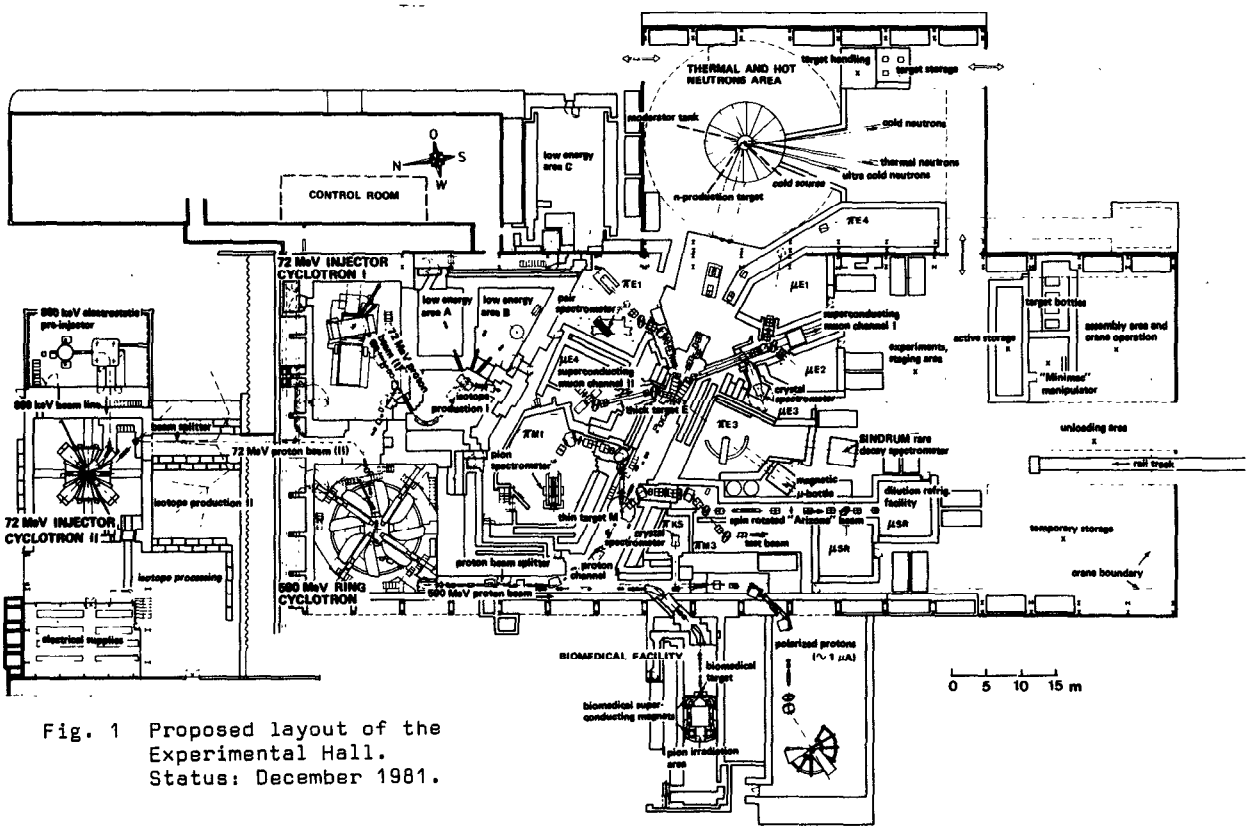

Fig. 1 Proposed layout of the Experimental Hall. Status: December 1981.

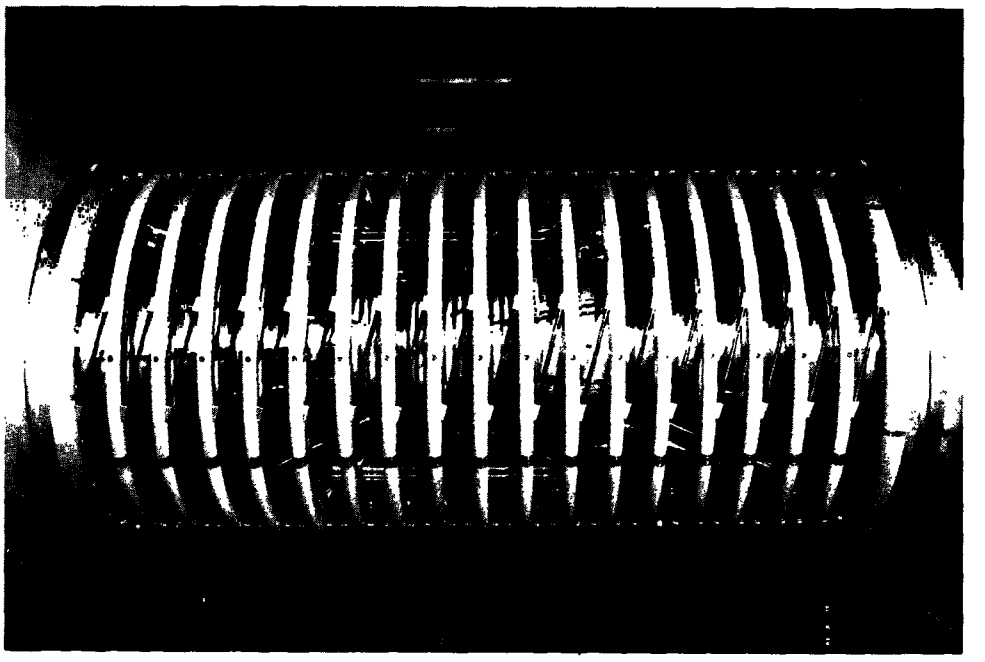

Fig. 2 The 800 keV acceleration tube installed at the Cockcroft Walton.

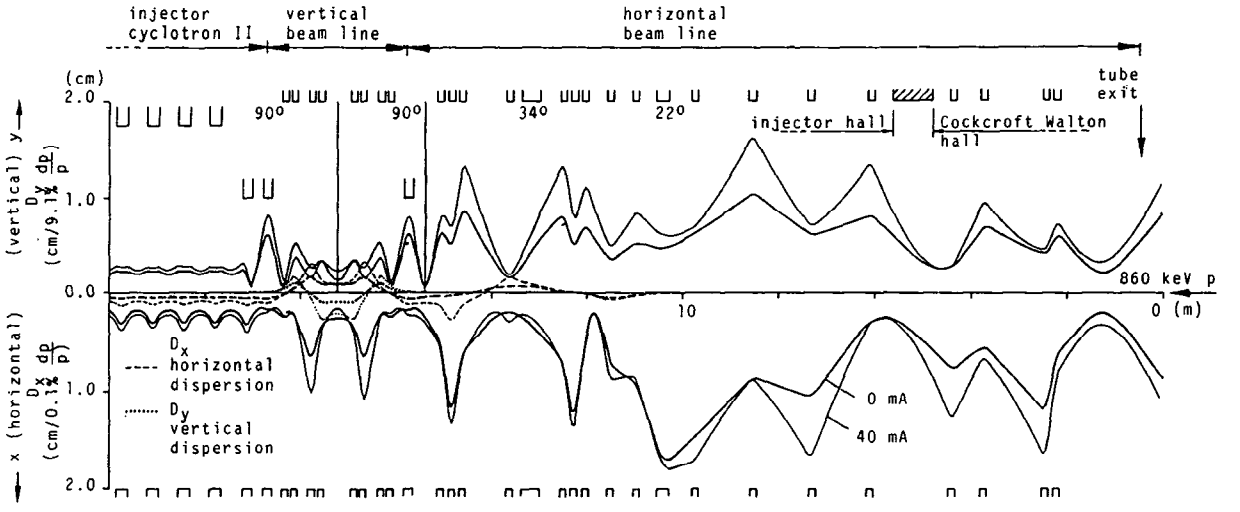

Fig. 3 Beam envelope and dispersion trajectories at 0 and 40 mA beam current in the 860 keV injection line.

solenoids and a diaphragm to remove most of the unwanted ions.

To transport this 60 keV beam, neutralisation of the space charge is essential. The neutralisation is a stationary state of a dynamic process: Electrons produced by collisions with residual gas atoms, are captured in the beam potential. These electrons are heated by the beam and diffuse back out of the potential[1]. Hence the stationary state electron density (and hence neutralisation) depend on the beam energy and current and the residual gas pressure. The 60 keV beam was shown to be more than 99 % neutralised at a pressure of about 10^{-5} Torr.

A photograph of the 800 keV acceleration tube, which was installed in summer 1983, is shown in Fig. 2.

2.2 The 860 keV beam line

There were two principle problems to be solved for the design of this beam line:

(a) Space charge: The neutralisation of the beam due to free electrons from collision is assumed to be weak and the space charge

effects from the full current will be felt.

(b) Since the beam incorporates both horizontal and vertical bends for axial injection, the matching of the beam emittance and the dispersions to the accelerator acceptance involves eight parameters.

Fig. 3 shows the beam envelope and dispersion trajectories at 0 mA and 40 mA, for the injection line from the acceleration tube exit to the first turn in Injector II. As can be seen, the matching depends on the intensity. This leads to the necessity of four quadrupole doublets in the vertical section just before injection. This part of the line is shown in Fig. 4.

The excitation for all quadrupoles will be beam current dependent, and will be adjusted automatically by the control system.

The part of this 860 keV beam line above Injector II may be seen in Fig. 5.

2.3 The 72 MeV cyclotron

This is an isochronous cyclotron with injection and extraction radii of 33 and 300 cm in the valley of the magnetic field. The guide field and focussing is provided by 4 sector magnets (see Fig. 5), each with the following parameters:

Weight	180 t
Pole-gap	35 mm
Magnetic field	10.4 kG (inner radius)
	10.9 kG (outer radius)
Power consumption	34 kW

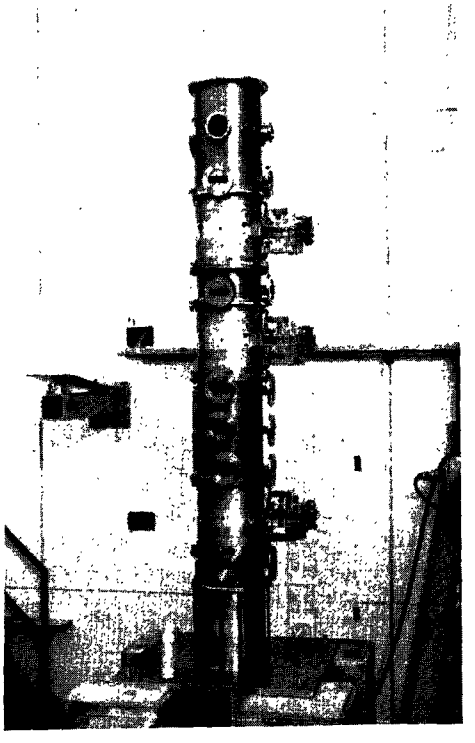

Fig. 4 Vertical insert for axial injection into the cyclotron. It contains eight quadrupoles and boxes for diagnostic elements.

Acceleration is provided by two 50 MHz λ/2-resonators each having two acceleration gaps. The power consumption is 150 kW per resonator. In order to obtain phase compression of the bunches during the whole acceleration time, the acceleration voltage increases from 125 kV/gap at the injection radius to 250 kV at extraction. Explanation of this effect may be found in reference 2.

By adding a third harmonic to the 50 MHz, and making a proper choice of amplitude (100 kV), the energy spread of the beam at extraction may be minimised. A 150 MHz cavity positioned between two of the sector magnets may be seen in Fig. 5. By adjustment of the phase between the fundamental and third harmonic, longitudinal space charge effects may be compensated to first order.

All these measures lead to a 'straightening' of the particle bunches in the cyclotron, to create clearly separated turns, which is essential for a good extraction efficiency.

Fig. 5 A view of the 72 MeV cyclotron, also showing part of the injection line.

PART II
THE NEUTRON SOURCE

1. INTRODUCTION

The present medium term plan for the SIN experimental program, shows the SINQ neutron source ready for operation in 1988. Money for construction should become available in late 1985; to meet this timetable, detailed engineering design work should commence in the early part of next year (1984).

2. THE TARGET

2.1 General

The production target is to be a vertical cylinder with a 20 cm diameter and 3 to 4 m length, of Pb/Bi eutectic mixture in the liquid phase. The design aim is to employ natural convection to transfer the beam heat about 3 m upwards. This allows three principal advantages; (i) no mechanical pumps for the liquid metal; (ii) the heat-exchanger and first conventional cooling circuit are removed well away from the high radiation field; (iii) the avoidance of complication and space conflicts, from cooling circuitry close to the neutron production region of the target. The 'extra' length also acts as the beam dump.

The two major concerns are the design for the proton-beam window and the thermofluid behaviour.

2.2 The beam window

With the expected proton current (1 to 3 mA) and beam distribution, a peak proton flux of 2 to $6 \cdot 10^{14}/cm^2/sec$ will be incident on the window. This is accompanied by a fast and HE neutron flux of 1 to $3 \cdot 10^{14}/cm^2/sec$. The window has to support a 'hydrostatic' pressure from the Pb/Bi which is 3 to 4 bar, and be corrosion resistant to the Pb/Bi. Ideally the window will be cooled on its inner face only by the Pb/Bi.

It is most likely that the beam window will be the limiting component on the target lifetime; we aim for this to be at least 1 year.

An experiment is in progress at the Los Alamos beam dump to examine the mechanical properties of stainless steel under proton irradiation comparable to that expected in operation. The samples are also being irradiated in contact with Pb/Bi to make a first attempt at seeing if there are any radiation induced corrosion effects. There are no results yet.

2.3 Thermofluid behaviour

Theoretical studies of the thermofluid behaviour of the target completed so far[3,4], have concentrated on obtaining results to increase our knowledge of the processes involved in natural convection in an enclosure and driven by internally generated heat. Parameter surveys have been made which include the effect of target height, beam size and power and the effect of sidewall cooling.

Targets with aspect ratio (height/diameter) up to 15 and beam current to 1 mA have been examined. These calculations may be summarised as follows:

(i) The Pb/Bi flow shows a simple total circulation throughout the target following establishment of the steady state, in all cases studied.

(ii) The maximum temperature at the steady state and the deposited energy show a simple power law relationship (Fig. 6).

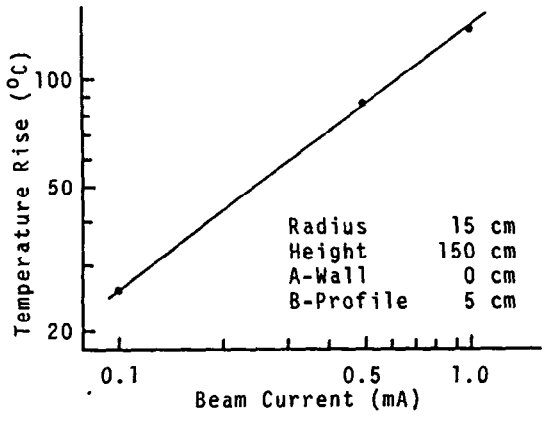

Fig. 6 Maximum temperature rise in the target as a function of beam current.

(iii) There is no need to cool the lower 1 m of the target (in the region of the moderator) as long as sufficient area is available for heat transfer in the region above.

More detailed aspects of the thermofluid behaviour are given in a separate report to this meeting by Takeda[4].

The theoretical studies are being backed up with an experimental program, leading eventually to a full scale test including Pb/Bi. The first large scale test-rig is now in operation and is shown in Fig. 7. These initial tests are being made with water; preliminary results may be found in[4].

2.4 Target activation

The effect of fission on target activation has been examined. The calculated fission probability is 0.09/proton and leads to the mass distribution shown in Fig. 8. In terms of gross activation and decay power the effect of fission is small. There are two principal effects; the production of nuclides in the 50 to 150 mass region; the production of delayed neutrons.

In terms of overall neutron-source safety, the production of Kr, Xe and Iodine are of particular note: The 'hazard rating', based on potential ingested dose without holdback factors, for Iodine is greater than that for Hg, one of the most populous products, but is about three orders of magnitude below Po-210. Both Po and Iodine will be a major consideration in the design of containment systems.

The delayed neutron precursor activation is about 230 Ci, corresponding to $8.4 \cdot 10^{12}$ n^o/sec, the flow velocity of the Pb/Bi (60 cm/sec) and short half life (0.2 sec up to 1 min), lead to about $5 \cdot 10^{10}$ n^o/sec at the top of the target.

The decay-power and energy release as a function of time after 1 year of irradiation at 1 mA, is shown in Fig. 9. The thermal capacity of the target is about 0.15 MJ/°C, hence after

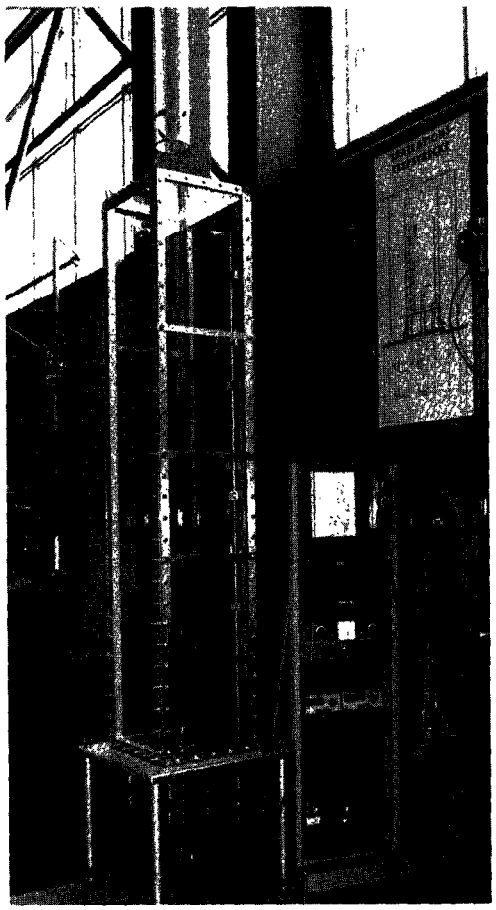

Fig. 7 General view of the thermofluid dynamics test-rig.

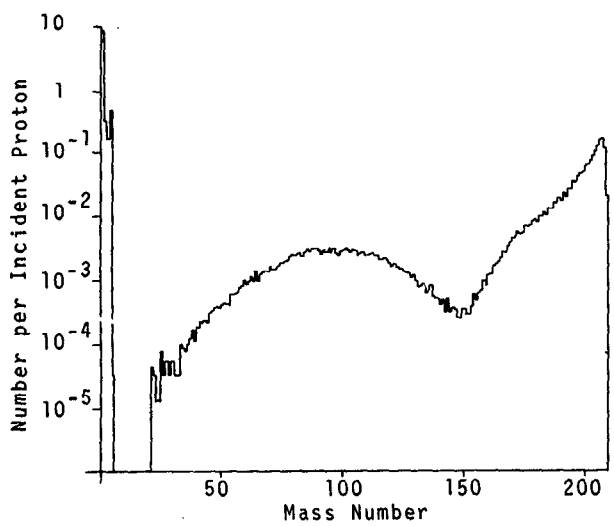

Fig. 8 Mass distribution for 590 MeV proton bombardment of Pb/Bi including fast fission.

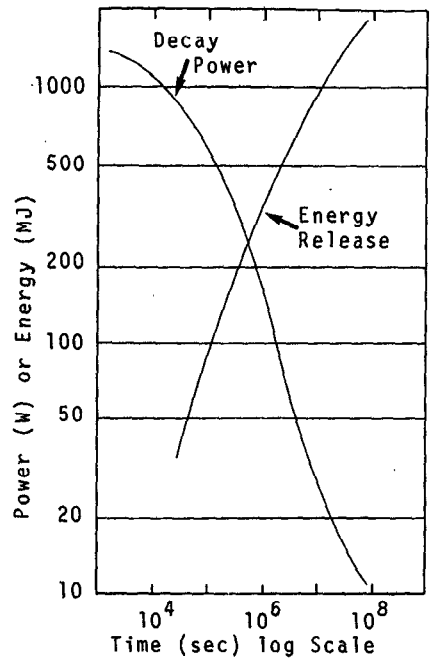

Fig. 9 Decay power and accumulated energy release from the decay of spallation product activity following 1 year irradiation at 1 mA.

1 day, a totally thermally isolated target will have a temperature rise of about 490° C. If cooling at the 0.5 kW level is maintained, the maximum temperature rise in the system is limited to about 270° C.

2.5 Vapour pressure above Pb/Bi surface

There will need to be an interspace above the Pb/Bi surface to accumulate the gaseous products. The hydrogen and helium will be accompanied by gaseous fission products and the vapours from (principally) Hg and Po. First estimates for Hg and Po using the methods of Hellwig et al.[5], give the following results for a 15 cm radius free surface.

(i) Mercury. Of the ∿78 kCi at equilibrium, about 76 % (49 kCi) will be liberated at a temperature of 200° C; this rises to 87 % (67 kCi) at 325° C.

(ii) Polonium. The equilibrium activity is about 5 kCi and produced via the channel $^{209}Bi(n,\gamma)^{210}Bi$ followed by β-decay. The released activity and evaporation rates ($g/cm^2/sec$) as a function of temperature are as follows:

T(°C)	Activity (Ci)	Evap. Rate
177	0.0007	$1.3 \cdot 10^{-17}$
227	0.04	$7.0 \cdot 10^{-16}$
277	1.1	$2.0 \cdot 10^{-14}$
327	19.0	$3.4 \cdot 10^{-13}$
377	200.0	$3.6 \cdot 10^{-12}$

3. THE MODERATOR

3.1 General

Tritiation of the D_2O is a known and expected consequence of source operation. The estimated activation levels are 0.8 Ci/litre at one year, 2.3 Ci/litre at three years and an equilibrium activity of 14.4 Ci/litre.

To limit corrosion and to remove gas (mainly from dissociation of the D_2O) a processing plant will be required. The plant is to consist of resin beds and degassifying equipment; at this stage we do not plan to include catalytic recombiners. In view of the need to have continuous processing and a pumped D_2O circuit, we now plan to incorporate the moderator heat exchanger into this system.

3.2 Cold source I: General

There are two possibilities for the cold source, (i) a large volume of D_2 or (ii) a small grooved H_2-type. Values from[6] show an optimal D_2-source to have a 50 % to 100 % higher gain factor compared with an optimal H_2 source. Recent measurements at Orphée[7] show higher gain factors than in reference 6; also the results of Inoue et al.[8] show a doubled gain factor for a grooved compared to an ungrooved methane source. These results would indicate that a grooved H_2 source could have a performance at least as good as for D_2.

As available refrigeration power is enough for two small H_2 sources and this leads to a more satisfactory overall source layout, the relative performance of these two cold source types with the SINQ geometry is to be measured experimentally by the KFA-SIN-TU Munich collaboration, in an experiment starting in the first half of next year (1984).

3.3 Cold source II: Heat deposition

Results from the recent heat deposition measurements made at TRIUMF[9], allow new estimation of the expected power. Heat generation in H_2 and D2 were deduced to be 36 and 19 mW/g, and for Al (a probable construction material) measured as 1.9 mW/g.

For a 1 litre H-source with a 5.0 mm thick spherical Al shell container, the estimated total heat load is 419 W/mA, the principal contributions being 224 W in H and 133 W in Al from fast neutrons and γ's; 37 W in H_2, and 25 W in Al from neutron capture.

For the D_2 source, a volume of about 20 litres will be required. Again using a spherical geometry, the large size requires taking the neutron flux variation into account. The heat distribution for the D_2 along the diameter perpendicular to the target and in the Al shell, are shown in Fig. 10. The fast neutron contribution dominates and is based on the flux distribution:

$$\phi = r^n \cdot \mathrm{Exp}\,(-\lambda r)$$

By fitting to diffusion calculation results, values of $n = -1.3$ and $\lambda = 0.021$/cm were obtained.

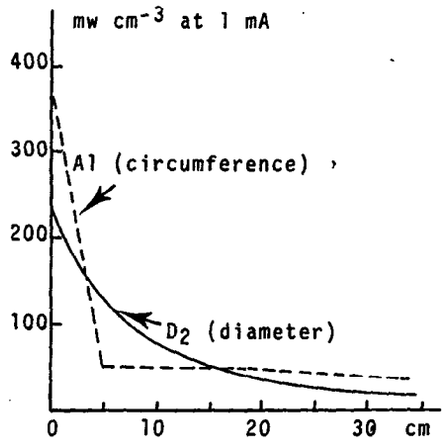

Fig. 10 Power deposition in the wall and D_2 for a 20 litre D_2 cold source.

Approximate integration of the power distribution gives a value of about 1.5 kW/mA. Fig. 10 also shows that this relatively large power may be reduced considerably by removing the cap beside the target, if this should turn out to be neutronically ineffective.

4. OVERALL SOURCE LAYOUT

4.1 General

A plan view of a preliminary version of the SINQ layout is shown in Fig. 11 and a vertical cut, in the central region of the source, in Fig. 12.

We plan to make the beam-tube tips replaceable as the possibility of failure of a beam-tube window cannot be entirely excluded. The central column containing the target and proton beam entrance line (see Fig. 12) will be subject to similarly high radiation damage and this is also planned to be replaceable. Collimators will be mounted in this central column; carbon in the region of the moderator and iron below. These are necessary to limit the consequences of a proton beam mis-steer.

Target extraction is from the top and will be made directly into a transport flask. The top plug can also be removed, allowing in principle replacement of the D_2O tank. The use of a light water layer outside the D_2O to increase the thermal flux[10] is now considered unwise in view of the consequences of leakage.

Three layers of containment are envisaged: (a) Outside the D_2O tank to contain any spillage as might occur with a beam-tube window failure. (b) An underpressure He atmosphere for the inner part of the shield. (c) An underpressure air system just outside the He containment, this air to be extracted via the proton beam tunnel ventilation system.

4.2 Beam tube layout

Current plans for the scattering facilities include both cold and thermal beam tubes, cold guides and thermal guides. The geography of the SIN site constrains the angle between the proton beam and thermal-guide bundle. There is sufficient room to accommodate guides up to about 150 m long.

There are two principle constraints to the layout of the beam-tubes; (i) their axes should be close to tangential to the target; (ii) we need to be able to replace the tips.

The thermal flux distribution allows use of two vertically displaced beam-tube layers and overall, six pairs of beam tubes are incorporated in the latest version. It is not clear that all twelve beam-ports could be used simultaneously as this depends on monochromator design and types of instruments.

Two cold sources are shown, both small H_2 rather than the single large D_2 of earlier versions: With slight changes, the two cold tube pairs and the cold-guides can be accommodated onto a single D_2 source.

One beam tube pair (HO2) could be available to view a hot-source if there is a requirement for such a facility.

4.3 Bulk shield

The source requires 4 m of iron and 1 m of concrete for the main biological shield. The first layer will require water cooling and we plan to include the inner 20 to 40 cm inside the moderator tank and use the D_2O for this. In view of corrosion problems, this first layer may be built from Pb.

Access for changing the beam tube tips will need to be through the bulk shield. Minimisation of the shield thickness is particularly relevant for the beam tubes. As the question of background is also intimately linked, we are investigating ways of building in as much flexibility as possible. Two schemes are under consideration:

In the first (Fig. 11), we provide 'user' boxes allowing mounting of collimators, monochromators etc. starting from a nominal 3 m radius. The size of box shown is based on the inclusion of a particular type of monochromator and would be determined in any final version by better consideration of the equipment to be mounted.

The second scheme (Fig. 12), is to provide a fixed part of the bulk shield at about 4 m radius, with full containment and no access for user equipment. The outer shielding would be built up from 'loose' blocks built up around the collimators, monochromators, etc.

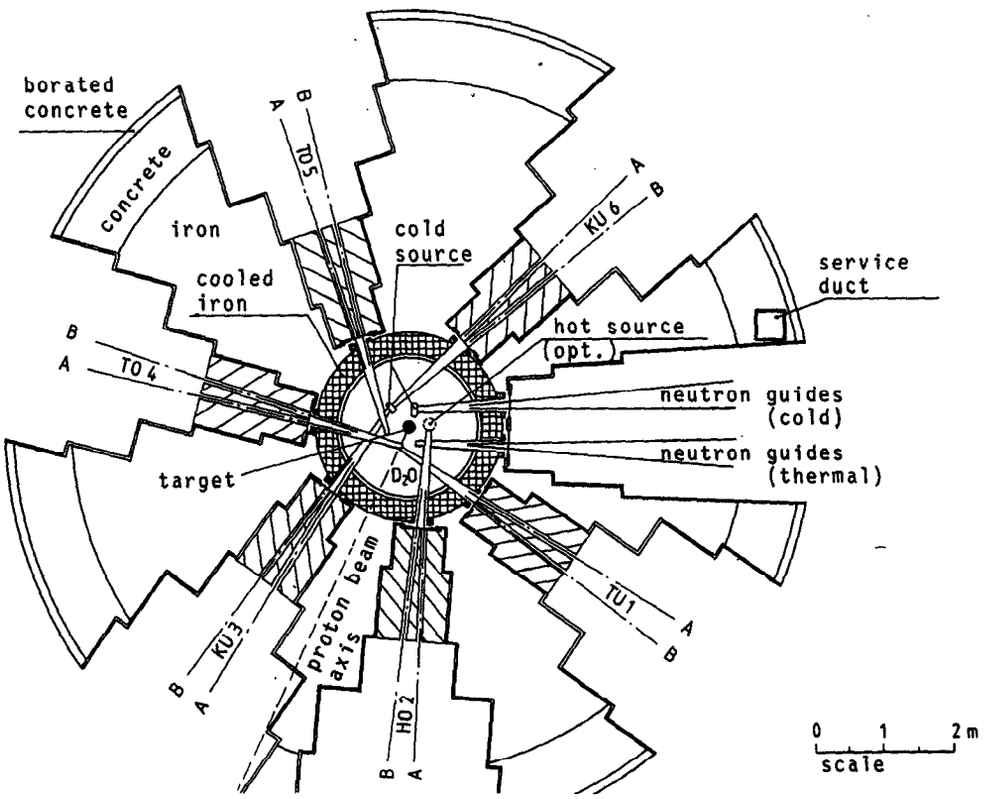

Fig. 11 A plan view of SINQ.

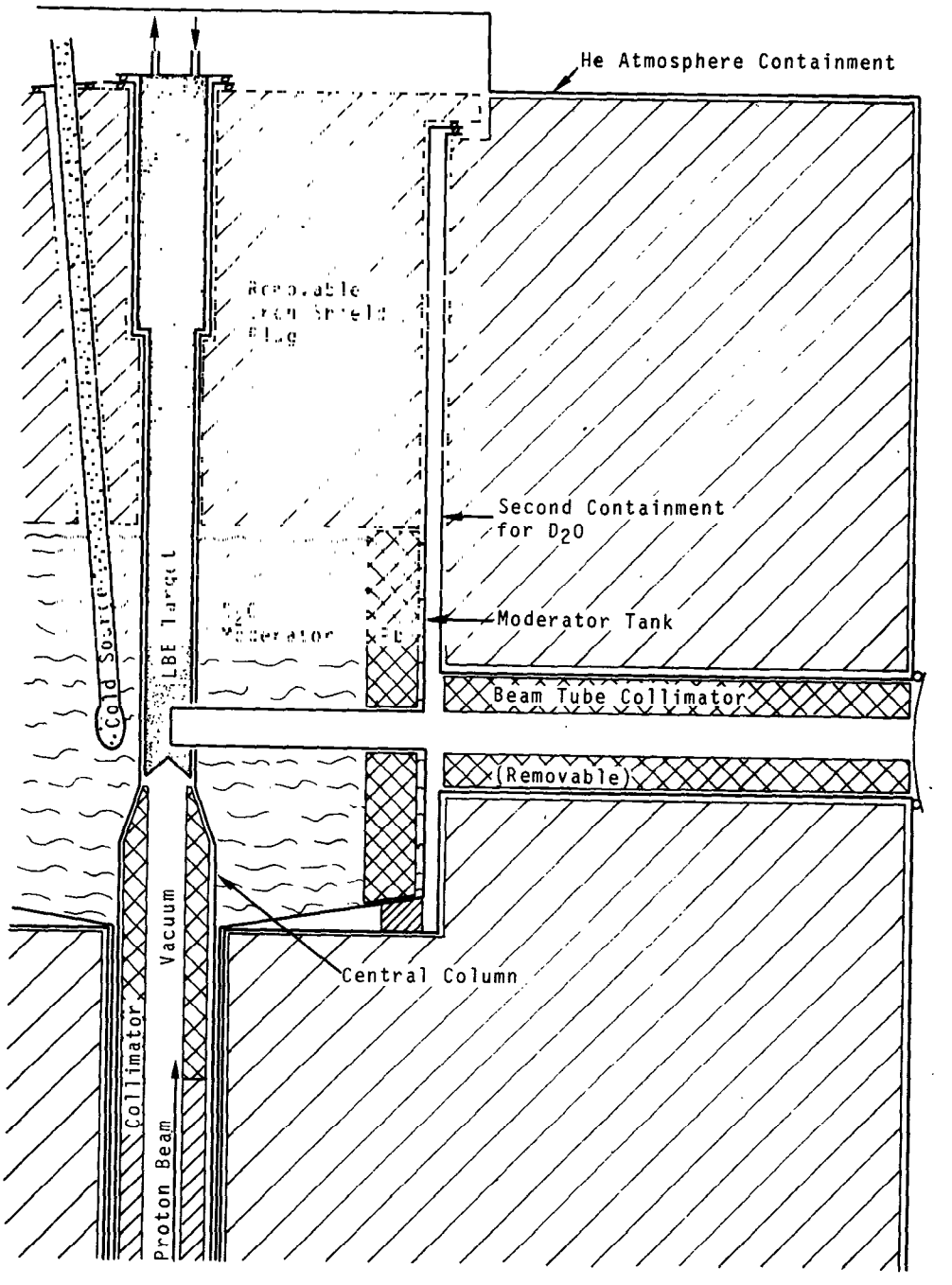

Fig. 12 A vertical cut through the central region of SINQ.

REFERENCES

1. A.J.T. Holmes, Phys. Rev. A19, 389 (1979)
2. W. Joho, Part. Accel. 6, 41 (1974)
3. Y. Takeda, Proc. ICANS-VI, 357 (1982)
4. Y. Takeda, These Proceedings
5. L. Hellwig et al., Realisierungstudie SNQ, Teil III, Annex I, JüL-Spez-113 (1981)
6. H.D. Harig, Thesis, University of Grenoble (1967)
7. D. Cribier, Private Communication (1983)
8. K. Inoue et al., Proc. ICANS-VI, 391 (1982)
9. W.E. Fischer et al., SIN preprint PR-83-09 (1983)
10. F. Atchison et al., Proc. ICANS-VI, 441 (1982)

Proceedings of International Collaboration on Advanced Neutron Sources (ICANS-VII), 1983 September 13-16
Atomic Energy of Canada Limited, Report AECL-8488

TRIUMF THERMAL NEUTRON FACILITY

I.M. Thorson, J.J. Burgerjon, R.E. Blaby and T.A. Hodges
TRIUMF
4004 Wesbrook Mall
Vancouver, B.C. Canada
V6T 2A3

Introduction

The TRIUMF Thermal Neutron Facility (TNF) has been described previously[1,2] as it was originally installed for operation in 1978. In the January/March 1983 shutdown of the TRIUMF facility the moderator assembly and target were replaced to increase the beam current disipation capability of the facility in anticipation of increased currents from the 500 MeV isochronous cyclotron. This report will outline these modifications[3,4,5] and others aimed at increasing the overall operating reliability of the TNF. Some preliminary commissioning test results of the molten target temperature distribution are also reported.

2. Moderator/Target Assembly Modifications

The most significant change in the moderator tank assembly is shown in Fig. 1; in the previous assembly the 15 cm diameter, 25 cm long stainless-steel target container sat in an open cavity at the bottom of the 46 cm diameter water moderator/coolant tank. The heat developed in the target by the residual proton beam was dissipated at the outside of the container by nucleate pool boiling of the water after transfer to the target can wall by convection of the molten lead. The pool-boiling mechanism limited the power dissipation capability of the target to approximately 50 kw based on a conservative estimate of 125 w cm^{-2} heat flux limit. To raise this limit the target design was changed to a forced flow regime by enclosing the stainless-steel target can in a secondary aluminum container with pumped H_2O cooling flow over both the front face of the target - as with the original design - and the other target surfaces. The coolant exhausts into the top moderator/coolant tank and the heat is disipated in a local external heat exchanger, as before. The new target design is estimated to be capable of dissipating 125 kw of heat. Because only about 75% of the proton beam power appears as heat in the target and the upstream meson production targets remove at least 25% of the initial beam the new target design is expected to satisfy TRIUMF's operational beam dump requirements for accelerated beams in excess of 200 kw.

The moderator/coolant assembly was replaced with one that accomodates the new, larger target assembly. The new design, like the old, has a D_2O moderator chamber below the centre plane of the target. Because no use has been made of the neutron beam tubes viewing the lower through-tube section of the D_2O moderator compartment - and none are currently contemplated - the through-tube port was eliminated to reduce the leakage from the D_2O moderator and thereby improve the flux to the existing beam tube and irradiation facilities. The other substantial change to the moderator/coolant tank asssembly was the elimination of the vertical access port to the front of the target, originally intended to accomodate a proton irradiation facility; such facilities have now been installed at a site 75 cm upstream and no further developments are envisaged.

The change to a forced-flow cooling regime for the target did introduce a complication in the cooling circuit design. The loss of pump power during high current operations leaves an inventory of heat in the target that would boil away all of the water in the target coolant channels. To avoid the uncontrolled thermal cycling that could result from the repeated voiding and reflooding (through the coolant outlet port) of the target coolant channel a standby inventory of water was installed at a height to have a pressure head comparable to the operating pump pressure. The inventory is sufficient to supply full target flow for 1-2 minutes following loss of pumping power and the

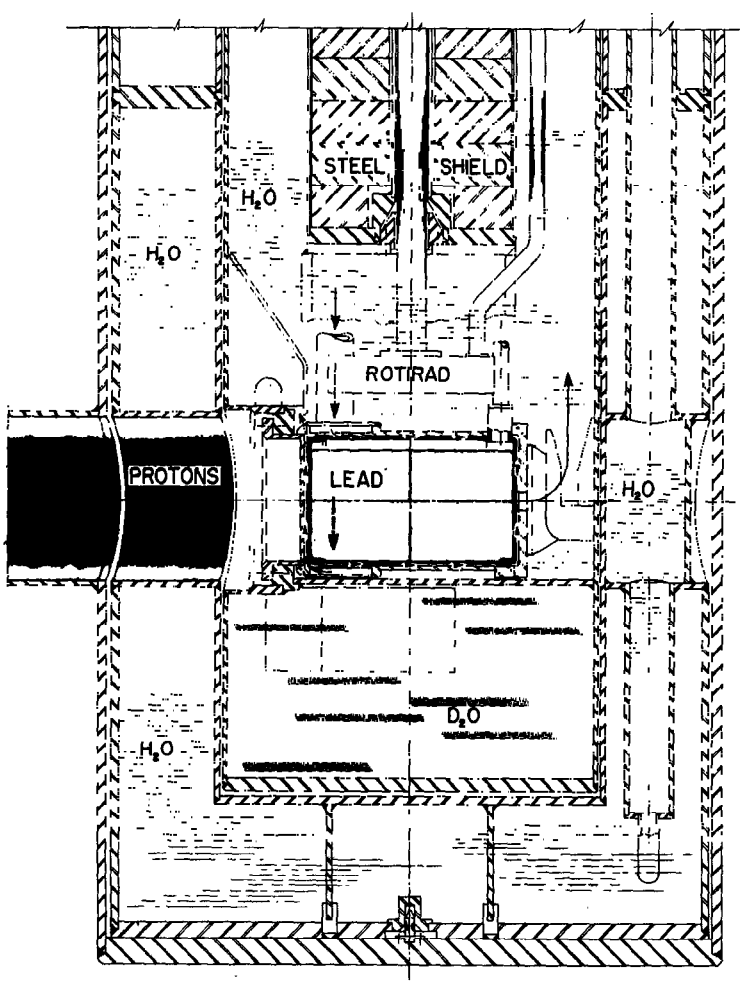

Figure 1. TRIUMF MKII TNF moderator/ coolant/target assembly

0 10 20 cm

resulting beam trip.

The first target installed in the new assembly has been extensively instrumented with thermocouples to measure the temperature distribution in the lead as a function of beam power and for varius operating conditions. Fig. 2 shows the positions of the 24 thermocouples held by thin stainless-steel baffle plates at five planes of various depths from the front face of the container.

Note that the void space at the top of the target above the lead target core is evacuated and it's pressure monitored to give an early warning of target containment failure, as in the previous design. With the exception of some minor operating problems, since rectified, with the mechanical refrigeration system used to cool the cold-traps needed to remove the volatile activities evolved from the molten lead, this monitoring system has worked well and gives us considerable confidence in the continuing integrity of the target containment system.

The design of the AISI347 stainless-steel target container was based on the ASME pressure vessel code taking into account effects of fatigue due to thermal stress and cycling, radiation and corrosion. The 347 stainless steel was chosen over the type 316 previously used on the basis of slightly better strength and thermal conductivity characteristics at the operating temperatures expected. The wall thicknesses produced by this design are reduced from the previous design to minimize the bulk lead temperature at the higher heat fluxes intended to dissipate the increased power. The least conservative design indicator was that of fatigue life time of the container wall which was estimated to be in the range of 5000 cycles; the thermal cycling rate has not been a closely established parameter of the system. We are implementing a thermal cycle monitoring system to measure not only the number but also the amplitude of the temperature variations actually experienced by the critical part of the target container.[6] The thermal stresses in the container, the dominant stress component, are estimated to peak at the onset of melting at the can wall and do not change significantly at higher power levels.

3. Commissioning Test Results

The temperatures shown in Fig. 2 were measured in commissioning tests during operations at 135 A transmitted from the cyclotron down beamline I without significant loss following removal of the meson production targets. Because of stability problems with the proton beam at these power levels there is a rather high noise level on these measurements and some of the apparent anomalies are probably not significant. The general level and rough distribution is reproducible however.

The temperatures in the molten sections of the lead are only weakly dependent on the power level and do not changing significantly between 85 and 135 μ A incident beam current. Another interesting feature, from Fig. 2, is that only small sections, if any, of the stainless-steel container walls are in contact with molten lead.

Fig. 3 shows the time dependence of the lead temperatures measured by selected thermocouples during a pump failure test. The principal operating parameter to be determined by these tests was the throttling required in the auxillary cooling line from the inventory storage tank. Because of the limited inventory the flow rate must be matched roughly to the overall heat dissipation time constant for the target to avoid coolant channel boiling. Note that the length of the temperature plateau at the lead melting point is dependent on the depth of the measuring point from the container wall, as expected.

We intend to repeat these measurements at incident beam power levels up to 150 kw as the accelerator capabilities allow.

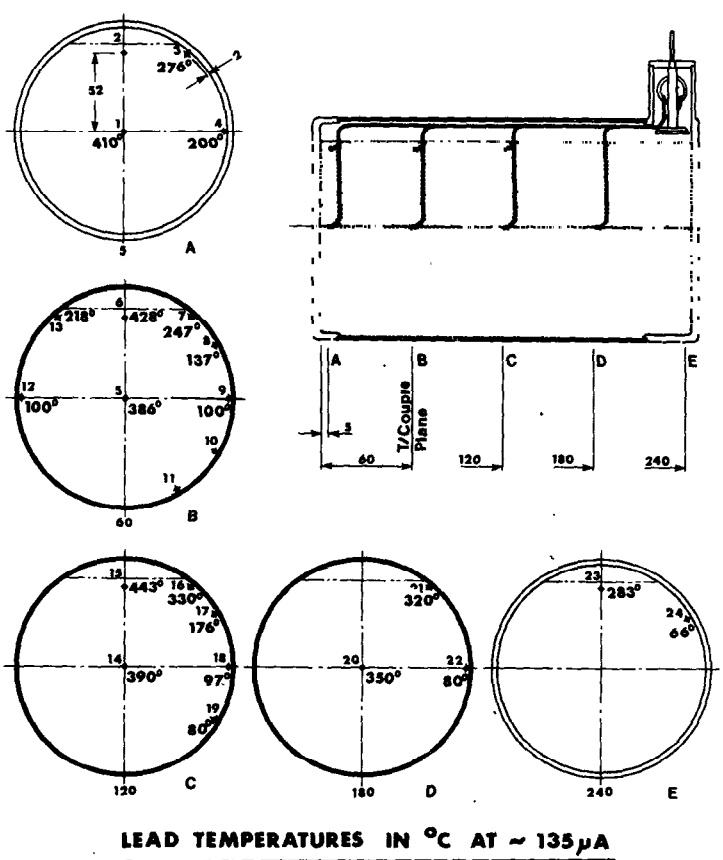

Figure 2. Thermocouple-Temperature Distribution in TNF MKII Target.

1. G.J. Russell, Proceedings of ICANS III Conference on Target Stations and Accelerator Technology, Los Alamos Scientific Laboratory March 19-22, 1979; pp.31.

2. A.S. Arrott et al, "The TRIUMF Thermal Neutron Facility as Planned for Operation in 1978" TRIUMF Report TRI-77-1 (1977).

3. T.A. Hodges, "TNF Lead Target - Thermal Analysis and Upgrading Feasibility" TRIUMF Design Note VPN-81-2 (1981).

4. J.J. Burgerjon, "Upgrading of the TNF Target," TRIUMF Design Note TRI-DN-80-10 (1980).

5. R.E. Blaby, et al, "TNF Cooling System" TRIUMF Design Note TRI-DN-86-6 (1982).

6. T.A. Hodges, "On-Line Measurement of Thermal Fatigue in the TNF Target", TRIUMF Design Note VPN-83-3 (1983).

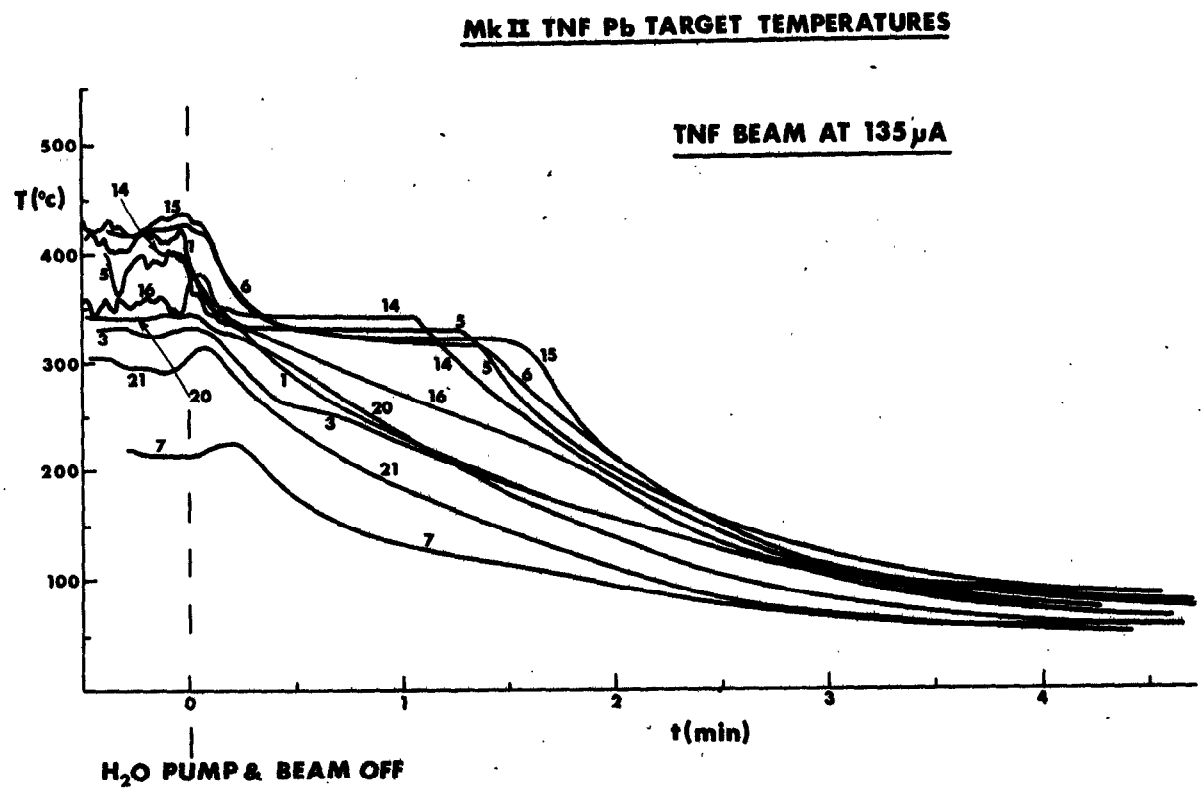

Figure 3. Temperature Decay Curves in MKII TNF Target

Proceedings of International Collaboration on Advanced Neutron Sources (ICANS-VII), 1983 September 13-16
Atomic Energy of Canada Limited, Report AECL-8488

PROGRESS ON CONSTRUCTION AND COMMISSIONING OF THE SPALLATION NEUTRON SOURCE AT THE RUTHERFORD APPLETON LABORATORY

G Manning

Rutherford Appleton Laboratory

ABSTRACT

This paper gives details of progress on the Spallation Neutron Source which is due to produce first neutrons in 1984. It updates similar reports given in ICANS-IV, V and VI. Since ICANS-VI the injector has been successfully commissioned to give 70 MeV H^- beams which have then been transported through the transfer line from the linac to the injection straight of the synchrotron.

PROGRESS ON CONSTRUCTION AND COMMISSIONING OF THE SPALLATION NEUTRON SOURCE AT THE RUTHERFORD APPLETON LABORATORY

G Manning
Rutherford Appleton Laboratory

1. INTRODUCTION

This is an update of reports given by myself at ICANS-IV and D A Gray at ICANS-V and VI. The main parameters of the SNS are given in Table 1, with a layout in Fig 1. A full description of the project is given in Ref 1.

Since the last ICANS meeting the first SNS milestone has been achieved with successful commissioning of the 70 MeV H^- injector system during January 1983. Subsequently H^- ions have been transported through the transport line from the linac to the injection straight of the synchrotron.

2. FINANCE

The financial approvals for capital have been updated to £15.58M for the machine and target station, and £2.45M for the 7 approved instruments. The update is purely for inflation. This does not include costs for staff nor for design, research and development costs. The allocation to cover all costs for the SNS in the current year is £10.15M.

Approximately £13M worth of capital equipment has been ordered for the machine and target station, and £1M for the initial instruments. The money is consistent with the planned date for first neutrons in October 1984.

3. PROGRESS

3.1 Injector and Injection System

70 MeV H^- ions were successfully accelerated in the linac during January 1983 and subsequently the beam has been transported through the transfer line over the synchrotron and back to the entrance to the injection straight of the synchrotron (see Fig 2).

TABLE 1: MAIN PARAMETERS OF THE SNS

Proton design energy	800 MeV
Proton design intensity	200 μA
Nominal repetition frequency	50 Hz
Injection scheme	H^- charge exchange
Injection interval	376 μs
Injection energy (protons)	70.44 MeV
Injected protons/pulse	5×10^{13}
Emittance H^- ions	25×10^{-6} rad m
Mean radius of synchrotron	26.0 m
Number of superperiods	10
Dipole field at 70.44 MeV	0.1764 T
Dipole field at 800 MeV	0.6970 T
Betatron tune (Q_h, Q_v)	4.31, 3.83
Beam emittance at 70.44 MeV H	$540\pi \times 10^{-6}$ rad m
V	$430\pi \times 10^{-6}$ rad m
Number of RF cavities	6
Frequency swing (harmonic No = 2)	1.34 to 3.09 MHz
Vacuum chamber in magnet	Ceramic
Target material	Depleted Uranium
Fast neutron production rate	3×10^{16} n per sec
Neutron current from surface of moderator	$10^{15} - 10^{13}$ s^{-1} $ster^{-1}$ eV^{-1} (.01 eV - 1 eV)

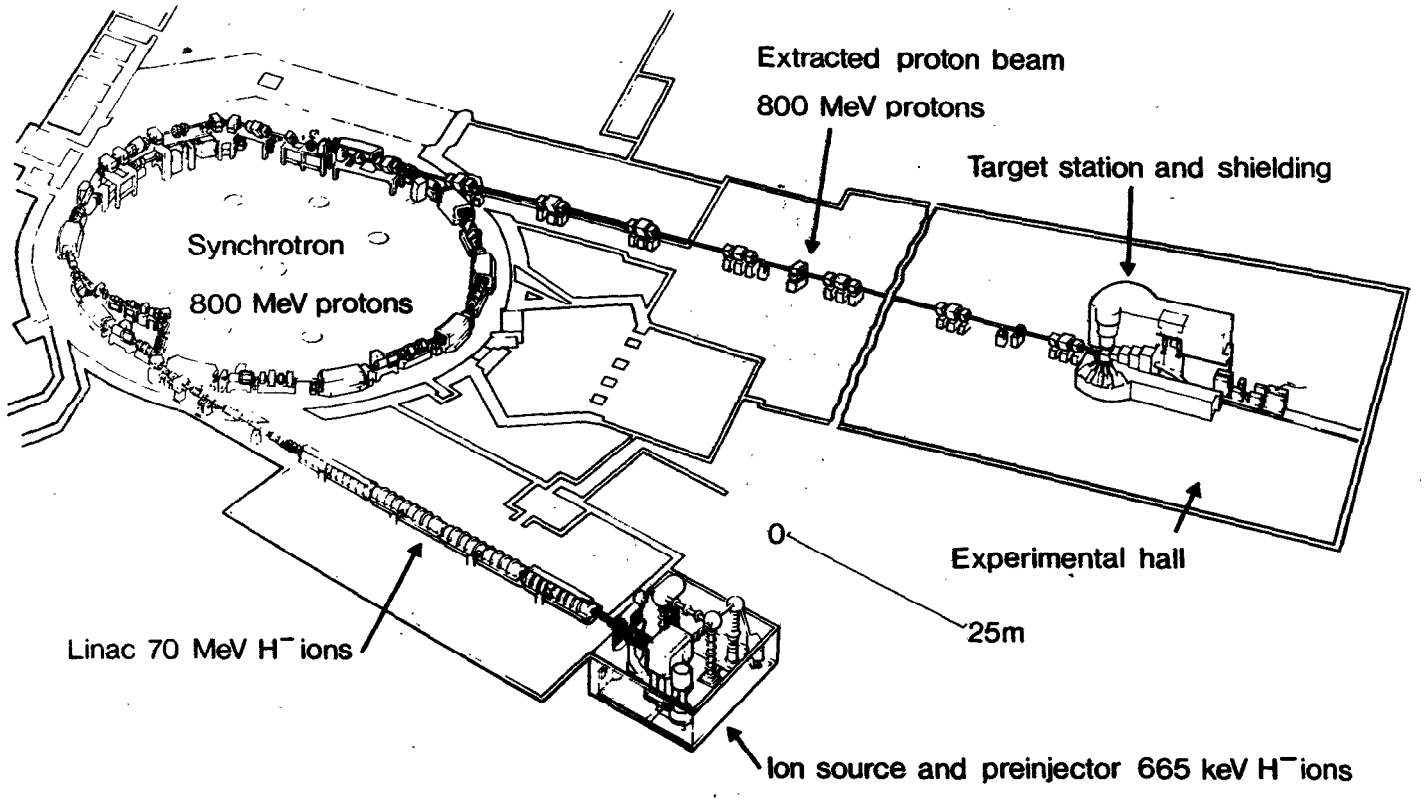

FIG 1 : LAYOUT OF THE SNS

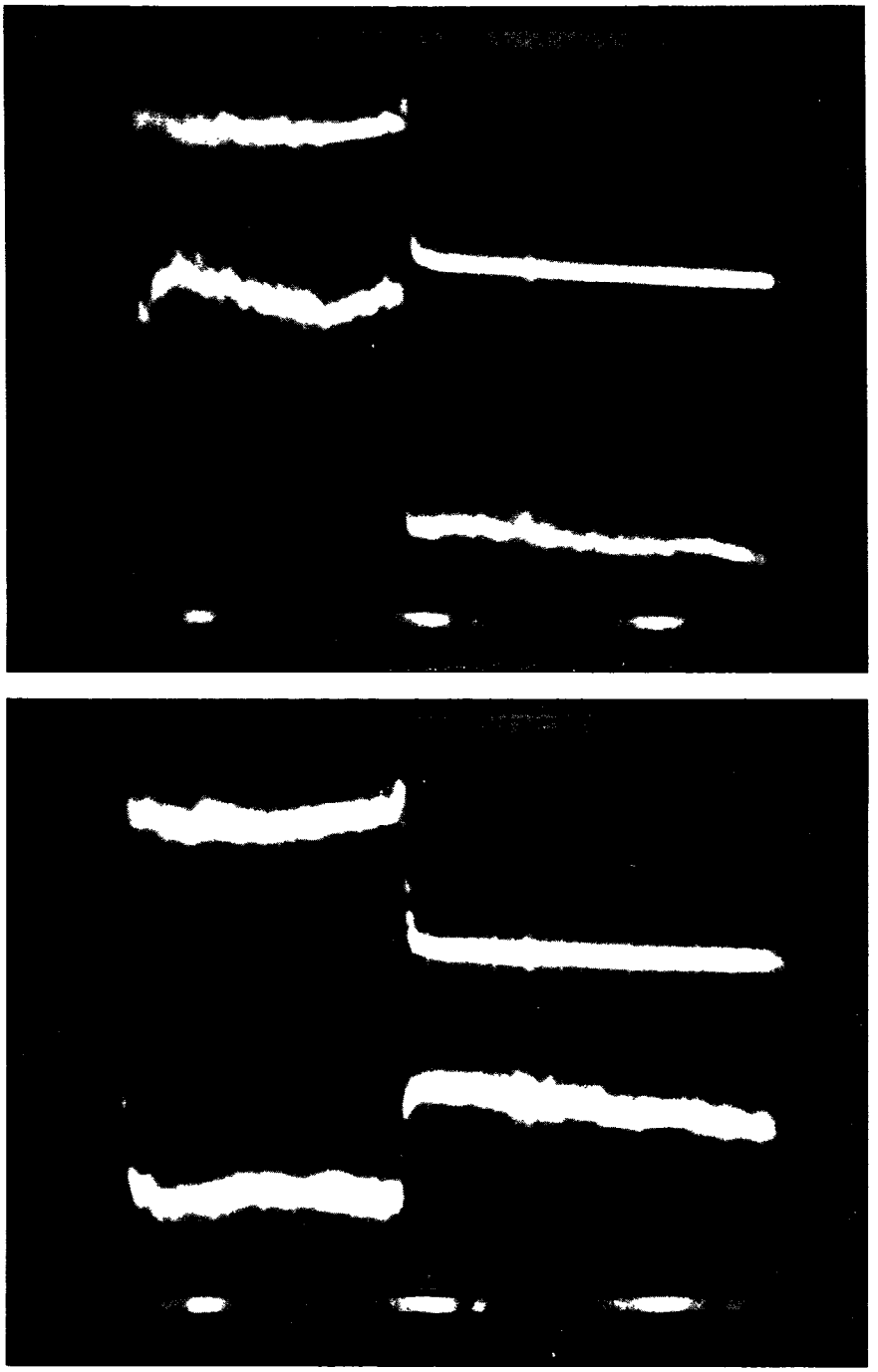

FIG 2 : FIRST 70 MeV H^- BEAM

Top trace - Input to Tank 1 4mA
Second trace - End of linac. 70 MeV foil out.
Third trace - Input to Tank 1
Bottom trace - End of linac. 70 MeV foil in.
Pulse length - 200 μs

The linac transmission is as expected with the buncher operational, viz 60%. The matching into the linac and the linac quadrupoles have been adjusted so that the beam loss is not measureable along the length of the higher energy part of the linac. To reduce induced activity levels in the 70 MeV beam stop the mean current during tests is kept to a maximum of 1 A (400 A mean is the design requirement). Pulsed currents of 3-4 mA have been used, the mean current is kept down by shortening the pulse length and reducing the repetition rate to typically 50/32 pps. The ion source arc is kept running at 50 pps. Ion source lifetime has been determined by the amount of caesium put into the caesium boiler. In one case 1 g of caesium lasted 120 hours of actual running. Another lasted 130 hours and is still working.

Emittances of the beam have been measured as follows for 99% of a 3 mA beam at 70 MeV:

	Horizontal	Vertical
Typical	12.5 π μmr	25.0 π μmr
Minimum measured	9.5 π μmr	10.2 π μmr
Specification (at 20 mA)	25.0 π μmr	25.0 π μmr

The linac is currently capable of producing enough 70 MeV beam to give about 30% of the design SNS high energy current.

Diagnostic devices in the linac and transfer line include toroids and 14 profile monitors using a scanning wire device to give horizontal and vertical profiles at each location.

The profile monitors are used for measuring emittance and steering and transfer matrix measurements in the transfer line and, by normalisation, can measure beam currents since the high vacuum quality toroids close to the synchrotron are not yet available.

A 'straight-through' branch of the transfer line at the final bending magnet is equipped with a scintillator and raster scan TV camera. The chopper, which will eventually be used to provide half-circumference length pulses in the synchrotron for injection studies, has been used to produce short pulses to prevent overheating of the scintillator. Beam has also been put down the third branch destined to be used, in collaboration with GSI, Darmstadt, for studies relevant to heavy ion fusion.

For the injection system, the septum magnet and its power supply are available. The 4 beam bump magnets have been installed in the injection straight. The power supply which supplies 14,000 A, 500 s long pulses at 50 pps is over a year late. It has passed its performance tests at the manufacturers and delivery is expected during August.

A batch of 5 stripping foils of the correct size have been successfully made. A further batch of 20 is being made.

It is planned to run a test of beam into a foil with the bump magnets powered some time during September.

3.2 Synchrotron ring

All components required for the next milestone, injection and trapping studies, are to hand except for the dipole magnets. The ring is expected to be ready for injection at the end of the year. Three of the 10 dipoles have been delivered and have successfully passed power tests. The effective magnetic lengths at both injection and extraction field levels were within ±0.5 mm as in the specification.

Supports for all synchrotron components are in position. Straight section components are being aligned without the aid of the bending magnet datum points. One straight section is completely installed with all vacuum joints made. A decision has been made that the ring will not be vacuum tested in sections following a satisfactory test on a section including the roughing line. Fitting together the modules especially those with RF shields and their associated capacitor rings requires careful work.

Trial fittings of the RF shield in the curved ceramic dipole vacuum vessel has been done to evolve the system for the production dipole installation.

Main ring diagnostic devices are installed in the ring, including position monitors, intensity monitors, profile monitors and a kicker magnet system for exciting betatron oscillation. Beam loss collectors will be installed initially for beam lost horizontally up to about 100 MeV. Ionisation chambers for beam loss detection will be installed around the ring (as well as along the injector and injection and extraction lines).

3.3 Magnet power supplies

Final wiring of the main magnet resonant power supply is in progress. The new make-up power supply consisting of a DC motor and singe phase alternator has been successfully run. The computer-controlled supplies for the trim quadrupole magnets are installed.

3.4 RF System

The next milestone requires 2 of the 6 RF systems for trapping studies. Two cavities have been installed in the synchrotron room. RF amplifiers have been built and are being installed. The 6 anode power supplies have been installed and tested into a dummy load. A potential problem of spikes into the mains from these supplies has been shown to be of no concern. Operation of the crowbar circuit of one supply does not trip another supply. Controls and ancillary supplies for two systems are ready for operation. The DC power supplies for the bias windings are installed. Trials on the prototype bias transistor regulator of about 50 kW showed a good frequency response. The first production regulator is installed. Sufficient low power RF equipment is available for the first system tests which are now in progress. Manufacture of the remainder of the four systems is proceeding well.

3.5 Services

Many raw water, demineralised water and chilled water systems have been installed and commissioned on systems as required.

3.6 Extraction

The extraction system consists of 3 kicker magnet systems with rise time of some 200 ns and a septum magnet to give a vertical deflection to the beam. Installation of the kicker power supplies is in hand. Each kicker is powered by two thyratron switched bumped delay lines. One complete system has been commissioned and is successfully powering one of the kicker magnets through the correct length of feeder. Boxes for the kicker magnets are being manufactured.

The septum magnet has been designed following work on a model to obtain field uniformity and sufficiently small fringe field into the working region of the synchrotron. The septum magnet power supply is installed but not yet wired up. The milestone date for extraction tests with 550 MeV protons is July 1984.

3.7 Extracted proton beam

The extracted proton beam takes the beam above and outside the synchrotron, back to target height through a shielded tunnel to the target.

The concrete plinths for supporting the beam components in the synchrotron room have been installed. The special bending magnet which comes after the extraction septum magnet to turn the beam horizontal has been manufactured and tested and is installed in the synchrotron room. Other components are being manufactured. The tunnel shielding walls have been installed and lined with concrete.

3.8 Target station

The progress on the target station will be reported in detail at this meeting by A Carne. Briefly:

i) Uranium target plates for 2 targets have been ordered.

ii) The target void vessel which contains the target, moderator, and reflector assembly is to be delivered in August.

iii) Target station main shield is being installed. Shielding wedges which support the neutron shutters have had a trial installation. Shutters are being delivered.

iv) The Remote Handling Cell and the Services area are being built up.

v) Refrigerators for the liquid hydrogen and liquid helium moderators have been ordered.

An important conclusion from the safety assessment is that the target plates will not melt, even if all cooling systems fail, provided the proton beam is turned off as soon as a fault condition is detected.

3.9 Controls

The controls system of 4 linked computers is being installed in a phased manner. The linac system has been used for the commissioning work on the linac. Many equipment designers are writing control programmes in the high level interpretive language 'GRACES'. Tuning of the system software has gone along in parallel.

4. SNS EXPERIMENTAL FACILITIES

Technical and scientific details of the first batch of SNS instruments were given at ICANS IV.

4.1 Liquids and Amorphous Materials Diffractometer (LAD) and High Throughput Inelastic Spectrometer (HTIS) - both LAD and HTIS are now in operation at the Harwell linac and will be transferred to SNS in the Spring of 1984.

4.2 High Resolution Powder Diffractometer (HRPD) - this is well advanced. The building is about half complete. The sample and detector tanks have been made, the glass guide tube sections have been delivered and the first octant of the scintillator detector is being tested. Completion is expected early in 1984 with final alignment of the guide in July 1984.

4.3 High Energy Transfer Spectrometer (HET) - the sample and detector tanks are nearing completion, the low angle ^{3}He counters have been delivered and a low cost, low background, scintillator detector module has been developed for use in the high angle bank. Completion is expected on the same time scale as HRPD.

4.4 Low Q Spectrometer (LOWQ) - a design change has recently been introduced, substituting a heavily shielded, supermirror bender for the in-shield nimonic chopper as a means of removing the high energy neutron background. Detailed design is just starting and completion of a 10 m long initial detector tank and part of the large scintillator detector is planned for Day One operation.

4.5 High Resolution Inelastic Spectrometer (IRIS) - the incident beam guide tube and disc choppers are being provided for Day One to serve a Be-Be window spectrometer being built by the Bhabha Atomic Research Centre (BARC) in India. IRIS itself will be provided in 1985.

4.6 In addition to the above, three development instruments will be built, viz: the polarised neutron spectometer POLARIS, using a polarising filter; an eV spectrometer using filter difference techniques and a single crystal diffractometer using an Anger Camera scintillator detector.

4.7 Development work on sample environment equipment such as cryofridges, sample changers etc is nearing completion and a batch of equipment for Day One operation has been specified.

A VAX 750 computer has been installed as a HUB computer together with the first three VAX 730's as Front End Mini Computers. Software development is now well under way.

5. FOREIGN PARTICIPATION

An agreement has been signed with BARC, India, for the supply of a beryllium window spectrometer for the High Resolution Inelastic instrument. In exchange, the BARC will have running time on this and other SNS instruments.

Instrument proposals have also been prepared by scientists from Italy (Constant-Q spectometer), Germany (inelastic crystal spectometer) and the Joint Research Centre Ispra (general purpose spectometer for radiation damage studies), and discussions are being held to define similar arrangements

Agreement has recently been reached with KFK, Karlsruhe, to provide a blockhouse and instrumentation for a neutrino experiment costing some 12 million DM. Engineering work on the foundations for the blockhouse and modifications to the experimental hall will start soon.

As part of a collaboration with KFA, Julich, six people from Julich are spending 6 months each working on the SNS. Also KFA and RAL are collaborating on studies of shielding of neutron lines at spallation sources.

6. OTHER USES OF THE SNS

A test beam for using secondary particles produced by high energy protons lost in the synchrotron is being installed.
An irradiation facility is being installed in the target void vessel for tests on materials where it is important to have a lower background of slow neutrons than in reactor irradiations.

A study has been made of a μSR facility derived from a transmission target in the extracted proton beam. This would be a very powerful facility. However funds are unlikely to be available initially for this. A simple test facility which will produce muons is being investigated.

7. DEVELOPMENT OF THE SNS

Until the SNS has run and it has been shown that losses in the synchrotron can be kept well below 1% at full energy, there is no point in a lot of work being done on increasing the SNS current using a new injector. Potentially bigger improvements to the SNS, particularly for lower energy neutrons, say at 4Å can be made by improving target arrangements. Two examples being studied in a collaboration between KFA Julich and RAL are a booster using a sub-critical target and a redesign of the existing SNS target system using fissile material. This will be reported in more detail at this meeting in a presentation by RAL/Julich.

8. CONCLUSION

The SNS is well on target to produce first neutrons in 1984 with some seven instrumental facilities. Foreign participation is welcome and is happening. There is good potential for an improvement to the SNS target arrangements which would be likely to yield up to a factor 10 improvement in useful neutron yields especially for slower neutrons.

9. ACKNOWLEDGEMENTS

I have reported here on the work of many people at RAL.

References

1. Spallation Neutron Source: Description of Accelerator and Target.
B Boardman (Ed). RL-82-006, March 82.

Proceedings of International Collaboration on Advanced Neutron Sources (ICANS-VII), 1983 September 13-16
Atomic Energy of Canada Limited, Report AECL-8488

STATUS REPORT AND FUTURE PLANS OF THE INTENSE PULSED NEUTRON SOURCE - ANL

G. H. Lander, J. M. Carpenter, R. L. Kustom, and T. K. Khoe

Argonne National Laboratory
Argonne, Illinois 60439

Abstract

A brief report is given of the status and current research at the Intense Pulsed Neutron Source (IPNS) at Argonne National Laboratory. Future plans for this facility involve an upgrade of the instruments, the installation of an enriched uranium (booster) target, and the construction of a small accelerator to serve as a prototype for a much more advanced source and, at the same time, deliver five times more protons to the IPNS facility.

Introduction

IPNS has been operating successfully since November 1981, and a number of new areas of science have begun to emerge. Some of these are now documented in the open literature and others are in preparation. Extensive reviews exist in the Proceedings of ICANS-VI[1] (July 1982) and the Yamada Neutron Scattering Conference[2] (September 1982). Other reviews from IPNS[3] are also available to the interested reader. In view of this, we shall confine to a minimum our remarks on condensed matter science now being performed at IPNS and use the remainder of the space to a discussion of future plans. Specifically, these include increasing our instrument capability with the building of an eV spectrometer, a quasielastic spectrometer on the cold source, and a major up-grading of the small-angle scattering diffractometer, also on the cold source. The second stage is the installation of an enriched (booster) target in the IPNS system and the third stage involves the building of a new accelerator, designed to deliver 100 μA at 500 MeV.

Present Scientific Activities at IPNS

Much of our emphasis at IPNS is on the use of epithermal neutrons. With the two powder diffractometers[4] a large number of structures are being solved with polycrystalline samples. The unique aspect of these diffractometers is the extremely high resolution ($\Delta d/d \leq 0.3$ %) which is independent of Q, the momentum transfer, and the availability of a complete Rietveld analysis methodology. An excellent example is given in Fig. 1. Another way of using the high resolution has been on simple systems that have been deformed. Examples here are determinations of residual stress in zircaloy[5] and tungsten carbide cermets.[6] Very small line shifts can be measured corresponding to strains of a few parts in 10^5. The single crystal diffractometer[7] is based on the Laue technique with an Anger type position-sensitive detector[8] and has continued to be used for solving crystal structures[9] and looking at the development of satellite reflections in reciprocal space. An example is given in Fig. 2. The small-angle diffractometer has been used for metallurgy (although until the cold source is operational this is severely limited), biology, and polymer science. An example of a biological program examined is given in Fig. 3. In the field of inelastic scattering the two chopper spectrometers[10] continue to perform extremely well. A major program concerns the study of single particle n(p) distributions using high energy (500 meV) incident neutrons. So far the most studied system is ^{4}He by the group from the University of Illinois.[11] Other interesting experiments concern S(Q,ω) distributions in amorphous systems, such as SiO_2, illustrated in Fig. 4. Again there are unique features here associated with being able to use very high incident neutron energies, and thus obtain large energy

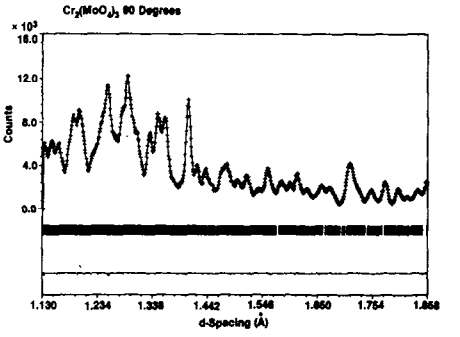

Fig. 1 Neutron diffraction study of chromium molybdate using the General Purpose Powder Diffractometer (GPPD). The + signs are experimental data after background subtraction. The solid curve is the calculated pattern. The vertical ticks show the positions of the independent hkl's in d-spacing. The differences between the data and calculation are plotted in the lower portion of the Figure. (A. K. Cheetham and P. Battle, Oxford University)

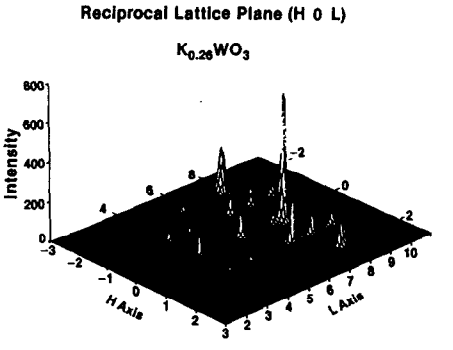

Fig. 2 Reciprocal lattice plane (HOL) of $K_{0.26}WO_3$ as observed below the phase transition with the single-crystal diffractometer. Superlattice reflections can be seen around some of the Bragg peaks and, in addition, there are weak peaks at positions with L odd, which denote a loss of a glide plane in the structural symmetry. Since these were not seen with x-rays they indicate shift of the oxygen atoms (B. Krause and G. Anderson, Northern Illinois University, and A. J. Schultz, ANL)

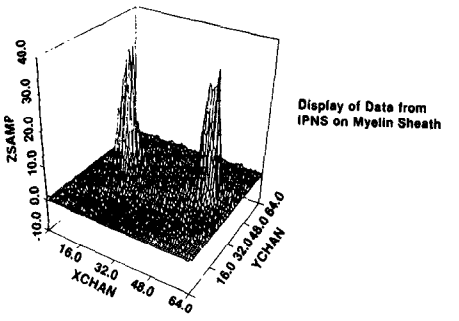

Fig. 3 Bragg peaks from a d-spacing of 87 Å as registered on the small-angle diffractometer from a sample of myelin sheath from a rat sciatic nerve. (D. Worcester and L. Braganza, Institit Laue Langevin, Grenoble)

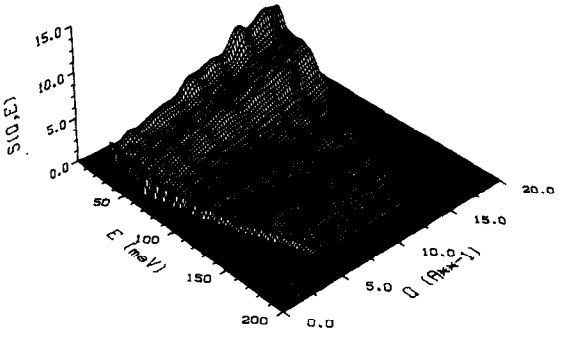

Fig. 4 The dynamic structure factor S(Q,E) of vitreous SiO_2 at 30 K, measured using the Low-Resolution Medium-Energy Chopper Spectrometer with 218 meV incident neutrons from IPNS. The data exhibit the overall Q^2e^{-2W} dependence expected for one-phonon scattering; at lowest energy transfers the intensity is due to oxygen atom rocking motions. Peaks at higher energy transfers are due to Si-O-Si group motions. The Q-dependent modulation of intensity contains information about the relative displacements of atoms in each mode of vibration. (J. M. Carpenter, D. L. Price and C. A. Pelizzari)

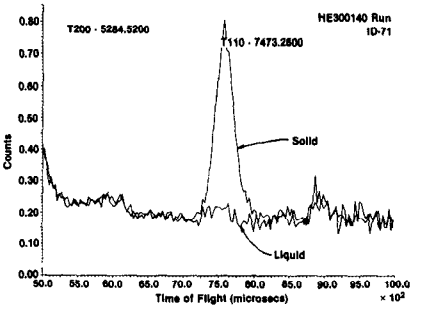

Fig. 5 Spectrum of liquid and single crystal ^3He as recorded in a single detector at the ultra-low temperature facility. The large peak is the (110) Bragg reflection from a crystal of ^3He at 0.010 K. (P. R. Roach, S. K. Sinha, B. K. Sarma and M. Vrtis, ANL and Northwestern University, and K. Skold, Studsvik, Sweden)

transfers, $\hbar\omega$ or E, at small momentum transfers Q. This is particularly important for magnetic problems, since the signal diminishes rapidly with Q, and a good example is the observation of a crystal-field transition at 130 meV in PrO_2.[12] The crystal analyzer spectrometer has been primarily used for H-mode spectroscopy. In addition to the above scattering instruments that are open to the user community, there are also 3 special beam experiments at IPNS. The effort on polarized neutrons initially focussed on development of the spin refrigerator, an ingenious method for polarizing a white (polyenergetic) beam of neutrons,[13] and is now being set up to measure the change in refractive index superconductors as a function of neutron wavelength and thus field penetration.[14] A large collaborating group is attempting to measure the nuclear spin ordering in ^3He below 1 mk. They recently succeeded in growing single crystals of ^3He and seeing a Bragg reflection, convincingly demonstrated in Fig. 5. Another effort is aimed at producing ultra-cold neutrons from a pulsed source by Doppler-shifting the neutrons with a large d-space mica crystal.[15]

The substantial effort on radiation damage at IPNS will not be discussed here, as it is covered in detail by Kirk in these Proceedings.

Future Plans in Scattering Instruments

The most immediate need at IPNS for the SAD, polarized beam and ^3He projects is a cold source. Our first attempt at a cooled (20K) methane moderator was not successful. We will have an 80K moderator source operating in October 1983 and are planning a new low-temperature moderator. The 80K moderator will already provide a substantial gain in the longer (4-6 Å) wavelength neutrons. [See paper by A. W. Schulke et al. in this Proceedings.]

At present, construction is taking place on the eV spectrometer designed to use high energy neutrons (> 1 eV) by counting secondary particles (initially γ-rays from the 4.28 eV Ta resonance) when the n-γ reaction takes place in a thin absorbing foil. Optimum use has been made of experience with machines of this kind at Harwell[16] and KENS, Japan,[17] although it should be realized that this kind of neutron spectroscopy is completely new. The ANL spectrometer should be operational late in 1983.

A new instrument to be built at IPNS is a quasielastic spectrometer. Plans for this are now in a preliminary state. This technique has been of special significance in chemical studies, often complementing either NMR or conventional neutron spectroscopy. At KENS the quasielastic machine, LAM-II, is based on inverse geometry with graphite monochromators and has a resolution of ~ 20 μeV.[18]

Target Development

With present proton currents (12 μA) and currents we envision in the near future (~ 16 μA), the heat-transport capabilities of the depleted-uranium targets and cooling systems of IPNS are not severely taxed. (They were designed[19] to operate with maximum center temperatures of 330°C at a current of 22 μA of 500 MeV protons.) We have begun an effort to provide higher neutron production rates and higher neutron fluxes by installation of a ^{235}U-enriched target.

Preliminary studies based on HETC-VIM calculations, indicate that a target identical in size to the present ones, decoupled from surroundings to maintain a short response time by 1.7 x 10^{22} $^{10}B/cm^2$ and with 65% ^{235}U, would have an effective multiplication

factor k_{eff} = 0.82, thus a nominal prompt-neutron gain factor $G = 1/(1-k_{ef}) \approx 5$. The pulse shape determined from the Monte Carlo simulations is not significantly broadened for energies below about 100 eV. The increase, above that for the depleted-U case, in slow-neutron beam current is about a factor 3.5. This is presumably because the distribution of primary spallation source neutrons is not identical to that of the fundamental multiplying mode of the booster. We estimate that the total power in the target would be about 100 kW for such a booster. Addition of about 1% ^{149}Sm to the alloy eliminates conclusively the possibility of thermal criticality. More-detailed KINO code studies now in progress indicate that $k_{eff} \approx 0.95$ if the ^{10}B layer were not present - we expect this to be a significant safety question. We find that the main influence upon the generation time is the water surrounding the target, with the specified ^{10}B layer, the prompt neutron generating time is 30 nsec. Assuming a total 100 kW power, distributed in part as in the depleted-U target and the remainder as in the fundamental booster mode, requires a minimum disk thickness of 12 mm. This minor reduction from 25 mm is due to the broader power-density distribution in the booster case. Fabrication procedures identical with those used for depleted uranium disks should be appropriate. Detailed studies of a loss-of-coolant occurrence indicate that the multiplying target cannot reach a temperature such as to melt the uranium (1100 C) or zircaloy cladding. Indications are that sufficient margin may exist in this respect, so that loss of coolant need not preclude continued use of the target. Delayed neutrons will increase from their present fraction (assumed to be the same as in ZING-P´) of 0.0053 to about 0.03, and we expect this to be tolerable background in most experiments since no instrument scientists have yet sensed any effect of the present delayed-neutron level. The additional neutrons will require only minor shielding changes (mostly at choppers and beam stops) since the neutron gain is entirely in easily-stopped fission neutrons.

Technical studies now in progress are aimed to refine the calculation of the loss-of-coolant temperature transient, to optimize the coupling of booster to the primary source (by changing target dimensions) and estimate more accurately the power density distribution and slow-neutron beam currents. Safety-and-security-related studies planned to begin shortly will address questions of criticality and security during fabrication, assembly and installation.

Detailed design will follow completion of these preliminary analysis and has not begun. A somewhat-optimistic estimate of the time when the booster will be installed is in early calendar year 1985.

Argonne Super Pulsed Spallation Neutron Source

Argonne Super Pulsed Spallation Neutron Source (ASPUN)[20] is a facility concept being studied at Argonne that would provide greater than $10^{17}n/cm^2$-sec in the 1 eV range. ASPUN is described in another paper at this conference. Argonne has concluded that a small-scale prototype could be built onto the IPNS facility affording critical tests of the principal ASPUN ideas and at the same time make an important increase in the scientific capabilities of IPNS.

The Mini-ASPUN plan uses a 500 MeV Fixed-Field Alternating Gradient (FFAG) accelerator[21] as the proton source. An FFAG accelerator has dc excited magnetic fields which increase with radius as $(R/R_o)^k$. Beam is injected into the inner radius, and as it is accelerated the equilibrium orbit radius grows to a larger value. Frequency modulated rf cavities are used to accelerate the beam following a voltage and frequency program that tracks the beam energy. The final energy is reached at the maximum radius, and beam is extracted in one turn.

Mini-ASPUN uses the IPNS 50 MeV Linac, 50 MeV transport line, 500 MeV transport line, and target. A plan view ov the IPNS facility with the 500 MeV FFAG drawn in place is shown in Fig. 6. The design goal for the average proton current of the 500 MeV FFAG is 100 μA.

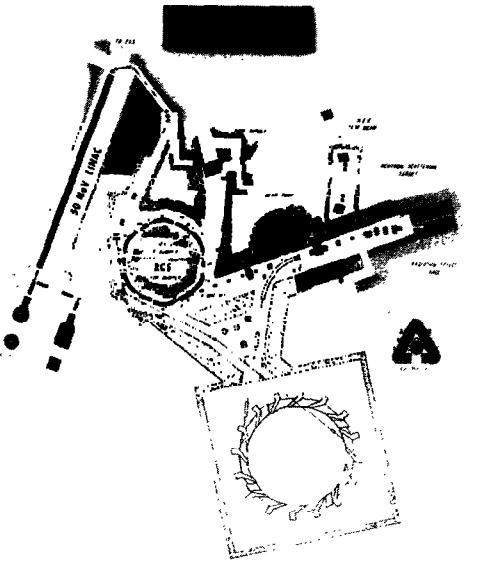

Fig. 6 Schematic of the proposed IPNS System including the mini-FFAG.

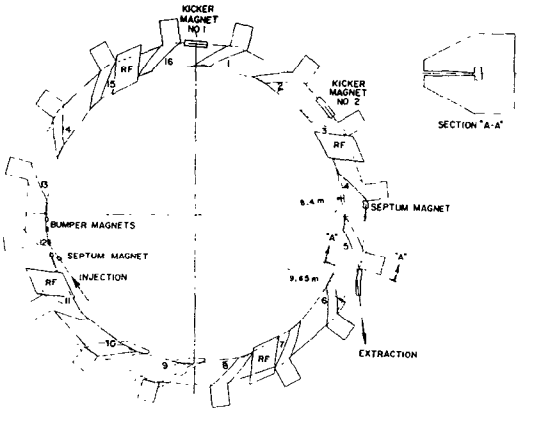

Fig. 7 Schematic of the 500 MeV FFAG ring.

A plan view of the 500 MeV FFAG ring is shown in Fig. 7. A table of parameters is given in Table 1. A total of 16 magnets are equally spaced around the ring. The combination of the entrance and exit edges and the field gradient in the magnet generates the transverse focusing in the vertical and horizontal planes. Each magnet and straight section corresponds to one cell of an accelerator lattice that is a DFFO configuration in the horizontal plane. Since there are sixteen magnets, there are sixteen identical lattice cells.

The injection scheme is $H^- \rightarrow H^+$ stripping using four bumper magnets and a septum magnet. A plan view of the injection is shown in Fig. 8. The dashed line indicates the normal unperturbed equilibrium orbit. The dot-dash line indicates the perturbed or bumped orbit produced by the four bumper magnets. The bumper magnet and septum magnet fields are reduced during injection to spread the beam more uniformly in space to reduce the space charge effect.

Table 1. FFAG for Mini-ASPUN

Injection Energy	50 MeV
Extraction Energy	500 MeV
Injection Radius	8.4 m
Extraction Radius	9.65 m
Injection Field	0.489 T
Extraction Field	1.5 T
Number of Sectors	16
Angular Width of Sectors	5.625°
Field Index, k	8
Spiral Angle, ξ	57°
Radial Betatron Frequency, ν_x	3.25
Vertical Betatron Frequency, ν_z	2.3
Space Charge Limit	4×10^{12}
Radial Beam Emittance @ 50 MeV	170 π mm-mr
Vertical Beam Emittance @ 50 MeV	120 π mm-mr
Frequency Range	1.784-3.748 MHz
Maximum RF Voltage per Turn	60 kV
Harmonic Number	1
Average Current	100 μa
Repetition Rate	180 Hz

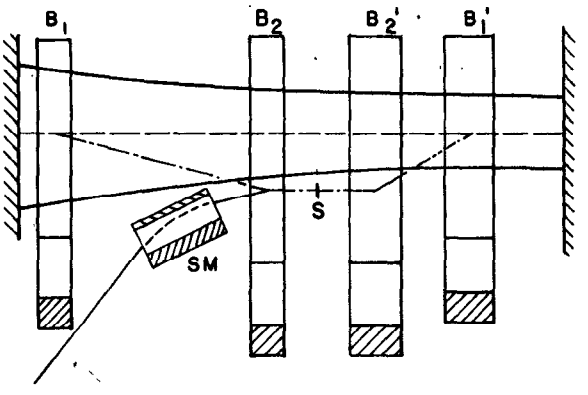

Fig. 8 Injection system showing four bumber magnets (B), Septum Magnet (SM), and Stripper Foil (S).

The 50 MeV linac would be operated at 180 Hz with a short beam pulse of about 50 μsec. The space charge limit is 4×10^{12}. The rf voltage and frequency programming technique will be the same as that described for the 1100 MeV FFAG in the full sized ASPUN except that only 60 kV total rf voltage is needed. This will be accomplished with four rf cavities spaces around the ring as shown in Fig. 7. The injection radius is 8.4 m and the extraction radius is 9.65 m. The spiral angle is 57° and the angular width of each magnet is 5.625°. The magnetic field in the magnet increases with average radius by the amount $B = B_o(R/R_o)^8$. The repetition rate will be 180 Hz. Internal stacking will be done by merging six pulses so that the extraction repetition rate will be 30 Hz. The betatron tune in the horizontal plane is 3.25 and in the vertical plane is 2.3. The magnetic field at the injection radius is 0.489 T and at extraction radius is 1.5 T. The magnet gap is 18 cm out to the 9.0 m radius, then contracts to 9 cm at the outside edge of the magnet.

One turn extraction will be accomplished using fast ferrite kicker magnets on the outside edge of the ring. The kicker magnet shown in straight section 16 of Fig. 7 kicks the beam inwards by 10 mrad. The beam undergoes an inward betatron oscillation for half a period. The second kicker magnet in straight section 2 produces an outward kick of 10 mrad. The extracted beam then enters the septum magnet in straight section 4 and finally the bending magnet outside of straight section 5. The pulse width will be about 140 nanoseconds. The fast ferrite kicker magnets are each 1 meter long and operate with 0.019 T-m integrated B-dℓ field. The septum magnet is 0.7 m long and operates with a 0.23 T field.

Several important elements of the full-sized ASPUN project will be tested on Mini-ASPUN. In particular, these include the development of magnets, highly efficient adiabatic capture, acceleration, and extraction, and internal stacking.

Transverse focusing of the beam in the ASPUN accelerator is provided by a combination of the entrance and exit edge angles and a radial gradient of the magnets. It is essential in the design of the machine that the fringing fields and edges can be accurately controlled so that the transverse betatron oscillations are sufficiently constant to avoid beam loss due to resonances. There are good reasons to believe that necessary accuracy can be achieved by coil shaping, shimming, and edge coils. Mini-ASPUN will provide the opportunity to test these various techniques and to determine the most flexible and easily controllable combination.

The injection efficiency needs to be exceedingly good or effective beam loss collectors need to be developed to avoid irradiation and damage to the machine components. Mini-ASPUN will provide the opportunity to perfect the rf voltage and frequency hardware and control to achieve theoretical predictions or to develop alternative approaches.

Beam stacking is required to reduce the external beam repetition rate of the ASPUN accelerator to a rate (~ 30 - 100 Hz) that is desired by many of the solid state science experimenters. Again, Mini-ASPUN provides an excellent research vehicle to develop this technique.

Mini-ASPUN will allow the development, testing, and demonstration of almost all elements of the full ASPUN facility. Benefits to the full ASPUN facility will accrue in not only the technical and economic elements but also in the speed at which the full design goals can be achieved after completion of construction. To the neutron scientists, this would represent a factor of five increase in intensity over the upgraded IPNS facility.

References

1. Proceedings of the ICANS-VI meeting at Argonne National Laboratory, July 1982, ANL Report ANL-82-80 (1982).
2. G. H. Lander, Physica 120B 15 (1983).
3. The IPNS User Bulletin is published twice a year; a Progress Report for 1981 - 1983 is in preparation. To obtain these documents and be placed on our mailing list write to the Scientific Secretary, IPNS-360, Argonne National Laboratory, Argonne, Illinois, 60439.
4. J. D. Jorgensen and J. Faber, in Ref. 1, p-105, (1982).
5. S. R. MacEwen, J. Faber, and A. P. L. Turner, Acta Metall 31, 657 (1963).
6. A. Kravitz, unpublished.

7. A. J. Schultz, R. G. Teller, and J. M. Williams, in Ref. 1, p. 115 (1982).
8. A. J. Schultz, R. G. Teller, J. M. Williams, M. G. Strauss, and R. Brenner, ACA Transactions 18 169 (1982).
9. A. J. Schultz, R. G. Teller, M. A. Beno, J. M. Williams, M. Brookhart, W. Lamana, and M. B. Humphrey, Science 220, 197 (1983).
10. D. L. Price, J. M. Carpenter, C. A. Pelizzari, S. K. Sinha, I. Bresof, and G. E. Ostrowski, in Ref. 1, p. 207 (1982).
11. R. O. Hilleke, P. Chaddah, R. O. Simmons, D. L. Price, and S. K. Sinha (to be published).
12. S. Kern, C.-K. Loong, J. Faber and G. H. Lander, Solid State Comm. (in press).
13. G. P. Felcher in Ref. 1, p. 179 (1982).
14. S. D. Bader, G. P. Felcher, K. E. Gray and R. T. Kampwirth, Physica 120B, 219 (1983).
15. J. W. Lynn, W. A. Miller, T. W. Dombeck, G. R. Ringo, V. E. Krohn and M. S. Freedman, Physica 120B, 114 (1983).
16. "Pulsed Neutron Scattering" by C. G. Windsor, Taylor & Francis, London, 1981.
17. J. M. Carpenter, N. Watanabe, S. Ikeda, Y. Masuda, and S. Sato, Physica 120B, 126 (1983).
18. N. Watanabe, H. Sasaki, Y. Ishikawa, Y. Endoh, and K. Inoue, in Ref. 1, p. 16 (1982).
19 J. M. Carpenter, U. Ahmed, J. R. Ball, F de Sousa, and T. Ewing, Argonne National Laboratory Report ANL-83-11 (1983).
20. T. K. Khoe and R. L. Kustom, IEEE Transactions on Nuclear Sciences, NS-30, (August, 1983).
21. F. T. Cole, R. O. Haxby, L. W. Jones, C. H. Pruett, and K. M. Terwilliger, Review of Sci. Inst. 28, 403 (1957).

Session B

Symposium on Advanced Concepts

Chairman - B.G. Chidley

Proceedings of International Collaboration on Advanced Neutron Sources (ICANS-VII), 1983 September 13-16
Atomic Energy of Canada Limited, Report AECL-8488

ASPUN, ARGONNE SUPER INTENSE PULSED SPALLATION NEUTRON SOURCE

T. K. Khoe and R. L. Kustom
Physics Division
Argonne National Laboratory
9700 S. Cass Ave.
Argonne, IL 60439

Introduction

Argonne has been in the process of developing plans for pulsed spallation neutron source facilities that would extend the flux levels by at least an order of magnitude over fluxes provided by facilities that are either now in operation or in construction. The ANL facility is called ASPUN for Argonne Super Intense Pulsed Spallation Neutron Source. The heart of ASPUN is a Fixed-Field Alternating Gradient (FFAG) proton synchrotron which, in our opinion, has great potential as a driver for a spallation neutron source.

The FFAG synchrotron was extensively studied in the 1950's and early 1960's at the Midwestern Universities Research Association (MURA) laboratories in Stoughton, Wisconsin.[1] An FFAG accelerator has dc excited magnetic fields into which beam is injected on the inside radius and as the beam is accelerated, the average equilibrium orbit radius grows. Frequency modulated rf cavities are used to accelerate the beam with a voltage and frequency program that tracks the beam energy.

The early FFAG accelerators were studied for use as high energy particle accelerators, a role which required a large momentum change from injection to extraction. The transverse focussing of the beam in an FFAG accelerator is accomplished through a combination of the entrance and exit edge angles and a field gradient from the inner radius to the outer radius of the machine. To achieve constant edge angles, the magnets spiral radially outwards, which for the early FFAG accelerators was quite extensive because of the large momentum difference between injection and extraction. However, the momentum range for use of an FFAG accelerator as a proton driver in a spallation source is about 2.5-2.7. Thus, the radial extent of the magnet is quite nominal, leading to a relatively simple FFAG accelerator design.

A discussion of the relative merits and potential of the FFAG driver is presented in Section III.

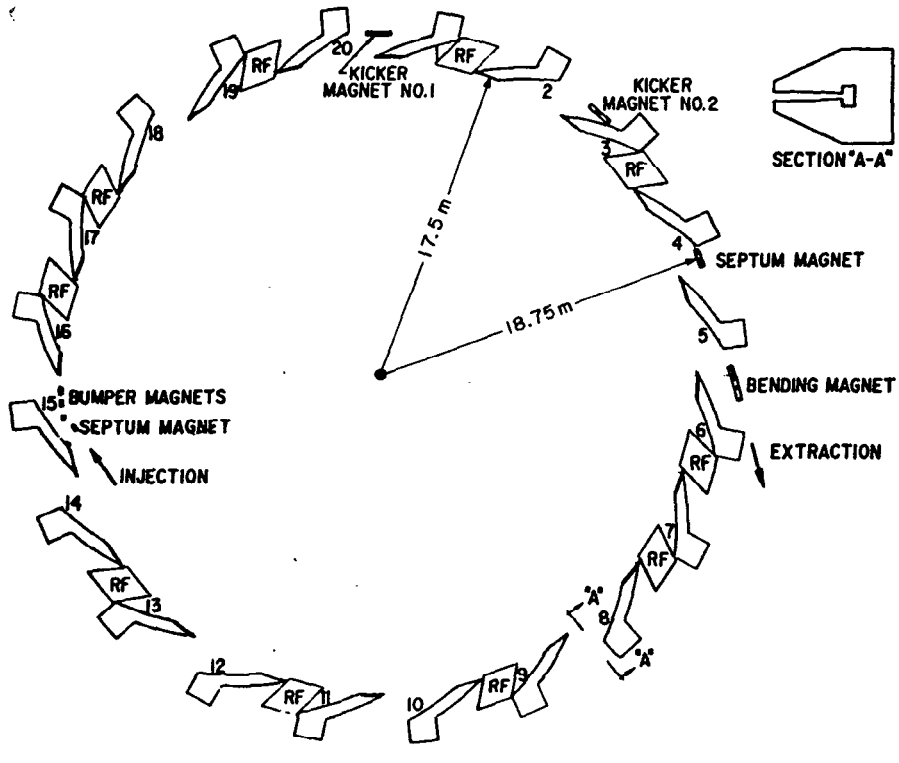

Fig. 1. Schematic view of FFAG ring.

Fixed-Field Alternating Gradient (FFAG) Design

The design is based on 200 MeV H^- to H^+ stripping injection. The extraction energy is 1100 MeV and the repetition rate without beam stacking is 220 Hz. The linac must provide 32 mA of H^- beam for 500 μsec at the 220 Hz repetition rate. The duty factor of the linac must be somewhat greater than 11% to allow for rf filling and stabilization before beam injection.

A schematic view of the FFAG ring is shown in Figure 1. Table 1 gives the machine parameters. The injection radius is 17.5 m. The injection system is shown in Figure 2. The normal equilibrium orbit is the dashed line shown in Figure 2. The four bump magnets, B_1, B_2, B_2', and B_1', deflect the equilibrium orbit along the dot-dash line through the stripper foil at point S. The 200 MeV H^- beam enters through the septum magnet, SM. The B' magnets operate with a maximum field of 0.39T and are 25 cm long and the B' magnets operate with a maximum field of 0.54T and are 37.5 cm long. The septum magnet operates at 0.6T and is 60 cm long. The horizontal phase-plane ellipse for 700π mm-mrad emittance at the stripper foil is shown in Figure 3. The bumper and septum magnet fields decrease so that the stripper foil effectively appears to start at $(x,x') = (o,o)$ and then moves inward along the negative major axis. Proper control of the decrease in field will produce uniform charge distribution in horizontal space leading to a smaller space charge effect. Magnets in the injection line will be used to distribute the beam uniformly in vertical phase space.

Table 1. Machine parameters

Injection energy (MeV)	200
Extraction energy (MeV)	1100
Injection radius (m)	17.5
Extraction radius (m)	18.75
Injection field (T)	0.489
Extraction field (T)	1.281
Number of sectors	20
Angular width of sectors (deg)	4.5
Field index k	14
Spiral angle ζ (deg)	65
Radial betatron frequency ν_x	4.25
Vertical betatron frequency ν_z	3.25
Space charge limit	10^{14}
Beam emittance at 200 MeV	
Radial (mm-mrad)	π 700
Vertical (mm-mrad)	π 500
Peak rf voltage per cavity (kV)	30
Frequence range (MHz)	1.5-2.259
Harmonic number	1
Number of cavities	10
Average current (mA)	≈3.5
Repetition rate (pulses/second)	≈220
Beam bucket area (eV-sec)	4.15
Output energy spread (MeV)	±19.5
Output bunch length (nsec)	136
Weight of sector magnet (ton)	
Pole and yoke	68
Coils	2.5
Power loss per sector magnet (kW)	140

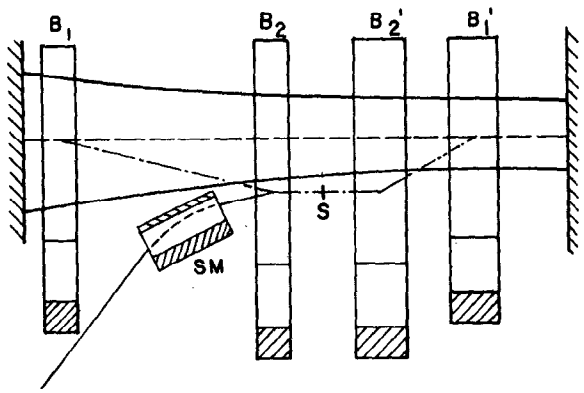

Fig. 2. Injection system showing four bumper magnets, septum magnet, and stripper foil.

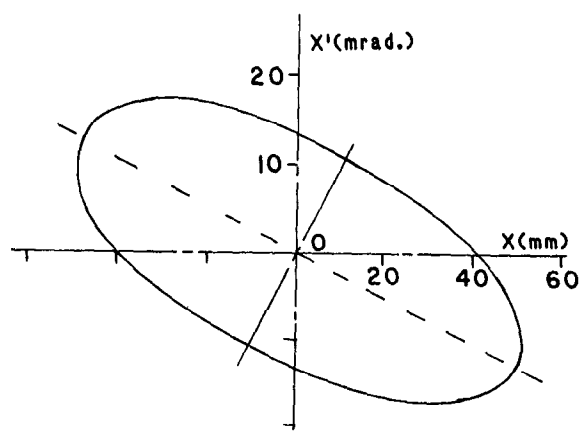

Fig. 3. Horizontal phase plane ellipse at stripper foil for 700 π mm-mrad emittance.

The energy of the linac beam will be modulated to give a coasting beam energy spread of ±3.2 MeV.

Adiabatic capture is accomplished by instantaneously exciting the rf cavities at 27 kV and linearly increasing the voltage to 150 kV in 150 μsec.

The guide field in an FFAG accelerator is given by

$$B = B_o\left(\frac{R}{R_o}\right)^k\left[1+\sum_{n=1}^{\infty} f_n \cos nN(\theta-\tan\xi \ln R/R_o)\right] \qquad (1)$$

where R is the radial distance from the machine center, $k = (R/B)(dB/dR)$ is the mean field index, θ is the azimuthal angle, f_n is the harmonic

component of the azimuthally varying field, N is the number of identical magnets, and ξ is the spiral angle. There are 20 magnets each with an angular width of 4.5° and a nearly sharp edge field so that the effective flutter, $(\Sigma f_n^2)^{1/2}$, is large. The pole of the magnet extends from R=17.4 m to 18.9 m. The magnet gap is constant from 17.5 to 18.0 m. The required field gradient in this region is supplied by pole face windings. The magnet gap is 220 mm, chosen to allow for 143 mm of peak to peak betatron amplitude, 20 mm of orbit error due to field errors and misalignment, 20 mm for pole face windings, 20 mm for the vacuum chamber wall, and 17 mm extra. The magnet gap decreases from 220 mm at a radius of 18.0 m to 111 mm at a radius of 18.9 m. The decrease is tailored to achieve the correct magnet gradient required by eq. (1). The magnet field at the injection radius of 17.5 m is 0.489T and at the extraction radius of 18.75 m is 1.28T. The magnet parameters are listed in Table 2.

The magnet will be designed to maintain the same flutter throughout the momentum range so that the betatron frequencies are independent of momentum. The values for the β and η functions for one period from straight section center to straight section center are shown in Figure 4 and the beam envelopes at injection with ε_x = 700 mm-mrad and ε_y = 500 π mm-mrad are shown in Figure 5.

Table 2. Magnet Characteristics

Width of sector	4.5°
Minimum pole radius	17.4 m
Maximum pole radius	18.9 m
Spiral angle	65°
Main coil ampere turns	9.7×10^4 A
Pole face windings amper turns	5.9×10^4 A
Weight of yoke and poles	68 tons
Weight of coils	2.5 tons
Power loss	~140 kW
Magnet height	2.5 m
Radial width	2.8 m

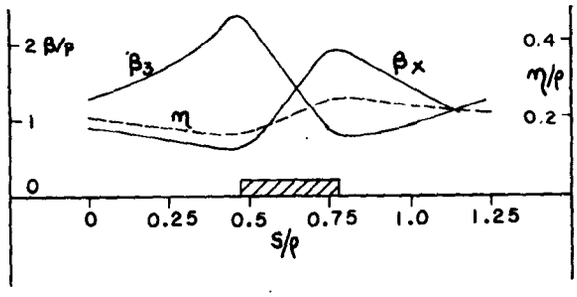

Fig. 4. β and η functions for one period starting at the center of a straight section.

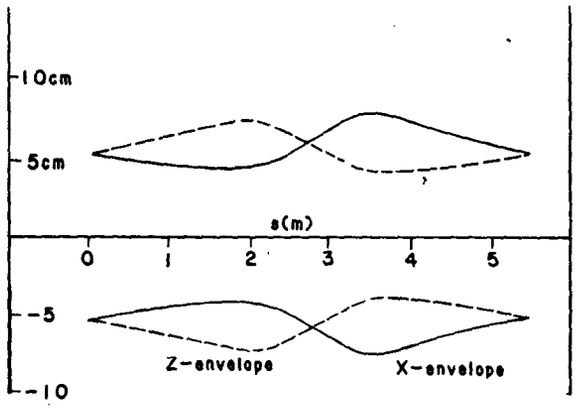

Fig. 5. Horizontal and vertical beam envelopes at injection for ε_x = 700 π mm-mrad and ε_y = 500 π mm-mrad.

The coherent space charge limit shortly after injection and bunching is 10^{14} ppp under the assumptions that the bunching factor is 0.45, the transverse charge distribution factor is 1.35, and the tune shift $\Delta\nu_z$ = 0.25. The additional increase in space charge limit due to the momentum spread is not included, providing some additional margin of safety. The rf voltage and frequency are initially programmed to maintain the product $B_f\beta\gamma^2 > 0.375$, where B_f is the bunching factor, and β and γ are the velocity in units of light velocity and the energy in units of rest energy, respectively. Later in the cycle when space charge is not a consideration, the voltage and frequency are programmed to achieve maximum practical energy gain per turn. The rf voltage and frequency as a function of time is shown in Figure 6. The acceleration voltage is provided by ten cavities spaced around the machine. The frequency varies from 1.5 MHz at injection to 2.259 MHz at extraction. After the initial capture period, the rf voltage is increased from 150 kV to 300 kV in approximately 750 μsec. The rf system parameters are listed in Table 3.

Table 3. Accelerating System Parameters

Number of cavities	10
Length of cavity	1.9 m
Cavity peak voltage	30 kV
Total volume of ferrite	11 m^3
Total peak ferrite losses	1.25 MW
Total peak beam power	6.48 MW
Cavity shunt resistance	7200 Ω
Coupling coefficient	6.2
Ferrite μ_Δ injection	26.8
μ_Δ extraction	12.5
Average rf flux density	0.0120T
Maximum rf flux density	0.0145T
D.C. biased H_{DC} (injection)	900 A/m
(extraction)	1800 A/m
Maximum H_{rf}	530 A/m
Power density in ferrite	114 kW/m^3

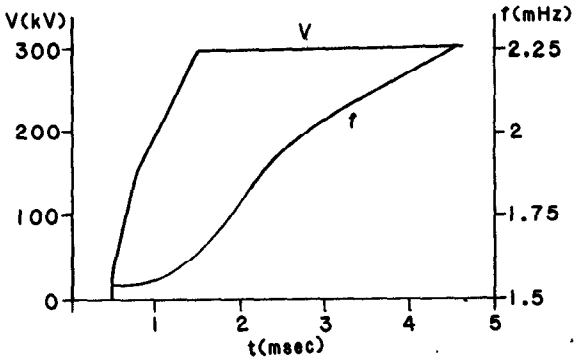

Fig. 6. Rf voltage and frequency as a function of time.

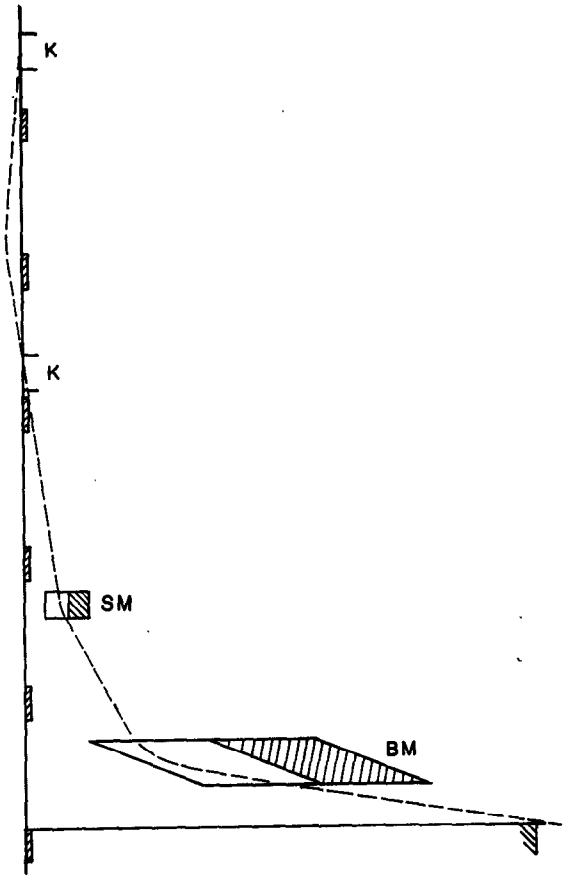

Fig. 7. The schematic plan view of the extraction system consisting of two fast ferrite kicker magnets, a thin septum magnet and a bending magnet.

Extraction is accomplished in one turn with two fast ferrite kicker magnets and a thin septum extraction magnet and a final bending magnet. A plan view of the extraction system is shown in Figure 7. The first fast kicker is located in straight section 20. The magnet provides an inward kick of 10.34 mrad. This produces a coherent betatron oscillation of the beam bunch. The location of the second kicker in straight section 2 is 180° in betatron phase from the first kicker. The second kicker produces a 10.34 mrad outward kick which adds to the deflection angle produced by first kicker. Each of the kickers is 1.0 m long and operates at 0.0625T. The extraction septum magnet provides a 62.3 mrad deflection angle. It is 1 meter long and operates at 0.376T. The final extraction benching magnet is 2 meters long, operates at 1.4T, and provides a 460 mrad angular deflection.

Discussion

Several features of an FFAG accelerator suggest that this concept is well suited to use as an intense pulsed spallation source. The injection and capture in a dc magnetic field using charge exchange $H^- \rightarrow H^+$ injection has the potential for extremely high efficiency (≈99%) since the rf voltage and frequency can be programmed with only that goal to achieve. The use of solid metal vacuum chambers provide very low impedances for beam instabilities, especially since the injection bumpers and extraction kickers are not seen by the beam beyond the immediate injection-extraction period. The energy gain per turn during acceleration can be made virtually constant so that most efficient use of the rf cavities is possible. More usable straight section space is available since the transverse focusing elements are contained totally within one magnet per lattice cell. The cost is much less than equivalent proton drivers.

Based on IPNS-I scaling, the peak neutron fluxes during the pulse would be 1.16×10^{17} n/cm^2-sec. This flux would be almost 23 times more than the WNR-PSR facility at the Los Alamos National Laboratory and the SNS facility at the Rutherford-Appleton Laboratory based on equivalent scaling. The ASPUN facility would equal the proposed SNQ facility the KFA Laboratory, Jülich, Germany.

This conceptual design is adequately complete to satisfy proof-of-principle and encourage further development. Argonne proposes to build a mini-ASPUN FFAG that could be used to test the design of the magnet, the efficiency of capture and acceleration, and the stacking process. The machine would be added to the IPNS-I facility using the existing 50 MeV linac, transport lines and target. The mini-ASPUN FFAG would operate at 500 MeV, 100 μa, and 30 Hz. This machine is described in some detail in the talk by G. H. Lander at this conference and so will not be described in further detail here.

References

1. F. T. Cole, et al., "Electron Model Fixed-Field Alternating Gradient Accelerator," Rev. Sci. Austr. 28, 403 (1957).

Proceedings of International Collaboration on Advanced Neutron Sources (ICANS-VII), 1983 September 13-16
Atomic Energy of Canada Limited, Report AECL-8488

ACCELERATOR PROJECT GEMINI FOR INTENSE PULSED NEUTRON AND MESON SOURCE AT KEK

H. Sasaki and GEMINI Study Group*

National Laboratory for High Energy Physics
Oho-machi, Tsukuba-gun, Ibaraki, 305, Japan

Abstract

A rapid-cycling synchrotron is designed for intense pulsed neutron and meson source at KEK. This 800 MeV accelerator aims to deliver proton beams of 500 μA in time average. This paper describes conceptual design of the accelerator and also points out some technical problems to be overcome in order to realize the project.

Introduction

Five hundred MeV Booster Synchrotron at KEK, which is delivering 2 μA proton beam in time average, is used as a pulsed neutron and meson source of Booster Synchrotron Utilization Facility (BSF) as well as an injector for 12 GeV Proton Synchrotron in a time-shared mode. At present, a project of H^- charge exchange injection is in progress to increase the beam intensity of the booster, and also energy-up of the present 20 MeV injector linac to 40 MeV has been discussed[1]. These correspond to a relatively short term program KENS-I', including the conversion of the present tungsten target to a depleted uranium. KENS-I' program aims to increase the neutron beam intensity by about one order of magnitude by improving the present accelerator and target system. On the other hand, a long-term future program of BSF was discussed informally since the fall of 1980. This is the construction of an intense pulsed neutron source (KENS-II program) and the extension of the present meson science experimental facility BOOM (Super-BOOM project). A tentative program has been presented at the meeting on the BSF future program on March 1982[2]. This was the first formal presentation. The most important part of this program is the construction of a high intensity proton accelerator.

Accelerator Design Principle

An accelerator system for KENS-II and Super-BOOM is called GEMINI, which is abbreviation of "a generator of meson-intense and neutron-intense beam". This is an 800 MeV rapid-cycling synchrotron aiming to deliver the proton beam of 500 μA in time average. Unlike the present meson factories or spallation neutron sources worldwide except those in BSF, GEMINI should deliver equally the pulsed proton beams to each of the meson and neutron experimental facility. And it may be possible that GEMINI will replace the 500 MeV booster as an injector for the present 12 GeV PS. This leads to the determination of the accelerator size to be a half of the circumference of 12 GeV PS, that is, 27 meters in average radius. In BSF, the unique features of the 70 nsec pulsed proton beam are effectively used for the time-of-flight technique in the neutron scattering experiments and for the studies on the relaxation phenomena of condensed matters with μSR. In GEMINI, it is also required that a single bunched beam is simultaneously supplied to each of the neutron and meson experimental facility. This determines uniquely the harmonic number of RF acceleration system is 2. Particularly, some kinds of μSR experiment ask a single short bunched beam less than 30 nsec in bunch length even at the sacrifice of beam intensity.

The accelerator parameters are listed in Table 1. The accelerator will consist of an H^- ion source, pre-accelerator including RFQ linac, 100 MeV Alvarez-type linac, and 800 MeV rapid-cycling synchrotron. The layout of the accelerator is shown in Fig. 1.

Table 1 A New Pulsed Neutron and Meson Source GEMINI

Maximum kinetic energy	800 MeV
Maximum intensity	6×10^{13} p/p
Repetition rate	50 Hz (100/3 Hz & 100 Hz)
Average beam current	500 μA
Injection energy	100 MeV
Injected H^- beam current	30 mA
Number of turns of injected beam	>240
Beam pulse width of injected beam	>330 μs
Magnet radius	7.00 m
Average radius	27.00 m
Number of period	24
Length of straight section	3.008 m
Structure	FBDO
Betatron frequency per revolution	
Horizontal	6.8
Vertical	7.3
Revolution frequency	0.757 - 1.489 MHz
Maximum beta-function	
Horizontal	12.4 m
Vertical	12.9 m
Momentum compaction factor	2.71×10^{-2}
Transition energy/rest energy	6.07
Beam emittance	
800 MeV	0.29×0.16 (mm rad)^2
100 MeV	0.97×0.52 (mm rad)^2
Number of bending magnets	24
Length of bending magnets	1.833 m
Length of quadrupole magnets	
Focussing magnet	0.525 m
Defocussing magnet	0.565 m
Bending magnet field	
800 MeV	0.697 T
100 MeV	0.212 T
Quadrupole magnet peak field gradient	4.18 T/m
Peak energy gain per turn	90.6 keV (60.4 keV)
Harmonic number	2
RF frequency	1.513 - 2.978 MHz
Maximum RF voltage	214 kV (166 kV)
RF bucket area	1.89 eV·sec
Number of RF stations	8
Incoherent space charge limit	7.2×10^{13} protons

Accelerator System

Lattice Structure

Four lattice structures were examined. Finally, a highly symmetric lattice with high tunes was chosen from them; 24 equal FBDO cells with a phase advance of about 90° per cell set the betatron tunes around 7. For a given mean radius of the accelerator, such high tunes lead to smaller aperture magnets for a constant space-charge limit. High tune means a high transition energy, which has advantages to both of the longitudinal and transverse instability of beam. On the other hand, this leads to a large number of unit cells, hence

* T. Adachi, H. Baba, S. Inagaki, Y. Irie, N. Kaneko, T. Kawakubo, M. Kumada, S. Matsumoto, M. Miki, I. Sakai, H. Someya and Y. Yano.

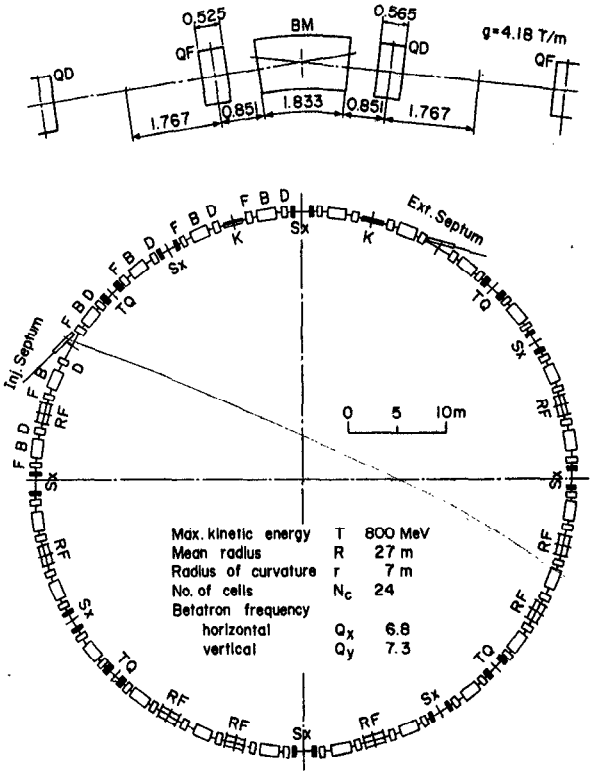

Fig. 1 GEMINI Layout

the shortening of the length of straight section where devices for extraction and acceleration are installed. The choice of horizontal and vertical tune of 6.8 and 7.3 is somewhat arbitrary, and more detailed studies might be considered on x-y coupling, acceptance choice, beam extraction optics, etc. Figure 2 shows amplitude and dispersion function along the beam orbit.

Injector Linac[3)]

100 MeV linac with a 30 mA H^- ion beam is assumed as an injector to the synchrotron. The accelerating structure of this injector system is divided into three stages: 50 ∿ 100 keV H^- ion source, 1 MeV RFQ or APF and 100 MeV Alvarez linac. Even thouth the attainable maximum energy through RFQ linac requires a deliberate

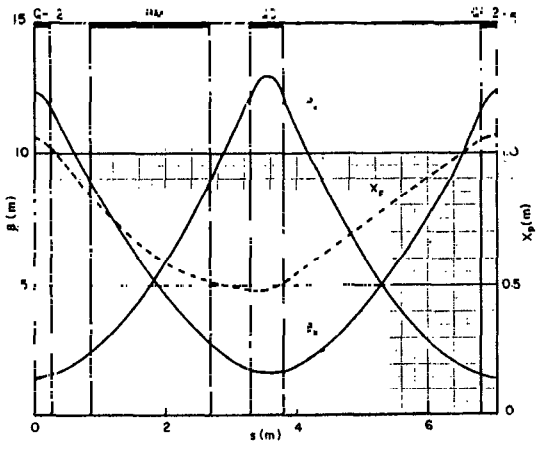

Fig. 2 Amplitude and Dispersion Functions

study, 1 MeV injection energy will certainly be attainable, which enables us to use klystron working around 400 MHz as RF power source. This will simplify the power system of the linac.

If the Alvarez linac is excited at 400 MHz, the diameter of cavity is reduced nearly to a half of the present proton linac at KEK, and the average accelerating field can be made higher, say, 3.5 MV/m. With the fixed dimensions of drift tube (bore diameter: 1.0 cm, outer diameter: 9.0 cm) and cavity (diameter: 48 cm), the values of transit time factor, effective shunt impedance, power loss, etc. were calculated as a function of the half-gap length. Table 2 shows accelerating energy by each cavity, cavity length, number of cells contained in a cavity and RF power for 6 partitions at the average accelerating voltage of 3.5 MV/m.

Table 2 Features of 100 MeV Injector Linac

Cavity Number	Energy (MeV)	Length (m)	Number of cells	Power (MW) Cavity	Beam	Total
1	18.37	7.267	81	0.852	0.521	1.373
2	35.57	7.138	41	0.835	0.516	1.351
3	52.68	7.305	33	0.870	0.513	1.383
4	69.93	7.483	29	0.911	0.517	1.428
5	85.38	7.180	25	0.898	0.464	1.362
6	100.39	7.458	25	0.929	0.450	1.379

The momentum spread of the beam at the exit is expected to be ±0.3 %, and the normalized acceptance in the transverse plane is estimated to be 20 mm•mrad with the first quadrupole magnet of 1.5 T/m in field gradient.

The build-up time of the cavity for $Q = 6.5 \times 10^4$ is about 275 μsec. If one adds 100 μsec as a margin to the minimum beam duration 350 μsec, the duty factor becomes 3.6 %. 400 MHz klystron with duty factor of 5 % and peak power of 2.5 MW is expected to be developed without much difficulty.

Injection

Beam injection will be carried out in horizontal plane. In order to store the number of protons of 6×10^{13} into the synchrotron with a 30 mA H^- ion beam, injection would occur at least over 240 turns requiring 330 μsec. We assume the normalized emittance of linac beam of 10 mm•mrad in both transverse planes. A phase-space area of 460 mm•mrad (H) x 246 mm•mrad (V) has to be filled with this beam. For the purpose of filling the horizontal phase space, injection starts with a horizontal bump orbit, which coincides with the injection orbit of the H^- ion beam at the exit of a focussing quadrupole magnet as shown in Fig. 3. A charge stripper of 120 $\mu g/cm^2$ carbon foil is set downstream the Q magnet, whose radial position must be outside the beam envelope at the end of injection. The bump orbit will be provided by means of a pair of bump magnets and a small trim quadrupole magnet. The density distribution of the beam after injection is regulated by choosing a proper decay waveform of the bump field. The maximum amplitude of the bump orbit requires bump field of 0.33 and 0.32 T for the 0.2 m long magnet B1 and B2, respectively. Filling of the vertical phase space will be achieved with a steering magnet introduced into the H^- injection line.

The beam intensity aimed by GEMINI is very huge and expected to be 6×10^{13} protons/pulse. Even though only one percent of the beam is lost, this is equivalent to the full intensity of the present 500 MeV booster synchrotron at KEK. Most of the beam loss in transverse planes at injection will come from the beam blow-up due to the multiple scattering and stripping inefficiency by the charge stripper. The charge stripped proton beam scans radially with decaying

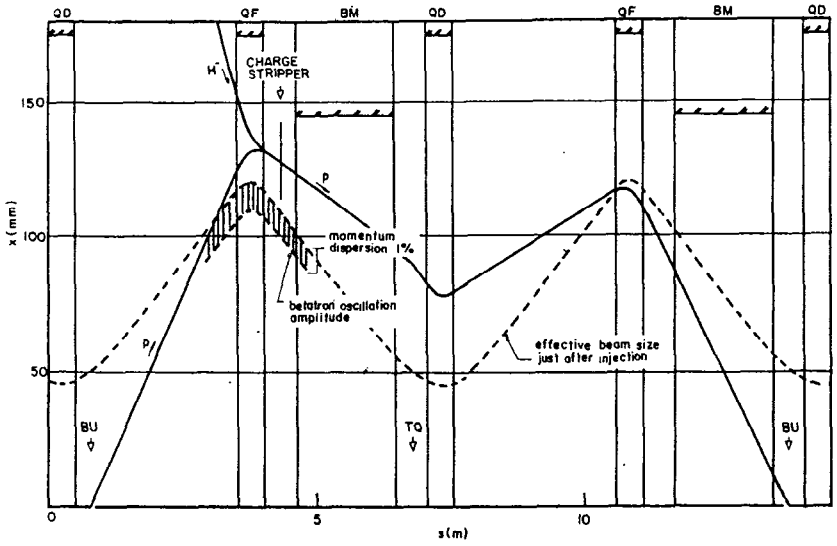

Fig. 3 Injection Optics

closed orbit. The effective number of traverse of the circulating proton beam through the stripper is at most forty times for a 30 mA, 20 % chopped H^- ion beam of 420 μsec in time duration. Using a 120 μg/cm^2 thick carbon foil, it is possible to keep the beam loss less than a fraction of percent and to localize the most likely unavoidable losses due to the stripping inefficiency by means of proper beam scrapers and collectors.

Ring Magnets

The accelerator ring is made of 24 bending and 48 quadrupole magnets. The required semi-aperture of good-field region is 11.5 cm x 7.4 cm and 13.5 cm x 9.0 cm in the bending and quadrupole magnet respectively. For the vacuum chamber, it is necessary to add 3 and 4 cm in horizontal aperture of the bending and quadrupole magnet respectively to allow the room for injection and extraction of beam. The cross-section of the ring-magnet is shown in Fig. 4.

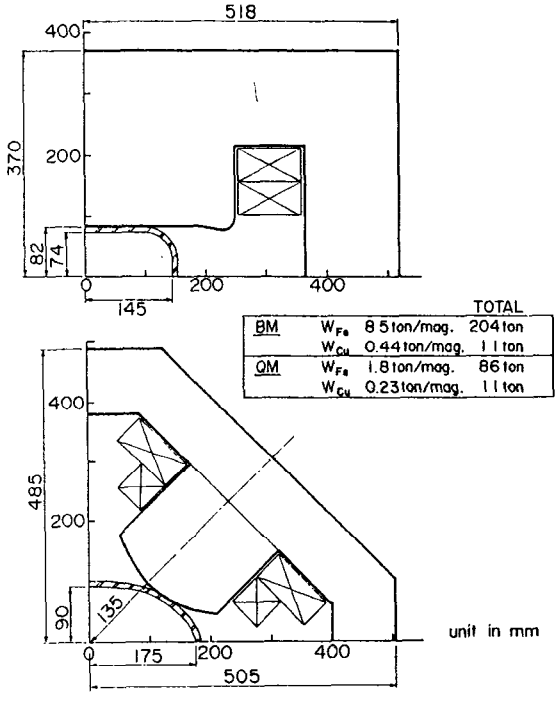

Fig. 4 Gap and Core Geometry of Ring Magnet

The ring magnet is excited with a repetition rate of 50 Hz. All of the bending and quadrupole magnets are divided into twelve groups. These are connected in series through resonant capacitors and forms a ring circuit. The dc bypass of the capacitors for the dc bias current is provided by installing chokes in parallel to the capacitors. In order to reduce the RF accelerating voltage, the magnet system would be excited by a dual-frequency system with resonant frequency of 100/3 and 100 Hz as proposed by M. Foss and W. Praeg at ANL[4]. This reduces the peak RF voltage of 214 kV to 166 kV. The switching system of resonant capacitor would be more simplified by replacing ordinary thyristor with GTO (gate turn-off) thyristor, which is capable of self-breaking. The test is under way[5].

The maximum voltage imposed on the exciting coil should be kept within 10 kV to the earth. This sets a limit to the number of turns of the coil and leads to a considerable power dissipation due to eddy current circulating in hollow conductor. Reduction of the eddy current loss will be achieved by using hollow conductors of parallel current circuits and by transposing those circuits each other at the connection points between coil pancakes as successfully applied at the KEK booster synchrotron magnet. Even though such a procedure is applied, a considerable amount of the eddy current loss takes place as shown in Table 3. Development of a stranded cable with cooling pipe for coil conductor would make free from eddy current loss, which leads to the reduction of the number of turns of coil and hence the voltage across the coil and the peak voltage applied to GTO thyristor.

RF Acceleration

We assume a 100 MeV injected beam with an effective full momentum spread of 0.75 %. The emittance of such an injected beam is 0.94 eV•sec for the acceleration system with harmonic number of 2. If the RF bucket area has to be twice of this emittance, the

Table 3 Power Consumption of Magnet System (100/3 & 100 Hz Dual Resonant Frequency Mode)

Magnet (24 BM, 48 QM)	BM	QM
P^{dc}_{ohm}	36.4 kW/mag.	19.4 kW/mag.
P^{ac}_{ohm}	5.2	2.7
P_{eddy}	12.5	6.7
P_{iron}	3.8	1.1

Energy-storage Choke (12 meshes)		Condenser (12 meshes)	
P^{dc}_{ohm}	32.5 kW/mesh	P_c	51.4 kW/mesh
P^{ac}_{ohm}	4.6		
P_{eddy}	8.4		
P_{iron}	7.5		

Total Power Loss		Total Stored Energy	
P_{dc}	2.19 MW	U_{dc}	990 kJ
P_{ac}	1.88 MW	U_{ac}	281 kJ

required peak RF voltage through the acceleration period is 166 kV in the 100/3 Hz operation of the guide field magnet. The RF voltage program and relevant parameters of RF bucket are shown in Fig. 5. The required RF voltage will be provided with eight RF stations, each of which is installed in a 3 m long straight section and consists of two reentrant ferrite-loaded cavities. A low impedance cathod-follower is proposed as a final-stage power amplifier in order to compensate for a large beam loading. Parameters of the RF acceleration system are listed in Table 4.

In GEMINI using the H^- charge-exchange injection scheme, the most likely beam loss at around injection will result from the inefficiency of beam trapping in the longitudinal phase space. RF capture efficiency in ordinary methods will be at most 80 % with reasonable parameters. Particularly in a high intensity machine such as GEMINI, therefore, the beam loss at RF capture should be significantly reduced. A chopper will be introduced into the beam line following the preaccelerator. Computer simulation showed that the inefficiency

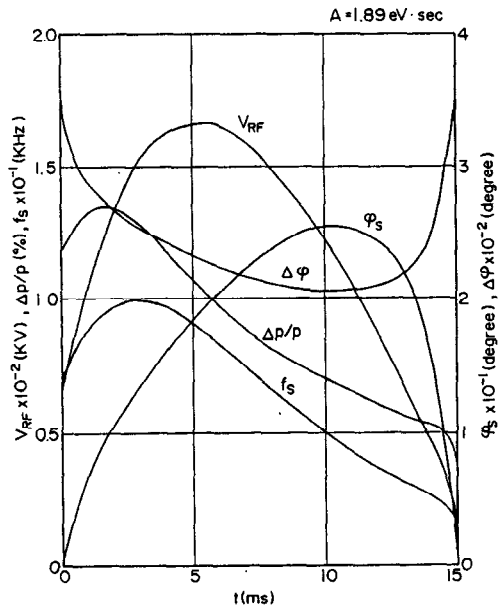

Fig. 5 RF Voltage Program and Relevant Parameters of RF Bucket

Table 4 Parameters of RF Acceleration System (100/3 and 100 Hz dual resonant freq. mode of guide field)

Harmonic number	2
RF acceleration frequency	1.513-2.978 MHz
Peak RF voltage	166 kV
RF bucket area	1.89 eV·sec
Number of RF stations	8
Number of cavities per station	2
Cavity length	1.2 m
Ferrite inner/outer diameter	0.30 m/0.50 m
Max. flux density of RF field in ferrite	∿100 Gauss
Bias current	550-2,050 A
Shunt impedance of RF cavity	2.7 kΩ
Total average RF loss of ferrite	125 kW
Average power delivered to beam	350 kW

of adiabatic trapping process is less than 1 % in the synchronous injection of a 20 % chopped beam into RF bucket.

While the required bunch length is some 200 nsec or less for the spallation neutron source, special μSR experiments require a very short single bunched beam, say, 30 nsec. This is one of the important options of the accelerator. Assuming typical RF accelerating voltage programs with a limited maximum voltage, the bunch length at the maximum energy was estimated in both cases of adiabatic damping and non-adiabatic method. In the later case, a sudden increase in the RF voltage around the maximum energy will cause the bunch to rotate in longitudinal phase space and the bunch would be upright after a quarter of a synchrotron oscillation period. Extraction should occur when the bunch length is a minimum[6]. It was confirmed by using the present 500 MeV booster at KEK that this method seems to be promising to realize the desired short bunched beam, provided at some sacrifice of beam intensity.

Extraction

Beam extraction is performed by the horizontal single-turn extraction. The emittance of the extracted beam is assumed to be twice of the expected one from adiabatic damping of the initial emittance. Then, the full size of the beam including a dispersion due to the momentum spread of 1 % is estimated to be 74 mm at the entrance of the septum magnet, which is located in a straight section following a defocussing quadrupole magnet. Kicker magnet, therefore, must give a kick sufficient to clear such a beam size plus a 10 mm thick septum. The available space for the kicker magnet is a 3 m long straight section located upstream the septum straight section by an amount of about π/2 radian in phase advance. The required kick angle is 28 mrad, which is too large to be achieved with one kicker magnet located in the 3m long straight section. Another kicker magnet, therefore, is installed at a straight section upstream the first kicker magnet by π radian to realize the required kick angle at the first kicker position. In addition to those kickers, several orbit bump magnets will be used to the purpose of manipulating the beam positions just before the extraction. Figure 6 shows the extraction trajectory of beam. The deflection by the kicker magnet is 15 mrad for the first and second magnet. The septum magnet is divided into two parts, each of which deflects the beam by 150 and 225 mrad, respectively. These bends provide a separation of 80 cm between the central orbit and the central line of the extracted beam at the exit of the septum magnet. This distance is long enough for the

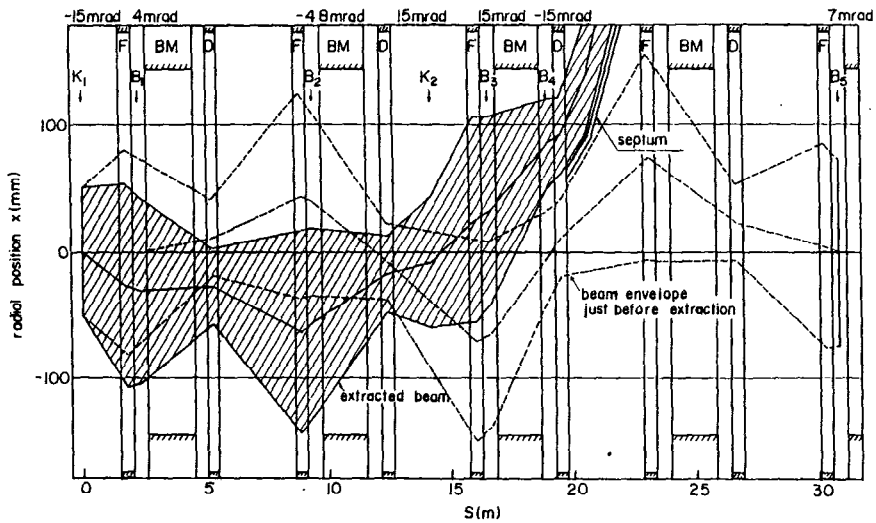

Fig. 6 Extraction Optics

extracted beam to clear the yoke of the quadrupole magnet following the septum magnet. Parameters of the kicker are listed in Table 5. Each kicker magnet, which is installed in a long straight section, is divided into two-different types K_u and K_d located to upstream and downstream side of the straight section according to the difference of beam size.

Table 5 Parameters of Ferrite-loaded Delay-line Type Kicker Magnet

	K_u (2 units)	K_d (3 units)
Deflection angle: Total (mr)	15	
Each (mr)	3	3
Gap height (mm)	180	120
width (mm)	200	200
Magnet length (mm)	600	350
Flux density in gap (T)	0.024	0.042
Exciting current (kA)	3.5	4.0
Impedance (ohm)	10	8.8
Inductance per cell (μH)	0.084	0.110
Capacitance per cell (nF)	0.84	1.4
No. of cells	10	10

Correction Lens System

For the sake of simplifying the power supply for the resonant network, the bending and quadrupole magnets are connected in series. Trim-quadrupole magnet system, therefore, must be introduced to keep the flexibility of tuning in the tune diagram. Assuming the variable range of tune is within ±0.5, four pairs of focussing and defocussing magnet are required, whose length and field gradient are 0.5 m and 1.53 T/m, respectively.

The natural chromaticity $\xi = \Delta Q/(\Delta p/p)$ is considerably high, that is, -9.1 for the horizontal plane and -10.2 for the vertical plane, respectively. If those chromaticities would be eliminated, eight sets of F-type and D-type sextupole magnet are required, whose field is 36.8 T/m^2 and -60.1 T/m^2 for a 0.3 m long magnet. Such quantities will be sufficient in practice to suppress head-tail effects, which might take place.

At present, it is an open question to introduce the octupole magnet for Landau damping.

Layout of the trim-quadrupole and sextupole magnets is shown in Fig. 1.

Vacuum Chamber

The vacuum chamber will be made from about 300 mm long sections of pure alumina, which are joined by metallizing the ends and brazing in vacuum. The lengths of vacuum chamber to be manufactured are within the limits of joining in this method, which enables us to attach directly metal flange at the end of the chamber.

Concluding Remark

The above-mentioned is only a preliminary design, and the design study is still in progress. Many problems are remained to be solved:

1) Design of each accelerator component in more detail,
2) Design studies of the items which have not been set about,
3) Layout including experimental facilities,
4) Cost estimation and time-schedule, etc.

R & D for some of technical problems is in progress; for example, construction of RFQ linac, manufacture of a permanent quadrupole magnet for linac drift tube and beam chopper for output beam of preaccelerator, application of GTO thyristor to the dual-frequency system of ring magnet power supply, development of stranded cable with cooling pipe as magnet coil conductor, etc. And also experiments such as beam bunch shortening test will be carried out by practical use of the existing accelerator and experimental facilities.

References

1) H. Sasaki, presented paper to this meeting.
2) T. Adachi (Ed.), Proc. of the Meeting on BSF Future Prospects, KEK Int. 82-6 (1982).
3) S. Inagaki, et al., Proc. of 7th Meeting on Linear Accelerators, KEK 82-14, 110 (1982).
4) M. Foss and W. Praeg, IEEE Trans. Nucl. Sci. NS-28, 2856 (1981).
5) H. Someya, et al., Proc. 4th Symp. on Accelerator Science and Technology at RIKEN, Japan, 317 (1982).
6) ANL-KFA Study Group, ANL-83-13.

Proceedings of International Collaboration on Advanced Neutron Sources (ICANS-VII), 1983 September 13-16
Atomic Energy of Canada Limited, Report AECL-8488

TRIUMF KAON FACTORY AS A POTENTIAL NEUTRON SOURCE

E.W. Blackmore

TRIUMF, Vancouver, B.C., Canada V6T 2A3

Summary

TRIUMF is considering the construction of a "kaon factory" post-accelerator to take the present 100 μA proton beam (6×10^{14} p/s) from 500 MeV to energies in the range of 15-30 GeV. This facility would produce secondary beams of kaons, antiprotons, neutrinos and other particles with an intensity of the order of 100 times present accelerators and would open up new fields in both nuclear and particle physics in the same way that the meson factories LAMPF, SIN and TRIUMF have done at sub-GeV energies. Although the production of neutron beams is not one of the prime motivations for constructing this facility, the high proton currents, in particular from the booster stage of acceleration, would make a unique spallation neutron source. This paper gives a brief report on the status of the kaon factory accelerator studies and describes the parameters of the proton beams which could be made available for neutron production.

Introduction

The TRIUMF cyclotron[1] is a six-sector isochronous machine accelerating H^- ions to a maximum energy of 520 MeV. Five H^- bunches per turn are accelerated, each bunch separated by 43 ns (23 MHz) and with a bunch width of 5 ns (±20°). A 5 mg/cm^2 carbon foil is used to strip the H^- to H^+ for extraction and at the present time three proton beams may be extracted simultaneously, two with an energy range 180-520 MeV and a low energy beam 60-100 MeV.

The cyclotron delivers currents of 150 μA cw with an emittance of 2π mm-mrad. A plan view of the facility is shown in Fig. 1. The proposed kaon factory will be fed by beam line 2A although for some of the schemes beam extraction by foil stripping will not be used as it is more advantageous to extract the H^- ions directly to allow for charge exchange injection to the next stage.

Accelerator Energy and Beam Characteristics

The physics justification for a kaon factory is well documented.[2,3] The interest in such a facility ranges from experimental studies of rare kaon decays, CP violation, neutrino and antinucleon interactions, hypernuclear physics to extensions of studies carried out at meson factories such as hadron-nucleon interactions and μSR. The energy chosen for a kaon factory accelerator depends on the range of secondary particles ($K,\bar{p},\nu$) desired, their intensities and momenta. Some typical cross sections[4] for low momentum kaon and antiproton production are shown in Fig. 2 as a function of incident proton energy. If the assumption is made that facility costs scale with proton energy, the Fig. 2(b) curves show how the relative cost/particle varies with incident energy. This puts the optimum energy between 15-20 GeV for the production of low momentum < 2 GeV/c secondary particles but higher if momenta > 5 GeV/c are required.

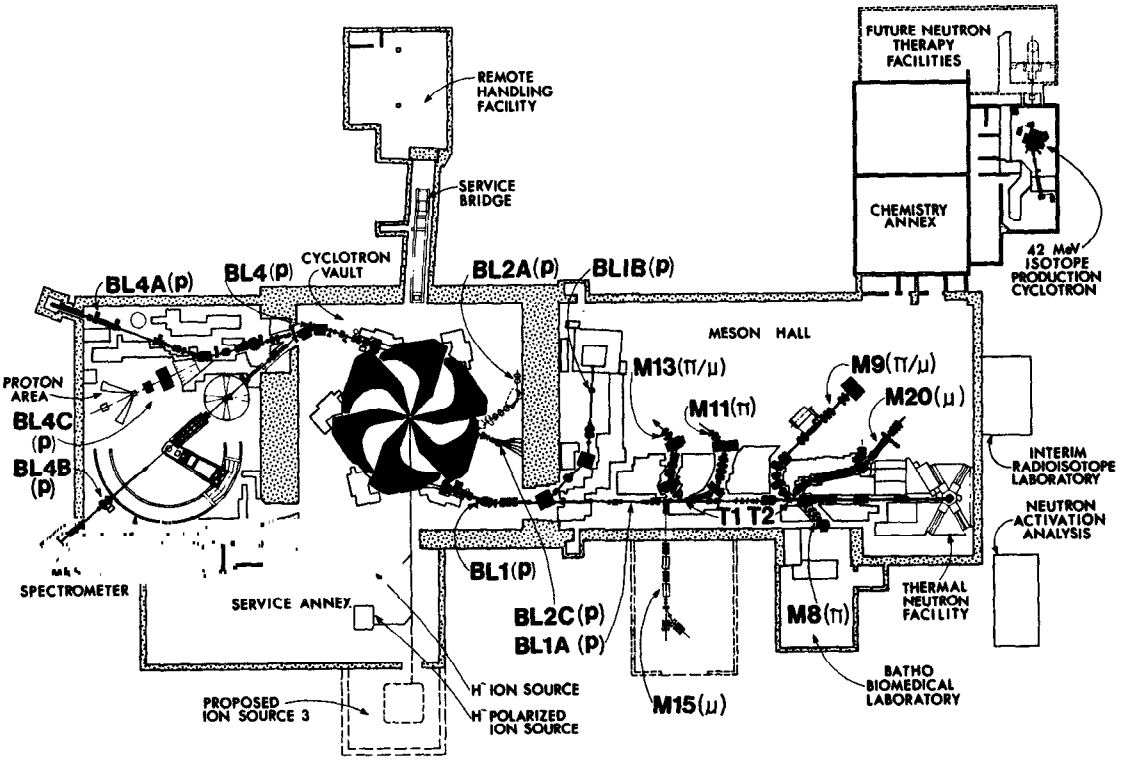

Fig. 1. Layout of TRIUMF cyclotron and beam lines (—— existing, ---- proposed).

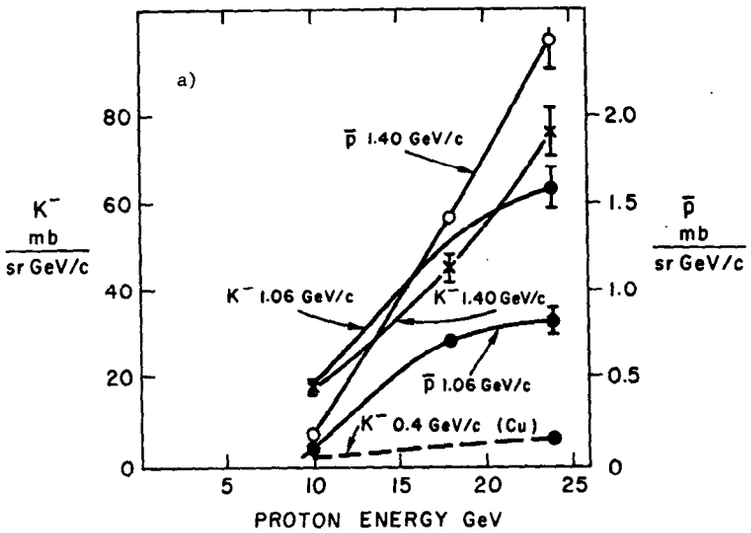

Fig. 2(a). Production cross sections on a 1 cm tungsten target as a function of proton energy.

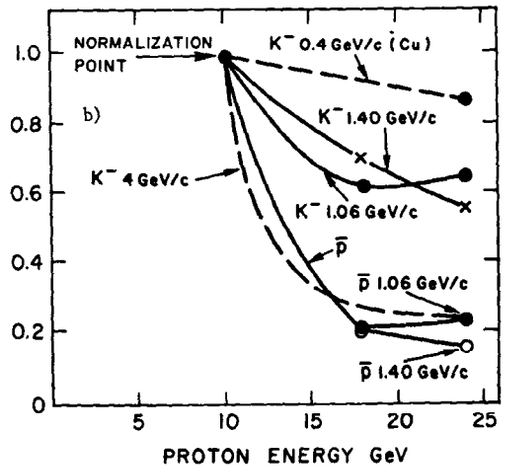

Fig. 2(b). Relative cost per particle assuming facility costs scale with proton energy.

The required time structure of the beam is continuous (cw) for most applications, in particular those requiring many-particle coincidences, but for neutrino experiments a macroscopic duty cycle of 10^{-5} or better is needed.

For a neutron spallation source the four parameters that establish the accelerator requirements are intensity, energy, pulse length and repetition rate. The intensity of 100 μA (6×10^{14}/s) would make the facility competitive with the SNS.[5] The energy of the kaon factory is too high for optimum neutron production from target, moderator and shielding considerations. The yield of neutrons is linear with (E(MeV) - 120) to approximately 2 GeV[6] and then rises more slowly due to range and moderator effects. An energy in the range of 1-3 GeV is therefore required.

The pulse length of existing or proposed facilities ranges from the 1 ns option of the LAMPF PSR[7] to 500 μs for the SNQ.[8] The repetition rates vary from 12-100 Hz. P. Egelstaff[9] has described two new directions for neutron scattering and their beam requirements:

- neutron diffraction with 100 eV neutrons
- single pulse diffraction

In the first case a pulse length of 100 ns or less is required but the repetition rate can be as high as 1-5 kHz. In the second case the maximum number of protons/pulse is desired ~10^{15} protons/pulse and the repetition rate can be less than 1 Hz.

The beam requirements for a neutron spallation source are very similar to those required for both a neutrino source and a pulsed muon facility, a fact recognized at LAMPF, SNS and KEK where these installations either exist or are planned. For a pulsed muon facility the pulse length must be a small fraction (<5%) of the muon lifetime which is 2.2 μs.

Accelerator Options

A number of accelerator options are being considered at TRIUMF and are shown in Fig. 3. Possible neutron sources within these accelerator schemes are also indicated.

Cyclotron Option

Matching to higher energy cyclotrons is obviously the most straightforward and designs have been made for a pair of superconducting cyclotrons with parameters as shown in Table I. Pole shape designs have been found which can maintain isochronism and vertical focusing to 15 GeV.[10] Although the proton beam would be cw, with the same 23 MHz microstructure as for the TRIUMF cyclotron, the possibility exists just as for the ASTOR[11] ring of using phase-expansion techniques to stack up to 500 turns in the intermediate ring at 3.5 GeV. These turns would then be extracted as a single turn giving a 10 kHz pulse structure to the beam. This pulse repetition rate could be reduced with commensurate reduction in average intensity by pulsing the ion source. However, there is no current limit to this scheme and it would be feasible to operate at the equivalent current of 400 μA cw.

Synchrotron Option

The intensity limit of a synchrotron is usually set at injection by space charge and phase-space considerations. The transverse space charge defocusing effects lead to an incoherent tune shift which from experience has to be kept to a value around 0.25.

Table I. Superconducting cyclotron specifications

Stage	I	II
Injection energy	430 MeV	3.5 GeV
Extraction energy	3.5 GeV	15 GeV
# sectors	15	42
Radius (max)	10.1 m	41.4 m
Radius (min)	7.5 m	40.6 m
# cavities (1 MV)	9	54
RF frequency	46 MHz	115 MHz
Harmonics	10	100
Excitation currents	2.1×10^6 At	2.5×10^6 At
Coil dimensions	8×60 cm^2	8×60 cm^2
Sector field	4 T	5 T
Gap width	7 cm	7 cm

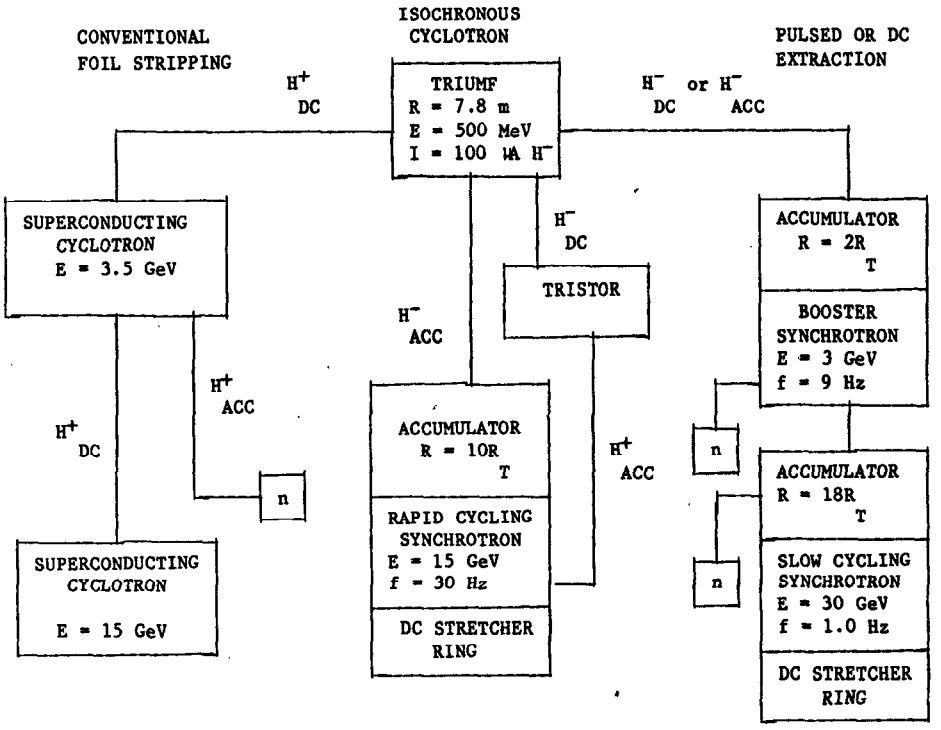

Fig. 3. Post-accelerator options using the TRIUMF cyclotron as injector.

Figure 4 shows the dependence of the total charge of protons (N) in the ring on energy for a tune shift $\Delta Q_y = 0.25$, a magnet aperture of 16 cm × 9 cm and a bunching factor of 2/3. At low energy (<<1 GeV) the self-force term dominates and $N \sim \beta^2\gamma^3$, and at higher energies the image force terms take over and $N \sim \gamma$. To achieve the desired 100 μA at 500 MeV injection energy, where the space charge limit is 11 μC, a repetition rate of 9 Hz is required. For a slow-cycling synchrotron with a repetition rate of 1 Hz an injection energy of 3 GeV is required. Two synchrotron options are being studied, a 16 GeV rapid-cycling synchrotron which would not need an injection booster for space charge reasons, although for rf reasons a booster would be an advantage, and a 30 GeV slow-cycling synchrotron injected from a 3 GeV booster.

The lattice design for these options will not be described here. Longitudinal defocusing effects at transition are eliminated by raising the transition energy to above the maximum energy of the synchrotron by imposing a superperiodicity close to the value of the horizontal tune: this can be achieved either by adding quadrupoles or by spacing the dipoles appropriately.

The matching of a 23 MHz isochronous cyclotron to a synchrotron operating at 9-30 Hz is perhaps the most difficult technical problem. Three schemes are being considered,[12] all of which require extracting the H^- ions from TRIUMF:

- stacking 160 turns in TRIUMF with pulsed extraction
- extracting as a cw H^- beam and stacking 15,000 turns in an external phase expansion ring TRISTOR
- extracting as a cw H^- beam and injecting directly into an accumulator ring using the extremely good emittance of the TRIUMF beam to reduce foil traversals

This extraction will be achieved using an auxiliary rf cavity shown in Fig. 5 to either decelerate the beam to provide turn compaction for the pulsed extraction or to accelerate the beam to provide sufficient turn separation for the installation of a septum for cw extraction.

Figure 6 shows one scheme for matching to a 1 Hz synchrotron. After rf stacking in the TRIUMF cyclotron a beam pulse consisting of 160 turns (800 TRIUMF pulses) is injected by charge exchange on a 200 μg/cm^2 carbon foil into a dc accumulator ring in the booster tunnel. Foil traversals are reduced by using a stripping foil much smaller than the accumulator magnet

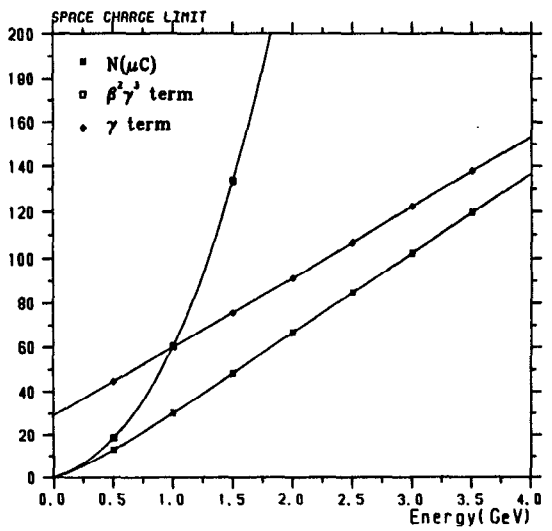

Fig. 4. Transverse space charge limit for the synchrotron option as a function of injection energy.

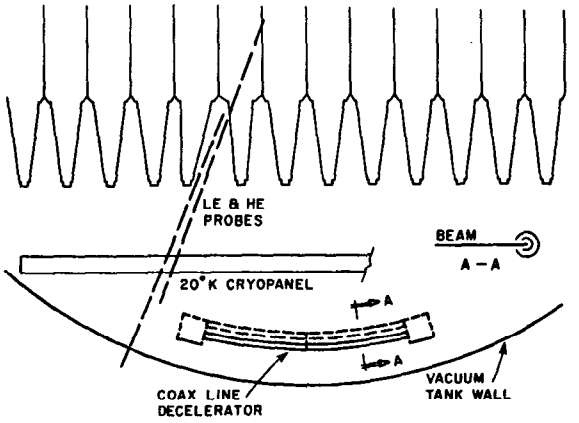

Fig. 5. Auxiliary rf cavity for decelerating or accelerating beam for H^- extraction.

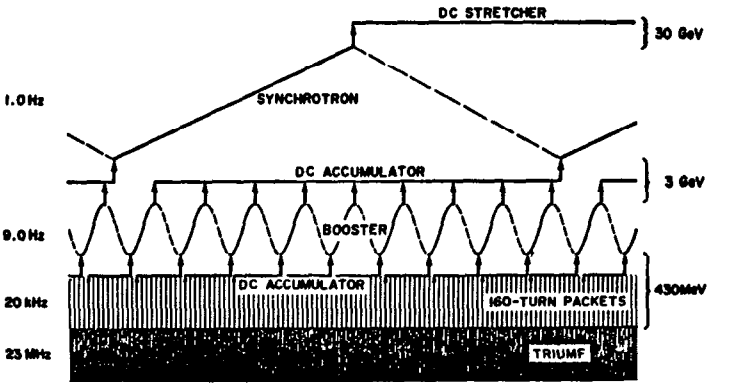

Fig. 6. Scheme for matching the TRIUMF cyclotron to a slow-cycling synchrotron.

aperture and by "painting" the beam across the magnet aperture in transverse and longitudinal phase space. The booster is then filled on each cycle and after acceleration the pulses are transferred in boxcar fashion to a dc accumulator in the main ring, which has a circumference 9 times the booster.

A layout of the proposed 30 GeV ring is shown in Fig. 7. The synchrotron tunnel would be approximately 1 km in circumference and buried 8-20 m below grade level.

Potential Neutron Sources

Both the 3.5 GeV intermediate stage of the cyclotron option and the 3 GeV booster/accumulator offer unique but quite different proton beams which could be used for a spallation neutron source. The relevant beam parameters are listed in Table II.

The short pulse length and high repetition rate of the cyclotron beam could provide a neutron source compatible with high energy (100 eV) neutron diffraction experiments. The large number of protons/pulse, especially from the main synchrotron accumulator ring could provide a high intensity neutron pulse for single pulse diffraction.

The kaon factory design study is still in progress, many problems remain to be solved, and none of the options has yet been singled out as the direction for detailed studies. This progress report is intended to indicate the potential of the proton beams from the proposed kaon factory and to elicit input from the neutron scattering community to ensure that their requirements are not overlooked in the design study.

Acknowledgements

Many colleagues at TRIUMF and visitors have contributed to the kaon factory design study. In the preparation of this paper I would like to acknowledge helpful discussions with M.K. Craddock, chairman of the design study, G. Mackenzie, I. Thorson and P. Egelstaff (Guelph).

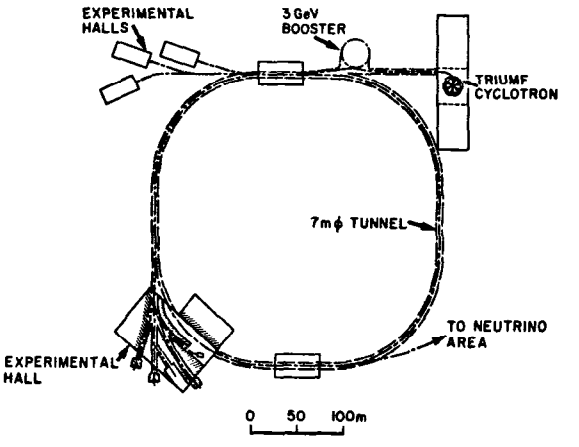

Fig. 7. Proposed 30 GeV accelerator layout.

Table II. Potential neutron sources using TRIUMF kaon factory

	booster synchrotron	slow-cycling accumulator	ring cyclotron
Energy	3 GeV	3 GeV	3.5 GeV
Radius	15 m	135 m	7.5-10.1 m
Repetition rate	9 Hz	1.0 Hz	dc or 10 kHz
Protons/second	6×10^{14} (100 μA)	6×10^{14} (100 μA)	6×10^{14} (100 μA)
Protons/pulse	7×10^{13}	6×10^{14}	6×10^{10} (10 kHz)
Pulse duration	0.32 μs	2.9 μs	0.22 μs
Pulse period	0.11 s	1 s	100 μs
Microstructure	2 ns/16 ns	2 ns/16 ns	10 ns/43 ns 0.3 ns/43 ns(dc)

References

1. J.R. Richardson et al., IEEE Trans. NS-22(3), 1402 (1975).
2. Proc. Second Kaon Factory Workshop, Vancouver, 1981, ed. R. Woloshyn and A. Strathdee, TRI-81-4.
3. Proc. Second LAMPF II Workshop, Los Alamos, 1982, ed. H.A. Thiessen et al., LA-9572-C.
4. J.F. Amann et al., LA-9486-MS (1982).
5. G. Manning, Proceedings of this conference.
6. R.L. Custom, IEEE Trans NS-28, 3115 (1981).
7. G.P Lawrence et al., Proc. of the XI Int. Conf. on High-Energy Accelerators, CERN, p. 103 (1980).
8. G. Bauer, Proceedings of this conference.
9. P. Egelstaff, Proceedings of this conference.
10. J.I.M. Botman et al., IEEE Trans. NS-30, 2007 (1983).
11. W. Joho, IEEE Trans. NS-30, 2083 (1983).
12. R. Laxdal et al., IEEE Trans. NS-30, 2013 (1983).

Session C

Targets I

Chairmen - W.E. Fischer and I.M. Thorson

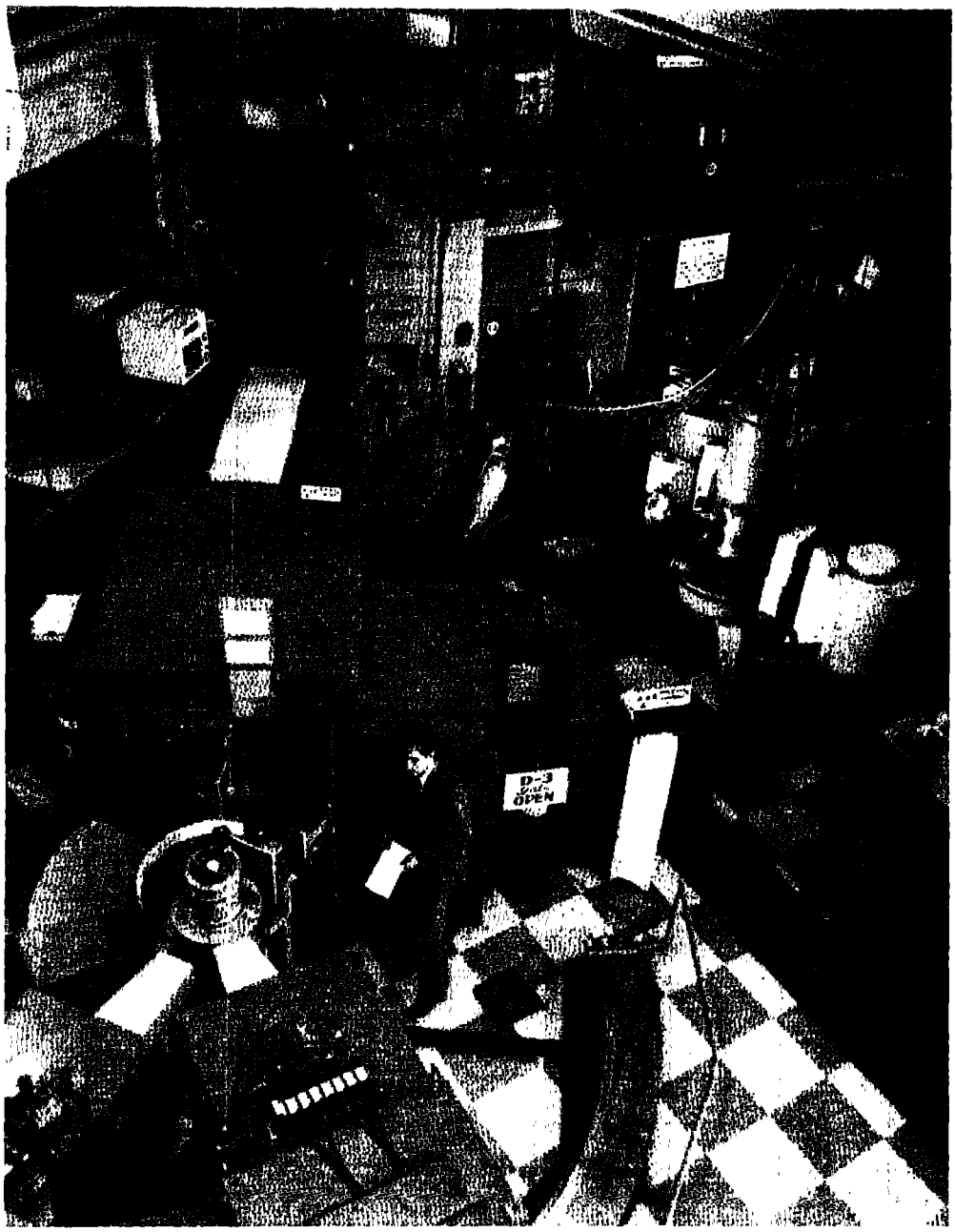

Proceedings of International Collaboration on Advanced Neutron Sources (ICANS-VII), 1983 September 13-16
Atomic Energy of Canada Limited, Report AECL-8488

PRODUCTION RATES OF SPALLATION AND FISSION PRODUCTS IN DEPLETED URANIUM AND NATURAL LEAD TARGETS BOMBARDED BY 600 MeV AND 1100 MeV PROTONS

W.AMIAN* , N.F.PEEK**, D.J.SHADOAN**, G.STERZENBACH*

* Institut fuer Reaktorentwicklung
Kernforschungsanlage Juelich GmbH
Postfach 1913
D-5170 Juelich, Germany

** University of California at Davis
Physics Department
Davis, California 95616
U.S.A.

ABSTRACT

Reaction rates for fission products and spallation products produced by bombarding natural lead and depleted uranium foils with protons at 600 MeV and 1100 MeV have been determined using Ge(Li) spectroscopy methods. The foils were placed on the beam entrance face of a thick rectangular target block of the respective material. Spectra of gamma-rays emitted in the decay of these products between one hour and one year after irradiation were obtained. Gamma-rays were assigned to the responsible products by matching gamma-ray energies and half-lives. Reaction rates were then obtained from the data by first determining the appropriate gamma-ray activity as of the end of the irradiation, correcting for detector efficiency and gamma-ray transition probability and dividing by the beam currant.
The resulting reaction rates are compared with model calculations at 1100 MeV. The general shapes of the distributions of reaction rates versus mass number agree fairly, but there are large discrepancies between individual data points and calculation. Reasons for this are discussed, especially regarding the effect of neutrons and secondaries which are produced in the target block.

INTRODUCTION

Lead and uranium are possible target materials for the German high flux neutron source SNQ. Therefore, it is required to study the production of residual activity in these target materials both from safety and maintenance aspects.

There are two possible ways to accomplish this task. The first is to study a nearly realistic spallation target in a mock-up experiment, map the induced activities at various positions inside the target and derive reaction rates at these points. This procedure has been adopted in the beginning of the SNQ study. It is, however, not possible to separate the combined influences of primary protons, secondary charged particles and fast or moderated neutrons. Thus, it is not straightforward to scale up the results to a real spallation target like the proposed target wheel.

Therefore, the second procedure, to study the fundamental high energy processes and to compare these results with model calculations, should be prefered. In this way, low energy neutron reactions, which are subject to normal reactor calculations, can be separated from high energy processes, and models for high energy spallation and fission processes can be compared with experimental data directely. This results in a combined effort to improve both the data basis and the model.

The present paper, actually, is between both procedures. Data which have been taken in connection with "infinitely thick" spallation targets have been reduced to obtain distributions of reaction rates as a function of mass number, so-called mass-yield distributions.
These have been compared with calculations for thin targets, although the influence of secondaries and neutrons could not be excluded.
The data for fission products and spallation products have been obtained in this study by gamma-ray assay of unseparated products in thin foils of uranium or lead. These foils have been bombarded by protons at 600 MeV and 1100 MeV and gamma-ray spectra have been recorded in time to follow the decay of individual gamma-ray lines.

EXPERIMENTAL

Target foils of 1.0 mm thickness and 30 mm diameter were placed on the beam entrance face of a large target simulating an "infinitely thick" spallation target. Two target materials were chosen for investigation, lead of natural composition and depleted uranium with an U-235 content of less than 0.5 %.
The experiments were conducted at Saturne National Laboratory (LNS) within the Centre d"Etudes Nucleaires de Saclay at proton energies of 600 MeV and 1100 MeV. The average beam intensity was up to 80 nA for the 1100 MeV runs and up to 25 nA for the 600 MeV runs. A more detailed description of the LNS experiments is given in reference /1/.
The uranium samples were vacuum encapsulated in aluminum cases to prevent the escaping of radioactive gases. Following each irradiation the samples were as quickly moved to the counting area as allowed by health physics considerations concerning the large target block. Short lived radioisotopes were out of the scope of this investigation.

A Ge(Li)-detector having an 80-cm^3 volume was used for the measurements. The output of the detector was amplified using standard equipment. The energy resolution for the 1332 keV line was 2.2 keV full-width at half-maximum. The detector was calibrated against IAEA and PTB standard reference sources with ±2% accuracy.
The samples were initially placed some meters from the face of the detector. When the counting rate had decreased, they were moved closer to the detector. Even at the closest distance of 23 cm, the detection efficiency is small enough to make true coincident gamma-ray summing negligible.

REACTION	cross section [mb]			REF.
	600 MeV	800 MeV	1100 MeV	
Al-27(p,3pn)Na-24	11.0+-3.3	10.5	9.9	[1]
	10.8+-0.7	10.5	10.2	[2]
		10.9+-0.2		[3]
		10.8		[6]
	11.0	10.75	10.4	[7]
Al-27(p,x)Na-22	19.6+-5.9	18	17	[1]
	13	12	11	[2]
	15	15.0+-1.5	15	[4]
		13.6		[6]
	17.3	16.3	14.8	[7]
Al-27(p,x)Be-7	4.0	5.4	7.0	[1]
	5	6.4+-0.6	8	[4]
			7.6	[5]
		5.7		[6]
	3.8	6.3	7.8	[7]
adopted values for beam monitor cross sections				
Al-27(p,3pn)Na-24	11.0	10.9+-0.2	10.5	
Al-27(p,x)Na-22	15.0		12.0	
Al-27(p,x)Be-7	5.0		7.6	

[1] G. FRIEDLANDER et al., Phys. Rev. 99(1955)263 based on a value of 10.8 mb for Na-24 at 450 MeV as given by L.Marquez, Phys. Rev. 86(1952) 405
[2] J.B. CUMMING, Ann. Rev. Nucl. Sci. 13(1963)261
[3] J.B. CUMMING et al.,Nucl. Instr. Meth. 180(1981)37
[4] H.R. HEYDEGGER et al., Phys. Rev. C14(1976)1506
[5[E. BAKER et al., Phys. Rev. 112(1958)1319
[6] G. RUSSELL et al.,ICANS-V, Juelich 1981
[7] J.TOBAILEM et al., CEA-N-1466(1)

TABLE 1. Cross sections for aluminum monitor reactions from literature and adopted values for the present work. Values are interpolated if no error is stated.

The spectra were recorded in time, starting at best half an hour after end of irradiation. The last data were taken one year thereafter. Counting time intervalls ranged between five minutes and 24 houres.

The number of protons per second hitting the target was determined from monitor reactions in aluminum. Cross sections from literature and the adopted values for the reactions Al-27 (p,3pn) Na-24, Al-27 (p,x) Na-22 and AL-27 (p,x) Be-7 are given in table 1. The number of residual nuclei at end of irradiation is determined by gamma-ray spectrometric measurements. The adopted nuclear properties are given in table 2. From these measurements the beam intensities in table 3 follow.

ISOTOPE	HALFLIFE	GAMMA-RAY	
		ENERGY [KeV]	INTENSITY [%]
Be 7	53.4 d	477.56	10.3
Na 22	2.6 y	511.00	179.8
		1274.54	99.94
Na 24	15.03 h	1368.55	100.00
		2754.10	99.85

TABLE 2. Adopted decay properties of Na 24, Na 22 and Be 7.

TARGET MATERIAL	ENERGY [MeV]	INTENSITY [PROTONS/SEC]	DURATION [h]
LEAD	600	1.1E+11	0.53
LEAD	600	1.1E+11	0.66
LEAD	1100	4.3E+11	1.03
URANIUM	600	3.9E+10	0.58
URANIUM	1100	4.9E+11	0.95

TABLE 3. Beam intensities and irradiation times of the experiment discussed in the present paper.

As a reference cross section only the Al-27(p,3pn)Na-24 value was used which is given in the literature with more precision than the values for the other two reactions. For a beam intensity as calculated from a given Na 24 production the agreement between calculated cross sections for the other two reactions and the litrature values is only reasonable.
For the calculatons we assumed a 15% error in the beam intensities which results from counting error, error in taking the correct irradiation time and mainly the errors in production cross sections.
The irradiation times durated up to 62 minutes. The beam intensity was monitored in five minutes steps by a secondary emission chamber. All irradiations ran with only slightly varying beam current so that for the longer lived nuclides no corrections were necessary.
The gamma-ray spectra obtained were recorded on magnetic tape for subsequent computer analysis and isotope identification. They were first corrected for analyzer deadtime and for random summing effects. Then the peak areas were extracted using the computer code AGAMEMNON /2/. These results were input to the halflife analysis and nuclide identification code YELLOW /2/, which determines the gamma-ray intensities as a function of time following irradiation and assigns to the decay particular products based on matching the gamma-ray energies and nuclide halflives. The results were then corrected for decay during irradiation and for gamma-ray attenuation in the samples.

For the present data it was sufficient to include only one parent and one daughter decay, since most of the precurser nuclides have short lifetimes and had decayed completely by the initiation of the first measurement which revealed the respective nuclide. Details of the methods are reported in reference /2/.

The discussion shows that the reaction rates which to obtain is the final goal of the experiments are not the direct information of the applied experimental method. The primary experimental informations deduced from the measured spectra are photon activities of particular gamma-ray transitions from decay of fission and spallation products produced by the irradiation. To determine the reaction rate of a given product, both the knowledge of its nuclear properties and the knowledge of experimental parameters are required. Nuclear properties are gamma-ray transition probabilities and halflives of the product and its parent. Experimental parameters are detector efficiency at the respective energy, the irradiation history and the beam intensity as discussed above.
All these properties and parameters are themselves possible sources of errors. For non-fission products, especially in the lead region, even the nuclear properties are not so well known.
Thus, it should be evident, that mass-yield distributions derived from gamma-ray spectrometrical methods
- miss many mass chains, which have either weak gamma-ray emitters or no gamma-ray emitters at all,
- will only give results for a defined set of products with high reaction rates, strong gamma-ray intensities and long enough halflives, unless radiochemical separation methods are applied,
- show fluctuations even relative to each other due to different nuclear properties and their quite different influences in deriveing reaction rates from the decay characteristics of a specific gamma-ray transition.

RESULTS

The measured reaction rates for 48 fission and spallation products in natural lead are given in table 4; the data for 56 products in depleted uranium in table 5. Uncertainties include statistical errors, fitting errors from the decomposition of a gamma-ray line as a doublet or triplet, counting rate associated uncertainties, errors in the detector efficiency calibration and the uncertainty in beam intensity. They do not include any errors in nuclear properties of the respective fission or spallation products. Therefore, the nuclear properties adopted for the calculations are also tabulated in tables 4 and 5.
Most of them were obtained from the Erdtmann and Soyka compilation /3/ of gamma-ray lines and have been checked for consistency with the Lederer and Shirley compilation /4/. For the shorter lived products errors in halflives would contribute considerably to the errors given for the reaction rates. Uncertainties in the absolute gamma-ray intensities should be considered for all products.

Reaction rates for fission and spallation products were obtained primarily for nuclides having halflives greater than about one day and having reaction rates greater than 2E-07 reactions per proton per g/cm^2 in lead , and greater than 1E-06 reactions per proton per g/cm^2 in uranium. Reaction rates were not obtained for all nuclides within this defined set, particularly not for those that decay almost entirely by beta-ray emisssion, but also for a few for which the primary gamma-ray had nearly the same gamma-ray energy as a more intense gamma-ray from another nuclide having a similar halflife.

There were gamma-rays observed for which reaction rates were not obtained, even though the gamma-ray could have been ascribed to the decay of a specific product. In these cases the assignments were not almost certain.
We were satisfied with analyzing one or two gamma-rays associated with the decay of a given product, usually but not always the gamma-ray with the highest intensity.

We attempted to obtain information for additional products, particularly for the light mass products Fe, Cu, Zn, Ga, which are of importance in corrosion studies /5/.
Even when observed, however, the extracted reaction rates for the expected gamma-rays were not adequate to determine unambigously correct assignments. In our opinion, this can be accomplished only if radiochemical separation methods are applied.
For some products which have been observed in the 1100 MeV experiments no results are given at 600 MeV. There are two reasons for that. Firstly, the 600 MeV experiments have been conducted at lower beam currents. This is especially true for the uranium experiment. As a consequence, almost exclusively fission products have been observed. Secondly, for these runs the decay in time could not be recorded as needed due to technical problems (sharing the multichannel analyzer with another group, delay in shipping the foils from France to our laboratory).

NUCLIDE	GAMMA ENERGY /keV/	GAMMA INTENSITY / % /	HALFLIFE	HALFLIFE OF PARENT NUCLIDE	REACTION RATE 1E-6 react./proton/(g/cm**2) @ 1100 MeV	@ 600 MeV
67 Ho 160	728.10	61.00	25.0 m	1.19 d	15.1 +- 4.3	n.d.
69 Tm 165	242.90	35.10	1.253d	10.5 m	32.4 +- 5.4	n.d.
	296.08	23.11				
69 Tm 166	2052.90	20.15	7.7 h	2.363d	32.8 +- 8.2	n.d.
	778.80	19.82				
69 Tm 167	207.80	42.00	9.25 d	17.7 m	45.6 +- 7.1	n.d.
70 Yb 169	197.97	36.00	30.70 d	1.417d	48.4 +- 8.4	14.3 +- 3.2
	177.18	22.00				
	130.51	11.50				
71 Lu 170	1054.28	4.614	2.02 d	16.0 h	78.4 +- 20.3	n.d.
71 Lu 171	739.82	52.77	8.22 d	12.09 h	51.6 +- 10.6	12.7 +- 2.6
	667.60	11.64				
71 Lu 173	272.01	12.50	1.37 y	23.6 h	101 +- 17.5	31.1 +- 6.7
72 Hf 175	343.40	86.92	70.0 d	10.5 h	68.7 +- 17.1	22.9 +- 5.0
	432.80	1.56				
75 Re 183	162.32	24.97	70.4 d	13.0 h	65.2 +- 9.5	59.2 +- 12.7
76 Os 185	646.11	81.00	94.0 d	14 h	73.9 +- 10.4	72.6 +- 15.8
	880.27	5.152				
77 Ir 188	155.03	33.40	1.73 d	10.3 d	85.1 +- 15.8	73.0 +- 20.3
	633.10	21.60				
	1210.00	6.75				
	2012.00	0.50				
78 Pt 191	538.87	13.40	2.8 d	3.2 h	107 +- 14.9	147 +- 26.0
	359.88	5.89				
79 Au 195	98.86	11.80	183 d	9.5 h	86.0 +- 12.7	118 +- 25.5
81 Tl 200	367.97	88.4	1.088d	21.5 h	86.0 +- 12.5	73.9 +- 14.9
	579.28	14.0				
	828.32	11.0				
81 Tl 201	135.34	3.70	3.063d	9.4 h	121 +- 24.6	115 +- 18.6
82 Pb 203	279.18	80.80	2.171d	11.76 h	129 +- 20.7	101 +- 18.4
	401.31	3.80				
83 Bi 204	899.15	99.0	11.3 h	3.52 h	14.5 +- 1.9	17.7 +- 3.2
	374.74	75.0				
83 Bi 205	703.30	28.0	15.31 d	1.8 h	19.7 +- 4.1	n.d.
	1764.27	27.0				
	987.80	17.0				
83 Bi 206	803.05	100.00	6.243d	8.83 d	9.9 +- 1.3	n.d.
	881.00	67.60				
	1718.65	34.00				
83 Bi 207	569.67	98.0	38 y	5.8 h	10.6 +- 1.7	9.7 +- 2.2
25 Mn 52	1434.30	100.00	5.7 d	8.3 h	0.71 +- 0.15	n.d.
25 Mn 54	834.81	99.978	312.2 d		0.95 +- 0.13	0.43 +- 0.11
30 Zn 65	1115.52	50.75	243.8 d	15.2 m	2.4 +- 0.2	n.d.
34 Se 75	264.65	58.60	120.4 d	1.63 h	3.7 +- 0.4	1.5 +- 0.4
	279.53	24.73				
	400.65	11.13				
37 Rb 83	529.54	30.0	86.2 d	32.4 h	5.8 +- 0.7	5.2 +- 1.1
	552.50	16.3				
38 Sr 85	513.99	99.28	64.73 d	2.7 h	6.1 +- 1.1	5.4 +- 1.1
39 Y 87	484.72	92.2	3.346d	1.6 h	6.5 +- 1.1	n.d.
39 Y 88	1836.01	99.36	106.6 d	83.4 d	8.4 +- 1.7	9.5 +- 2.2
	898.02	94.00				
40 Zr 89	909.20	99.87	3.268d	2.02 h	4.8 +- 0.7	n.d.
45 Rh 101m	306.77	86.7	4.34 d	8.5 h	8.2 +- 1.1	n.d.
45 Rh 102	475.00	93.00	2.89 y		3.0 +- 0.4	2.4 +- 0.7
	631.10	55.80				
	697.10	44.64				
47 Ag 105	344.20	40.9	41.3 d	56.0 m	3.5 +- 0.7	19.9 +- 4.5
	280.30	29.7				
	644.55	10.2				
	443.37	10.8				
50 Sn 113	391.71	64.17	115.1 d	6.74 m	0.2 +- 0.04	n.d.
	255.04	2.07				
52 Te 121	573.08	79.10	16.8 d	2.12 h	1.7 +- 0.2	1.5 +- 0.4
58 Ce 139	165.85	80.0	137.5 d	4.5 h	2.2 +- 0.2	n.d.
61 Pm 143	742.00	38.50	265 d	8.83 m	2.6 +- 0.4	n.d.
63 Eu 146	747.13	98.60	4.6 d	48.3 d	1.1 +- 0.2	0.43 +- 0.17
	1408.80	3.30				
63 Eu 149	327.70	3.8	93.1 d	9.4 d	10.8 +- 3.5	n.d.
21 Sc 46	1120.52	99.99	83.85 d		0.50 +- 0.15	n.d.
21 Sc 48	1311.80	99.99	1.825d		0.60 +- 0.15	n.d.
26 Fe 59	1099.22	56.50	45.1 d		1.7 +- 0.2	n.d.
	1291.56	43.20				
40 Zr 95	724.18	44.20	64.4 d	10.3 m	4.1 +- 0.4	3.9 +- 0.9
	756.72	54.80				
44 Ru 103	497.08	86.40	39.35 d	50 s	7.1 +- 1.5	8.0 +- 1.7
	610.33	5.30				
45 Rh 106	621.80	9.806	29.9 s	368.2 d	2.2 +- 0.4	n.d.
	1050.10	1.463				
47 Ag 110m	657.72	94.74	249.9 d		1.9 +- 0.4	2.6 +- 0.7
	884.67	72.86				
65 Tb 160	876.37	30.0	72.1 d		13.4 +- 3.2	22.3 +- 4.8
	966.17	25.5				
80 Hg 203	279.17	81.50	46.59 d		11.7 +- 1.1	15.1 +- 3.2

TABLE 4. Reaction rates of spallation and fission products produced by protons of 1100 MeV and 600 MeV at the beam entrance surface of a thick rectangular target of natural lead. The data are ordered by mass numbers in three groups each. The first group consists of spallation products, the second of neutron deficient high energy fission products, the third of neutron rich fission products and othar β^- emitters.

NUCLIDE	GAMMA ENERGY /keV/	GAMMA INTENSITY / % /	HALFLIFE	HALFLIFE OF PARENT NUCLIDE	REACTION RATE 1E-5 react./proton/(g/cm**2) @ 1100 MeV	@ 600 MeV
26 Fe 59	1099.22	56.50	45.1 D		0.73 +- 0.05	n.d.
	1291.56	43.20				
36 Kr 87	402.70	48.3	76.4 m	55.6 s	7.4 +- 0.9	n.d.
39 Sr 91	555.57	60.7	9.67 h	58 s	12.2 +- 1.1	n.d.
40 Zr 95	724.18	44.20	64.4 d	10.3 m	23.8 +- 2.2	17.5 +- 2.6
	756.72	54.80				
40 Zr 97	743.36	98.00	16.8 h	3.7 s	19.3 +- 2.2	20.5 +- 3.5
42 Mo 99	140.51	90.90	2.758d	2.6 m	17.7 +- 2.3	21.6 +- 3.6
44 Ru 103	497.08	86.40	39.35 d	50 s	32.4 +- 3.0	31.9 +- 5.3
	610.33	5.30				
45 Rh 105	319.24	19.6	1.473d	4.44 h	22.9 +- 2.1	19.1 +- 3.6
	306.31	5.44				
45 Rh 106	621.80	9.806	29.9 s	368.2 d	15.6 +- 1.5	15.4 +- 2.4
	1050.10	1.463				
47 Ag 112	1387.00	5.4	3.14 h	21.1 h	13.3 +- 4.8	10.3 +- 1.2
	616.80	43.5				
48 Cd 115	336.30	46.10	2.224d	20.0 m	7.6 +- 0.7	9.0 +- 1.6
	527.86	32.90				
	492.29	10.20				
51 Sb 125	427.95	29.60	2.77 y	9.64 d	6.3 +- 0.5	5.4 +- 0.9
	636.15	11.20				
	463.51	10.00				
51 Sb 127	685.50	35.7	3.85 d	2.1 h	6.2 +- 0.7	n.d.
	473.00	25.0				
	783.80	15.0				
52 Te 129	459.50	7.14	1.16 h	4.32 h	3.4 +- 0.4	2.9 +- 0.5
52 Te 132	116.30	1.95	3.246d	4.1 m	16.9 +- 1.8	13.6 +- 2.3
	228.16	88.50				
53 J 134	884.08	66.00	52.6 m	41.8 m	23.6 +- 4.3	n.d.
	847.03	96.00				
55 Cs 137	661.62	84.62	30.1 y	3.92 m	18.7 +- 1.8	17.6 +- 2.0
56 Ba 139	165.80	18.8	1.415h	9.3 m	18.8 +- 2.5	16.9 +- 2.8
57 La 140	1596.20	95.47	40.27 h	12.79 d	17.7 +- 1.4	17.4 +- 2.8
	815.80	22.32				
	487.03	43.00				
58 Ce 141	145.45	48.00	32.38 d	3.93 h	14.6 +- 2.1	9.4 +- 2.6
57 La 142	641.17	52.50	1.542h	10.7 m	11.9 +- 1.2	n.d.
58 Ce 143	293.30	43.4	33.7 h	14.0 m	10.6 +- 1.0	10.5 +- 1.8
58 Ce 144	133.53	10.8	284.2 d	39.8 s	11.9 +- 1.6	10.9 +- 1.9
60 Nd 147	531.00	13.5	11.06 d	12 m	7.6 +- 0.7	5.0 +- 1.1
63 Eu 156	2026.61	3.502	15.19 d	9.4 h	0.53 +- 0.2	n.d.
30 Zn 65	1115.52	50.75	243.8 d	15.2 m	0.25 +- 0.03	n.d.
31 Ga 68	1077.44	3.30	1.13 h	287 d	0.48 +- 0.15	n.d.
34 Se 75	264.65	58.60	120.4 d	1.63 h	0.51 +- 0.10	n.d.
	279.53	24.73				
	400.65	11.13				
37 Rb 83	529.54	30.0	86.2 d	32.4 h	1.4 +- 0.1	n.d.
	552.50	16.3				
39 Y 87	484.72	92.2	3.346d	1.6 h	0.73 +- 0.08	n.d.
39 Y 88	1836.01	99.36	106.6 d	83.4 d	2.1 +- 0.2	1.2 +- 0.4
	898.02	94.00				
40 Zr 89	909.20	99.87	3.268d	2.02 h	0.61 +- 0.08	n.d.
41 Nb 91m	1205.00	3.4	64 d	15.49 m	1.3 +- 0.3	n.d.
45 Rh 101m	306.77	86.7	4.34 d	8.5 h	1.3 +- 0.1	n.d.
47 Ag 105	344.20	40.9	41.3 d	56.0 m	1.3 +- 0.2	n.d.
	280.30	29.7				
	644.55	10.2				
	443.37	10.8				
50 Sn 113	391.71	64.17	115.1 d	6.74 m	0.89 +- 0.10	n.d.
	255.04	2.07				
52 Te 121	573.08	79.10	16.8 d	154 d	1.5 +- 0.2	n.d.
54 Xe 127	202.84	68.0	36.41 d	6.25 h	2.7 +- 0.3	1.9 +- 0.7
	172.10	25.4				
	374.96	17.7				
58 Ce 139	165.85	80.0	137.5 d	4.5 h	1.6 +- 0.2	n.d.
61 Pm 143	742.00	38.50	265 d	8.83 m	1.2 +- 0.1	n.d.
63 Eu 146	747.13	98.60	4.6 d	48.3 d	0.11 +- 0.01	n.d.
	1408.80	3.30				
79 Au 192	316.50	84.75	4.1 h	4.9 h	3.8 +- 0.3	n.d.
	295.98	32.63				
79 Au 194	328.50	60.90	1.646d	260 y	4.1 +- 0.4	n.d.
	293.60	10.663				
81 Tl 200	367.97	88.4	1.088d	21.5 h	3.8 +- 0.8	n.d.
	579.28	14.0				
	828.32	11.0				
83 Bi 204	899.15	99.0	11.3 h	3.52 h	3.6 +- 1.2	n.d.
	374.74	75.0				
83 Bi 205	703.30	28.0	15.31 d	1.8 h	1.8 +- 0.2	n.d.
	1764.27	27.0				
	987.80	17.0				
83 Bi 206	803.05	100.00	6.243d	8.83 d	1.9 +- 0.2	n.d.
	881.00	67.60				
	1718.65	34.00				
83 Bi 207	569.67	98.0	38 y	5.8 h	6.0 +- 0.7	n.d.
85 At 209	782.00	58.0	5.42 h	30 m	2.6 +- 0.3	2.0 +- 0.4
	792.00	37.0				

TABLE 5. continued on next page

NUCLIDE	GAMMA ENERGY /keV/	GAMMA INTENSITY / % /	HALFLIFE	HALFLIFE OF PARENT NUCLIDE	REACTION RATE 1E-5 react./proton/(g/cm**2) @ 1100 MeV	@ 600 MeV
86 Rn 211	947.20	27.0	14.60 h	3.1 m	2.3 +- 0.3	3.3 +- 0.6
	1135.00	18.0				
	250.10	10.0				
91 Pa 230	951.95	28.09	17.4 d		1.0 +- 0.1	1.3 +- 0.2
	918.50	7.95				
	898.65	5.618				
91 Pa 232	969.30	41.62	1.31 d		1.8 +- 0.3	2.3 +- 0.4
	894.30	19.84				
	150.10	10.84				
92 U 237	207.95	22.40	6.75 d	8.7 m	95.0 +- 8.6	63.5 +- 10.6
93 Np 239	277.60	14.10	2.355d	23.5 m	58.2 +- 5.6	59.5 +- 9.9
	228.19	10.72				

TABLE 5. Reaction rates of spallation and fission products produced by protons of 1100 MeV and 600 MeV at the beam entrance surface of a thick rectangular target of depleted uranium. The data are ordered by mass numbers in three groups each. The first group consists of neutron rich fission products, the second of neutron deficient high energy fission products, the third of spallation products.
(Continuation from previous page)

DISCUSSION

The primary purpose of this experiment was to measure reaction rates for fission and spallation products created during bombardement with high energy protons.
These reaction rates are plotted for the lead targets in figure 1 versus mass number of the residual nuclei both at 600 MeV and at 1100 MeV. All points are plotted with their experimental errors (one standard deviation). Arrows indicate that a stable reaction product is missing with certainty and, therefore, the total reaction rate of this mass chain is higher than indicated.

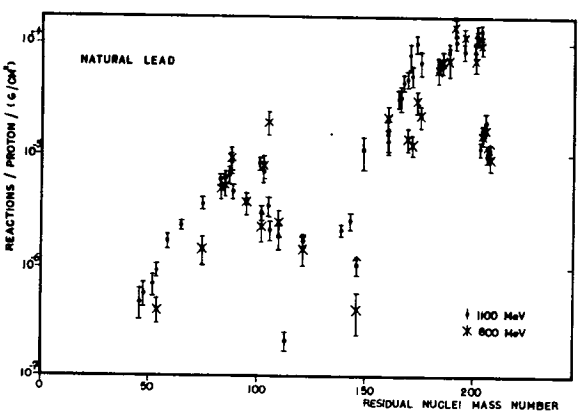

FIGURE 1 Distribution of reaction rates versus mass number for spallation and fission products produced by protons of 1100 MeV and 600 MeV, respectively, at the beam entrance surface of a thick rectangular target of natural lead.

The data for lead indicate that for mass numbers less than about 130 the reaction rates and, therefore, the shapes of the mass-yield distributions are nearly the same at 600 MeV and 1100 MeV. Also near to the mass numbers of the lead isotopes the reaction rates are nearly the same. In the intermediate region, however, there seems to be a difference in both shapes. While the 600 MeV data fall off steeply as mass number decreases (except for Ho 160, which is a β^- emitter), the 1100 MeV data seem to have a new maximum around 170 mass units and then the production rates fall off like at 600 MeV, with the location of the gradient shifted by about 10 mass units.

The 600 MeV results for uranium are compared in figure 2 to the 1100 MeV data. Because of the low beam intensity for this experiment, mainly fission products have been observed. It is not astonishing that their reaction rates agree well at 600 MeV and at 1100 MeV within the errors stated. Concerning the non-fission products with masses below 160 mass units there have been only two assignments which indicate that the reaction rates at 600 MeV are about one half the ones at 1100 MeV. There have been no assignments at 600 MeV for mass numbers between 160 and 208. Results for the higher mass numbers are similar within the experimental errors.

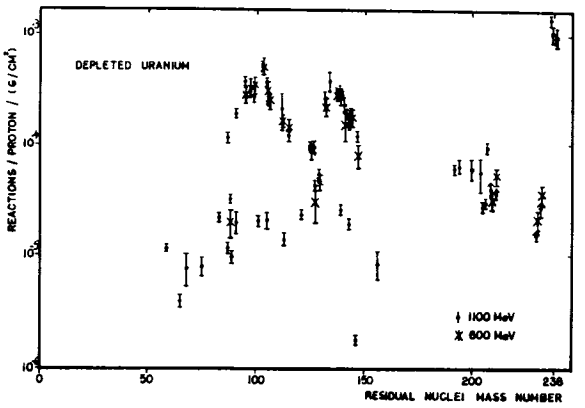

FIGURE 2 Distribution of reaction rates versus mass number for spallation and fission products produced by protons of 1100 MeV and 600 MeV, respectively, at the beam entrance surface of a thick rectangular target of depleted uranium.

The results shown in figures 1 and 2 are compared with HET calculations /6/ for 1100 MeV protons hitting lead targets, figure 3, and hitting uranium targets, figure 4. The calculations are for thin targets, i.e. no secondaries are considered to interact with a target nucleus. This situation is the easiest to calculate and gives only the residual nuclei left by high energy processes.
The calculated numbers of residual nuclei within a three mass unit interval are plotted as histograms in figures 3 and 4. The normalization is for a total inelastic cross section of 1.776 barns for the lead data and 1.983 barns for the uranium data. The errors from Poisson statistics of the calculated histogram are at worst 20%.

For natural lead, figure 3, calculation and experiment agree fairly only at the higher masses near to the masses of lead. At lower mass numbers it is evident that the calculated mass-yield distribution is shifted towards lower mass numbers by about 20 units. There is no obvious reason for that.
From the experimental point of view it is hard to imagine how a successive row of experimental points should be systematically too low by a factor of 4 while other points fit the calculation well. The only reason might be that we are missing stable nuclides and nuclides decaying from the opposite side towards the stability line. The influence of secondaries should go into the opposite direction.

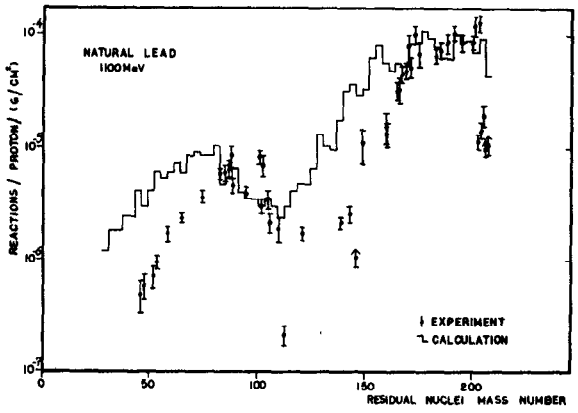

FIGURE 3 Comparison of experimental and calculated distributions of reaction rates versus mass number of, spallation and fission products produced by protons of 1100 MeV on lead. The calculations are done with HETC (JUEL-SPEZ-196) and apply to thin targets, whereas the measurements have been performed on the beam entrance surface of a thick rectangular target.

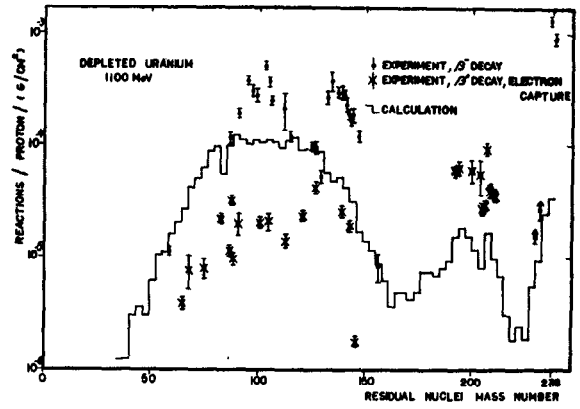

FIGURE 4 Comparison of experimental and calculated distributions of reaction rates versus mass number of spallation and fission products produced by protons of 1100 MeV on uranium. The calculations are done with HETC (JUEL-SPEZ-196) and apply to thin targets, whereas the measurements have been performed on the beam entrance surface of a thick rectangular target.

Turning to depleted uranium, figure 4, the agreement between experiment and calculation is bad again. In this figure we distinguish between nuclides which are β^- emitters and nuclides which decay by β^+ or electron capture. The β^- emitters between mass numbers 50 and 170 may be refered to as fission products. Their reaction rates are higher than anticipated from calculations for the thin target. The reason is that neutrons produced in the thick target initiate fissions in the thin target, too.
Referring to the calculations, however, high energy fisson products from bombarding uranium with protons do not only consist of neutron deficient isotopes as indicated by the crosses in figure 4, but also include some "normal" fission products, i.e. neutron rich isotopes. Thus, the high energy fission process is completely hidden by fissions from neutrons of intermediate energy.

A remarkable fact is that the center of the calculated fission peak is shifted towards lower mass numbers relatively to the experimentally observed double fission peak by about 15 to 20 mass units.
The satellite peak at masses around 200 units is reproduced, but the experimental values are about half an order of magnitude higher. The same is true for the steep decrease below mass number 238. Not reproduced by the calculations are the reaction rates for U 237 and Np 239. The latter, however, is produced by neutrons and not by protons.

In conclusion, the experimental and calculated mass-yield distributions given for uranium and lead are far from being consistent. Both experiment and model may be in error. Especially for uranium, the comparison with a thin target experiment would be of great interest.

CONCLUSION

The goal of the present experiment was to deduce reaction rates of fission products and spallation products produced during irradiation of natural lead and depleted uranium with protons at 600 MeV and 1100 MeV.
Although the basic spectral data appear quite complicated, for most of the gamma-rays given in tables 4 and 5 data reduction was not unusually difficult. Experimental errors have been given which include statistical errors, fitting errors for the decomposition of a gamma-ray line as a doublet or triplet, counting rate associated uncertainties, error in detector efficiency and uncertainties in beam intensity.
The major weakness in determining reaction rates for fission and spallation products by this technique is the rely on nuclear data; such data have different influences on the various products and result in nonuniform scatter in the data. Errors of these nuclear data have not been included in the experimental errors given, because they are normally not tabulated in the compilations /3/,/4/.
It is apparent that the reaction rates given in tables 4 and 5 will change as nuclear data measurement become more accurate.

The comparisons of the present experimental data and model calculations with HETC /6/ do not give encouraging consistencies, although the genaral shape is similar. At small and intermediate mass numbers the calculated mass-yield distributions seem to be shifted by 15 to 25 mass units towards smaller masses. It has to be pointed out, however, that the calculations are made for thin targets, whereas the measurements have been performed on the surface of an "infinitely thick" spallation target.
To reduce the influence of secondaries and neutons, an experiment to measure the production rates of thin targets has been planned at 800 MeV proton energy.

REFERENCES

/1/ W.AMIAN, N.F.PEEK, D.J.SHADOAN, Gamma-Ray Measurements of Isotopes Produced by 1.1 GeV Protons on Lead and Uranium Targets, ICANS-V, Juelich 1981
/2/ W.AMIAN, N.F.PEEK, D.J.SHADOAN, Measurements of the Spallation and Fission Product Production for Depleted Uranium and Natural Lead Targets Bombarded by 1100 MeV Protons, ICANS-VI, Argonne 1982
/3/ G.ERDTMANN, W.SOYKA, The Gamma-Rays of the Radionuclides, Verlag Chemie, Weinheim and New York 1979
/4/ C.M.LEDERER, V.S.SHIRLEY, Tables of Isotopes,Seventh Edition, John Wiley & Sons, New York 1978
/5/ W.LOHMANN, A.RIBBENS, private communications
/6/ P.CLOTH, D.FILGES, G.STERZENBACH, T.W.ARMSTRONG, B.L.CALBORN, The KFA-Version of the High-Energy Transport Code HETC and the Generalized Evaluation Code SIMPEL, JUEL-SPEZ-196, March 1983

Proceedings of International Collaboration on Advanced Neutron Sources (ICANS-VII), 1983 September 13-16
Atomic Energy of Canada Limited, Report AECL-8488

FERTILE-TO-FISSILE CONVERSION AND FISSION MEASUREMENTS FOR THORIUM BOMBARDED BY 800-MeV PROTONS

J. S. Gilmore, G. J. Russell, H. Robinson, and R. E. Prael
Los Alamos National Laboratory
P.O. Box 1663
Los Alamos, New Mexico 87545, U.S.A.

Summary

Axial distributions of fertile-to-fissile conversion (^{232}Th to ^{233}U), four spallation products, and 34 fission products have been measured for a thick thorium target bombarded by 800-MeV protons. Uranium-233 production was determined by measuring the amount of ^{233}Pa produced, and the number of fissions was deduced from the fission product yield curves. The axial distributions were integrated to get the total conversions and fissions occurring in the target. Our preliminary experimental results are 1.25 ± 0.06 atoms of ^{233}Pa produced per incident proton, and 1.56 ± 0.25 fissions per incident proton. Corresponding calculated results are 1.267 ± 0.007 and 1.543 ± 0.006.

Introduction

The work reported here is part of the Fertile-to-Fissile Conversion (FERFICON) program at the Los Alamos National Laboratory.[1, 2, 3] The experiment was conducted at the Weapons Neutron Research Facility (WNR)[4] using the 800-MeV proton source of the Clinton P. Anderson Meson Physics Facility (LAMPF).[5] We have measured ^{233}U production, thorium fission, four spallation products, and 34 fission products in a thick thorium target irradiated with 800-MeV protons. We determine ^{233}U production by measuring the amount of ^{233}Pa formed, and deduce the number of fissions from fission product mass-yield curves. Our experimental approach has been described previously.[3] Briefly, we explicitly measure the axial distribution of products by sampling various planes perpendicular to the target axis; the radial integral for each plane is performed by combining sampling-foils from the plane. We integrate the measured axial distributions over the target to obtain the total number of each reaction.

This measurement is a "clean" integral experiment, and the data are relevant to spallation neutron source development, accelerator breeder technology, and validating computer codes used in these applications. We compare measured quantities with calculated predictions.

Calculational Approach

At Los Alamos, we have the following Monte Carlo codes integrated into a package for use in spallation physics computations: a) the Oak Ridge National Laboratory (ORNL) code HETC[6] for particle transport >20 MeV, and b) the Los Alamos code MCNP[7] for neutron and photon transport <20 MeV. The Los Alamos code HTAPE, written by Dick Prael, is used to analyze the Monte Carlo results. We have operational the latest ORNL HETC version which includes high-energy fission effects for $Z \geq 91$, and the Rutherford Appleton Laboratory (RAL) HETC version, as modified by Atchison,[8] which allows high-energy fission with essentially no restriction on Z. With MCNP, we do continuous-energy Monte Carlo using pointwise ENDF/B-V cross sections.

In our calculations, we do a precise mockup of target geometry, target canister, proton beam window, and air paths. We simulate the measured proton beam profile with eleven concentric ring-sources, and obtain the proton fraction in each ring from the measured distribution.

Experimental Setup and Procedures

We used a 19-rod clustered target having the physical characteristics given in Table I. The axial distributions of reaction products were determined from ninety 41.94-mm-diameter by 0.254 mm-thick thorium foils. Ten weighed-and-matched, four-gm foils were placed in each of seven planes perpendicular to the target axis within the target, and on the front and back target faces (see Fig. 1). Each plane contained one foil in the central rod and nine foils loaded symmetrically in three of the six target sectors. We chose this loading for mechanical reasons, and to minimize any effects from misalignment of the proton beam, which was focussed on the central rod.

After the target assembly was irradiated with 1.91 x 10^{16} protons, nine solutions were prepared for counting by dissolving the foils in nitric acid containing small amounts of hydrochloric and hydrofluoric acids. For each plane, representative sampling was accomplished by combining one half of the solution of the central foil with the solution of the remaining nine foils. Five ml (2.5%) of the final solution was used for Ge(Li) gamma assay. One additional sample was prepared utilizing 5% of the foil on the front face of the central rod.

To determine the number of protons striking the target, a 0.254-mm-thick Al monitor foil (sandwiched between two 0.0254-mm-thick Al guard foils to compensate for recoil loss) was placed ~60 cm in front of the target. The number of $^{27}Al(p,x)^{7}Be$, $^{27}Al(p,x)^{22}Na$, and $^{27}Al(p,3pn)^{24}Na$ reactions occurring in the monitor foil were used to determine the incident proton dose (see Table II). The center of the beam was known from the discoloration of a cellophane foil which covered the monitor foil packet, and the proton beam profile was measured by counting concentric rings cut from one of the guard foils. The measured proton beam profile is shown in Fig. 2. Ninety-seven percent of the protons were within the diameter of the central rod.

All dissolved thorium samples were counted using a Ge(Li) detector and associated pulse height analyzer which had been calibrated against a mixed radionuclide gamma-ray reference standard.* The gamma-ray spectra were analyzed by the GAMANAL computer program.[9] After the samples had been counted 15 times over a period of 40 days, the decay data were processed by the CLSQ program.[10] Strontium-89, ^{90}Sr, ^{96}Nb, ^{96}Tc, ^{105}Rh, ^{141}Ce, and ^{147}Nd had to be resolved from interfering activities by decay. Cesium-134, ^{137}Cs, and ^{85}Sr were determined by gamma-counting radiochemically separated samples, while ^{89}Sr and ^{90}Sr were measured on beta counters which had been calibrated by the method of Bayhurst and Prestwood.[11] Atoms of gamma emitting nuclides were calculated from specific gamma-rays using the gamma branching intensities and half-lives given in the Gamma-Ray Catalog by Reus, Westmier and Warnecke.[12] All nuclides were corrected for decay during the irradiation and for beta or gamma attenuation in the samples.

Experimental Results and Conclusions

Yields for 39 isotopes, either independent (direct formation) or cumulative (produced by direct formation plus the beta-decay of predecessors) were sought in each of the 10 samples. Fig. 3 shows the axial distribution of four of these products: (a) ^{233}Pa, formed by radiative capture which maximizes near z = 9 cm, (b) ^{95}Nb, the fission product with the highest cumulative yield among those we measured, which maximizes near z = 3 cm, (c) ^{227}Th, a high-mass spallation product produced by the p,p5n reaction, which peaks at about 5 cm, and (d) ^{205}Bi, a low-mass spallation product whose yield decreases monotonically with distance into the target. Although certain details of the fission product mass-yield curves change from the front to the back plane, the main features are quite similar. This point is illustrated by Fig. 4 which shows the ratio of the yields of selected fission products to the cumulative yield of ^{95}Nb as a function of axial position. As might be expected, the largest changes occur in the less probable modes of fission, e.g., for low independent yields such as ^{95}Nb and ^{134}Cs, or for neutron deficient isotopes such as ^{87}Y and $^{119}Te^{m}$.

Figure 5a shows the fission product yield-curve from the front-face-foil of the central rod. This mass-yield curve is two-peaked and exhibits several signs of high-energy fission: (a) the shape of the mass-yield curve defined by the cumulative yields (open circles) is quite asymmetric with the heavy peak lower and narrower than the light; (b) the independent

* Amersham Corporation solution number R9/270/46.

yields of antimony isotopes near stability in the mass 120-126 region are comparable to the cumulative yield of ^{127}Sb which would comprise the total 127 chain yield at low energies; and (c) several neutron-deficient isotopes (shown by filled points) were readily measured.

Fission product yields from the outer 9 foils at the front face of the target have been calculated by subtracting the center foil from the data for the entire first plane (see Fig. 5b). None of the neutron-deficient products were observed in these foils. The mass-yield curve appears similar to that from 14-MeV neutron fission of ^{232}Th,[13] which is also shown normalized at mass 99.

Turkevich and Niday proposed that mass yield distributions could be represented by a two-mode-of-fission hypothesis (TMFH)[14] and Ford demonstrated its applicability at intermediate energies.[15] This hypothesis, which suggests that any fission yield curve can be expressed as the combination of symmetric and asymmetric components, has been applied to this data to aid in understanding the curves and to determine the number of fissions. Fourteen-MeV neutron fission of thorium was chosen for the asymmetric or "low-energy-fission" mode since it appears to approximate the secondary fission in the first plane; the amount of fission by this mode was determined from the yields of the four heaviest masses which were measured, ^{140}Ba, $^{141,143}Ce$, and ^{147}Nd. The yields remaining after subtracting the low-energy component are shown in Fig. 5c. The points represent average values, from combining the data from all 10 samples. The Gaussian distribution ("symmetric") which was determined by least squares analysis of the data for ^{72}Zn, ^{89}Sr, ^{95}Nb, ^{103}Ru, ^{105}Rh, and ^{112}Pd, centers about mass 108, has a standard deviation of 14 mass units (FWHM = 33), and has been normalized to 200%.

Figure 5d shows the axial distributions for "symmetric" and "asymmetric" fission and their sum. For the central rod at z = 0.0, the ratio is 2.34, the highest we observed. Figure 6 compares the mass yield curve produced by the TMFH with the experimental data for the entire first plane. The "symmetric to asymmetric" ratio is 1.03. The point at mass 97 is probably low because of independent formation of ^{97}Nb, and mass 115 is low by the yield of $^{115}Cd^m$, neither of which were measured. Data for masses 127, 132, and 137 are also expected to be low because of the large charge dispersion in this region in high-energy fission. The lowest ratio of "symmetric to asymmetric", 0.633, occurs at z = 13.11 cm, and the agreement between experimental data and TMFH curve is somewhat better (see Fig. 7). The number of fissions in the sample is determined by summing the mass-yield curve (unnormalized) and dividing by two. A mass-yield curve defined by connecting the data points with straight lines for these two planes gave results that were 12% and 8% lower than the TMFH curves, respectively.

The axial distributions of ^{233}Pa, ^{227}Th, ^{205}Bi, ^{95}Nb, and fission were used to determine the total production per proton in the target. The total number for each reaction is:

$$\text{Total}_i = \frac{M}{\ell \cdot p} \int N_i(z)\, dz$$

where M is the mass of the target in grams, ℓ is the target length in cm, p is the number of protons, and N_i is the number of atoms produced per gram of thorium. The integral was evaluated using Simpson's rule and points read from the graphs as illustrated in Figs. 3 and 5d. Some of our experimental results are shown in Table III. The uncertainty on the number of fissions includes the possibility of a somewhat higher number due to insufficient information on the charge distribution and the yield of nuclides near stability.

In Table III, we also show computational results with and without high-energy fission. For no high-energy fission, we used both the ORNL and RAL models; such a comparison tests differences in evaporation schemes. We used the RAL model with two level density parameter (B_o) values to study high-energy fission effects.

When high-energy fission is neglected, we see the following comparisons between measured and calculated quantities: a) both models predict ^{233}U production to better than 6%, b) the calculated fissions are low by a factor of ~3, c) both models significantly underpredict ^{95}Nb (a fission product) formation and overpredict ^{205}Bi and ^{277}Th production, and d) model predictions intercompare well except for the ^{205}Bi values. When high-energy fission is included, we note the following: a) for B_o = 8 MeV, the calculated ^{233}U production and number of fissions agree very well with measured values, b) for either B_o, the calculated ^{95}Nb and ^{205}Bi production is signficantly improved over the no high-energy fission

case, but there are still marked differences with measured values, and c) for both B_0 values, the calculated ^{227}Th formation is low by a factor of ~2. Based on the comparisons in Table III, we would say that with high-energy fission, the RAL model with B_0 = 8 MeV gives better overall agreement with measurements than with B_0 = 14 MeV (which is the RAL recommended value). This tentative conclusion agrees with that recently reached by the Juelich group.[16]

Further calculated results for the 19-rod clustered thorium target are shown in Table IV. We utilize the $\bar{\nu}$ values to give us an "average" energy for low-energy neutron fission which is then used to predict the low-energy production of the measured fission products. We note for a "frame-of-reference" that the $\bar{\nu}$ values could be attained with a fission mixture of ~70% fission spectrum neutron fission and ~30% 14-MeV neutron fission. Also, the inclusion of high-energy fission adds ~29% to the energy deposition in the target.

A final publication of this thorium conversion measurement is being readied, and will include the effects of a mass-dependent B_0 in the computations as well as measured versus calculated results for more of our experimental data.

Acknowledgements

This work was performed under the auspices of the U.S. Department of Energy. We appreciate the support of E. R. Whitaker, J. R. Baldonado, and K. J. Hughes in setting up the experiment, and the assistance of the counting room personnel in the Los Alamos Nuclear and Radiochemistry group. Many thanks to Antoinette Sandmeier for her typing help.

References

1. G. J. Russell, "Applied Spallation Physics Research at Los Alamos," ICANS-VII, International Collaboration on Advanced Neutron Sources, Chalk River Nuclear Laboratories, Chalk River, Canada, Sept. 12-16, 1983.

2. G. J. Russell, J. S. Gilmore, R. E. Prael, H. Robinson, and S. D. Howe, "Spallation Target-Moderator-Reflector Studies at the Weapons Neutron Research Facility," Symp. on Neutron Cross Sections from 10-50 MeV, Brookhaven National Laboratory, Upton, NY, May 12-14, 1980, BNL-NCS-51245, Vol. I, pp. 169-192 (July 1980).

3. G. J. Russell, J. S. Gilmore, H. Robinson, and R.E. Prael, "Fertile-to-Fissile and Fission Measurements for Depleted Uranium Bombarded by 800-MeV Protons," ICANS-V, Proc. of the 5th Meeting of the International Collaboration on Advanced Neutron Sources, Juelich, West Germany, June 22-26, 1981, Juel-Conf.45, ISSN 0344-5789, pp. 621-639 (Oct. 1981).

4. G. J. Russell, P. W. Lisowski, S. D. Howe, N. S. P. King, and M. M. Meier, "Characteristics of the WNR - a Pulsed Spallation Neutron Source," Nuclear Data for Science and Technology, K. H. Bockhoff, ed., 1983, pp. 831-835.

5. M. S. Livingston, LA-6878-MS, UC-28 and UC-34, Los Alamos National Laboratory (1977).

6. K. C. Chandler and T. W. Armstrong, "Operating Instructions for the High-Energy Nucleon Meson Transport Code HETC," Oak Ridge National Laboratory, Report ORNL-4744 (January 1972).

7. Los Alamos Monte Carlo Group, "MCNP - A General Purpose Monte Carlo Code for Neutron and Photon Transport, Version 2B," LA-7396-M, Revised (April 1981).

8. F. Atchison, "Spallation and Fission in Heavy Metal Nuclei under Medium Energy Proton Bombardment," Meeting on Targets for Neutron Beam Spallation Sources, Juelich, West Germany, June 11-12, 1979, Juel-Conf-34, ISSN 0344-5798, pp. 17-45 (January 1980).

9. R. Gunnink and J. B. Niday, "Computerized Qualitative Analysis by Gamma-Ray Spectrometry," University of California, NTIS, USAEC report UCRL-51061 (1972).

10. J. B. Cummings, "Applications of Computers to Nuclear and Radiochemistry," National Academy of Sciences National Research Council Report NAS-NS-3107, pp, 25-33 (1962).

11. B. P. Bayhurst and R. J. Prestwood, "A Method for Estimating Beta-Counting Efficiences," Nucleonics, 17, No. 3, pp. 82-85 (1959).

12. U. Reus, W. Westmier and I. Warnecke, "Gamma-Ray Catalog," Gesellschaft fuer Schwerionenforschung, Darmstadt, GSI-Report 79-2 (1979).

13. T. R. England, "Preliminary ENDF/B-VI Yields," private communication.

14. A. Turkevich and J. B. Niday, "Fission of ^{232}Th with Pile Neutrons," Phys. Rev. 84, pg. 52 (1951).

15. G. P. Ford, "Analysis of the Two-Mode-of-Fission Hypothesis," Phys. Rev. 118, pg. 1261 (1960).

16. T. W. Armstrong, P. Cloth, D. Filges, and R. D. Neef, "An Investigation of Fission Models for High-Energy Radiation Transport Calculations," Juel-1859, ISSN. 0366-0885 (July 1983).

TABLE I

Physical Characteristics
of the 19-Rod Clustered Thorium Target

Density (g/cm^3)	Diameter (cm)	Length (cm)
11.38	18.28[a]	36.31

[a] Effective diameter ($D = d\sqrt{n}$) for the 19-rod clustered target with an individual rod diameter of 4.194 cm.

TABLE II

Al Monitor Foil Data

Reaction	Cross-Section (mb)		Measured Number of Protons	Statistical Error (%)
$^{27}Al(p,x)^{7}Be$	5.7		1.89×10^{16}	±1.4
$^{27}Al(p,x)^{22}Na$	13.6		1.91×10^{16}	±1.1
$^{27}Al(p,3pn)^{24}Na$	10.8		1.93×10^{16}	±1.3
		Average	1.91×10^{16}	±0.7

TABLE III

Preliminary Experimental Data Compared to Calculated Results
for the Thorium Conversion Measurement

	Experiment	Calculation			
		Without High-Energy Fission		With High-Energy Fission	
		ORNL B_0 = 8 MeV	RAL B_0 = 8 MeV	RAL B_0 = 8 MeV	RAL B_0 = 14 MeV
^{233}U Production (atm/p)	1.25 ± 0.06	1.321 ± 0.009	1.248 ± 0.008	1.267 ± 0.007	1.120 ± 0.007
No. of Fissions (fiss/p)	1.56 ± 0.25	0.550 ± 0.004	0.486 ± 0.004	1.543 ± 0.006	1.444 ± 0.006
^{95}Nb Production (atm/p)	0.068 ± 0.003	0.0300 ± 0.0005	0.0265 ± 0.0005	0.0551 ± 0.0009	0.0523 ± 0.0009
^{205}Bi Production(atm/p)	0.0056 ± 0.0003	0.0500 ± 0.0011	0.0362 ± 0.0010	0.0077 ± 0.0004	0.0080 ± 0.0004
^{227}Th Production(atm/p)	0.046 ± 0.002	0.0644 ± 0.0016	0.0658 ± 0.0016	0.0221 ± 0.0007	0.0236 + 0.0007

TABLE IV

Calculated Thorium Target Characteristics

	Without High-Energy Fission		With High Energy Fission	
	ORNL B_0 = 8 MeV	RAL B_0 = 8 MeV	RAL B_0 = 8 MeV	RAL B_0 = 14 MeV
Protons				
Leakage > 20 MeV (p/p)	0.226 ± 0.003	0.231 ± 0.003	0.228 ± 0.002	0.229 ± 0.002
$\overline{E}$ (Mev)	234.7 ± 4.4	235.6 ± 4.4	239.0 ± 3.2	237.9 ± 3.2
Neutrons				
Leakage > 20 MeV (n/p)	1.019 ± 0.007	1.013 ± 0.006	1.012 ± 0.005	1.040 ± 0.005
$\overline{E}$ (MeV)	93.15 ± 0.97	92.84 ± 0.97	93.12 ± 0.68	90.93 ± 0.67
Leakage < 20 MeV (n/p)	21.01 ± 0.11	19.45 ± 0.11	20.79 ± 0.09	18.82 ± 0.09
$\overline{E}$ (MeV)	---	---	---	2.093 ± 0.017
Capture < 20 MeV (cap/p)	1.321 ± 0.009	1.248 ± 0.008	1.267 ± 0.007	1.120 ± 0.007
$\overline{\nu}$ for Neutron Fission < 20 MeV (n/fiss)	2.773 ± 0.029	2.754 ± 0.029	2.761 ± 0.025	2.840 ± 0.027
$\overline{\varphi}$ < 20 MeV (n/cm^2.s)[a]	---	---	---	$(2.00 \pm 0.01) \times 10^{13}$
Fissions				
High-Energy > 20 MeV (fiss/p)	---	---	0.986 ± 0.005	0.884 ± 0.004
Low-Energy Neutrons < 20 MeV (fiss/p)	0.550 ± 0.004	0.486 ± 0.004	0.557 ± 0.004	0.560 ± 0.004
Energy Deposition				
E > 20 MeV (MeV/p)	421.2 ± 0.8	447.2 ± 0.9	588.2 ± 0.6	583.4 ± 0.6
E < 20 MeV (MeV/p)	122.3 ± 0.8	109.1 ± 0.7	123.9 ± 0.6	122.5 ± 0.6

[a] Average neutron flux inside target for 100 μA of 800-MeV incident protons

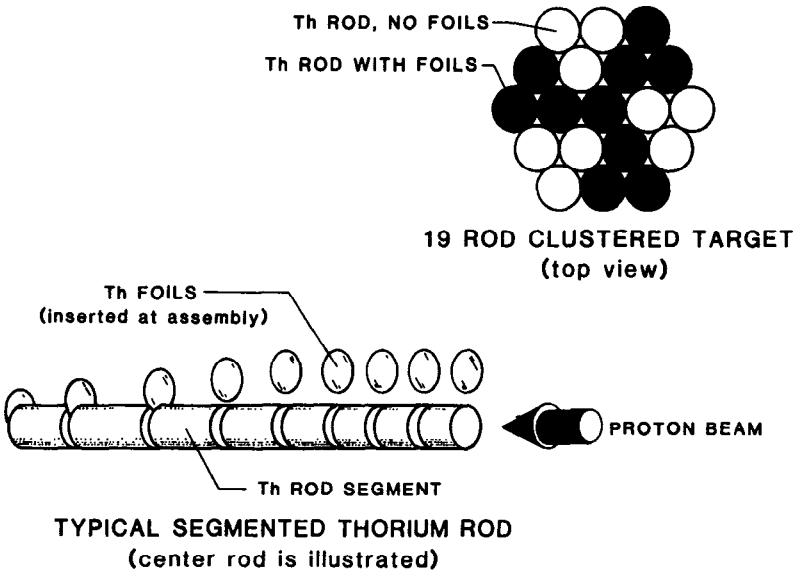

Fig. 1 Illustration of the 19-rod clustered thorium target, the location of the foils in the array, and the foil positions within a rod.

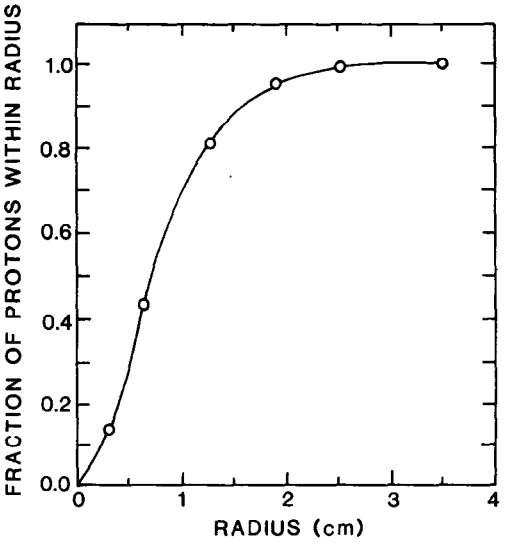

Fig. 2 Measured proton beam profile.

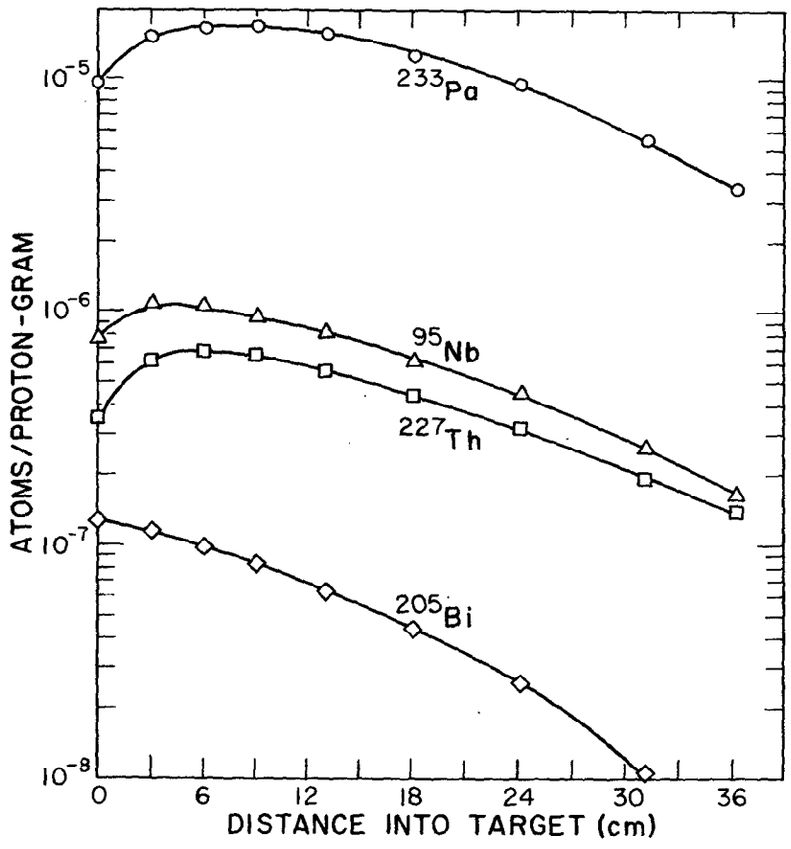

Fig. 3 Axial distributions of ^{233}Pa, ^{95}Nb, ^{205}Bi, and ^{227}Th in the thorium target.

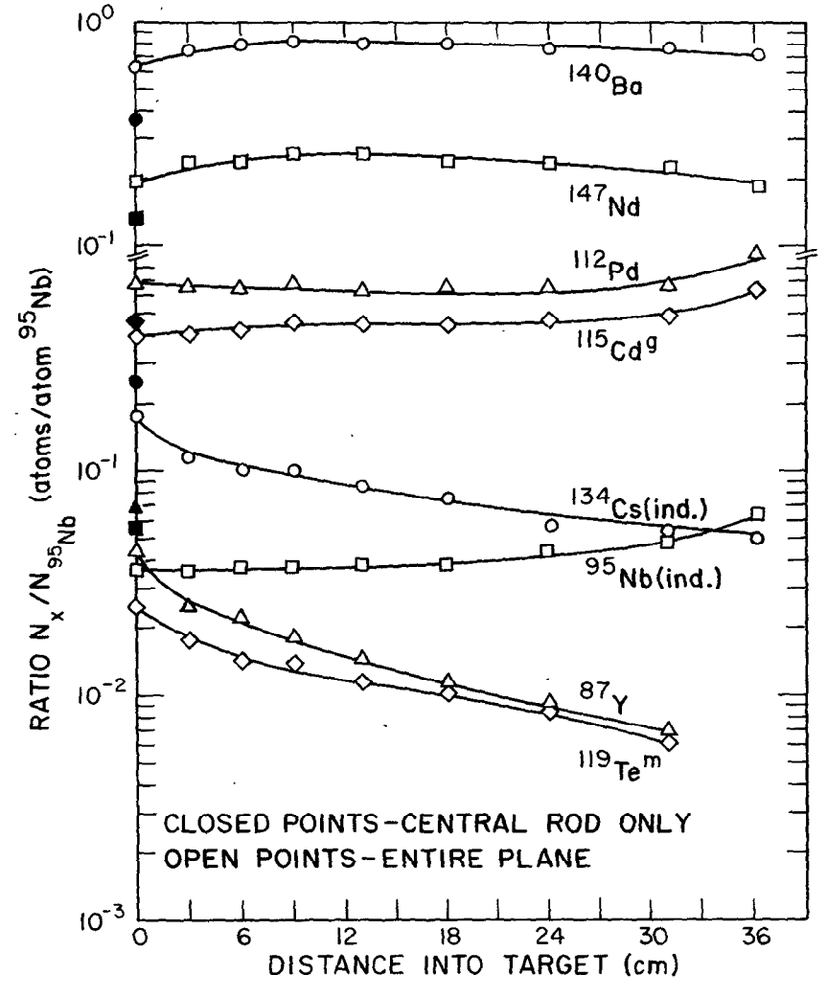

Fig. 4 Ratio of the yields of selected fission products to the cumulative yield of ^{95}Nb as a function of axial position in the thorium target.

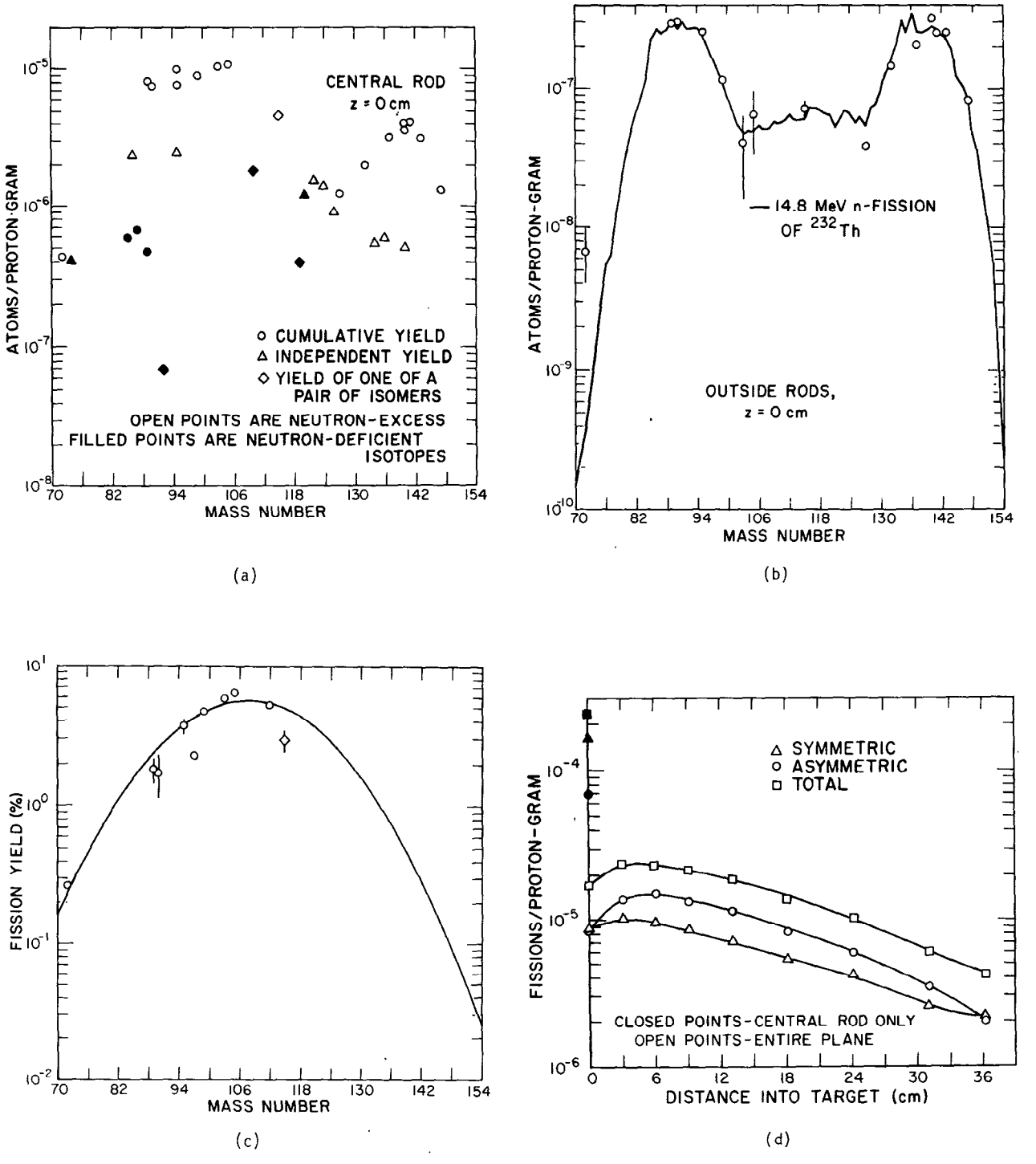

Fig. 5 Fission data from the thorium target: (a) fission product yields from the central rod, z = 0.0 cm, (b) comparison of the fission product yields from the outside rods, z = 0.0 cm, with yields from 14.7-MeV neutron- fission of ^{232}Th, (c) normalized mass-yield curve for hypothetical "symmetrical" fission mode, and (d) axial distribution of fissions, and of hypothetical "symmetrical" and "asymmetrical" fission modes in the thorium target.

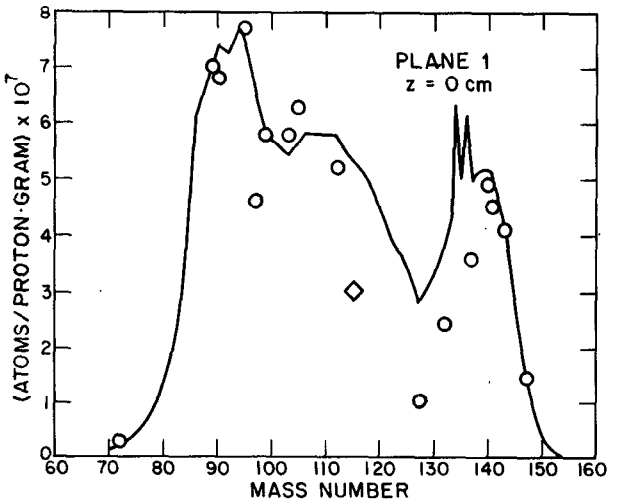

Fig. 6 Comparison of the TMFH mass-yield curve with experimental data from the z = 0.0 cm plane of the thorium target.

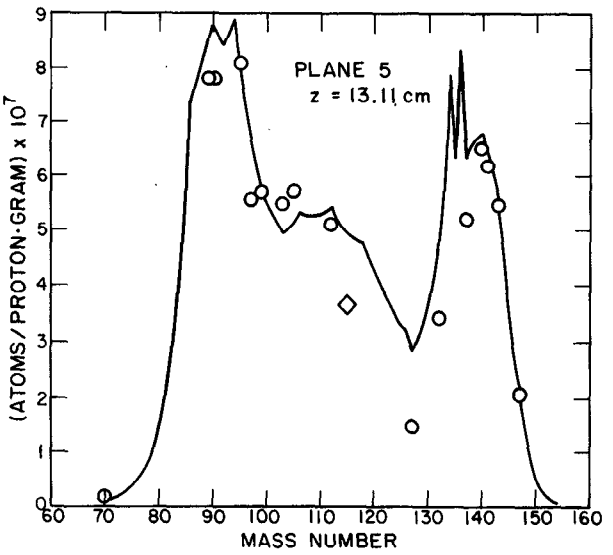

Fig. 7 Comparison of the TMFH mass-yield curve with experimental data from the z= 13.11 cm plane of the thorium target.

Proceedings of International Collaboration on Advanced Neutron Sources (ICANS-VII), 1983 September 13-16
Atomic Energy of Canada Limited, Report AECL-8488

RECENT TARGET DESIGN CALCULATIONS AT KFA

P. Cloth, D. Filges, R.D. Neef, H. Schaal

Institut für Reaktorentwicklung, Kernforschungsanlage Jülich GmbH
Postfach 1913, D-5170 Jülich, Germany

ABSTRACT

The target design calculations described here were performed for the two proposed proton beam energies (350 MeV and 1100 MeV) and different target material mixtures as tungsten, lead and uranium. The results for some important nuclear parameters as neutorn production, neutron fluxes and energy deposition were discussed. Preliminary calculations for the high energy source shielding and "grooved" moderator design were also shown.

INTRODUCTION

The recent target design calculations made by KFA are mainly performed for comparisons of nuclear parameters of the SNQ target station at the two forseen proton beam energies of 350 and 1100 MeV. One aim of these calculations was to optimize the targets for different materials and beam energies.

EVALUATIONS FOR PROTON BEAM ENERGIES OF 350 MEV VS 1100 MEV

All calculations were performed with HETC/KFA-1 /1/ and based on the 3-D target model described in detail in Ref. /2/. The main parameters for the calculations are shown in Table I.

Table I Parameters for Calculations

Beam Parameters:	
- kinetic energy:	350 MeV/1100 MeV
- particles:	protons
- average current:	5 mA
- pulse current:	200 mA
- pulse width:	0.25 ms
- pulse frequency:	100 s^{-1}
- beam profiles:	gaussian 4 cm FWHM truncated at radius = 4 cm
Targets:	
- geometry:	rotating "wheel"
- materials:	U_{dep}(0.2 nat% ^{235}U)-, Pb-, W-H_2O/Al mixtures*, and solid W
- cladding/structur:	aluminium
- coolant:	H_2O
Moderators:	H_2O/D_2O
Shielding-Material:	cast iron and concrete

*mixture: heavy material 76.5 %
cladding 7.0 %
coolant 16.5 %

1. Neutron production, neutron fluxes in H_2O moderator and energy deposition for different target materials (W, Pb, U_{dep})

In table II the neutron yields (< 15 MeV) per proton in the target are compared for proton beam energies of 350 and 1100 MeV and for different target compositions as described in table I. Additionally in table III the particle production for the uranium case is given.

Table II Neutron Yield per Proton in Target-Region

(n/p < 15 MeV)

Material	350 MeV	1100 MeV	ratio 1100/350
U_{dep}-H_2O-Al	5.15	30.12	5.8
Pb-H_2O-Al	3.43	19.53	5.7
W-H_2O-Al	4.16	21.3	5.12
W_{solid}	4.49	23.3	5.19

Table III Comparison of Particle Production for U_{dep}-Targets

	350 MeV	1100 MeV	ratio 1100/350
Neutrons produced per proton in the system			
< 15 MeV	5.87	35.6	6.1
Neutron yield per proton in target			
< 15 MeV	5.15	30.12	5.8
> 15 MeV	0.51	3.7	2.3
Charged particle yields per proton			
protons	0.44	4.0	9.0
pions	1.7×10^{-3}	2.8×10^{-1}	170
(neutral pions)	2.0×10^{-3}	1.9×10^{-1}	95

A comparison of thermal neutron fluxes (10^{-5} - 0.41 eV) in the fast moderator (size: length x height x width 20x12x15 cm^3) is given in table IV. The given thermal fluxes are the average omnidirectional thermal fluxes within that position of the moderator defined by the total moderator length of 20 cm (along the beam direction), the total moderator height of 12 cm (direction perpendicular to beam tube axis), and the central 5 cm region of the 15 cm moderator width (direction along beam tube axis). For details see Ref. /2/. In all calculations the moderator had the same positions and size, therefore none of these data were optimized for the special target composition and beam energy.

Table IV Thermal Neutron Fluxes in Fast Moderator*
(thermal energy 10^{-5} - 0.41 eV)

Target	Φ_{th} (a) ($n/cm^{-2}\ s^{-1}$/proton) 350 MeV	1100 MeV	Φ_{th} (b) ($n/cm^{-2}\ s^{-1}$) 350 MeV	1100 MeV
U_{dep}-H_2O-Al	4.9×10^{-3}	2.65×10^{-2}	1.5×10^{14}	8.3×10^{14}
Pb-H_2O-Al	2.9×10^{-3}	1.6×10^{-2}	0.9×10^{14}	5.0×10^{14}
W-H_2O-Al	3.5×10^{-3}	1.8×10^{-2}	1.1×10^{14}	5.6×10^{14}
W-solid	3.9×10^{-3}	2.0×10^{-2}	1.2×10^{14}	6.2×10^{14}

(a) neutron fluence per beam proton
(b) average neutron flux for I = 5 mA
*same system for all calculations, not optimized

The depth distributions of the calculated energy deposition inside the target "mixture" (i.e. the homogenized region of the target wheel) are shown in Figure 1. The deposition for 350 MeV beam energy is predominately due to ionization by primary protons and secondary protons for all target materials. However, for 1100 MeV beam energy in case of uranium as target material only about 30 % of the energy deposition is caused by primary and secondary protons, whereas the rest comes from high energy fission and low energy neutron induced fission. From Figure 1 it can be seen that cooling problems for 350 MeV beam energy may arise from Bragg-peak energy deposition at the end of the proton range. In table V the peak energy deposition corresponding to a single pulse for different target materials and 350 MeV and 1100 MeV beam energy is given. In table VI the total deposition in the target wheel for an average proton beam current of I = 5 mA for both energies and all target materials is compared. If the proton beam energy is increased to 1100 MeV the energy deposition in the lead is enlarged by a factor of 2 whereas for the uranium target the deposition increases by factor of about 5.

Table V Peak Energy Deposition for U_{dep}, Pb, W as Target Material

Target	350 MeV(1) MeV/cm^3-proton	Peak Deposition kJ/cm^3 per pulse**
U_{dep}-H_2O-Al	4.3	0.215
Pb-H_2O-Al	3.63	0.18
W-H_2O-Al	4.5	0.225
W-solid	4.36	0.218

Target	1100 MeV (2) MeV/cm^3-proton	Peak Deposition kJ/cm^3 per pulse**
U_{dep}-H_2O-Al	3.0	0.15
Pb-H_2O-Al	1.2	0.06
W-H_2O-Al	-	-
W-solid	-	-

** pulse current I = 200 mA, pulse width 0.25 ms
pulse frequency 100 s^{-1}
(1) for radial intervall about beam axis r=1.0 cm
(2) for radial intervall about beam axis r=1.5 cm

Table VI Comparison of Heating for U_{dep}, Pb, W as Target Material*

Deposition in Target (MeV)	350 MeV U_{dep}	Pb	W_{mix}	W
> 15 MeV	366	292	288	287
< 15 MeV	210	6	30	10
Total Deposition MeV/P	576	298	318	297
Total Deposition in MW for I=5 mA	2.88	1.49	1.59	1.48

Deposition in Target (MeV)	1100 MeV U_{dep}	Pb	W_{mix}	W
> 15 MeV	973	542	-	-
< 15 MeV	1515	29	-	-
Total Deposition MeV/P	2488	571	-	-
Total Deposition in MW for I=5 mA	12.44	2.86	-	-

*Depth of systems not optimized

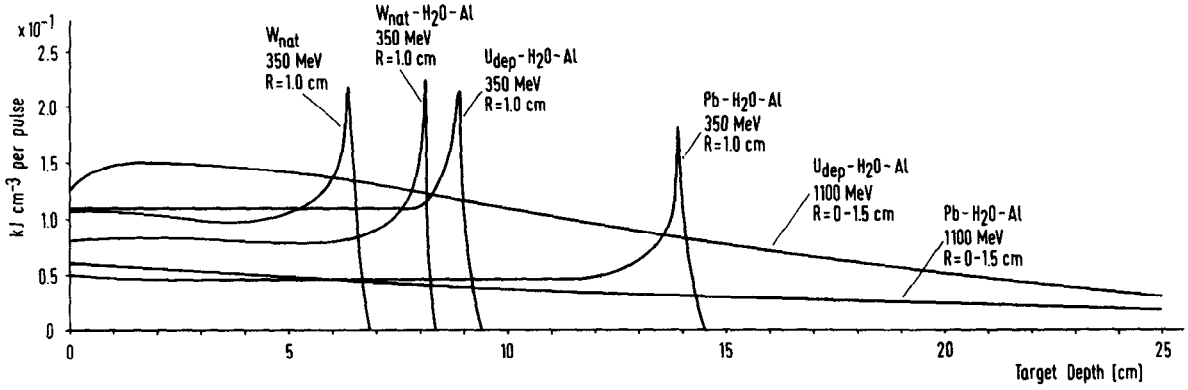

Figure 1 Energy deposition inside target wheel (axial)

2. High Energy Source Shielding

The calculations were done in a coupled procedure with the Monte Carlo code HETC/KFA-1 and the one-dimensional transport code ANISN /3/. For the HETC calculations the target area was surrounded by a sphere of 5 m thickness, consisting of cast iron. HETC calculated the angular dependent fast neutron flux (E_n > 50 MeV) at spherical shells around the target center (see fig. 2) thus generating a shell source for ANISN. For the ANISN calculations a sphere with 4 m of cast iron and 1 m of concrete was supposed. The cross section data were taken from LANL-library. ANISN calculated the neutron flux and the dose rate inside the shield.

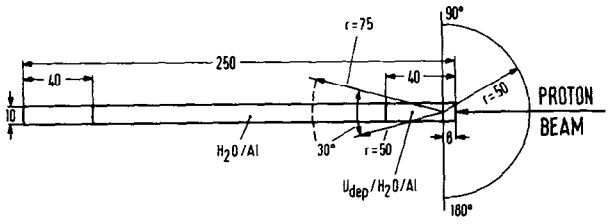

Figure 2 Simulation of high energy source for 1-D ANISN shielding calculations

The first question was, whether it would be useful to build different shieldings for 350 MeV and for 1100 MeV proton beam energy. Fig. 3 shows the dose rate vs. sphere radius for both cases. The curves have different intensities, but the same shape. So to get same dose rate at the outer edge of the shield, the dose rate curve for E_p=1100 MeV has to be extrapolated as shown in Fig. 4. Then the difference ΔL=80 cm means, that the cases 350 MeV and 1100 MeV have to be different in 80 cm thickness of iron only. So it does not seem to be reasonable to build different shields.

The second question was, whether the shield thickness should be the same in forward as in backward direction for 1100 MeV beam energy. A comparison of angular dependent fast neutron yields (from HETC calculations) lead to a dose rate ratio forward to backward (for constant thickness of the shield) of about 20, but coupling calculations give a ratio of about 1000. The reason for this difference lies in the fact, that the energy spectrum (see Fig. 5) in the forward direction is much harder than in the backward direction and that the angular shape in backward direction is more isotropic than in forward direction. So it can be stated that different shield thicknesses in forward and backward direction should be taken into account. Detailed studies are planned.

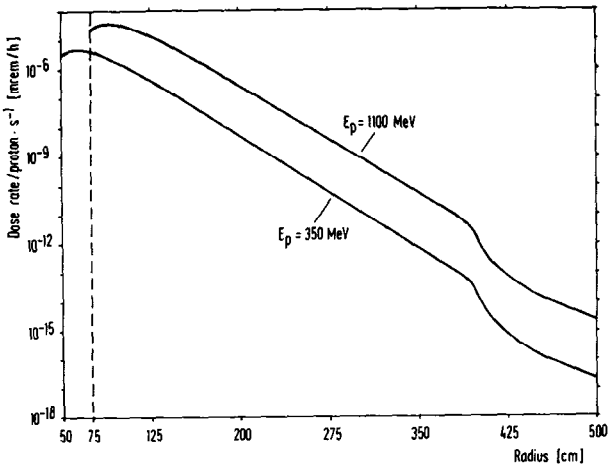

Figure 3 Coupled dose rate calculations (HETC/ANISN) in forward direction

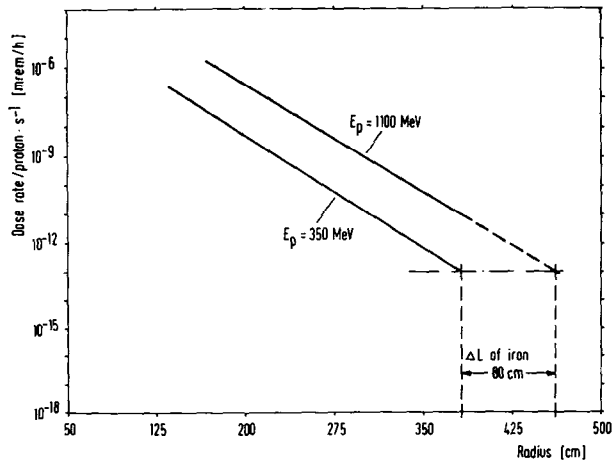

Figure 4 Determination of additional shielding thickness comparing 350 MeV and 1100 MeV proton beams

STUDIES FOR TARGET OPTIMIZATION

1. Target Depths and Fast Moderator Position for 350 and 1100 MeV Proton Beam Energy

To determine optimal target depths dependent on the different target material compositions the following criteria have to be taken into account

- proton range
- spatial dependent neutron production in the target
- escape distribution on the surface of the target
- spatial dependent energy deposition
- material saving
- minimum of radioactive inventory

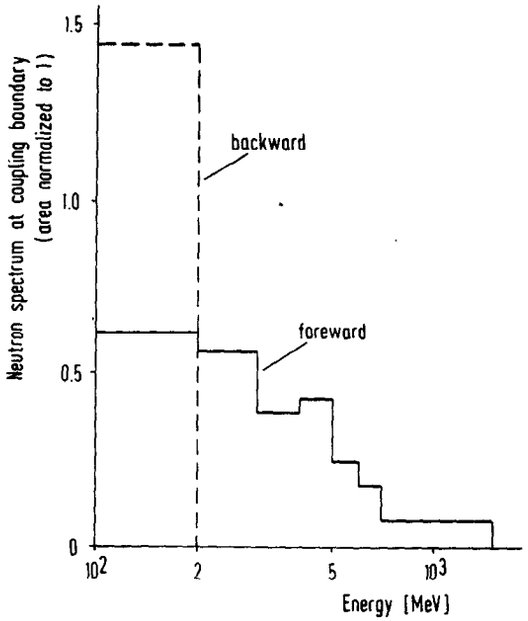

Figure 5 Neutron spectra for 1100 MeV proton beam energy for uranium target in forward and backward direction (coupling surface R=75 cm see Fig.2)

The proton ranges for the relevant targets are given in table VII.

Table VII Proton Ranges and Bragg Peak Position

Target	Bragg Peak Position 350 MeV (cm)	Proton Range (cm) 350 MeV	1100 MeV
U_{dep}-H_2O-Al	8.8	9.0	48.3
Pb-H_2O-Al	13.8	14.0	75.9
W-H_2O-Al	8.12	8.25	44.4
W-solid	6.3	6.75	40.0

In Figure 6 the spatial dependent neutron production in the target for 350 MeV beam energy is plotted. From these calculations the cummulative production rates were determined and are shown in Fig. 7. To avoid the high energy deposition in the "Bragg"-peak area (see Fig. 1) the target depth should not include the "Bragg"-peak position. This condition is fullfilled if one cuts the cummulative curve of neutron production at 85%. In the 1100 MeV case, the optimal target depth was estimated from the cummulative escape distributions of neutrons in proton beam direction. This was done because the proton range is very large compared to range of the 350 MeV protons therefore the escape distribution of neutrons determines the depth of the target system. In table VIII the optimal target depths for both energies are given.

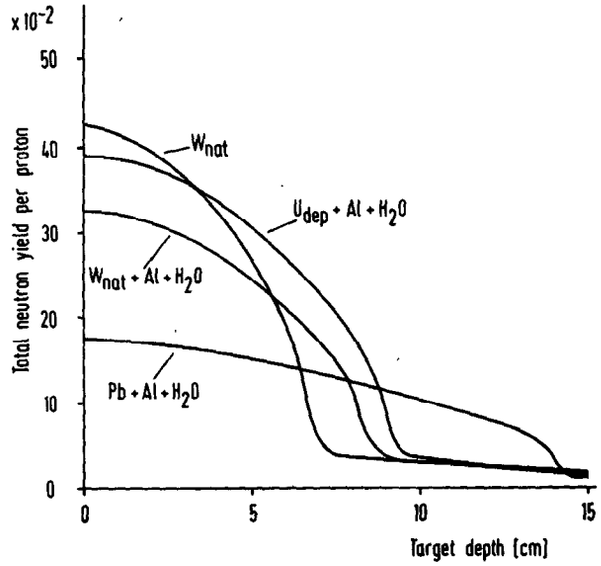

Figure 6 Spatial dependent neutron production rates in target wheel (350 MeV beam energy)

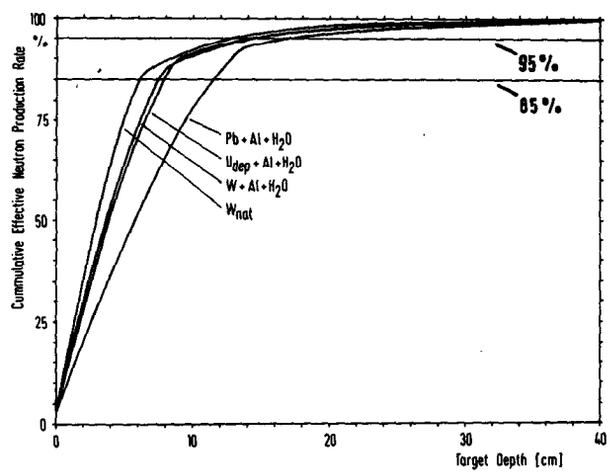

Figure 7 Cummulative effective neutron production rate vs. target depth (350 MeV beam energy)

The position of the fast moderator for 350 MeV and 1100 MeV proton energy depends on the spatial neutron flux or neutron current distributions. The center of the moderator should be located below the maximum of the escape distribution or flux distribution of the targets. In Figures 8 - 10 the distributions are shown. From these distributions the moderator positions for 350 MeV and 1100 MeV beam energy and different target mixtures are determined and given in Table IX.

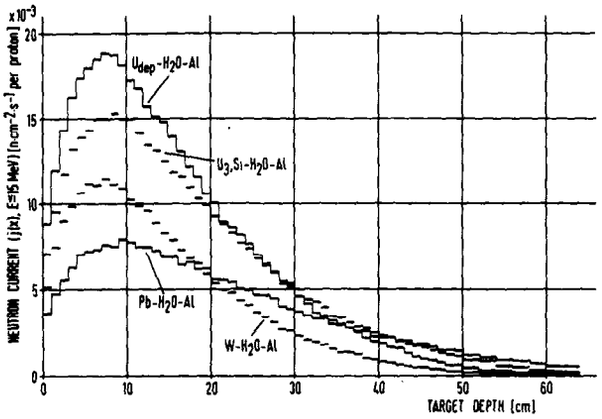

Figure 8 Escape distributions for different target mixtures vs. target depth (1100 MeV beam energy)

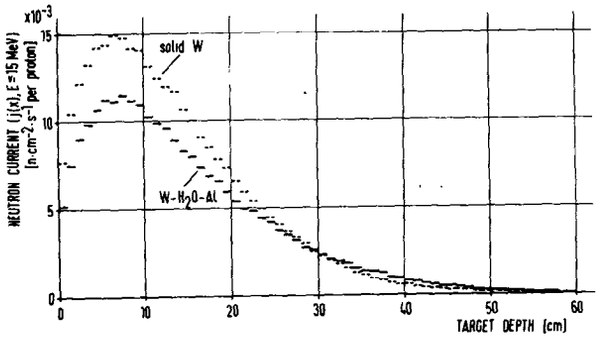

Figure 9 Escape distributions for W-mixtures and W-solid targets vs. target depth (1100 MeV beam energy)

Table VIII Target Depth for 350 MeV and 1100 MeV proton beam energy

Target	Target Depth (cm) 350 MeV 85% cummulative neutron production	1100 MeV 95% cummulative neutron escape distribution
U_{dep}-H_2O-Al	8.0	36.0
Pb-H_2O-Al	12.0 (13.0 for 90%)	68.5
W-H_2O-Al	7.75	36.0
W-solid	6.0	31

Table IX Moderator Positions for 350 MeV and 1100 MeV Proton Energy

Target	350 MeV	1100 MeV
	Peak Position=Center of Moderator (cm)	
U_{dep}-H_2O-Al	4.0 - 5.0	7.5 - 8.5
Pb-H_2O-Al	6.0	8.0 - 11.0
W-H_2O-Al	4.0	7.0 - 8.0
W-solid	3.0 - 4.0	6.5 - 7.5

2. Moderators

Fast Moderators have to be optimized in their geometrical dimensions as well as in their structural material components. Experiments show in special cases that "grooved" moderators give higher detector responses for thermal neutrons than solid moderators. To study this phenomenology a special fast running 3-D geometry model for HETC/MORSE Monte Carlo calculations was developed /4/. The advantage of this geometry model is easy parameter variation for overall size of the moderator and description of grooves and fins including structure and moderator material. Point detector estimation of escaping neutron fluxes and currents in energy time and space with importance sampling is used. Some preliminary results to show possible gains for grooved moderators (24 grooves)

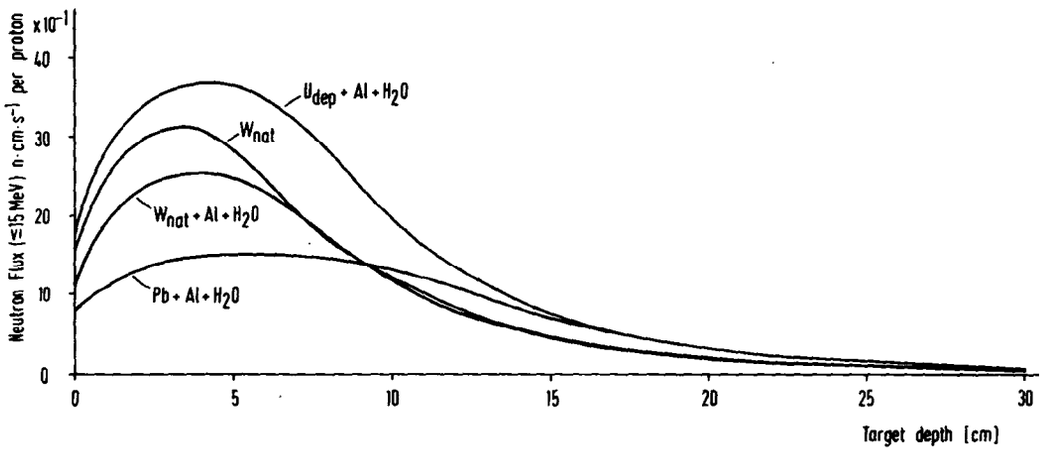

Figure 10 Neutron flux distributions for different target mixtures vs. target depth (350 MeV beam energy)

compared with solid moderators are shown in Figure 11. The study is in progress. Results will be published.

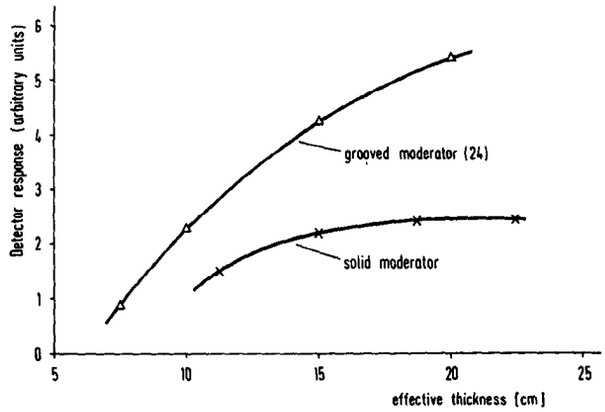

Figure 11 Comparison of detector responses (thermal energy 10^{-5} - 0.4 eV) for solid and grooved moderators of same overall size

Investigations on cold sources were started evaluating cross section for hydrogen (H_2) at 20° K for different mixtures of para- and orthohydrogen. The new cold source of KFA-DIDO research reactor has been designed with these data and is now under construction. Results should be available in about one year. Details of the data evaluation and the design will also be published.

REFERENCES

/1/ P. Cloth, D. Filges, G. Sterzenbach, T.W. Armstrong, B.L. Colborn
The KFA-Version of the High-Energy Transport Code HETC and the generalized Evaluation Code SIMPEL
KFA-Report Jül-Spez-196, March 1983

/2/ T.W. Armstrong, P. Cloth, D. Filges, R.D. Neef
Theoretical Target Physics Studies for the SNQ Spallation Neutron Source
KFA-Report Jül-Spez-120, July 1981

/3/ H. Schaal, M. Kloda, G. Sterzenbach
Internal Note, SNQ 3 J../BH 191082

/4/ To be published as KFA-Jül-Report

/5/ To be published as KFA-Jül-Report

Proceedings of International Collaboration on Advanced Neutron Sources (ICANS-VII), 1983 September 13-16
Atomic Energy of Canada Limited, Report AECL-8488

PROGRESS IN MATERIALS INVESTIGATIONS FOR SNQ - TARGETS

P. Krautwasser *
W. Lohmann **

Kernforschungsanlage Jülich GmbH, D-5170 Jülich, FRG
* Division for Reactor materials (IRW)
** Solid State Division (IFF-SNQ)

Summary

The materials investigations and development program for heavily loaded components of the SNQ-target wheel is presented. This broad program includes the target elements, proton beam windows, the slide ring sealing and the water chemistry of the cooling systems. Two examples are discussed as highlights in more detail: the thermal cycling effects on uranium (part of the target element development) and the possible use of sinter aluminium product for the stationary proton beam window.
During thermal cycling of uranium alloys at a lower temperature of 55°C and temperature differences ΔT = 10, 35 and 65 K, the growth rate per cycle approaches at higher cycle numbers a constant value for each ΔT. The growth rate increases with increasing ΔT and seems to be less influenced by differences in uranium alloy composition or material microstructure than by the amplitude of the temperature cycle.

Introduction

The achievement of a safe and reliable operation of the SNQ-target wheel introduces to a great extent new requirements to be met by the used materials. This holds especially for heavily loaded components from irradiation effects and from thermomechanical stresses; Fig. 1 shows such components, which therefore must be investigated in detail.

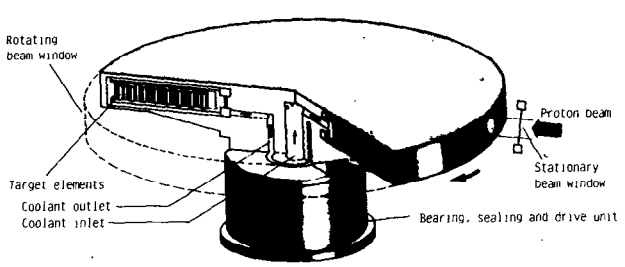

Fig. 1:
The SNQ-target wheel and its components exposed to intense irradiation and high thermomechanical load

A corresponding materials testing, qualification and development program has been worked out and is depicted in Tab. 1.
The most extensive task is the target element development, where three operational target elements based on Pb, W, and U are the ultimate goal. Problem areas do not only exist for the target material itself - particularly for the U-case -, but also concerning the development of a reliable combination of target material - bonding - cladding (preferably Al). The investigations dedicated to the cladding material will also reveal useful data for the rotation proton beam window and the general structural material of the target wheel.

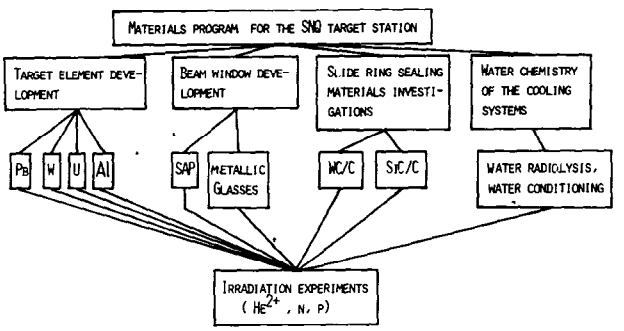

Tab. 1:
SNQ-target station materials program and promising materials for the different applications

The highest materials performance is required for the stationary proton beam window, which is considered as a desirable, but not imperatively needed component. The emphasis is presently put on materials with extremely high irradiation resistance; Al-alloys like sinter aluminium product (SAP) and metallic glasses with high thermal stability like $Nb_{40}Ni_{60}$ seem to be promising.
Because of the unusual SNQ-operating conditions, the concern in the case of the slide ring sealing materials is the applicability of conventional combinations (WC/C); hence, also new developments, e.g. SiC/C have been included.
The water chemistry investigations are primarily devoted to radiolysis and concomitant enhanced corrosion effects under intense proton- and neutron irradiation. The data evaluated hereby are the basis of a technical design for the water conditioning systems and of the operations parameters to be set and controlled.
All branches of this material program end up in irradiation experiments, which are described in detail elsewhere (Lohmann, 1983). Their basic idea is a staged procedure from simulation experiments with He-implantation or n-irradiation to a variety of experiments under conditions at least close to SNQ, which are performed at the LAMPF-proton accelerator (800 MeV/1 mA). Their final step will be the proof test of a complete small target wheel.
In order to illustrate the recent progress of this program, two examples - one of the target element development and another of the beam window development - are discussed below in more detail.

Thermal cycling of Uranium

Purpose of Study

By increasing the effective target area, the rotating target planned for SNQ reduces the thermal load for a specific target area by a factor of 200, i.e. increases the cooling period from 10^{-2} (proton pulse frequency: 100 Hz) to 2 sec compared to a stationary target with the same proton beam power. This leads to a far lower operation temperature for the rotating target. Both, lower temperature and longer cooling period reduces the thermal cycling growth rate of alpha-uranium, as discussed later. Although the operation temperature and the cycle frequency, i.e. number of cycles during target wheel operation ist reduced, requirements for spallation materials, bondings and claddings are still high.
The lower operation temperatures T_0 and the amplitude of thermal cycling ΔT of an uranium target for the first and second stage of SNQ are $T_0 \leq 160°C$, $\Delta T \leq 65$ K (350 MeV, 5 mA) and $T_0 = 125°C$, $\Delta T = 65$ K (1100 MeV, 5 mA) respectively. The corresponding data for the initially considered first stage of 1100 MeV and 0.5 mA were $T_0 = 55°C$ and $\Delta T = 10$ K. For the orthorhombic alpha-uranium with a highly anisotropic thermal expansion coefficient, the interaction of adjacent grains leads to high local stresses and plastic strain during thermal cycling and thus to thermal cycling growth.
A number of studies mainly by Mayfield, 1958, Zegler, 1958, Lloyd, 1958, and Pugh, 1956, shows a relationship between thermal cycling growth and lower temperatur T_0, ΔT, heating and cooling rate, time at temperature and material texture. The available data for alpha-uranium cycling groth were measured in a temperature range above 350°C and are therefore not applicable for SNQ temperatures (Fig. 2).

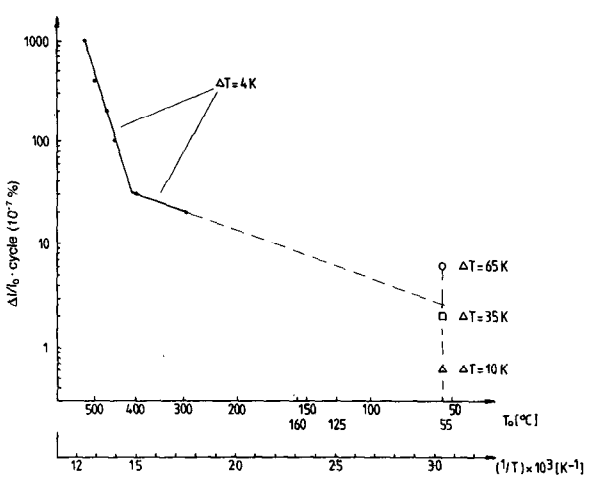

Fig. 2:
Extrapolation of thermal cycling growth data (ΔT = 4 K) by Mayfield, 1958, and results of this study

To investigate the influence of thermomechanical cycling on the behaviour of the specific materials to be used for the SNQ target under conditions relevant for SNQ, three techniques are used: 1. thermal cycling by immersion of samples in liquids of different temperatures and automatic sample transfer, 2. thermal cycling of samples by inductive heating and water cooling in a medium frequency furnace (4 kHz) and 3. simulation of thermal cycling by high cycle fatigue. First results of method /1/ will be reported in this paper.

Measurements of thermal cycling growth at lower operation temperatures of the SNQ variants T_0 of 55, 125, and 160°C and cycling temperatures ΔT of 10, 35, 65, 100 K, will provide the functional relationship of cycling growth with T_0 and ΔT (Table 2) for four uranium alloys. Subsequently, the effect of time at temperature will be studied.

Lower temperature T_0 (°C)	Temperature Amplitude ΔT (K)			
55	+10	+35	+65	
125		+35	+65	+100
160		+35	+65	+100

Tab. 2:
Lower temperatures and temperature differences of the cycling program

Experimental

To study thermal cycling growth at a lower temperature of $T_0 = 55°C$ and temperature amplitudes of ΔT = +10, +35, + 65, four thermostats with liquid-temperatures of 55, 65, 90 and 120°C were used. The samples were transferred between the two corresponding thermostats by an electronically controlled, pneumatic driven sample handler. Stabilized polydimenthylsiloxane (BAYSILONE-M 50) was used as liquid. Time at temperature (sample immersion time) was 15 sec each, to keep the temperature difference between the liquid and the center of the sample under 12% of ΔT. With a transfer time of 2-2.5 sec, the total cycle period was 35 sec.
At intervals of about $1.5 \cdot 10^4$ cycles, the length and weight of the samples were measured.

Samples

For the first study, four uncladded uranium-alloys "off the shelf", machined to cylinders of 9.0 mm diameter and 50 mm in length were used:
pure uranium, U - 5 W/o Mo, U - 3.7 W/o Zr, U - 0.75 W/o Ti.

Results

The weight loss of the uncladded samples due to corrosion is shown in Fig.3 as a function of the number of cycles, i.e. time, for ΔT = 10, 35 and 65 K. Up to $6 \cdot 10^4$ cycles the measurements were performed in air, later on in nitrogen. Pure uranium had the highest corrosion rate, followed by the U - 3.7 W/o Zr alloy. U - 0.75 W/o Ti and U - 5 W/o Mo showed the lowest weight loss. In all cases, the corrosion rate was proportional to ΔT.
Assuming a uniform surface corrosion, a correction factor for the sample length was calculated from the weight loss of a sample. From the difference in sample lenght at a given number of thermal cycles and the original length of the uncycled sample and in consideration of the correction factor the thermal cycling growth per cycle ($\Delta l/l_0 \cdot$cycle) was calculated. The results for the cycling amplitude of ΔT = 10 K is shown in Fig. 3. The scale of the ordinate (10^{-7} %), provides $\Delta l/l_0$ in % for an operation-time of the target of about one year (10^7 cycles).
At low cycle numbers, the different alloys show distinct variations, caused in part by the normalization of $\Delta l/l_0$ to a small number of cycles, in part by non-typical dimensional changes due to internal stresses introduced by sample machining. At cycle numbers higher than 10^5, the mean thermal cycle growth rate per cycle reaches a constant value and seems to be fairly independent on alloy composition or sample microstructure with a somewhat lower value for pure uranium.

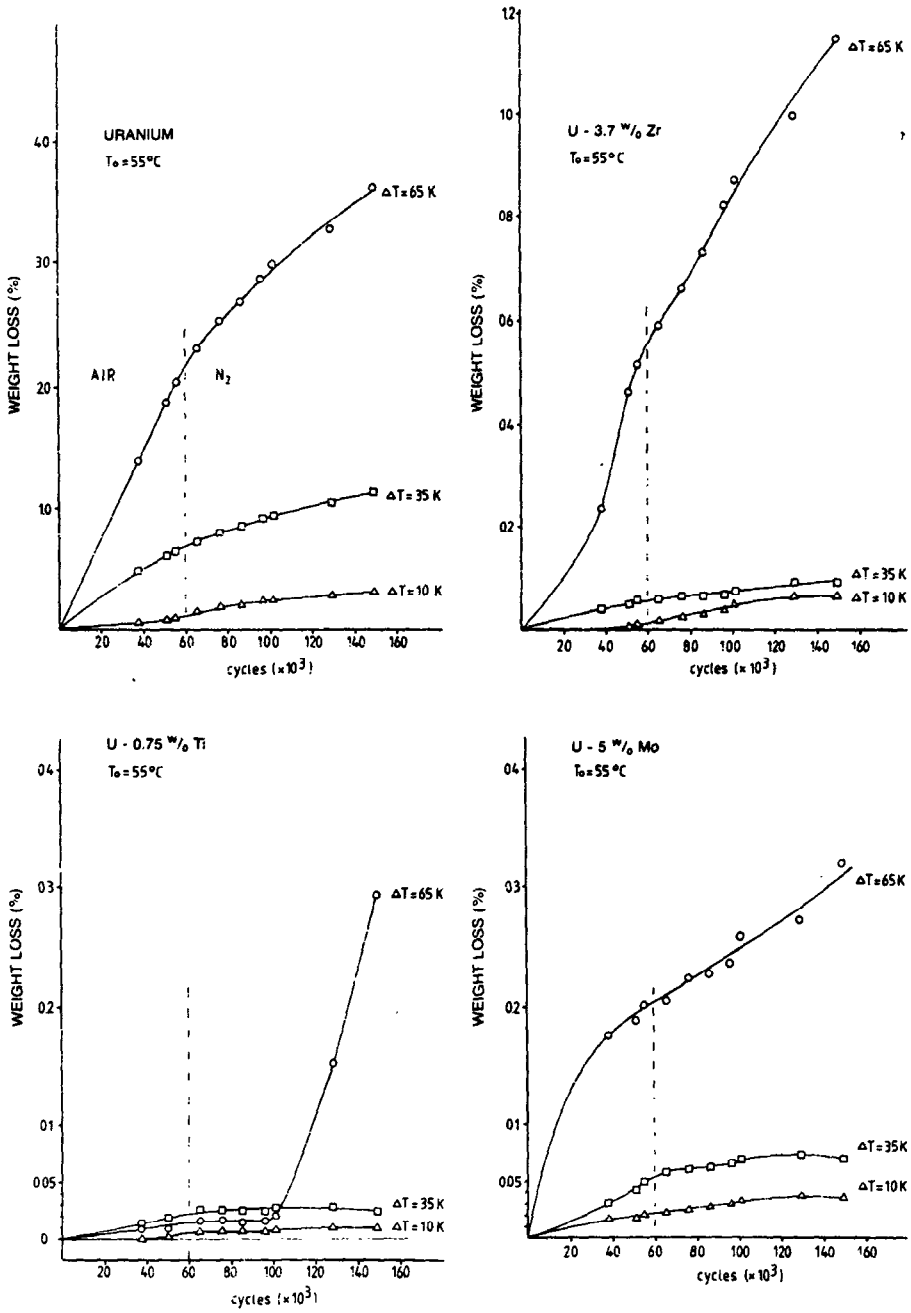

Fig. 3:
Weight loss of uncladded uranium alloys during thermal cycling

Except for pure uranium, the same is true for the three uranium alloys cycled at $\Delta T = 35$ K shown in Fig. 4.
Fig. 5 shows the corresonding growth rates for a cycling amplitude of $\Delta T = 65$ K. Again pure uranium yields a somewhat higher value than the uranium alloys, which seem to converge at $15 \cdot 10^4$ cycles to about the same growth rate per cycle.
A comparison of the results listed in table 3 shows an increase in thermal cycling growth with increasing ΔT.

Alloy composition	$\Delta l / l_0 \cdot$ cycle (10^{-7} %)		
	ΔT = 10 K	ΔT = 35 K	ΔT = 65 K
Uranium	-1.4	6.1	8.5
U-3.7 w/o %	-0.1	1.1	5.7
U-5 w/o %	0.6	2.0	4.7
U-0.75 w/o %	0.2	1.6	3.4
	≦ 0.6	≦ 2.0	≦ 6.0

Tab. 3:
Thermal cycling growth rates at $1.5 \cdot 10^5$ cycles and at a lower temperatur T_0 = 55°C and ΔT of 10, 35, and 65 K

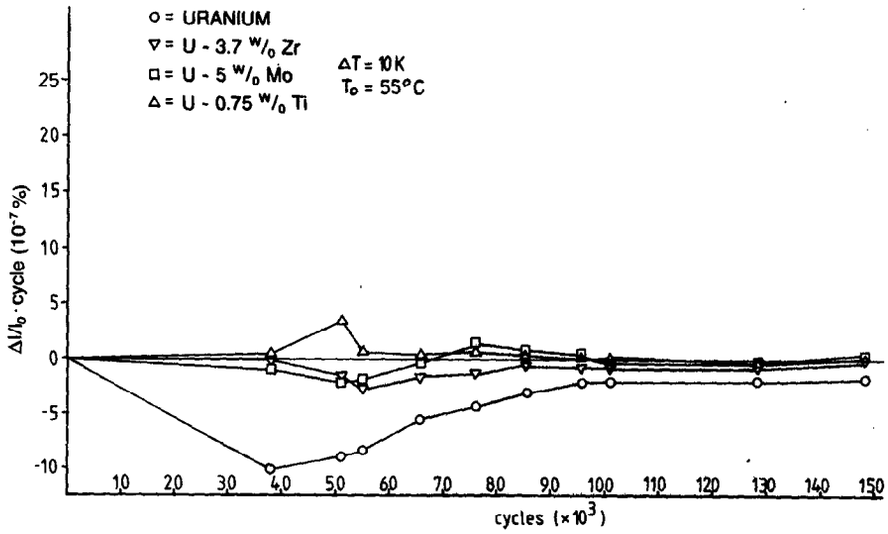

Fig. 4:
Thermal cycling growth per cycle at a lower temperature of 55°C and a cycling amplitude of + 10 K

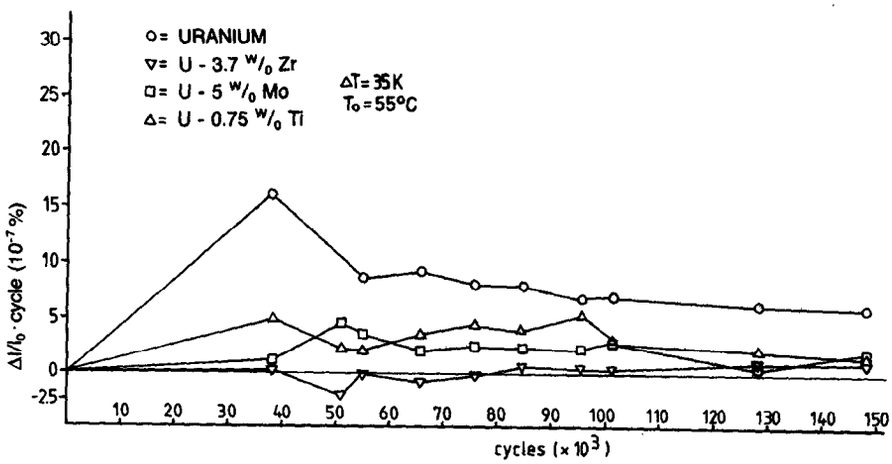

Fig. 5:
Thermal cycling growth per cycle at a lower temperature of 55°C and a cycling amplitude of + 35 K

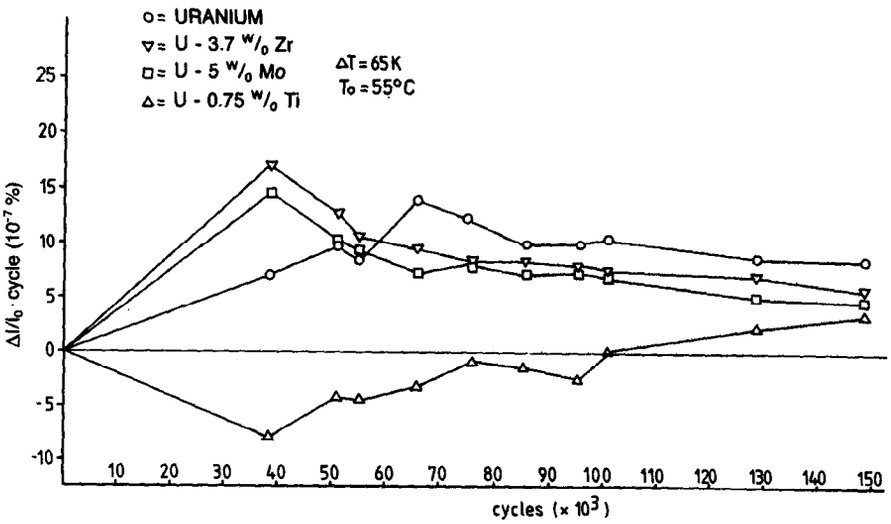

Fig. 6:
Thermal cycling growth per cycle at a lower temperature of 55°C and a cycling amplitude of + 65 K

In Fig. 4 through 6 $\Delta l/l_0$ per cycle is the mean value of the growth rate at a given total cycle number, leading to smaller systematic errors at higher cycle numbers. In contrast to this, the data shown in Fig. 7 are the mean values of the growth rate per cycle of cyle number intervals of about $2 \cdot 10^4$ cycles. Although the scatter is larger, the growth rate per cycle seems to be constant for cycle numbers larger than $8 \cdot 10^4$. The growth rate date for the basic temperatures of T_0 = 125 and 160°C are expected to be higher according to Mayfield, 1958 (Fig.2). In addition, the higher cooling rate of 2 sec of the target wheel compared to 15 sec in our test facility may increase the growth rate to some extend (Mayfield, 1958), although the cooling rate of the rotating target is still lower than the cooling rate of a stationary target.

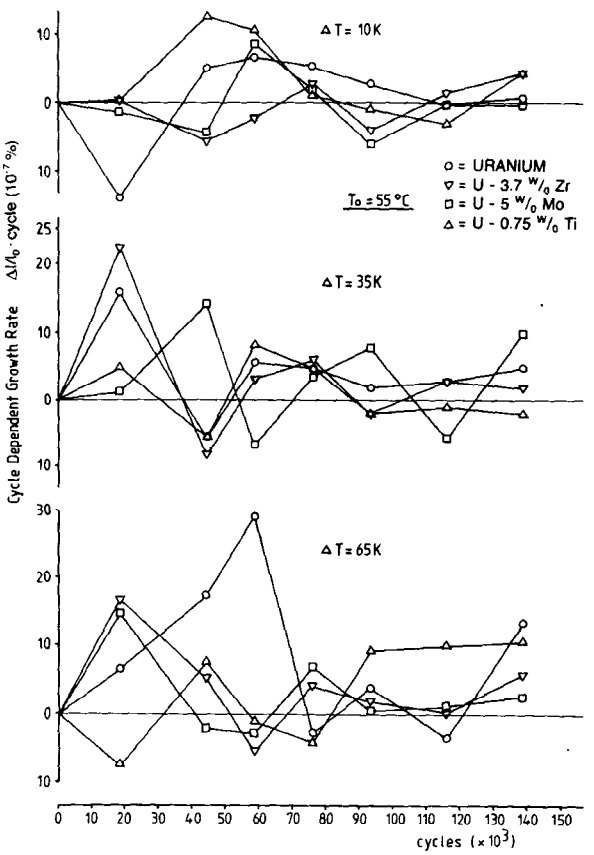

Fig. 7:
Growth rates per cycle calculated for subsequent cycle number intervals of about $2 \cdot 10^4$ cycles

Beam window development

SAP-AlMgSi-composite alloy

There are three essential requirements for the stationary proton beam window (cf Fig. 1):

- sufficient strength at elevated temperatures,
- both low heat production and proton radiation damage favouring thus material with low atomic and mass number,
- acceptable technological properties.

Al-based alloys seem to be promising from this point of view. One has further to distinguish between sintered and usual, wrought material.
The sintered alloy SAP (Al-matrix + 7 % Al_2O_3) has reasonable strenght up to 400°C and - more important - shows no He-/H-embrittlement up to 1700 appm each at least for high-oxide SAP (Maziasz, 1979). On the other hand, SAP is a brittle material with poor technological properties (e.g. weldability).
AlMgSi-alloys - chosen as general structural material for the target wheel - are limited to an upper operations temperature below 150°C. A high irradiation resistance is known from neutron irradiations (Farrell, 1979), but there are no data on proton irradiation effects with the concomitant high He- and H-production. These Al-alloys are ductile and possess good and well known technological properties.
Combination of the favourable properties of both materials led to the development of a SAP-AlMgSi-composite alloy, consisting of a SAP core surrounded by an AlMgSi-border. Preliminary tests on prototype disks reveal a good quality of the transition zone from optical metallography and a high gas-tightness, indicated by a leakage-rate of less than 10^{-9} mbar·l·s^{-1} at 200°C.

Radiation effects on Al-based alloys

Calculations have been performed for the case of a proton beam power of 0.6 MW (1100 MeV, 0.5 mA, prev.first SNQ-stage) assuming equal damage effects for SAP and pure Al. The results are compiled in Table 4.

	Displacement rate (dpa/sec)	He-production rate (appm He/sec)	H-production rate (appm H/sec)
Protons	2.2×10^{-7}	7.3×10^{-5}	3×10^{-4}
Fast neutrons	1.4×10^{-8}	2.6×10^{-13}	2.4×10^{-13}
Total	2.3×10^{-7}	7.3×10^{-5}	3×10^{-4}

Tab. 4:
Radiation damage of an Al-based stationary proton beam window for 0.6 MW proton beam power

The neutron contribution to the total damage can be neglected. At least for high-oxide SAP, a theoretical window lifetime of about 6.500 h is possible from the He-produktion rate; the corresponding dpa-damage is less than 6 dpa, which should not affect the materials integrity (H-embrittlement) because of a high H-diffusivity at SNQ-operating temperatures (see below).

Stress and temperature considerations for SAP

A simple assessment of the mechanical and thermal load on a SAP-based beam window has been made assuming a double-disk plate geometry as depicted in Fig. 8.
The maximum temperature T_{max} can be estimated (Lohmann, 1982) from the energy balance, inserting a coolant temperature of 300 K and assuming a heat transfer coefficient of 1 W/(cm^2·K). The time-averaged power density from beam heating turns out to be about 500 W/cm^3 for a 0.6 MW proton beam power.
The maximum stress σ_{max} from bending moments is calculated (Lohmann, 1982) as a fuction of the window thickness d and the pressure differential p (1 and 3 bar, resp.). Results are shown in Fig. 9, together with the expected maximum temperature T_{max}.
The T_{max}-values corresponding to a given d are indicated on the upper scale. Referring to this scale, the temperature-dependent yield strength $\sigma_{0.2}$ (T) and the ultimate tensile strength σ_{UTS} (T) of SAP - 7 % Al_2O_3 has also been drawn in. The intersection of the strenght curves with σ_{max} (T,p) denotes the minimum thickness d_{min} at a fixed p. The corresonding data can be read from the insert of Fig. 9, assuming $\sigma_{max} \leq \sigma_{0.2}$ (T).

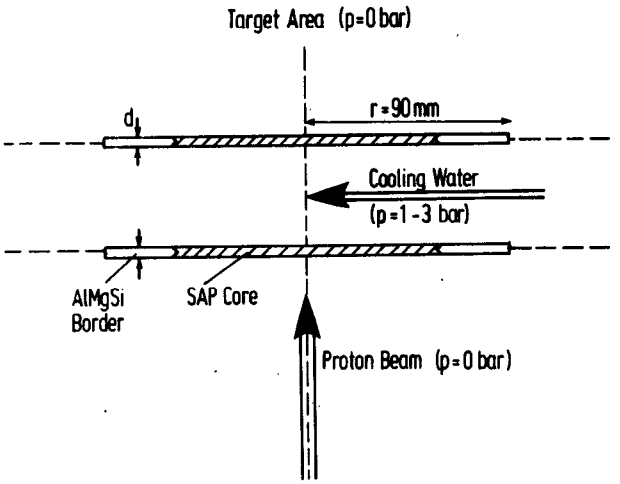

Fig. 8:
Internally water cooled, double-disk plate beam window with thickness d and plate radius r = 90 mm, determined by the proton beam size

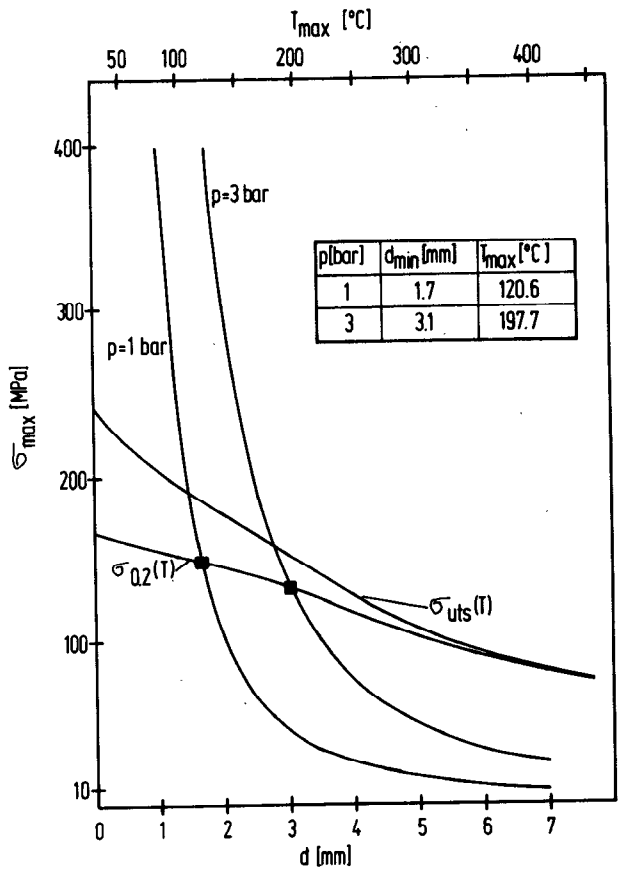

p[bar]	d_{min} [mm]	T_{max} [°C]
1	1.7	120.6
3	3.1	197.7

Fig. 9:
Evalution of the needed beam window plate thickness d from stress and temperature calculations (see text)

From these results, a moderate operations temperature combined with sufficient strenght is indicated. Ongoing investigations will deal with irradiation effects from He and proton irradiations. The He-experiments are dedicated to the change of mechanical properties of preimplanted material as a function of its Al_2O_3-content, because there is a ductility improvment by a lower oxide fraction. The LAMPF proton irradiation tests (Lohmann, 1983) will be performed on complete proton type disks under operating conditions close to SNQ. Additionally, Al-C has been included into the current program as an alternative Al-based sintered alloy offering a substantially higher ductility than SAP, but with the lack of data on its irradiation behaviour.

References

Farrell, K.; King, R.T.
"Tensile Properties of Neutron Irradiated 6061 Aluminium Alloy in Annealed and Precipitation-Hardened Conditions"
Proc. Conf. on Effects of Radiation on Structural Materials, ASTM-STP 683 (1979), 440

Lloyd, L.T.; Mayfield, R.M.
"Microstructural Changes of Uranium upon Thermal Cycling"
Trans. Amer. Soc. Metals, 50 (1958), 954

Lohmann, W.; Hammad, F.M.
"On the Possibility of Using Sintered Aluminium Product (SAP) as a Beam Window Material for SNQ-I"
Technical Note SNQ (August 1982)

Lohmann, W.
"Irradiation Effects in Candidate Materials for the SNQ-Target Station"
Proc. ICANS-VII (1983), this volume

Mayfield, R.M.
"Effects of Cycling Variables upon Growth Rate of 300°C Rolled Uranium"
Trans. Amer. Soc. Metals, 50 (1958), 926

Maziasz, P.J.; Farrell, K.
"The Tensile Properties of High Oxide SAP Containing Helium and Tritium"
J. Nucl. Mat. 85+86 (1979), 913-917

Pugh, S.F.
"Radiation Damage in Fissile Materials"
Progr. Nucl. Energy, Ser. V, 1 (1956), 652-671

Zegler, S.T.; Mayfield, R.M. and Mueller, M.H.
"Effects of Fabrication and Heat Treatment Variables upon the Thermal Cycling Behaviour of Uranium"
Trans. Amer. Soc. Metals, 50 (1958), 905

Proceedings of International Collaboration on Advanced Neutron Sources (ICANS-VII), 1983 September 13-16
Atomic Energy of Canada Limited, Report AECL-8488

SOME TOPICS OF RECENT DEVELOPMENT ON MONTE CARLO COMPUTATION OF TARGET SYSTEMS IN JAPAN

Motoharu Kimura
Laboratory of Nuclear Science, Tohoku University
Sendai, 982 Japan

Abstract

NMTC code was refined by Nakahara of JAERI to make workable up to 250 of mass number. The code was used to explain the experimental results of high energy fission C.S. and the shoulder of spallation neutron spectra measured by KfK and LANL. Tsukada gave a theoretical basis for it assuming 10% ∿ 50% longer MFP of proton and neutron in nuclei.

Kimura made extensive computer simulation experiment of Monte-Carlo calculation, expecting possible cut down of computation cost, introducing James-Stein-Estimator (JSE). JSE proceedure will be useful for the data of large statistical fluctuation in general.

Introduction

Accelerator based neutron beams were used for condensed matter research for more than 15 years in Japan, and Accelerator breeder system is being studied systematically for 5 or more years now.

I would like to talk on some related topics recently developed by our study group.

On hadron transport Code

Nakahara et al[1] refined the NMTC/JAERI code which takes into account the high energy fission. He tried various cases of chosing formulae and parameter values related to the high energy fission and compared with the experimental results[2]. Mass dependence of the calculated nonelastic cross sections is also shown in comparison with the experimental data[3]. I will show just a small part of their results in the following three view graphs. The first view graph shows the comparison of their results with the experiments of Steiner et al[2] on the proton induced fission cross sections for Bi^{209}. Here, A_f and A_n are level density at Saddle point and equil. deformation. Ordinate is $\sigma_f(Bi)/\sigma_{non-el}(Pb,Bi)$. It is not clear yet if there is a real physical meaning in the discrepancy between proton and neutron bombardments. In Fig 2, for ^{238}U, comparison between Il'inov's[4] and Kupriyanov's[5] idea of double humped structure of fission barrier was made.

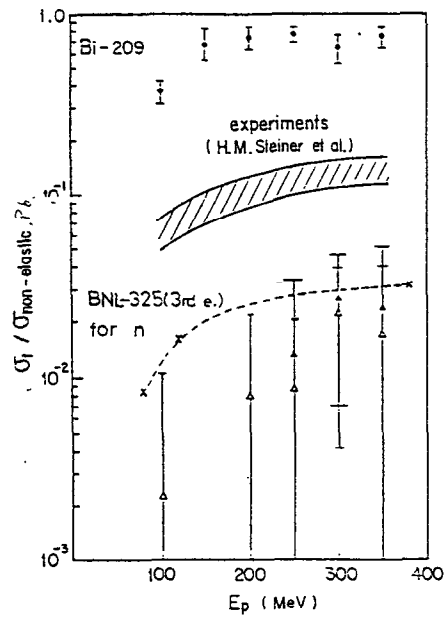

Monte Carlo calculations :
- • a_f/a_n (Vandenbosch – Huizenga) a_n (Le Couteur)
- ▲ a_f/a_n (Il'inov et al.), $a_n = A/10$.
- △ a_f/a_n (Il'inov et al.), $a_n = A/20$.

Fig1 Proton induced fission on ^{209}Bi

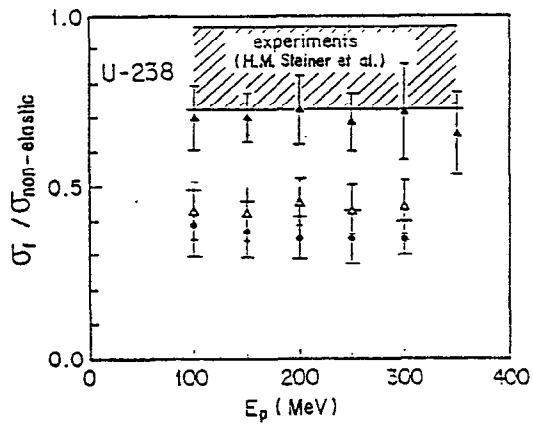

Monte Carlo calculations :
- ▲ Weisskopf - Bohr - Wheeler theoery with a_f/a_n due to Il'inov et al. and $a_n = A/10$.
- △ Same as the case ▲ except $a_n = A/20$.
- • Kupriyanov et al's model (Double humped)

Fig 2 Proton Induced Fission on ^{238}U

Fig 3 is for ^{232}Th.

A ≦ 250 made possible.

Nakahara made possible to handle mass number up to 250 which is needed to study actinide incineration and other problems.

On Energy Spectra of Spallation Neutrons

The evidence of slight shoulder near 100 MeV in the energy spectrum of spallating neutrons bombarded by high energy protons on heavy nuclei was explained by Tsukada[6] assuming longer mean free path of nucleons in the nuclear matter. Nakahara, using NMTC/JAERI code[1] calculated the energy spectra of neutrons for the case of Pb and U cylinder of 60 cm in length and 10 cm dia, bombarded axially by 590 or 800 MeV protons, obtained results which suggest the existence of such a shoulder. The KfK[7] and LANL[8] groups performed extensive measurements at different emerging angles of neutrons from various targets and the shoulder becomes more conspicuous for smaller emerging angles.

Both the NMTC or HETC calculational results ever obtained assuming free nucleon interaction cross sections have never given such shoulders, irrespective of the inclusion of high energy fission process or not.

Tsukada, therefore, assumed smaller interaction, that is, longer MFP of nucleon-nucleon collisions inside the nucleus. This will enhance the leakage of high energy neutrons from the nucleus and the number of evaporating neutrons will be suppressed.

Fig 4 is a NMTC/JAERI results assuming 10% and 50% increase of MFP. Even though the statistics is not yet very good, we can see a slight bamp in the energy spectrum at about 100 MeV.

However, Nakahara found decrease of the total neutron yield as shown in Fig 5. It seems a good compromize may exist at about 10% increase of MFP. However, if the target dimension is much larger than the one of KfK experiment, total yield may be larger independent of MFP.

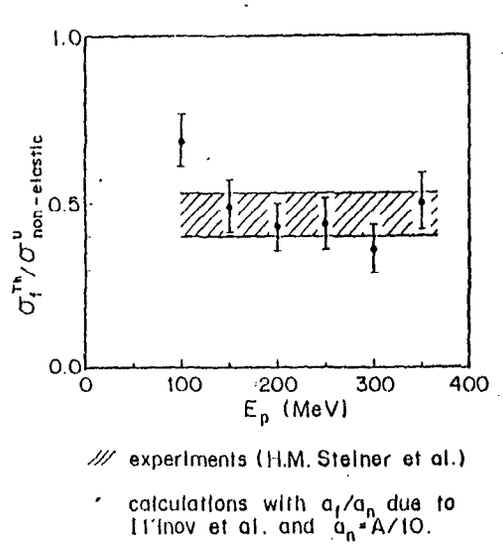

Fig 3 Proton induced fission on ^{232}Th

Tsukada carefully analysed the spectra and suggested existence of the third component as shown in Fig 7 and Fig 8. He assumed exponential forms like

$$A_i(E/E_{0i})\exp(-E/E_{0i}) \qquad i = 1, 2, 3$$

for the evaporation part, high energy tail and also for the third component.

The third component, that is, of intermediate energy of around 20 MeV may correspond to the pre-equilibrium component as suggested by Nakai et al.[9] This component is included in the cascade calculations of Nakahara.

Molten salt target Molten salt of $LiF-BeF_2-UF_4$, for example, looks very promising, with many advantagious features. A molten salt accelerator breader system is being proposed by Furukawa et al.

Our study group for A.B. system proposes to construct an 800 MeV × 500 μa proton synchrotron, GEMINI, as the first step to the 1 GeV × 300 ma proton linac which will be the final demostration machine of A.B. system. We hope it will be realized in the early 2000's. On GEMINI, Sasaki talked yesterday. We think we need at least 2∿3 more accelerators as the intermediate test machine of rather low energy but of high current. This is needed for the R & D of target system for the final design.

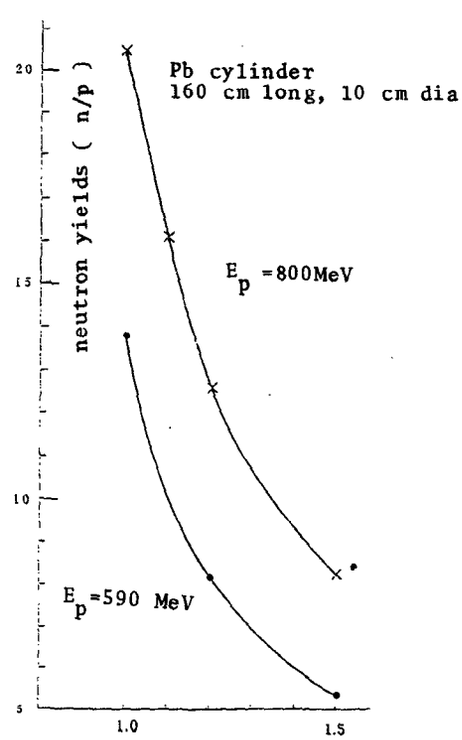

Fig 6

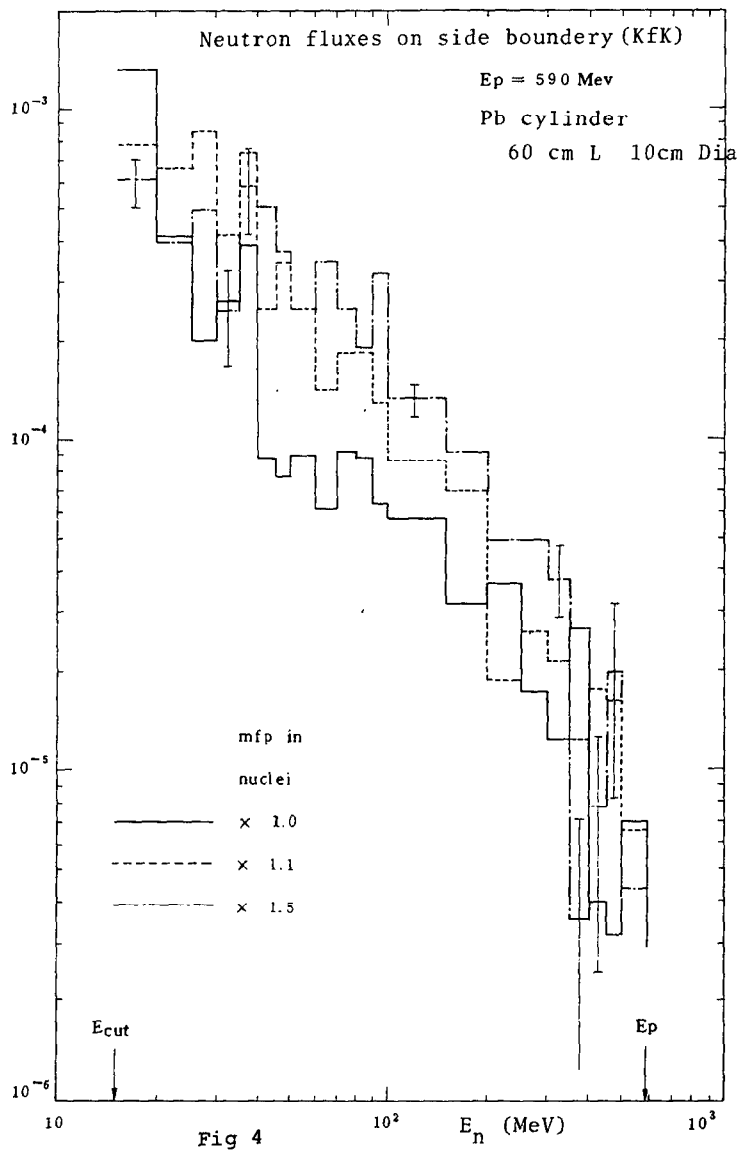
Neutron fluxes on side boundery (KfK)
Ep = 590 Mev
Pb cylinder
60 cm L 10cm Dia
mfp in
nuclei
× 1.0
× 1.1
× 1.5
Ecut
Ep
10^{-3}
10^{-4}
10^{-5}
10^{-6}
10
10^2
10^3
E_n (MeV)

Fig 4

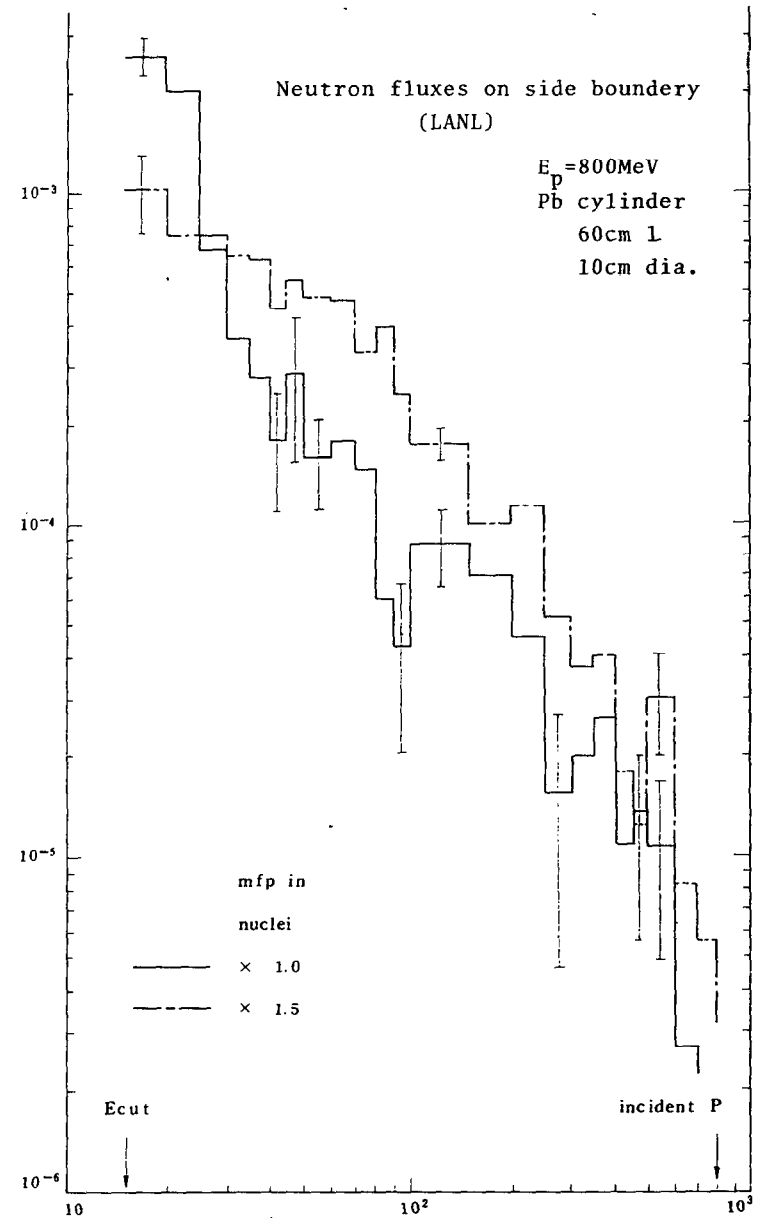
Neutron fluxes on side boundery
(LANL)
E_p=800MeV
Pb cylinder
60cm L
10cm dia.
mfp in
nuclei
× 1.0
× 1.5
Ecut
incident P
10^{-3}
10^{-4}
10^{-5}
10^{-6}
10
10^2
10^3

Fig 5

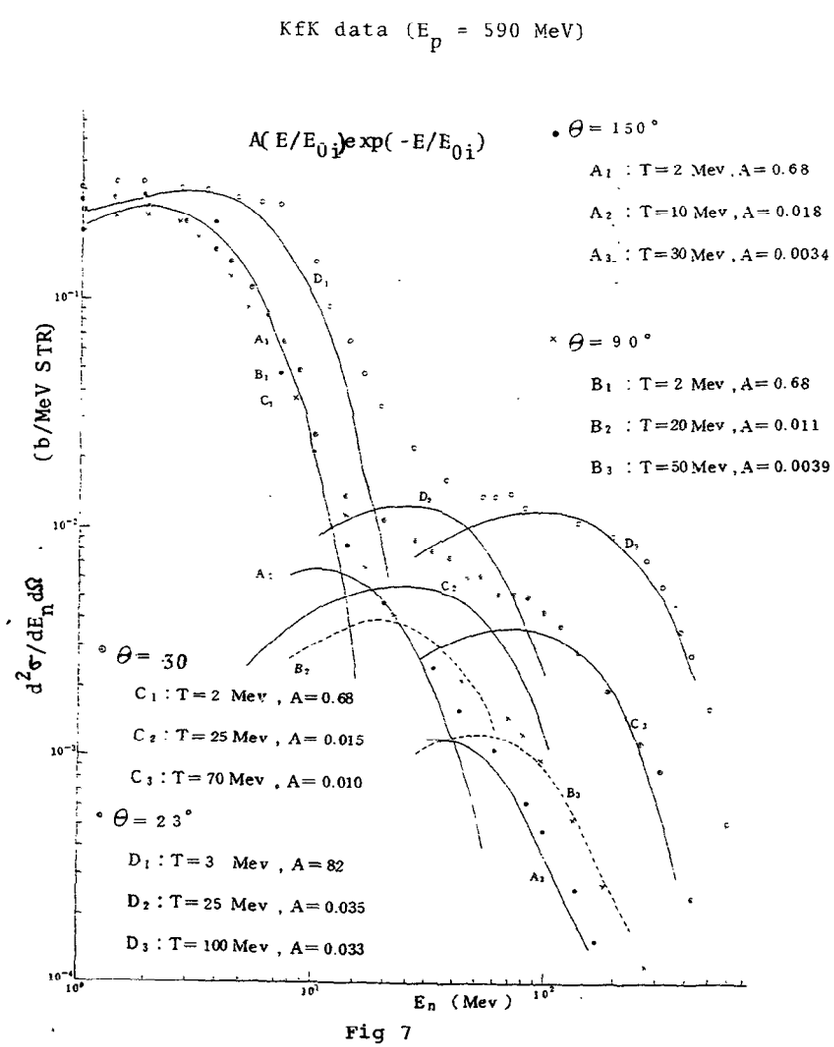
KfK data (E_p = 590 MeV)
$A(E/E_{0i})\exp(-E/E_{0i})$
• θ = 150°
A1 : T=2 Mev, A=0.68
A2 : T=10 Mev, A=0.018
A3 : T=30 Mev, A=0.0034
× θ = 90°
B1 : T=2 Mev, A=0.68
B2 : T=20 Mev, A=0.011
B3 : T=50 Mev, A=0.0039
θ = 30
C1 : T=2 Mev, A=0.68
C2 : T=25 Mev, A=0.015
C3 : T=70 Mev, A=0.010
θ = 23°
D1 : T=3 Mev, A=82
D2 : T=25 Mev, A=0.035
D3 : T=100 Mev, A=0.033
$d^2\sigma/dE_n d\Omega$ (b/MeV STR)
E_n (Mev)

Fig 7

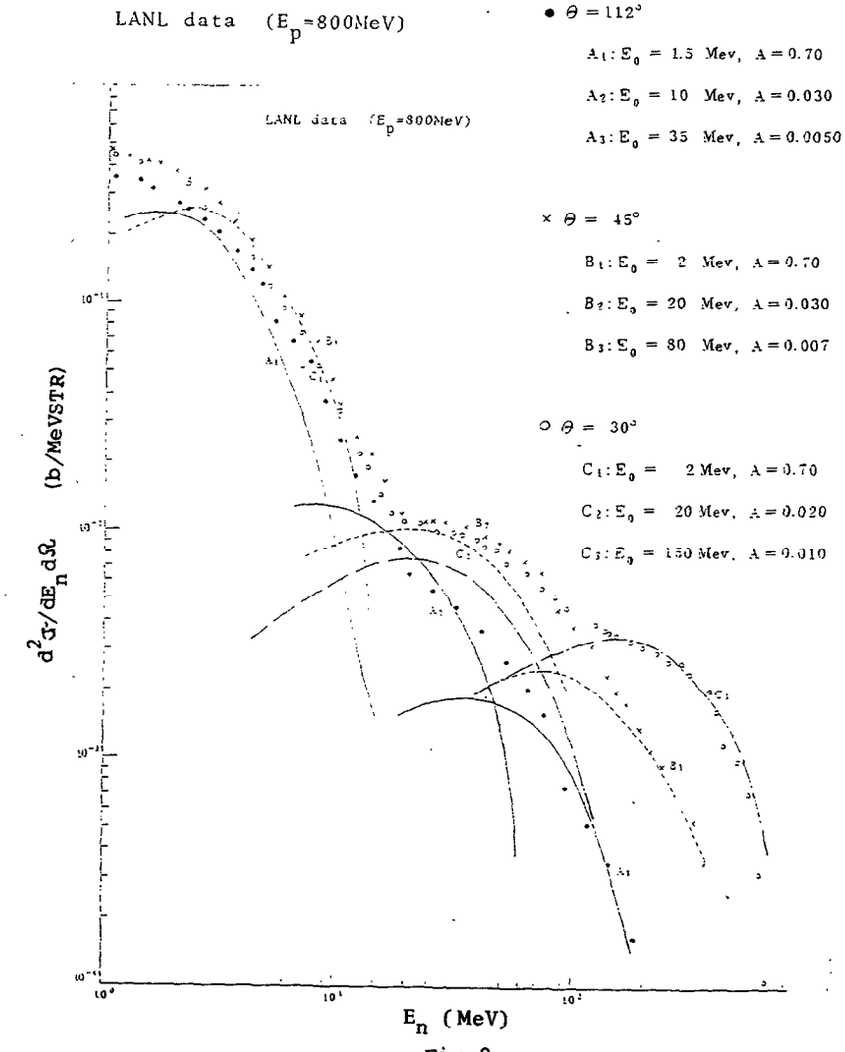
LANL data (E_p=800MeV)
• θ = 112°
A1 : E_0 = 1.5 Mev, A = 0.70
A2 : E_0 = 10 Mev, A = 0.030
A3 : E_0 = 35 Mev, A = 0.0050
× θ = 45°
B1 : E_0 = 2 Mev, A = 0.70
B2 : E_0 = 20 Mev, A = 0.030
B3 : E_0 = 80 Mev, A = 0.007
○ θ = 30°
C1 : E_0 = 2 Mev, A = 0.70
C2 : E_0 = 20 Mev, A = 0.020
C3 : E_0 = 150 Mev, A = 0.010
$d^2\sigma/dE_n d\Omega$ (b/MeVSTR)
E_n (MeV)

Fig 8

Possible Application of James-Stein Estimator to cut Monte-Carlo Computation Cost.

This is a study done mainly by Kimura with a help of Matsubara, a mathematical statistician. J.M. Carpenter noticed the theory of James-Stein Estimater may work.

What is James-Stein-Estimator. The notion of James-Stein Estimator was first introduced on 1960 by C. Stein[10] who pointed out the possibility of improving the usual estimator in the case of multivariate normal (Gaussion) mean.

Simplest example. Suppose we have k test pieces, designated as j = 1, 2, ··· k, of various metals whose length were measured by a certain person using a certain instrument. The length depends on the temperature X. Suppose the results are shown by A_{ij} in Fig 9. It is not possible to know the true length f_{ij}. We usually take the estimate Y_{ij} by the least square fitting against X.

The measurement for A_1, for example, is independent of the measurements for A_2, A_3··· and it is quite natural to take separately the least square fitting. We have, however, missed to use other information obtainable from the data of A_2, A_3 ···. By taking into account all the data of all other samples simultaneously, we might be able to shift somewhat the data points like (as shown in Fig 9)

A_{ij} = The original measurements
$A_{ij}^{(1)}$ = A_{ij} shifted vertically in some way
Y_{ij} = The regressed value of A_{ij}
$Y_{ij}^{(1)}$ = The regressed value of $A_{ij}^{(1)}$.

We conjecture that when a proper shifting is applied, then the total "risk" might be less. Here, the risks are defined as follows:

$$\text{RISK 0} = \sum_{j=1}^{k} \sum_{i=1}^{n} (A_{ij} - f_{ij})^2 \qquad (1)$$

$$\text{RISK 1} = \sum_{j=1}^{k} \sum_{i=1}^{n} (A_{ij}^{(1)} - f_{ij})^2 \qquad (2)$$

$$\text{RISK 2} = \sum_{j=1}^{k} \sum_{i=1}^{n} (y_{ij} - f_{ij})^2 \qquad (3)$$

$$\text{RISK 3} = \sum_{j=1}^{k} \sum_{i=1}^{n} (y_{ij}^{(1)} - f_{ij})^2 \qquad (4)$$

If we can observe a tendency

$$\text{RISK 1} \leqq \text{RISK 0}, \quad \text{RISK 3} \leqq \text{RISK 2} \qquad (5)$$

then it may be allowed to say that the shifted data points $A_{ij}^{(1)}$ and their regressed values $y_{ij}^{(1)}$ are closer to the true values. And there does exist such a case actually.

The most essential point to reduce $A_{ij}^{(1)}$ and $y_{ij}^{(1)}$ in this James-Stein proceedure is the introduction of "Shrinkage factor ρ" which plays the central role to take into account the fluctuation of measurement in total.

The "sectioned" data at each X = Xi, that is A_{ij}(j = 1, 2,···k) will be processed by the James-Stein proceedure (called JSE) to give rise to

$$A_{ij}^{(1)} = \bar{\mu}_i + \rho_i \, (A_{ij} - \bar{\mu}_i) \qquad (6)$$

$$\bar{\mu}_i = \text{average of } y_{ij} \text{ over } j = \frac{1}{k} \sum_{j=1}^{k} y_{ij} \qquad (7)$$

and ρ_i is given by

$$\rho_i = 1 - \frac{k-3}{k-1} \cdot \frac{\sigma^2 \{\frac{1}{n} + (X_i - \bar{X})^2 / \sum_i (X_i - \bar{X})^2\}}{\sum_j (y_{ij} - \frac{1}{k} \sum_j y_{ij})^2} \qquad (8)$$

ρ_i are usually less than 1 and have a function to smear out the fluctuation. A large A_{ij} may have larger chance to have fluctuated to the positive side from the true value and vice versa. In case $\rho_i < 0$, we should put it equal to 0. σ^2, the true variance, which we can not know, but can be replaced by its estimate S^2 which is the average over j of residual variances S_j^2 from the sample regression lines, (that is as shown in the graph)

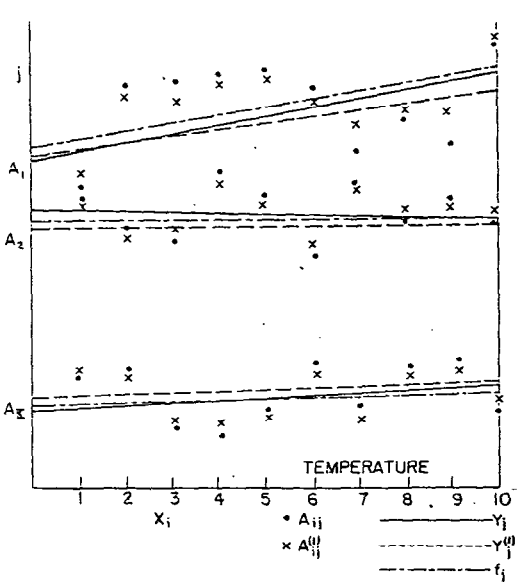

Fig 9

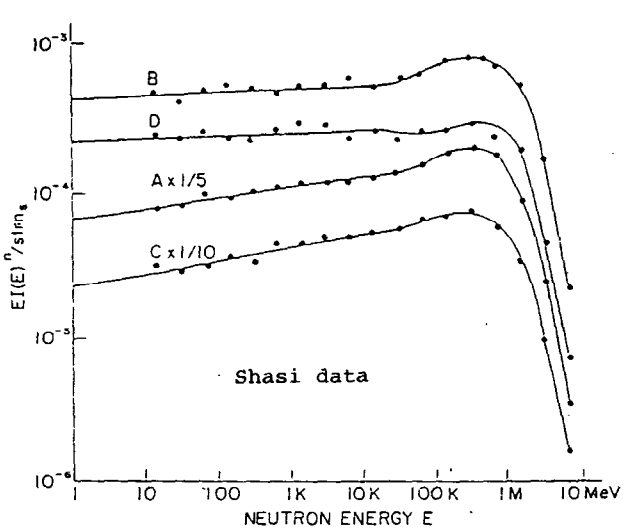

Fig 10

$$S^2 = \frac{1}{k} \sum_j^2 S_j^2,$$

$$S_j^2 = \frac{1}{n-2} \{\sum_i (A_{ij}-\bar{y}_j)^2 - \frac{\sum_i (X_i-\bar{X})(A_{ij}-\bar{y}_j)}{\sum_i (X_i-\bar{X})^2}\} \quad (9)$$

$$y_j = \frac{1}{n} \sum_i y_{ij}$$

Thus we can calculate $A_{ij}^{(1)}$ and $y_{ij}^{(1)}$. We define the Figures of Merit (FOM) as follows:

$$\text{FOM 1} = \text{RISK 0/RISK 1}$$
$$\text{FOM 2} = \text{RISK 2/RISK 3} \quad (10)$$

FOM 1 and FOM 2 may be of some measure how much the data were improved. FOM 1 and FOM 2 are generally larger than 1 and tend to 1 when the measurement of A_{ij} is more accurate.

Shashi data.[11] This is the raw data of neutron spectra from target-reflector-moderator system of various configurations for the intense pulsed neutron source (IPNS) of Argonne. A, B, C and D correspond to different neutron beams. We will limit our interest to the 10 eV ∿ 10 KeV region, where log E vs log (EI) have straight lines. See Fig10

Hand calculations using above formulae gives the result that all the ρ_i's are very close to 1 and $A_{ij}^{(1)}$ do not differ from A_{ij} more than 0.5% or so. This is because the fluctuation of all the data are rather small and there remains not much room to shift the regression lines. The Monte-Carlo results of Shashi are already too accurate to allow the JSE proceedure work substantially. (Table1)

Computer experiments simulating the problem. We have done some computer experiment to understand the problem more systematically.

(1) Number of data k was increased to 12, the first 4 of which are the regression lines of Shashi data, 8 others were arbitrarily created. Each of these 120 points on the 12 straight lines are designated by f_{ij} representing the true values which we can not know. The 12 straight lines have different inclination and average.

As a reference, we created another data set, which is consisted of 12 identical horizontal lines of the same height, that is $f_{ij} = 0.5000$, $i = 1, 2 \cdots 10$, $j = 1, \cdots 12$, and compared with the result using above data set. An I-number KR(1, 3) was introduced to compute more general way, that is,

KR = 1 : k = 4, Shashi data (A, B, C, D)
KR = 2 : k = 8, A, B, ···H
KR = 3 : k = 12, A, B, ···L.

To simulate the Monte-Carlo out put, we called randon number generator, of Gaussian, Uniform or Poisson type. In the case like Shashi data for neutron spectra, Poisson should be applied, but we also tried to use other subroutines.

The Shashi data possesses a certain amount of variance S^2 which was calculated to be (0.025). We wanted to take the magnitude of S^2 widely changed, covering the one of Shashi data. For this, we introduced another I number NR(1, 9) to cover wide range of standard deviation as follows:

$$\sigma_G = 2^{(n-NR)} \quad \text{(Ganssian)(10)} \quad NR(1, 9)$$

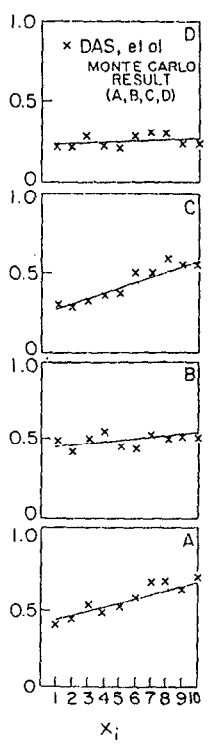

Fig 11a

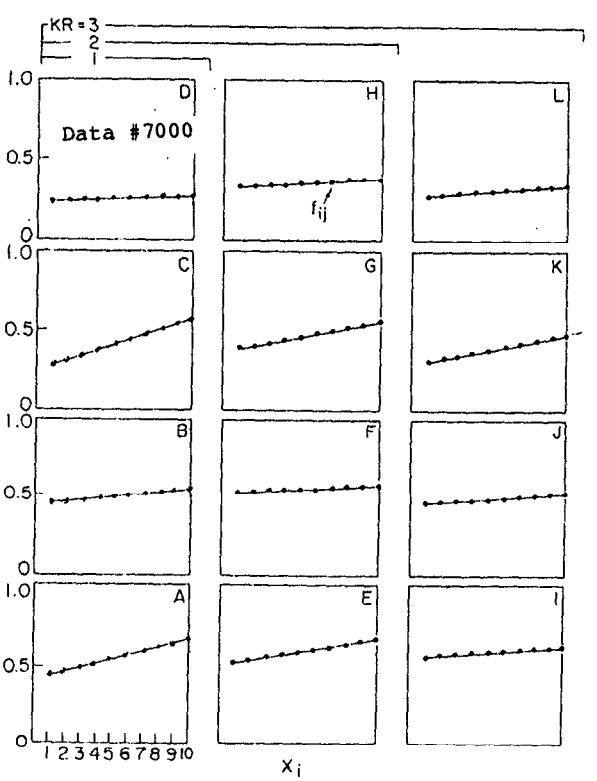

Fig 11b

$$\sigma_U = 2^{(n-NR)/2}\sqrt{f_{ij}(1-f_{ij})} \quad \text{(uniform)} \quad NR(1, 9) \tag{11}$$

$$\sigma_P = \sqrt{f_{ij}/\lambda} = 2^{(n-NR)/2}\sqrt{f_{ij}} \quad \text{(Poisson)} \quad NR(1, 7) \tag{12}$$

with $\lambda = 2^{(NR-n)}$
(n is not the max of i)

n is an integer to shift the range of survey. Usually it is taken 1. We had better taken $\sigma_G = 2^{(n-NR)/2}$ to make the correspondence to the other cases more clearcut. In case of Poisson, we introduced λ to keep the standard deviation independent of absolute number of count of neutrons. In case of uniform, we must call the uniform random number $2^{(NR-n)}$ times and compare it with f_{ij}. Central limit theorem will be applied in the case of σ_U and σ_P.

We obtain from the above 3 equations

$$\ln \sigma_G = (n-NR)\cdot\ln 2 \tag{13}$$

$$\ln \sigma_U = (n-NR)/2\cdot\ln 2+\frac{1}{2}\ln f_{ij}+\frac{1}{2}\ln(1-f_{ij}) \tag{14}$$

$$\ln \sigma p = (n-NR)/2\cdot\ln 2+\ln\sqrt{f_{ij}} \tag{15}$$

The computer also prints out

$$\sigma_{EX} = \sqrt{RISK\ 0/n\cdot k}, \quad n = 10, \quad k = 4, 8 \text{ or } 12. \tag{16}$$

When the repetition of the computer experiments is increased, σ_{EX} quickly converges into one of above σ's. Therefore, the graphic representation by print out taking the number of lines for NR instead of σ_{EX} is quite adequate.(Fig 12 a, b)

Summary of results. Now, each (*) in Fig 12 a, b is the average of 10 repetitions of rondom number generation. Similar proceedure was repeated 6 times generally, and plotted on the same figure. Fig 13 etc. are plotted the averaged FOM's vs ln σ_{EX}.

Comparison with Shashi data. We must find FOM1 or FOM2 in Fig 14(with Poisson, and for k = 4) corresponding to σ = 0.025 of Shashi's data. Unfortunately, our Poisson subroutine did not work for wide range of NR. It is essentially nothing but a gaussian for small σ_P as 0.025. So, we refer to Fig 13, and find

FOM 1-1 = 0.0054, FOM 2-1 = 0.002.

Thus the application of James-Stein Estimator for Shashi's Monte-Carlo results will improve the data by only 0.5% for FOM1 and 0.2% for FOM2, which are very small, as seen in Table 1 of hand calculation.

Some interesting results. We could find some interesting facts as seen in Figs 12 & 13.

(1) FOM1-1 is larger than FOM2-1 for the same σ_{EX}. This is understandable.
(2) In the normal case, ln(FOM1,2-1) are linear to ln σ_{EX} for wide range, But not exactly of straight lines.
(3) The data points ([illegible] fluctuate very much for FOM1-1 < 0.02 or > 1.0 and also in all region for FOM2.

We can not explain these facts just now.

Another data set #4190. We have tried another data set, that is f_{ij} = 0.500000 for all i, j. (We call this #4190. The enlarged data set including Shashi's is called #7000.) We also tried many other data sets between #7000 and #4190, introducing η and ζ, two parameters to approach to #4190 from #7000. The curves of Fig 12a, b gradually go up to higher level and become horizontal, that is, the FOM's become independent of NR or standard deviation, as shown in Fig 15. The fluctuations of FOM's become very large as can be guessed from Fig 12a, b. The total times of calling random number were almost 10^8 to obtain the results as shown in Table 2, in which some FOM's show very large fluctuations due to some capricious results. If we exclude these extremely deviated cases, we obtain (FOM1), (FOM2) or ((FOM1)), ((FOM2)) excluding more cases.

If we are allowed of some conjecture, these numbers may coincide to 10(k-3) and 2(k-3). All are integers in the range of standard deviation, with one exception of the case of KR = 2 and (FOM2) or ((FOM2)).

We can not find the reason just now.

Discussion. Finally, I must come back to the first problem, that is : Can we cut the computation cost of Monte-Carlo calculation ?

Suppose we have cut down to 1/100 of what Shashi had spent, the standard deviation may be 10 times larger. It may be allowed to say that the amount of information contained will be proportional to the inverse of standard deviation squared, generally. Fig 13 shows that the degree of improvement (FOM1-1 or FOM2 -1) are almost proportional to σ^2. Does this fact mean that the saving of expenses to 1/100 will result in the improvement of reliability by JSE proceedure but, inevitably accompanied by the decrease of usefulness to 1/100 ? In other words, does the JSE processing give nothing good ? It is not so. The increase of standard deviation is the results of saving cost to 1/100, but the size of standard deviation did not change very much by JSE processing itself.

JSE proceedure will not be vary powerful when the raw data are enough accurate. If the raw data are consisted of sevaral (> 4) regression lines considered as distributed in multi-variate normal distribution, the JSE application will be recommendable, especially when the counting rate, for example, is very low and can not be measured again.

Table 1 Hand Calculated Results

i = 1: Xi = $\log E_i$ = 1.197

A	= 3.830×10^{-4}	B	= 4.800×10^{-4}
$A^{(1)}$	= 3.828 "	$B^{(1)}$	= 4.390 "
C	= 3.056 "	D	= 2.388 "
$C^{(1)}$	= 3.060 "	$D^{(1)}$	= 2.397 "

Similar results are obtained for i = 2, ···10.

Table 2

FOM 1 and FOM 2 of #4190 averaged NR=(1,9)

KR=	1	2	3
FOM 1	12.3+4.4	98.8+135	101.2+27.2
FOM 2	2.1+0.1	13.3+ 12.6	18.6+ 2.6
(FOM 1)	11.2+1.7	47.9+2.0	89.9+ 7.6
(FOM 2)	2.07+.04	8.9+0.5	17.9+ 1.6
((FOM 1))	9.53+0.8	47.9+2.0	89.9+ 1.6
((FOM 2))	2.06+0.03	8.9+0.04?	17.9+ 1.6
k	4	8	12
k-3	1	5	9
10(k-3)	10	50	90
2(k-3)	2	10 ?	18

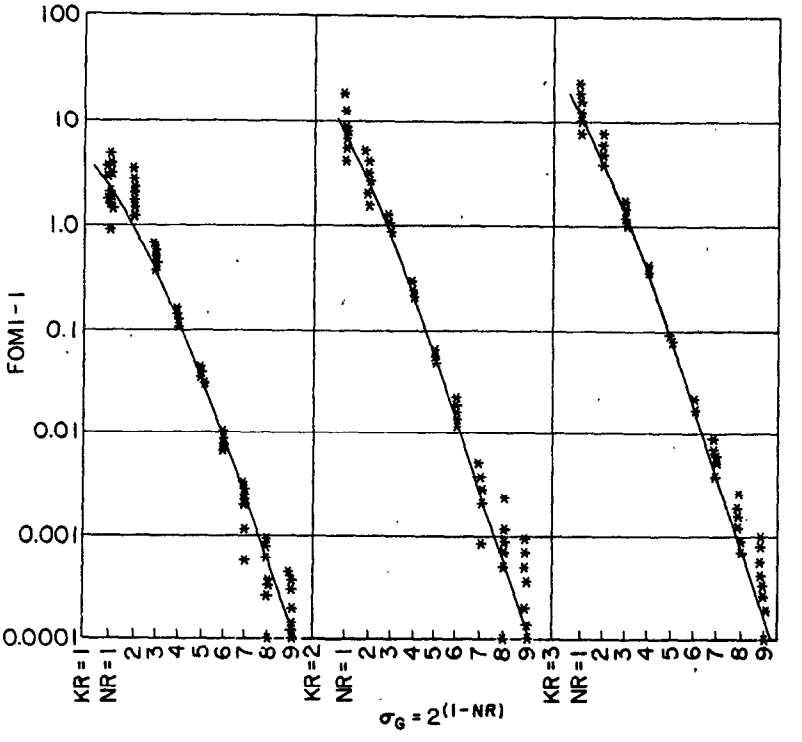

Fig 12a

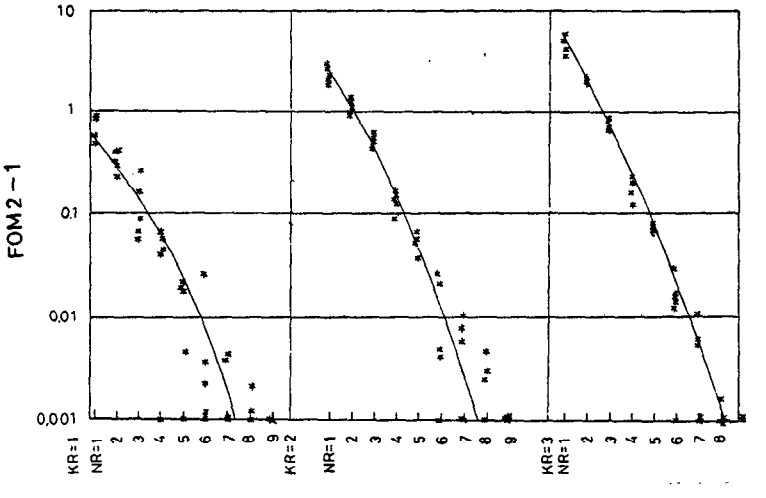

Fig 12b

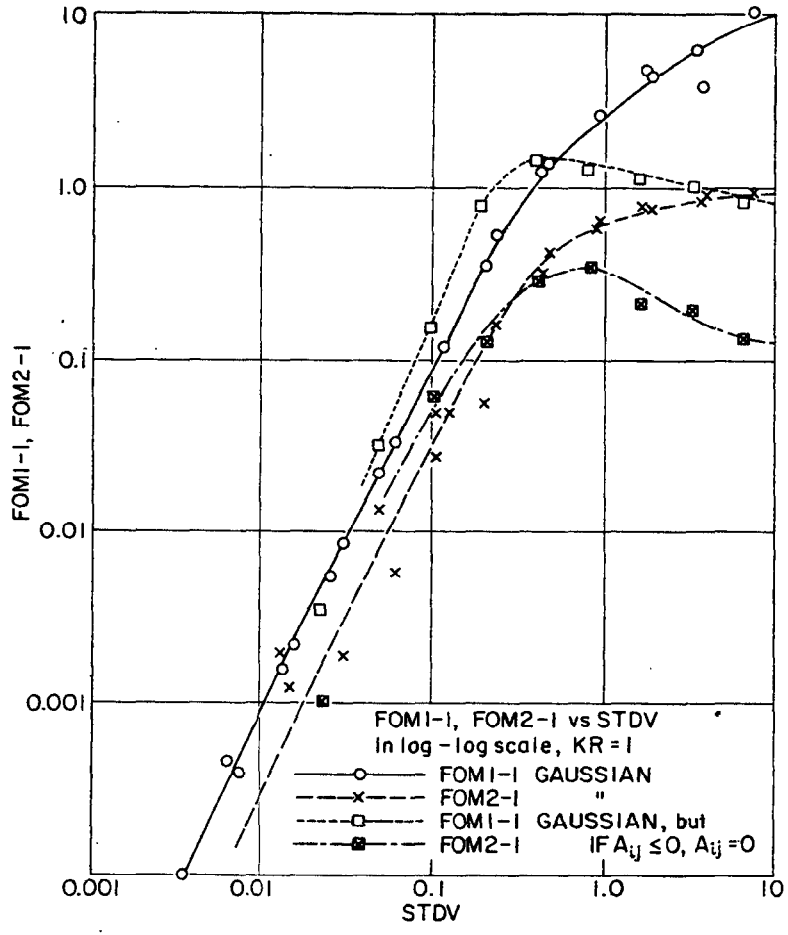
FOM1-1, FOM2-1 vs STDV
In log-log scale, KR = 1
FOM1-1 GAUSSIAN
FOM2-1 "
FOM1-1 GAUSSIAN, but
FOM2-1 IF $A_{ij} \leq 0$, $A_{ij} = 0$
FOM1-1, FOM2-1
STDV
10
1.0
0.1
0.01
0.001
0.001
0.01
0.1
1.0
10

Fig 13

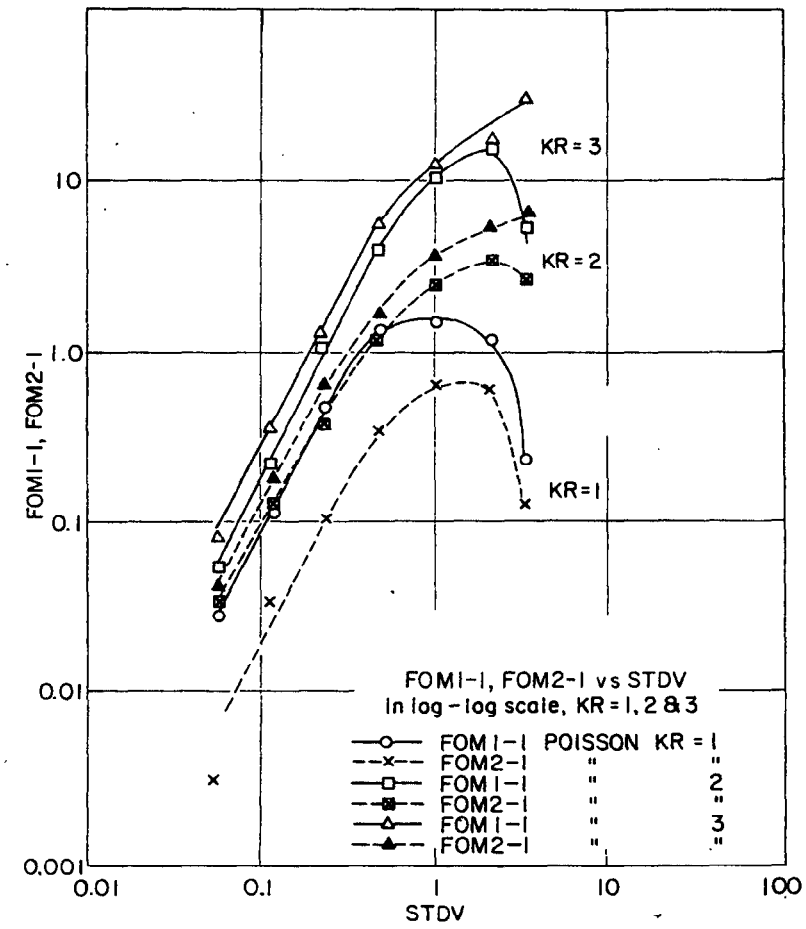
KR = 3
KR = 2
KR = 1
FOM1-1, FOM2-1 vs STDV
In log-log scale, KR = 1, 2 & 3
FOM1-1 POISSON KR = 1
FOM2-1 " "
FOM1-1 " 2
FOM2-1 " "
FOM1-1 " 3
FOM2-1 " "
FOM1-1, FOM2-1
STDV
10
1.0
0.1
0.01
0.001
0.01
0.1
1
10
100

Fig 14

This procedure is somewhat similiar to religious liturgy, certifying you that you are now closer to the truth or to God.

References

1) Nakahara Y. and Tsutsui T., JAERI-M 82-198 (1982)
Nakahara Y. Nucl. Sci. & Tech. 20(6) 511 (1983)
2) Steiner H.M. and Jungerman J.A. Phys. Rev. 101, 807 (1956)
3) Schimmerling W., et al.; Phys. Rev. C, 7, 248 (1973)
4) Il'inov A.S., Cherepanov E.A. and Chigrinov S.E.: Sov. J. Nucl. Phys., 32, 166 (1980)
5) Kupriyanov V.M., et al.: Sov. J. Nucl. Phys., 32, 184 (1980)
6) Tsukada, K. and Nakahara, Y. to be published
7) Cierjacks et al. ICANS IV, 1981. KEK p. 215, Autwork Conf. 1982
8) S.D. Howe, private communications, preliminary
9) Nakai et al. Physics Letters, Vol. 121B, 373 (1983)
10) Stein, C. Proceedings of the Third Berkeley Symposium on Mathematical statistics and Probability, Vol.1, Berkeley; University of California Press, 1955, 197-206.
James, W. and Stein, C. ibid. 1961, 361-206
Efron, B. and Morris, C. Stein's Paradox in Statistics, Scientific American, May, 1977, 119-127.
11) J.M. Capenter et al. IPNS project, Argonne National Laboratory Report 1975. IPNS-1, ANL78-88, p.126, Fig 4 (1978)
Shashi data means the Monte-Carlo results by Mrs Shashikara Das

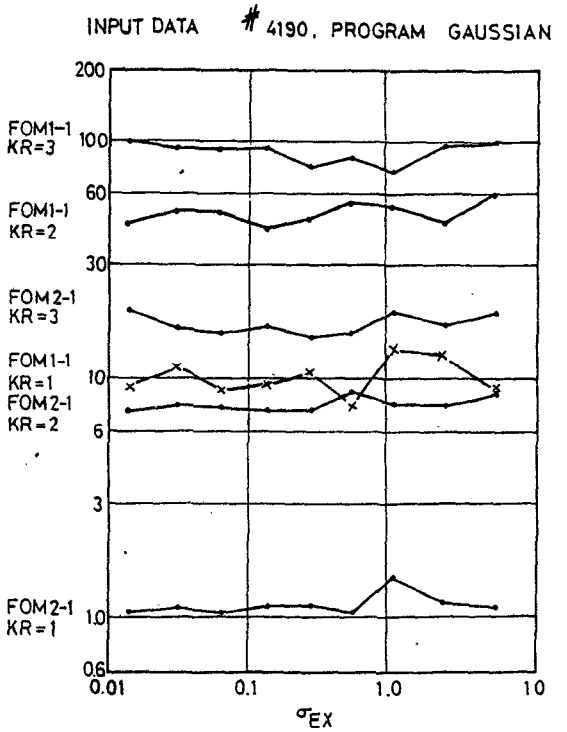

Fig 15

Proceedings of International Collaboration on Advanced Neutron Sources (ICANS-VII), 1983 September 13-16
Atomic Energy of Canada Limited, Report AECL-8488

MULTIPLYING BOOSTER TARGETS ON THE SNS

RAL (UK)-KfA (FRG) Collaboration*

Presented by A Carne

1. Introduction

The SNS at the Rutherford Appleton Laboratory is due to produce its first neutrons late in 1984 and to achieve full design intensity in 1986. The parameters of the SNS have been reported at a number of Conferences (1, 2) and in the literature (3).

No facility should be built without the potential for development and expansion. It is certainly a goal that the SNS should realise full utilisation of its beam lines, which are capable of supporting 20-25 instruments: to this end the SERC/RAL is actively seeking international collaboration and is in various stages of negotiation with a number of countries. This paper however is concerned with the development of the SNS as a source, in particular with the provision of an enhanced "booster" target. As pointed out in reference (3), the intrinsic brightness of the SNS is comparable to that of the ILL in the thermal energy region, somewhat inferior in the low energy region served by the ILL cold source but is markedly superior at higher energies (x 10 at 100 meV and x 1000 at 1 eV). Any improvement in the performance of the SNS in general, and of its target in particular, should therefore concentrate mainly on upgrading the facility in the cold neutron regime with any concommitant increase in the thermal and epithermal regions being an added bonus.

A collaborative project was set up early in 1983 between the RAL and Kernforschungsanlage, KfA Jülich, to study multiplying, sub-critical booster targets. The collaboration is also privileged to have the help of a number of individuals with special expertise contributing to this work. The project is divided into a number of broad headings, including the scientific case (future instrument demands, new science), high power booster concepts (targets with or without enrichment, with or without a fissile core or blanket), neutronic performance and moderator fluxes, technical problems (choice of fuel and coolant). At this early stage safety requirements are not included explicitly, but are of course always borne in mind. These topics will now be discussed in a little more detail.

* Members of the Collaboration are (RAL) A Carne, G H Eaton, D A Gray, W S Howells, G C Stirling (KfA) G Bauer, H Brockmann, W Scherrer, together with D Beynon, D Picton (Birmingham University), W Kley, H Reif (Ispra), M Kuchle (KfK), G Constantine (Harwell).

2. Scientific Case and Requirements

Whether or not a booster target is built depends firstly on the strength of the scientific case. The SNS as being presently built will be a leading pulsed source into the 1990's and is expected to outperform all present sources, including high flux reactors, in the neutron energy regime > 100 meV. At lower energies the relative performance is less clear and in the cold neutron regime < 10 meV, may be inferior to reactors (due to lower intensity and, in some cases, lack of compatibility between cold neutron experiments and the time of flight technique).

The scientific case for a booster target thus falls into two parts: (a) to provide an uprate of performance of known instruments especially in the cold neutron regime and (b), which is more difficult, to envisage scope for new science in the 1990's. These in turn set the requirements on the system of pulse intensity, length and shape, resolution, repetition rate, background, etc.

As a first step to defining the source parameters, Table 1 lists some "typical" performance figures for reactor (ILL) and pulsed (SNS) instruments over four main activities of cold neutron science. Column 4 envisages new instruments which give a, say, factor 10 better performance. Care is required in defining "better" since, depending on the case, it may mean more intensity, or wavelength window or repetition rate, etc. Column 5 indicates the pulsed source parameters required to serve this "x 10 instrument". It can be seen that the broad requirement is for an increased (x 10) intensity per pulse at 20 (25) or 50 Hz, with pulse lengths (and shapes) similar to the present SNS. The high repetition rate is required to achieve the highest time-averaged intensity, within the frame overlap limitation, and most instruments can operate at high (∿ 50 Hz) frequency.

3. High Power Booster Concepts for the SNS

Monte Carlo, point kinetics and neutron transport calculations are being performed by the member institutions on two basic concepts for a booster target, these are :

(a) An enriched uranium target, not dissimilar to the present SNS parallel plate target, with closely coupled moderators within a reflector assembly (e.g. beryllium).

(b) A spallation target (perhaps enriched) mounted within a core, or blanket of fissile material, surrounded by a reflector (e.g. nickel), with the moderators located at optimal positions to be determined.

The concept of an enriched SNS-type target is being studied mainly at RAL with the codes (HETC/05R) used in the design of the original ^{238}U target (4). Similar calculations have been performed for the IPNS target by Carpenter et al (5) and similar results are expected. Emphasis is being placed on varying the ^{235}U enrichment along the target to increase the neutron production at the downstream and where the cold moderators are located (including the para-H_2 one). First preliminary indications are that by increasing the enrichment to produce a flat fast neutron output increases the power (from the original 230 kW) by a factor $\sim$ 4 with a similar increase in neutron flux coupled to the downstream moderator. Such gains are within the reach of the present services and so this concept is of interest also to the existing target station. It also serves as a baseline for a booster based more on reactor concepts.

The concept of a fast neutron target surrounded by a small sub-critical fast assembly is also being studied, mainly at KfA. Initial work was done by Constantine and Taylor (6), based on the "Superbooster" studies for the Harwell electron linac (7). The one dimensional neutron transport code ANISN was used to consider the affects of (oxide) fuel volume fraction in the core, nickel reflector thickness, criticality k and the use of ^{239}Pu instead of ^{235}U. The target was the ^{238}U SNS and sodium was the assumed coolant throughout. The results indicated that a subcritical assembly (k = 0.95, corresponding m = 20) of 50% volume fuel and a 200 mm reflector would achieve a compact core of about 15ℓ (30% PuO_2) or about 20ℓ (UO_2) only. Table 2 shows the performance of such a 15ℓ core (30/70 Pu/U fuel) for a 5 and 10 MW mean power booster, taking into account the delayed neutron background (delayed neutron fraction $\beta \sim$ 0.48%). Significant numbers are the prompt multiplication m and the mean fuel temperature rise per pulse (q.v.). The values of m are greater than the actual gains achievable in the neutron flux feeding a moderator for such a system because of the increased surface area compared with the SNS target: the neutron flux is 2.7 x SNS value at 50 Hz, 13.5 x at 10 Hz.

The preliminary estimates have been followed by more sophisticated computations at KfA. Calculations have been performed using the time dependent homogeneous diffusion equation, point kinetics (with time) and MORSE on cylindrical and spherical modèls of a booster. Comparisons have been made between the codes in determining criticality k, neutron lifetime and pulse lengths, with the result that the simple equations appear adequate to make a survey of booster geometry and parameters before needing the full Monte Carlo codes. As an example, figure 1 shows a "typical" spherical configuration with a $k_{eff} \sim 0.97$. Outgoing fluxes were compared with and without booster (i.e. with the Ni reflector in contact with the spallation target). With the booster a neutron lifetime of 0.5 μs was obtained and neutron flux enhanced by x 3 compared with a conventional target. Pulse length from the moderator was again calculated using the 3 methods above, showing the simple calculations to be adequate for first optimisations. Pulse lengths ($\sim$ 50 μs) were dominated by moderation times.

An interesting model has been proposed by Kuchle using a pancake core of 4 MW (Th) with horizontally arranged plutonium fuel rods in a 0.3 x 0.3 x 0.2 m^3 assembly with Na cooling. A prompt multiplication of m = 50 at 10 Hz within a 5 MW power ceiling gives a x 10 gain in cold neutron yield. Using a 150 or 200 mm diameter parahydrogen moderator yields a x 100 flux at 4 Å compared with the ILL cold source.

4. Neutronic Performance and Moderators

Evaluation of neutronic performance using different calculational methods has already been referred to. Further codes in common usage by the collaboration are ENDF 8/2, 8/3 and 8/4, derived data libraries for neutron and γ-photon data and ORIGEN II, for fission products, burn-up and induced activity studies.

The design of a cold moderator and its optimisation in the wavelength range 0.5 Å < λ < 20 Å required pulse length $\gtrsim$ 100 μsec are being studied at Birmingham. Clearly moderator performance is intimately linked with the booster due to its relative size and location within the assembly. The optimum booster-moderator assembly is one which satisfies the experimental requirements, within its own physics, engineering and (ultimately) safety constraints. Of the basic orientations for a moderator, wing geometry is strongly preferred to suppress the γ-flash and fast neutron backgrounds. A likely material for the cold moderator is para-hydrogen, if the purity can be maintained. Whilst the thickness of a moderator determines, to first order, its pulse length (e.g. it is $\sim$ 50 mm on the SNS), increasing the transverse dimensions can increase the neutron flux with small or no increase in pulse length if suitable heterogeneous poisoning is introduced. Delayed neutron background becomes an important problem in the paramaterisation and experimental utilisation of the moderator. The suggestion has been made of using close-in choppers to reduce this problem.

5. Technical Problems, Choice of Fuel and Coolant

The choice of fuel for the booster lies with uranium enriched with ^{239}Pu or ^{235}U, in the form of oxide, ceramic, or alloyed with molybdenum. The use of plutonium offers a number of advantages, including shorter pulse times available because of the smaller delayed neutron fraction and the smaller core sizes achievable. As indicated in the examples above the latter is particularly important since it permits a higher neutron brightness at the surface feeding the moderator. Some of the disadvantages of plutonium are obvious and need not be discussed.

Alternative candidates for the fuel material are oxide and metal, possibly as an alloy (8%-10%) with molybdenum as used in the PFR. In either case reactor experience indicates pin rather than plate-type fuel will be required to give the high volume fraction of fuel needed to achieve high k_{eff} in a small, hard-neutron spectrum core, at the same time giving good heat transfer performance and (by virtue of its shape) superior resistance to swelling and fission product build-up. The impossibility of attaining bonding for oxide fuels virtually makes pins imperative.

The central problem in the use of any fuel is indicated in Table 2, i.e. the behaviour under pulsed conditions. Stress problems arise not only

with the rapid rise of temperature during the pulse, but also of quenching due to accelerator beam trips. Further problems include fatigue and possibly ratchetting of the fuel within the clad. Whilst there is experience of oxide fuels to 8-10% burn-up in fast reactors, the more arduous operating conditions in a booster might suggest that much lower design levels (say 2%) be considered initially. The question of reprocessing has yet to be studied.

The choice of coolant is dictated by the projected high power densities and the requirement (via its moderating properties) for a short ($\sim 10^{-7}$ sec) neutron generation time. The power densities in the range of 300-500 kW/l suggest the use of liquid sodium on the coolant. However D_2O is also a candidate if the increased pulse lengths are acceptable. In either case it may be necessary to use 1/v and resonant absorbers in the core.

The combination of these power densities, the nature and magnitude of the fuel inventory and the pulsed-power operation of the system (let alone the problem of high power density pulsed cryogenic moderators) necessitate a detailed series of safety and criticality studies to ensure safe operation of the booster. The safety studies must produce a design which minimises the possibility of power excursions, coolant channel blockage and core melt-down incidents.

6. Conclusions

The development of the SNS by the provision of an enhanced "booster" target and optimised for cold neutrons offers a facility which will outperform all known sources into the 1990's. A goal of the order of 10 x improvement is aimed at: whether and how this will be achieved and what compromises have to be made will be the subject of study by this collaboration over the next few years. We look forward to this exciting prospect.

7. References

1. Spallation Neutron Source Working Group (Presented by G H Rees) "A Pulsed Spallation Source for Neutron Scattering Research" 1977 US National Particle Accelerator Conference, Chicago, March 1977

2. See for example: A Carne "SNS Target Station Progress Reports" ICANS IV (KEK Japan, 1980) and ICANS VI (ANL, USA, 1982)

3. B E F Fender, L C W Hobbis and G Manning "The UK Spallation Neutron Source" Phil. Trans. R. Soc. London B290 657 (1980)

4. F Atchison "A Theoretical Study of a Target, Reflector and Moderator Assembly for SNS" Rutherford Appleton Laboratory Report RL-81-006 (1981)

5. J Carpenter et al Internal Laboratory Memos ANL 1981

6. G Constantine and N P Taylor Private Communications 1982, 1983

7. G Constantine, V S Crocker et al "The Physics of the Superbooster" AERE Report AERE R5205 (1967)

TABLE I

Scientific activity	ILL Instrument	SNS Instrument	Ten times "better" instrument than currently available	Pulsed source parameters required to achieve "x 10" instrument
LOW-Q small angle scattering (metallurgy, magnetism, polymers, chemistry, biology)	D11 $Q = 0.001 - 0.3Å^{-1}$ Intensity ~ 10^6 n cm^{-2} s^{-1} at 10Å ($\Delta\lambda/\lambda$ ~ 10%)	LOW-Q $Q = 0.003 - 1.0Å^{-1}$ Intensity ~ 3×10^5 n cm^{-1} s^{-1} for $1 < \lambda < 10Å$	$Q = 0.001 - 5Å^{-1}$ Intensity ~ 3×10^6 n cm^{-1} s^{-1} for $1 < \lambda < 20Å$	$0.5 < \lambda < 20Å$ prf = 20 Hz Intensity/pulse = 25 x SNS
Broad resolution quasielastic scattering (rotational diffusion in liquids etc.)	IN5 Resolution = 90 μeV Wide $\hbar\omega$ Intensity ~ 10^5 n cm^{-2} s^{-1}	IRIS(PG) Resolution = 13 μeV $\hbar\omega$ = 1 meV Intensity ≡ IN5	Intensity/pulse = 10 x SNS	$\lambda = 6.7Å$, δt_{mod} ~ 100μs prf = 50 Hz Intensity/pulse = 10 x SNS
			Intensity/pulse = 10 x SNS $\Delta\lambda$ = 2.5 x SNS	$\lambda = 6.7Å$, δt_{mod} ~ 100μs prf = 20 Hz Intensity/pulse = 10 x SNS
High resolution quasi-elastic scattering (eg. jump diffusion processes in metals, etc.)	IN10 Resolution = 1μeV $\hbar\omega$ = ± 15μeV Intensity ~ 10^4 n cm^{-2} s^{-1}	IRIS(S1) Resolution = 1.2μeV $\hbar\omega$ = 80μeV Intensity/μeV ≡ IN10	Intensity/pulse = 10 x SNS	δt_{mod} ~ 100μs prf = 50 Hz Intensity/pulse = 10 x SNS
			prf = 500Hz Intensity/pulse ≡ SNS	δt_{mod} ~ 100μs prf = 500 Hz Intensity/pulse ≡ SNS
Ultra-high resolution quasielastic scattering (eg. polymer segmental diffusion)	IN11 (1982) Resolution = 10 neV $Q = 0.02 - 1.5Å^{-1}$ Intensity ~ 1.5×10^7 n cm^{-2} s^{-1}	SES (RL-81-019) Resolution = 70 neV $Q = 0.04 - 2.2Å^{-1}$ Intensity ~ 1.5×10^6 n cm^{-2} s^{-1} $4.5 < \lambda < 7.5Å$	Resolution = 70 neV Intensity = 1.5×10^8 n cm^{-1} s^{-1}	$2 < \lambda < 10Å$ δt_{mod} ~ 2 x SNS prf = 20 Hz Intensity/pulse = 250 x SNS

TABLE 2

prf n (Hz)	Multi-plication m	Fraction of Useful Power	Pulse in MJ	Mean temp rise C in 80 kg as oxide
1	106.4 (140.8)	0.49 (0.32)	2.45 (3.24)	91 (120)
2	71.4 (106.4)	0.66 (0.49)	1.64 (2.45)	61 (91)
5	36.0 (61.3)	0.83 (0.71)	0.83 (1.41)	32 (52)
10	19.7 (36.0)	0.91 (0.83)	0.45 (0.83)	17 (32)
25	8.3 (16.9)	0.96 (0.92)	0.19 (0.37)	7 (14)
50	4.3 (8.3)	0.98 (0.96)	0.098 (0.19)	3.6 (7)

Operating Modes at 5 and (10) MW mean power, allowing for delayed neutron fraction; 30/70 Pu/U fuel as oxides, Na coolant

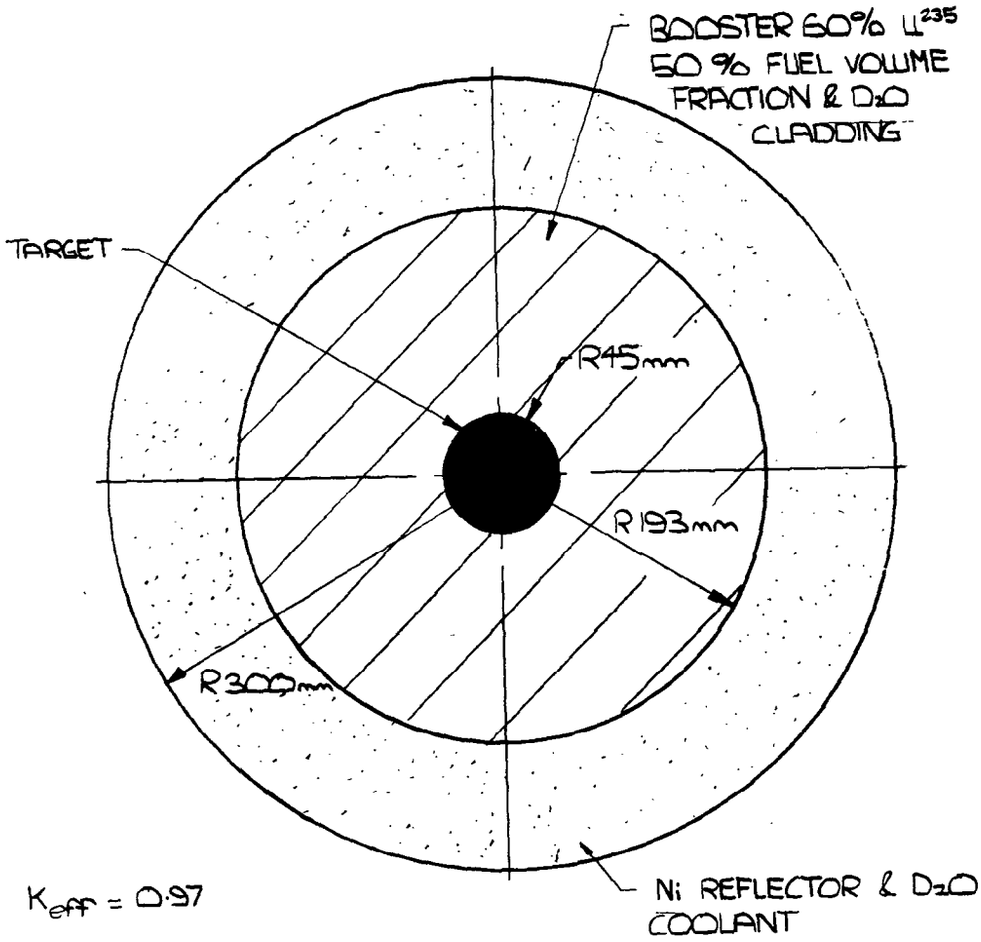

FIGURE : 1 BOOSTER GEOMETRY & MATERIALS STUDIED BY K.F.A. GROUP

Proceedings of International Collaboration on Advanced Neutron Sources (ICANS-VII), 1983 September 13-16
Atomic Energy of Canada Limited, Report AECL-8488

ENHANCEMENT OF THE SNS SPALLATION TARGET BY U-235 ENRICHMENT

H. Brockmann and W. Scherer

Kernforschungsanlage Jülich GmbH

Institut für Reaktorentwicklung

Introduction

A collaboration between Rutherford Appleton Laboratory (RAL) and Kernforschungsanlage Jülich GmbH (KFA) was initiated in the early 1983 to study a multiplying subcritical booster target for the SNS (1). One proposal to realize a booster target is to enrich the present U-238 target in U-235 or Pu-239 and to enhance the neutron output by additional fissions of these isotopes without changing the overall design of the target. Another concept is to design a totally new booster target regarding from the beginning all requirements of such a type of neutron source. Since there was no preference for one of these proposals at the beginning it was decided to consider first the development potential of the present SNS target assembly and to use this as a baseline for the design of a new subcritical booster target.

For estimating the potential of the enhanced SNS target two-dimensional neutron transport calculations were made for different enriched targets and the original SNS target which is used as reference. In the following, the potential performance of the present SNS target is discussed and first results of the neutronic calculations for the enriched SNS target are given.

Potential Performance of the SNS Target

The power density distribution in the present SNS target is not uniform along the target axis (2, 3) and emphasis is being placed on varying the U-235 enrichment along the target to increase the neutron production at the downstream part. A further measure is to operate the SNS target up to its design limit.

The average power density in the uranium plate with the highest thermal load is 270 W/cm^3 for the present SNS target. Regarding the safety factor 3 in the target cooling system the average power density in the enhanced target could be raised to 810 W/cm^3. This leads to a total power of 1.6 MW in the enhanced target or a total energy deposition of 8100 MeV/p for a proton current of 200 µA.

The energy deposition due to high energy reaction is 646 MeV/p in the present SNS target. Since the high energy deposition will be changed only insignificantly by the enrichment the number of low energy fissions, n_{fiss}, will be increased from 2 fissions /p in the present target to about 38 fissions /p in the enriched target. The average number of fission neutrons per fission is about 2.5 in the enriched target so that 96 fission neutrons /p are created in the enhanced assembly.

In the present SNS target, 28 neutrons are produced per incident proton of which 23 neutrons are due to high energy reactions. Denoting the total number of neutrons per proton by n_{SNS} and the number of spallation neutrons by n_{spall} the neutron gain of the enriched target is given by

$$\text{neutron gain} = \frac{n_{fiss} + n_{spall}}{n_{SNS}} = 4$$

The resulting effective multiplication constant defined by

$$k_{eff} = \frac{\text{fission source}}{\text{absorptions + leakage}} = \frac{n_{fiss}}{n_{fiss} + n_{spall}}$$

will be 0.8 for the enhanced target.

Calculational Model

The model of the target assembly used in the neutron transport calculations is shown in Fig. 1. The target is simulated by a 9 cm diameter by 33.9 cm long cylinder containing a uniform mixture of uranium, coolant, and cladding in their appropriate portions. The coolant is heavy water and the cladding material is Zr. The target is surrounded by pressure vessel which is approximated by a 1 cm thick region made of stainless steel. The reflector, which consists of beryllium rods cooled by heavy water, is represented by a homogeneous mixture of 80 % (vol.) Be and 20 % (vol.) D_2O.

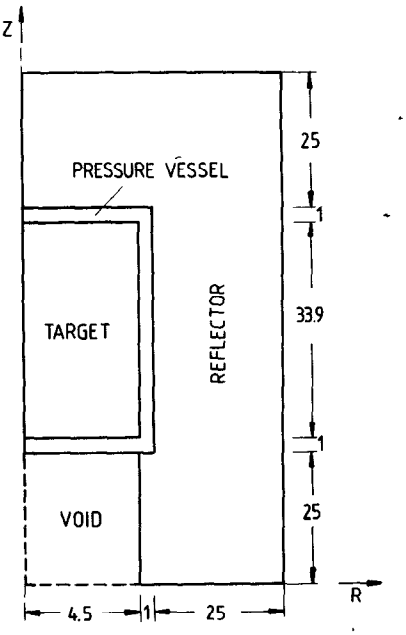

Fig. 1 Model for Transport Calculations (Dimensions in cm).

In the neutronic calculations, the target was divided into eight regions of nearly the same volume in which the enrichment in U-235 was changed (see Fig. 2). The U-235 enrichment increase in the direction of the proton beam to account for the decrease of the primary neutron source. To regard the influence of the Be-reflector the enrichment in the outer radial regions is lower than in the inner regions.

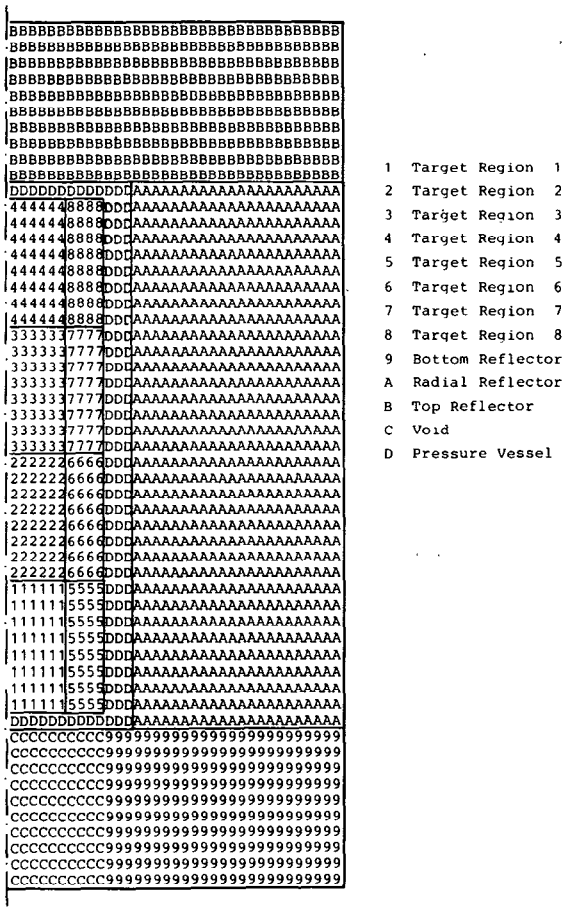

Fig. 2 Zone Number by Interval in Transport Calculations.

The neutronic calculations were made with the diffusion code CITATION (4) and the discrete ordinates transport code DOT-IV (5), using the P1S4 approximation. A 15 broad group library was used in the transport calculations which was collapsed from a 123 fine group cross section library (94 fast plus 30 thermal groups). The weighting functions were calculated by the 1-D discrete ordinates transport code XSDRNPM (6) using infinite cylinder geometry. For this purpose, two spectrum calculations with U-235 enrichments of 30 % and 50 % were made regarding the different enrichments in the lower and upper target zones.

The primary spallation neutron source was approximated by a two-dimensional step function shown in Fig. 3. The source strenght data were taken from Ref. 2.

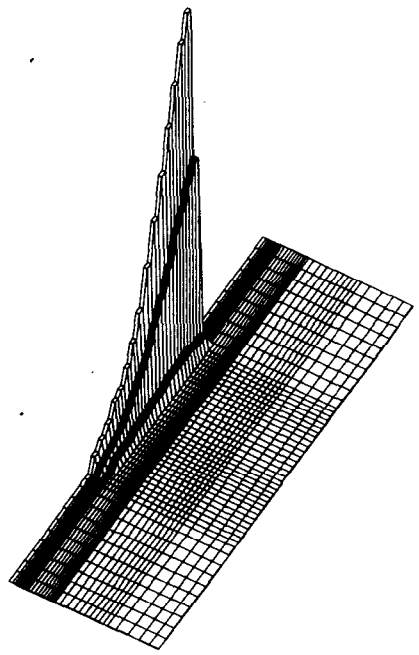

Fig. 3 Neutron Source Distribution (E < 15 MeV) in Target.

Discussion of Results

Two series of calculations were made using the diffusion code CITATION and the discrete ordinates transport code DOT. In the first series, the original SNS target which is used as reference was calculated. The results were compared with earlier results of RAL to make sure that the calculational model is adequate. In the second series of calculations, the U-235 enrichment in the 8 target regions was changed in such a way that a nearly uniform power density distribution with the desired power level of 810 W/cm^3 was achieved regarding also the contribution of the incident proton beam in the front regions of the target. Some quantities of interest obtained from these calculations are given in Table I. To calculate the total power a fixed amount of 125 kW due to the high energy reactions was added to the fission power. It was furthermore assumed that an energy of 6 MeV is released in a neutron capture event.

Further results of the CITATION AND DOT calculations for the enriched target are given in Figs. 4 and 5. They present the required U-235 enrichment and the fission power densities in each of the eight target regions. In order to quantify the benefits of the enriched target at the present stage of calculations, the neutron gain was calculated as the ratio of the radial outflow from the enriched target to the radial outflow from the present SNS target.

The gain in the total radial outflow for the enriched target in comparison to the present SNS design is about 3. The enhancement varies from 2 in the region near the proton beam entrance to 7.7 at the downstream region. The increase in the neutron currents feeding the moderator boxes is 2.3 for the first half of the target and 5.7 for the second half.

TABLE 1

Summary of CITATION and DOT Results.

		Fission Power (kW)	Total Power (kW)	Multiplication Factor	Radial Outflow from Target
Reference	CITATION	57	194	0.1542	$5.06 \cdot 10^{16}$
	DOT	68	207	0.1878	$5.60 \cdot 10^{16}$
Enriched	CITATION	1415	1560	0.7972	$1.49 \cdot 10^{17}$
	DOT	1480	1640	0.8062	$1.71 \cdot 10^{17}$

U-235 ENRICHMENT

FISSION POWER DENSITY (W/CM^3)

		NEUTRON GAIN
REGION 4 70 % 734	REGION 8 50 % 746	7.7
REGION 3 45 % 670	REGION 7 35 % 749	4.3
REGION 2 35 % 662	REGION 6 30 % 749	2.6
REGION 1 25 % 514	REGION 5 25 % 617	2.0

Fig. 4 U-235 Enrichment, Fission Power Density, and Neutron Gain in the 8 Target Regions obtained from the DOT Calculation.

U-235 ENRICHMENT

FISSION POWER DENSITY (W/CM^3)

		NEUTRON GAIN
REGION 4 90 % 659	REGION 8 70 % 733	7.1
REGION 3 60 % 664	REGION 7 45 % 754	4.1
REGION 2 40 % 572	REGION 6 35 % 736	2.5
REGION 1 30 % 440	REGION 5 30 % 628	1.9

Fig. 5 U-235 Enrichment, Fission Power Density, and Neutron Gain in the 8 Target Regions obtained from the CITATION Calculation.

Conclusion

One way to design a multiplying subcritical booster target for the SNS is to enrich the present target in U-235 or Pu-239. First calculations show that an operation of the target up to the design limit by enriching in U-235 leads to gains in the radial neutron outflow from the target that further investigations of this proposal seem to be worthwhile. The next task will be the study of the time structure of the neutron pulse from the target and the moderator. A further important problem to be investigated will be how the coupling between target and moderator will be influenced by the large increase of the fission power in the target.

References

1. A. Carne, "Multiplying Booster Targets on the SNS," Proceedings of this Conference.

2. F. Atchison, "A Theoretical Study of a Target Reflector and Moderator System for SNS," RL-81-006, Rutherford and Appleton Laboratories (1981).

3. M. Holding, "SNS Target Station, Calculations to Determine the Uranium Plate Thicknesses for the SNS Target," SNS/TS/N8/82, Rutherford and Appleton Laboratories (1982).

4. T.B. Fowler et al., "Nuclear Reactor Core Analysis Code: CITATION," ORNL-TM-2496, Rev. 2, Oak Ridge National Laboratory (1971).

5. W. A. Rhoades et al., " The DOT-IV Two-Dimensional Discrete Ordinates Transport Code with Space-Dependent Mesh and Quadrature," ORNL/TM 6529, Oak Ridge National Laboratory (1978).

6. N. M. Greene and C. W. Craven, Jr., "XSDRN: A Discrete Ordinates Spectral Averaging Code," ORNL-TM-2500, Oak Ridge National Laboratory (1969).

Proceedings of International Collaboration on Advanced Neutron Sources (ICANS-VII), 1983 September 13-16
Atomic Energy of Canada Limited, Report AECL-8488

Target Designs for Stepwise Developement of SNQ

Horst Stechemesser*, Gerd Thamm**
Kernforschungsanlage Jülich GmbH, D-5170 Jülich, FRG,
* Zentralabteilung Allgemeine Technologie
* SNQ - Projekt Targetstation

Summary

The construction of the SNQ accelerator in two stages (stage I: 350 MeV or above, stage II: 1100 MeV, 5 mA average proton current for both) requires a staged concept for some areas of the proton target station too. Chiefly the target depth dimensions for the various materials such as lead and/or tungsten as well as uranium, in stage I only one fifth of stage II but unchanged outer dimensions of the target wheel, is influenced. Cooling systems for the target, moderators and shielding will also be constructed in two stages. In contrast other components like target block shielding and cooling water pipes embedded in the shielding block respectively target trolley are to be constructed in stage I already in identical size designed for stage II.

1. Introduction

On occasion of last years ICANS-VI meeting at Argonne National Laboratory G. Bauer reporting on the "Status of the SNQ Projekt at KFA Jülich" /1/, pointed out that the facility should be built in a staged way.

Stage I:

Accelerator type LINAC with a mean proton current of 5 mA and about 350 MeV proton energy or

SYNCROTRON with a mean proton current of 0,5 mA and 1,1 GeV proton energy. Both types first using al-cladded lead as target material, followed later by al-zircaloy/claded depleted uranium.

Stage II:

Accelerator type LINAC with 1.1 GeV proton energy and 5 mA mean current using al-cladded lead first and finally al-zircaloy/cladded depleted uranium as target material.

Stage III:

Implementation of a proton pulse compressor - (pulse length 0.5 µs)

Both possibilities of stage I had been studied to such an extent till january 1983 that a choice on the accelerator type could be made. In february 1983 the scientific advisory committee of the SNQ project recommended to build a LINAC in stage I (see /2/). The main data are given in Table 1.

TABLE 1: MAIN PROTON BEAM PARAMETERS OF SNQ

	STAGE I	STAGE II
ENERGY	350 MEV	1100 MEV
AVERAGE PROTON CURRENT	5 mA	
PULSE PROTON CURRENT	200 mA	
PROTONS/PULSE	$3.12.10^{14}$	
REPITITION RATE	100 Hz	
PULSE WIDTH	250 µs	

Since then the plant lay out work is concentrating on designing a target station using first lead or tungsten[1.)] and finally 238-uranium target rods cladded by al or zircaloy and directly cooled by light water. The concept of the target station is to be elaborated in such a manner that it would allow as easily and fast as possible the technical adaption necessary to be operated with a 1100 MeV/5 mA proton beam in stage II and with the same sequence of target materials as in stage I.

The main results of the work achieved so far will be given in this report.

2. Basic Design of the Targetstation

(Table 2)

During operation, the target is located in

1.) tungsten has become a serious canditate for targets in stage I and II (see/3/)

the centre of the target block, where it is hit by the proton beam (Fig. 1). The fast neutrons emerge from the upper and lower surface of the disc-shaped target wheel at the position of proton incidence. These neutrons are slowed down in moderators of different design (small H_2O moderator below the target and large D_2O tank with cold neutron source and irradi[illegible] cies

TABLE 2: MAIN DATA OF THE TARGET BLOCK

- OUTER DIAMETER TARGET BLOCK	12 M
- TOTAL HIGHT TARGET BLOCK	13 M
- DIAMETER CAST IRON CENTER	10 M
- THICKNESS CONCRETE SHELL	1 M
- HIGHT TARGET BLOCK ABOVE TARGET-WHEEL	5 M
- BEAM HOLES (MULTIPLE), LOOKING AT H_2O-MODERATOR	8 HOLES
- BEAM HOLES (MULTIPLE), LOOKING AT COLD NEUTRON SOURCE	2 HOLES
- DIAMETER ROTATING BEAM SHUTTER	2 M
- NEUTRON BEAM LINES (MULTIPLE, 6 EACH)	2 LINES
- TOTAL WEIGHT CAST IRON	8.10^6 KG

above the target) (Fig. 1)
Several beam tubes and neutron guide tubes which view these moderators and penetrate through the surrounding shielding lead to the experimental areas where the neutron scattering instruments are located (Fig.2).

Inspection, maintenance and eventually repair cannot be carried out in the operational position of the target wheel, because it is not accessible for any tasks inside the shielding block. Therefore the target wheel is mounted on a trolley also carrying the lower moderator and parts of the shielding. For such IWR (Inspektion-Inspection, Wartung-Maintenance, Reparatur-Repair) tasks the target wheel will be moved by remote handling from its operational position into the service cell, which is directly linked to the target block.
The target wheel has to rotate on the fixed target trolley when in operational position, whereby cooling water for the removal of heat, which is mainly generated by spallation, has to run trough the weel. The wheel has to be connected to a device called KLA (Kühlung-Cooling, Lager-Bearing, Antrieb-Drive water supply system) which supplies the wheel's cooling water, acts as bearing and drives the rotation /4/.

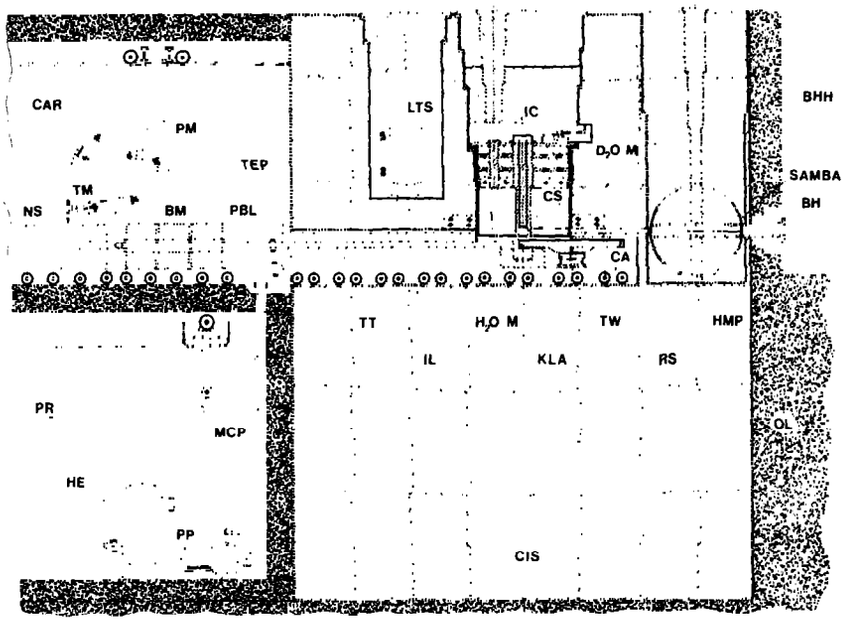

FIG. 1: TARGET BLOCK (VERTICAL VIEW)

BH Beam Hole
BM Bending Magnet
CA Cavern
CAR Cavern Ante Room
CIS Cast Iron Shielding
CS Cold Neutron Source
D_2O-M D_2O-Moderator
HE Heat Exchanger
HMP Heavy Metal Plug
H_2O-M H_2O-Moderator
IC Irradiation Channel
IL Inner Liner
KLA German shortcut for Cooling, Bearing and Rotating Drive Water Supply
LTS Low Temperature Supply
MCP Main Cooling Pipe
NH Neutron Hall
NS Neutron Stop
OL Outer Liner
PBL Proton Beam Line
PM Power Manipulator
PP Pressure Pumps
PR Pump Room
RS Rotating Shutter
SAMBA Size Adaptable Multiple Beam Aperture
TEP Trolly End Plate
TM Telemanipulator
TT Target Trolly
TW Target Wheel

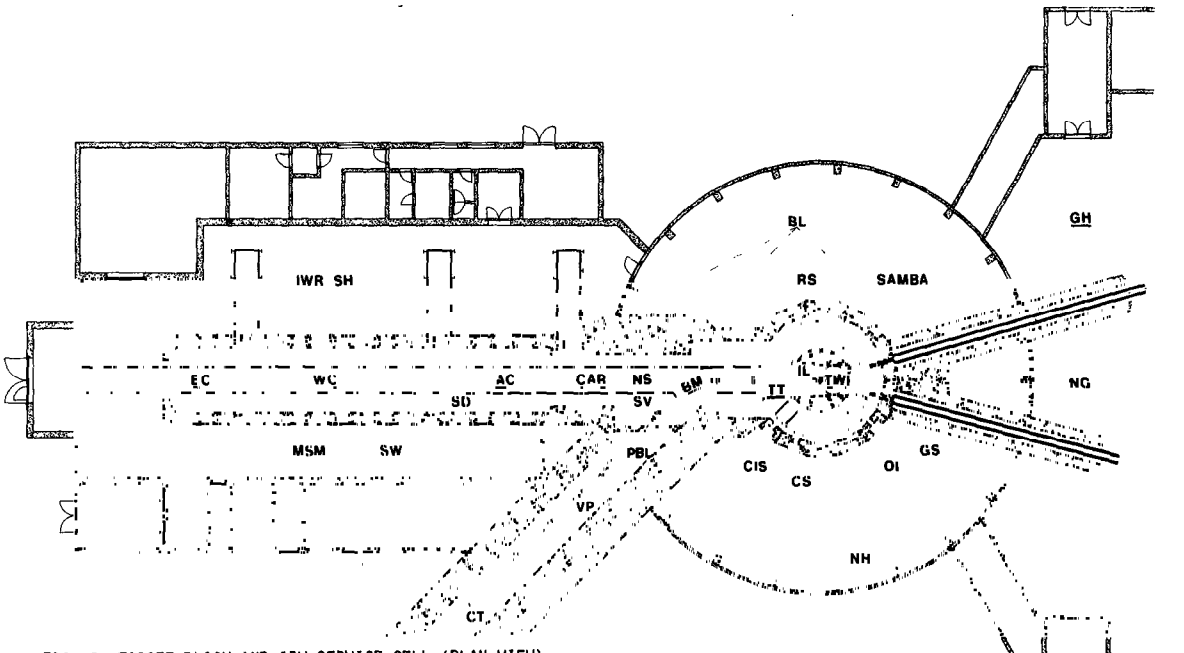

FIG. 2: TARGET BLOCK AND IRW-SERVICE CELL (PLAN VIEW)

AC	Assembling Cave	EC	Entrance Cave	OL	Outer Liner
BL	Beam Line (Neutrons)	GH	Guide Hall	PBL	Proton Beam Line
BM	Bending Magnet	IL	Inner Liner	RS	Rotating Shutter
CAR	Cavern Ante Room	MSM	Master Slave Manipulator	SAMBA	Size Adaptable Multiple Beam Aperture
CIS	Cast Iron Shield	NG	Neutron Guide	SW	Shielding Window
CS	Concrete Shield	NH	Neutron Hall	TT	Target Trolly
CT	Cold Trap	NS	Neutron Stop	VP	Vaccum Pump
				WC	Workshop Cave

The rotating target is a unit consisting of the connection of the target wheel and the so-called KLA.
Target wheel and KLA are connected force-locking and water-tight by bolts and metallic sealing rings. This connection can be unscrewed in the IWR-service cell.

3. Nuclear Target Data of Stage I and II

The nuclear data for stage I and II using lead, tungsten and depleted uranium as target materials have been calculated by D. Filges et al /5/. Those which are of particular importance for the technical lay out of the targetstation are given in Table 3: range of protons, target depth for 85 % (stage I) respectively 95 % (stage II) of the neutron production, target depth for the centre of moderators, peak energy deposition per pulse, time-averaged total target power.
The proton range for the same material is about five times greater in stage II compared to that of stage I, nearly twice as great for lead than for tungsten and uranium the proton ranges of which are nearly of equal size. The target depths up to which 85/95 % of all neutrons are produced show the same relations between the different target materials and the two stages. It is smaller than the range of

TABLE 3
THERMO/NUCLEAR DATA OF SNQ TARGETS
(STAGE I AND II)

	R (cm)		D-85 (cm)	D-95 (cm)	D-MAX (cm)	
	I	II	I	II	I	II
Pb - TARGET[1]	14,0	75,9	12,0	66-70	4,0	9,5
T - TARGET[1]	8,3	44,4	7,8	36	4,0	7,5
U - TARGET[1]	9,0	48,3	8,0	36	4,5	8,0

	E-MAX (KJ/cm³) / PULSE		E-TOT[2] (MW)		ΔT (K)	
	I	II	I	II	I	II
Pb - TARGET[1]	0,182	0,06[3]	1,5	2,9	124	41
T - TARGET[1]	0,225	—	1,6	≈3,0	90	-
U - TARGET[1]	0,215	0,149	2,9	12,5	91	63

R RANGE OF PROTONS
D-85(95) TARGET DEPTH FOR 85(95)%[4] OF THE NEUTRON PRODUCTION
D-MAX TARGET DEPTH FOR MAX NEUTRON LEAKAGE CURRENT
E-MAX PEAK ENERGY DEPOSITION PER PULSE
E-TOT TIME AVERAGED TOTAL POWER IN TARGET
ΔT TEMPERATURE RISE AT HOT SPOT IN TARGET
1.) AVERAGE MATERIALS COMPOSITION IN THE TARGET
Pb/T/U = 76,5%, H_2O = 16,5%, Al = 7%
2.) RADIAL INTERVALL ABOUT BEAM AXIS 1,0CM
3.) RADIAL INTERVALL ABOUT BEAM AXIS 1,5CM
4.) 85% → STAGE I, 95% → STAGE II

FIG. 3: ENERGY DEPOSITION IN DEPLETED URANIUM TARGETS VERSUS TARGET DEPTH (STAGE I AND II)

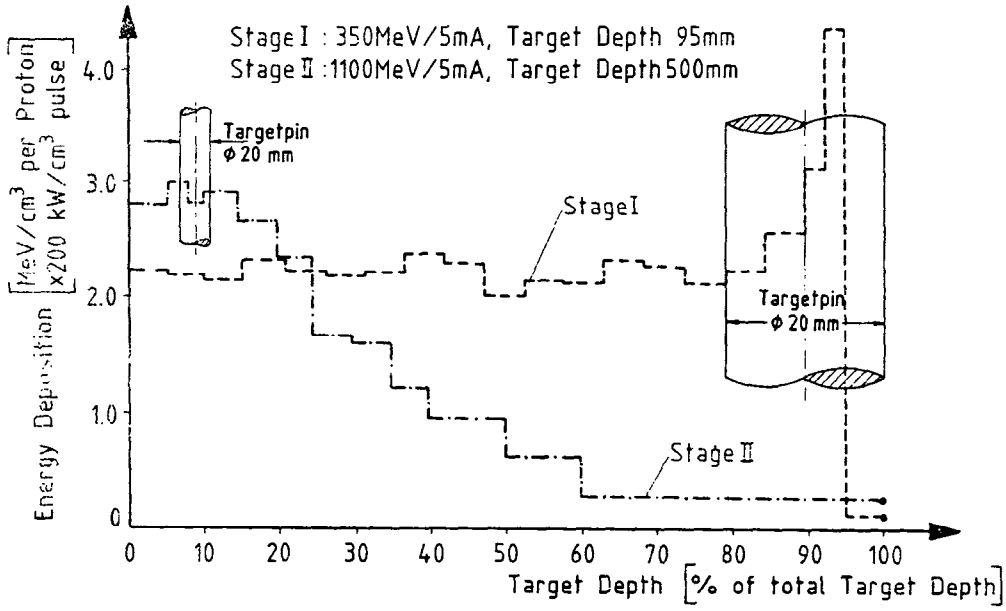

protons and therefore determines the "technical" target depth in stage I and II.

The different target depths for the centre of the moderators have to be taken into account for the optimal coupling especially of the H_2O-moderator, whereas they are of minor importance in the case of the large (2 m diameter) D_2O-moderator.

The maximum peak energy deposition per pulse is significantly greater in stage I. Furthermore shape and position of the peaks are different, within stage I and II. Fig. 3 shows the curve of the peak deposition versus the target depth for uranium targets in stage I and II. Typical target pin diameters (20 mm) are indicated for both stages. The very narrow ("Bragg") peaks in stage I at the end of the target, which are much smaller than the pin diameters result in an unsymmetric radial temperature distribution and additional thermal stress, that could be avoided by a reduction of the "technical" target depth in stage I. The uniform radial temperature distribution in stage II. does not require any technical extra-measures.

Table 3 reveals that the time averaged total power generated in the target is significantly higher for the uranium target in stage II compared to all targets in stage I and even the "non-uranium" targets in stage II. This leads to a 2 step concept of the target cooling system.

4. Design for Stage I and II

The concept of constructing SNQ in several stages permits the stepwise construction for some of the components too, whereas other component groups either are needed for functional reasons in their final design right from the start or will, because of construction reasons be used in stage I and II. identically, even though a lesser version would suffice in stage I.

4.1 Target Wheel

The stepwise concept has its strongest influence on the design of the target of course. The target, a large wheel, rotating in the pulsed proton beam in a high energy density is a novel component of a high potential with respect to design, selection of materials, welding techniques and depending upon this its operation life. Because of this it was decided to have identical design and structural materials for the target wheels of all stages in order to use the operation experience for

TABLE 4 TECHNICAL DATA OF SNQ TARGET-WHEELS

	UNIT OF MESURE-MENT	1. STAGE (350 MeV)			2. STAGE (1100 MeV)		
		LEAD	TUNGSTEN	URANIUM	LEAD	TUNGSTEN	URANIUM
-FREQUENCY OF REVOLUTION	sec^{-1}	0,5			0,5		
-DIAMETER TARGET-WHEEL	mm	2490	2490	2490	2560	2560	2560
-TARGET DEPTH FOR 85% NEUTRON PROD.	mm	120	77,5	80	—	—	—
-TARGET DEPTH FOR 95% NEUTRON PROD.	mm	—	—	—	700	360	360
-TECHNICAL TARGET DEPTH	mm	121,2	82,2	82,2	700	360	360
-NUMBER OF STAGGERED PIN ROWS		7	5	5	37	20	20
-NUMBER OF TARGET PINS	pieces	2184	1560	1560	9304	5916	5916
-TARGET PINS SERVING AS TIE-RODS	pieces	0			232	0	0
-DIAMETER OF TARGET-ELEMENTS-	mm	23-20,7	23-21,5	23-21,5	24,0-18,0	24,0-18,0	24,0-18,0
-COOLING WATER FLOWRATE	m^3/h	250	250	250	250	250	500
-PRESSURE DROP IN TARGET DEPTH	bar	0,13	0,09	0,09	1,01	0,35	0,94
-CLADDING MATERIAL		AlMgSi1			AlMgSi1	AlMgSi1	(Zircaloy)
-HIGHT OF TARGET-ELEMENTS	mm	100			100		
-HIGHT OF TARGET-WHEEL	mm	156			156		
-STRUCTUREMATERIAL TARGET-WHEEL		AlMgSi1			AlMgSi1		
-TOTAL WEIGHT TARGET MATERIAL	kg	1045	1283	1262	3350	3508	3460
-TOTAL WEIGHT TARGET-WHEEL	kg	2945	3093	3072	4600	5145	5095

improving the life expectancy. The design life of the first target wheel is two years corresponding to 12.000 h of full power /6/.

The main load for the target wheels does not arise from the weight of the target material but from the hydraulic pressure of the cooling water flow onto the wheel discs comprising the inner walls of the target wheel. The wheel discs of the lead target of stage II (700 mm target depth) are loaded that much, so that they are to be held together by 232 tie rods in order to avoid excessive elastic deformation. The elastic buckling of the target discs is thus reduced from 3,5 mm down to 0,2 mm. These tie rods comprising target pins with stronger canning and threaded bolts on either end /4/ are not needed for tungsten and uranium targets of stage I and II as well as for the lead target of stage I, as the lesser target depth reduces the hydraulically stressed areas of the wheel discs especially because the inner target zones with a smaller number of cooling water channels are not existing in those designs. Because of this the pressure loss and thus the average static water pressure at the same cooling water flow in the target (table 4) are reduced. The same is valid for a cooling water flow through the uranium target of stage II doubled from 250 m^3/h to 500 m^3/h.
The cooling water channels within the target structure of the uranium target have been altered with respect to save after-heat removal. All water inlet and outlet channels within the target structure are designed like a syphon, so that in the first instance the target pins remain under water in the case of loss of coolant. (fig. 4 and 5)

4.2 Target Pins

The target material itself is also strongly influenced by the staged concept. It is arranged in form of pins in the inner of the target wheel for better heat removal. For each construction stage of the accelerator different target materials are to be used starting with lead and/or tungsten and ending with uranium (Table 4) The target pins will always be inserted in cans to avoid direct release of spallation products from the pin surfaces of the target materials into the cooling water. Direct contact of water with uranium because of the well known uranium-water reaction has to be avoided in any case. For minimising the release of spallation products from the canning surfaces surrounded by cooling water the canning material must have a low atom weight and a low density. Therefore aluminium is a suitable canning material especially, as aluminium has in addition a low neutron and proton damage rate /3/, a good corrosion resistance and a high heat transfer coefficient. As a back-up material for targets at higher temperatures, likely to occur in

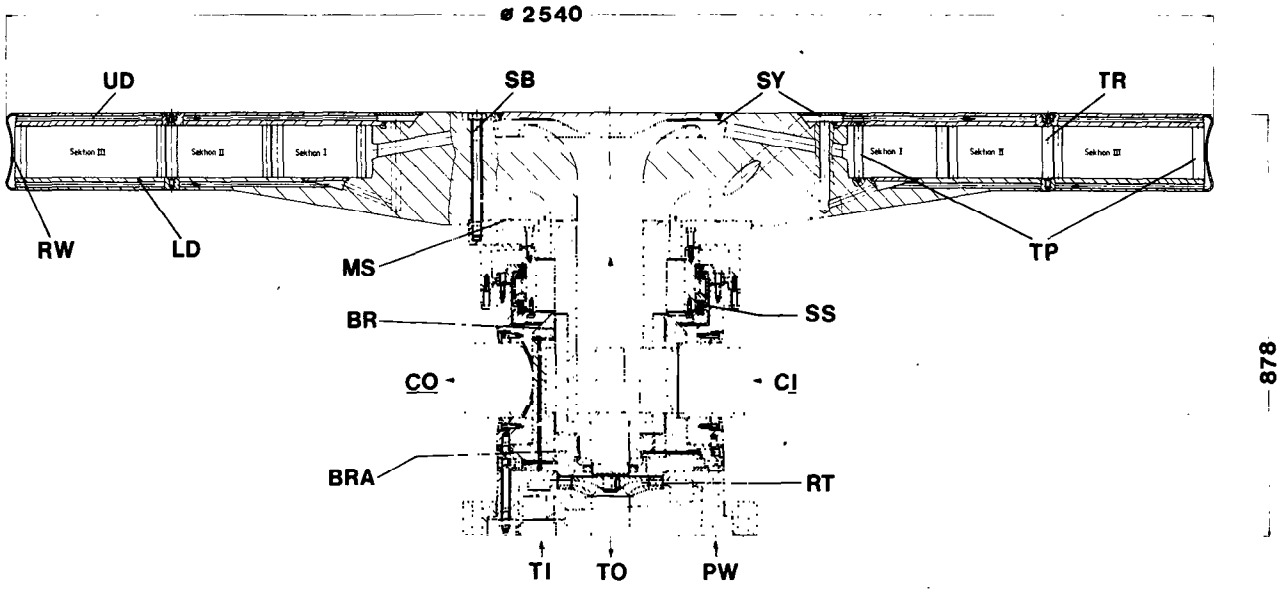

FIG. 4: PB-TARGET, 1100 MeV, MOUNTED ON KLA TYP I
(KLA TYP I: HYDROSTATIC AXIAL AND RADIAL BEARINGS, RADIAL TURBINE)

BR	Radial hydrostatic Bearing	PW	Pressurized Water Inlet hydrostatic radial Bearing	TJ	Turbine Water Inlet
BRA	Radial and axial hydrostatic Bearing	RT	Radial Turbine	TO	Turbine Water Outlet
CI	Coolingwater Inlet	RW	Rotating Window	TP	Target Pin
CO	Coolingwater Outlet	SB	Screw Bolt	TR	Tie Rod Pin
LD	Lower Wheel Disc	SS	Slide Ring Seal	UD	Upper Wheel Disc
MS	Metallic Seal	SY	Syphon		

uranium pins with failed cooling, circaloy is considered.
Special attention must be paid to the manufacture of the canning. Galvanic processes or evaporation of nickel and chromium layers are not favourably looked at because their higher atom weights are of disadvantage (see above) and there are doubts concerning radiation resistance of these materials.

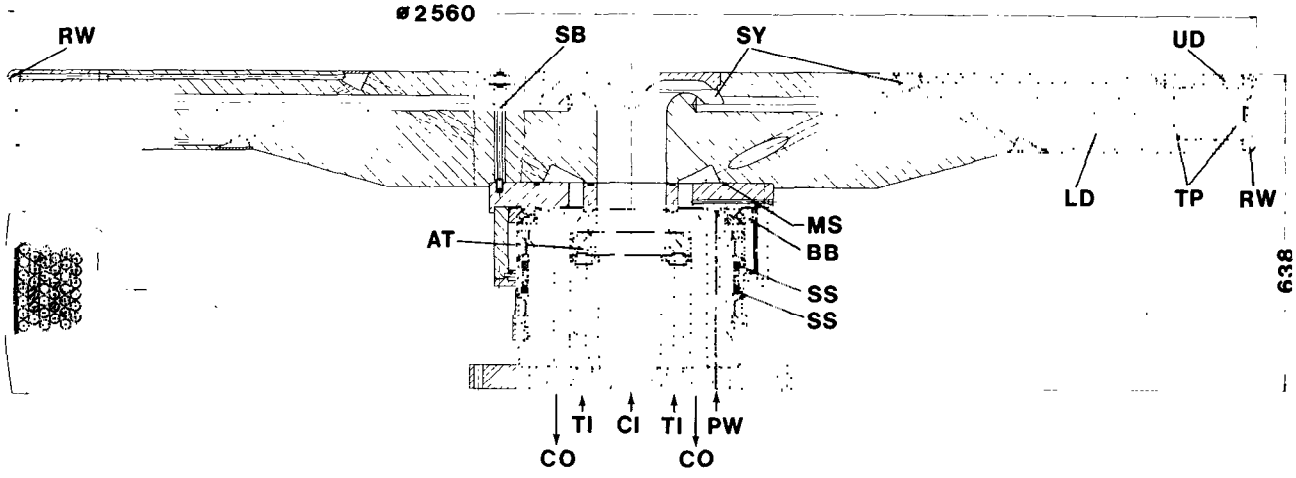

FIG. 5: U-TARGET, 350 MeV, MOUNTED ON KLA TYP II
(KLA TYP II: HYDROSTATIC AXIAL BEARING, RADIAL BALL BEARING, AXIAL TURBINE)

AF	Axial Turbine	MS	Metallic Seal	SS	Slide Ring Seal
BB	Ball Bearing (radial)	PW	Pressurized Water Inlet for hydrostatic axial Bearing	SY	Syphon
CJ	Coolingwater Inlet	RW	Rotating Window	TI	Turbine Water Inlet
CO	Coolingwater Outlet	SB	Srew Bolt	TP	Target Pin
LD	Lower Seal Disc			UD	Upper Wheel Disc

The canning in the form of tubes is to be put over the target pins and it is important to achieve a maximum surface contact ratio as the heat transfer coefficient and therefore the temperature level in the target pin is influenced by this. Table 3 shows the importance of this at high local energy depositions of stage I. For a lead target pin it is sufficient to push a lead pin of a tight fit into the aluminium tube. When the proton beam hits the lead it is heated up and expands against the water-cooled aluminium tube, so that lead and aluminium press against each other. As lead possesses virtually no elasticity a high plastic deformation at the surfaces takes place giving a ratio of surface contact of over 95 %.

This principle does not work with the hard and non-plastic materials tungsten and uranium. These materials require a plastic deformation of the cladding material at the surfaces of the target pin. In this case the aluminium tube is to be pressed onto the core of tungsten and uranium by isostatic pressing. Manufacturing processes of different pressing methods and the measuring of surface contact ratio are under preparation.
The differences of the stage concept and the variation of target materials caused by it present themselves only in the number of rows of target pins, that means the depth in the inner of the target wheel (table 4).
The targets of stage II with the same material are about five times deeper than the ones of stage I and the lead targets are always about double as deep as the tungsten or uranium targets (tungsten and uranium target are of the same depth).
Fig. 4 shows the target wheel with the largest target depth using lead at 1100 MeV. In contrast the uranium target at 350 MeV shown in fig. 5 is extremely short. The targets of stage I are problematic because of extremely high energy deposition at the end of the proton range due to an eminently narrow "Bragg"-peak. As shown for a uranium target of stage I in fig. 3, the specific heat deposition in a part of the pin abruptly increases by about 100 % leading to significantly increased hot-spot temperatures compared with its surrounding and leads to problems concerning thermal stress due to an asymmetric temperature profile. This unwandet thermodynamic effect has to be avoided either through "thinning" of target material in the area of the "Bragg"-peak or through reduction of target depth (replacement of last pin row by water). The losses in neutron production in the order of about 15 % (see table 3) due to shortening of the target seem to be tolerable, as they occur for the probably short time operating targets of stage I only. Therefore the latter method will be preferred in the design.

4.3 KLA-unit

Fig. 4 and 5 show target wheels mounted on KLA units. The KLA-unit carries the load of the total target wheel (table 4), moves it at 30 rotations per min. in a vacuum atmosphere and has openings for cooling water entry and outlet for the rotating target wheel /4/.
Already now this KLA unit as an important part is extensively beeing tested, taking into account radiation damage of materials for slide ring seals /3/ as well as overall mechanical performance of the KLA unit. The dynamic behaviour of a KLA unit type I as shown in fig. 4 without radiation damage has been tested in original size. This type I unit has hydrostatic axial as well as radial bearings. Repeatedly problems occurred with the hydrostatic radial bearings leading to mechanical damages. These problems seem to be related to thermal causes and testing is continued. In any case, the developement of a KLA unit typ II (Fig. 5) has been started in parallel, which features the well performing hydrostatic axial bearing and a special stainless steel roller bearing as a radial bearing. In addition the remote handling of the KLA unit is facilitated, as there are no more outer

cooling water inlet and outlet pipes like for type I.
A stainless steel roller bearing in original size is unter test right now.

4.4 Diameter of Target Wheel

The diameter of the target is determined essentially by thermodynamical parameters. During one rotation at a pulse distance of 10 ms (frequency 100 Hz) the same area at the wheel circumference has to be hit by one proton pulse only. That gives a circumferential velocity of 40 mm/10 ms = 4 ms^{-1} with a proton beam diameter of 40 mm (FHWM see /5/). Furthermore a sufficiently long cooling period of about 2 seconds was chosen before reentering the proton beam, from which a wheel diameter of 2,5 m results.
The target station is designed for the uranium target of stage II. The two moderators, located above and below the target wheel, have to be placed in an optimum position depending on the neutron flux distribution emerging from the target wheel. This is a target depth of 8 cm (see table 3) and of special importance for the small H_2O-moderator. Eight neutron beam tubes are directed at the H_2O-moderator. As they are in fixed positions in the target block, they thus determine the location of the H_2O-moderator in the cavern. Table 3 shows, that for the same target material the target depth for the optimum positioning of the moderator for stage I is about 3,5 cm smaller than for stage II. In addition, the depth for lead compared with tungsten and uranium, for which the depth is about the same, is about 1,5 - 2 cm more. These differences are taken into account by reducing the radius of target wheels of stage I by 3,5 cm in comparison with stage II wheels. For lead a further adjustment of the target wheel radius does not seem to be necessary, as the existing wide maximum of the neutron flux distribution /5/ will compensate differences of 1 to 2 cm in the moderator arrangement. Final optimisation calculations for real geometries will have to decide wether or no

TABLE: 5
THERMOMECHANICAL DATA OF SNO-TARGET - COOLING SYSTEMS
(STAGE I AND II)

I. KLA-H_2O-MODERATOR SYSTEM

	Stage I	Stage II
Total Heat Dissipation		
in Target + Structure	4 MW	13,5 MW
in H_2O - Moderator	0,2 MW	0,4 MW
Flowrate		
Turbine (max)1.)	126 m³/h	
Bearings (radial, axial)1.)	4,5 m³/h	
Target Cooling	250 m³/h	500 m³/h
H_2O-Moderator	15 m³/h	30 m³/h
Total	265 m³/h	530 m³/h
1.) in Target Cooling included		
Purification	20 m³/h	
Pressure		
Turbine	37 bar	
Bearings (radial/axial)	60 bar /	30 bar
Target (Entry/Outlet)	7 bar /	2 bar
H_2O-Moderator	3,5 bar	
Coolant Temperature at Entry	50° C	
Temperature Rise in Coolant	14,5 K	24,0 K

	Stage I	Stage II
II. D_2O-MODERATOR SYSTEMS		
Total Heat Dissipation	0,5 MW	1,0 MW
Flowrate	6 Kg/s	10 Kg/s
Pressure	2 bar	
Temperature at Entry	45° C	
Temperature Rise	20,0 K	30,0 K
III. SHIELD COOLING SYSTEM		
Total Heat Dissipation	1,0 MW	2,0 MW
Flowrate	40 m³/h	70 m³/h
Pressure	4 bar	
Temperature at Entry	45° C	
Temperature Rise	21,5 K	24,5 K
IV. SHUT DOWN COOLING SYSTEM		
Total Heat Dissipation		
immediately after shut down	100 KW (U)	450 KW
1 d after shut down	7 KW (U)	30 KW
Flowrate	1,5 Kg/s	
Pressure	3 bar	
Temperature at Entry	45° C	
Temperature Rise	(max) 20 K2.)	

1.) Uranium
2.) within 1st hour after shut down

radius adjustments have to be carried out.

4.5 Cooling systems

It can be seen in table 5, that for stage II only the use of uranium leads to significantly higher heat deposition in the target, the H_2O- and D_2O-moderators and the shield systems. Therefore, for the cooling systems of these components a stage concept was adopted too. The first stage of this concept provides for save heat removal for all targets of stage I and for the non-uranium targets of stage II.
All cooling systems are of a modular design for the components influencing the cooling capacity.
The increase in cooling capacity for stage II is carried out by adding pumps and heat exchanger moduls in parallel. All necessary provisions for extra space have to be made in stage I of course. All parts, which can lateron not be altered, like the pipes fixed into the targetblock and the target trolley, have to be of the dimensions necessary for stage II at stage I already.

4.6 Shielding Block

With regard to /5/ the shielding of the target wheel (fig. 1 and 2) in stage I could be constructed some what smaller (shielding thickness of stage I 5 to 10 % lesser than for stage II). As a later increase would be very time consuming and costly a stepwise construction of the target block shielding is not considered.

References

/1/ Bauer, G.S. "Status of the SNQ Projekt at KFA-Jülich", Proc. ICANS-VI, report ANL-82-80, Argonne National Laboratory

/2/ Bauer, G.S. (1983) "The SNQ-Projekt" Proc. ICANS-VII, this volume

/3/ Lohmann, W. and Krautwasser, P. (1983) "Progress in Materials Investigation for the SNQ-Target" Proc. ICANS-VII, this volume

/4/ Stechemesser, H. "Mechanical Design of the Target Station DIANE of the German Spallation Neutron Source Project and its Rotating Target" Atomkernenergie/Kerntechnik 41 (1982), p 259-263

/5/ Filges, D. et. al. (1983) "Recent Target Design Calculations at KFA" Proc. ICANS-VII, this volume

/6/ Thamm, G. et. al. (1983) "Operational, Handling and Safety Aspects of the SNQ-Target Station" Proc. ICANS-VII, this volume

Proceedings of International Collaboration on Advanced Neutron Sources (ICANS-VII), 1983 September 13-16
Atomic Energy of Canada Limited, Report AECL-8488

HEAT-UP EFFECTS OF GAMMA SHOWERS ON NINE SAMPLE MATERIALS IN TRIUMF NEUTRON SOURCE GEOMETRY

M. Pepin
Swiss Institute for Nuclear Research
CH-5234 Villigen, Switzerland

SUMMARY

The Monte-Carlo programme EGS[1] was used to follow the propagation of electron-gamma showers through the geometry of the TRIUMF neutron source, and to estimate the resulting energy deposition in nine sample materials.

INTRODUCTION

Following the Monte-Carlo study[2] of the heat-up of samples of 9 materials by the nuclear cascades of protons at 520 MeV in the approximate geometry of the TRIUMF neutron source, the Monte-Carlo programme EGS was used to investigate the additional, simultaneous heat-up of the same 9 samples by the effect of:

i) the gamma showers from neutral pion decay, and

ii) the prompt nuclear gamma showers

which are produced in the lead target by the nuclear cascades. The 9 sample materials are Be, C, Al, Fe, Cu, W, Pb, Bi, and heavy water. The effects of proton beam lateral displacement and beam spot size were also briefly examined.

In order to allow the flexible handling of the somewhat complicated geometry of the target arrangement (see Fig. 1), the geometry package of HET was linked to the EGS code and used in this study.

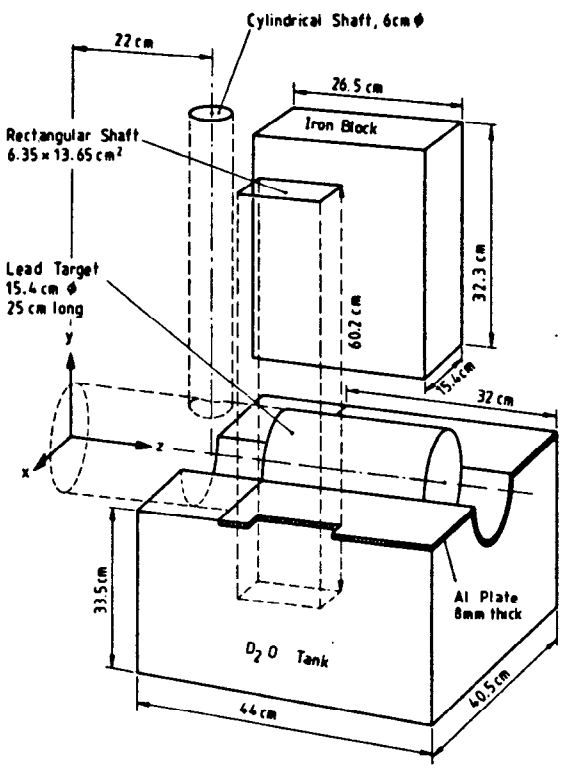

Fig. 1 Simplified geometry of the central region of the TRIUMF neutron source, as used in the Monte-Carlo study.

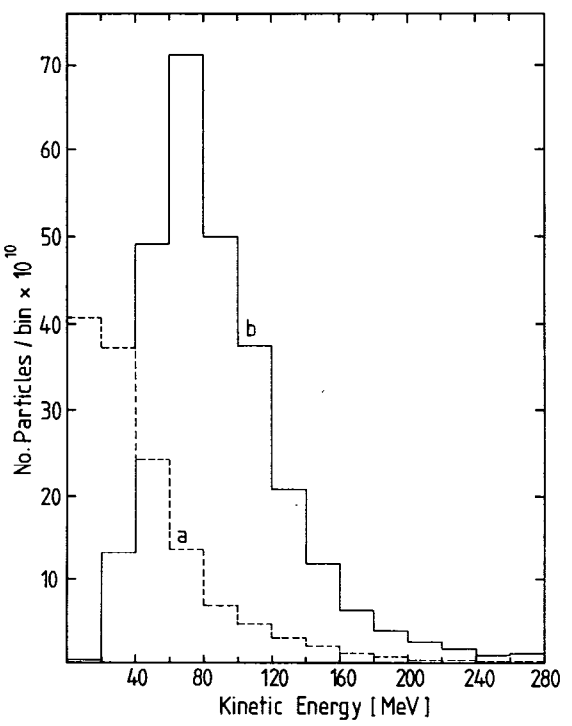

Fig. 2 Kinetic energy spectrum of a) the neutral pions generated in the nuclear cascades, and b) the resulting decay gammas.
Histogrammes are normalised to 10 μAs of incoming proton beam.

PARAMETERS OF THE SOURCE GAMMAS

For the gammas from neutral pion decay, the pion energy spectrum and the normalisation factor of one pion per 46 incident protons were taken from the 520 MeV nuclear cascade study. The pion spectrum and the resulting spectrum of the original gammas, obtained under the assumption that the pions are produced isotropically in the lab, are shown in Fig. 2. The mean gamma energy is 89.7 MeV, the mean z-value (z is the direction of the proton beam) lies 4.6 cm deep in the lead target. The distribution of shower origins in the plane perpendicular to the proton beam was assumed identical to the beam shape, i.e. gaussian, with 95 % of the probability within a spot of 3 cm diameter; tails outside a radius of 5 cm were cut off.

For the prompt nuclear gammas, the same x, y, and z distributions were taken as for the gammas from neutral pion decay. Following F. Atchison, W.E. Fischer and B. Sigg[3], the normalisation factor was taken to be 1.2 gammas per incident proton, and the source spectrum was assumed to be in good approximation rectangular between 1 and 9 MeV.

METHOD

In order to save computing time, the propagation of all shower particles was suspended when the particles escape the surface of the lead target. All escaping particles were then rotated by that multiple of 60 degrees which was necessary to bring them into the 60 degree sector of the target which faces the sample; the propagation of the shower was then resumed. The shower particles were also rotated by 60 degrees more and 60 degrees less than necessary, in order to judge the contribution of the neighbouring sectors to the flux incident on the sample. The spectrum of photons incident on the sample was obtained, and EGS was used again to estimate the energy deposits in the sample.

RESULTS

Table I presents compared values of particle energies and fluxes for the neutral pion decay and the prompt nuclear gamma showers (photons below 1 MeV were not included in these statistics, as they contribute considerable numbers of particles, but less than 10 % of the energy). The energy spectra of the gammas incident on the sample are shown in Fig. 3. Table II gives the sample heat-ups for the 9 materials. All results are normalised to 10 µAs of incoming protons.

CHECK OF THE RESULTS

In a very rough hand calculation, the gamma source was assumed to be a mono-energetic, isotropically emitting point, located at the centre of mass of shower origins. The energy incident on the sample was then given by the source strength, times the solid angle factor, times (for each intervening medium) the product of the thin-beam attenuation for that thickness of medium and the energy fluence buildup factor for the mean photon energy at entrance to that medium (the mean photon energy was taken from the EGS intermediate results). The heat deposited in the samples of Al, Fe, Pb and heavy water, for which buildup factors could be found in the literature, were estimated by calculating in a similar way the energy transmitted through the sample and assuming the complements of energy to have been deposited.

In these calculations, and for photon energies below 10 MeV, the buildup factors were taken

	π^0 decay showers	Prompt nuclear showers
No. of incoming protons	$6.24 \cdot 10^{13}$	$6.24 \cdot 10^{13}$
No. of electron-gamma cascades	$2.71 \cdot 10^{12}$	$7.49 \cdot 10^{13}$
Total energy of initial gammas (MeV)	$2.43 \cdot 10^{14}$	$3.75 \cdot 10^{14}$
Mean energy of initial gammas (MeV)	89.7	5.0
No. of particles above 1 MeV escaping target from side	$0.45 \cdot 10^{12}$	$2.15 \cdot 10^{12}$
Total kin. energy of the above (MeV)	$3.70 \cdot 10^{12}$	$7.50 \cdot 10^{12}$
Mean kin. energy of the above (MeV)	8.1	3.5
Composition of the above	96 % gammas	99 % gammas
No. of particles above 1 MeV incident on the sample	$1.10 \cdot 10^{10}$	$1.90 \cdot 10^{10}$
Total kin. energy of the above (MeV)	$4.20 \cdot 10^{10}$	$6.70 \cdot 10^{10}$
Mean kin. energy of the above (MeV)	3.8	3.5
Composition of the above	98 % gammas	99 % gammas

Table I Some parameters characterising the flux, energy content, and composition of the electron-gamma showers at various stages of their propagation: at source, at the side exit point from the cylindrical lead target, and at the point of incidence on the sample.

Sample	π^0 decay showers		Prompt nuclear γ showers		Nuclear cascades	
	E_{dep} [MeV/sec cm^3]	$(dT/dt)_o$ [^{o}C/sec]	E_{dep} [MeV/sec cm^3]	$(dT/dt)_o$ [^{o}C/sec]	E_{dep} [MeV/sec cm^3]	$(dT/dt)_o$ [^{o}C/sec]
D_2O	$0.38 \cdot 10^8$	$0.13 \cdot 10^{-5}$	$0.42 \cdot 10^8$	$0.15 \cdot 10^{-5}$	$8.62 \cdot 10^9$	$3.0 \cdot 10^{-4}$
Be	$0.46 \cdot 10^8$	$0.21 \cdot 10^{-5}$	$0.80 \cdot 10^8$	$0.38 \cdot 10^{-5}$	$7.47 \cdot 10^9$	$3.5 \cdot 10^{-4}$
C	$0.76 \cdot 10^8$	$1.10 \cdot 10^{-5}$	$1.24 \cdot 10^8$	$1.81 \cdot 10^{-5}$	$5.28 \cdot 10^9$	$7.6 \cdot 10^{-4}$
Al	$0.82 \cdot 10^8$	$0.54 \cdot 10^{-5}$	$1.50 \cdot 10^8$	$0.99 \cdot 10^{-5}$	$3.68 \cdot 10^9$	$2.4 \cdot 10^{-4}$
Fe	$2.92 \cdot 10^8$	$1.32 \cdot 10^{-5}$	$4.12 \cdot 10^8$	$1.86 \cdot 10^{-5}$	$6.79 \cdot 10^9$	$3.1 \cdot 10^{-4}$
Cu	$3.50 \cdot 10^8$	$1.63 \cdot 10^{-5}$	$5.52 \cdot 10^8$	$2.57 \cdot 10^{-5}$	$6.76 \cdot 10^9$	$3.8 \cdot 10^{-4}$
W	$6.00 \cdot 10^8$	$3.72 \cdot 10^{-5}$	$9.62 \cdot 10^8$	$5.97 \cdot 10^{-5}$	$6.06 \cdot 10^9$	$3.8 \cdot 10^{-4}$
Pb	$4.38 \cdot 10^8$	$4.79 \cdot 10^{-5}$	$7.42 \cdot 10^8$	$8.11 \cdot 10^{-5}$	$2.98 \cdot 10^9$	$3.3 \cdot 10^{-4}$
Bi	$3.70 \cdot 10^8$	$4.81 \cdot 10^{-5}$	$6.58 \cdot 10^8$	$8.57 \cdot 10^{-5}$	$2.66 \cdot 10^9$	$3.5 \cdot 10^{-4}$

Table II Energy deposition E_{dep} per cm^3 of sample and per sec, and initial rate of sample heat-up $(dT/dt)_o$ for nine sample materials and for pion decay and prompt nuclear γ showers. Pro memoria, the corresponding quantities for nuclear cascades (results of ref. 2), are also shown. All figures are normalised to a 10 μA incoming proton beam.

from the Engineering Compendium on Radiation Shielding[4]. For the propagation of the neutral pion decay showers through the lead target of 7.7 cm radius, a kind of "buildup factor" was defined by estimating the unscattered escaping energy (thin beam approximation) and comparing it with the total energy transmitted through a 7.7 cm thick lead slab, as given by Messel and Crawford[5]. A value of 199 was obtained.

Comparison of these hand calculations with the EGS results shows good agreement (discrepancies between 2 % and 15 %) whenever the photon energies are below 10 MeV, i.e. everywhere except for the propagation of the pion decay showers through the lead target. In this last situation the hand calculation leads to a value 42 % larger than the value given by EGS.

EFFECTS OF BEAM VARIATION

In order to ascertain the effects of lateral beam displacement and beam spot size on the sample heat-up, EGS was used to estimate the amounts of energy incident on the sample when the distribution of shower origins was displaced laterally by 1.5, 3.0 and 4.5 cm towards the sample, and when the distributions of shower origins in the x-y plane were assumed uniform within concentric rings with limiting radii of 1.1, 2.2, 3.3, 4.4, 5.5, 6.6, and 7.7 cm. Because of the limited computing time available, only the showers from neutral pion decay were thus investigated, and the statistics used in these studies were considerably reduced, so that the number of photons above 1 MeV incident on the sample was as low as 8 (for shower origin

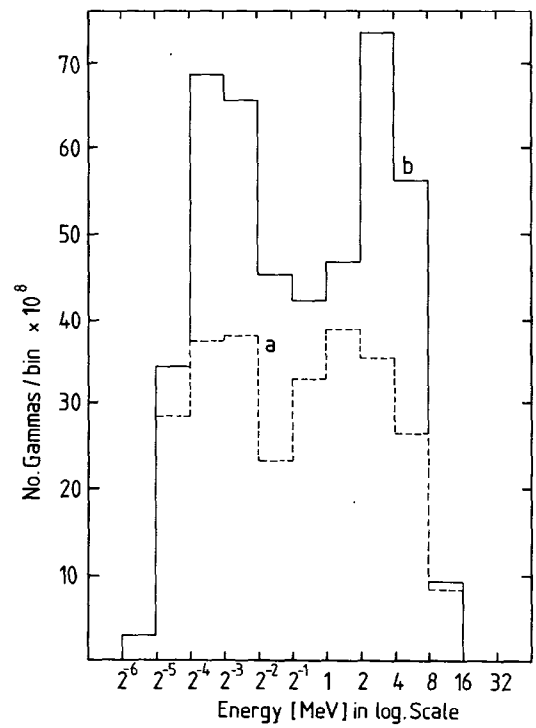

Fig. 3 Energy spectra of gammas incident on the samples under study for a) showers originating in neutral pion decay, and b) showers from prompt nuclear gammas. Histogrammes are normalised to 10 μAs of incoming proton beam.

Description of incoming proton beam	Energy incident on sample	
	Absolute in MeV (for 10 μamp sec beam)	As multiple of case with "standard" beam
a) "Standard" beam	$4.2 \cdot 10^{10}$	1.0
b) Beam 1.5 cm off-center	$7.0 \cdot 10^{10}$	1.5
Beam 3.0 cm off-center	$12.0 \cdot 10^{10}$	2.7
Beam 4.5 cm off-center	$76.0 \cdot 10^{10}$	16.4
c) Ring 1 $0 \leq r < 1.1$ cm	$2.4 \cdot 10^{10}$	0.5
Ring 2 $1.1 \leq r < 2.2$ cm	$2.9 \cdot 10^{10}$	0.6
Ring 3 $2.2 \leq r < 3.3$ cm	$3.4 \cdot 10^{10}$	0.7
Ring 4 $3.3 \leq r < 4.4$ cm	$14.1 \cdot 10^{10}$	3.0
Ring 5 $4.4 \leq r < 5.5$ cm	$22.2 \cdot 10^{10}$	4.8
Ring 6 $5.5 \leq r < 6.6$ cm	$21.1 \cdot 10^{10}$	4.5
Ring 7 $6.6 \leq r < 7.7$ cm	$122.0 \cdot 10^{10}$	26.0

Table III Energies incident on the sample in the form of γ showers for a) the original, "standard" beam, b) the same beam laterally displaced towards the sample by various amounts, and c) seven centered but ring-shaped beams. The results are given in absolute values (normalised to 10 μAs of protons on the lead target), and as a multiple of the energy incident on the sample in the "standard" case.

distributions concentrated near the axis of the target). The statistical errors are correspondingly large.

The results, given in Table III, show that beam mis-alignment and blow-up could account for gamma heat-up effects up to an order of magnitude greater than the values obtained with the "standard" beam.

ACKNOWLEGEMENTS

F. Atchison pointed out the possibility of linking the HET geometry package to the EGS code and showed me how it is done. His help in tracing and eliminating the ensuing bugs no doubt saved me a very great amount of time.

REFERENCES

1. R.L. Ford and W.R. Nelson, The EGS code system, SLAC Report No. 210 (June 1978).
2. M. Pepin, Monte-Carlo study of the energy deposition of a flux of spallation neutrons in various samples, Proceedings of ICANS-VI, page 629.
3. F. Atchison, W.E. Fischer and B. Sigg, Some aspects of the neutronics of the SIN source, Proceedings of ICANS-VI, page 441.
4. Engineering Compendium on Radiation Shielding, Springer Verlag 1968, Volume I, pages 167 and ff.
5. H. Messel and D.F. Crawford, Electron-photon Shower Distribution Function, Pergamon Press 1970.

Proceedings of International Collaboration on Advanced Neutron Sources (ICANS-VII), 1983 September 13-16
Atomic Energy of Canada Limited, Report AECL-8488

SINQ BULK SHIELD ANALYSIS USING THE S_n -METHOD

by

v. Herrnberger, P. Stiller
Federal Institute for Reactor Research
5303 Wuerenlingen, Switzerland

SUMMARY

Two available high neutron energy cross section libraries for shield design were checked and corrected. Comments are given to the corrections and the errors found. Homogeneous iron and heterogeneous iron/concrete bulk shields were analysed by direct and adjoint S_n-method using these libraries. Some results were comparable to published data. Conclusions are drawn for the utility and accuracy achieved with these data libraries. This investigation was made for the project of a spallation source (SINQ) at the Swiss Institute for Nuclear Research (SIN).

1. INTRODUCTION

The design of a spallation source shield involves the same types of problems as for nuclear reactor shields - viz. designing the bulk shield, the beamholes and shutters, and the determination of sky- and groundshine. However, the energy range of the neutron and gamma radiation created by the spallation processes is much wider and the necessary cross-section data and models are less accurately known than for nuclear reactor shielding. An intercomparison of cross-sections (c.s.) and methods is useful in determining the effects of these uncertainties on the target quantities of interest, e.g. radiation damage, radiation heating and dose rates. For the bulk shield analysis of the SINQ we restricted ourselves to the established deterministic method of discrete ordinates using a version of ANISN in connection with two different high energy neutron c.s. libraries.

We proceeded in three steps:

a. Preparing the necessary group cross section libraries for the transport calculations.
b. Analysing a high energy neutron benchmark of a homogeneous iron shield with respect to equilibria spectra, relaxation length and build-up factors.
c. Analysing a heterogeneous bulk shield of iron and concrete and comparing the outer dose rates with rule of thumb results.

2. COMMENTS ON THE STATE OF THE HIGH ENERGY NEUTRON CROSS SECTION LIBRARIES

Two cross-section libraries which include the necessary neutron c.s. are available for use. The first, from the Oak Ridge National Laboratories, USA, will be refered to as HILO[1]. The other from the Los Alamos National Laboratory is termed LANL[2]. The main characteristics of the libraries are compared in Table 1. The LANL library is relatively old (1972) compared to HILO (1978) and it has been recommended, that it should be applied with caution[3]. It is neither adjusted to experiments nor based on the latest c.s. files. The energy resolution (number of groups) in the low-energy range is similar to that of HILO. In the high energy range HILO has a much better resolution. HILO may, therefore, be expected to be better suited for problems with strong spectrum variation in the high energy range, as is the case for an iron shield.

Table 1

Summary of the Characteristics of the HILO and LANL Libraries
(HE: high energy / LE: low energy range)

Characteristics	HILO	LANL
Coupled n & γ	yes	no γ
Number of n groups	HE: 31, LE: 35 } 66	HE: 11, LE: 30 } 41
n-energy range	HE: 14.9-400 MeV LE: 10^{-10}-14.9 "	HE: 17.-800 MeV LE: $1.39 \cdot 10^{-10}$-17.MeV
γ- energy range	10^{-2} - 14 MeV	-
Legendre expansion	HE: P_5 LE: P_3	P_3
Elastic scatter	Yes, except for Pb & W in HE	no in HE
Origin of data	HE: Intranuclear cascade/evaporation and optical model LE: VITAMIN-C from ENDF/B-IV	Intranuclear cascade/evaporation LE: ENDF/B-III
Adjusted to experiments	yes	no
References	(1) (5) (7)	(2) (5) (7)

Because of the obvious importance of the c.s. data in the calculations both libraries have been recently checked, corrected and compared directly to each other and to available measurements. The results were satisfactory with three exeptions:

LANL-library:

a. The c.s. of molybdenum in the energy range 17-20 MeV (group 11) seemed to be wrong, if compared to the neighbour groups. They were replaced by those generated by the NJOY-data-processing system[4] from ENDF/B-IV. To be consistent the corresponding values in the P_1-P_3 moments were generated and replaced too[5]. Table 2 compares the original LANL data with those from NJOY and ENDF/B-IV for the P_0-moment only.

b. The c.s. of lead is questionable above 100 MeV, if it is compared to measurements and HILO-c.s. data: This error was found by T. Armstrong too[6]. See Fig. 1.[7]. For lead the HILO c.s. is recommended for use instead of the LANL values.

HILO-library:

c. The HILO c.s. (except for Pb and W) are much too large above 100 MeV. This is due to an increase in the elastic c.s. obtained from optical model calculations, where global parameters were used[8]. Figure 2 shows the huge differences in comparison to the basic BNL-325 data for iron[5]. Therefore transport calculations for an iron bulk shield will generally give lower fluxes and dose rates with HILO c.s. than with LANL c.s., which don't contain elastic scattering in this energy range. (See table 1 and figure 2).

The influence of the c.s. differences on the calculated outer dose rates and the shield thickness is of major concern and can be examined by typical bulk shield benchmarks.

Table 2: Comparison of P_0-scattering transfer moments $\sigma_{11\to g'}$ for molybdenum [barn]

g'	LANL	NJOY/ENDF/B-IV
11	0.	1.61990
12	1.65616-4	2.83250-1
13	-1.48324-3	1.29320-2
14	-1.11616-3	1.44870-2
15	-5.31374-4	2.54750-2
16	-5.49201-4	4.28840-2
17	-2.01767-4	6.70790-2
18	5.80335-5	2.73350-1
19	-1.17007-4	2.17190-1
20	1.72217-4	2.57970-1
21	2.82994-6	2.97200-1
22	7.15650-4	3.39110-1
23	-5.24013-4	7.39910-1
24	5.60998-4	6.97120-1
25	1.36244-3	5.02510-1
26	-7.13660-4	2.85860-1
27	7.63087-5	2.00580-1
28	-2.94215-4	3.47000-2
29	-2.02188-5	3.96010-3
30	-1.68503-5	0.
31	-3.24634-5	0.
32	-7.98184-6	0.
33	2.70260-5	0.
$\sigma_{T,11}$	-0.0025	5.91547
$\sigma_{tot,11}$	1.3513	3.65390
$\sigma_{abs,11}$	1.353	-2.26157

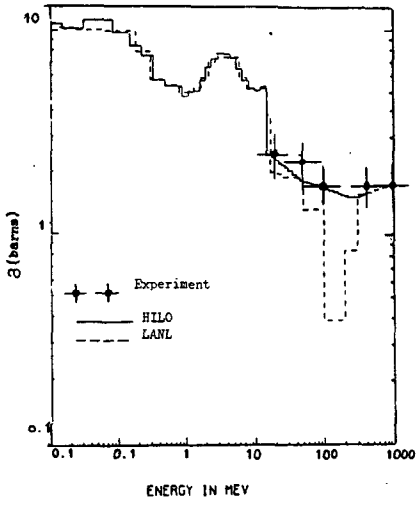

Fig. 1 Comparison of total/unelastic Pb c.s.

3. THE HIGH ENERGY NEUTRON BENCHMARK

A good tool for the analysis of the effect of cross section uncertainties on the dose rates is a so called "benchmark" configuration.

It has a simple definition of source material, composition and geometry to avoid unnecessary complexities of its analysis. Important characteristics of the real physical problem are, however, maintained so as to provide adequate physical insight. The benchmark, which was defined by EIR, SIN and KFA, has an isotropic spherical neutron source of 300 - 400 MeV of 10 cm diameter in an iron sphere of 10 m diameter. Spectra and dose rates were calculated by S_{16}/2.5 cm - mesh sizes. The source was normalized to 1 n/cm^3 sec.MeV. From the dose rates curves of Fig. 3 the relaxation lengths and the dose build-up factors were determined.

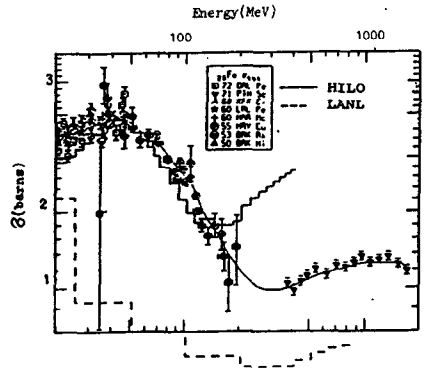

Fig. 2 Comparison of HILO-, LANL- and Barn Book data for total/nonelastic Fe c.s.

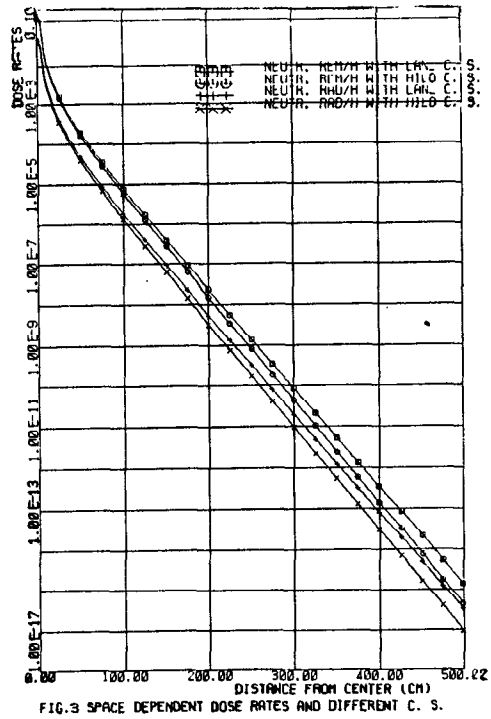

FIG.3 SPACE DEPENDENT DOSE RATES AND DIFFERENT C. S.

Equivalent and absorbed dose rates were limited to neutron energies above 15 MeV (Fig. 3), because they are the dominant contributions to the surface dose rate in a shield, which also includes concrete. From the spatial dose distribution relaxation lengths λ (Table 3) and dose build-up factors were derived (Fig. 4), which are useful for hand calculations.

The main conclusions are:

a. LANL c.s. show less attenuation than the HILO c.s., as it was concluded from the differences in their total c.s. (Fig. 1). The LANL c.s. give about a factor of 2 - 3 higher equivalent dose rates for penetration depths between 2 and 5 m.

b. Absorbed dose is a factor of 5 lower than the equivalent dose through the whole shield thickness. However the energy dependences of the dose conversion factors are different. Therefore the spectral changes are small and the absorbed dose can be easily estimated from the equivalent dose.

Table 3: Relaxation lengths λ for 300 - 400 MeV neutrons in iron

Reference	Penetration depth [cm]	λ [cm]
HILO	10 - 200	18.4
	200 - 300	17.8
	300 - 500	17.3
LANL	10 - 500	∿ 19.
(10)	100 -	17.

c. The relaxation length found with the HILO calculations is due to the space dependent build-up of scattered neutrons in the broad energy intervall of 100 MeV. No equilibrium above 60 MeV is reached after 2 m iron thickness. The LANL value of λ is constant and close to the value calculated in the HILO for the first 2 m. For greater penetration depth the HILO value gets smaller and approaches that of 17 cm[10].

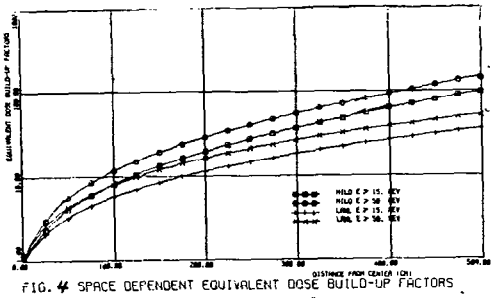

FIG. 4 SPACE DEPENDENT EQUIVALENT DOSE BUILD-UP FACTORS

Including the full spectrum above 15 MeV λ gets larger: 19.6 and 20.3 in the case of HILO and LANL respectively. The values are near to λ = 22 cm obtained by extrapolation back to 400 MeV the values quoted in reference 9.

d. The build-up factor increases with depth to a value of about 100. The build-up factor taken in conjunction with the relaxation length determines completely the dose rate greater penetrations depths. The HILO library gives 3 x higher values than LANL. The contribution of neutrons between 15 and 50 MeV to the dose rate is only about 30%.

The comparison of these results with Monte Carlo calculations performed by Atchison at SIN and with coupled Monte Carlo/S_n-calculations by Schaal et al. at KFA are underway. Finally the difference in the surface dose rates calculated by both libraries is relatively small, with respect to the deep penetration thickness of 5 m iron or 25 - 30 relaxtion lengths. The greater λ of LANL calculations is compensated to some extent by lower build up factor values. Relaxation lengths of the HILO calculation approaches published values. Therefore both libraries may be recommended for deep penetration problems in iron.

4. THE HETEROGENEOUS IRON/CONCRETE BULK SHIELD

Behind an iron shield thickness of 4 - 5 m the neutrons scattered below 15 MeV contribute more than 90% to the dose rate. This contribution may be eliminated by inclusion of concrete.

As a rule of thumb about 1/4 of the iron thickness is added from a rough balance between size and cost.

A first estimate for the bulk shield of the SINQ[12] indicated 3.9 m iron and 1 m of concrete would reduce the dose rate at the outer radius of 6 m to 0.25 mrem/h·mA (The inner radius of the iron shield is 1 m to contain the heavy water tank). Using the same method as in the benchmark analysis above this configurations has been examined for the importance of the source neutron energy with respect to the outer dose rate.

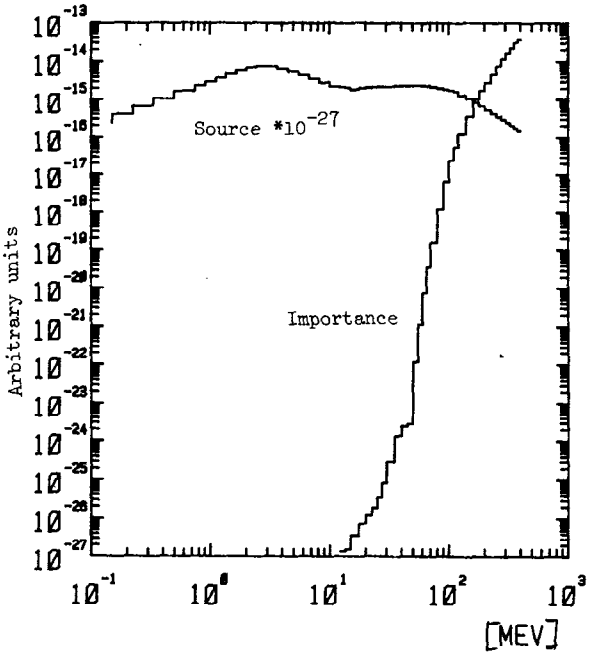

Fig. 5 Measured 90 source spectrum and its importance function for surface dose rate.

This can be done either by series of direct calculations with different monoenergetic sources or in a more economic way by one adjoint calculation with the dose rate response as source. The importance is defined as the dose rate per source neutron and unit lethargy. This together with the source spectrum is shown in Fig.5.

By folding both quantities, the outer dose rate can be calculated. The importance decreases with decreasing energy. Source neutrons below 50 MeV make only a very small contribution to the dose rate.

As the neutrons above 100 MeV are of primary importance direct calculations were performed with three different source energies to obtain more spectral information within the shield. The spectral shapes were all very similar below 100 MeV. Dose rates from the direct and the adjoint calculations are compared in Table 4. They agree within 25% or better, which shows the sufficient quality of the numerical approximation.

Table 4
Outer dose rate at a cast iron/normal concrete shield. Source diameter: 20 cm.

Calculation type	Source 1 n/cm^3·sec·MeV [MeV]	Dose rate [mrem/h]
adj. dir.	375 - 400	6.8 - 11*) 6.5 - 11
adj. dir.	250 - 275	1.8 - 11 1.8 - 11
adj. dir.	100 - 110	2.1 - 14 1.7 - 14

*) 10^{-11} = - 11

To check the bulk shield estimates direct and adjoint transport calculations were repeated with 90° source spectrum measured by Cierjacks et al.[13] and a total source strength [14] of

$$8.6 \cdot 10^{16} \text{ n/sec mA.}$$

The dose rates at the surface of the shield were calculated to

(adjoint): 0.226)
(direct): 0.234) mrem/h·mA

which are in excellent agreement. The rule of thumb estimate gave 3.9 m or 30 tons/m^2 iron. Our calculation assumed 4 m or 29 tons/m^2 cast iron (ρ = 7.15 to/m^3). Hence the iron shield thickness is overestimated by 1 relaxation length (λ = 17 cm) with respect to the more sophisticated calculations. However we compared pure iron to cast iron, where the C and Si content may have implications for the attenuation characteristics. The spatial dose distribution is shown in Fig. 6. The gamma dose contribution is neglegible.

Fig. 7 illustrates the efficient elimination of neutrons below 10 MeV with increasing concrete depth. The spectrum shifts to higher energies. Therefore the gradient of the dose rate is the steepest in the first 20 cm of concrete (Fig. 6).

For more than 50 cm concrete depth the gradient gets much less steep than in the iron: Therefore the effective concrete thickness is at least about 30 cm. If the remaining 70% are replaced by an equivalent thickness of 20 cm iron, the overall shield thickness is reduced by 10% to 4.5 m.

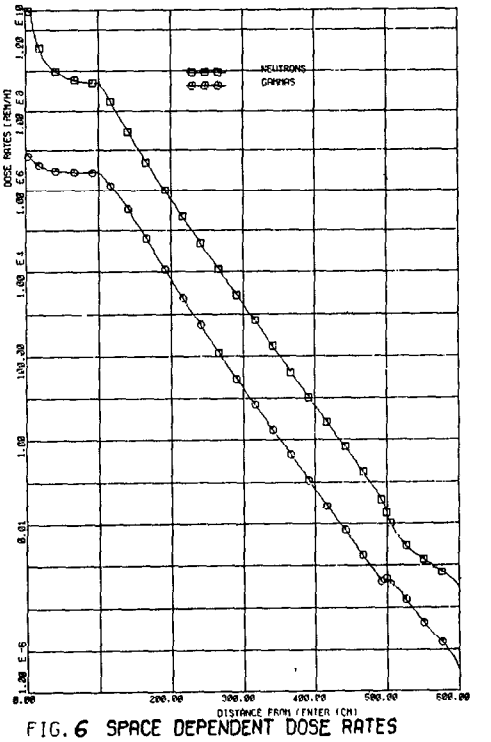

FIG. 6 SPACE DEPENDENT DOSE RATES

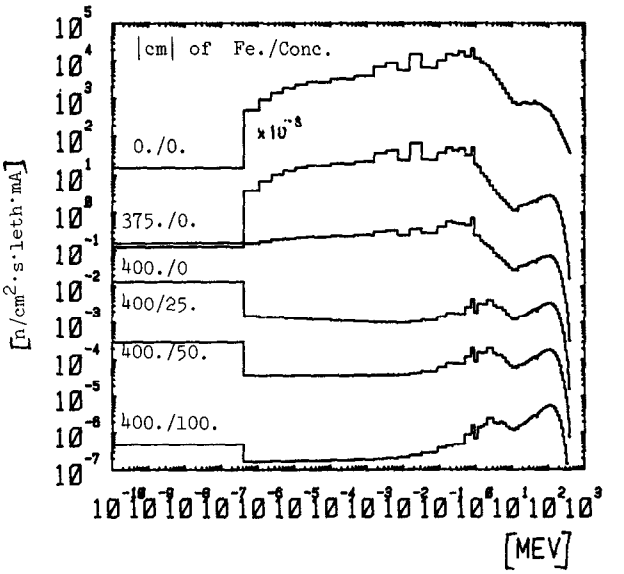

Fig. 7 Space dependent neutron spectra through the bulk shield

The main conclusions for the bulk shield design of the SINQ are:

a. Only neutrons above 100 MeV are important.

b. Adjoint calculation are economic and sufficiently precise.

c. The rule of thumb seems to overestimate the iron shield thickness by only one λ with respect to the more sophisticated transport calculations.

d. From the shielding point of view the thickness of an effective concrete layer at the surface of an bulk iron shield is 30 cm. The result should be relatively insensitive to the thickness of iron.

REFERENCE LIST

1. R.G. Alsmiller, Jr., J. Barish
Neutron-photon multigroup cross-section for neutron energies $\leq$400 MeV.
ORNL/TM-7818 June 1981, RSIC/DLC-87

2. D.G. Foster, Jr., D.R. Harris, and W.B. Wilson, "Medium Energy Nuclear Data Library", in "Applied Nuclear Data Research and Development Quarterly Progress Report, Jan. 1 through March 31, 1974", Los Alamos, LA-5655-PR, July 1974

3. W.B. Wilson, Private Communication 1982.

4. R.E. MacFarlane, R.M. Boicourt, "NJOY: A Neutron and Photon Cross Section Processing System", Trans. Am. Nucl. Soc. 22, 720, 1975

5. V. Herrnberger et al.,
Revision, check and documentation of LANL (HILO) cross-section library for neutron energies up to 800 (400) MeV
TM-22-83-2, 11.6.83 (TM-22-82-41, 11.11.82)

6. T. Armstrong, Private Communication 8.8.1983

7. V. Herrnberger et al.,
A direct comparison of the high energy neutron cross section libraries from LANL and ORNL.
TM-22-83-13, 26.1.83

8. R.G. Alsmiller, Private Communication 10.1.1983

9. SNQ, Realisierungsstudie zur Spallationsquelle. Teil II, pg. A-440/441, Mai 1981, KFA Jülich

10. T.A. Broome, The Attenuation of Neutrons in Concrete.
Rutherford Laboratory, SNS/TS/N1/81

11. V. Herrnberger, Analysis of the High Energy Neutron Shielding Iron Benchmark, EIR internal report, TM-22-82-54, 12.11.82

12. F. Atchison, Beam Shutter Problems in AF-SSP-123, May 1983

13. S. Cierjacks et al., Messung der absoluten Ausbeuten .. , 11.04.05 P 12 A KfK, Karlsruhe, Februar 1980.

14. V. Herrnberger et al., Some Estimates of the Fusion Radiation Damage Simulation by Spallation Neutrons. Proceedings of the 6th ICRS, Tokyo, Mai 1983.

Session D

Accelerator Components and Technology

Chairmen - J.H. Ormrod and C.D. Bowman

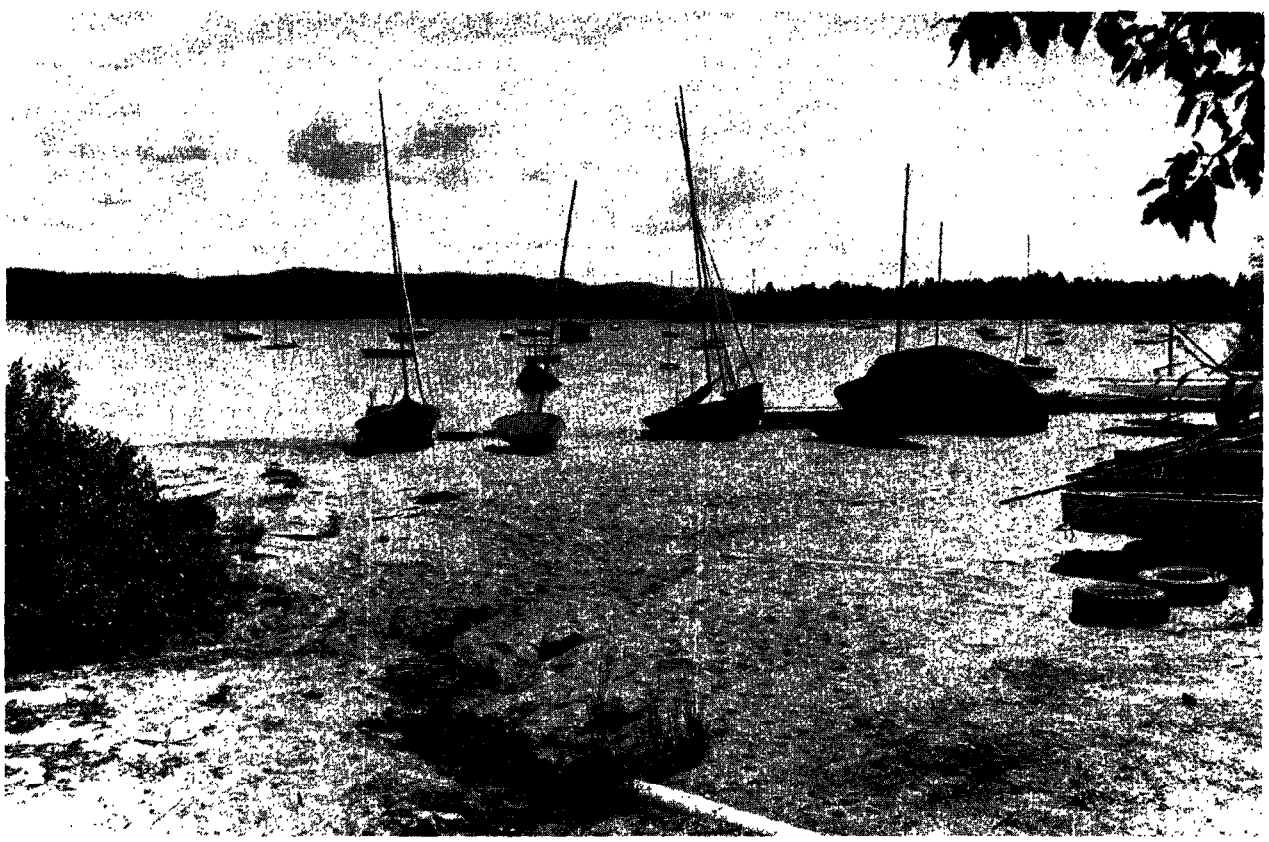

Proceedings of International Collaboration on Advanced Neutron Sources (ICANS-VII), 1983 September 13-16
Atomic Energy of Canada Limited, Report AECL-8488

Proton Storage Ring (PSR) Diagnostics and Control System*

Peter Clout
Los Alamos National Laboratory
AT-3, MS H808
Los Alamos, New Mexico 87545

Summary

When any new accelerator or storage ring is built that advances the state of the art, the diagnostic system becomes extremely important in tuning the facility to full specification. This paper will discuss the various diagnostic devices planned or under construction for the PSR and their connection into the control system.

The PSR Control System

The PSR is a major new facility at LAMPF. The beamline, Line D, provides a short, high-intensity burst of protons to the Weapons Neutron Research (WNR) spallation neutron source. The nature of most of the experiments at the neutron source is such that the neutron pulse length determines the energy resolution. As beam is taken directly from LAMPF, this length also determines the total, time-averaged neutron flux and hence the signal-to-noise ratio of the experiments. Thus the setting of the existing WNR facility is a compromise between resolution and signal strength. The PSR will remove this compromise by accumulating LAMPF beam for up to 750 μs, a complete LAMPF cycle, and then delivering the accumulated charge with a time structure suitable for the experiment. The overall gain is dependent on the particular experiment, but usually it will be over two orders of magnitude. Figure 1 shows the PSR in some detail.

The existing controls for Line D and WNR consist of a single computer with ∿950 channels connected to it. The new PSR control system[1-5] will take over these channels and will add ∿1500 new channels. However, the controls problem does not scale with channels. The PSR adds a new dimension of complexity to the facility, and the machine physicists and the operators need much more help than the existing controls system on WNR can give. WNR has been operational for some years, and the PSR is due to take first beam in April 1985.

Requirements

The PSR control system's overall requirements are

- the system must provide the operator with full and responsive facilities for bringing on-line all the equipment that makes up the PSR;
- the system must automatically monitor equipment for normal operation and report exceptions to the operator;
- the system must present information to the operator about the current state of the PSR, or any selected section, in an easily understood form;
- the system must maintain a log of significant events; and
- the system must be flexible enough to add new equipments and channels easily, as well as to add new programs for operator interaction.

These requirements specify two kinds of processing required of the computers in the system. The first kind is single-word input/output (I/O) processing associated with reading values from and writing them to the interfaces connecting the PSR's equipment to the control computers. This task also will include simple routine conversions and range checks, and the magnitude of the task scales with the amount of equipment and number of channels. The second kind of processing relates to the provision for operator interaction, and the magnitude of this task scales with the number of operators and their activity.

The choice of microprocessors for the first task and a computer system for the second task is a natural one. To simplify the software development, the microprocessors and the computer were chosen from a compatible range and are Digital Equipment Corporation (DEC) LSI 11/23's running RSX 11S and a VAX 11/750 running VAX/VMS. Thus the LSI 11/23's are memory-only systems that are down-line loaded from the VAX 11/750.

The third requirement calls for not only a connection to all the power supplies, etc., but also

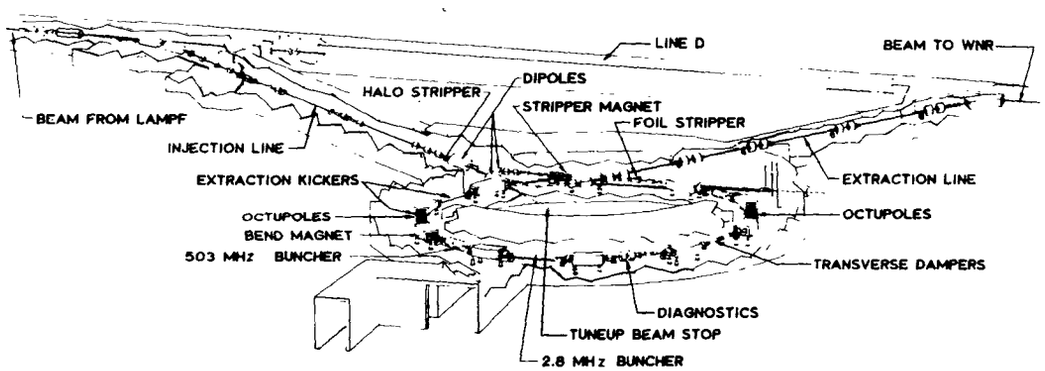

Fig. 1.
Proton storage ring schematic.

*Work supported by the US Department of Energy.

suitable, well-placed diagnostics in the beamlines and the storage ring that are connected into the control system. These diagnostics present extra challenges to the software designers because invariably they are more complex than power supplies, vacuum systems, etc. The second half of this paper will examine this aspect in more detail.

For many reasons, CAMAC was chosen as the interface system between the computers and microprocessors of the control system and the equipment of the PSR. This is also an excellent choice for the diagnostics because of the wide range of suitable CAMAC plug-ins available on the market. Nothing in the design of the software or hardware of the system precludes the use of other interfacing systems, for example, IEEE 488, where appropriate. A recent analysis of the software overhead, hardware costs, and performance showed that, given the communications needs of the system, a serial CAMAC system was the best choice for the communications between the VAX 11/750 and the LSI 11/23's.

Detailed Hardware Description

Figure 2 shows schematically the hardware of the system, which is located in several buildings. The computer-related items on the two operator consoles are six color-graphics displays with touch screens, twelve computer-assignable knobs, and a conventional computer terminal. The remainder of the console is taken up with oscilloscopes, TV monitors, and other dedicated instrumentation. Although the touch screens and color-graphics systems are commercial products interfaced to the VAX 11/750 Unibus, the programmable knob units are being constructed in-house and are interfaced through CAMAC modules. These devices make up the main hardware of the operator interface with the control system. The console consists of ten bays arranged to form two operator consoles and one single-bay alarm console.

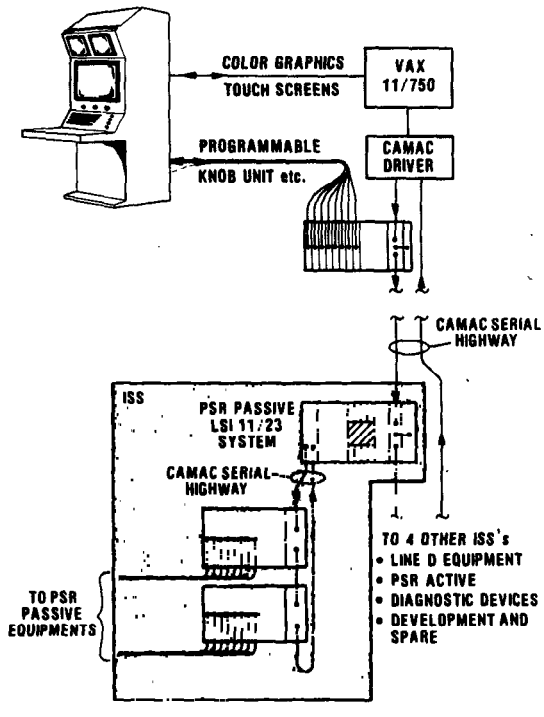

Fig. 2.
PSR Control system hardware.

The CAMAC driver on the VAX is a powerful interface with extensive direct-memory access (DMA) facilities, and it has a software driver under VMS, the VAX operating system. As can be seen in Fig. 2, the serial highway from the VAX 11/750 controls the CAMAC crates in which are mounted the LSI 11/23 microprocessors. One component of the LSI 11/23 system is a module that gives CAMAC access to the Q-bus of the LSI 11/23. It is this module and the DMA facilities of the CAMAC driver that allow the VAX 11/750 to keep databases up to date with minimum VAX software overhead and almost no LSI 11/23 software overhead. Both processors also are able to interrupt the other by CAMAC Look-at-Me (LAM) interrupts.

There are five such LSI 11/23's planned, including one for development, and each will have a serial highway of its own to connect its CAMAC crates. These crates hold the CAMAC plug-ins that connect to the equipment of the designated area for the LSI 11/23. A watchdog system in each LSI 11/23 crate will ensure that if a fault occurs in the LSI 11/23, the run permit for the PSR will be dropped within 1 s. The LSI 11/23 and its associated CAMAC system is termed an Instrumentation Sub-system (ISS); the "PSR Passive" ISS is the shaded area in Fig. 2.

Presently, there is one LSI 11/23 allocated to act as the "Diagnostics" ISS. However, some diagnostic devices are better placed on the CAMAC serial highway of the VAX and controlled directly by the VAX. Another diagnostic is in fact controlled by an 8085 microprocessor, and this communicates directly with the VAX like any ISS.

Data in the System

In the control system, data exist in one of four forms. Binary data are used to represent two-valued inputs and outputs, such as on or off. Analogue integer data represent I/O values that are covered by an integer in the range -32 000 to +32 000. Analogue real data are used for all other single-valued channels. Finally, analogue vector channels are used where an array of integers is required, for example, to specify a waveform. Each of these forms can be in a number of different types:

- Interface units--the value in primary SI units at the front panel of the CAMAC or IEEE 488 unit.
- Hardware units--the bit pattern read or written across the I/O bus.
- I/O units--hardware units modified to a legal PDP/11 and VAX/11 data type (the form in which data are stored in the run-time database).
- Engineering units--value in meaningful units to an operator; for example, pounds per square inch, amperes, degrees Celsius.
- Physics units--value converted to a higher level unit that in some cases is a more meaningful indication of the physics of the process; for example, tesla.
- Process units--high-level units that cannot directly translate to a single I/O channel, for example, tune.

Not shown on the diagram of the software, Fig. 3, is that the conversion between I/O units and engineering or physics units is carried out by a conversion module. This module has coded into it the various required algorithms and has access to the run-time database to obtain the parameters needed for each conversion.

Detailed Software Description

The overall software has been broken down into a number of modules, each having a well-defined function

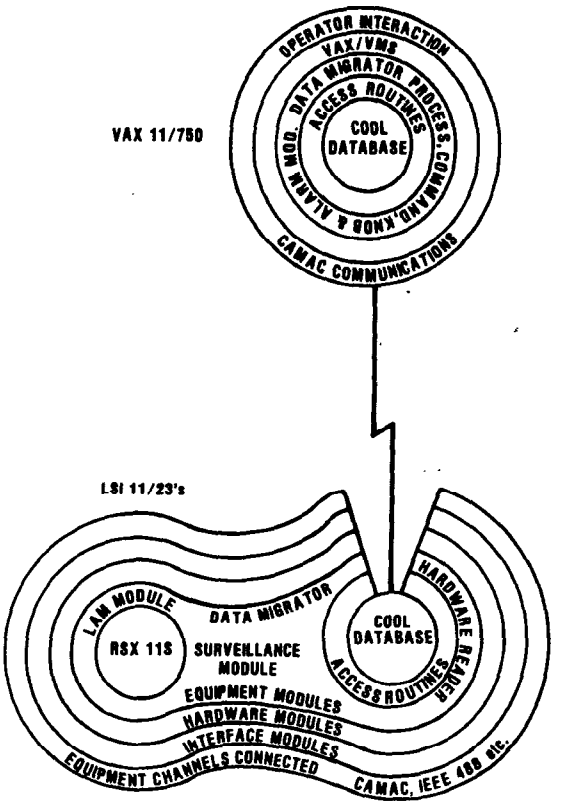

Fig. 3.
PSR control system software.

and a clear interface to the rest of the system. In fact, the modularity of the software reflects that of the hardware, allowing ease and flexibility in making changes. The modules are defined so that

- one or more modules make up a program or task;
- ideally, each module should be less than one month's work to code and test; and
- the intermodule interface is chosen to isolate future changes.

The first step was to isolate in a single database all information that relates to the individual equipment and its associated channels. The information in this database is held in an ASCII file established and maintained using a DEC product, DATATRIEVE. DATATRIEVE allows easy maintenance of a database and easy-to-use sorting of the data and report writing.

From this database is generated a machine efficient, run-time Control (COOL) database. It is this database that exists in main memory of the VAX 11/750 and the LSI 11/23's, and that which the programs reference. As an example, the address of a CAMAC plug-in will take several ASCII characters in separate fields in the ASCII database from which the run-time database generation program will produce packed binary addresses. The format of the packed address will be defined by the CAMAC coupler, so that it can be used directly at run-time. The run-time database generation also will produce any data tables required by individual programs or tasks. Thus the generation of a new database will at least mean relinking much of the system.

Figure 3 shows schematically the system's software layers. Generally, the LSI 11/23's act as intelligent I/O controllers to the VAX 11/750, enabling the VAX 11/750 to carry out operator-requested functions.

At the center of the VAX 11/750 software is the COOL database that is referenced through access routines to isolate the detailed structure of the database. On top of the access routines come all the other modules of the system.

The Command Module is responsible for the interaction with the operator to assign knobs or start specific operator-interaction programs. It is also responsible for keeping track of console resources. This is the module that comes up first at the console when the system is started.

The Knob Module is responsible for accepting knob assignments, taking knob input, and making the corresponding changes in the COOL database. It also maintains the one-line display on the knob unit.

The Alarm Module is responsible for maintaining the alarm screen and the log of significant events. Each channel, soft or hard, will have three sets of limits associated with it. Warning and alarm limits are self-explanatory, but the log-by-exception limits are less clear. These define a delta so that when an input channel is more than this delta from its last logged value, the new value is logged with the time and date. For control channels, these data are maximum range, normal range, and maximum rate of change.

The Data Migrator ensures that the varying data and the flags that indicate changes are kept current between the VAX 11/750 and the individual LSI 11/23's. For this the CAMAC system is used as described above.

Although all the above are single modules, the Process Modules are many and varied. It is here that the expansion takes place, and the system is tailored to the particular needs of the PSR. Selected Process Modules are started by the Command Module on the request of the operator. The running Process Modules have full access to the graphics devices on the console and the COOL database, which includes the last inputs from the touch screens. Thus they have full information on the state of of the PSR and full control of the PSR equipment. It is in the Process Modules that the flexibility of the system exists.

The next layer of the software is the operating system, VAX/VMS, through which goes all communication with the real world. For this purpose, VAX/VMS includes the I/O drivers added for CAMAC and the Lexidata color-graphics system.

Finally comes the Operator Interaction and CAMAC communications layer, which represents the main functions of the VAX 11/750.

There are two fundamental differences between the VAX 11/750 software layout and the LSI 11/23 software layout. The first is that the RSX 11S operating system is used only for task management and not for I/O management. This gives rise to the double-centered representation of the software. The second difference is that, as shown, the VAX 11/750 has direct access to the LSI 11/23 COOL database. This is a simplification in some respects, because the VAX 11/750 Data Migrator has control access to the Data Migrator in the LSI 11/23 to ensure that the LSI 11/23 takes action on the changed data.

Input channels are handled differently from output channels by the ISS. Two software modules, the LAM Module and the Hardware Reader, are responsible for ensuring that the COOL database input-channel data in the ISS are up-to-date. The LAM Module does this for I/O plug-ins that are interrupt or LAM based, whereas the Hardware Reader does the updates on a timed basis. All the other software modules access input data from the COOL database.

The Surveillance Module is responsible for checking input data against specified limits and reporting exceptions to the Alarm Module in the VAX 11/750 through the COOL database.

All changes to be made to equipment parameters must be made through an Equipment Module, which is a separate program for each set of equipment. This module can check input channels in the COOL database and apply the change in a manner specific to that equipment. This allows checks to be programmed into the system to ensure safe and correct operation. The Equipment Module also implements soft channels. These channels do not relate directly to a single hardware channel, but to two or more channels in a specific way. A simple example might be the on-off control of an equipment where a single soft on-off channel might be translated by the equipment module into a pulse output on one of two binary output channels.

All access to the I/O plug-ins by the LSI 11/23's is through the Hardware modules and the Interface Modules. These modules are designed to hide the differences between, for example, I/O plug-ins of similar function but different detailed design. Thus the code in an Equipment Module need only reflect the type of I/O, not the details of the actual I/O plug-in used. The Hardware Module also has no need to know the details of how the I/O bus is connected to the computer, but rather it issues calls in terms of the I/O bus (CAMAC, IEEE 488 etc.) to the Interface Module that localizes the code reflecting the actual connection of these buses. To illustrate: if a pair of wires bringing a 0- to 10-V signal to a CAMAC plug-in were to be moved to a similar IEEE 488 unit, all that would need changing would be the run-time database.

Diagnostics Interfacing for the PSR

Beam-Position-Monitor System

This system has already been described in some detail elsewhere.[6] It consists of a large number of detection units with an rf multiplexer system to select the unit of interest. The output of the multiplexer is then processed by rf signal-processing electronics that provides an X- and Y-position signal to two fast analogue-to-digital converters as well as a beam-present signal. Some further linearization of the signal is then required before the two X- and Y-positions of the centroid of the beam are obtained.

The detectors used consist of four pickup plates equispaced around and just inside the beam pipe. As such, they do not intercept the beam and so give a nondestructive read-out of the beam position.

To control the timing and sequencing of data acquisition and take account of the operating modes of the PSR, a microprocessor system has been implemented based on an Intel 8085. This has two control ports. One is an RS 232 port that allows an exerciser to operate the system locally for initial setup and trouble-shooting. The second port is a 16-bit parallel port connected to the VAX 11/750 computer. This second port is implemented with commercial 16-bit FIFO I/O CAMAC units. In addition, there are separate signals to allow the 8085 to interrupt the VAX to indicate that there is a message in the input FIFO and to allow the VAX to initialize the 8085. Thus, rather like the LSI-11/23's, the comunications are CAMAC based although they are message orientated. The 8085 therefore can be looked on as a single-purpose ISS as far as the hardware is concerned.

When it comes to the software, the Process Module that is called by the operator to handle the beam-position-monitor system communicates directly with the system through the CAMAC driver in the VAX. Messages have been defined that cause the 8085 to set the various delays and multiplexers and collect position data. When all the requested data are collected, the 8085 places a message in the input FIFO and sets a CAMAC LAM so that the Process Module in the VAX will be started, will read the data, and will present it to the operator.

The high speed of the ADC's allows the collection If a large amount of data from a single detector during one cycle of the PSR. However, the delays involved in resetting the multiplexers and the associated delay settings preclude taking data for more than one detector in a single cycle, and thus some of the commands to the system can take from a considerable fraction of a second to several seconds to complete, depending on the repetition rate of the PSR as well as on the actual command.

The current status of the beam-position-monitor system is that the final details of the timing and the VAX interface are being worked on, and it will then be ready for installation.

Beam-Profile Monitors - Harps

The harp units consist of an X-Y grid of wires that is placed in the beam-transport lines. The current on each wire is proportional to the integrated intensity of the beam along the wire. Thus, measuring the charge collected in one cycle of the PSR on all the wires gives an X- and Y-profile of the beam. The resolution of this profile depends on the spacing of the wires, and the sensitivity depends on the thickness of the wires and the noise in the electronics.

The harps will perturb the beam, especially in the injection line where they will cause the beam to be partially stripped from H^- to protons. For this reason, the harps are introduced into the beam only when a measurement is needed. In the storage ring itself, the high circulating charge precludes the use of harps.

The read-out of harp wires will be by specially constructed multiplexers. The input stage of the multiplexers has a sufficiently high impedance that over a cycle of the PSR it will integrate the accumulated charge. After a cycle of the PSR, the multiplexers will cycle through the 32 X and 32 Y wires and provide an output voltage and trigger pulse for an ADC to digitize the beam profile. This ADC will be operated by the diagnostics ISS and the results will be migrated to the VAX in the normal way. In this case, commands to insert a harp, make a measurement, adjust the gains of the ADC, etc, will be normal output or control channels to the ISS.

Loss Monitors

These monitors are designed to study the beam spill at various positions along the transport lines and storage ring. The actual monitors are mounted on the walls of the tunnel and consist of 1-pint cans filled with Nuclear Enterprises scintillator 235A viewed by an RCA 4552 phototube. The amplifier electronics has two outputs. The first allows the loss to be seen on an oscilloscope as a function of time and the second is connected to a gated analogue to digital converter so that the loss as a function of time can be recorded by the Control System. This will be done by the diagnostics ISS and the result then is migrated to the VAX in the normal way.

Activation Protection Monitors

These monitors are the same as the Loss Monitors but the electronics differ. The amplifiers have a longer time constant than the Loss Monitors and the output is compared with a preset trip level. If the level is exceeded, the output will activate a fast-protect system so as to either stop injection or

rapidly dump the stored beam, depending on the time and location of the trip. The fast-protect system is quite separate from the control system, although the control system is able to read out the inputs that caused a fast-protect trip. Each new cycle of LAMPF and the PSR will attempt to reset fast protect. The Activation Protection electronics provides a dc output that is proportional to the average loss expressed as a percentage of the trip level. The Activation Protection monitors are used to regulate the spill budget of the facility. As such, each monitor will be set to a trip level appropriate to its location.

Phosphor Screen

One insertable phosphor screen will be installed in the region downstream of the injection-line stripper magnet before the injection point. At this point, the beam is a neutral hydrogen atom beam. Read-out of the phosphor screen is by a television camera, and thus no read-out to the control system is planned. The screen will be inserted by command from the control system, however.

Energy Measurement

The energy acceptance range of the PSR, $\Delta p/p$, is less than about 0.1%, requiring stabilization of the energy of the beam from LAMPF. At 800 MeV, the protons and H^- ions are not fully relativistic, traveling at about 0.8 c; thus, a time-of-flight measurement can be used to determine the energy. This requires two pickups with a time measurement made as a bunch traverses between them. A flight path between the pickups of about 100 m is needed, assuming a 100-ps time resolution. Quite standard commercial CAMAC units are able to achieve this; therefore, the energy measurement in this case would be a simple input channel on the diagnostics ISS. Another approach being studied is to partially strip the beam with a laser. The stripped electrons have an energy of about 0.5 MeV and can be deflected out of the beam and energy analyzed with an electrostatic analyzer. This approach is somewhat more complex but it does not rely on the bunch structure of the beam.

The last approach for measuring the energy is to use the injection line and/or the storage ring as a magnetic spectrometer. In this case, existing beam-position-monitor detectors provide the read-out.

The present beam from LAMPF has no stringent requirement on absolute energy. On the short term, it has been observed to vary by 0.5 MeV from its nominal 800 MeV. This variation is within the acceptance of the PSR, but closer control is desirable. Long-term variations of up to 10 MeV have been seen, and clearly these are outside the acceptable limits. One solution to reduce the fluctuations is by controlling the phase of the last rf tank of LAMPF. This would be a feedback loop from the energy measurement through the diagnostics ISS.

Quadrupole Moment Detector

The quadrupole moment detector uses the same design of pickup as the beam-position-monitor system, but processes the signal in a different way to generate the X- and Y-widths of the beam, which then give the quadrupole moment. The pickup will be placed in a straight section of the ring rather than inside the quadrupoles as are the position-monitor pickups in the ring. The output voltage of the pickups will be read by a gated ADC attached to the CAMAC system of the diagnostics ISS. The result is a single-valued channel migrated to the VAX in the normal way.

Frequency Monitor

The frequency monitor in the ring consists of a simple pickup inside the pipe with a fast spectrum analyzer to analyze the signal detected. As the spectrum changes with time, a real-time spectrum analyzer is required. The signal can be observed simply with the CRT of the analyzer, but the system is much more versatile if the frequency spectrum is read into the control system. This will allow reading the spectrum as a function of time as well as further processing of the information. As with the beam-position-monitor system, such an instrument will be connected directly to the VAX.

Satellite Detector

The chopper's function is to prepare the time structure of the H^- beam to be accelerated by the linac so that it suits the particular operating mode of the WNR/PSR facility. Satellites are defined as bunches or parts of bunches appearing before or after the desired bunch. They could arise if the chopper does not deflect the beam sufficiently or if it is incorrectly phased. Thus, a satellite detection system is essential to adjust the chopper. The satellite detector consists of a foil that can be inserted into the beam in the transport line between the end of LAMPF and the storage ring. The flash of γ-rays is recorded with a fast detector as a function of time to obtain the time structure of the injected beam with respect to the chopper frequency. A time-to-digital converter in the ISS CAMAC will be used to store the information in the control system.

Ring Profile Monitor

For a ring profile monitor, two ideas are currently being discussed, but so far no actual design or construction has been started.

One idea is to have a gas curtain across the beam. The interaction of the protons with the gas will produce electrons in proportion to the proton density. These electrons then can be imaged, using suitable electrostatic or magnetic lenses, into a two-dimensional detector. The distortion of the image due to the potential well of the proton beam means that further processing is necessary to reconstruct the true profile.

The second idea is to pass a wire rapidly through the beam, collecting the current on the fly.

Both of these ideas need considerable development and they are unlikely to be available for some time.

Current Monitors

These will be ferrite toroids with the beam acting as the primary winding. The secondary winding will have about 100 turns, the output of which is then amplified and passed through a voltage-to-frequency converter. A gated scaler as part of the diagnostics ISS will then measure the beam charge for the gate period. The injection line current monitors will be an existing LAMPF design. The ring monitor cannot be highly inductive and so a wall current monitor will need to be developed. For the extraction line, the behavior of the LAMPF monitor needs to be investigated for peak currents of up to 46 A.

Conclusion

The basic design philosophy for the PSR control system has been presented, together with those aspects specific to the diagnostics of the PSR. Each of the

diagnostics currently being considered or implemented has been briefly described, together with the planned implementation of the interface to the control system where appropriate. The development of the diagnostics for the PSR is limited by resources but is driven by the need to understand the operation of the machine in order to reach full design current. First beam for the PSR is scheduled for April 1, 1985 with a tune-up period of about 18 months to full current.

Acknowledgments

This work reports the contributions of many other people to the PSR project. S. Bair, A. Conley, R. Ford, M. Fuka, and N. Greene all contributed significantly to the design and implementation of the control system. E. Higgins and F. Wells were responsible for the beam-position-monitor system and R. Hardekopf and A. Jason together are responsible for the remainder of the PSR diagnostics. I would also like to acknowledge the many helpful suggestions made at the proof stage by R. Hardekopf and A. Jason.

References

1. P. Clout, "Proton Storage Ring Instrumentation and Control System, Overall Philosophy," Los Alamos National Laboratory, Accelerator Technology Division, Group AT-3, PSR Technical Note 47 (February 1980).

2. P. Clout, "PSR Control Console, Conceptual Design Document," Los Alamos National Laboratory, Accelerator Technology Division, Group AT-3, PSR Technical Note 88 (June 1981).

3. P. Clout, "PSR Instrumentation and Control Data Base System," Los Alamos National Laboratory, Accelerator Technology Division, Group AT-3, PSR Technical Note 106 (May 1982).

4. P. Clout, "Proton Storage Ring Instrumentation and Control System, Signal Connection Manual," Los Alamos National Laboratory, Accelerator Technology Division, Group AT-3, PSR Technical Note 108 (November 1982).

5. P. Clout, S. Bair, A. Conley, R. Ford, M. Fuka, and N. Greene, "The Proton Storage Ring Control System," IEEE Trans. Nucl. Sci. 30, Vol. 4, p. 2305 (1983).

6. E. F. Higgins and F. D. Wells, "A Beam Position Monitor System for the Proton Storage Ring at LAMPF," IEEE Trans. Nucl. Sci. 28, Vol. 3, p. 2308, (1981).

Proceedings of International Collaboration on Advanced Neutron Sources (ICANS-VII), 1983 September 13-16
Atomic Energy of Canada Limited, Report AECL-8488

PSR Beam-Pulse Formation and Control*

R. A. Hardekopf
Los Alamos National Laboratory
Los Alamos, New Mexico 87545

Introduction

The Proton Storage Ring (PSR) is a major addition to the Weapons Neutron Research Facility (WNR) at LAMPF. It will act as a bunch compressor for the relatively long linac macropulses from LAMPF, tailoring them into short, intense pulses ideally suited for neutron-scattering research. This paper concentrates on the methods used to form these pulses before injection into the linac, to multiplex the PSR beam with other LAMPF users, and to synchronize the storage ring with pulse arrival time at injection and with the WNR mechanical neutron chopper at extraction.

WNR Pulse Characteristics

To understand the pulse structure required by the PSR, it is useful to begin with the operation of WNR in its present configuration. The LAMPF accelerator produces 800-MeV proton beams with a 750-μs-long macropulse structure at a 120-Hz repetition rate. Within the macropulses are many 200-MHz micropulses, each containing 3-5 x 10^8 protons. WNR operates in one of two modes, micropulse or microsecond.

For high-energy neutron work, single micropulses at a minimum spacing of 1 μs throughout an entire macropulse are selected. Thus, this is a low-intensity mode, wasting the capability of the LAMPF accelerator during that macropulse. Furthermore, because other LAMPF users must be satisfied, only one macropulse in ten can be diverted to WNR, resulting in a maximum 12-Hz overall rate. As Fig. 1 depicts graphically, this combination provides very narrow pulses but with low peak intensity and only about 0.25-μA average current.

For slow-neutron (thermal and epithermal) work, much longer pulses can be used, up to 10 μs in length, and these are taken at the end of each LAMPF macropulse. To maintain high average intensity, both the pulse width and the repetition rate must be higher than desired for many experiments. A typical 5-μs-long pulse, as depicted in Fig. 1, contains 1000 micropulses and gives an integrated intensity of 5 x 10^{11} protons/pulse for an average current of about 10 μA.

PSR Pulse Characteristics

The PSR will remove the limitations imposed by compromise between intensity and resolution, converting much more of the LAMPF beam to pulses suitable for neutron work without seriously impacting other LAMPF users. It operates both as a pulse compressor, squeezing the 750-μs-long LAMPF pulses into much shorter ones (270 ns), and as an accumulator and repetition-rate shifter, accepting pulses at the normal LAMPF rate of 120 Hz and ejecting them at 720 Hz. It accomplishes these operations with a significant gain in time-averaged beam intensity.

Figure 1 depicts graphically the gain in integrated protons/pulse for the two operating modes of PSR compared with the two WNR modes discussed earlier. The short bunch (SB) mode, shown on the left, will replace the existing WNR micropulse mode for high-energy neutron applications. In this mode, protons are accumulated in six equally spaced 1-ns bunches

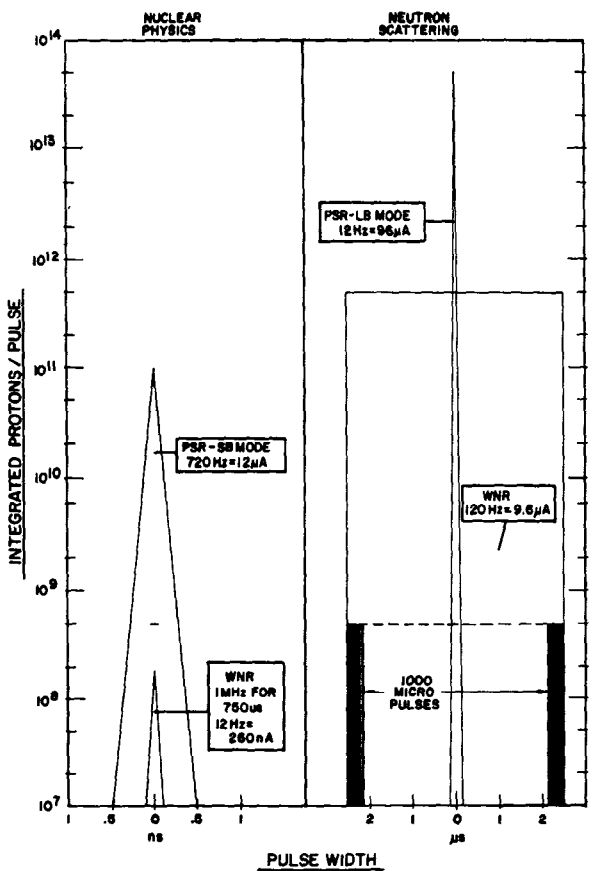

Fig. 1
Comparison of WNR and WNR/PSR pulse characteristics for the two modes of operation. On the left (nanosecond time scale) is the SB mode used for high-energy nuclear physics experiments and on the right (microsecond time scale) is the LB mode used for slow-neutron scattering experiments. The peaks are schematic representations of the important parameters for neutron production: integrated protons per pulse versus pulse width. Overall repetition rates and average beam currents for these operational modes are indicated in the labeled boxes.

during the last 108 μs of each LAMPF macropulse. The LAMPF beam is modified during this injection period by a chopper buncher system in the low-energy linac transport to form a sequence of pulses spaced at 60-ns intervals. The ring circulation period is synchronized with this incoming pulse train so that 300 micropulses are accumulated in each of the six ring bunches. The 1-ns bunch width is maintained during accumulation and storage by a 503-MHz buncher system in the ring. Individual bunch extraction takes place between LAMPF injection cycles at a constant 720-Hz rate. Each bunch contains 1 x 10^{11} protons, yielding an average current in the SB mode of ∿ 12 μA.

*Work supported by US Department of Energy.

The long-bunch (LB) mode, shown on the right in Fig. 1, replaces the WNR microsecond mode for low-energy neutron applications. Here the gains are even more dramatic as the bunch width is decreased to 270 ns, the protons/pulse is increased to 5 x 10^{13}, the repetition rate is lowered to 12 Hz, and the average current is increased to about 100 μA. For this PSR mode, one out of ten LAMPF macropulses are chopped at the injector into 270-ns-long segments at a 360-ns period, synchronous with the ring circulation period. The entire macropulse is accumulated by the PSR into a 270-ns-long pulse with a 46-A peak circulating current. The pulse width is maintained by a 2.8-MHz harmonic buncher in the ring, and the pulse is extracted about 100 μs after injection is complete.

PSR Control Summary

It is clear that PSR operation places new requirements on beam preparation and transport at LAMPF, including synchronization and timing aspects that are crucial to successful operation. Figure 2 is a schematic of the accelerator, storage ring, and WNR target area showing major components that affect PSR operation. Here I will mention only briefly these components, with more detailed descriptions of some of the active components to follow.

The injection scheme for PSR requires H^- beam produced in a new, intense H^- source at LAMPF. The beam is chopped and bunched in the low-energy transport line, accelerated to 800 MeV in the linac, kicked into Line D in the LAMPF switchyard, and bent into the PSR injection line where it is magnetically stripped to neutral atoms just before entering the ring orbit. A foil stripper in the first section fully strips the beam to protons. A PSR injection kicker magnet and foil stripper in the Line D by-pass allow multiplexed operation between PSR and direct LAMPF beam for WNR. Thus the old modes of WNR operation can be provided to experimentors while PSR operates at a low duty cycle for tune up and machine physics tests. After accumulation of the pulse in PSR is complete, the bunches are kicked out by two extraction kickers that perturb the orbit so that the pulse passes into the extraction septum magnet. The firing circuit for the extraction kicker allows synchronizing the target pulses with a WNR mechanical neutron chopper operating at 30000 rpm.

Low-Energy Beam Chopper

One of the keys to PSR operation is preparation of the pulse structure before the beam is accelerated so that incoming bunches are synchronized with the ring period and active bunchers in the ring. A traveling-wave beam chopper has been designed for the H^- injector transport line to provide pulses not only for the two PSR modes, but also for the existing WNR direct modes and other LAMPF users of H^- beam. The design is a careful balance between several factors that influence chopping efficiency and state-of-the-art pulsed electronics capability. To achieve clean micropulse selection with high intensity, a pulse rise time of <5 ns is required, and the chopper must be coupled with a subharmonic prebuncher

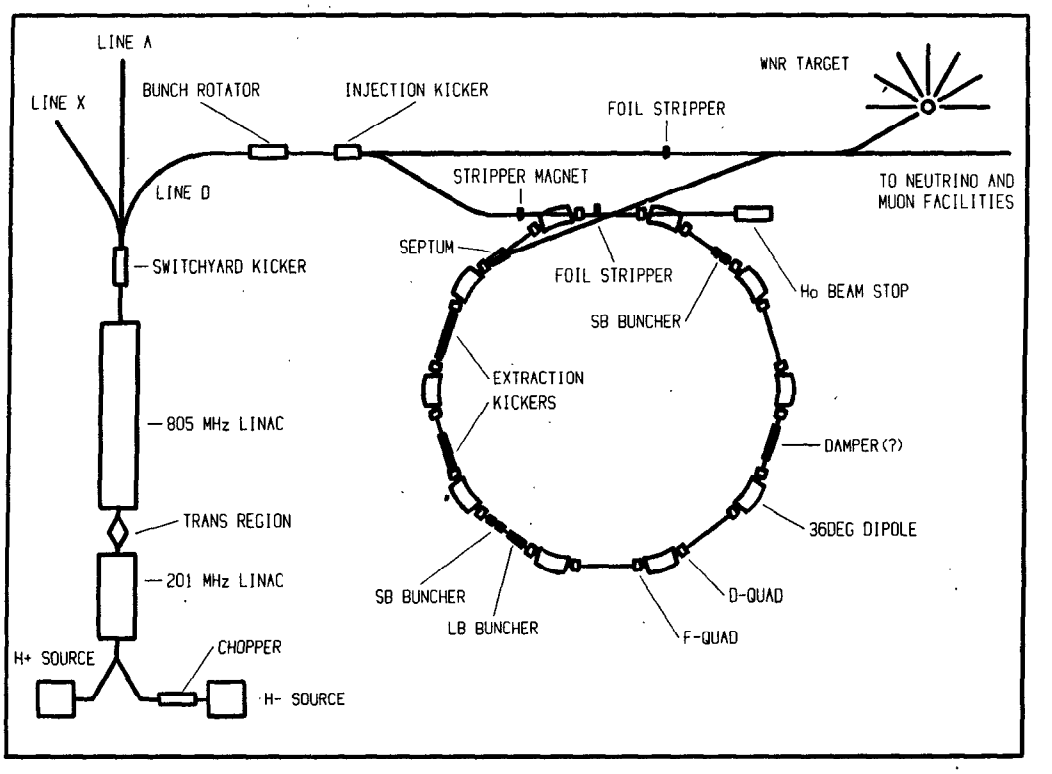

Fig. 2.
Overview of the LAMPF/WNR facility showing how the PSR interacts with other LAMPF beams. New equipment at LAMPF being built for the PSR includes the intense H^- source, the chopper, and the switchyard kicker magnet. The injection kicker allows beam to be multiplexed between PSR and WNR-direct during PSR tune-up. A tune-up beam dump under the PSR extraction line can receive up to 5-μA average beam.

to compress transmitted beam into the acceptance of LAMPF's 201-Mz bunching system. The beam optics of the newly designed H^- transport system dictated 20-mrad deflection as a minimum for complete separation of the chopped beam, taking into account the expected 2π cm·mrad emittance from the ion source. For this deflection angle and for pulses of less than 1 kV, a deflector ∿1-m long is required. The 750-keV ions travel at 1.2 cm/ns, taking about 80 ns to traverse this distance. Therefore, a traveling-wave principle must be used, with the deflecting pulse longitudinal velocity matched to the beam velocity.

Figure 3 shows the coax-plate deflecting structure that we have designed for the chopper. It uses flat plates on the structure's beam side soldered to and supported by short lengths of coaxial cable that connect adjacent plates across the back of the ground plane. The lengths of the cables are adjusted to match pulse propagation to beam velocity. The plate width and spacing thus can be chosen to give the best compromise between efficiency and coupling. Because the coaxial cable provides most of the path length, deleterious effects from mismatch at the corners are avoided, as well as coupling between turns on the structure's back. The shape of the plates and their spacing from the ground plane are adjusted empirically, providing 50-Ω impedance with minimum perturbation at the coaxial-cable transition. Individual plate replacement is accomplished easily without disturbing the rest of the structure.

The thickness of the plates influences plate-to-plate coupling; therefore, we used 0.4-mm-thick spring steel for desirable stiffness, with copper plating for better conductivity. We can thus maximize efficiency by making the plates 7.9 mm wide on a 10.2-mm center-to-center spacing for a 78% aspect ratio and a 94% calculated dc efficiency. The chopper's bandwidth with an assumed spacing of 2.8 cm between deflecting structures is ∿200 MHz.

Two power amplifiers (positive output and negative output) with the following characteristics are required for driving the deflection structures.

Rise and fall times	<5 ns
Voltage output into 50 Ω	>600 V
Pulse width	<15 ns to > 1 ms
Duty factor	10% maximum
Time jitter	<1 ns

An amplifier configuration using eight paralleled planar triodes has been developed to meet these requirements.

A paper[1] describing this development, including the POISSON calculation studies and laboratory measurements, was presented at the 1983 Particle Accelerator Conference in Santa Fe. Completion of the two power amplifiers, the deflecting structures, and the vacuum box is scheduled for completion in the spring of 1984.

Switchyard Kicker Magnet

The change from protons to H^- beam for PSR/WNR has necessitated a complete redesign of the LAMPF switchyard area, where beams are directed into the major experimental areas. The positive and negative beams, simultaneously accelerated by LAMPF, are first spatially separated by a vertical bending magnet. Low-intensity negative beam is directed into Line X (nuclear physics) while the chopped, high-intensity negative beam is bent into Line D (PSR/WNR) by a fast kicker magnet and a septum magnet.

In the SB mode of PSR operation, each macropulse is shared with other LAMPF H^- users; therefore it is desirable to minimize the kicker rise time, during which time no beam can be transmitted (the chopper

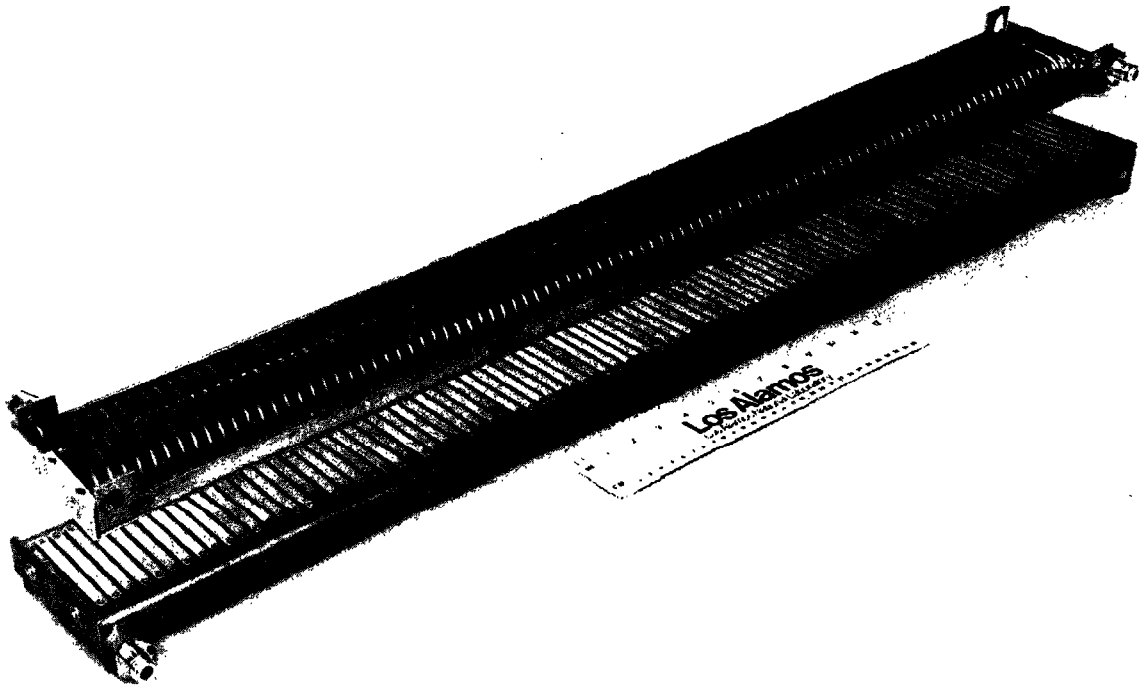

Fig. 3
Photograph of coax-plate traveling-wave deflection structure used in the beam chopper. This device, located in the H^- linac injection line, must product a variety of pulse patterns with <5-ns rise time for both WNR and PSR beams.

provides the gap required). A time of 40 μs was chosen as a reasonable compromise between beam efficiency and driver capability. The magnetic field must be established and settled to within 0.3% during this period.

The fast rise time, variable pulse length (100 to 1000 μs), high duty factor, and high degree of amplitude regulation required by the kicker magnet have determined the design. We have chosen a single-turn conductor, lumped-inductance ferrite magnet for the basic element, partly in order to use existing ferrite bricks and support equipment. However, to have the required current in the range of 2 kA where solid-state regulator circuits are applicable and at the same time keep the magnet inductance and peak voltage to low values, we chose to construct the kicker magnet in two identical sections with separate drivers. The mechanical construction of each section is a 1-m-long stack of ferrite blocks with a 5-cm-high by 10-cm-wide aperture. The unit has a calculated inductance of 3 μH, and both sections together yield a 1.2° kick for 2-kA current.

The modulator design uses a three-loop current driver to supply current to the kicker magnet. The circuit uses a high-current transistor amplifier in conjunction with a dual pulse forming network (PFN) to establish, sustain, and regulate the required current wave. The transistor amplifier/regulator and the dual PFN energy store share in the overall current development; the amplifier supplies 10-15% of the total while the PFNs supply the remainder. Active feedback is used in the amplifier/regulator to deripple the PFN contribution and provide a constant current to the kicker during the required pulse interval. Adjustment of the pulse length is achieved by a PFN line-length-changing circuit that couples appropriate sections of the PFN together through semiconductor switches. Kicker magnetic-field level is set by adjusting the PFN charge voltage and a reference voltage level supplied to the feedback circuit.

PSR Extraction Kicker

Once the injection cycle is complete, the extraction process can begin. Long-bunch extraction takes place soon after injection at the same rate. Short-bunch extraction is at six times the injection rate and takes place at equal intervals throughout the 8.3 ms between LAMPF cycles. The short-pulse mode of PSR operation requires the extraction of single 1-μs proton bunches from up to six bunches circulating at 60-ns intervals in the ring. This requires the kicker magnet to turn on and off quickly and to turn off cleanly so as not to disrupt the remaining proton bunches. These requirements led to the choice of a kicker "magnet" that is a carefully terminated strip transmission line. For transverse electromagnetic waves, the pulse must propagate through the electrodes in the direction opposite to the beam propagation so that the electric and magnetic forces deflect the beam in the same direction.

The pulse power supplies[2] provide ±45-kV pulses to the plates with rise times of 30 ns (SB mode, 720 Hz) or 50 ns (LB mode, 12-24 Hz). For the LB mode, the pulse must be sustained for 300 ns with a flat-top specification of ±1%. These power levels are obtained by resonant charging of an intermediate energy-store capacitor bank that is switched into a Blumlein PFN a few microseconds before extraction time. Discharge of the PFN into the load is through high-voltage thyratrons especially developed for this application.

Extraction pulses must be synchronized within 1 ns of the circulating beam and, for the SB mode, must provide complete flexibility in the extraction sequence. This will allow nonuniform loading of the bunches, extraction of alternate bunches to reduce instabilities, and possibly nonuniform extraction times for experimental purposes. For the LB mode, the circuit provides a 200-μs window during which time a fire signal synchronized with the WNR mechanical chopper can extract the pulse, subject to the 360-μs ring period.

Timing and Synchronization

The interaction with LAMPF is complicated by the many pulse-selection options required: 800-MeV or dual-energy LAMPF operation, PSR and/or WNR running in either of two basic modes with possible multiplexed operation, tune-up of PSR with reduced repetition rate and modified pulse structure, and simultaneous chopping of H^- beams for LAMPF experimenters when required. As indicated schematically in Fig. 4, the system is intimately connected with LAMPF timing, and close coordination is essential.

A computer-to-computer link is envisioned to establish the basic mode requests between PSR and LAMPF operations. The LAMPF master timer then provides the appropriate timing gates as indicated in Fig. 4. Independently of these "slow" gates, PSR establishes the fast chopping patterns through CAMAC commands to the chopper control and pattern generator (CCPG) located in the LAMPF injector area near the H^- chopper. These patterns are synchronized to the two basic PSR frequencies, 2.8 MHz and 16.7 MHz, which are transmitted by the frequency and synchronization generator (FSG) to the CCPG, to the PSR master synchronization system, and to a new low-frequency buncher (16.7 MHz) in the H^- injection line. The patterns are selected and multiplexed within the CCPG by the LAMPF master timer gates and applied to the amplifiers driving the fast H^- chopper.

There are three levels of control that provide the needed flexibility: first, the frequency of the indicated gate patterns on a macropulse basis (for example 12 Hz for LB mode, 120 Hz for SB mode); second, the length of the gates that establish the PSR or WNR portion of the macropulse; and third, the synchronized pattern structure produced by the CCPG. Selection at all three levels will be provided at the PSR control console within boundaries established by LAMPF.

Although the bunchers in the ring are synchronized to the same frequencies (or multiples) used in pulse selection, there is a phase uncertainty because of the different transit times for the beam pulses and rf signals. The PSR master synchronization system will establish the correct phase relationship by comparing the arrival time of beam in the PSR injection line with the rf signals in the buncher cavities. Synchronized operations, such as position monitors and beam extraction, will derive their signals from these phase-locked reference frequencies. Slower operations, such as turn on of the injection kicker magnet and start of orbit-bumper programming, will be gated by pulses from the PSR timing processor, which receives trigger pulses from the LAMPF master timer.

Figure 5 displays the relation between LAMPF beam gates for a few macropulses in the two basic PSR modes. The patterns indicated in the figure on a nanosecond time scale are developed by the chopper for the two modes during the enable time determined by the gates. Low-intensity H^- beam can be accelerated simultaneously with the high-intensity H^+ beam from LAMPF. Thus the SB mode, in which only one out of twelve micropulses is admitted, does not impact meson production in Area A. However, H^- beam in the LB mode will be nearly equal in intensity to the H^+ beam, and rf-cavity loading precludes simultaneous acceleration. Up to 10% of LAMPF production (12 out

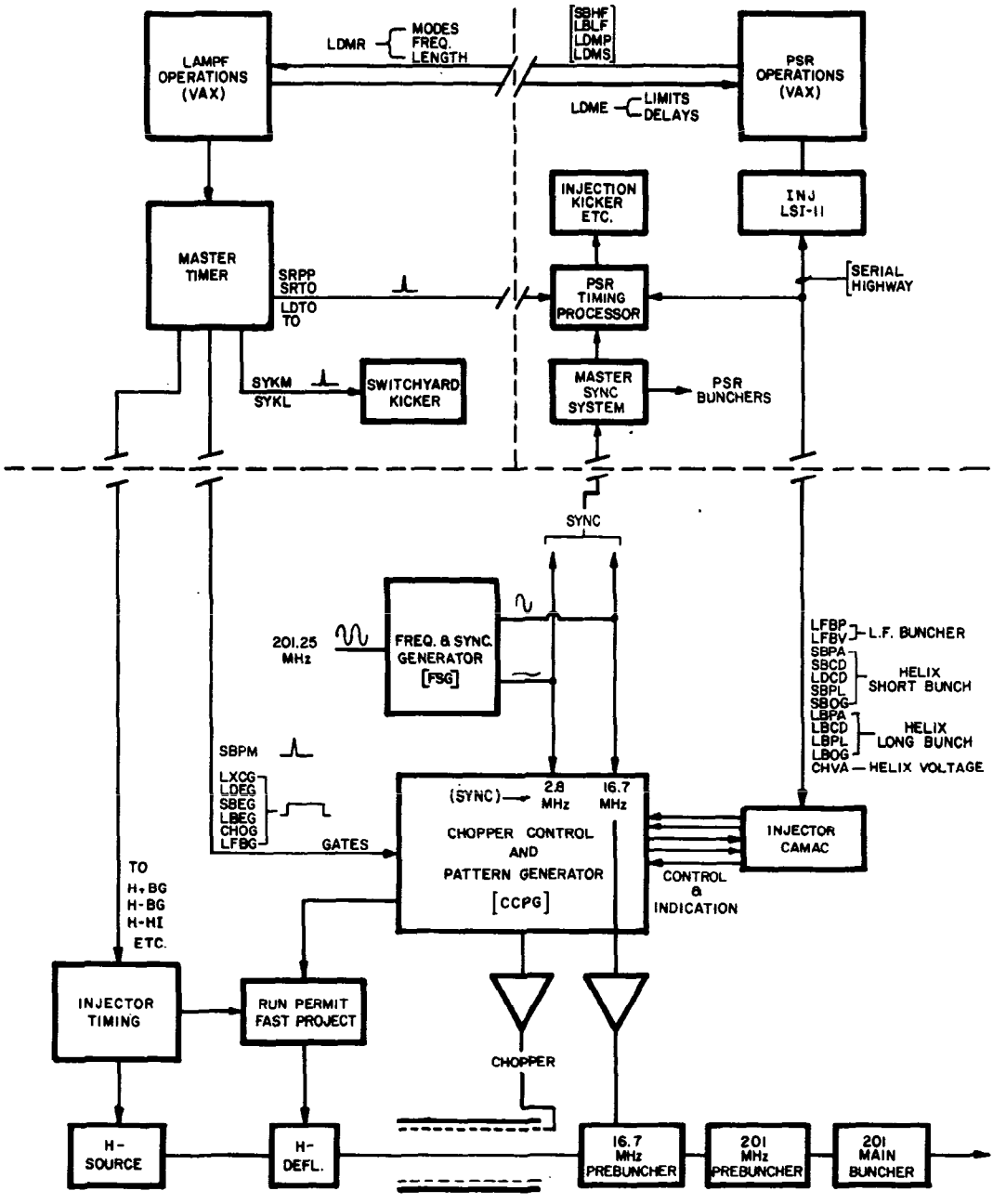

Fig. 4
Schematic diagram to illustrate timing and synchronization communication between PSR, LAMPF, and the H^- injector area. The focus of the control for PSR is the CCPG which generates pulse trains to drive the chopper amplifier. Although the patterns are controlled from PSR, overall timing gates must be provided by LAMPF through the master timer. The FSG derives the rf needed to synchronize chopper patterns with the PSR bunchers.

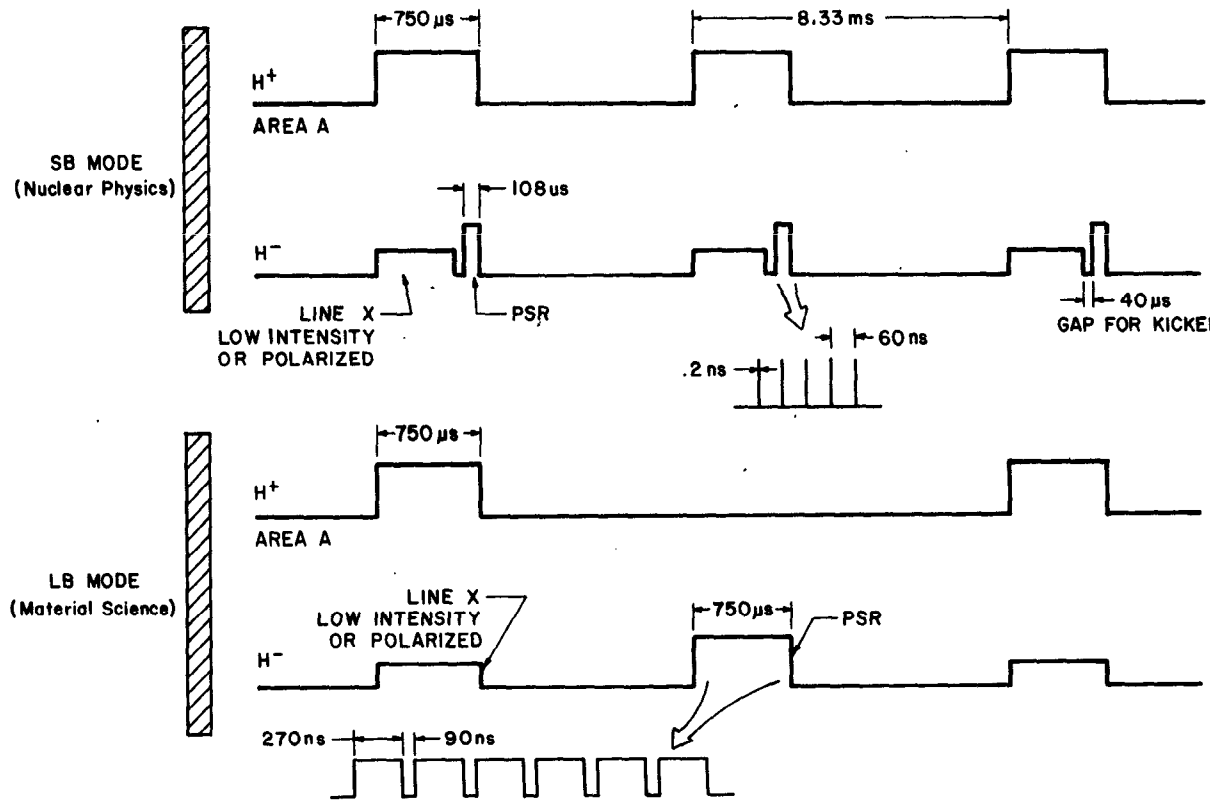

Fig. 5.
This diagram shows the interlacing of PSR beam with other LAMPF beams for the two basic modes of operation. Low intensity H^- beam, either from the H^- or polarized source, or chopped for the SB mode, can be accelerated simultaneously with the high-intensity H^+ beam. In the SB mode, PSR takes the last 108 μs of each (nominal) 750-μs-long macropulse. For the LB mode, the chopping pattern retains much of the intense H^- beam, requiring that H^+ macropulses be skipped during PSR injection. Many other combinations are possible, including multiplexed operation with different types of chopped beams.

of 120 Hz) will be made available for PSR in the LB mode.

Conclusion

Four different kinds of pulse structures are required for chopped beam destined for the PSR/WNR complex. Within these types, a great deal of flexibility must be provided so that WNR can operate in a stand-alone mode, or with PSR, or multiplexed during the PSR commissioning period. PSR beams must be fully synchronized with the ring bunchers and must be adjustable in frequency, length, and micropulse selection pattern for tune-up operations. The beam chopper, kicker magnets, and synchronization scheme necessary to achieve these aims have been described. Close coordination with the LAMPF linac rf and timing system will be required to successfully implement all of the beam requirements.

References

1. J. S. Lunsford and R. A. Hardekopf "Pulsed Beam Chopper for the PSR at LAMPF," IEEE Trans. on Nucl. Sci., NS-30, No. 4, 1983, p. 2830.

2. J. F. Power, W. C. Nunnally, K. R. Rust, J. S. Samuels, and G. Spalek, "Fast Extraction Modulators for the Los Alamos Proton Storage Ring," Proc. of 4th Int. Pulsed Power Conf., 1983, to be published.

Proceedings of International Collaboration on Advanced Neutron Sources (ICANS-VII), 1983 September 13-16
Atomic Energy of Canada Limited, Report AECL-8488

PRELIMINARY TESTS OF A SECOND HARMONIC RF SYSTEM FOR THE INTENSE PULSED NEUTRON SOURCE SYNCHROTRON*

J. Norem and F. Brandeberry
Argonne National Laboratory
Argonne, Illinois 60439

Summary

The Rapid Cycling Synchrotron (RCS) of the Intense Pulsed Neutron Source (IPNS) operating at Argonne National Laboratory is presently producing intensities of 2-2.5 x 10^{12} protons per pulse (ppp) with the addition of a new ion source.[1] This intensity is close to the space charge limit of the machine, estimated at ~3 x 10^{12} ppp, depending somewhat on the available aperture. With the present good performance in mind, accelerator improvements are being directed at 1) increasing beam intensities for neutron science, 2) lowering acceleration losses to minimize activation, and 3) gaining better control of the beam so that losses can be made to occur when and where they can be most easily controlled. We are now proposing a third cavity for the RF system which would provide control of the longitudinal bunch shape during the cycle which would permit raising the effective space charge limit of the accelerator and reducing losses by providing more RF voltage at maximum acceleration.[2]

This paper presents an outline of the expected benefits together with recent results obtained during low energy operation with one of the two existing cavities operating at the second harmonic ($2f_o$). These results show that bunch lengthening does occur as expected and switching from harmonic to fundamental operation during acceleration can be done with minimal losses.

Expected Benefits

Recent experimental evidence using the new high current ion source seems to confirm the existance of the space charge limit of the RCS near 3 x 10^{12} protons per pulse. Figure 1 shows losses during capture and acceleration as a function of injected current. These curves are typical, but do not indicate the dependence on machine parameters such as trim quadrupoles and injection conditions. Capture losses rise when the injected beam approaches 3 x 10^{12} (equivalent to 14.4 μA) and these losses are too large to permit operation. As neutron users desire high intensities, we have studied ways in which intensity improvements could be compatible with lower losses and improved reliability, both of which are critical in a machine where essential components can reach radiation levels of ~1 rem.

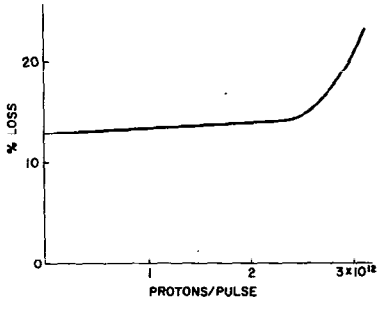

Fig. 1. Total beam losses between injection and extraction. The increase in losses at high intensity is primarily due to capture losses.

* Work supported by the U. S. Department of Energy.

Both theoretical and experimental[3,4,5] studies have shown that increasing the bunch length decreases the charge density and increases the maximum space charge limited intensity at injection. Since the sinusoidal acceleration field of the RCS requires that the synchrotron phase and longitudinal phase space acceptance of the accelerator change significantly during acceleration, acceleration losses during midcycle are also a problem that can be improved using RF. Present operation of the RCS is shown in Fig. 2. We have plotted beam energy (E), RF acceleration voltage (V), synchrotron phase (ϕ_s) and space charge tune shift ($\Delta\nu$) of the beam as a function of time in the acceleration cycle, for typical 500 MeV acceleration.

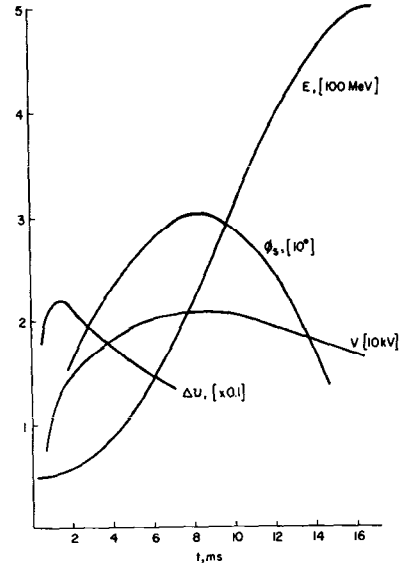

Fig. 2. Present operating conditions of the RCS.

The proposed system would utilize a third cavity capable of operating at the second harmonic ($2f_o$) for the first part of the acceleration cycle to stretch out the bunch length, and at the fundamental (f_o) for the remainder of the cycle to provide additional acceleration voltage. The voltage and frequency of the two components (f_o and $2f_o$) are plotted in Fig. 3. The phase space acceptance (A) as a function of accelerating voltage and time in the acceleration cycle for both the existing and proposed systems, together with the measured longitudinal emittance (ε_z) are shown in Fig. 4. This plot also shows how the present RF voltage program limits the acceleration efficiencies to roughly 85%.

It has been shown on the RCS (described below) and other accelerators[3,4,5] that the second harmonic RF component can increase the space charge limit of an accelerated bunch by 30-40% when used through the whole acceleration cycle. Because of the low peak RF voltage (21 kV) and the undesirably large losses of 1 x 10^{13} protons/s in this 30 Hz synchrotron, it was decided that the third cavity should also be capable of operating at the fundamental frequency to provide additional longitudinal acceptance when needed. This constraint made operation above 5.5 MHz inefficient,

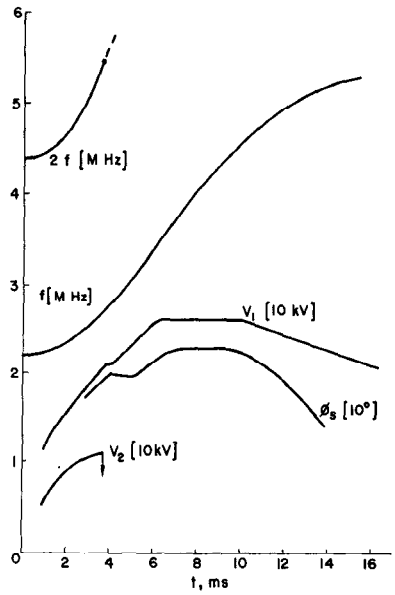

Fig. 3. Voltage and frequency programs for the two harmonics.

and slightly reduced the available gains in the space charge limit to

$$G = \frac{\Delta\nu_{max}}{\Delta\nu(t)}$$

where $\Delta\nu_{max}$ is the maximum space charge induced tune shift and $\Delta\nu(t)$ is the incoherent tune shift when the harmonic component is turned off, that is,

$$\Delta\nu(t) \propto \frac{Nf(\phi)f(x/a)f(y/b)}{\nu\gamma^3\beta^2 a(a+b)}$$

where N is the number of particles in the bunch, ν is the tune, γ and β are the relativistic energy and velocity factors, a and b are the half width and height, and $f(\phi)$, $f(x/a)$, and $f(y/b)$ are dependent on bunching and the beam distribution in the x and y planes. A detailed computer analysis was done of bunch shapes and areas using experimental data (Fig. 4) and a variety of RF voltage programs, assuming constant, and slowly varying, invarient emittances ε_x, ε_y and ε_z, with the result that the gain in intensity is essentially determined by $1/\gamma^2\beta$ at the instant the harmonic is shut off. If the harmonic is turned off too early, space charge effects will produce beam losses and if the additional RF voltage at the fundamental is provided too late, additional losses will be produced due to insufficient longitudinal acceptance. Optimum beam efficiency is obtained when beam losses due to space charge detuning and phase space are both minimized. This requires that the transition between second harmonic and fundamental must be made as quickly as possible at roughly 4 ms into the acceleration cycle.

Two other operating modes are possible. If space charge considerations become less important than losses, it would be possible to maintain the third cavity at the fundamental through the whole cycle. It is also possible to operate the third cavity at the second harmonic through the whole cycle, if problems occur with switching or if maintaining a long bunch through the acceleration cycle becomes important. At PETRA, it has been found that the addition of a higher harmonic cavity increases the threshold of the vertical instability that limits the beam current. This threshold has been increased by a factor of five

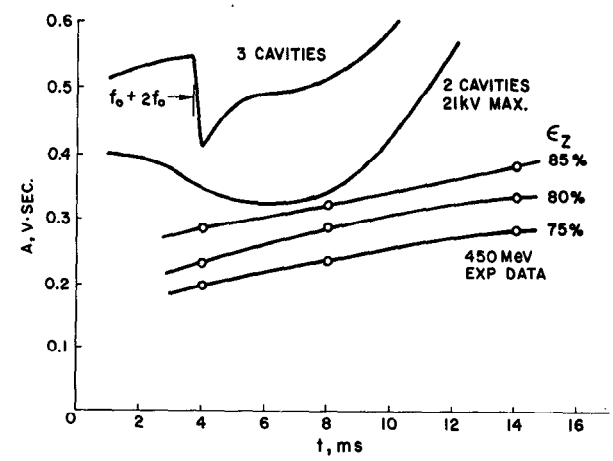

Fig. 4. Phase space acceptance and measured longitudinal emittance as a function of time, for 2 and 3 cavities.

when the bunch length increases by a comparable factor.[6] Operation of the proposed cavity above 5.5 MHz requires changes in the cavity design however, either a reduction in ferrite or gap capacitors accompanied by a change in the cavity bias system.

System Description

Existing System

The existing system is described in detail elsewhere[2,7] so only a short overview will be provided here. The present RF accelerating system for the RCS produces a total peak accelerating voltage of 21 kV across two single gap ferrite loaded cavities located 180° apart. The frequency swing of the fundamental operating mode is 2.2 to 5.3 MHz. The frequency program is generated from an integrated $\dot{B}$ signal using a third order polynomial expansion. Beam phase and position signals are added to correct the program. The low level electronics, located in the main control room, generate the low level drive and phase control signals required by the two cavities. Two separate amplifier systems, located near the accelerator, generate the cavity gap and bias potentials. A block diagram of the existing system is shown outside the dashed box in Fig. 5.

Proposed Addition

The third cavity system would have the capability of operating in three modes: 1) fundamental mode throughout the whole acceleration cycle, 2) second harmonic operation for the first 4 ms and fundamental operation for the remainder, and 3) second harmonic through the whole acceleration cycle. The system, in the first two operating modes, would provide additional voltage requirements at $\dot{B}$ maximum and, in the last two modes, would be capable of increasing the space charge limit of the RCS. In addition to the previously stated advantages, other considerations are: 1) all three cavities could be operated at lower levels decreasing component stresses if the full voltage increase is not required, and 2) failure of one of the systems would not significantly hinder the IPNS experimental program since the RCS could quickly resume operation with two acceleration cavities at reduced intensity, with repairs postponed to the next shutdown period. Space for the third cavity in the RCS ring can be provided by combining the trim quadrupole and octupole magnets.

For the third accelerating system, the cavity and amplifier chain would be identical to the ones presently in use, simplifying the design and construction. The construction can be accomplished without jeopardizing any existing accelerator components or significantly interrupting the anticipated IPNS operating schedule. Costs will be held down by using existing spare ferrite and cavity parts, as well as the existing reserve of the final stage dc power supply. Some additions and changes will be required in the low level controls. The main electronic design effort will center on the problems of switching from the harmonic to the fundamental mode and phase locking to the other cavities under the various conditions. A block diagram of the proposed system is shown in the upper portion of Fig. 5.

Experimental Results

Limited experiments on the feasibility of the planned approach have been done by modifying the existing system. In one experiment, the low level electronics of one of the cavities was modified by adding a diode frequency doubler to allow operation on the second harmonic. Another doubler was added to the output of the capacitive divider on the fundamental cavity permitting the measurement and control of cavity to cavity phase. An additional function generator was added to allow independent control of the voltage functions to each of the cavities. During initial tests, no attempt was made to revert the system operating on the second harmonic back to the fundamental. Also, since the high level RF equipment is limited to a maximum of 5.3 MHz, the harmonic system could not be operated beyond several milliseconds after beam capture.

Initial tests were conducted with the normal 450 MeV magnet program. Although stability of the beam was not optimized, the beam was captured into a visibly larger bunch. Since only one cavity was operating on the fundamental, only half of the required voltage was available and all of the beam was lost by $\dot{B}$ maximum. The peak energy was then lowered to 225 MeV, which decreased the maximum B and allowed beam to be accelerated and extracted at full energy with only a single cavity. Cavity to cavity phase problems were corrected with regulator accuracy $<\pm 10^{\circ}$. Under these conditions, the effects of fundamental and harmonic voltage, as well as cavity to cavity phase programming were studied. A typical set of conditions is shown in Fig. 6. A photograph showing the bunch formation under fundamental and harmonic operation and the transition to fundamental

ACCELERATING SYSTEM BLOCK DIAGRAM

EXISTING AND PROPOSED ADDITION

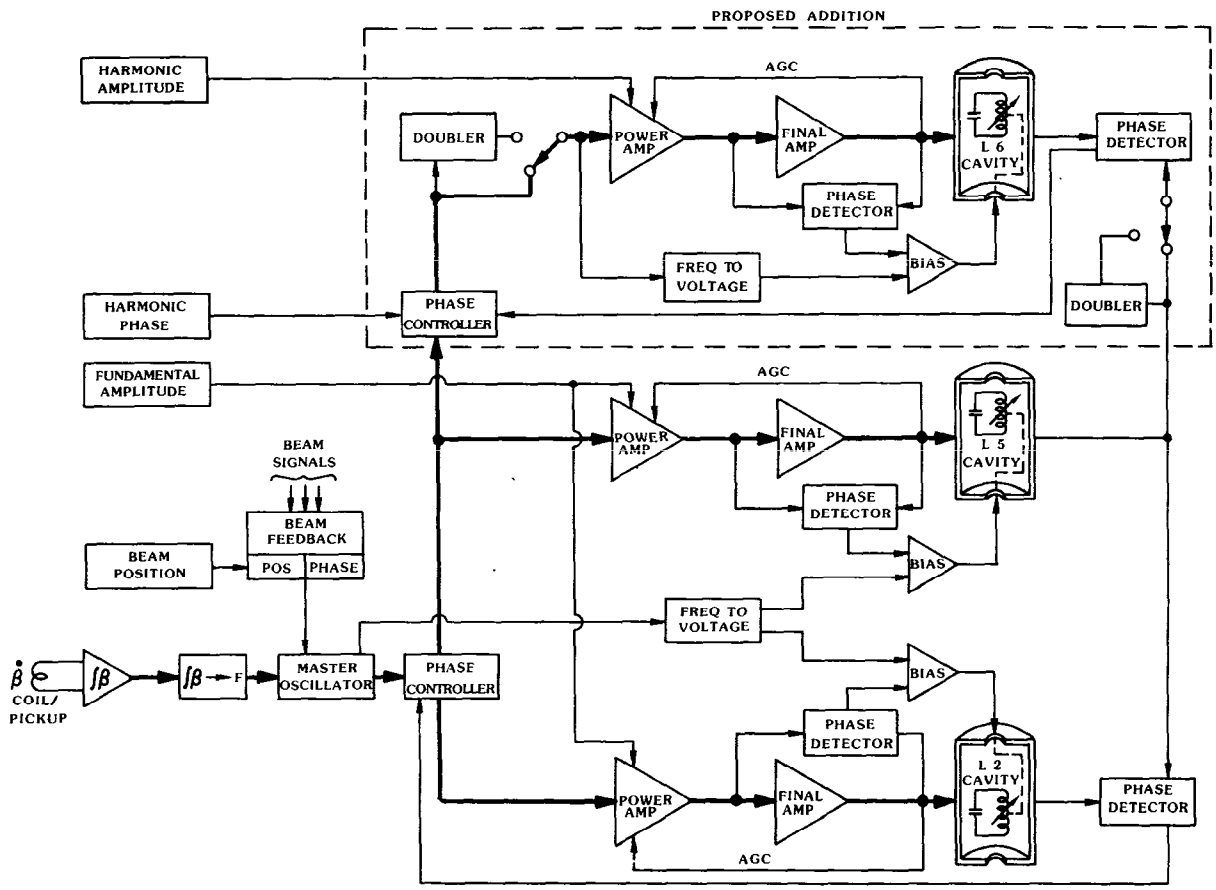

Fig. 5. Block diagram of the existing and proposed accelerating systems.

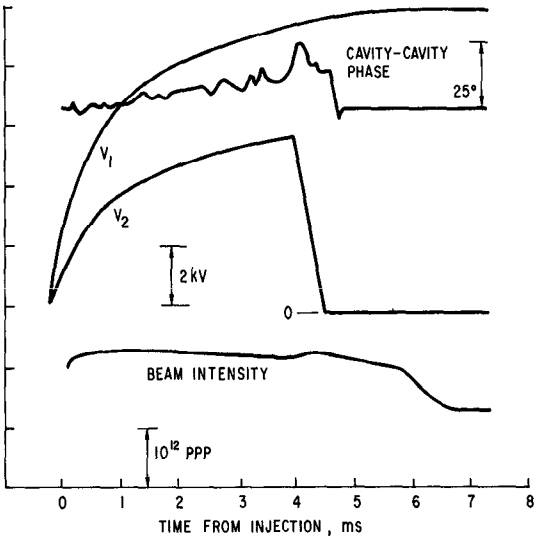

Fig. 6. Typical harmonic operating conditions.

is shown in Fig. 7. No increase in beam losses or instabilites was noted because of the harmonic voltage operation. In addition, no instabilities or bunch oscillations were encountered when the harmonic system was shut down rapidly ($\tau \sim 100$ μs ~ 1/2 synchrotron period).

Most recently, switching one RF cavity from the second harmonic to the fundamental was done during acceleration to 450 and 300 MeV using one cavity operating at the fundamental. During these tests, the voltage on the second harmonic cavity was reduced to zero in 0.5 ms, the cavity was off for ~0.7 ms while the cavity was switched to the fundamental and the voltage was then raised to ~10 kV in ~0.5 ms. Beam losses during this transition period were consistent with predictions based on the available longitudinal phase space (Fig. 4) and the small losses which did occur during switching seemed to be directly related to the RF voltage during this period as shown in Fig. 8. Additional effort will be required on the cavity to cavity phase and beam phase servo systems.

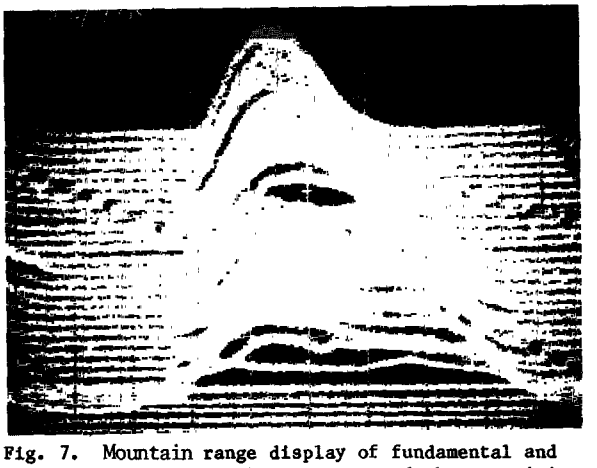

Fig. 7. Mountain range display of fundamental and harmonic bunch structure and the transition to the fundamental.
Horizontal scale - 50 ns/division.

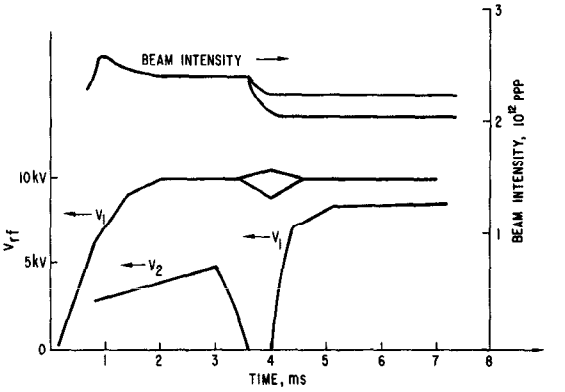

Fig. 8. Beam intensity during transition from harmonic to fundamental operation. The range of beam losses due to changes in the fundamental voltage is shown.

Conclusions

The limitations of inadequate RF voltage in the present accelerating system are clearly evident. A third cavity system has many advantages, even when operating on the fundamental frequency. Since the RCS is approaching the theoretical space charge limit, the added "bonus" of using the harmonic mode to increase this limit, should have a positive impact on the whole IPNS experimental program. Initial tests have shown that bunch lengths can be extended and the transition from harmonic to the fundamental acceleration seems to produce no adverse effects on the beam bunch or beam stability.

References

1. V. Stipp, A. DeWitt and J. Madsen, "A Brighter H^- Source for the Intense Pulsed Neutron Source Accelerator System," IEEE Trans. Nucl. Sci., Vol. NS-30, No. 4, p. 2743 (August 1983).

2. J. Norem, F. Brandeberry and A. Rauchas, "A Proposed Second Harmonic Acceleration System for the Intense Pulsed Neutron Source Rapid Cycling Synchrotron," IEEE Trans. Nucl. Sci., Vol. NS-30, No. 4, p. 3490 (August 1983).

3. T. Bertuccio, et al., "Improvement in the RF Capture By Using Nonsinusoidal Accelerating Voltages," IEEE Trans. Nucl. Sci., Vol. NS-16, No. 3, p. 533 (1969).

4. E. G. Sandels, et al., "A 2nd RF System for Nimrod," IEEE Trans. Nucl. Sci., Vol. NS-20, p. 418 (1973).

5. J. P. Delahaye, "Shaping of Proton Distribution for Raising the Space-Charge of the CERN PS Booster," Proc. of 11th Inter. Conf. on High Energy Accel., Geneva, p. 299 (1980).

6. R. D. Kohaupt, "The Experimental Study of a High Harmonic RF System in PETRA," Desy Report M-83-07 (March 1983).

7. T. W. Hardek and F. E. Brandeberry, "Intense Pulsed Neutron Source (IPNS-I) Accelerator RF System," IEEE Trans. Nucl. Sci., Vol. NS-26, No. 3, p. 3021 (June 1979).

Proceedings of International Collaboration on Advanced Neutron Sources (ICANS-VII), 1983 September 13-16
Atomic Energy of Canada Limited, Report AECL-8488

INTENSE PULSED NEUTRON SOURCE ACCELERATOR STATUS*

C. W. Potts, F. R. Brumwell and V. F. Stipp
Argonne National Laboratory
Argonne, Illinois 60439

Introduction

The Intense Pulsed Neutron Source (IPNS) facility has been in operation since November 1, 1981. From that date through August 1, 1983, the accelerator system was scheduled for 7191 hours of operation. During this period, 627 million pulses totaling about 1.1×10^{21} protons were delivered to the spallation target. The accelerator has exceeded goals set in 1981 by averaging 8.65 μA over this two year period. This average beam current, while modest by the standards of proposed machines, makes the IPNS synchrotron (Rapid Cycling Synchrotron [RCS]) the highest intensity proton synchrotron in the world today. Table I, Figs. 1 and 2 provide more detailed data on accelerator operation. Weekly average currents of 12 μA have been achieved along with peaks of 13.9 μA. A great deal has been learned about the required operating constraints during high beam current operation. It should be possible to increase the average beam current during this next year to 12 μA while observing these restraints. Improvement plans have been formulated to increase the beam current to 16 μA over the next three years.

Operating Summary - General

The original IPNS accelerator system has been previously described in detail elsewhere.[1,2] Extensive modifications[3] to the base system were made in 1980 and 1981. As Fig. 1 implies, with these modifications in place, it was a reasonably straightforward activity to get the accelerator currents up to the 8 μA short-term goal. The H^- ion source in operation at that time could deliver a charge of only 8×10^{12} ions 30 times per second. When the various transport and acceleration efficiencies were considered, a time average of only 10.0 μA of 50 MeV H^- ions could routinely be delivered to the synchrotron for acceleration to full energy. This was, in a way, fortunate since it encouraged us to make the beam handling more efficient and put a greater premium on reliability. We were able to limit average beam losses to only about 4×10^{11} protons/pulse and maintained a combined acceleration and extraction efficiency of about 85% in the synchrotron. The residual radiation level in the synchrotron tunnel stayed reasonably low, with only 4 locations reading greater than 300 mrem after a 4 day shutdown. In fact, maintenance personnel were exposed to a total of only 7.55 man-rem of radiation in 1982.

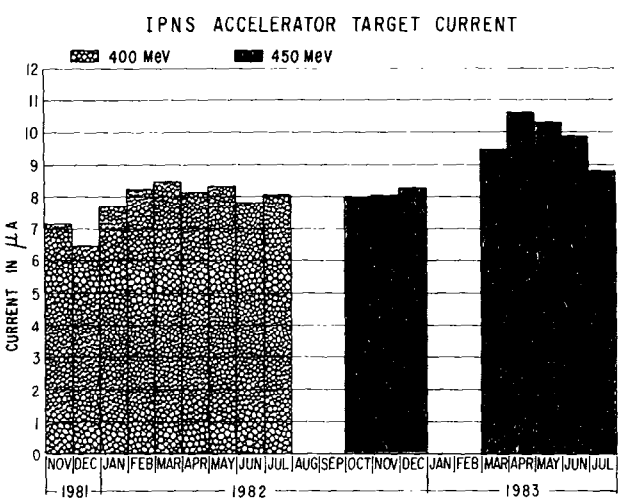

Fig. 1. IPNS Accelerator average target current.

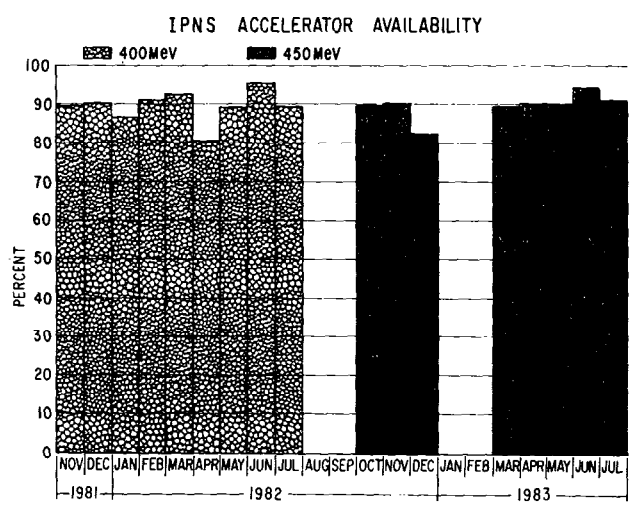

Fig. 2. IPNS accelerator availability since turn-on.

Table I.

Accelerator Operating Summary

	Nov. 1981-July 1982	Oct. 1982-July 1983
Proton beam energy	400 MeV	450 MeV
Average beam current	8.02 μA	9.21 μA
Operating efficiency	88.9%	90.2%
Scheduled operating time	3358 hours	3833 hours
Available operating time	2985 hours	3458 hours
Total pulses on target	2.94×10^8	3.33×10^8
Total protons on target	4.44×10^{20}	6.39×10^{20}

*Work supported by the U. S. Department of Energy.

In March of 1983, a more intense H^- ion source became operational and the beam current became limited by the losses that could be tolerated in the RCS tunnel. The 12 μA beam current noted above was achieved with loss of 5.5×10^{11} protons per pulse. We feel this is about the maximum long-term average beam loss that can be tolerated and still allow for hands-on maintenance. The RCS tunnel has a mean diameter of 50 feet, a width of 7.5 feet and a mean height of 8 feet, so little room is available for temporary shielding, special handling fixtures, etc. Future higher intensities can only be achieved by more efficient beam capture and acceleration.

Automatic devices are set to shutdown the beam when the losses exceed an average of 7.5×10^{11} for one second. When the machine is operating at 30 Hz at 5.5×10^{11} loss (normal conditions), a slight power supply current change or beam instability will easily cause a beam shutdown. While restart is simple, some neutrons are lost and an undesirable target thermal cycle has occurred. The IPNS accelerator is, therefore, a machine that has to be "tuned" very deliberately. This means that the trial and error tuning that usually produces the highest accelerator current is difficult if not impossible on this accelerator. Power supply instability due to phase slip with respect to the power line phase (when the accelerator is synchronized to a neutron chopper) and a pesky high energy longitudinal beam instability have been previously described.[3] Substantial improvement has been made in these two operating problems, but they are not totally cured. These two effects keep the accelerator system on the verge of a beam shutdown at all times when maximum proton currents are required.

The Preaccelerator and H^- Ion Source

The H^- ion source in use at start-up in 1981 used double charge exchange to produce the low energy H^- ion beam. This source was quite reliable but was limited to a current of 20 mA (on good days!). To reach planned future goals of the accelerator system, at least 40 mA of H^- was required. Earlier Argonne studies of a Penning H^- ion source[4] were somewhat discouraging due to unreliability and high hydrogen gas flow requirement. A magnetron H^- ion source developed at Fermi National Accelerator Laboratory (FNAL)[5] has worked reliably for several years. With the standard FNAL magnetron source, sufficient beam could be obtained but the pulse width was limited by excess cathode temperature to 30 μs at a 30 Hz rate. The high arc current required (120-150 A) tended to overheat the cathode. By incorporating a focusing groove in the source cathode, the required arc current decreased to 40 A. The focusing groove technique was discovered at Brookhaven National Laboratory (BNL).[6]

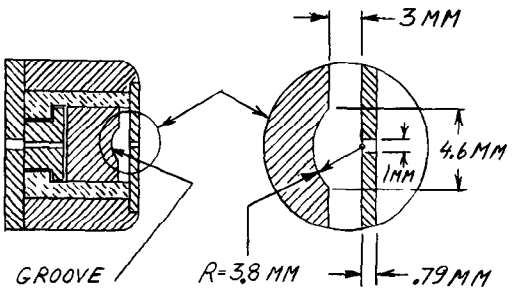

Fig. 3. Magnetron H^- ion source with grooved cathode.

The new IPNS source[7] can produce a 50 mA, 70 μs wide pulse at 30 Hz with the cathode temperature reaching only ~370°C. The grooved cathode also produces a more stable arc with less low frequency noise. The lower arc currents also require less hydrogen flow to maintain a discharge. A cross section of the magnetron with a groove in the cathode is show in Fig. 3.

In the IPNS preaccelerator an extended transport line is required to connect the source into the preaccelerator high voltage column. Space charge neutralization is required to prevent blowup in this transport line. A flow of ~0.2 atmospheric cm^3/min of dry nitrogen seems to be adequate. Good neutralization requires about 30 μs of mixing time. This early portion of the beam pulse is chopped out before it reaches the linac by a 750 kV traveling wave beam chopper.[8] This chopper is also used in the safety system to enable the source to continue to operate at constant temperature when operating requirements dictate no beam, a change in pulse width or a change in repetition rate.

The performance of the new ion source has been excellent. During a total running time of 3100 hours, in that period only one two-hour unscheduled source shutdown occurred and this resulted from an ancillary power supply problem. The source body was opened and inspected after a 5 month period. It took less than 2 man-days to clean the source up and get it operational again. We feel the lower temperature operation is responsible for the long operating life and lack of internal damage.

The ion source is capable of delivering up to 30 μA of average current to the RCS while only about 15 μA maximum is presently usable in the synchrotron. It is thus possible to run the preaccelerator voltage and linac RF levels lower to improve reliability since maximum beam transport efficiency from the preaccelerator to the RCS is not required. We have recently added feedback circuits to exactly regulate the amount of beam delivered to the synchrotron each pulse. This helps to control the number of excess beam loss trips since we operate so close to a beam loss trip limit most of the time.

Linac

The linac has now been running for two years with input RF power at 150% of the initial design level. Overall linac reliability has been excellent with breakdowns accounting for 1% of scheduled operating time. The life of the expensive RCA type 7835 final power amplifier tube is equal to that obtained during Zero Gradient Synchrotron (ZGS) operation when average RF power levels were about 3% of present levels. The dc blocking capacitors on the final power amplifier have been the most troublesome component, but when they are properly fabricated 200-300 million pulses can be expected. There has been no appreciable buildup of residual radiation in the linac components.

Rapid Cycling Synchrotron

Reliability and Cost Improvement

The extraction kicker magnet has 4 quarter turn coils each originally designed to be driven by and terminated in 7 Ω. The planned operating voltage of 68 kV proved difficult to handle because of cable breakdowns and corona discharge at connections. Judicious impedance mismatching has reduced the operating voltage to 49 kV without effecting the current pulse rise time or creating harmful reflections. Beam extraction efficiency remained at

essentially 100%. The driving point impedance is now 4.67 Ω and the terminating resistors are 6 Ω. The power supply presently contains four $14,000 CX1192 deuterium thyratrons. Originally estimated for a life of 10^8 pulses, the tube life has, in fact, averaged over 3 x 10^8 pulses with these modifications in place. Since 10^8 pulses is only 7 weeks of operation, this is a significant cost saving. The lower required voltage will allow future operation to be conducted with the cheaper CX1175 type tube.

Beam Intensity Improvement

In October of 1982, the beam energy was increased from 400 MeV to 450 MeV without loss of average current. This meant an increase in the neutron per proton ratio of about 18%. The new ion source became operational in March of 1983. Within 2 months, the weekly average current increased from 8 μA to almost 12 μA. Several changes in the synchrotron operating mode made this possible. A change in the injection working point of 0.03 increased the efficient capture intensity from 2.4 to 3.0 x 10^{12}. This required a trim quadrupole current of about 7 A. Sustaining this small tune shift beyond about 5 ms into the cycle actually made high energy operation more unstable.

The threshold of the high energy longitudinal instability that bothered the RCS from its first days was raised in early 1982 from about 1.3 x 10^{12} to 2.4 x 10^{12} protons/pulse by reducing reflections in the low level RF portion of the beam phase feedback system. The increased current from the new source made the problem reappear above 2.4 x 10^{12}. This problem has now been solved again, at least at present intensity, by artifical bunch dilution. Figure 4 shows traces of the high energy longitudinal beam profile with and without bunch dilution. The diluted beam signal (upper) clearly shows a bunch with decreased localized particle density. Following a technique employed at the Japanese National Laboratory for High Energy Physics (KEK)[9], we deliberately inject a controlled amount of noise into the RF master oscillator for about 2 ms starting shortly after $\dot{B}$ maximum. The frequency of this noise is fixed a few % above the beam synchrotron oscillation frequency. Counter phasing the two RF cavities at this noise frequency did not produce the same result as it did at KEK. New equipment is now being installed to allow the noise frequency to linearly track the changing synchrotron frequency in hopes of reducing the longitudinal problem even more.

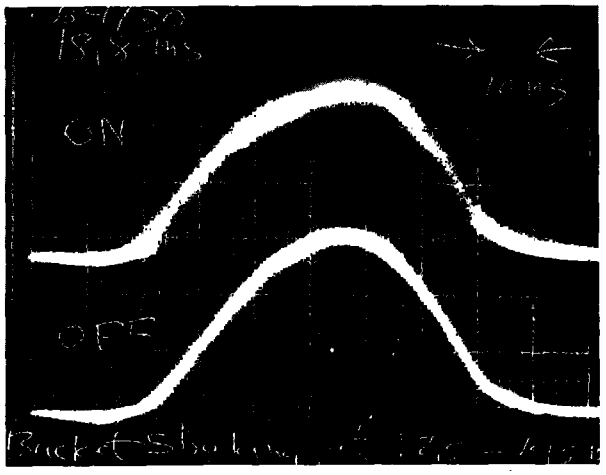

Fig. 4. IPNS beam bunch at 430 MeV.
Upper trace - artifically diluted by synchrotron noise. Lower trace - undiluted.

The higher currents available from the new ion source also made the problem of "beam noise" more acute. These beam generated electrical signals effect numerous low level signals but have been particularly troublesome in the ring magnet power supply where under certain circumstances beam noise causes a ring magnet current change which causes an orbit shift which, in turn, causes greater beam noise, etc. An adverse positive feedback loop thus exists which, over several cycles, will cause beam losses large enough to trip the machine. Extensive efforts at filtering have been at least partially successful. This noise effect was also diminished by installing a circuit to correct the RF capture frequency in proportion dc drifts in the $\dot{B}$ integrator that feeds the RF function generator. All efforts to "clean up" signals by trial and error filtering are severely handicapped in that radiation levels prevent "beam-on" access to troubled equipment.

H^- Stripping Foil

There has been no major effort employed to change the stripping foil material or methods of foil suspension this last year. The brighter ion source allows a pulse narrower in time. The narrow pulse, combined with changed operating modes on the injection bumper magnet have decreased the time that already stripped protons recirculate through the stripping foil. With these techniques operable, a typical well conditioned foil lasts about 1-1/2 weeks (20 million pulses). Techniques to "condition" the foil include a larger than normal injected beam size, exposure of as much of the foil as possible to beam, and a slow buildup of current over about 3 hours. Foils have lasted as long as 55 million pulses with up to 1.5 x 10^{20} ions stripped.

Operating Problems

Little has been done thus far to localize the damaging effects of lost beam. A protective carbon block has been installed just upstream of the kicker magnet vacuum chamber. This protective block has clearly reduced vacuum leak problems in this area. Installation of remotely movable carbon shield blocks has been contemplated in the S-4 straight section for some time. This installation has not been given nearly as much priority as increasing beam intensity.

We have known for some time that the injection bump magnets and some diagnostics show some signs of radiation damage. However, the first serious problem directly attributable to excessive lost beam occurred in late May when the machine was operating at 13 μA. The beam intensity suddenly dropped by a factor of two. After many hours of tests and observation, we determined that the aperture inside ring triplet magnet #6 was partially occluded. Residual radiation readings and brief crude viewing indicated a problem at a point where the vertical beta function reached is maximum. A temporary repair restored 10 μA capability. The accelerator ran a little over two months until August 1 with this restricted condition.

A more detailed inspection in August after a 3 week cooldown revealed that the beam had burned completely through one of the "hoops" of the RF liner. Figure 5 shows the damaged piece protruding slightly into the aperture. We think that when heated by the magnet and beam, the hoop droops further into the aperture. We plan to cut this out with some remotely operated shears during the present shutdown.

A similar damaged hoop was discovered at the entrance to ring singlet magnet #5. This was not at a point of maximum vertical beam size, so its origin is

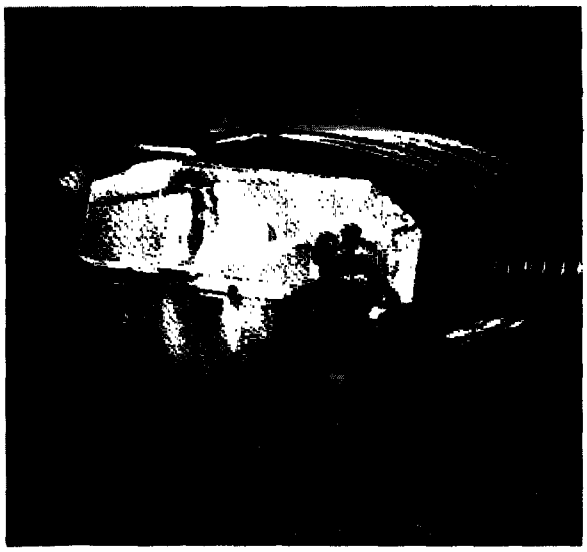

Fig. 5. Damaged liner of triplet magnet #6. End view with mirror reflected view from bottom.

more puzzling. Vertical orbit distortions may be playing a part in the problem. The alignment will be checked before operation resumes in late September. Problems like this make the operators long for vertical trim dipoles. Carbon scrapers will be installed at one or more points in the ring in an attempt to protect the liners from future problems.

Future Plans

Taking into account both beam current and beam energy changes, the IPNS accelerator is now producing about 80% more neutrons per pulse than it did at the beginning of 1982. We expect to increase the beam energy to 500 MeV in October, which will provide a further 18% increase. The RF liner problem in May forcefully reminded us that we are running a pretty "hot" machine. Despite this, we feel it is possible to increase the average (not peak) current to 16 μA within 3 years.

A plan to accomplish this and provide better long-term viability has been established. This plan includes the following:

1. Construct an additional spare ring magnet of each type.

2. Replace the aging ring magnet tuning choke with a higher inductance choke.

3. Improve beam loss monitoring and loss monitor data logging.

4. Replace single phase apparatus on linac transmitter with three phase.

5. Install 2 (perhaps 4) trim horizontal and vertical dipoles for injection orbit optimization.

6. Install a third RF transmitter with option to run this transmitter on the second harmonic for all or part of the acceleration cycle.

7. Install internal adjustable collimation to protect synchrotron apparatus from missteered beam.

As stated before, the key to successful higher current operation of this accelerator is beam loss control. The items above should help provide better orbit stability, tunable aperture optimization and reduction of the charge density within the aperture—all consistent with beam loss control.

References

1. A. V. Rauchas, F. R. Brumwell and G. J. Volk, "Commissioning of the Argonne Intense Pulsed Neutron Source (IPNS-I) Accelerator," IEEE Trans. Nucl. Sci., Vol. NS-26, No. 3, p. 3006 (June 1979).

2. J. M. Carpenter, T. H. Blewitt, D. L. Price and S. A. Werner, "Pulsed Spallation Neutron Source," Phys. Today, Vol. 32, No. 12, p. 42 (December 1979).

3. C. W. Potts, F. R. Brumwell, Y. Cho, A. V. Rauchas and G. J. Volk, "Status Report on the Rapid Cycling Synchrotron," IEEE Trans. Nucl. Sci., Vol. NS-28, No. 3, p. 2104 (June 1981).

4. D. R. Moffett and R. L. Barner, "An Intense H^- Source for the IPNS Rapid Cycling Synchrotron," IEEE Trans. Nucl. Sci., Vol. NS-28, No. 3, p. 2678 (June 1981).

5. C. W. Schmidt and C. D. Curtis, "A 50 mA Negative Hydrogen Ion Source," IEEE Trans. Nucl. Sci., Vol. NS-26, No. 3, p. 4120 (June 1979).

6. J. G. Alissi and Th. Sluyters, "Regular and Assymetric Negative Ion Magnetron Sources with Grooved Cathodes," Rev. Sci. Instr., Vol. 51, No. 12, p. 1630 (December 1980).

7. V. Stipp, A. DeWitt and J. Madsen, "A Brighter H^- Source for the Intense Pulsed Neutron Source Accelerator System," IEEE Trans. Nucl. Sci., Vol. NS-30, No. 4, p. 2743 (August 1983).

8. A. Rauchas and R. Zolecki, "Injected Beam Chopper System for the Intense Pulsed Neutron Source Accelerator System," IEEE Trans. Nucl. Sci., Vol. NS-30, No. 4, p. 2947 (August 1983).

9. Y. Mizumachi and K. Muto, "RF Phase Shake and Counterphasing at Phase Transition," IEEE Trans. Nucl. Sci., Vol. NS-28, No. 3, p. 2563 (June 1981).

10. J. Norem, F. Brandeberry and A. Rauchas, "A Proposed Second Harmonic Accelerator System for the Intense Pulsed Neutron Source Rapid Cycling Synchrotron," IEEE Trans. Nucl. Sci., Vol. NS-30, No. 4, p. 3490 (August 1983).

Proceedings of International Collaboration on Advanced Neutron Sources (ICANS-VII), 1983 September 13-16
Atomic Energy of Canada Limited, Report AECL-8488

PRESENT DESIGN OF THE LINAC OF THE SNQ PROJECT

J. Schelten and C. Zettler

Abteilung für Beschleuniger-Technologie des SNQ-Projektes der
Kernforschungsanlage Jülich GmbH,
D-5170 Jülich, West-Germany

The present concept of the linear accelerator for the spallation neutron source project is described. The need for two 100 MHz RFQ's and for a funneling section in front of a 200 MHz Alvarez structure and the usefulness of single cells with separate RF power supplies following the alvarez accelerator is discussed. The single cell concept asks for a sophisticated control of the amplitude, phase and timing of the RF power. Because of the large number of components a special handling of failures is required. The consequences of beam loading are considered.

Introduction

The linear accelerator concept of the SNQ project was further developed since 1982 in the KFA Jülich after the joint KfK/KFA study was completed in 1981[1]. The user community of the SNQ, which was steadily growing during the study of the SNQ project, was asking for more flexibility in particular for a variable end energy of the accelerated proton beam and for shorter pulses with higher currents. According to this development the new design of the linear accelerator was governed by the changed pulse structure with an average pulse current $\overline{I}_p$ = 200 mA, a pulse length of 250 µsec, and a repetition rate of 100 Hz, as well as by the variable end energy $E \geq 350$ MeV, and by a stage concept as described by G. Bauer in the SNQ status report at this conference.

It is the purpose of this paper to describe the new linear accelerator concept. This has to be done at a time when the basic design values have been frozen in while however many essential parameters are still negotiable.

Basic design

Alvarez

The middle part of the new linear accelerator of the SNQ project consists of a 200 MHz Alvarez structure as is indicated in Fig. 1. In the Alvarez a proton beam at an injection energy of 2 MeV is accelerated to an energy of about 100 MeV. A 200 MHz Alvarez is a well

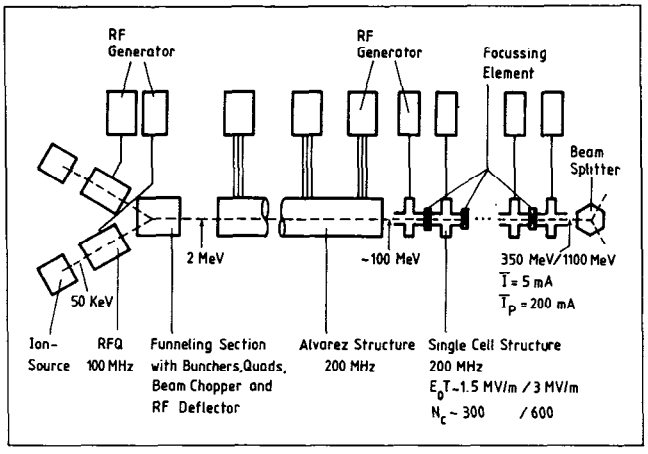

Fig. 1 Schematic view of the SNQ linear accelerator

known, reliable accelerator due to the experience of many years of operation at BNL, CERN and FNAL. In table 1 a few parameters of the SNQ Alvarez are compared with parameters of three existing Alvarez accelerators. The table indicates that the energy and the pulse current values of the SNQ Alvarez are comparable with those of the existing machines. However, the average current of the SNQ project exceeds the other average currents by at least an order of magnitude. This means that one has to emphasize the minimization of beam losses in the SNQ Alvarez which is for the existing machine not an important feature. At present, beam dynamic studies are performed to demonstrate that beam losses can be

	SNQ	BNL	CERN	FNAL
U_i[MeV]	2	0.75	0.75	0.75
U_f[MeV]	100	200.03	50	200.03
$\hat{I}$ [mA]	200	220	150	300
$\bar{I}$ [mA]	5	0.44	0.016	0.04
f_p[Hz]	100	10	1	15
f [MHz]	201.25	201.25	202.56	201.25

Table 1 Parameter of operating 200 MHz Alvarez accelerators and of the SNQ Alvarez. U_i injection energy, U_f Alvarez end energy, $\bar{I}_p$ averaged pulse current, $\bar{I}$ average current, f_p repetition rate and f rf frequency.

sufficiently suppressed by avoiding any possible effect, which leads to emittance growth, such as resonances, beam instabilities and mismatch[2].

RFQ

The fairly high injection energy of 2 MeV which ultimately allowed to choose a 200 MHz rf frequency for the Alvarez accelerator can only be achieved by a RFQ injector. At present there is no RFQ accelerator in permanent operation. However, a few successful beam tests with RFQ's have been reported. In table 2 parameters of projects with four vane RFQ structures are listed for which beam tests

Four Vane RFQ projects under beam test							
Laboratory	I_{design} [mA]	f [MHz]	U_i [KeV/amu]	U_f [MeV/amu]	$\Delta\tau/\tau$	Part q/A	Status
IHEP (USSR)	150	148.5	100	0.620	$2.5\cdot10^{-5}$	p	200 mA (1974)
IHEP (USSR)	>200	148.5	100	1.98	$1\cdot10^{-5}$	p	130 mA (1979)
ITEP (USSR)	240	148.5	89	3.00	$3\cdot10^{-5}$	p	100 mA (1982)
Los Alamos (USA)	60	425	100	0.64	$<1\cdot10^{-3}$	p	30 mA (1980)
Los Alamos (USA)	167	425	100	2.072	$1\cdot10^{-3}$	H^-	18 mA (1983)
CERN (Switz.)	-	202.56	50	0.52	-	p	70 mA (1983)
INS (Japan)	4	100	5	0.138	cw	≥1/7	H^+, H_2^+, H_3^+ beam test (1983)
LBL (USA)	0.9·A/q	199.3	7.1	0.2	$2\cdot10^{-3}$	≥1/7	beam test (1983)

Table 2 Parameters of four vane RFQ structure under beam tests, $\bar{I}$ = design current as designed, f - rf frequancy, U_i, U_f initial and final RFQ energy $\Delta\tau/\tau$ duty cycle, q and A charge and atomic number, respectively.

have been performed[3]. According to these beam tests it has been demonstrated that proton currents of about 100 mA can be accelerated in four vane RFQ's at a frequency of about 100 MHz starting from an energy as low as 50 KeV to a few MeV. Because of these promising results it seems to be justified that the injector of the SNQ linac is based on this recent development in accelerator technology.

The current limited by space charge, which can be accelerated in an RFQ structure, depends on the initial particle energy and on the frequency. In a linearized model a current limit can be estimated, which is represented by the solid line in Fig. 2. The validity of this current limit has been demonstrated by multi particle calculations since

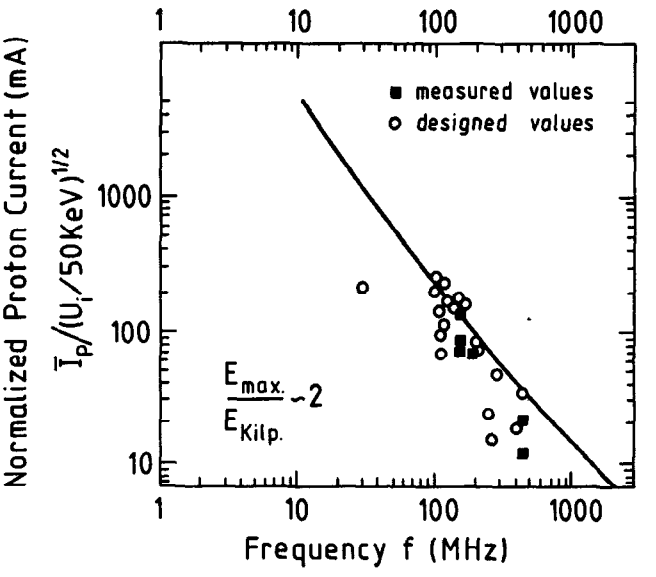

Fig. 2 Maximum RFQ proton current as a function of frequency and injection energy U_i

■ - measured currents from table 2

O - results from many particle calculation

▬ - current limit estimate by a linearized model.

the calculated currents of designed RFQ accelerators lie at or below the solid line (see Fig. 2). A promissing result is that the measured currents of the six known RFQ's under beam test are close to the current limit. One reads from Fig. 2 that a current of 200 mA can probably not be accelerated in a 200 MHz RFQ from 50 KeV to 2 MeV as is required. However, by using two 100 MHz RFQ and by funneling the beam in order to feed the Alvarez accelerator with 200 MHz bunches, the situation is fourfold relaxed since each of the RFQ operates at the lower frequency of 100 MHz with higher current limit and has to accelerate only half of the current.

Funneling section

The funneling section consists of beam transport components as bunchers and quadrupoles, the fast choppers for cutting gaps in the current pulse and a rf deflector for merging the two 100 MHz bunches on a common beam axis. A detailed treatment of the beam dynamics with the linear model by regarding space charge and constraints due to the beam properties at the end of the RFQ and in front of the Alvarez has shown that sufficient space can be provided for the rf deflector and for the fast choppers if the latter are placed in the 100 MHz lines[4]. Multi particle simulations of the 11 m long funneling section are in progress.

Because of the beam funneling two identical ion sources are needed, each of it yielding a pulsed current of 100 mA. At present, a prototype of a magnetic multipole source and of the 50 KeV extraction system is under development.

High energy part

The high energy part of the SNQ linac consists of single cells with negligible rf coupling between the cells. Each single cell should be supplied with rf power by its own generator. The amplitude, phase, and timing of the rf power is electronically controlled and can be changed considerably during operation if required. The operation frequency is 200 MHz, the same as in the Alvarez accelerator, i.e., there is no frequency jump between the two accelerator parts. With an average accelerating voltage gradient E_0T of about 1.5 MV/m about 300 single cells are needed to accelerate the proton beam from 100 MeV to the end energy of 350 MeV (stage I). By installing another 300 single cells and by upgrading the rf power supply for stage II the voltage gradient can be increased to about 3 MV/m in order to reach the ultimate end energy of 1.1 GeV. It is this flexibility besides many other options and a large variety of advantages to be discussed in the next paragraph which has led to the concept of uncoupled accelerator structure.

Transverse focussing elements are placed between single cells. The number of elements will be optimized with respect to beam optics and beam losses. A large number of small magnetic quadrupole lenses has the additional advantage of reducing the electric power losses in the quads due to smaller aperture radii.

In Fig. 3 the estimated power consumption of the SNQ linac in stage II is compiled. The

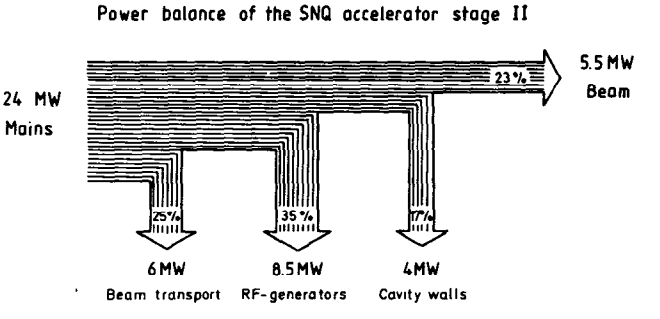

Fig. 3 Preliminary energy flow diagramme of the SNQ accelerator stage II

fraction of power going into the beam is relatively large because of the large effective shunt impedance of single cells (see Fig. 4) because of the large beam loading of 75 % and 62,5 % in stage I and II during the pulse, and because of the focussing via many small lenses.

Single cell concept

The alternative to the single cell concept, where each cell has its own relatively small rf power generator and its own control system,

is an accelerator with coupled structures, e.g. side-coupled structure or Disk and Washer (D+W) structure with the rf power supply from large generators.
The single cell concept has a variety of advantages which will be discussed in the following by comparing it with a coupled structure concept.

Shunt impedance

It is generally accepted that a single cell has a higher shunt impedance ZT^2 than any coupled structure, provided the resonator wave mode and the ß value are the same. While in a coupled structure the length of the cell is a fixed parameter set for instance $ß \cdot \lambda/2$, it is an additional adjustable parameter for uncoupled single cells. Knapp et al. estimated that ZT^2 values of coupled structures are 20 % less of that of single cells[5]. For a further comparison of shunt impedances of coupled and uncoupled structures, Disk and Washer values from literature were scaled according to $ZT^2 \sim f^{1/2}$ to the frequency of f = 200 MHz and corrected to a beam hole radius R_H = 3.5 cm with data from Manca and Knapp[6]. The scaling works quite well since the D+W values calculated originally for frequencies of 1.32 GHz by Schriber and of 324 MHz in the KFA/KfK study agree within 5 % as can be seen in Fig. 4[7,1]. These scaled ß-dependent values may be compared with calculated ZT^2 values for single cells at 200 MHz with bore radii of 3.5 cm diameter calculated by Lehmann[8]. Fig. 4 shows that the calculated shunt impedance of single cells in the E_{01} resonator mode is for $ß \leq 0.7$ larger than the shunt impedance of the D+W structures at the E_{02} resonator mode. However, taking into account the relatively high losses due to the supporting structure in the D+W, the shunt impedance of single cells becomes even for the highest energy larger than the shunt impedance of D+W.

Variable end energy

Since the stable phase angle φ_s is an adjustable parameter in the single cell concept, particles at any velocity can be accelerated. This property can be utilized to operate the

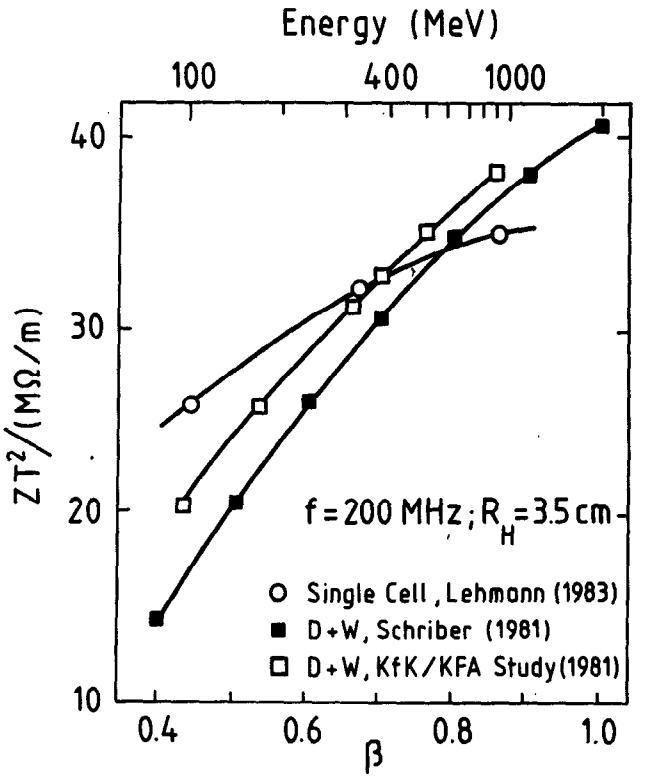

Fig. 4 Corrected, scaled and calibrated effective shunt impedances ZT^2 vers. ß for D+W structures and for single cells at 200 MHz and bore radius of 3.5 cm.

SNQ linac in other modes at higher end energies with smaller beam currents. In the single cell concept it is possible to use the extra rf power which is gained by reducing the beam current to increase the accelerator voltage gradient and hence the end energy. In a coupled structure the voltage gradient can not be changed without additional phase slip and therefore the extra RF power can not be used otherwise. In Fig. 5 the relation between end energy and current is shown for the SNQ linac of stage I. In addition it is shown how the neutron yield decreases if the end energy is increased at the expenses of a current reduction.
By decreasing the average current to 2 mA the end energy increases to 450 MeV. In this case the neutron intensity is reduced to 50 %, however, an important energy window for nuclear physic experiments can be scanned in this way.

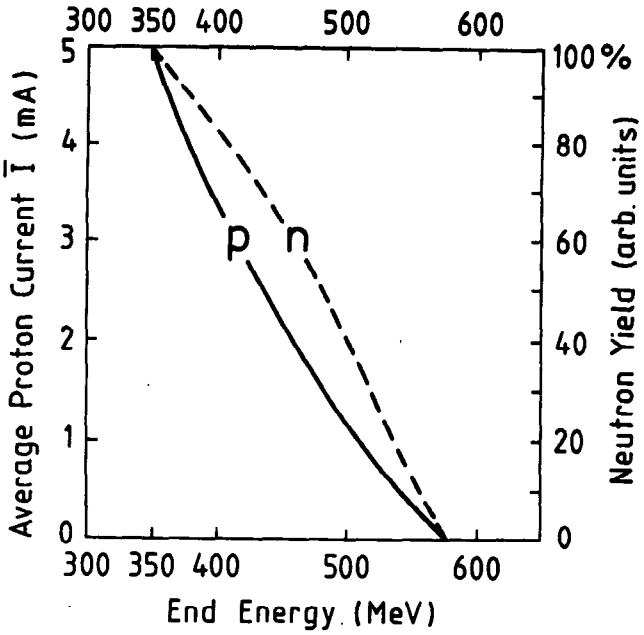

Fig. 5 Average proton current of the SNQ linac in stage I and the neutron yield in the target versus the end energy for constant rf power.

Beam losses

A limit of the beam losses in the order of 10^{-6} or less is required along the high energy part of the SNQ linac because otherwise it will not be possible to enter the accelerator tunnel 24 h after a shut-down of the accelerator. It is certainly a delicate task to predict beam losses at this low level and it is a big effort to estimate them with multi particle calculations. Nevertheless there are qualitative arguments which favorize the single cell concept in this respect:

1. The transverse focussing of the beam can be performed with many narrow spaced magnetic lenses, ultimately with a lens between consecutive cells. This way of transverse focussing assures a minimum of beam breathing implying less beam losses than the alternative solution of widely spaced lenses in the case of coupled structures.

2. An attempt can be made to reduce longitudinal beam losses in the single cell concept by changing to a more negative stable phase angle with the consequence of a decreased end energy. This flexibility of the single cell concept, which will widely be used when operation begins and during the test phase, does not exist with coupled structures except when stable angle and rf power are changed simultaneously.

3. In coupled structures the rf power is transported along the accelerating cells with the group velocity V which is of the order of 10 % (D+W: 50 %) of light velocity and thus smaller than the beam velocity. This situation leads to a ringing of the rf amplitude at the head of the current pulse, responsible for beam losses. For single cells the rf power is not transported along the cells and the term group velocity is meaningless in this concept. Consequently this source of beam losses does not exist. Similarly, the problem of rf amplitude gradient along the coupled structure is absent in the single cell concept.

4. Since each single cell has its own tuner a shift of the resonance frequency due to temperature or stress changes can be compensated by retuning. However for a coupled structure local temperature and stress changes lead to field distortions which cannot be compensated by the one tuner per tank. As a consequence additional phase slip occurs which may also lead to beam losses.

Mass production

The large number (300 and 600 for stage I and II, respectively) of identical components as cavity, control system, rf power generator and focussing device lowers the price per item because of mass production. On the other hand considerable effort can be spent to cost-optimize all items which are purchased in such large quantities. This leads to another reduction of cost. In addition, smaller items will atract more firms for tender.

Flexible stage concept

There are different ways to realize stage I of the SNQ linac and to reach the ultimate design values depending on the cash flow.

One has to assume that already in stage I the tunnel will have its final length of about 400 m for the high energy part of the linac

as is required for stage II. One way of realisation of stage I and II is to keep the E_oT voltage gradients at the maximum value of 3 MV/m and to install in stage I the minimum number of single cells with the full rf power installation per cell. In this case only 1/4 of the tunnel would be used. A better way is according to Fig. 6 to fill about half the

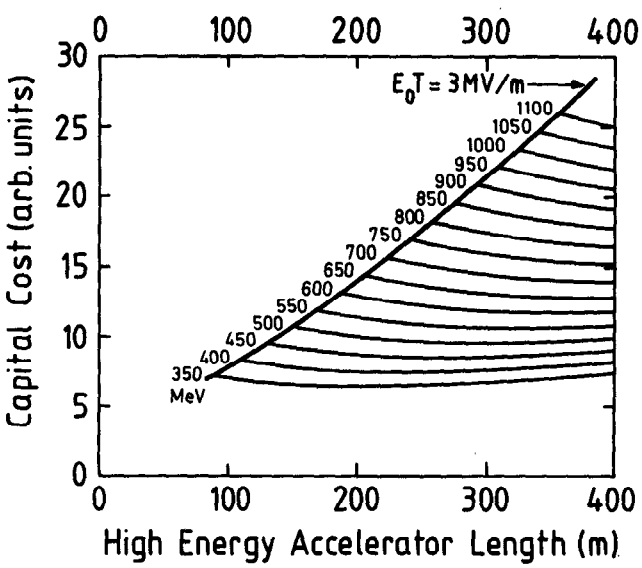

Fig. 6 Capital cost versus accelerator length of the high energy part of the SNQ linac in the range of $E_oT \leq 3$ MV/m. The results are based on a shunt impedance of 30 MΩ/m, a rf filling factor of 82 %, a stable phase angle of -20°, a current of 200 mA and an injection energy of 100 MeV and last not least on the costs per meter of rf structure, beam optics and tunnel, and on the cost per Watt of rf power.

tunnel with single cells. In this case the voltage gradient is only 1.5 MV/m and hence less rf power has to be provided. According to the cost estimates of rf structure, beam optics, tunnel and rf power, Fig. 6 indicates that the stage I linac with the smaller voltage gradient, which means more reliability, is less expensive. Due to the merits of the single cell concept one then can change over to an intermediate stage I' by simply upgrading the rf power and increasing the E_oT value to its maximum of 3 MV/m. In this case the end energy is 600 MeV at the same current $\bar{I}_p$ = 200 mA which means for instance a neutron intensity gain of about 2. The major advantage however is that one can gain experience about the operation of stage II before its installation (characterized by E_oT = 3 MV/m and energies up to 600 MeV) already in stage I'.

For the final upgrading to the end energy of 1.1 GeV all components used so far remain still in use.

In summary the single cell concept has the advantage that the rf power losses of the structure are smallest, that the mode of operation can be varied, that beam losses should be smaller in comparison to coupled structures and that the investment cost can be considerably reduced by mass production.

Failure compensation

Because of the large number of components a failure will frequently occur in the high energy part of the linac. The by far weakest component is certainly the amplifier chain. Assuming Poisson statistics and a life time of 8000 h of operation for the rf generator, one has to expect on average one failure per day with the 300 units of stage I. This large failure rate cannot be treated in the conventional way by switching off the linac, diagnosing the error, replacing the faulty component and then turning back to normal. This would cause too long shut-down periods. The situation is even more severe with the 600 components in stage II.

Fortunately, the single cell concept allows to continue operation if the rf power generator of one or even more single cells failed. A consequence of a single cell which does not accelerate any more is a change of the phase advance in the following cells. The phase mismatch is 1.30 and 0.20 for all following cells if the failure occurs at a cell operating at 100 MeV and 350 MeV, respectively, provided the single cell is detuned in order not to be charged up with rf power by the beam. Otherwise the phase change increases to values of 4.6° and 0.7° while the batch is passing. The presence of a non-accelerating single cell is signaled to the control system and the phase of the rf power in the following cells is changed to compensate for the resulting beam delay. As a result the beam is

accelerated to an end energy which is by about 1 MeV smaller than the normal value. If necessary the correct end energy can be obtained by slightly decreasing the absolute value of the stable phase angle. This correction is performed by the end energy control circuit. It should be emphasized that the described means to compensate for a faulty rf generator of a single cell are performed within msec, i.e. between two pulses and that the operation of the accelerator continues without any interruption. Then, during operation the error can be further diagnosed and the faulty component may be replaced. Thereafter the operation turns back to normal.

The single cavity control system which is one part of the three level linac control system is shown in Fig. 7. The inner three control loops to the left of the cavity are conventional. By mechanical tuning the resonance

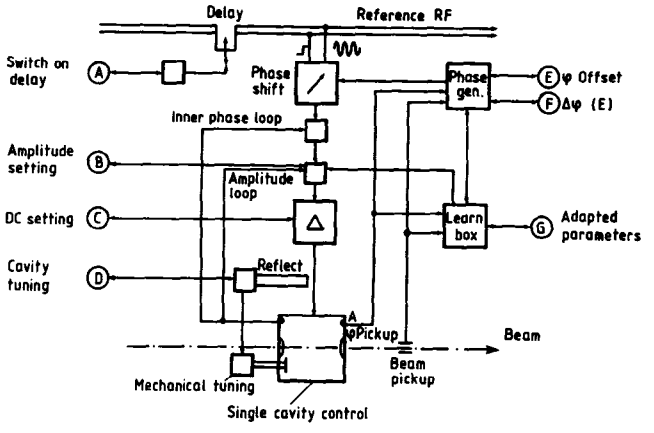

Fig. 7 Block diagramme of the single cavity control[9].

frequency is kept constant. In the other two loops the rf amplitude and phase are held at the same value. Because of the options to operate the high energy part of the SNQ accelerator at different stable phase angles, with small and large rf amplitudes and for different pulse currents the control loop needs input settings (E) for the phase generator, (D) for the amplitude loop, (C) for the amplifier chain, and (B) for the tuner. The phases are set with respect to a 200 MHz reference rf signal which is delayed for each single cell according to the arrival of the bunches in the center of the accelerator gap of a single cell. In a similar way the "switch on" signal is delayed in order to assure the precise charge-up with rf power when the first bunch of a batch enters the single cell.

The more advanced control loops are on the right hand side of Fig. 7. Pick-up signals for the rf phase and beam are fed into the phase generator for determining the actual phase advance φ_s which is compared with the setting value (E) in order to activate properly the phase shifter device. The offset value is corrected by the feed back value $\Delta\varphi(E)$ which originates from the end energy measuring device at the end of the accelerator.

An still more sophisticated part in the cavity control system is the learn box which observes the error signals during many batches in order to learn how to improve the control. For this purpose the learn box is provided with the actual phase advance value and setting value and with the phase generator response. Based on an analysis of this information collected from many batches the learn box may change directly the setting value for rf phase and amplitude or create with the support of a computer from a higher level a complete new set of parameter values (G) which are better adapted to the actual situation than the original settings.

An example should illustrate the way how the learn box works. For this purpose it is assumed that the current has suddenly changed to a lower value. Consequently, from then on at the beginning of each batch the rf amplitude becomes too large because of the reduced beam loading. Then the amplitude will be lowered by the inner amplitude loop and simultaneously the phase control becomes active. After some damped oscillations the control system will be quiet again. This procedure at the beginning of each batch would take place for ever if the learn box would not interfere. After having observed and analysed the actions of the control system for many batches the only reaction of the learn box should be to decrease the rf amplitude setting adapted to the changed beam loading.

RF power generation

In the single cell concept it would be possible to feed the cells with rf power from the largest rf generators of 4 MW power by distributing the rf power to a set of eight cells via power splitters and phase shifters. The advantages of the single cell concept quoted above exist however only if small rf generators, one for each cell, are used. Otherwise the discussed options of operation cannot be fully utilized. This restriction of small generators is in contrast to coupled structures where small and/or large generators can be used. A rather comprehensive study on the rf power generation at 200 MHz has been performed[10]. A few results of this study are compiled in table 3. With the listed life times of the driver chains the costs of the rf installation and of the replacements per watt are not very different between the three cases of small tetrodes, large triodes and klystrons. Table 3 indicates also that the solution with tetrodes which could be used as rf generators for the single cells is at medium cost compared to the other two. This relation holds for stage I and II. The major difference between the tetrode and klystron cases lies in the device failure rate as listed in table 3.

200 MHz RF Systems			
RF Amplifier	Small Tetrode 250 kŴ	Large Triode 1.5 MŴ	Large Klystron 3.0 MŴ
Single cell	Yes	No	No
Coupled cells	Yes	Yes	Yes
Number of power modules	I: 300 II: 1200	60 240	30 120
Device life time	8000 h	8000 h	40,000 h
Cost of installation [DM/W]	I: 0.6 II: 0.4	0.5 0.3	0.8 0.6
Replacement cost [DM/W]	0.05	0.025	0.08
Device failure rate	I: 1/d II: 4/d	1/5d 1/d	1/2m 2/m

Table 3 200 MHz RF systems with the pulsed power KW and MW, I, II refers to the stages.

Beam loading

With respect to the cavity accelerating voltage there are an rf cavity current I_{cav} and a beam current I_{beam} flowing into and out of the cavity. Their ratio I_{beam} / I_{cav} is the beam loading which is 75 % and 62.5 % in stage I and II, respectively. The fairly large beam-loading has consequences which will be discussed in the following:

1. In stage I about 1/4 of the cavity current is needed to maintain the voltage gradient E_oT while 3/4 are required for acceleration. Thus, for charging-up the cavity with rf power before each batch the total current, which is four times larger than the current needed to maintain the E_oT value, can be used. Therefore, the charge-up time is considerably shortened. By charging at resonance frequency the voltage change is given by (1)

$$\frac{dv}{dt} = I_{cav} \cdot (R/Q) \cdot \frac{\omega}{2} \exp\left(-\frac{\omega \cdot t}{2Q}\right) \qquad (1)$$

One calculates with a typical R/Q value of 330 Ω/m (Ohmic, not including transit time factor) for single cells that the voltage of 1/4 $I_{cav} \cdot R$ is reached after 20 μsec. If the design voltage would be reached assymptotically by charging with the needed current $I_{cav} - I_{beam}$ the charge-up time would be much larger since the characteristic time constant is already 100 μsec (= 2Q/ω). The rapid charge-up with full power within 20 μsec requires a precise timing for the onset of rf filling into the cavities with respect to the arrival of the first bunch of a batch.

2. In the case of a break down of a generator unit the beam will recharge the cavity. Assymptotically, a voltage gradient is

reached which is about four times as large as the value of normal operation in stage I. The voltage gradient becomes twice as large in stage II. Its polarity is such that the beam is decelerated. The characteristic time constant is again 100 μsec. The heavy loading of a cavity by the beam must be suppressed in order to avoid sparking in the cavity and energy modulation of the beam during the batch. Possible remedies are a fast short-circuiting of the cell or a strong mechanical detuning which unfortunately is slow. Both methods are expensive. It seems also possible to damp the cavity via the amplifier line even if the amplifier is out of service.

3. During a gap, i.e. a missing string of bunches as is deliberately produced by the fast choppers in the funneling section, the cavity voltage rises. The relative increase per missing bunch is $\Delta V/V = 2.10^{-4}$ with the parameters of stage I. For a typical switch gap in the batch of 20 missing bunches corresponding to 100 nsec the relative voltage rise is 0.4 % followed by a ringing of about the same magnitude. The voltage rise during the gap can be reduced by decreasing appropiately the cavity current I_{cav}. Such a measure requires however an amplifier with a band width of infinity. With a large band width of e.g. 20 MHz which might be achieved with small power generators the voltage rise is reduced to the tolerable value of 0.1 %.

4. The stable phase angle $\varphi_s \neq 0$ causes a reactive component of the beam current which is passed on to the generator. The reactive component can be compensated for the duration of a batch by working with an appropiately detuned cavity. For linacs the resonance frequency ω_{cav} must be larger than the generator frequency ω_g. During the charge-up with $\omega_g < \omega_{cav}$ the phase angle between the cavity current I_{cav} and the accelerating voltage $E_oT \cdot L$ increases from 0° to a value of about 20° as can be calculated from the data of stage I. A phase jump by just this value is then required to turn the cavity current I_{cav} in phase with the accelerating voltage, when the first bunch of a batch arrives and the design E_oT value has been reached. Because of the finite bandwidth of the driver chain the phase jump will result in some ringing effects of small amplitude even if the bandwidth is of the order of 20 MHz.

We are grateful to our colleagues in the ABT division for many helpfull discussions and valuable informations and to Mrs. Lydia Fuckardt for carefully typing the manuscript.

References

1 Realisierungsstudie zur Spallations-Neutronenquelle der Arbeitsgemeinschaft Spallations-Neutronenquelle der Kernforschungsanlage Jülich (KFA) und des Kernforschungszentrums Karlsruhe (KfK) (1981).

2 M. Pabst, private communication (1983).

3 H. Klein, "Development of the different RFQ Accelerating Structures and Operation Experience", Proc. of Part. Acc. Conf., Santa Fé (1983).

4 K. Bongardt, private communication (1983).

5 B.C. Knapp, E.A. Knapp, G.J. Lucas, and J.M. Potter, "Resonantly Coupled Accelerating Structures for high-current Linacs", IEEE Trans. Nucl. Sci. 12 (1965), 159.

6 J.J. Manca and E.A. Knapp, "TM_{01} Mode Accelerating Cavity Optimization, LA 7323 (1978).

7 S.O. Schriber, "Accelerator Structure Development for Room-Temperature Linacs", IEEE Trans. Nucl. Sci. 28 (1981), 3440.

8 R. Lehmann, "Coarse Optimization of Single Cells", private communication (1983).

9 H. Halling, A. Hardt, A. van der Hart and S. Martin, "Control of the High Energy Part of the Jülich SNQ Linac (Single Cell Arrangement)", private communication (1983).

10 A. Mitra, "Tetrode Amplifier for the High Energy Linac Structure", private communication (1983).

Proceedings of International Collaboration on Advanced Neutron Sources (ICANS-VII), 1983 September 13-16
Atomic Energy of Canada Limited, Report AECL-8488

IPNS ACCELERATOR SYSTEM AND NEUTRON CHOPPER SYNCHRONIZATION*

A. Rauchas, G. Ostrowski, C. Pelizzari† and G. Volk
Argonne National Laboratory
Argonne, Illinois 60439

Introduction

Several of the neutron scattering instruments at the Intense Pulsed Neutron Source (IPNS) at Argonne use neutron choppers for monochromatization of the neutron beam. Since the neutron burst is produced by a proton beam extracted from the Rapid Cycling Synchrotron (RCS), precise synchronization must be maintained between the RCS and the chopper aperture to minimize the degradation of energy resolution. The first attempts at synchronization were made in 1978 on the ZING-P' facility with a single chopper. Synchronization was further complicated after IPNS began operating in 1981 when a total of three chopper experiments came on-line. The system in use during that period of time was able to maintain synchronization with typical data collection efficiencies ranging from 20 to 70%. A synchronization system improvement, installed in late 1982, increased the data collection efficiencies of all the IPNS chopper systems to 99+%. The development of the RCS and neutron chopper synchronization system is described together with a detailed description of the present system.

RCS System Description

The RCS was originally designed to operate at 30 Hz synchronized to the 60 Hz power line. The synchrotron ring magnets are part of a biased 30 Hz resonant circuit which is driven by a 24 phase power source made up of two solid state power supplies.[1]

*Work supported by the U. S. Department of Energy.
†Now at Dept. of Radiology, University of Chicago.

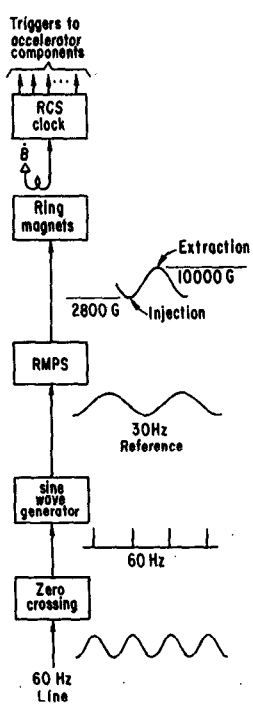

Fig. 1. Accelerator timing block diagram.

The reference 30 Hz sine wave for the ring magnet power supply (RMPS) is generated from the 60 Hz power line by an analog series approximation circuit.

The timing for the other accelerator components (H^- ion source, linac, injection and extraction magnets, etc.) is provided by the RCS clock which is synchronized to the magnetic field in the ring magnet by monitoring the zero crossings of the $\dot{B}$ signal from a pickup loop in one of the magnets. The clock has an uncertainty of ±0.5 μs and all timing adjustments have a resolution of 10 μs. A block diagram of the accelerator timing system is shown in Fig. 1.

The proton beam is extracted from the RCS in a single turn by a fast, 100 ns rise time, kicker magnet,[2] a pulsed transformer septum magnet[3] and a conventional dc septum magnet. The timing pulse from the RCS clock to the extraction kicker system arms the trigger circuitry. A signal derived from the circulating beam triggers the high current thyratron switches to charge the magnet after the tail of the circulating beam bunch has passed the kicker magnet creating an uncertainty of ±100 ns in the actual extraction time in respect to the timing pulse from the RCS clock.

Chopper System Description

The neutron beam chopper is a cylinder made of a neutron absorbing material with a curved slot containing a slit package which permits neutrons to pass through. The revolution frequency, and the width and curvature of the slits determine the range of energies that are transmitted to the experimental sample. The chopper is rotated at a frequency multiple of 30 Hz (typically 270 Hz) by a fractional horsepower synchronous motor. The motor-chopper assembly is enclosed within a vacuum tight housing which contains windows for neutron beam entry and exit. Cooling for the motor and bearings is provided by water cooling loops on the outside of the vacuum enclosure at the armature end and by a 0.5 torr helium exchange gas within the enclosure which provides cooling by convection but does not create significant aerodynamic drag on the chopper rotor. The total amount of cooling provided established the practical limit on motor size. The chopper rotor and vacuum enclosure are shown in Fig. 2.

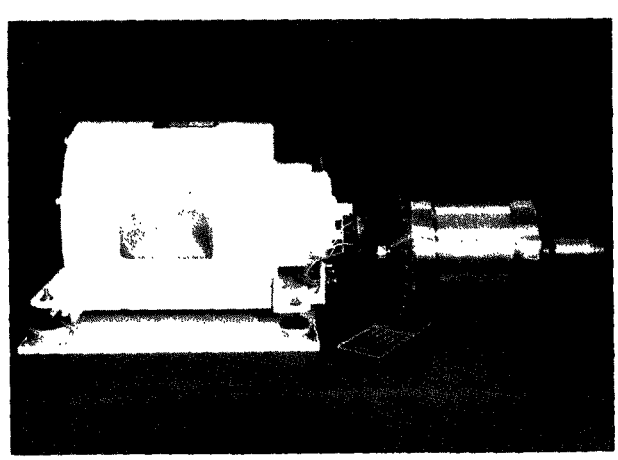

Fig. 2. Chopper rotor and vacuum enclosure.

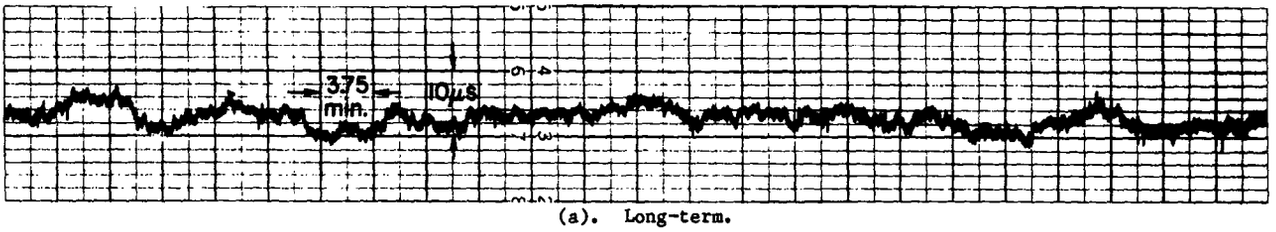

(a). Long-term.

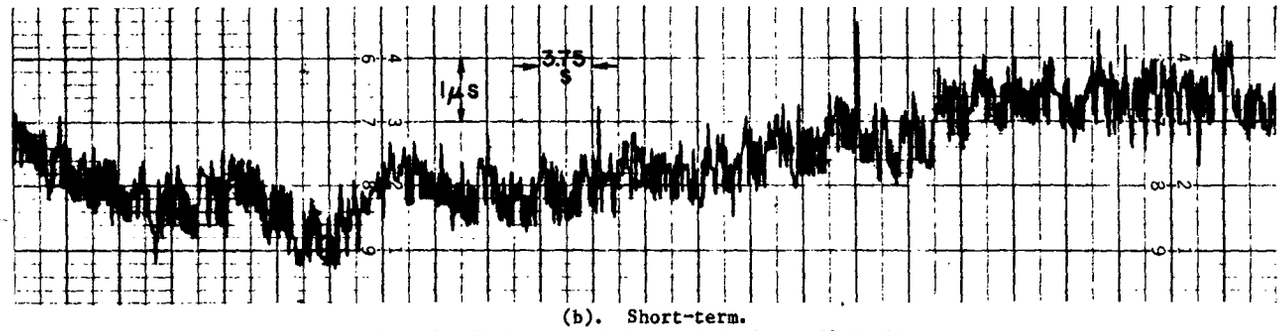

(b). Short-term.

Fig. 3. Variation of the period of the 60 Hz line.

The chopper drive system provides the power required to operate the chopper at a chosen speed, monitors the chopper operating parameters and shuts down the chopper power if a potentially damaging condition exists. A frequency synthesizer produces two phase sine waves in the frequency range of 1 Hz to 960 Hz to drive the chopper motor power amplifiers. The synthesizer also has provisions to be phase locked to an external 30 Hz reference and provide an output at any harmonic of 30 Hz. A magnetic pickup, located on the chopper housing, provides a signal indicating the position of the chopper opening. A separate accelerometer is mounted on the armature bearing end plate and acts as a monitor for chopper vibration.

Initial Synchronization Attempts

The first logical step for synchronization, at least from the accelerator standpoint, was to operate the chopper system synchronized to the 60 Hz power line. Investigation of the power line stability was begun and the "stable" line frequency was found to be unacceptable. A typical plot of long-term 60 Hz line period is shown in Fig. 3(a). Short-term variations are shown in Fig. 3(b). With the chopper's high moment of inertia, the low torque motor had no possibility of tracking the short-term variations of the power line. The phase change response of the chopper magnetic pickup signal to the reference drive signal is shown in Fig. 4 for a 0.001% change in the frequency of the drive signal. As a point of comparison, a 1 μs change in the 60 Hz period is equivalent to a 0.006% change. The difference in the large inertias and time constants of the chopper system and the RCS ring magnet system made synchronization to the line impossible.

The next synchronization attempt was to operate both systems locked to a common crystal oscillator.[4] This was a familiar mode of operation for the chopper system since it is used at reactor facilities, however, it was a totally new approach for the accelerator. The output of a 3.932 MHz oscillator, stable to ±1 part/million (ppm), was divided down to generate the required 60 Hz pulses for the RMPS, as well as the drive frequencies for the chopper. Studies of extraction from the RCS were conducted and the timing limits for efficient extraction and transport were established. Efficient extraction was possible within ±250 μs of the peak of the ring magnet field and within ±120 μs of the peak of the extraction septum pulse. Thus, it was possible to allow the chopper to initiate the extraction from the RCS within the efficient extraction time, the extraction window (EW). Two different means of controlling extraction were attempted. The first allowed the chopper system to control the triggering time of the extraction septum, with the kicker trigger occurring a fixed time after the septum. The second method fixed the septum time to the ring magnet field and allowed the chopper to control the arming time of the kicker system. Although the former allowed the use of a large EW

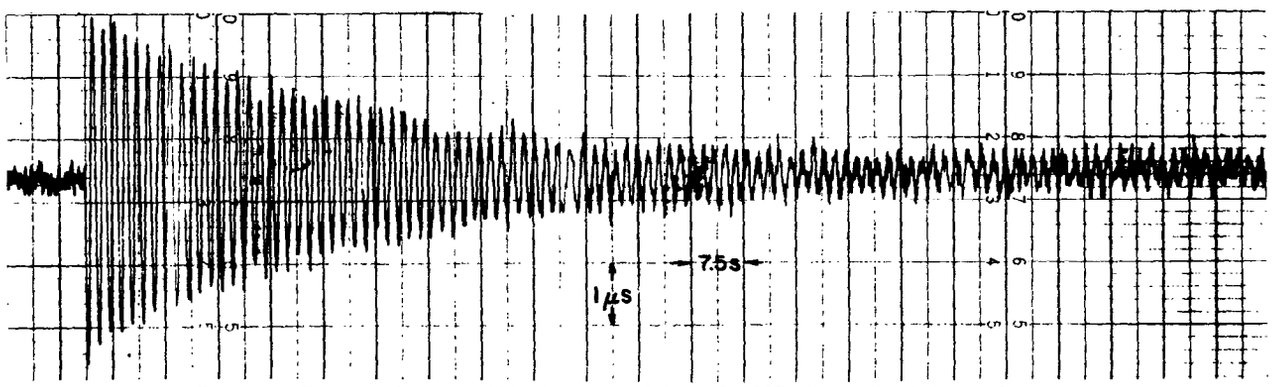

Fig. 4. Chopper phase oscillation caused by a 0.001% change in driving frequency.

(±250 μs), some degradation in the neutron energy resolution was detected due to the additional timing uncertainties caused by the longer delay between the chopper extraction command and the neutron burst from the target. Therefore, the second method became the standard mode of extraction control.

Further problems were encountered due to phase shifts between the master clock, the RMPS voltage and the ring magnet magnetic field. The phase shifts between the RMPS voltage and magnetic field were primarily caused by temperature variations in the RMPS resonant circuit and the subsequent detuning. This effect was minimized by installing a circuit to vary the capacitance of the tuned circuit in small steps to maintain the system within ±150 μs of resonance. Due to its nature, this was a relatively long-term effect. Several other factors on phase shifts were short-term. The first was caused by "beam noise", the coupling of circulating beam into various control lines causing instabilities in RMPS control circuits such as the sine wave generator and RMPS regulator. The second was caused by power line related ripple in various RMPS control circuits causing variation in system operation, a problem which due to the asynchronous operation to the line became a factor in many RCS systems, and in beam acceleration efficiency. The effect of "rolling" in respect to the power line frequency resulted in a 10% lower average current delivered on target. In addition, since the rate of "rolling" varied as the line frequency varied, the tuning of the accelerator was difficult because of the constantly changing conditions. Attempts were made to pinpoint the various causes for the beam handling instabilities. The effect on the RMPS caused variations in the injection field creating changes in the beam noise pattern which in turn affected the RMPS causing a further change in the injection field, etc.; a servo loop with positive feedback. Some variation of the injected beam properties due to ripple on the 50 Mev transport line magnets were also noted, but the position and size variations were too small to account for the beam instabilities. Any variation in the energy distribution of the injected pulse due to power supply ripple in the linear accelerator could not be studied for lack of an injection energy spectrometer.

After careful study, the effects of the RMPS were minimized; however, the total phase shift between the master clock and the ring magnet field and subsequently the EW remained in the range of ±200 μs. The chopper control system was redesigned to enable the chopper to track the phase variations of the EW. However, due to the low torque of the chopper drive motor, the maximum correction rate was limited to 0.5 μs/s since a higher rate would cause demagnetization of the motor armature. Because of the low correction rate, the chopper was not able to maintain synchronization with the RCS for 100% of the time. In fact, with multiple chopper operation, since only the master chopper can control extraction and because of the unequal inertias and time constants of the choppers, the data collection efficiency of the slave choppers was as low as 20%.

Synchronization System Operation

The operation of the RCS on the master clock is straightforward and has already been described in the previous section. The interfacing of the RCS to the chopper electronics and chopper system operation will be described here. Figure 5 shows the block diagram of the system.

In order for the chopper to stay in phase with the RCS, the chopper frequency $1/\tau_c$ must be a multiple of the 30 Hz RCS frequency. The fundamental condition

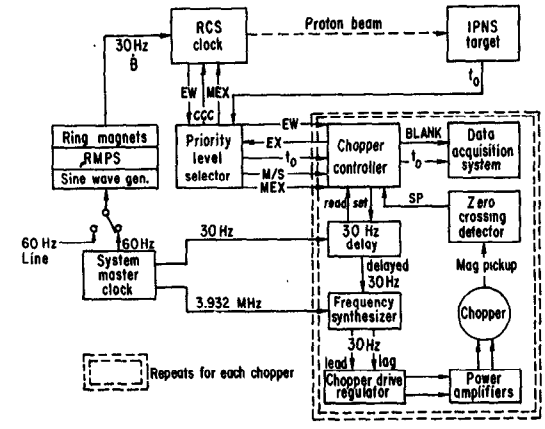

Fig. 5. RCS and neutron chopper synchronization system block diagram.

which must be met is that the chopper opening time follow the protons on target signal (t_o) by the required phase delay time T_c, within a tolerance of ΔT_c. The chopper phasing system controls proton beam extraction and, therefore, t_o, so all that is required to establish the desired phase is to send an extraction command (MEX) at a time such that

$$t_o + T_c = t_2 + \tau_c \quad ,$$

where t_2 is the chopper opening before t_o. The EW is provided by the RCS clock during which MEX is accepted; if an MEX arrives within this window then it will be used, but only if the chopper can control (CCC) level is true. The CCC is used to make it possible for the RCS to control extraction on those RCS cycles when a MEX cannot be issued within the EW; when the CCC is false, the RCS clock will generate its own extraction trigger at the midpoint of the EW, the optimum instant from the accelerator's point of view. As long as the CCC is true, the RCS clock will wait for a MEX until the last possible moment; if none arrives, the beam will be extracted at the trailing edge of the EW. In this case, the pulse will not be usable by the chopper experiment, but will be available to other experiments. The phasing system checks every t_o pulse to make sure that the phase condition is satisfied, i.e., that

$$t_o - t_2 = \tau_c - T_c \pm \Delta T_c/2 \quad .$$

If this condition is not satisfied, an inhibiting level is sent to the data acquisition system so data will be accumulated only for correctly phased pulses. The final function of the phasing system is to adjust the phase of the chopper with respect to the RCS when necessary in order that a legal MEX (i.e., in the EW) can be sent. This is accomplished by introducing a delay in the 30 Hz pulses to the frequency synthesizer from the master clock.

The priority level selector is the communications link to the RCS. It also communicates with up to six chopper controllers and prioritizes the information it receives from them. Each controller receives EW and t_o from the priority level selector and sends back its own extraction trigger, EX. The priority level selector sends to the RCS clock, as the MEX, the highest priority legal EX signal it receives for each RCS cycle. Thus, if the first priority EX signal is not within EW, the second priority EX will be used, etc. If there is no EX from any of the six inputs which is within EW, the priority level selector sets the CCC false until a legal EX pulse comes in again from one of the chopper controllers. At any instant,

the highest priority chopper providing a legal EX is defined to be the master, all others are slaves. This status information is sent back to each chopper controller and is used during phase shifting. Only the master chopper tracks the EW, all the slaves track the MEX, the extraction command issued by the master chopper.

Although it is not shown on Fig. 5, the system also contains a 60 Hz backup clock. In the event of interruption of the master 60 Hz signal to the RMPS, the backup clock synchronously switches the RCS over to its own 60 Hz reference signal. This is done to protect the RMPS from possible damage due to sudden removal of the reference 30 Hz sine wave and to prevent the RCS from shutting down when something goes wrong with the master clock or associated cabling. The backup clock does not provide any signals to the chopper system, so the choppers do not synchronize to the RCS in this mode of operation.

Synchronization System Improvements

Although tolerable, the data collection efficiency of the chopper experiments was far from ideal and further methods were investigated to improve the efficiency. It did not take long to realize that the RMPS could be phase shifted much more rapidly in respect to the master clock than the 0.5 μs/s maximum chopper correction rate. A system was designed and built to phase shift the RMPS and to interface to the existing controls with the least amount of effort. The changes to the basic system of Fig. 5 are shown in bold on Fig. 6.

The basic concept of neutron chopper controlled extraction remained the same, however, the EW was replaced by two: 1) the RCS extraction window (REW) and 2) the chopper extraction window (CEW). The REW is generated the same way as the EW and occurs centered about the peak of the extraction septum field and denotes the maximum allowable time range for extraction. The CEW is identical in width to the REW, but starts on the positive transition of the 30 Hz square wave from the master clock. The chopper phasing circuits use the CEW as the reference to phase the choppers so that the EX occurs in the center of the CEW. Since the CEW is referenced directly to the same clock that provides the reference signal to all the choppers, the phase relationship between the clock and the CEW is fixed and, therefore, no phase corrections are required by the choppers except for any internal mechanical variations, such as, bearing

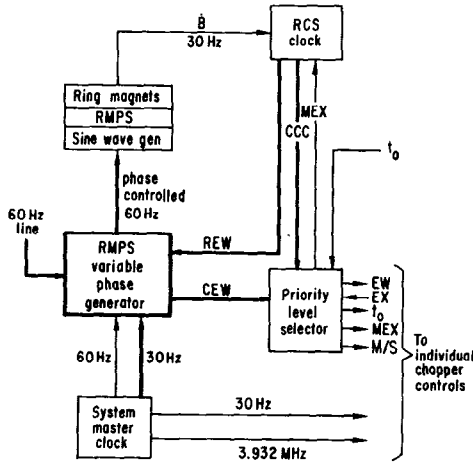

Fig. 6. Synchronization system improvements.

wear. In addition, the CEW provides a fixed synchronization reference point for choppers operating on various harmonics of 30 Hz.

The RMPS variable phase generator monitors the two windows, CEW and REW, and maintains synchronization between the two by phase shifting the RMPS and, therefore, the whole accelerator system. This is accomplished by varying the delay of the 60 Hz pulses between the master clock and the RMPS sine wave generator. No correction is made if the phase difference between the REW and CEW is less than 50 μs. If the phase difference exceeds the window width, corrections are made at a rate of 450 μs/s. When the phase difference is less than the window width, corrections are made at a rate of 30 μs/s. Once a correction is begun, it continues until the phase error is zero. Phase corrections are enabled only when the RMPS is operating synchronized to the master clock and the beam is on. The RMPS variable phase generator has a control range of ±5 ms. If the control range is exceeded during a correction, the electronics switches the RMPS to the backup clock, resets the delay to midrange, switches the RMPS back to chopper clock and resumes correction. A manual delay is included to allow the RCS operator to set the variable delay to the center of the control range.

As part of this improvement, the direction of the CCC signal was reversed. It now provides a status indication to the chopper priority level selector that, when true, the RCS clock is accepting the MEX command. It is true only when the phase error between CEW and REW is less than the window width. When the phase error is greater than the window width, CCC is false and extraction occurs at the midpoint of REW.

An additional feature of the RMPS variable phase generator is the synchronization of the transfer from master clock to 60 Hz line operation. Since the accelerator operation is more stable when the RMPS is operating synchronized to the 60 Hz line, whenever the chopper experiments are not operating even for short periods of time, the accelerator is operated synchronized to the line. The synchronized transfer feature allows the transfer to be made in both directions without shutting down the beam; and for a fast cycling accelerator, the previously required 5 minute switchover time resulted in quite a few missed pulses on target.

Conclusion and Future Plans

The final evolution of the RCS and neutron chopper synchronization system has brought about data collection efficiencies of 99+% to all the neutron scattering experiments using choppers. However, it has not eliminated the accelerator instabilities related to the beat frequency of the master clock to the 60 Hz line. This manifests in a 10% lower average current delivered on target with master clock operation compared with 60 Hz line operation.

Work is presently underway on a compromise solution, a master clock which tracks the variations of the 60 Hz line within the tracking capabilities of the chopper system. Additional circuitry would improve the tracking capability of the chopper by damping any oscillation induced by the phase shifting required by the new clock. Initial tests of a prototype system look promising but an operational system is still in the future.

Finally, the ideal system, from the accelerator's point of view, is under consideration; a redesign of the total chopper system to allow the chopper to track the 60 Hz line.

References

1. W. Praeg and D. McGhee, "Ring Magnet Power Supply for a 500 MeV Synchrotron," Conference Record IEEE-IAS-1978 Annual Meeting, Toronto, Canada (October 1-5, 1978).

2. D. E. Suddeth and G. J. Volk, "The Rapid Cycling Synchrotron Extraction Kicker Magnet Drive System," IEEE Transactions on Nuclear Science, Vol. NS-28, No. 3, p. 3017 (June 1981).

3. M. Foss, K. Thompson, and W. Praeg, "A Transformer Septum Magnet," IEEE Transactions on Nuclear Science, Vol. NS-26, No. 3, p. 4024 (June 1979).

4. W. Praeg, D. McGhee and G. Volk, "Phase Lock of Rapid Cycling Synchrotron and Neutron Choppers," IEEE Transactions on Nuclear Science, Vol. NS-28, No. 3, p. 2171 (June 1981).

Proceedings of International Collaboration on Advanced Neutron Sources (ICANS-VII), 1983 September 13-16
Atomic Energy of Canada Limited, Report AECL-8488

DEVELOPMENT OF A HIGH CURRENT INJECTOR FOR A SPALLATION NEUTRON SOURCE

B.G. Chidley, G.E. McMichael and M.R. Shubaly

Atomic Energy of Canada Limited
Chalk River Nuclear Laboratories
Chalk River, Ontario, Canada K0J 1J0

Summary

A spallation neutron source for breeding fissile material must have high efficiency and reliability to be competitive with other sources of fissile fuel. A study by Tunnicliffe et al in 1976[1] suggested a breeder based on a proton linac with an output of 300 mA average current at 1 GeV. Although such an accelerator is feasible with present technology, development work is needed before a practical device can be built. Bartholomew[2] at ICANS-V described an accelerator breeder development program that included the ZEBRA[3] accelerator (300 mA average at 10 MeV) and its precursor RFQ1[4] (75 mA average at 600 keV). This paper describes the injector development program at Chalk River, including the ion source, transport line, and structure to accelerate a proton beam to an energy suitable for further acceleration in a drift tube linac.

Injector Requirements

The injector for a spallation neutron source must deliver a high current proton beam at 100% duty factor at an energy suitable for further acceleration in a drift tube linac. For this discussion we shall assume the values of ZEBRA[3] (300 mA at 2 MeV). The injector is a relatively small component of a large and expensive installation, so system parameters must be chosen to optimize the cost and efficiency of the entire installation rather than for economy or convenience of the injector. High reliability and long component lifetime are essential requirements of the injector. Low beam spill and high efficiency of conversion of rf power to beam power are important only if they influence reliability or erosion of components.

In addition to providing an output beam matched to the admittance of the drift tube linac, the injector must have the capability of variable current operation from zero to full design value while maintaining the emittance match.

The most suitable configuration for the injector is to use a dc column operating below 100 kV followed by a radio-frequency quadrupole (RFQ) accelerator. At CRNL high current operation of a 750 kV dc column proved to be very troublesome and the largest 100% duty factor 750 keV proton beam ever obtained spark-free for 30 minutes was below 50 mA.

To obtain pertinent design information and operating experience prior to ZEBRA construction, RFQ[4] is being built to accelerate 75 mA of protons to 600 keV. RFQ1 operating at 2.5 times the ZEBRA frequency and at a lower surface electric field will have relatively similar space charge and beam loading. RFQ1 has been designed for conservative electric fields and modest currents, so that operation near the space charge limit can be conveniently studied and operation will be possible over a range of voltages. Basic specifications for the two RFQ's are given in Table 1.

Table 1

	RFQ1	ZEBRA
dc injector output	50 keV	75 keV
RFQ output	600 keV	2 MeV
output current	75 mA	305 mA
frequency	269 MHz	108 MHz

The aims of the RFQ1 experiment are to gain practical experience with design, construction, operation and diagnostics. Of particular interest will be the operation near the current limit and a comparison of observed transmission with the results from computer particle dynamics codes.

Figure 1 shows the dc injector to the start of the radio-frequency quadrupole of RFQ1. Requirements are summarized in Table 2.

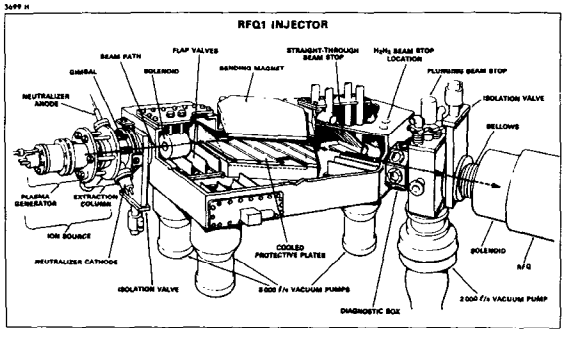

Fig. 1 RFQ1 dc injector.

Table 2

DC Injector Requirements

1. High dc current

RFQ1	115 mA H_1^+	(> 230 mA total)
ZEBRA	375 mA H_1^+	(> 750 mA total)

2. Fixed energy

RFQ1	50 keV
ZEBRA	75 keV

3. Low emittance - High brightness

RFQ1	$\varepsilon_n = 3\ \pi$ mm-mrad
ZEBRA	$\varepsilon_n = 6\ \pi$ mm-mrad

4. Variable current

Zero to full current with ramp times of tens of seconds to tens of minutes.

5. Reliable operation

   - freedom from sparking
   - long component lifetimes
   - stable output (low noise and minimum oscillation of beam envelope)

6. Match to RFQ acceptance

   - over full current range

Ion Source, DC Column, and Low Energy Beam Transport

To provide the high brightness beam required by the RFQ it is planned to start a high quality beam and minimize the length and number of transport elements between the source and the RFQ. Multiple apertures are required for high currents so the plasma generator must give a uniform current density over the extraction area to reduce mismatch between apertures. The plasma must be quiescent to reduce both "time-averaged" mismatch and deleterious effects on space charge neutralization in the beam transport line. In addition all components must be designed with adequate cooling to have long lifetime and provide stable, repeatable operation.

A duoPIGatron meets most of these requirements. It has high arc and gas efficiency, and although the proton fraction is low, it is not much different from other plasma generators of the same size. An experimental program to improve its proton fraction is in progress.

The electrode geometry is designed to minimize aberrations and so produce a bright beam with a minimum of halo. Beamlet stacking can be used to reduce the effective emittance from the multi-aperture array. The extraction column must operate at high gradient to handle the high current density. To provide reliable operation of the accelerator, sparking in the extraction column must be reduced. To achieve this, electron backstreaming and sensitivity to x-ray fields must be minimized. Backstreaming is reduced by minimizing beam spill, by effective suppression of electrons from the beam generated plasma, and by minimization of electron production in the extraction gap. Sensitivity to x-ray fields is reduced by effective shielding of the ceramics and by the proper choice of electrode materials. Figure 2 shows a cross section of the triode accel-decel extraction column used at Chalk River for up to 500 mA total output.

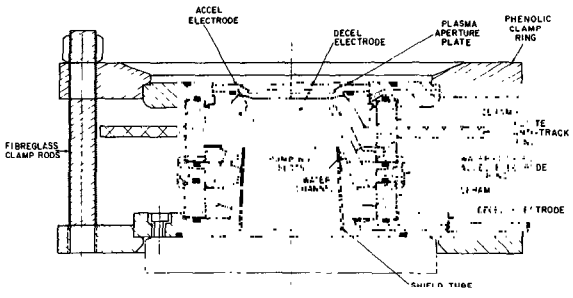

Fig. 2 Triode accel-decel extraction column.

The transport line is kept as compact as is consistent with species selection, vacuum pumping, and diagnostics to reduce convective instabilities. Matching from the extraction column is achieved with a double focusing bending magnet (which also provides for species selection) and two solenoids. For low energy high current beams, good space charge neutralization is necessary to reduce growth in beam size and emittance. This can be achieved by keeping the gas pressure in the transport system relatively high (4-9 x 10^{-3} Pa) although this leads to high charge exchange losses so a preferable alternative may be a plasma bridge neutralizer and this approach is being investigated. Scraping of the neutralized beam is to be avoided as this often leads to emittance growth.

Variable beam current at a fixed energy is obtained by operating the plasma generator on a mixture of argon and hydrogen and varying the argon fraction to vary the proton current from zero to design value while keeping the perveance constant. This requires careful control of the two gas flows and the arc current but does provide variability from zero to full current with the emittance decreasing slowly as the proton current decreases. The required variation of gas flows and arc current are shown in Fig. 3.

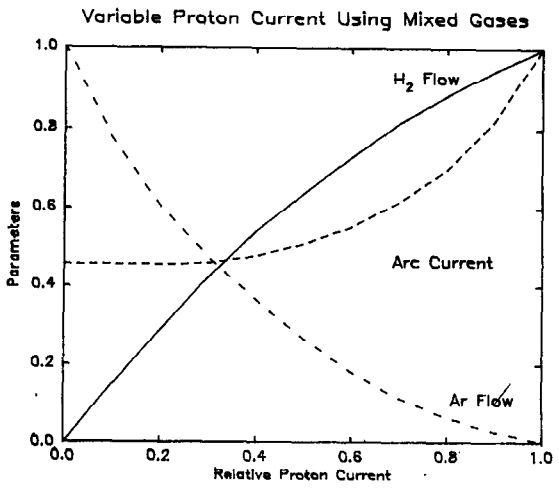

Fig. 3 Variation in gas flow and arc current to give variable beam current.

From measurements on a test stand, single beamlet normalized emittance is 0.34 π mm•mrad for 93% of 85 mA (total current). For a triangular array, as will be used on RFQ1, the effective emittance is 2.4 π mm•mrad and for a full array of 7 apertures, as will be used for ZEBRA, the emittance is 4.9 π mm•mrad. Spark free runs of 3.5 hours at 475 mA (total current), 42 keV have been achieved.

RFQ Accelerator

The current limit for no emittance growth in an RFQ is $3 * 10^4 \beta^3$ amps, where β is the particle velocity expressed as a fraction of the speed of light. Above this limit, emittance growth will occur although operation without beam loss is possible if the structure admittance is large enough to tolerate the increasing emittance until β is larger. The upper current limit for 50 keV injection with manageable emittance growth is about 100 mA. RFQ1 can be operated at 50 keV input but ZEBRA must have a higher injection energy (75 keV in the present design). Design parameters for the RFQ of RFQ1 are given in Table 3.

Table 3

RFQ1

Input Energy	50 keV
Output Energy	600 keV
Input Current	90 mA
Output Current	75 mA
Maximum Electric Field	24.86 MV/m (1.5 * Kp)
Vane Length	2.32 m
Vane Voltage V	
Design	73 kV
Maximum	88 kV
Average Bore Radius r_0	0.464 cm
Minimum Radius a_{min}	0.399 cm
CURLI Current Limit at 300 keV	125 mA
Nominal Input Conditions	
ε (normalized)	3 π mm-mrad
α	1.1175
β	5.454 cm/rad
Structure Power	up to 310 kW
Beam Power	45 kW

The large power dissipation makes cooling of the structure a major design consideration, with the region of rf contact between sheel and vanes being particularly troublesome. To eliminate the need for dynamically adjustable end tuners with their rf contact problems, strapped vanes and adjustable vane supports will be used.

The large beam spill (15 mA) represents a high gas load in the RFQ. Adequate pumping will be required for the RFQ structure as well as for the injector and beam stop. The complete RFQ1 vacuum system has 3 diffusion pumps (25000 L/s), 8 cryopumps (16000 L/s), one ion pump (2000 L/s), and one titanium sublimator (4000 L/S) for a total pumping capacity of 47000 L/s.

The present design value of the maximum electric field on the vane surface is 1.25 times the Kilpatrick limit (1.25 * Kp) but it will be operated at 1.5 * Kp or higher for improved performance. Typical values used in pulsed RFQ's are 2.0 to 2.5 * Kp but there have been doubts expressed that these can be maintained in a cw device. Recent results on the Japanese LITL accelerator[5] show satisfactory cw operation at 1.8 * Kp and an experiment is in progress at CRNL to measure sparking limits in an unmodulated cw RFQ. For RFQ1 a very conservative limit has been used to ensure that an adequate measurement regime is possible to determine space charge current limits over a wide range of operating parameters.

A schematic cross section of RFQ1 is shown in Fig. 4 with the region of interest from a beam dynamics viewpoint indicated by the central hatched square. Within this region the quasistatic approximation can be used in which the vane tips are considered to be equipotential surfaces and the effects of rf currents can be neglected.

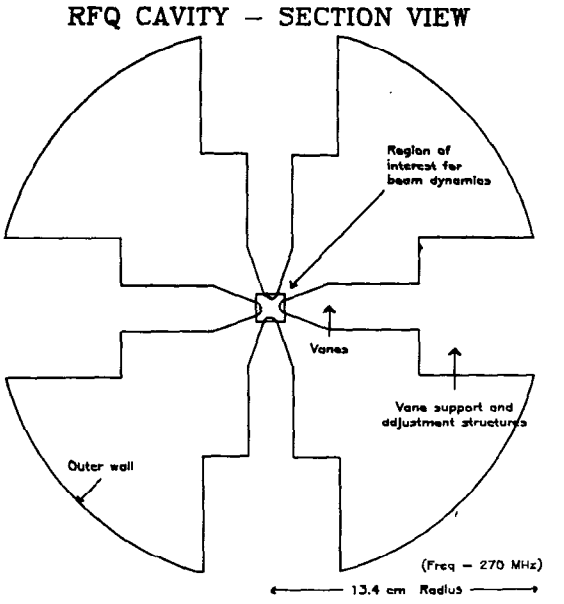

Fig. 4 RFQ1 cross section.

Vane tip shapes have been investigated that allow an increased vane voltage for a specified peak surface field. In this way focusing fields can be reached which are closer to the optimum before being limited by sparking problems. Vane profiles considered were a) the idealized 2-term potential (which cannot be built in practice), b) POP[6] style (the radius of curvature at the tip is the same as for the idealized, but uses a circular arc rather than hyperbolic), c) a constant radius of curvature tip (rather than varying with aperture), and d) a tip with constant center of curvature. The transmission calculated for the various vane shapes using the computer program PARMTEQ are shown in Fig. 5. These curves show how the vane tip profile influences the output current.

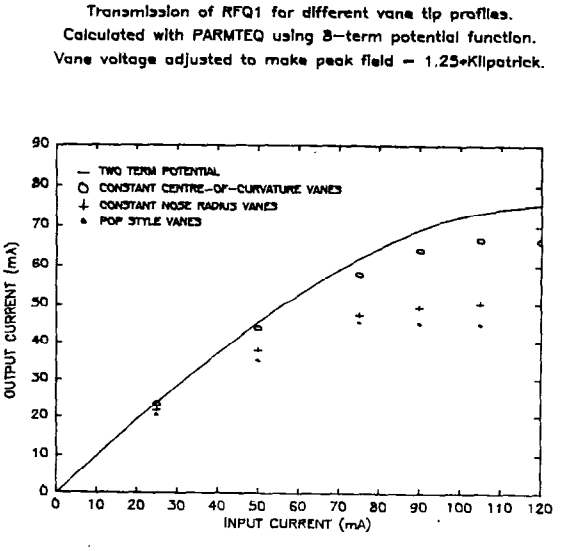

Fig. 5 Calculated transmission for various vane tip profiles.

Participants from the United States, Germany and Japan took part in a design review of RFQ1 held at Chalk River in June. All aspects from conceptual design to mechanical details were involved in the review. Suggestions in numerous areas are being implemented - in particular on the mechanical design (the present phase of our work).

The present status of RFQ1 is as follows. The ion source has been tested. Some parts of it will be used as they are presently designed and fabricated. Drawings are finished for the injector with construction expected to be finished mid-1984. The drawings for the RFQ are expected to be completed at the end of 1984 with the RFQ operational at the end of 1986.

Acknowledgements

The authors would like to acknowledge the work of members of the ZEBRA group, including S.O. Schriber for system requirements, L.D. Hansborough, R.B. Turner, A. Walton, T. Tran Ngoc, D. Beaulieu, and J.E. Anderchek for mechanical design, J. Ungrin, R.M. Hutcheon and J.C. Brown for rf discussions, and L.W. Funk and M.S. deJong for diagnostics and tranport lines.

References

1. P.R. Tunnicliffe, B.G. Chidley, J.S. Fraser, "High Current Linear Accelerators and Nuclear Power", Proc. 1976 Proton Linear Accelerator Conf., Atomic Energy of Canada Limited, Report AECL-5677, 36 (1976).
2. G.A. Bartholomew, "Research Opportunities with Prototype Accelerators for an Accelerator Breeder", ICANS-V Proceedings ISSN 0344-5789, 89 (1981).
3. B.G. Chidley, J.C. Brown, G.E. McMichael, S.O. Schriber, M.R. Shubaly and J. Ungrin, "Design and Constraints for the ZEBRA Injector, RFQ and DTL", Proc. 1981 Linear Accelerator Conf., Los Alamos National Laboratory, Report LA-9234-C, 49 (1981).
4. M.R. Shubaly et al., "RFQ1: A 600 keV, 75 mA CW Proton Accelerator", IEEE Trans. Nucl. Sci., NS-30, No. 2, 1428 (1983).
5. N. Ueda, T. Nakamishi, S. Arai, T. Hattori, T. Fukushima, Y. Sakurada, T. Honma, N. Tokuda, S. Yamada, M. Takanaka, A. Otano, A. Mizobuchi, Y. Hirao, "Design, Construction and Performance of the INS RFQ Linac LITL", IEEE Trans. Nucl. Sci., NS-30, No. 4, 2975 (1983).
6. J.E. Stovall, K.R. Crandall, R.W. Hamm, "Performance Characteristics of a 425 MHz RFQ Linac", IEEE Trans. Nucl. Sci., NS-28, No. 2, 1508 (1981).

Proceedings of International Collaboration on Advanced Neutron Sources (ICANS-VII), 1983 September 13-16
Atomic Energy of Canada Limited, Report AECL-8488

BEAM LOADING AND BEAM INSTABILITIES IN HIGH CURRENT ACCELERATORS

K.C.D. Chan and J. McKeown

Atomic Energy of Canada Limited
Chalk River Nuclear Laboratories
Chalk River, Ontario, Canada K0J 1J0

Summary

Accelerators with intense beams are important components of spallation neutron sources. This paper summarizes past experiments and present studies on beam induced effects in accelerators with intense beams carried out at Chalk River on the Electron Test Accelerator (ETA).

Introduction

Beam loading and possible beam instabilities from beam induced effects are important in accelerators proposed for spallation neutron sources. At Chalk River, electrons have been used to study the behaviour of intense beams in coupled cavity linac systems[1,2]. Experiments on beam loading with a cw beam up to 20 mA have examined how changes in load impedance of an accelerator structure resulting from changes in beam current can be controlled. These experiments have measured the changes in coupling, quality factor and shunt impedance at different beam loading factors, providing information for optimal design of high current linacs. At the same time, the beam induced TM_{110} deflection mode was used successfully to detect the position of the beam centroid[3,4].

The means for a systematic study of beam loading and beam stability have been gradually acquired over the past seven years. Recently, a pulsed electron gun[5] with 22 nC/pulse has been manufactured so that a study of beam excitations of higher order modes can be undertaken at a beam intensity typical of recently proposed accelerators[6]. Such modes have serious implications for beam stability in high current accelerators. The experimental program has been complemented by theoretical work using the computer codes SUPERFISH[7], URMEL[8], BCI[9] and TBCI[10]. These codes have been used to assist with the design of new structures and predict the consequences of interactions between the beam and the structure.

This paper summarizes past work done at Chalk River on the beam cavity interaction and reports on the ongoing physics program. This includes the preparation for injection of pulses from the pulsed electron gun into the graded-β section of ETA, with the aim of demonstrating the space charge effect at high current level, and the physics design for the HERA proton ring linac structure, demonstrating the use of the design codes in calculating beam induced effects.

Underlying Physics

When a beam bunch passes through a cavity, e.g., an accelerating cell in an accelerator structure, transient cavity electromagnetic fields are induced in the cavity volume. Figure 1 depicts a time sequence of a beam bunch passing through a pair of accelerating cavities. The amount of energy U deposited in the cavity is equal to the square of the charge q in the bunch multiplied by a proportional constant k which is a function of cavity geometry and material only. The excitation of the cavity can further be expanded into eigenmode excitations. The excitation of an eigenmode is governed by the Condon[11] formula:

$$\frac{d^2p_m}{dt^2} + \frac{\omega_m}{Q_m}\frac{dp_m}{dt} + \omega_m^2 p_m = \frac{\omega_m}{2U_m}\int \vec{J}\cdot\vec{E}_m \, d^3r$$

where p_m = eigenmode expansion coefficient
ω_m = mode angular frequency
E_m = mode electric field
J = beam current density
Q_m = mode quality factor
U_m = mode stored energy = $1/2\ \varepsilon_0 \int \vec{E}_m\cdot\vec{E}_m d^3r$

This has the form of the equation for a forced harmonic oscillator. In the case of a cw beam, if the bunch frequency is close to the frequency of an eigenmode or its harmonics, the resonant excitation condition will drive the excited mode to an amplitude significantly in excess of its transient value.

A beam particle experiences the induced fields from all the previous particles in addition to the externally applied electromagnetic fields. In recently proposed accelerators, because of their high current, the effects of these induced fields are very significant. They can affect the beam emittance and rf controls in various ways besides being a source of energy loss which must be compensated. The longitudinal electric fields induced by charge at the head of a bunch tend to slow down the particles at the tail and give rise to a variation in particle energy within the bunch. The resonantly induced fundamental mode field gives rise to a beam dependent component of rf acceleration which the control loops have to compensate by adjusting the drive to the external rf source. The dipole mode transverse magnetic fields will deflect beam away from the axis. The quadrupole mode fields give rise to beam dependent focusing and defocusing forces. Therefore, in order to obtain a stable beam system under heavy beam loading and avoid beam induced instabilities, beam induced effects must be studied in detail.

Past Experiments with Intense Beams

The beam loading experiments have been described in detail in references 1 and 2. The graded-β structure of the Electron Test Accelerator was used to deliver a cw electron beam up to 20 mA at 1.4 MeV, and beam loading experiments were carried out in a β=1 structure. The latter is a side-coupled structure consisting of 18 accelerating cells. Both structures operate in the π/2 coupled mode of the TM_{010}-like passband at a frequency of 805 MHz. Beam loading of 80% was achieved in the β=1 structure at an average accelerating gradient up to 0.2 MV/m.

Under high beam loading conditions and at different field gradients, the progressive shift from over to undercoupling between the accelerating structure and the rf source was observed. No significant change of the shunt impedance was found for accelerating gradients of 0.1 to 0.8 MV/m and beam loading factors of 80 to 10%, respectively. The relationship between the admittance phase angle and the beam phase angle was found to be a strong function of beam loading. Also the beam induced power at the operating mode was observed to vary as the square of the current. These experiments provide necessary design information for

systems at the more economically desirable gradients of 1 MeV/m and beyond.

The beam position monitors were described in references 3 and 4. The beam induced TM_{110} mode oscillation in a cavity, often a major cause of beam instability because of the mode magnetic field normal to the beam, was used to advantage for detecting beam displacement. The beam position was measured by measuring the beam induced power that is proportional to the square of the product of the beam current and beam displacement. The position information obtained correlated well with that derived from self-powered detectors[12] and had a position sensitivity of 0.14 $mW \cdot mm^{-1/2} \cdot mA^{-1/2}$. The position information was subsequently used in a feedback loop to control the drive current in a steering magnet upstream, thereby maintaining the beam on axis. At 1 mA, the beam was maintained on axis to better than a fraction of a millimeter.

Present Work with Intense Beam

Pulsed Electron Gun Injection

Fabrication details and properties of the pulsed gun have been described in reference 5. The gun produces electron pulses at 5 kHz with 1.4×10^{11} electrons (22 nC) per pulse and a pulse half width of 3 ns. This section describes the calculations of the injection of these high intensity pulses into ETA, including space-charge effects. Similar calculations have been reported recently for the free electron laser at LANL[13] and for the Stanford Linear Collider[14].

Some beam properties in the injection line are shown in Fig. 2. A series of four coils (K1-K4) are required to produce an approximately uniform longitudinal magnetic field of 15 mT to compensate for the transverse space charge force along the bunching distance between the buncher and M4 accelerator. A gap lens (L1) is used to tailor the beam for injection to this length and another gap lens (L2) for going into M4. The transverse beam envelope is also shown. With no buncher power, the scalloping of the beam envelope is limited to 0.2 mm around a beam radius of 9 mm. With the buncher turned on, the radial buncher field produces a time dependent deflecting force on the off-axis particles and increases the effective transverse emittance of the beam. This effect increases with larger beam radius. At a beam radius of 9 mm, the estimated increase in divergence of 9 mrad will increase the effective beam emittance by as much as 10.31 $\pi \cdot cm \cdot mrad$ compared to the gun intrinsic emittance of 5.66 $\pi \cdot cm \cdot mrad$. This effect is included in the calculations and results are shown as the dashed curves in Fig. 2.

Results of longitudinal bunching calculations are shown in Fig. 3. In the calculations, the electron pulse is represented by disks of charge distributed along the axis. Each disk is further divided radially into two rings. The radii of these rings are assumed to be constant. The forces taken into consideration are the buncher field and Coulomb forces between the rings and their image charges on the beam pipe.

With a buncher peak voltage of 9.79 kV, the beam continues to bunch up to 60 cm from the buncher with 60% of the electrons falling into a phase interval of 100°. After 60 cm, the density of electrons at the center of the bunch becomes very large producing a debunching effect as demonstrated by the bunch widening at 80 and 100 cm. Results also show that the space charge effects are milder for the outer rings because they receive greater compensating forces from the image charges on the beam pipe. Therefore, at this buncher voltage and a current level of 5.2 A, the bunching efficiency is limited by the longitudinal space charge effect.

HERA Proton Ring Structure Design

HERA[6] is a proton-electron collider designed for 820 GeV protons and 30 GeV electrons or positrons at the DESY laboratory in Hamburg. The proton beam contains high density bunches with 3×10^{11} protons/bunch. At an accelerating gradient of 0.868 MV/m and an average beam current of 0.53 A, the beam loading is as high as 94%. Calculations show that the induced field in the accelerating mode is 0.8 MV/m which is of similar magnitude to the field from external rf sources.

Figure 4 shows a proposed [15] cavity geometry (208.5 MHz) derived by scaling the dimensions of an optimized PETRA cavity (500 MHz). The scaled geometry was further optimized with SUPERFISH[7] calculations by varying the gap length to give maximum ZT^2 of 27.74 MΩ/m at a ratio of gap length to cavity length (g/L) of 0.56.

The beam induced fields in the cavity were calculated with the codes SUPERFISH[7], URMEL[8], BCI[9] and TBCI[10] (Fig. 5). For axially symmetric modes, the energy loss to higher order modes (k_{hm}) is 1.13 times the energy loss to the fundamental mode and increases with larger gap length. The total energy loss to all axially symmetric modes (k_T) is 0.293 $V \cdot pC^{-1} \cdot m^{-1}$ and increases by 10% due to the increase of k_{hm} when g/L increases from 0.5 to 0.7. The energy loss parameter k_{110} to the first dipole mode (TM_{110}-like) is 0.0053 $V \cdot pC^{-1} \cdot m^{-1}$ and decreases by 70% when g/L increases from 0.5 to 0.7. The opposite trends of k_{hm} and k_{110} indicate that there is an optimum g/L value for loss of energy to higher order modes. The optimum value can be obtained by using the above information with the shapes of wake functions calculated from BCI and TBCI in beam dynamics tracking programs like WAKETRAC[16], which has been successful in predicting the threshold beam current, and energy and phase spread in PETRA and LEP rings[17]. Beam instabilities for a wake field accelerator have been similarly studied[16]. It is apparent from these calculations that the conventional method of accelerator structure optimization by changing the shape to improve the shunt efficiency is inappropriate for high current accelerators. Indeed at high beam loading the overall efficiency must be optimized by considering fields excited by an external source and those by the beam.

Conclusion

Understanding of the beam cavity interaction is increasing. Effects of beam loading in a biperiodic coupled structure were observed and beam induced TM_{110} mode fields in cavities were used successfully to measure beam displacement. The injection of the beam pulse from a new high intensity pulsed gun was studied. At a current of 5.2 A, the bunching efficiency was limited by the longitudinal space charge forces. The time dependence of radial buncher fields was found to introduce significant beam emittance growth. Design codes were used to obtain information on beam induced fields in a proposed HERA proton ring accelerating cavity. This information can be used for cavity design and beam stability studies with beam dynamic tracking computer codes.

References

1. G.E. McMichael, J. McKeown and J.S. Fraser, "Beam Loading Experiments with a Side Coupled Structure", Proc. Lin. Acc. Conf., BNL-51134, 180 (1979).
2. J. McKeown, J.S. Fraser and G.E. McMichael, "Field Control in a Standing Wave Structure at High Average Beam Power", Proc. Proton Linear Acc. Conf., Atomic Energy of Canada Limited, Report AECL-5677, 291 (1976).
3. J. McKeown, "Beam Position Monitor Using a Single Cavity", IEEE Trans. Nucl. Sci., NS-26 (3), 3423 (1979).
4. K.C.D. Chan, R.T.F. Bird, M.F. Coulas, J. McKeown and Y.M. Shin, "Experiments with Beam Position Sensors", IEEE Trans. Nucl. Sci., NS-28 (3), 2328 (1981).
5. K.C.D. Chan, R.T.F. Bird and J. McKeown, "The Construction of a Pulsed Electron Gun", Atomic Energy of Canada Limited, Report CRNL-2448 (1983).
6. ECFA Study on HERA, DESY HERA 80/01 (1980).
7. K. Halbach and R.F. Holsinger, "SUPERFISH, A Computer Program for Evaluation of RF Cavities with Cylindrical Symmetry", Particle Accelerators 7, 213 (1976).
8. T. Weiland, "URMEL User Guide", DESY M82-24 (1982).
9. T. Weiland, "BCI - A Computer Program for Transient Electromagnetic Fields of Bunched Beams in Accelerators", CERN/ISR-TH/80-45 (1980).
10. T. Weiland, "Transverse Beam Cavity Interaction, Part 1: Short Range Forces", DESY 82-015 (1982).
11. E.U. Condon, "Forced Oscillations in Cavity Resonators", J. Appl. Phys. 12, 129 (1941).
12. R.B. Shields, "Gamma-Radiation-Induced Current Between Insulated Dissimilar Electrodes", Atomic Energy of Canada Limited, Report AECL-3564 (1970).
13. J. Fraser, "Subharmonic Triple Buncher for a High Efficiency Free Electron Laser", IEEE Trans. Nucl. Sci., NS-30 (4), 3115 (1983).
14. M.B.James and R.H. Miller, "A High Current Injector for the Proposed SLAC Linear Collider", IEEE Trans. Nucl. Sci., NS-28 (3), 3461 (1981).
15. "Proposal, Canadian Participation in the HERA Electron-Proton Colliding Beam Facility at DESY", The Institute of Particle Physics, Canada, 1983.
16. T. Weiland and F. Willeke, "Particle Tracing with Collective Effects in Wake Field Accelerators", to be published, presented at the 1983 High Energy Accelerator Conference.
17. T. Weiland, "On the Quantitative Prediction of Bunch Lengthening in High Energy Electron Storage Rings", DESY 81-088 (1981).

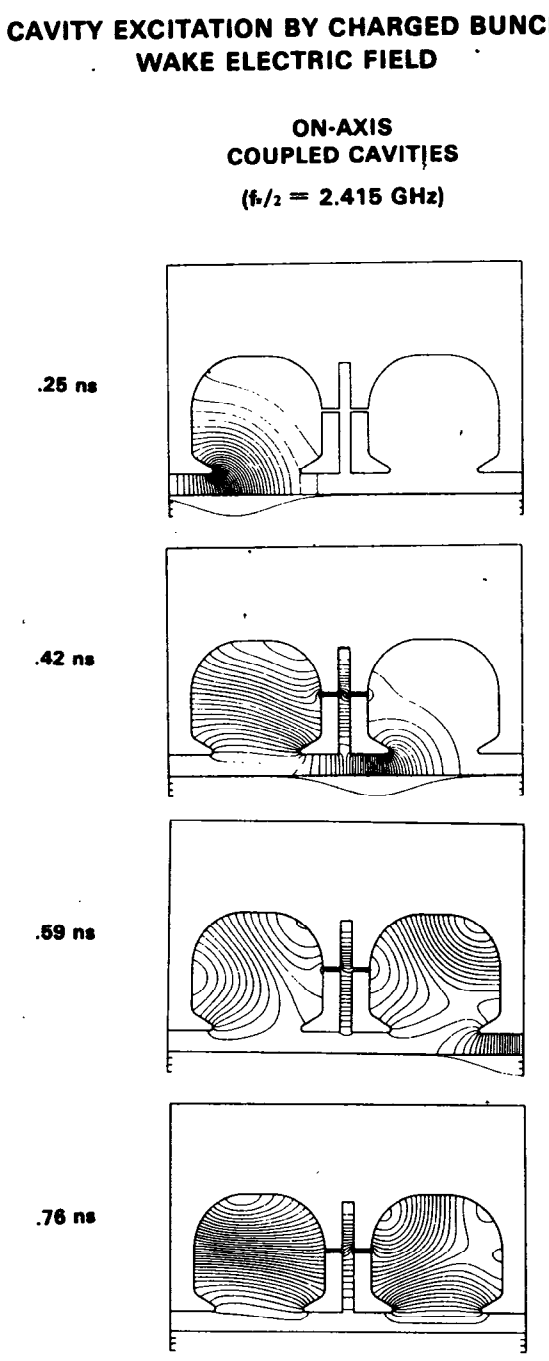

Fig. 1. A time sequence of a beam bunch passing through a pair of accelerating cavities. Induced electric fields are shown as calculated using the computer code BCI. Time zero is when the leading edge of the bunch enters the first cavity.

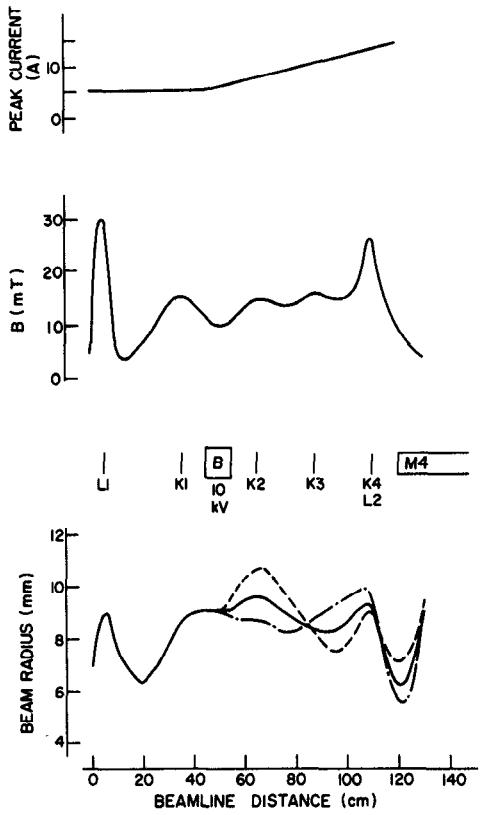

Fig. 2. Transverse beam envelope calculation. L1, L2 = gap lenses; K1, K2, K3, K4 = coils; M4 = accelerator, B = rf buncher. The solid curve is beam radius with buncher off and the dashed curves are with buncher on.

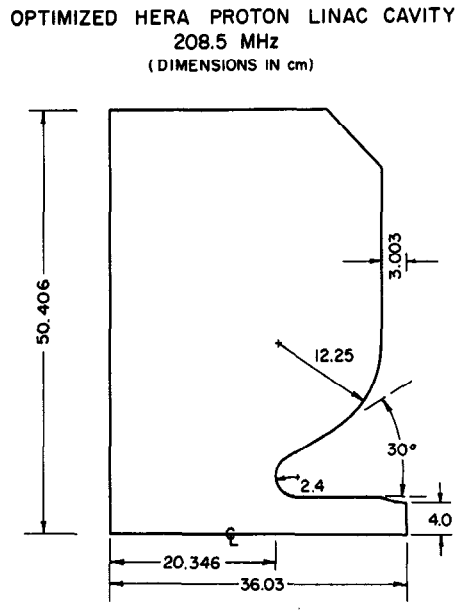

Fig. 4. A proposed cavity shape for the HERA proton ring linac. A half cell is shown with the left boundary at the middle of the cell.

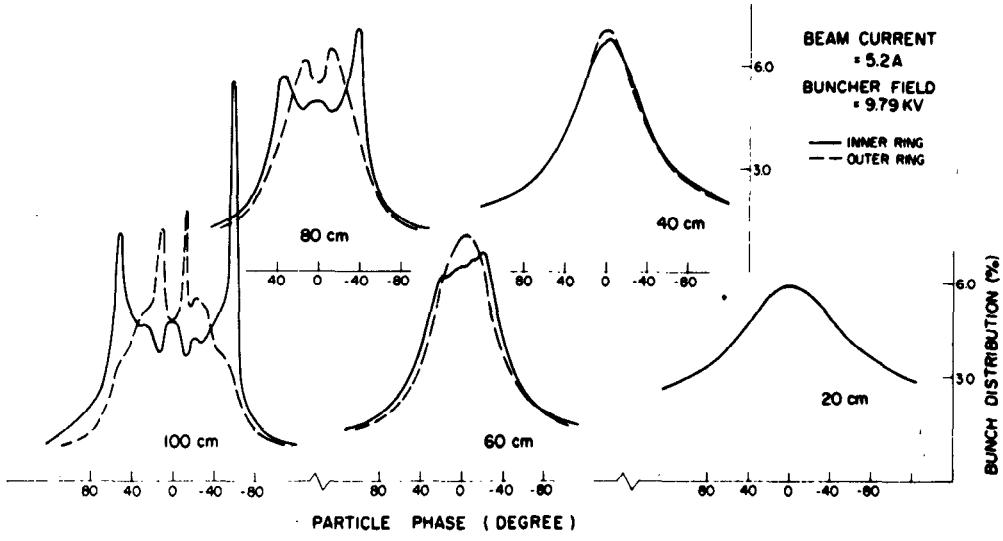

Fig. 3. Calculated longitudinal bunch shape with bunching distance for a current of 5.2 A.

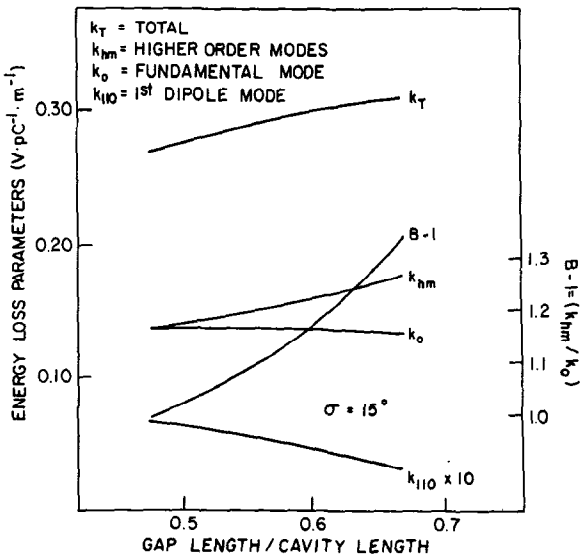

Fig. 5. The energy loss parameters. k_{hm} and k_o are for cylindrical symmetric modes. The calculation was done for a gaussian beam bunch with σ = 15° B-1 is defined as k_{hm}/k_o and is a measure of the amount of energy going to higher order modes.

Session E

Science Applications of Accelerator Based Sources

Chairman - T.M. Holden

Proceedings of International Collaboration on Advanced Neutron Sources (ICANS-VII), 1983 September 13-16
Atomic Energy of Canada Limited, Report AECL-8488

CONDENSED MATTER PHYSICS WITH NEUTRONS

R N Sinclair

Materials Physics Division, AERE Harwell
Didcot, Oxon, OX11 ORA, UK

The basic principles of the usage of slow neutrons as a probe for the study of condensed matter are presented and discussed. Various categories of experiment are defined and illustrated to show the limitations of existing neutron sources. The possibilities opened up by the introduction of advanced accelerator based sources are examined and the importance of simultaneously decreasing relative background counting rates is emphasised.

INTRODUCTION

The use of slow neutrons as a probe for the study of the properties of condensed matter has grown continuously since the first research reactors become available. Physics, in the title of this paper, must now be taken to include chemistry, biology and metallurgy in both pure and applied forms. Over a thousand papers based on the results of neutron scattering experiments are published each year. Recent reviews[1,2] have emphasised the breadth and depth of information being produced from all types of source while the proceedings of ICANS-VI[3] gives a good illustration of the quality of data obtained to date using accelerator-based sources. Today even the UK is prepared to spend the equivalent of more than US$ 20M each year on the provision of neutron sources, experimental equipment and manpower for pure condensed matter research with neutrons. At AERE Harwell, as well as our pure research programme of neutron based experiments, we have an applied neutron programme which yields a significant income from research and development programmes. Some of them come from within the UKAEA, others from other government departments and private industry. I have found myself investigating copper clustering in pressure vessel steels, metallurgy of maraging steels, the structure of nuclear waste storage glass and low energy methods for the production of ceramics and glasses.

If we take the facility at the Institut Laue-Langevin as a model for an advanced neutron source, then about 500 experiments can be expected to be performed each year which will result in about 400 research papers in the open literature. Some papers will have greater scientific significance than others. These statistics will depend on the scheduling policy adopted and it could be decided to aim for a lower throughput of key experiments.

Why is the slow neutron such a useful probe into the condensed state when available flux has been so much lower than for electromagnetic radiation sources? Put at its simplest, the reasons are fourfold.

- Slow neutron wavelengths (0.1 - 10 Å) are of the order of interatomic spacings and energies (.001 - 10 eV) covers the range of excitations up to binding energies.
- The interaction with the nucleus is via scattering lengths $b(A, I_A \pm \frac{1}{2})$ which varies unsystematically with both variables. A is the atomic weight of the isotope and I_A the nuclear spin.
- An interaction between the magnetic moment of the neutron and that of the ion produces a magnetic scattering length.
- The mean free path in an average sample is a few centimetres.

These properties combine to make the particle ideal for studying both structures (atomic and magnetic) and dynamics using bulk samples. The almost random variation of b ensures that structural information usually complements that from X-ray studies and provides the opportunity to vary the isotopic content and give extra information. When observing excitations, finite momentum is always transferred to the scattering system allowing, for example, dispersion to be uniquely investigated.

THE MEASURED-CROSS SECTIONS

The experimentalist places his sample in a beam of either white or monochromatic neutrons and measures the scattering from his sample with or without final energy and scattering angle analysis. Table 1 shows the relationship between the quantity measured and the information obtained. E and E^1 are the neutron energies before and after scattering, respectively, and 2Θ is the scattering angle. A complete measurement of the double differential cross-section over a wide range of energy transfer and scattering angle or incident energy contains all the information to describe the structure and dynamics of the system (extracting the information may well need more than one experiment). According to Van Hove[4]

$$\frac{\partial^2\sigma}{\partial\Omega\partial E^1} = \frac{\sigma}{4\pi}\left(\frac{E^1}{E}\right)^{\frac{1}{2}} S(\underline{Q},\omega) \qquad (1)$$

$$\text{where } S(\underline{Q},\omega) = \frac{1}{2\pi}\iint \exp i(\underline{Q}.\underline{r} - \omega t)G(\underline{r},t)d\underline{r}dt \qquad (2)$$

The wave vector transfer $\underline{Q}$ has magnitude

$$|Q| = \left[\frac{2m_n}{\hbar^2}\left(E + E^1 - 2\sqrt{E}\sqrt{E^1}\cos 2\Theta\right)\right]^{\frac{1}{2}}$$

and the energy transfer ω is given by

$$\hbar\omega = E - E^1$$

The double differential cross-section is thus related to a double Fourier transform of $G(\underline{r},t)$ a space-time correlation function. With present neutron sources the complete function is rarely measured completely enough in both variables (Q and ω) for structural information to be obtained. This is found from $G(r,\alpha)$ (elastic scattering, $\omega = 0$) or $G(r,0)$ (total scattering, S(Q) via a single differential experiment without final energy analysis. This means that corrections have to be made for the effects of inelasticity in the experiment. Limited structural information can be obtained from an even simpler measurement; that of the total scattering cross-section as observed in a transmission experiment which integrates over both final energies and scattering angles.

EXAMPLES

I have chosen three examples of areas where pulsed neutron experiments at accelerator based sources are attempting to solve long standing problems in respect of three very common materials - mild steel, vitreous silica and ice. It perhaps means that the new sources are performing as expected if useful contributions can be made for such well studied materials. Most of the experiments were made at the Harwell electron linac pulsed source[5] which has a low fast neutron source strength at present of 10^{14} fn/sec and thirteen instruments in routine operation or development.

Internal Stress in Steels

Internal stresses within a sample are difficult to measure but can be important. Weld failures may arise from propagation of cracks due to residual stress around a weld. Conventional measurements are made with strain gauges and a stripping technique or X-ray diffraction which only observes surface strains. Other techniques are very sensitive to texture. Neutron diffraction experiments[6] can observe stress in a bulk sample via a corresponding lattice strain. There is an extention of the lattice spacings d along the stress and a contraction perpendicular to the stress and a fractional change is observed between 10^{-3} and 10^{-4}. Experiments on welds of commercial importance are underway with the aim of optimising the welding technique. Recent measurements have revealed the variation of the strain for different lattice spacings and directions in an experiment with a rectangular bar stressed beyond its elastic limit. Work is in hand to try to reduce the data via the known elastic constants to see if a simple interpretation is possible. The widths of the observed Bragg peaks is also a function of the stress and indicates the regions where microscopic strains occur.

The shifts due to stress can also be seen in a measurement of the total cross-section as a function of wavelength (λ) since an edge is produced when $\lambda = 2d$. The edge is assumed to be rectangular and appears broadened only by the resolution function of the spectrometer and any material effects. Recent data from a transmission spectrometer on the same bent steel bar have shown that the edges can be fitted accurately and used to derive the average strain through the bar. The results so far are in good qualitative agreement with the diffraction results and show that strain measurements can be made very rapidly by this technique. With the increasing availability of area neutron detectors, it may be possible to make stress measurements simultaneously with millimetre resolution and perform stress radiography.

Structure of Vitreous Silica

This subject has been brought to the forefront again by a recent paper by Phillips[7]. Over recent years a continuous random network model of SiO_4 tetrahedra has been accepted as satisfying the experimental evidence from many techniques. Phillips believes that the failure of such models to predict the details of observed vibrational spectra means that a model based on paracrystalline regions is necessary. He supports this view by citing some electron microscopy evidence and also the failure of hand built and computer built random models to fit the measured total pair correlation function. His model comprises 50 A diameter paracrystalline regions of β-cristobalite with surfaces stabilised by a large number of Si = O bonds. Pulsed neutron experiments offer the best opportunity to study the Si - O bond length distribution and coordination. Gaskell[8] has compared our results[9] to a variety of random network models and finds the comparison to be relatively insensitive to the medium range structure or topology. However none of the models gives a good representation of the data in this region. The evidence for the existence of Si = O would come from an analysis of the first peak in the correlation function. To date there is no evidence for a distribution of bond lengths such as might be given by a mixture of Si - O and Si = O[10] The way forward however is clear in this respect. More accurate diffraction data to Q values up to 60 A^{-1} will reduce experimental widths in the correlation function and enable a more accurate analysis of the first peak.

Phillips basic objection is however to the prediction of polarised Raman spectra and the density of vibrational states as measured by neutron inelastic scattering. Raman spectroscopy is difficult to interpret uniquely so a full high resolution measurement of $S(Q,\omega)$ is needed to derive a density of states that can be closely compared to model predictions. The source at Harwell is not capable of this and progress must await experiments with progressively stronger sources.

The Dynamics of Ice

Although the vibrational spectra of H_2O at low temperatures has been extensively studied, it is only the advent of accelerator based sources with a relatively rich epithermal energy spectrum that has allowed neutron measurements to reach the intramolecular vibration region with any accuracy. The problem has been that the vibrational density of states extends up to nearly 0.5 eV. As well as being of interest to established the force constants applying to the ice structure for its own sake, it is hoped that a thorough understanding may lead to a better picture of the structure and dynamics of amorphous ice and water. Measurements published this year[11] have at last succeeded in obtaining a clear picture of features in the density of states to its upper limit. The width of the O-H stretching mode was found to be in close agreement with optical data. A more complete experiment has recently been performed with IPNS[12] spanning a region of $S(Q,\omega)$ which enables the assignment of features to be critically examined. One of the great advantages of neutron spectroscopy over optical spectroscopy is the absence of selection rules.

The other major advantage lies in the ability to directly measure the dispersion of excitations in chosen directions in a single crystal sample. In an experiment with the Constant-Q spectrometer at Harwell, the dispersion of the O-D stretching modes in a single crystal of heavy ice was observed[13] for the first time. Several flat branches were found in the energy range between 230 meV and 330 meV. Although this was an incomplete experiment, it did demonstrate the capability of accelerator based sources to provide the most detailed dynamical information in previously inaccessible region of energy transfer.

POSSIBILITIES WITH ADVANCED SOURCES

Almost all of the results discussed above come from experiments with a low flux accelerator-based source. It is interesting to speculate on the effect of increased source strength on the scientific applications.

a) Improved Statistical Accuracy and/or

Resolution
- leading to more detailed and accurate interpretation.

b) More Samples can be Studied
- systematics in alloy systems, temperature variation etc, can be extended. Applied experiments become more attractive.

c) Smaller Samples can be used
- isotopic substitution with rare isotopes becomes possible and the study of difficult to grow single crystals. Small samples mean easier to make multiple scattering corrections.

d) More Accurate Techniques can be employed
- more structural derivations based on $S(Q,\omega)$ measurements or elastic diffraction, more polarised neutron experiments.

e) New Experiments
- mainly deriving from the rich epithermal spectra or the pulsed nature of the source. An extended range of excitations involving small cross-sections could become possible. Diffraction with short wavelength neutrons can minimise corrections for inelasticity. Kinetic experiments on relaxation phenomena.

The count rate an experimentalist records contains two components. Firstly, the signal from the sample which is proportional to the flux incident on the sample, the number of atoms in the beam and the desired cross-section. Secondly, there is a background component which has to be measured separately and subtracted. The consequences c) d) and e) above in particular rely in many cases in improving the signal to background ratio as the flux on the sample is increased by moving to a more powerful source. This arises since the criterion for a minimum sample size or limit of energy transfer often comes from an unacceptable signal to background ratio. The requirement is that the background does not go up in proportion to the flux on the sample. Pulsed accelerator-based sources are in a favourable situation here since the fast neutron source is switched off during the experiment. The remaining problem is to deal with the fast neutrons which have interacted with the sample and shielding materials and this becomes more important as the neutron energy used in the experiment is raised. In this energy region (> 1 eV) the background in the beam itself can be important and it is no longer good enough to remove the sample to measure the background. This discussion emphasises the need for innovatary source, beam tube and instrument design as the flux is raised, so that scientific results can be gathered in new areas.

References

1. "The Neutron and its Applications (1982) Ed P Schofield (Inst of Phys Conf Series 64).
2. "Neutron Scattering in Biology, Chemistry and Physics" Phil Trans Roy Soc B 290 (1980)479-681.
3. "ICANS-VI", Argonne Lab Report ANL-82-80.
4. Van Hove, L., Phys Rev 95 (1954) 249-262.
5. Windsor C.G., and Sinclair R.N., Phys Bull 33 (1982) 290-292.
6. Allen, A., Andreani, C., Hutchings, M.T., and Windsor, C.G., NDT International, October 1981.
7. Phillips, J.C., Solid State Physics 37 (1982) 93-170.
8. Evans, K.M., Gaskell, P.H., and Nex, C.M.M., "The Structure of Non Crystalline Materials 1982" (Taylor and Francis, 1983) 426-438.
9. Wright, A.C., and Sinclair, R.N., (1978) "Physics of SiO_2 and its interfaces". Ed Pantelides, S.I. (Oxford, Pergamon) 133-138.
10. Johnson, P.A.V., Wright, A.C., and Sinclair, R.N. J Non Cryst Solids (1983). In Press.
11. Andreani, C., Boland, B.C., Sachetti, F., and Windsor, C.G., J Phys C 16 (1983) L513-L516.
12. Andreani, C. Private Communication.
13. Andreani, C., Bosi, P., Muzzega, E., Sachetti, F. and Windsor, C.G., J Phys C 16 (1983) 3055-3060.

TABLE 1

QUANTITY MEASURED	CLASS	INFORMATION DERIVED	RANGE	SCIENTIFIC FIELDS
$\sigma_s(E \to E^1, 2\theta)$; $\frac{\partial^2\sigma}{\partial\Omega\partial E^1}$ barns $st^{-1}eV^{-1}$	Inelastic	Dynamics [Structure]	10^{-6}eV → 1eV	Tunnelling, Molecular Spectroscopy, Diffusion, Surface Studies, Lattice Dynamics, Amorphous Dynamics, Spin Dynamics, Momentum Distribution
$\sigma_s(E,2\theta)$; $\left(\frac{\partial\sigma}{\partial\Omega}\right)_{eff}$ barns st^{-1}	Diffraction	Structure [Dynamics]	1000 Å → 1 Å	Biological Structures, Mixed Phase Systems, Crystallography, Magnetic Structures, Amorphous Structures, Surface Structures, Molecular Structures
σ_s (E) Barns	Total Scattering Cross-section	Structure [Dynamics]	1000 Å → 1 Å	Mixed Phase Systems, Applied Crystallography, Amorphous Structures, (Multiple Scattering Corrections)

Proceedings of International Collaboration on Advanced Neutron Sources (ICANS-VII), 1983 September 13-16
Atomic Energy of Canada Limited, Report AECL-8488

NUCLEAR AND PARTICLE PHYSICS WITH HIGH INTENSITY PULSED NEUTRON SOURCES

T. Dombeck

University of California
Los Alamos National Laboratory
Los Alamos, New Mexico 87545

Summary

Prospective high intensity pulsed neutron sources should have profound implications in nuclear and particle physics not only in studies involving neutrons but also neutrinos and muons. This talk surveys the physics interests in the experiments that can be performed. The running conditions and target requirements necessary to optimize each experiment are also discussed. A comparison is made between the experimental results possible at current facilities and those possible with the highest intensity sources under consideration for the future.

Introduction

The development of high intensity pulsed neutron sources (10 to 200μA) at Tsukuba,[1] Argonne,[2] Los Alamos,[3] and Rutherford[4] laboratories will open new frontiers in nuclear and particle physics just as they are now doing in condensed matter research. Other sources of still higher intensity (5mA) as porposed at Julich[5] and Argonne[6] should extend this research even further. As scientists look deeper into the potential of these sources, it becomes evident that they will be important not only for neutron related studies but also for neutrino[7,8] and muon[9] studies; all of which have generated great interest in the physics community.

For nuclear physics studies the energies of the various probes, neutrons, neutrinos and muons available from these pulsed sources (~ many MeV) match the levels inside the nucleus. Furthermore, the high intensities produced permit searches for rare processes to test symmetry rules in particle physics. The pulsed nature of these sources reduces backgrounds and allows energy determination by time-of-flight techniques. In the next section I will discuss in detail the advantages and unique capabilities that pulsed sources provide for each type of particle probe. I will emphasize the running conditions that will optimize each case. Because of familiarity, I have relied on event rates, etc., as observed at the neutron scattering (WNR) complex at Los Alamos (see Fig. 1); however, extrapolations can easily be made for performance at other sources.

The last section of this talk describes specific experimental topics to be addressed at high intensity pulsed sources of neutrons, neutrinos and muons. The list is by no means intended to be a complete overview but to provide more of a flavor for the physics of interest.

Optimized Running Conditions

Neutrons

A large class of nuclear scattering experiments require neutrons from the high energy part of the spectrum (0.1 to 800 MeV) generated in spallation sources, but not found in reactor beams (see Fig. 2). Short pulse widths are required to allow a determination of the neutron energy by time-of-flight techniques. Because of the higher energies involved moderators and reflectors are not relevant and usually thinner

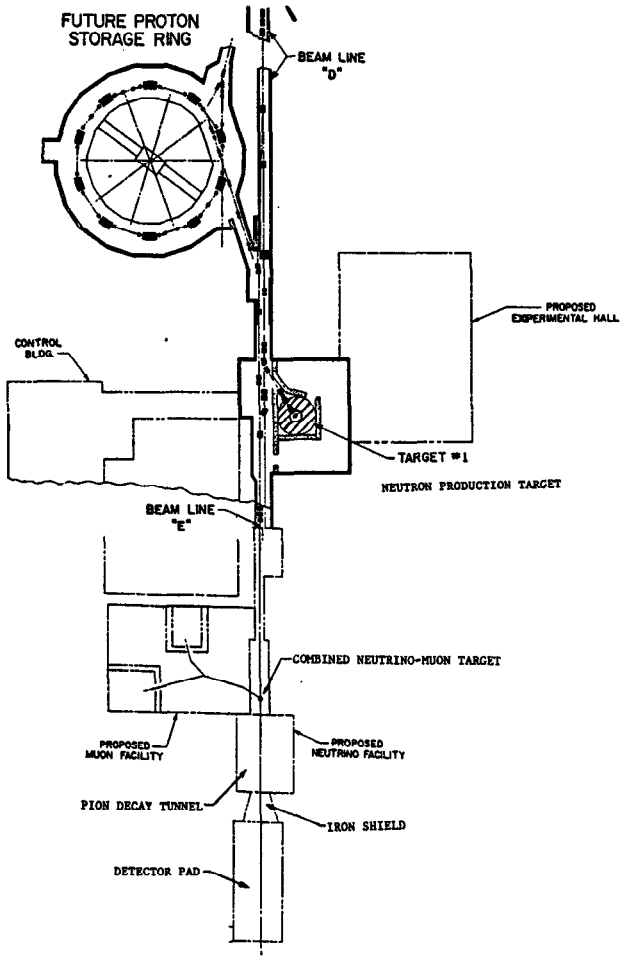

Fig. 1 A schematic diagram of the WNR complex at Los Alamos National Laboratory is shown. Existing and future facilities are pointed out.

diameter or shorter length targets than used for condensed matter research are employed so as not to degrade neutron energies or pulse widths. Also, as discussed below, the target has a higher-Z to enhance neutron production than that required for neutrino or muon production.

Neutrons in the 0.1 to ~100 MeV range can be viewed at right angles to the incident proton direction. This requires a thin diameter (~1cm) target in order not to degrade pulse widths. The best energy precision in time-of-flight requires pulses ≤1ns wide, which is more restrictive than that required for condensed matter research. The very high energy neutrons (>100 MeV) are produced at small angles and require a short target to maintain pulse widths. Here pulse widths of a fraction of a nanosecond are required for best results. For neutrons produced near 0° there is

another potentially useful feature. A high polarization due to Schwinger scattering[10] can be achieved.

Another class of particle physics experiments requires neutrons at the opposite end of the spectrum, i.e., ultracold neutrons (UCN). These long wavelength neutrons can be stored for long periods in material bottles[11] thus increasing the measurement time for experiments on fundamental properties of the neutron. A Doppler-shifting technique has been developed at

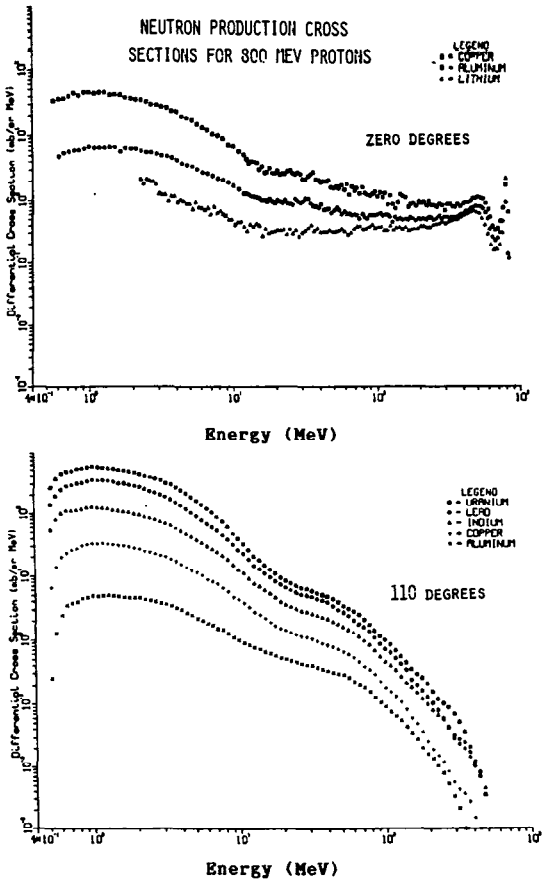

Fig. 2. High energy neutron production cross sections for various target materials are given for 800 MeV incident protons. The data were taken at Los Alamos.

Argonne[12] to generate UCN at pulsed neutron sources. It has been shown that UCN can be stored with this technique at a density corresponding to the peak intensity of the source, which can be much higher than at a reactor.

A UCN source can use the same target-reflector system required for condensed matter research with the addition of a cold moderator. However, for optimum running conditions the moderator should be isolated from decouplers and poisons that absorb the low energy tail of the neutron spectrum. Furthermore, to take full advantage of the peak intensity of the source, the Doppler-shifter should be placed as close to the moderator as practical to avoid pulse broadening due to a long flight time. For example, if the Doppler-shifter were placed 500 cm from a cold moderator at the WNR and using 100μA of Proton Storage Ring (PSR) beam, it is estimated that a 30ℓ bottle can be filled to ~250 UCN/cm^3. The Doppler-shifter makes use of neutrons around 400m/s. Their pulse width after the 500 cm flight path is ~250μs which matches the pulse width emerging from the cold moderator that is dominated by the neutron slowing-down time. Of course if the pulse rate can be increased, as planned at higher intensity sources,[5] the filling rate will permit larger bottles. Nevertheless, the stored density of UCN cannot be increased unless the peak neutron flux is increased. This may be possible at the higher intensity sources[5] with the addition of accumulator rings or at the WNR with a boosted target yielding more neutrons per proton.

Neutrinos

Neutrinos result from pion production in the source. The pion decay chain yields neutrinos through the reactions

$$\begin{aligned} P+N &\rightarrow \pi^+ + X \\ &\quad\hookrightarrow \mu^+ + \nu_\mu \\ &\qquad\hookrightarrow e^+ + \nu_\mu + \bar{\nu}_e \quad . \end{aligned} \tag{1}$$

If a π^- meson decays, the neutrinos and anti-neutrinos in (1) are interchanged. Thus by sign selection of pions, a pure beam of one type of neutrino over another type can be generated. Another way to isolate a specific type of neutrion is by timing. The pion decay time is 26ns while that for the muon is 2.2μs, allowing in principle a separation of the various neutrino types in the decay chain (1) if the incident proton burst has a width no more than a few hundreds of nanoseconds. In the discussion that follows I will discuss the three major methods to produce neutrino beams and their properties; (i) beamstop sources; (ii) in-flight pion decay beams, and (iii) muon bottle sources.

In the beam stop source, such as the one in operation at the Los Alamos Meson Facility (LAMPF) line A beamline,[13] a long target with a large diameter is employed to interact all the protons, to contain the generated pions and to degrade their energy until they come to rest. Capture rates for π^- mesons are large in all substances and they are eliminated by absorption before they can decay. Capture rates for π^+ are small if low-Z targets are used. Thus, only π^+ mesons and their associated neutrinos survive. The

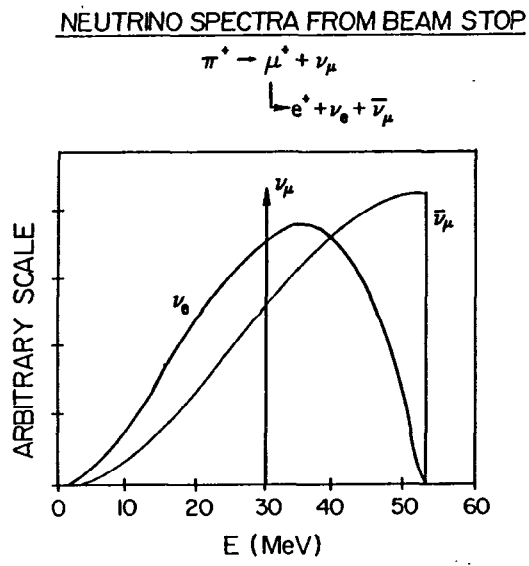

Fig. 3. The neutrino energy spectra for each type of neutrino produced in a beam stop source is shown.

subsequent μ^+ from these decays will also come to rest in the target and decay. The energy spectrum of the resulting neutrinos is shown in Fig. 3. Note that the stopped pion decay is two-body and results in a nonoenergetic ν_μ ~30 MeV and with a line width of a few keV. The muon decays yield neutrinos with a Michel spectrum.

Fluxes of 5 x 10^7 ν/cm^2-s for each neutrino type have been observed at a 6 m distance from the LAMPF line A beam stop with an incident current of 600μA of protons at ~600 MeV. One disadvantage of the LAMPF source is the long pulse width (~500 μs) making it impossible to separate neutrinos by timing. At LAMPF this will be rectified when the PSR is available.[7] At the Spallation Neutron Source (SNS) in England, a stopping beam of neutrinos has been proposed using the same target where spallation neutrons are being produced.[8] This latter source will not be optimized because of the high-Z material in the target which will result in half the π^+ mesons being absorbed when compared to the Cu-water beamstop at LAMPF. Even so, the reduced pulse width at the SNS (~100ns) does permit timing separation of neutrino types and the SNS experiment will have a lower cosmic ray background rate in the detector than the on-going LAMPF experiment.[13] This should permit lower energy thresholds to be used resulting in comparable event rates for the two experiments.

Higher energy neutrino beams can be produced by in-flight decays of pions and muons. In each case, a low-Z target (generally carbon) with a small diameter is employed which permits the generated pions to escape without much absorption or energy loss. The pions are permitted to traverse a 12-m-long free region of space and decay in-flight (see Fig. 1). Because the pions are moving upon decay, the neutrinos are generally directed forward so the detector is placed at the end of the decay channel but behind about 9 m of iron shielding which keeps neutrons from the target from striking the detector. Both π^+ and π^- escape the target and decay in-flight yielding ν_μ and $\bar{\nu}_\mu$ fluxes with energy spectra shown on Fig. 4 for an 800 MeV incident proton beam.

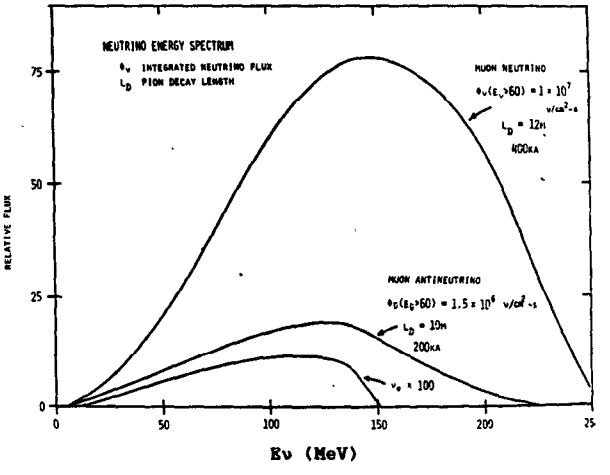

Fig. 4. The neutrino energy spectra for an in-flight pion decay source are shown for 800 MeV protons incident on a carbon target.

The pion beam originating off the target has a broad angular divergence and as much as an order of magnitude increase in neutrino flux can be gained through a magnetic focusing device placed in the pion beam. This "horn" device is a shaped current sheet as shown on Fig. 5. It turns the large angle pions parallel to the decay channel axis such that their decay neutrinos are more likely to hit the detector. In Ref. 7, it has been estimated that ν_μ fluxes in excess of $10^7 \nu/cm^2$-s and $\bar{\nu}_\mu$ fluxes of ~1.5 x 10^6 ν_μ/cm^2-s are possible for 100μA of incident protons at 800 MeV. The horn can sign select the pions by defocusing the unwanted ones, yielding pure beams of either ν_μ or $\bar{\nu}_\mu$. The beam is also free of ν_e background to the 0.1% level. These can arise from the

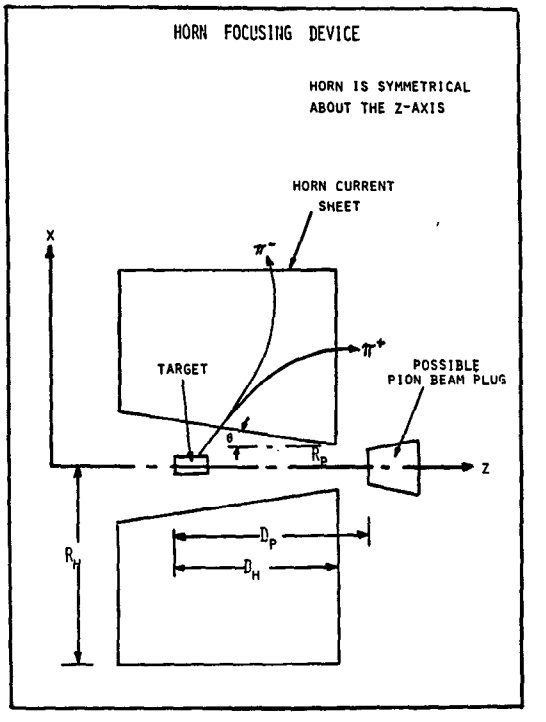

Fig. 5. A magnetic pion focusing device composed of a single current sheet is shown schematically relative to the production target.

muons which originate from pion decays in the channel. However, muons require a decay path of many kilometers due to their long lifetime and this accounts for their low number of decays for a 12m decay channel. (Below, I discuss how pure ν_e beams can be generated by employing muon bottles.)

The parent pions in the decay channel have relatively low energies and are not relativistic. This fact and the large pion energy spread results in a useable correlation between the kinetic energy of the neutrinos and their arrival times in the detector. If a pion decayed close to the target, the neutrino moving at the speed of light would arrive in the detector (a distance ~21m) in ~70ns. If part of the flight path were taken up by the pion before it decayed, the time of arrival would be later for the neutrino with the time difference given roughly by

$$\Delta t = \frac{\ell}{c}\left(\frac{1}{\beta} - 1\right), \qquad (2)$$

where ℓ is the pion flight path. Taking ℓ ~6m (half the decay channel length), and $0.75 \leq \beta < 1$ for pions produced by 800 MeV protons, the arrival time differences have a range from 0 to 5ns. The higher energy neutrinos are the products of the higher energy pions

(larger β) and it is expected these neutrinos will arrive sooner in the detector than the lower energy ones.

Another factor which enhances the timing separation is that the neutrino production angle is thrown more forward in the laboratory as the pion energy increases. Thus, a low energy pion decaying near the target is less likely to have its neutrino hit the detector than a similar pion decaying at the far end of the decay channel. This is because the ratio of detector solid

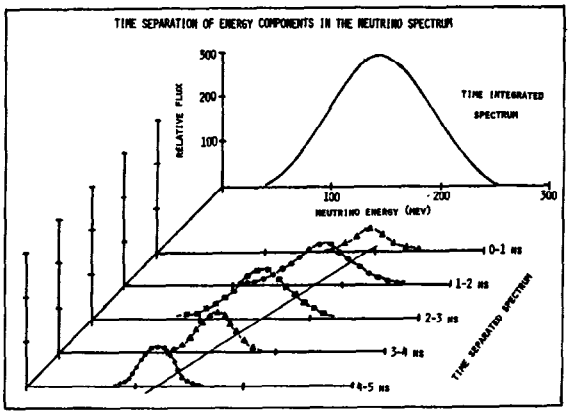

Fig. 6. The neutrino-energy-arrival-time correlation in the detector is shown as computed using a Monte Carlo calculation.

angle to the decay solid angle is less at the target end of the decay channel than it is at the detector end. Therefore, the low energy neutrinos in the detector will have resulted from pions that travelled a large portion of the flight path at the relatively low β yielding the longest arrival times.

The results from our Monte Carlo computer simulations[7,33,34] for the WNR neutrino beam is shown on Fig. 6. All neutrinos above ~60 MeV cross the same plane in the detector separated by at most 5ns in arrival times. This fortuitously matches the LAMPF pulse microstructure which is 1/4ns wide pulses separated by 5ns. We find that the average neutrino energy decreases by ~20 MeV/ns and in each 1ns wide bin the energy spectrum has a $\Delta\sigma/E$ ~ 12 to 16%. This can be compared to the time integrated spectrum which has a 35% width. Therefore measuring neutrino arrival times in the detector relative to the LAMPF microstructure should yield an unprecedented precision on the incident neutrino energy for such experiments.

As I pointed out, the timing-energy correlation is a result of the relatively low energy pions generated at LAMPF. Some portion of this correlation will probably survive for incident proton energies up to a few hundred MeV higher in energy, but probably disappears around 1.5 to 2 GeV where most pions are relativistic. Though I have not investigated the correlation at higher energies, I believe that longer decay channels (>12m) will be necessary to enhance any residual effect.

As one final remark about the timing correlation, neutron backgrounds in the neutrino detector resulting from proton interactions in the target and beam stop arrive at times >20ns relative to the neutrinos. Unfortunately, frame overlap does not permit a separation of these neutron backgrounds using the LAMPF microstructure. In some neutrino experiments where event rates are relatively high but low neutron backgrounds are important, the PSR in the short pulse mode (1ns wide pulses at 720HZ) may provide a means to perform these measurements in a background free environment while allowing full advantage of the neutrino energy-timing correlation as well.

All of these timing considerations should be kept in mind for future generations of pulsed sources. It may be important to retain some microstructure in the beam at the highest intensities, even if this means throwing away some of the flux by chopping, to obtain the highest precision measurements.

The last neutrino source I wish to discuss uses a muon bottle.[14] In order to obtain higher energy electron neutrinos (ν_e) from muon decays than result in a stopped source, an in-flight method is necessary. However, the long muon decay times translate into long flight paths. The only practical means to produce a source is to bend the muon path into orbits in a magnetic trap. A low-Z target is embedded into a dipole magnetic field such that pions emerging from the target are trapped in orbits in the magnet gap. The pions decay and a portion of the muons are also trapped by the field. In Ref. 14, it is estimated that a source of ν_e can be produced with a relatively planar flux of about 10^6 ν/cm^2-s for 100 μA protons incident on the target. The optimum proton energy depends in part on the magnet pole face diameter and on the field strength. For a 5T field in a 1.5m diameter gap a proton energy near 650 MeV is optimal. Noone has yet made a muon bottle as it requires superconducting technology in a high radiation field. It should be pointed out that all the timing separation of neutrino types discussed above for the beamstop source apply to the muon bottle as well.

Muons

Muons are the decay products of pions through reactions given in (1). There are two types of muon sources; (i) a surface beam, and (ii) an in-flight pion decay beam. Both sources require a target of low-Z material with a thin diameter (~5cm) to reduce absorption of the parent pions. In general, low momentum muons (<80 MeV/c) are desired for most applications and these are the products of low momentum pion decays (<160 MeV/c) which have a maximum production at angles greater than 90° off the target (backward angles).[9] Because the target parameters are similar for in-flight neutrino production as well as muon production it may be possible to have a combined production target; the neutrinos originating from higher energy forward pions and muons originating from lower energy backward pions.

A surface muon beam arises from the decay of positive pions at rest in the skin of the target. Such muons have a momentum of 30 MeV/c and are 100% polarized. Negative muons cannot be made this way because all stopped π^- mesons are absorbed in the target. Negative muons or higher momentum positive muons are obtained only from in-flight pion decays. In this case, a beam transport including a long superconducting solenoid in which the pions decay is necessary to enhance the yield of muons. With either type of muon source the spread of momenta is large and requires a special achromatic transport to allow a large acceptance of muons. For instance in Ref. 9 it is estimated that a 100 μA beam of protons at 800 MeV will produce 8 x 10^7 μ^+/s from an in-flight source with a 20% momentum acceptance. This beam will have about 70% polarization. A negative muon beam will be down by a factor of four or five from the positive. A surface beam of 2 x 10^7 μ^+/s and with a 10% momentum spread can also be produced by this source.

The timing characteristics of the muon beam are also important and can change from one class of experiments to another. Some experiments require high powered pulsed lasers to pump transitions. These are best matched by muon beams having a width of one nanosecond up to a few hundred nanoseconds. Enhancements of up to 10^5 in event rates over a dc-experiment are possible.[9]

Discussion

The characteristics and special requirements for neutron, neutrino, and muon pulsed sources are given in Table I. These requirements of target parameters and pulse widths for the incident protons are generally incompatible, except perhaps for muon and in-flight pion decay neutrino beams. This suggests that shared operations will be required to meet all requirements, either by real-time scheduling of beam or by multiplexing proton current to different target stations. Both of these methods are being employed at the WNR complex at Los Alamos to allow a broad physics program to exist.

The Los Alamos facilities; some of which are in operation, under construction or proposed, are shown schematically in Fig. 1. Not shown is the Line A beam-stop neutrino source which is to the east of LAMPF whereas all WNR facilities are to the south. The main WNR target cell can be used for nuclear neutron experiments by the replacement of the target for condensed matter research with one more appropriate for nuclear physics. Because the proton beam strikes the target vertically, the flight paths can only view the target at 90°. For the highest energy neutrons a separate target and beam is situated in the Line D tunnel and is viewed at 0° by a flight path going straight out to the south. These two target stations cannot be used simultaneously because different settings of dipole bending magnets in the proton channel are required in each case. At present both beams use chopped LAMPF macropulses to achieve high resolutions in time-of-flight.

The in-flight neutrino facility is under construction just to the south of the Line D channel. It will have a target about 50m away from target cell one. At present it will be fed LAMPF macropulses in a multiplexed mode eventually sharing pulses with PSR and running simultaneously with all other programs at the WNR. It is hoped that PSR beam can also feed the neutrino target by further multiplexing with the WNR. This would permit a muon physics program veiwing the neutrino target at backward angles as well as an extension of the neutrino program using the PSR duty factor reduction, simultaneously a neutrino program using LAMPF macropulses, and if current permits a full neutron scattering program at the WNR, all at the same time.

As can be seen by the above remarks, there are many targets stations at Los Alamos and a complex plan for multiplexed operation to allow beam time to each user. The reason that this scheme is possible is due to the high intensity of proton currents (~1mA) available from LAMPF. and the fact that no single user at this time can use it all. In fact, shielding in the WNR limits the maximum current to about 100μA of protons for neutron scattering, leaving current for other targets. This is perhaps an historical accident and will not be the case at other pulsed sources.

The research program at the SNS at Rutherford Laboratory is more concentrated than at Los Alamos. The full 200μA beam at the SNS can be accomodated by the neutron target and almost all of the available current will be used for neutron production. Therefore, the neutrino source (stopped) must use the same target which has not been optimized for neutrinos. Also, I do not believe there is an in-flight neutrino source planned at this time.

The SNS machine will have a pulsed muon program centered around a 5-cm-long carbon target placed upstream of the neutron target. The muon source is designed primarily as a surface beam without an in-flight decay beam. It should provide a total μ^+ flux in two 100ns bursts about twice that quoted in Ref. 9 for Los Alamos. However, a chopper will be required for shorter pulse widths which will reduce the muon flux to about 1/3 that at Los Alamos where PSR can

Table I. Characteristics and Requirements for Pulsed Sources of Neutrons, Neutrinos, and Muons for Nuclear Physics Studies

Source	Energy or Momentum Range	Target Specifications	Pulse Width Requirements	Comments
Neutron	10^{-6} eV (ultracold)	High-Z, large diameter	~200μs	requires cold moderator
	0.1 to 25 MeV	High-Z, thin diameter (~1 cm)	$\lesssim$-1ns	neutrons viewed at 90°
	>25 MeV	High-Z, short length	~500 ps	neutrons viewed at 0°
Neutrino	0 to 53 MeV (ν_μ,ν_e stopped source)	Low-Z, large diameter, stopping length	~200 ns	timing allows separaation of neutrino types
	60 to 300 MeV (ν_μ in-flight source)	Low-Z, thin diameter, ~1 interaction length	$\lesssim$1ns	timing allows E_ν determination
	50 to 150 MeV (ν_e in-flight source)	Low-Z, thin diameter	~200 ns	Muon bottle required
Muon	30 MeV/c (μ^+ surface beam) 50 to 80 MeV/c (μ^+ and μ^- in-flight)	Low-Z, ~5 cm diameter	<1 to 300 ns	view target at backward angles

generate the short pulse widths. The double target scheme will probably degrade the proton flux on the neutron target by about 15% which should be acceptable to the condensed matter program.

The basic imcompatibility between the different nuclear physics and condensed matter sources is inherent in the target specifications and pulse width requirements for each case. This incompatibility will persist at the higher intensity sources being designed now unless they have enough current to service all users simultaneously. I suspect this is a hollow dream because each user would like to take full advantage of all the available current for his specific program; this is especially true for neutrino experiments where event rates are so low. Thus, each target station will probably be designed for the maximum current. Therefore, if a broad program including nuclear and particle physics is desired, special consideration must be given to scheduling the proton beam. This sharing should be possible as no user can use all of the beam all of the time. However, it implies that the laboratory will require a broad based program advisory committee to help set its priorities.

Details of the Physics Interest and Experiments for Nuclear Physics Studies at Pulsed Sources

Theoretical Introduction

The following discussion about modern ideas of particle structure and the forces of nature is cursory and intended to provide a backdrop for the experiments that can be performed at high intensity pulsed sources. The discussion borrows from various reviews and popularized articles to be found in the literature, such as Abdus Salam's Nobel Prize acceptance speech[27] and Ellis-Nanopoulos on cosmology.[28]

Most experiments in nuclear and particle physics are designed to test symmetry properties in nature. Some of these symmetries involve the space-time properties of the interactions between particles, such as parity and time. Other symmetries involve the underlying classification or grouping of particles by their similar properties, such as charge, spin, color, isospin, etc.

The "standard model" claims that the universe is composed of fermions interacting by the exchange of bosons. All observed fermions are left-handed, i.e., spining counter-clockwise along the direction of motion, which would be an exact statement if the fermions were massless. Anti-particles are right-handed. The elementary fermions can be grouped into families, known as the SU(3) xSU(2)xU(1) grouping

$$\begin{pmatrix} u \\ d \end{pmatrix} \quad \begin{pmatrix} c \\ s \end{pmatrix} \quad \begin{pmatrix} t \\ b \end{pmatrix}$$
$$\begin{pmatrix} \nu_e \\ e \end{pmatrix} \quad \begin{pmatrix} \nu_\mu \\ \mu \end{pmatrix} \quad \begin{pmatrix} \nu_\tau \\ \tau \end{pmatrix} , \qquad (3)$$

the top row refers to quarks which comprise the hadrons. The bottom row refers to the leptons which can be placed in one to one correspondence with the quarks. There are specific questions which such a classification scheme produces. How many families are there? Are the leptons on the same elementary level as the quarks which compose protons and neutrons, rather than on the level of the protons and neutrons? For example, we know that the quarks found in nature are admixtures of the ones given in (3), i.e, they exhibit mixed properties. Do leptons exhibit a similar behavior, and is the relative admixture the same as for quarks? Such a mixing of leptons could appear as a transformation or oscillation of one type of neutrino into another.

Another question is whether the scheme (3) is the manifestation of a higher group symmetry, i.e., do quarks and leptons have a substructure such that they are all composed of the same subparticles? This unification of leptons and quarks into the same larger group, say SU(5), permits new interactions which can transform quarks into leptons. In this scheme Baryon number is not conserved and protons can decay. Furthermore, neutrons may be able to oscillate into antineutrons ($\Delta B = 2$ interaction).

The boson exchange involves particles such as the γ, $W^{\pm}$,Z°, gluons and gravitons, which mediate the forces in nature. Are all of these particles just different manifestations of the same substructure? Can all the forces be unified within the same picture? Indeed Weinberg and Salam recently found a theory that joins the electromagnetic and weak forces; the γ, Z°, and $W^{\pm}$ particles. They predicted neutral currents in weak interactions and many other effects in nuclei; the testing of which is the goal of many planned experiments. Out of this theory came one fundamental parameter, the Weinberg angle θ_W, giving the relative weak-electromagnetic strengths. A precision measurement of θ_W would yield information such as how many families of quarks and leptons there are, and which of the higher groups, (SU(5), O(10), etc) used in unification schemes is correct.

The space-time symmetries of the interactions in nature are not necessarily conserved. For instance, parity is not conserved by weak interactions and this is related to why only left-handed fermions have been found. Is the universe truly asymmetric or can we find evidence for right-handed particles? Another violated symmetry is time, which has appeared in nature in only one interaction in the K° -$\bar{K}^{\circ}$ system. What is its nature and are there other reactions where T is violated? In fact, it has been suggested that the small T violation that has been observed may explain the basic asymmetry of the universe, why we live in a matter dominated world as opposed to one with equal amounts of matter and anti-matter. Understanding the origins of T-violation could explain this fundamental question.

There are other space-time symmetries to be tested in particle interactions, such as whether they exhibit scalar (S), pseudoscalar (P), vector (V), axial-vector (A), or tensor (T) properties. Each of these can be related to the properties of the bosons being exchanged. In some cases, we only know this property of the forces to the 10 to 20% level.

The quest to answer these questions do not necessarily require the high energies found at CERN, Fermi Lab or Brookhaven. Useful information can be obtained from background free, precise measurements of fundamental quantities. This is the way many of the nuclear experiments that can be done at high intensity pulsed sources can have an impact in this field. In some cases the interactions are between elementary particles, such as neutrino-electron scattering or atomic states in muonium. In other cases, fundamental properties of neutrons and muons are studied, such as the neutron electric dipole moment. In still others the nucleus itself is considered a laboratory in which to study the interactions, such as compound resonances. A list of such experiments is given in Tables II through IV. Because of time limitations I can only give a brief description of a few selected from this list, but these should demonstrate the techniques involved and precisions that can be obtained.

Neutron Electric Dipole Moment (EDM)

If observed, the EDM would be an example of parity and time symmetry violations. Theoretical models explaining the violations seen in the K°-$\bar{K}^{\circ}$ system predict a finite EDM. As observed in Ref. 30, progressively smaller limits placed on the EDM have eliminated certain theories from contention.

The experiment uses the nuclear magnetic resonance method[15,30] extended by Norman Ramsey in which the EDM coupled to an electric field causes a shift in the NMR line. The line width is inversely proportional to the time a neutron spends in the perturbing electric field and inversely proportional to the square root of the neutrons counted. Therefore, storing neutrons in a bottle throughout the measurement can increase the

Table II Nuclear Physics Experiments Using Neutrons

Reaction	Present or Planned Limits	Possible Limits	Comments
Electric Dipole Moment	5×10^{-25} e-cm[15]	10^{-28}e-cm	Test Fundamental Symmetries of Time and Baryon conservation. Use ultracold neutrons stored in bottles
n-$\bar{n}$ oscillations	10^{6}s [16]	10^{9}s	
Gravity Effects			Use room temperature and long wavelength interferometers [29]
$n\rightarrow pe^{-}\bar{\nu}_e$	10^{-3} [17]	10^{-5}	Search for T-violation, use polarized neutrons
Compound Resonances			Search for T-violation
Giant Dipole Resonances			Nuclear Structure Studies: High ℓ-states, non-nuclear degrees of freedom. Use polarized neutrons and TOF techniques in 0.1 to 25 MeV range
Nuclear Fission			
$He^3(n,\gamma)He^4$			look for few body correlations
$He^3(n,\gamma\gamma)He^4$			tests of QED-presently disagrees by factor of 30
Cross Sections of unstable nuclei			Astrophysics implications
A(n,n)A'			Nuclear data measurements of cross sections. A' may be unstable. Take advantage of MeV range of neutrons in pulsed sources.
A(n,p)A'			
A(n,α)A'			

Table III Nuclear Physics Experiments Using Neutrinos

Reaction	Present or Planned Limits	Possible Limits	Comments
$\nu_\mu\rightarrow\nu_e$ osc.	0.001 eV^2 [7] $\sin^2 2\theta < 10^{-5}$	10^{-4} eV^2 10^{-7}	Need low backgrounds. Cosmic ray backgrounds reduced by pulse source
$\nu_\mu\rightarrow\nu_\mu$ osc.	0.01 eV^2 [7] 10^{-3}	10^{-3} eV^2 10^{-4}	
$\nu_\mu e\rightarrow\nu_\mu e$	100-1500 events [7,8,19,20]	10^5 events	Measure y-distribution and $\sin^2\theta_W$ to 1%
$\nu_e e\rightarrow\nu_e e$	300 events [8,18]	3000 events	Use muon bottle to get higher energy neutrinos. Use pulse structure to eliminate backgrounds from other neutrino types.
$\nu_\mu P\rightarrow\nu_\mu P$	1200 [19]	12000	Look for induced pseudoscalar, at low energies have no problem with form factors
A(ν,μ)A'			Nuclear structure studies [31]
A(ν,ν)A'			Map out axial-vector strength in nucleus. Complimentary to electron scattering which gives vector strength [32]

Table IV Nuclear Physics Experiments Using Muons

Reaction	Present or Planned Limits	Possible Limits	Comments
muonium	10^{-5} [21]	10^{-8}	Test QED, Weak Interactions -- study hyperfine structure using pulsed lasers matched muon pulse length
muonic atoms	4×10^{-4} [22]	10^{-5}	
$\mu e \to \bar{\mu}\bar{e}$	muonium produced in vacuum [23]	10^{-5}	lepton conservation, T-violation
$\mu^- A \to e^- A$		10^{-8}	lepton conservation
$\mu^- A$ capture	~15-20% [24,25,26]	~2-3%	Nuclear structure studies -- use lasers and observe decays, need polarization information tests PCAC, CVC
Rare μ decays			Test for right-handed currents [35]

sensitivity over beam types of experiments. Ultimately, the limit can be pushed to $\sim 10^{-28}$ e-cm using this method, about three orders of magnitude beyond present experimental limits.

The advantages of a pulsed source over a reactor for this experiment include a higher peak flux of neutrons meaning the bottle can be filled to a higher density. As future pulsed sources increase in intensity the EDM limits should be progressively improved.

Nuclear Data Measurements

These measurements are intended to study and catalogue in a systematic fashion neutron-nucleus cross sections over a broad range of nuclei. Total, capture, elastic and inelastic cross sections will be measured as well as (n,p) and (n,α) processes. Such measurements are currently carried out at the Oak Ridge Electron Linear Accelerator but planned proton spallation sources will have much higher intensities in the higher energy region (>10 MeV) which should permit observation of smaller cross section processes and correlation measurements in multiparticle final states. Backgrounds should also be decreased at a proton accelerator especially when attempting to observe gamma transitions from excited nuclear states. Electron machines produce gamma rays profusely by Bremstrahlung making it difficult to perform such measurements.

Even though these measurements are interesting in their own right, they also provide useful numbers for application in the fission and fusion reactor programs. Embrittlement of materials due to hydrogen build up through (n,p) reactions can be studied. Also, neutron cross sections up to tens of MeV are of interest for materials used in fusion reactors. Capture cross sections of neutrons on various isotopes are unknown and needed for fission reactors.

Neutrino Oscillations

At low energies neutrino oscillations can be looked for in the transition $\nu_\mu \to \nu_e$ (appearance mode) or in the $\nu_\mu \to \nu_\mu$ (disappearance mode) in which a faster than normal flux drop off with distance is searched for. This last mode is complimentary to the $\bar{\nu}_e \to \bar{\nu}_e$ mode observed at reactors.

For neutrino transitions to take place in free space there must be a finite mass difference between the neutrino types. Thus, if observed, neutrino oscillations will also provide evidence for neutrino masses. The oscillation wavelength is given by

$$\lambda = \frac{E_\nu}{1.27\ \Delta m^2}\ , \qquad (4)$$

where λ is in meters, E_ν is the neutrino energy (MeV) and Δm^2 is the square of the mass difference between neutrino types (eV^2). For a viable experiment, it is optimal to have a low E_ν to have a short wavelength.

Another parameter to be determined is the mixing angle ($\sin^2 2\theta$) that gives the strength of the transition. This parameter may be related to quark mixing. The sensitivity to the mixing angle is given by the statistical uncertainty in the measurement,[7] and the backgrounds present. This is why pure beams of ν_μ are important as small amounts of ν_e contamination can be misinterpreted as a $\nu_\mu \to \nu_e$ transition.

In principal the experiment would attempt to map out an oscillation length to prove the effect is due to oscillations. This could be accomplished by changing the detector position which is no small feat for a multi-hundred-ton device. Another approach is to change λ by varying the neutrino energy as given by (4). Because of the E_ν-arrival-time correlation discussed above, different E_ν components can be isolated simultaneously during the measurement.

Neutrino-Electron Elastic Scattering

Neutrino electron scattering is a fundamental reaction involving only the weak neutral current for $\nu_\mu e$ and a combination of neutral and charged currents for $\nu_e e$. This latter process is the only interaction available in which the interference term between the two currents can be observed.

The Weinberg angle can be determined by comparing $\nu_\mu e$ and $\bar{\nu}_\mu e$ scattering.[7] A high precision measurement is conceivable because of low backgrounds at the low neutrino energies generated at these pulsed sources. For instance a neutral current reaction producing backgrounds is

$$\nu N \to \nu N \pi^0 \hookrightarrow \gamma\gamma \hookrightarrow e^+e^-e^+e^- \ . \qquad (5)$$

On Fig. 7, we show the production cross section for (5) as a function of neutrino energy. At low energies (~200 MeV) the cross section is five orders of magnitude below the observed rate at the Brookhaven AGS (~1000 MeV).

Another unique feature of the low energy experiment is the differential y-distribution where y is the energy sharing given by

$$y = E_e/E_\nu \quad . \tag{6}$$

Because of the broad neutrino spectrum (σ/E~100%) at the AGS energies, no determination of the y distribution has ever been accomplished. With the E_ν-arrival-time correlation the precision on E_ν will be ~10%[33,34] allowing a determination of y by measuring the electron energy and its time of production in the detector.

The y-distribution for neutrinos has a constant and quadratic term, the coefficients in front of each is related to Θ_W. If a linear term exists, it will be evidence for other space-time components in the neutral current beside vector and axial-vector.

Neutrino-Nucleus Interactions

J. D. Walecka[32] has pointed out that our knowledge of the nucleus is half-missing. The distribution of its vector currents has been studied in detail using electrons and photons as probes, but we have little experimental knowledge about the axial-vector currents. These are best studied with neutrinos having low energies that can exchange energies to the nucleus comparable to its energy levels (~ tens of MeV).

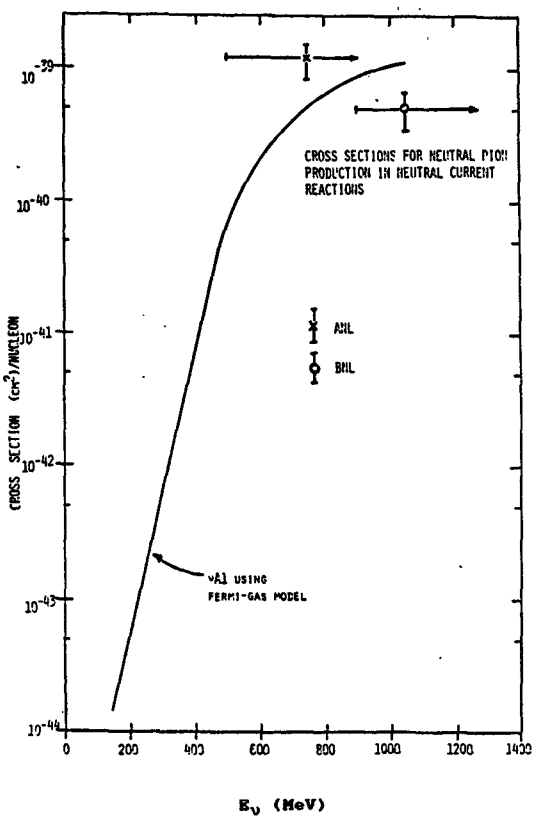

Fig. 7. The neutral current pion production cross sections are given as a function of the neutrino energy.

Also, so as not to disturb the nucleus excessively, there actions should involve only the weak neutral currents which do not change protons to neutrons as the charged currents do.

An interesting theoretical question of astrophysics interest is whether neutrinos can coherently interact with all the nucleons in the nucleus at the same time.7 If so these coherent cross sections will vary with increasing mass number as A^2. Such coherent processes for νHe scattering could play an important role in supernovae as outgoing neutrinos could exert a pressure preventing collapse.

Experiments can be performed using liquid detectors; some cryogenic such as He and O[2]. Only the recoil nucleus is seen and its energy is determined by the natural scintillation light generated in the fluid. Thus a large vat with phototubes immersed in it may suffice for the measurement. It may be necessary to segment the detector to observe any gamma rays emitted from nuclear excited states. The same detector may be used for a large number of experiments by replacing the liquid.

The study of neutrino-nucleus scattering could not have been contemplated in past years at LAMPF because of the long pulse length (~500μs) which would have allowed cosmic ray induced backgrounds to swamp the detector. With the prospect of a duty factor reduced by five orders of magnitude or more using the PSR, the prospect of performing these measurements is once again being investigated,[7] especially in view of the use of the energy-arrival time correlation that defines the incident neutrino energy. In this case, it is only necessary to measure the recoiling nucleus energy to obtain all the relevant information in the interaction, such as the cross section dependence on the exchange of the four-momentum squared.

Because the recoil is very low energies (<10 MeV for He and decreases with A of the nucleus) it is imperative to have a background free environment for the experiment. Beside cosmic rays, neutrons generated in the neutrino beamline can cause knock-on scatters imitating neutrino events with cross sections fifteen orders of magnitude higher. As I mentioned above, the PSR short pulse mode (1ns-wide pulses at 720Hz) seems appropriate to eliminate this source of background by timing as the neutrons arrive at times beginning 20ns later than the neutrinos. Unfortunately, the PSR in this mode will only be able to deliver ~12μA of current and event rates will be only a couple per day per ton of detector. These events will also be divided among the 5-timing bins. This is a study where future high intensity pulsed sources could certainly improve the experiments in a direct way by increasing the event rate.

Muonium Production

Muonium is an atomic system composed of a μ^+ and an electron. The interesting measurements involve the hyperfine splitting, Δν (between the ground state triplet and singlet states), and the Lamb shift ($2S_{1/2}$-$2P_{1/2}$ splitting). Because the system does not involve a nucleus, precision comparisons with quantum electrodynamics between the two elementary particles are possible.[9]

The experimental technique stops μ^+ in a gas cell in a magnetic field. Microwave radiation induces transitions between Zeeman levels by flipping the muon spin. The effect is then monitored by measuring the μ decay asymmetry. A high incident μ^+ polarization is therefore required.

The experimental precision is related to the Zeeman line width. A significant reduction can be effected by using only muonium atoms that have been immersed in the magnetic field for a relatively long time, $t \sim 2.2\mu s$ (muon decay time, τ_μ). Taking into account counting rates, the optimal source would have a pulse width $\Delta t < \tau_\mu$ and a repetition rate $\nu \ll 1/\tau_\mu$. A proposed experiment at Los Alamos[7] using the PSR would improve present QED test precision by a factor of 4. Higher intensity sources of muons may provide an additional order of magnitude improvement.

Conclusion

A broad program in nuclear and particle physics at a pulsed source would include neutrinos and muons as probes as well as neutrons. Optimization of experiments for each probe requires different target parameters and pulse widths. With proper scheduling or multiplexing of the proton current, I believe that a successful program in nuclear physics can proceed and can co-exist with a condensed matter neutron scattering program. This may require a broad based program advisory committee to help set priorities.

The pulsed nature of the source is most useful in determining energies by time-of-flight. The energy-timing correlation is present even for neutrinos due to the non-relativistic nature of the parent pions. However, the energies are such for nuclear probes that short pulse widths are necessary for a large class of experiments, on the order of one nanosecond or a fraction of a nanosecond. This implies that future sources should allow for some microstructure in their pulses, even if this means reducing intensity by chopping the beam.

For the nuclear and particle experiments I have considered in this talk, the upcoming generation of pulsed sources offer significant improvements in precision over present results. All of these experiments are and probably will remain statistics limited for the immediate future, therefore, as intensities increase at planned pulsed sources precision in these experiments should improve even further.

References

1. KENS, Y. Ishikawa, Proc. of International Collab. on Advanced Neutron Sources IV, Tsukuba, 89 (1981).
2. IPNS, R. Kustum, IEEE Trans. Nucl. Sci. NS-28, 3115 (1981).
3. WNR, R. Silver, Proc. of Int. Collab. on Advanced Neutron Sources VI, Argonne, 51 (1982).
4. SNS, G. Manning, Proc. of Int. Conf. on Neutron Physics and Nuclear Data, Harwell, 829 (1978).
5. SNQ, G. Bauer et al., Jul-Spez-118, KFK 3175 (1981).
6. R. Kustum and T. Khoe, BAPS 28 91 (1983).
7. G. Stephenson et al., "Proposal for a High Intensity Los Alamos Neutrino Source" Los Alamos (1982).
8. R. Maschuw and B. Zeitnetz, "Research Proposal for Neutrino Physics at SNS," Kernforschungzentrum, Karlsruhe (1982).
9. R. Heffner et al., "Proposal for a Pulsed Muon Facility," Los Alamos (1983).
10. J. Schwinger, PR 73, 407 (1948).
11. A. Steyerl, Springer Tracts on Mod. Phys. 80, 57 (1977).
12. T. Dombeck et al., NIM 165, 139 (1979); and T. O. Brun et al., PL75A, 223 (1980).
13. H. Chen, Univ. of Cal. at Irvine Report UCI-Neutrino No. 44 (July, 1980).
14. V. Lobashov and O. Serdyuk, NIM 136, 61 (1976).
15. I. S. Altarev et al., PL 102B, 13 (1981).
16. G. Fidecaro, Neutrino '81 Conference on Neutrino Physics, Maui, Hawaii, July (1981).
17. R. Steinberg et al., PRD13, 2469 (1976).
18. H. Chen et al., LAMPF proposal 225 (1977).
19. A. Mann et al., Brookhaven AGS proposal 734 (1978).
20. K. Winter, Proc. of Europhysics Study Conf. on Electroweak Effects, Erice, Sicily, Feb. 1-10 (1983).
21. P. O. Egan, "Muonium," Proc. of Workshop on Muon Science, Los Alamos, March (1982). Los Alamos report LA-9582-C.
22. E. Zavattini et al., Brookhaven AGS proposal 745 (1979).
23. P. Bolton et al., PRL 47, 1441 (1981).
24. J. Walecka, "Muon Capture in Nuclei," Proc. of Workshop on Muon Science, Los Alamos, March (1982). Los Alamos report LA-9582-C.
25. A. Aberigi et al., PR 177, 2118 (1969), and G. Bardin et al, PL 104B, 320 (1981).
26. L. Ph. Roesch et al., PRL 46, 1507 (1981).
27. A. Salam, Science 210, 723 (November, 1980).
28. J. Ellis and D. Nanopoulos, CERN Courier, 211 (July, 1983).
29. A. Klein and S. Werner, Rep. Prog. Phys. 46, 259 (1983).
30. N. Ramsey, Rep. Prog. Phys. 45, 95 (1982).
31. T. Donnelly and R. Peccei, Phys. Rep. 50, 1 (1979).
32. J. Walecka, "Neutrino Interactions With Nuclei," Proc. of LAMPF II Workshop, Los Alamos, July 19-22 (1982).
33. T. Dombeck, "LANLNU," Los Alamos report LA-UR-82-1589.
34. R. Carlini, private communication on "NUBEAM" results, a program from CERN.
35. J. Carr et al., PRL 51, 627 (1983).

Proceedings of International Collaboration on Advanced Neutron Sources (ICANS-VII), 1983 September 13-16
Atomic Energy of Canada Limited, Report AECL-8488

STUDIES OF NEUTRON IRRADIATION EFFECTS AT IPNS-REF*

M. A. Kirk
Materials Science and Technology Division
Argonne National Laboratory
Argonne, Illinois 60439

Neutron irradiation effects studies at the Radiation Effects Facility (REF) at the Intense Pulsed Neutron Source (IPNS) located at Argonne National Laboratory (ANL) are reviewed. A brief history of the development of this user facility is followed by an overview of the scientific program. Experiments unique to a spallation neutron source are covered in more detail. Future direction of research at this facility are suggested.

Introduction

Argonne National Laboratory has been a center for neutron irradiation effects studies for over 20 years. The somewhat simple ambient temperature studies of the 1950's at ANL were followed in the 1960's and 1970's by more sophisticated low-temperature studies in the CP5 reactor. This latter effort was led at ANL by Thomas Blewitt. The CP5 irradiation facilities consisted of two liquid helium cooled irradiation cryostats, one for thermal neutron irradiations and the other with a ^{235}U converter for fast neutron irradiations, ambient temperature irradiation positions including a rabbit tube, and high temperature (up to 700°C) irradiation thimbles. These facilities were designed, constructed and characterized by Blewitt and coworkers.[1,2] The CP5 facilities at ANL along with somewhat more limited facilities at Oak Ridge National Laboratory (ORNL) were for 20 years the mainstay of the U.S. program in basic research on neutron irradiation effects. The low-temperature (4.2 K) fast-neutron irradiation facility in CP5 was the only such facility in this hemisphere and one of only 5 in the world during this 20 year period. The situation today is approximately the same, but at ANL, the CP5 reactor has been replaced by IPNS-REF.

Major areas of research during the days of CP5 were the following: Irradiation hardening in Cu, Cu alloys and Nb single crystals was studied at temperatures between 4.2 and 600 K.[3] Simultaneous measurements of resistivity, lattice parameters and anomolous x-ray transmission in fast-neutron irradiated Cu at T < 50 K yielded information on migrating defect species and annihilation and clustering effects.[4] Dislocation loops of interstitial and vacancy natures were detected by changes in length and resistivity during thermal neutron irradiation of uranium.[5] Low-temperature irradiations of superconductors gave information on the effects of crystal structure and metallurgical variables on various superconducting parameters.[6] The most accurate neutron sputtering yields and spatial distribution of sputtered atoms were determined for single crystals of gold.[7] Simultaneous measurements of changes in length and resistivity during low-temperature irradiations of Cu and Ni have revealed aspects of the structure of defect cascades.[8] Measurements of disordering in ordered alloys by magnetization, resitivity, and transmission electron microscopy (TEM) have revealed fundamental mechanisms of neutron damage production.[9] Finally, low-temperature defect production measured by resistivity techniques, along with a state-of-the-art determination of neutron flux and spectrum, has produced the first meaningful comparison with similar data from other reactors, ion accelerators, and fission fragment experiments.[2] These one-sentence descriptions of some past research at CP5 will give, perhaps, a perspective on any comparison of the usefulness of fission and spallation neutron sources for this area of research.

The Radiation Effects Facility at IPNS

For several years before and immediately following the close-down of CP5 in 1979, the Blewitt group, including R. Birtcher, B. Brown, M. Kirk, B. Loomis and T. Scott, prepared designs, calculations and mock-up experiments[10,11] for the IPNS-REF. Construction took place in 1980-81 and the first experiments at 4.2 K were performed in January, 1982. The facility is operated by ANL as a national user facility for both an in-house irradiation effects program and outside users. A Program Committee reviews all research proposals. The instrument scientist with major responsibility of facility management for users is R. C. Birtcher. About 50% of research at the REF is performed by outside users (non ANL).

The facility itself consists of two irradiation cryostats (5 cm inner dia.) with controllable temperatures between 4.2 K and about 400 C and neutron fluxes of about 1×10^{12} n/cm^2 sec ($E_n > 0.1$ MeV, synchrotron current of about 10 μA delivered on a ^{238}U target), and a smaller ambient temperature irradiation position. These irradiation facilities are located adjacent to a separate irradiation effects target and surrounded by lead to produce a fast neutron flux without significant moderation. Figure 1 displays the resultant neutron energy spectrum and compares it with pure and degraded fission spectra. A close similarity between degraded fission and spallation can be noted, with the exception of the high energy "tail" from spallation which accounts for about 3% of the neutron flux and about 15% of the damage in a typical material. These neutron fluxes, energy spectra and flux gradients have been measured to the highest accuracy achievable today (about 10% in the flux defined for neutron energies > 0.1 MeV). A more approximate measure of secondary proton fluxes and energy spectra have been made, and an upper limit on the gamma flux has been determined. More details of these measurements and the facility can be found in references 12-14.

It is important at this point to emphasize those features that are unique to the accelerator based spallation neutron source. The most important for research to date has been the low gamma flux relative to a typical fission source. We have measured the gamma flux to be at least one order of magnitude lower than a fission source with the same neutron flux. Of next importance has been the ability, through the accelerator controls, to turn the neutron flux on or off, to precisely control the total neutron dose (especially very low doses) and the neutron dose rate. Of more minor importance to present research, but of possible future importance, is the high energy "tail" in the neutron spectrum and the pulsed nature of the neutron flux (100 n sec pulses at 1, 5, 10, 15 or 30 Hz repetition rates).

The low gamma flux (especially from a non fissioning spallation target) makes the consideration of a "next generation" REF with the capability of low temperature irradiations in a neutron flux of 10^{14} - 10^{15} n/cm^2 sec very attractive. This would be

*Work supported by the U. S. Department of Energy.

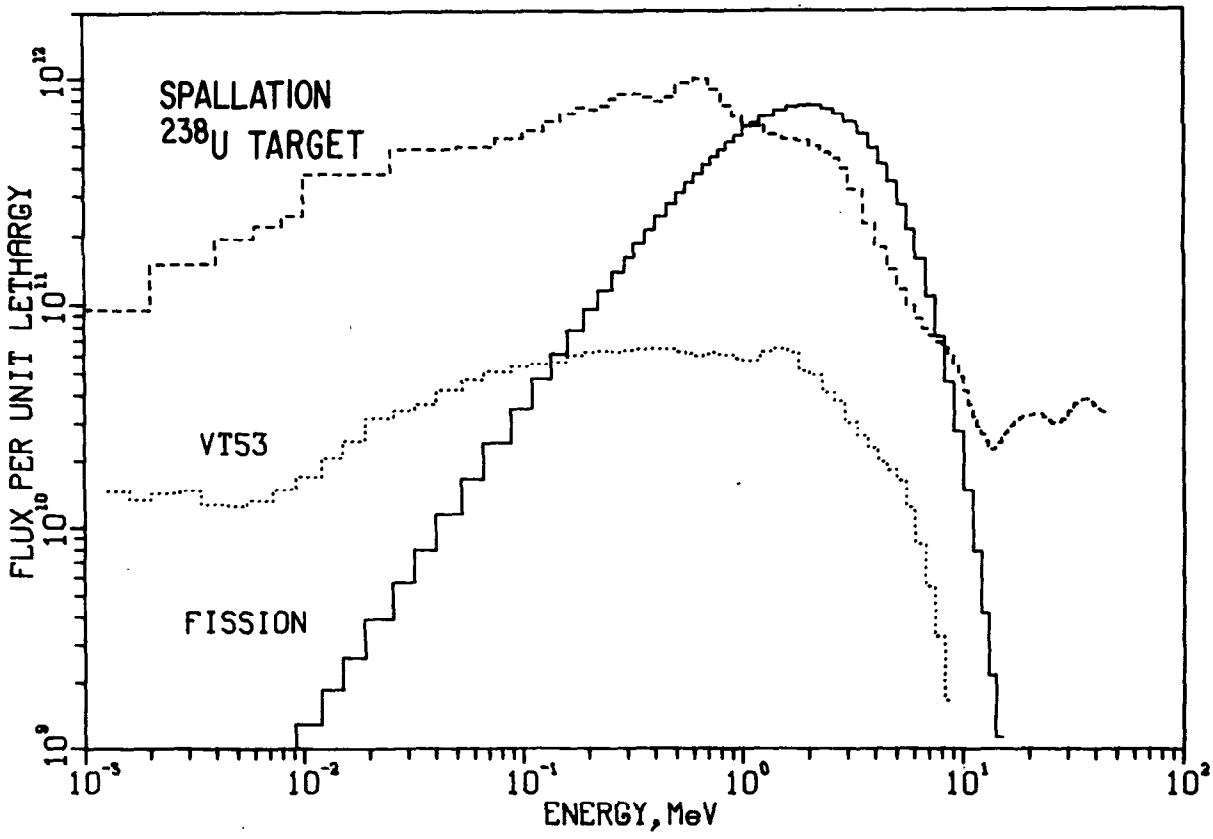

Figure 1. Comparison of neutron spectra (with arbitrary normalization) from pure fission, degraded fission (VT53 facility in CP5 reactor), and spallation from ^{238}U (500 MeV proton energy).

impossible in a fission reactor due to gamma heating. It is for this reason that we consider the REF at IPNS to be an experiment in itself. It is the first and only REF at a spallation source. It is currently the only low-temperature neutron irradiation facility in the USA. It is the only national user facility in this field in the world.

Coming from our long experience with a fission source, we should discuss briefly those features of an accelerator based spallation source that we have found to be disadvantages. We expected and have measured rather severe flux gradients in irradiation positions near the target. This can impose some restrictions, but to now they have been only a minor constraint. Irradiation rig design, sample design and placement, and sample rotation have all been used to minimize the effects of these flux gradients. Inherent in accelerator systems and extensive safety interlocking has been rather numerous beam shutdowns during daily operation. This is of little or no consequence to either low-temperature irradiations or many sample irradiations at ambient temperature. However data can be affected in those in situ experiments at controlled temperatures when defects are mobile. Temperature control itself can be affected, and equilibrium defect concentrations temporarily changed.

Finally, the use of a dedicated target for these studies has both advantages and disadvantages. Total control of the accelerator for precise on, off, dose and dose rate values has tremendous advantages for some in situ experiments. However, the irradiation effects target is programmed to receive the proton beam only 1/4 of total IPNS running time, placing a severe restriction on the length (dose) and number of experiments that can be done. A limited number of small samples can be irradiated at ambient temperature near the neutron scattering target. The flux is lower and the energy spectrum is moderated somewhat.

Overview of Scientific Program

The Radiation Effects Facility at IPNS was designed and constructed (with support from the Basic Energy Sciences Division of the U. S. Department of Energy) to be a basic research tool in this field. In most instances research performed here is designed to contribute to a fundamental understanding of irradiation effects in metals, semiconductors, superconductors, and insulators in support of both the fission and fusion energy programs. The ANL program is designed to investigate the production by neutron irradiation of point defects and defect cascades, defect migration, annihilation, clustering, and interaction of point defects with other defects such as impurities and dislocations. Electron, proton, ion and gamma irradiations are also performed to complement neutron irradiation data in several experiments. The influence of these various defect states upon the physical properties of materials is examined.

The primary emphasis of the ANL program is the use of the unique aspects of this pulsed spallation neutron source. Thus major experimental efforts are in progress studying neutron irradiation effects in organic insulators, semiconductors, and ordered alloys. Irradiation effects due to a gamma flux can be quite important in both organic insulators and semiconductors. This facility is unique in that fast-neutron irradiation effects can be independently studied in these materials. Precise control of dose and dose rate has been essential in the semiconductor and ordered alloy work. It is believed that in the near future the pulsed nature of the source will be

utilized in these same two areas of experiment. A more detailed discussion of these unique experimental areas is postponed until the following section while the balance of the experimental program is briefly reviewed.

Spallation and 14 MeV Neutron Irradiation of Stabilized NbTi Superconductors[15]

Experiments are being performed on the irradiation behavior of NbTi, a leading candidate for the superconducting magnets in a fusion energy device. The effect of cyclic neutron irradiation at 5 K and annealing to 300 K is being investigated for various metallurgical states of NbTi. Critical current density (j_c) is measured as a function of applied field up to 9 T at 4.2 K after each cycle of irradiation and annealing. Generally, small decreases have been measured in j_c after 2 cycles and the smallest decrease is for materials with a high degree of final cold work and optimized initial annealing temperature (380 C).

Observations in an HVEM of in situ Tensile Deformation and Fracture in Neutron-Irradiated Niobium[16]

High-purity and O-doped (200 appm) Nb single-crystal tensile specimens were irradiated in IPNS-REF at 300 K. Observations of the in situ tensile deformation in the ANL-High Voltage Electron Microscope (HVEM) have shown the deformation processes that give rise to irradiation induced embrittlement and/or deformation. This process consists of dislocations gliding in channels which are thus cleared of the defect clusters produced by the neutron irradiations. Video tape recordings of details of the process have been made with the HVEM.

Non-ANL User Experiments

Both Los Alamos National Laboratory (LANL) and Oak Ridge National Laboratory (ORNL) has been major outside users of IPNS-REF in programs to study neutron irradiation effects in fusion energy magnet materials. The LANL experiments on organic insulators will be discussed in the next section. The ORNL experiment (R. Coltman and C. Klabunde) is designed to study changes in magnetoresistivity of copper at 5 K under cyclic neutron irradiation and annealing. It now appears that the copper stabilizer in the superconducting magnets for a fusion reactor may be the most irradiation sensitive component.[17] Initial data has been taken on the increase of resistivity and magnetoresistivity in copper after 3 irradiation and anneal cycles. Analysis of results is underway. These results coordinate nicely with the NbTi work described above. To perform these experiments the ORNL group constructed an irradiation rig capable of in situ measurements in applied magnetic fields up to 7 T.

Other experiments in progress include: continuation of the semiconductor work (see next section on silicon) by the University of Missouri group (J. Farmer and J. Meese with R. Birtcher, ANL) with measurements of Deep Level Transient Spectroscopy in irradiated germanium; a study of neutron irradiation effects in the amorphous metal superconductor, Mo-Ru-B at 4.2 K with in situ magnetic fields to 7 T (R. Scanlan, Lawrence Berkeley Laboratory); a study of fatigue in neuron irradiated copper single crystal (D. Luzzi and M. Meshii, Northwestern University); diffuse x-ray scattering studies of neutron irradiated nickel, copper, and their dilute alloys and Si and Be (R. Averback, ANL and P. Ehrhart, KFA, Jülich, West Germany); and a study of the effects of solutes on neutron damage production and recovery in zirconium (S. MacEwen and R. Zee, Chalk River Nuclear Laboratory, with R. Birtcher, ANL).

Experiments Unique to a Spallation Neutron Source

Neutron Irradiation Effects in Organic Insulators

Two sets of experiments have been taking place at IPNS-REF in this field. Work at ANL in collaboration with the Japan Atomic Energy Research Institute (S. Egusa, visiting scientist at ANL) is in progress to investigate changes in mechanical properties of composite organic insulators following fast neutron and gamma irradiations at 5 K and 300 K. Mechanical and electrical property changes were measured in the composite G-10CR by a LANL group (G. Hurley, J. Fowler and D. Rohr) following 5 K irradiation at IPNS-REF. Both programs will be able to isolate those irradiation effects due only to neutrons; a result of the low gamma flux at IPNS. The interest in these materials for use as magnet materials in fusion energy devices is high.

The LANL results to date show small but significant changes in mechanical and electrical properties of G-10CR irradiated at 5 K with neutrons to 2.5 MGy.[18] Flexural strength was reduced and fracture surfaces show dependence on temperature and irradiation. Both DC and AC resistivities decreased slightly with this irradiation dose, but dielectric breakdown strength showed no significant change.

Four kinds of cloth-filled organic composites were irradiated in IPNS-REF at 300 K and 5 K and mechanical property changes were studied at ANL.[19] The same study was also made for composites irradiated with 2 MeV electrons at 300 K for comparison.[20] Gamma irradiations are currently taking place at ANL on these materials. The neutron results to date show the shear modulus and ultimate strength unchanged in all samples after 400 Mrad. However the fracture propagation energy in the glass fiber/polyimide matrix is seen to change with neutron irradiation at a much higher rate than with electron irradiation.

Fast Neutron Irradiation Effects in Semiconductors

Knowledge of the defect structure in semiconductors following fast neutron irradiation has been severely limited by the concurrent production of defects or charge carriers due to high gamma fluxes in fission reactors. The low gamma flux at IPNS-REF allows, for the first time, meaningful measurements of DC conductivity, annealing, and Deep Level Transient Spectroscopy (DLTS) during and following low-temperature fast-neutron irradiations. These measurements have yielded information on damage production, thermal recovery and defect identification.[21]

Resistivity measurements on several semiconductors during irradiation at 5 K are displayed in Fig. 2. The somewhat surprising behavior illustrated in this figure can be well described by the exponential relation:

$$\sigma(\phi) = \sigma_o \, e^{-K\phi}$$

where σ is conductivity, ϕ is fluence (in protons on spallation target in Fig. 2) and K is a damage constant dependent on material. This form of relation has been observed in metals and when analyzed in a similar fashion here yields information on defect cascades. In silicon the average cascade volume was determined to be 4.7×10^5 atom volumes with a defect density in this volume of 5.5×10^{-4}.

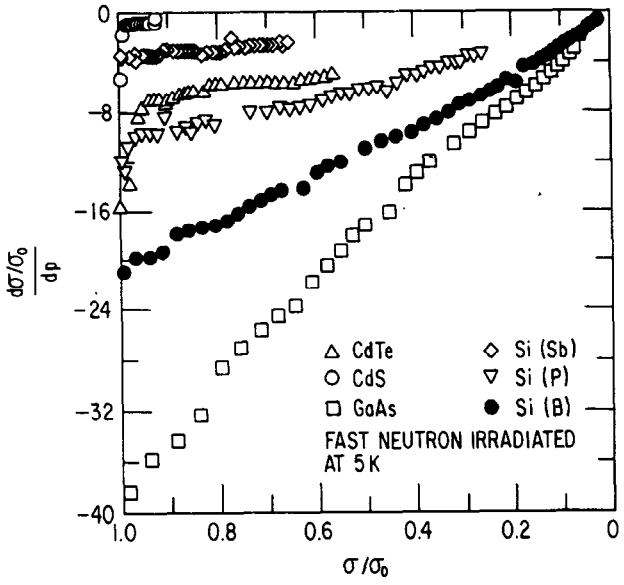

Figure 2. The normalized rate of conductivity change, $d(\sigma/\sigma_0)/dp$, vs. fractional normalized conductivity, σ/σ_0.

The annealing results in silicon yielded a very low temperature process at 22 K which has not been observed before. Results in CdTe indicated the vacancy may be mobile below room temperature which, if true, would be the only known vacancy in a II-VI semiconductor to possess this property.

DLTS has been used to determine the defect energy levels introduced into the band gap of n-type silicon following fast-neutron irradiation at 5 K.[22] The thermal production and annihilation of these defect energy levels during annealing is shown in Fig. 3. The increase of the defect level E_1 (known to be the vacancy-oxygen A center) occurs at the expense of a defect with a deeper electronic energy level whose concentration can only be inferred by the behavior of the low-temperature shoulder of its DLTS signal. This annealing is consistent with the single vacancy which is known to thermally migrate below 150 K. Decreases in the E_1 and E_3 (divacancy) levels between 250 and 300 K may be a result of the appearance of the E_0 level which suggests that this level may be associated with an interstitial type defect. Above 350 K the divacancy level E_3 anneals out while E_1 and E_2 grow. E_2 may be associated with larger vacancy clusters. These results suggest, in agreement with conductivity measurements, that the fast-neutron defect cascade in silicon is very diffuse and at 5 K contains primarily single vacancies and divacancies.

Fast Neutron Irradiations of Cu_3Au

Ordered alloys have been useful to study irradiations effects from the earliest days of nuclear reactors. The formation of displacements or defects usually causes a larger number of replacements during the process. These replacements result in the disorder of ordered alloys which can be measured in several different ways. Also, the migration of a defect, say a vacancy, can cause the ordering of many

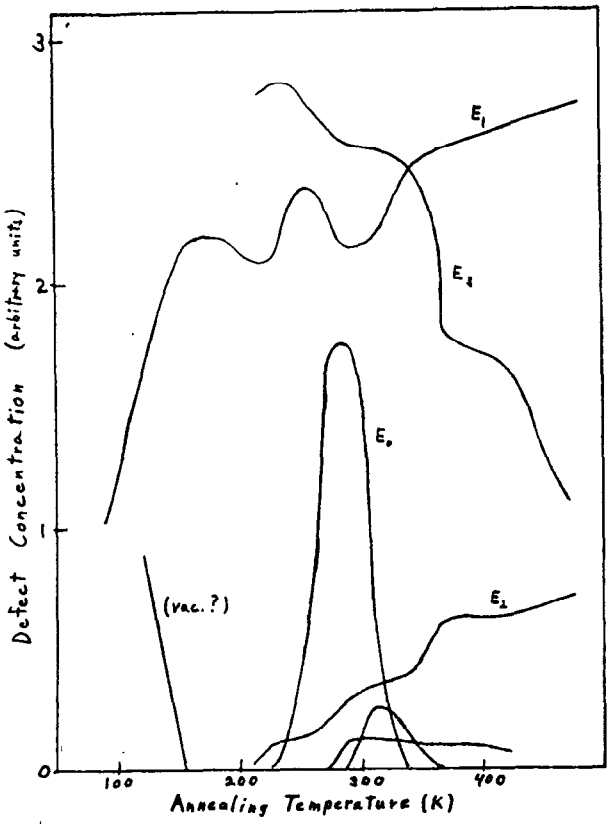

Figure 3. Annealing behavior of defect levels in fast-neutron irradiated n-type Si as measured by Deep Level Transient Spectroscopy (DLTS).

atoms and thus reveal itself to measurement more easily. We have been active for many years at ANL in the use of ordered alloys to reveal fundamental mechanisms of neutron irradiation effects.[9] Recent experiments on Cu_3Au reveal or take advantage of unique features of IPNS-REF.

Individual defect cascades produced by fast-neutron irradiation can be revealed clearly as disordered zones in an ordered matrix by the appropriate transmission electron microscopy (TEM) technqiue.[23] One study was designed to compare images and sizes of disordered zones produced by fast neutrons from a fission source, CP5, and a spallation source, IPNS. We expected a strong similarity in size distributions based on the very similar distributions of neutron energies as seen in Fig. 1. This was indeed demonstrated in Fig. 4. In addition, some quite large disordered zones were observed and sized in the specimens irradiated with spallation neutrons. Although the numbers of disordered zones examined in this specimen was not sufficiently large to make a firm conclusion, it was probably true that we were observing a few disordered zones created by the very high energy neutrons in the spallation spectrum. Further study is currently in progress. This limited study, however, reveals the subcascade nature of these high energy events.

More extensive experiments on Cu_3Au are currently underway to study the irradiation enhancement of vacancy diffusion in this ordered alloy.[24] Several experimental runs over the past year have revealed

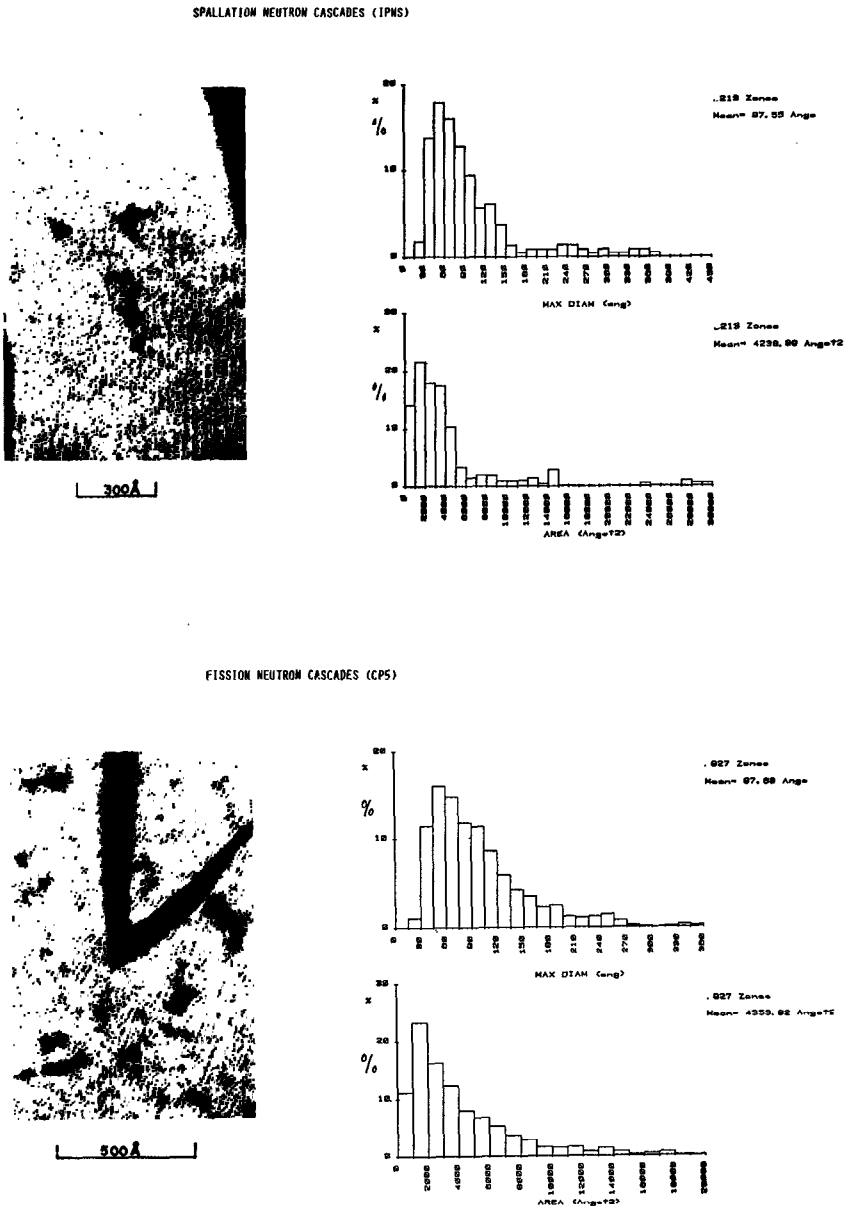

Figure 4. TEM high resolution images and size distributions of disordered zones (or cascades) in neutron-irradiated Cu_3Au. Images are recorded in dark-field superlattice reflection ($\vec{G}$ = 110). Heavy dark lines are anti-phase domain boundaries.

very systematic behavior in the data. Changes in degree of long range order are measured by resistivity changes. Analysis with respect to theory is in progress. The data consists of the effect on ordering rate per incident neutron ($dS/d\phi$) of neutron dose (ϕ), dose rate ($\dot{\phi}$), irradiation temperature (T) and the sample order parameter (S). An example of the variation of ordering rate as a function of irradiation temperature and order parameter is shown in Fig. 5. This demonstrates that ordering is by vacancy diffusion only, and is not affected by interstitial diffusion; a result which has been demonstrated earlier by electron irradiation.[25] Note in the S ≈ 1 sample that ordering by the vacancy diffusion is not possible and only disordering by the cascade disordered zones is observed. However some reordering of these disordered zones is apparently revealed and shows a temperature dependence.

Theoretical expressions combining the reaction rate theory of irradiation enhanced diffusion[26] with the reaction rate theory of ordering[27] have already been proposed by Zee and Wilkes.[28] We believe our data will be a quantitative test of both theories.

The effect of the pulsed irradiation structure has been investigated by us. No effect can be found in this particular experiment which demonstrates that time average values of flux, fluence and resultant damage parameters are suitable. This is in agreement

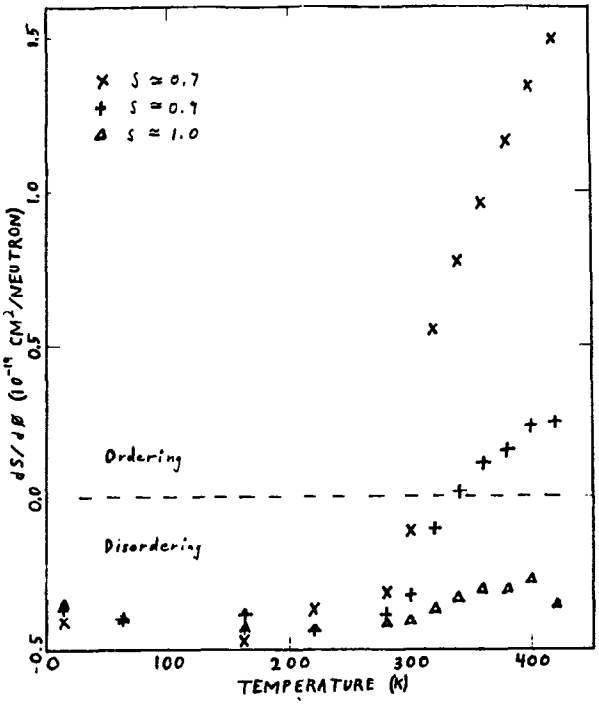

Figure 5. Ordering and disordering rates in fast-neutron irradiated Cu_3Au as a function of irradiation temperature in three samples with different degrees of long-range order (S).

with recent theoretical calculations appropriate to our experiment.[29] However, new experiments will begin soon in which an effect of the pulsed structure of the irradiation flux is anticipated.

A new and direct measure of the irradiation produced vacancy concentration and lifetime is proposed in Fig. 6. The change in sample order as a function of time is shown during irradiation and immediately following a precise shutdown of the flux. The decay of the irradiation produced vacancy concentration is observed over about 75 seconds. The difference in interception of the two straight lines at the precise time of shutdown is proportional to the vacancy concentration. The second linear slope was unexpected. Further investigation of this effect has suggested that we are observing a second mechanism for production of migrating vacancies, which may be the emission of vacancies by dislocation loops produced by the irradiation.

A central point to be made here is that precise control of neutron dose, dose rate and irradiation temperature is far easier with an accelerator based spallation neutron source (and dedicated target) than with a fission reactor. Precise and instantaneous full-flux start up and shutdown is possible only with a facility like IPNS-REF.

Summary and Observations

In this article we have described briefly the Radiation Effects Facility (REF) of the Intense Pulsed Neutron Source (IPNS) at Argonne National Laboratory and how it was designed, constructed and characterized by the group of Tom Blewitt. Coming from our experience with the CP5 research reactor we discussed the advantages and disadvantages of a pulsed spal-

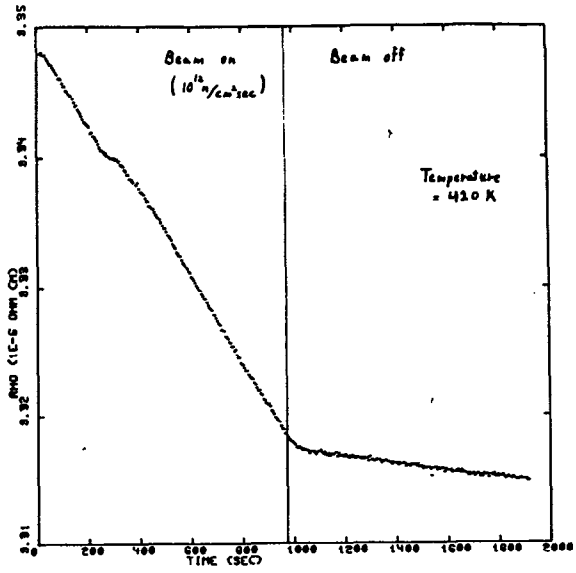

Figure 6. Ordering in Cu_3Au during neutron irradiation (beam on) at 420 K and following cessation of irradiation at 970 sec. Note decay of irradiation-produced vacancy concentration near 1000 sec and evidence for a continuing vacancy diffusion for time > 1000 sec.

lation neutron source for irradiation effects research. The central advantages are the low gamma flux relative to a fission reactor source and a more precise control of irradiation parameters such as dose, dose rate, and instantaneous turning on and off. Two other differences of note are the high energy tail in the neutron energy spectrum and the pulsed structure of the irradiation flux (100 nsec pulse normally at a 30 Hz repetition rate). The high energy neutrons are few (3%) and of little or no consequence to irradiation studies in this, a degraded fission-like, neutron flux. The pulse structure, while little utilized at present, is expected to be useful to certain future experiments studying the kinetics of mobile defects.

The research program has been reviewed with a special emphasis on those experiments that employ the unique features of IPNS-REF. Approximately 50% of the research is performed by outside users of this national user facility; the balance is performed by the Neutron Irradiation Group in the Materials Science and Technology Division at ANL. Irradiation experiments on organic insulators and semiconductors are both strong components of this program as they require the relatively low-gamma flux. The experiments on irradiation enhanced diffusion in Cu_3Au require the precise control of irradiation parameters afforded by control of the accelerator. A neutron source such as IPNS-REF, essentially dedicated to this research, facilitates control of dose and dose rate without competition from other users.

If a next generation of spallation sources is constructed (with protons currents ~5 m·Amp.), it will be possible to include facilities for irradiations in neutron fluxes of 10^{14}–10^{15} neutrons/cm^2 sec and at controlled temperatures to as low as 4.2 K. This would exceed the highest practical neutron flux for this kind of research facility in a fission reactor by about an order of magnitude, and such a source would permit qualitatively new research in areas such as

irradiation effects on mechanical properties. For this reason we view the IPNS-REF as prototypical and as an experiment itself.

It is possible, however, that the experiment will end within two years of the time of this writing. During this time a new facility in the Bulk Shielding Reactor at ORNL will be opened for use by the irradiation effects community. The new facility will have 5 times the flux of IPNS-REF and be available for experiments nearly year round. It will not have those features unique to a pulsed spallation source that we have been discussing. A foregone conclusion by many, including the funding agency, is that there is insufficient demand for two facilities. This author would seriously question such a conclusion in view of unique research opportunities at a pulsed spallation source and the possibility of a future facility. At the same time there is a need for more fundamental and applied research in the field of neutron irradiation effects. A recent study concluded as much if we are to have fission and fusion reactors as energy sources in the future.[30] The need is especially critical for students in this and related fields.

Any new facility in the future will need a strong in-house program in neutron irradiation effects. Good fundamental research is exceedingly difficult for outside users. The complexity and construction of many experiments make them impractical for the occasional visiting scientist. However, enlisting the aid of a local scientist at the facility can overcome much of this problem.

Acknowledgements

The author would like to thank his many coworkers and colleagues at ANL and other institutions for their generous help and instruction.

References

1. A. C. Klank, T. H. Blewitt, J. J. Minarik and T. L. Scott, Bull. Inst. Int. Froid Suppl. 5 (1966) 323.
2. M. A. Kirk and L. R. Greenwood, J. Nucl. Mater. 80 (1979) 159.
3. T. H. Blewitt and C. A. Arenberg, Suppl. to Trans. Japan Inst. Metals, 9 (1968) 226.
4. E. E. Gruber, T. H. Blewitt and T. O. Baldwin, J. Appl. Phys. 45 (1974) 542.
5. B. A. Loomis and S. B. Gerber, Phil. Mag. 18 (1968) 539.
6. B. S. Brown and T. H. Blewitt, J. Nucl. Mater. 80 (1979) 18.
7. M. A. Kirk, R. A. Conner, D. G. Wozniak, L. R. Greenwood, R. L. Malewicki and R. R. Heinrich, Phys. Rev. B19 (1979) 87.
8. R. C. Birtcher and T. H. Blewitt, J. Nucl. Mater. 98 (1981) 63.
9. M. A. Kirk and T. H. Blewitt, J. Nucl. Mater. 108 & 109 (1982) 124.
10. M. A. Kirk, R. C. Birtcher, T. H. Blewitt, L. R. Greenwood, R. J. Popek and R. R. Heinrich, J. Nucl. Mater. 96 (1981) 37.
11. B. A. Loomis, H. R. Thresh, G. L. Fogle and S. B. Gerber, Nucl. Tech. 55 (1981) 617,
12. R. C. Birtcher, T. H. Blewitt, M. A. Kirk, T. L. Scott, B. S. Brown and L. R. Greenwood, J. Nucl. Mater. 108 & 109 (1982) 3.
13. R. C. Birtcher, M. A. Kirk, T. H. Blewitt and L. R. Greenwood, ICANS-1982, ANL 82-80, p. 407.
14. L. R. Greenwood, J. Nucl. Mater. 108 &109 (1982) 21.
15. P. Hahn, B. S. Brown, H. W. Weber and M. W. Guinan, to be published in proceedings of the International Cryogenic Materials Conference, Colorado Springs, August 15-19, 1983.
16. B. A. Loomis and M. P. Otero, to be published in proceedings of the Third Topical Meeting on Fusion Reactor Materials, Albuquerque, September 19-22, 1983.
17. R. R. Coltman, Jr., J. Nucl. Mater. 108 & 109 (1982) 559.
18. G. F. Hurley, J. D. Fowler and D. L. Rohr, submitted to Cryogenics.
19. S. Egusa, M. A. Kirk, R. C. Birtcher, M. Hagiwara and S. Kawanishi, to be published in Rad. Effects as proceedings of Second International Conf. on Radiation Effects in Insulators, Albuquerque, May 30 - June 3, 1983.
20. S. Egusa, M. A. Kirk, R. C. Birtcher, M. Hagiwara and S. Kawanishi, accepted for publication by J. Nucl. Mater.
21. R. C. Birtcher, J. M. Meese and T. L. Scott, to be published in proceedings of the Fourth Neutron Transmutation Doping Conference, Washington, D.C., June 1-3, 1982.
22. R. C. Birtcher and T. L. Scott, to be published.
23. M. L. Jenkins and C. A. English, J. Nucl. Mater. 108 & 109 (1982) 46.
24. M. A. Kirk and L. L. Funk, to be published.
25. J. Gilbert, D. Herman and A. C. Damask, Rad. Effects 20 (1973) 37.
26. R. Sizman, J. Nucl. Mater. 69 & 70 (1978) 386.
27. G. J. Dienes, Acta. Met. 3 (1955) 549.
28. R. H. Zee and P. Wilkes, J. Nucl. Mater. 97 (1981) 179.
29. V. Naundorf and C. Abromeit, Rad. Effects 69 (1983) 261.
30. Report of the Working Group on Low Temperature Neutron Irradiation, DOE/ER-0138, July 1982.

Session F

Targets II

Chairman - G.J. Russell

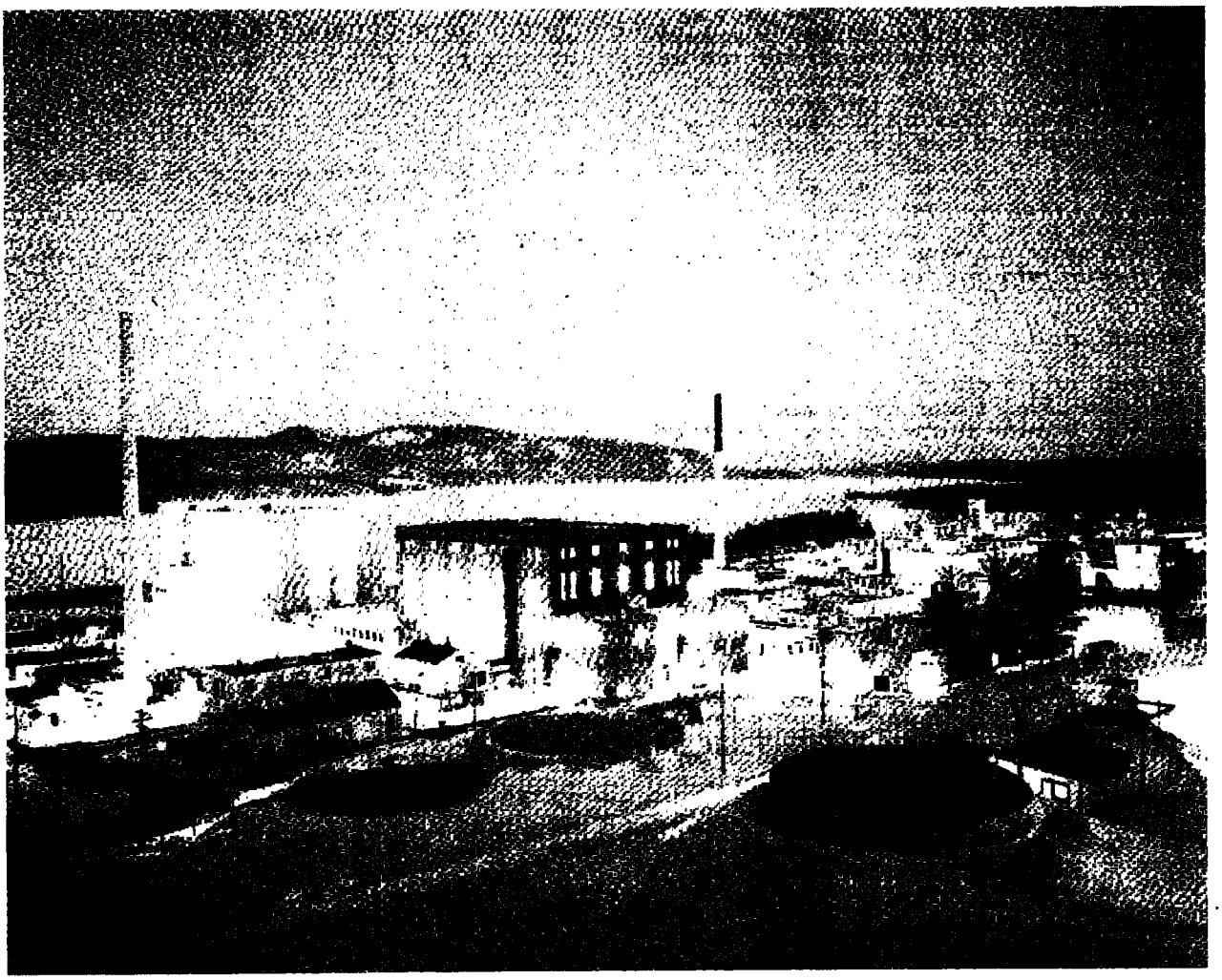

Proceedings of International Collaboration on Advanced Neutron Sources (ICANS-VII), 1983 September 13-16
Atomic Energy of Canada Limited, Report AECL-8488

VALIDATION OF SPALLATION MODELS FOR PARTICLE PRODUCTION

D. Filges, T.W. Armstrong*, P. Cloth

Institut für Reaktorentwicklung, Kernforschungsanlage Jülich GmbH
Postfach 1913, D-5170 Jülich, Germany
*KFA Consultant, P.O. Box 2807, La Jolla California 92038, USA

ABSTRACT

The intranuclear-cascade-evaporation model has been used to predict the neutron production from nonelastic interactions of protons with several target materials as U, Pb, Ta, In, Nb, Fe, Al and C. These model predictions for a 590 MeV proton beam were compared with measurements of Cierjacks et al. /1/ made at the SIN facility. In general the model predicts approximately the correct neutron production in the evaporation region, whereas in the high energy region (>100 MeV) are substantially discrepancies between measurement and model predictions. As an example calculated yields for ^{3}He and ^{4}He production were also compared with measured cross sections. From these limited comparisons shown here it is evident that there are large differences between theoretical evaluations and measurements.

INTRODUCTION

As part of a study to assess the accuracy of state-of-the-art high-energy models for spallation neutron source applications, the intranuclear-cascade-evaporation model has been used to predict the double differential neutron production cross sections for nonelastic collisions of protons with uranium, lead, tantalum, indium, niobium, iron, aluminium and carbon nuclei. The purpose here is to predict some comparisons of model validation calculations mainly with experimental data for neutron spectra produced in thin targets.

CALCULATIONAL PROCEDURE

The calculations are made using HETC/KFA-1 /2/ with the so- called "thin target setup" with 590 MeV protons. For uranium the Rutherford and Appleton high energy fission model (RAL) /2/ with B_0 = 8 MeV and the production of secondary evaporation particles isotropically in the lab system were used /2/. For all other targets the variable B_0-option of HETC/KFA-1, without high energy fission and a non isotropic emission for evaporation was assumed.

All cases were run with about 30000 real collisions per target with 1 hour computer time on IBM-3033. The cases were measured by S. Cierjacks et al. /1/ and the final evaluation of the measured data for materials U, Pb, Ta, In, Nb, Fe, Al and C measured at angles of 30°, 90° and 150° were compared. The materials input for HETC/KFA-1 is given in Table I and the energy and angle grids for the analysis is shown in Table II.

Table I Material Input

Target	Z	A	N_A(Atoms/cm^3 x 10^{-24})
U	92	238	0.0483
Pb	82	207	0.0329
Ta	73	181	0.0552
In	49	115	0.0382
Nb	41	93	0.0554
Fe	26	56	0.0846
Al	13	27	0.0602
C	6	12	0.1104

Table II Energy and Angle Grid for Analysis of HETC/KFA-1 Results

Energy	Grid	θ Grid
0	15	0°
0.15	20	5
0.2	30	10
0.3	40	15
0.4	60	20
0.6	80	25
0.8	100	35
1.0	150	40
1.5	200	50
2.0	300	65
3.0	400	80
4.0	500	100
6.0	600	120
8.0		140
10.0		160
		180
27 ΔE Intervals		15 ΔE Intervals

For evaporation particles the following angle grid is used

Calculated Evap.	Angle in Experiment
0° - 60°	23° / 30°
60° - 120°	90°
120° - 150°	150°

The following results were evaluated from the HETC/KFA-1 calculations

double-differential yield spectra for each particle type

Y_i (E,θ), no./(MeV.str) per incident proton

where i= emitted particle type
= n(evap+cascade), p(evap+cascade), d, t, ^{3}He, α, π^+, π^0, π^-.

- marginal distributions, summed over angle:

Y_i (E), no./MeV per proton

- marginal distributions, summed over energy:

  Y_i (θ), no./str. per proton

- total yield, over all energy and angle:

  Y_i , no. per proton

To compare with the KfK data in terms of cross sections, the "yield spectra" must be multiplied by the inelastic cross section σ_{in}, computed by HETC, which can be obtained in the following way:

From HETC listing (printed information at beginning of run) the value for the macroscopic geometric cross section, Σ , is printed (in units of cm^{-1}).

Then, in units of barns:

$$\sigma_{in} = \Sigma_{in}/N_a = 1/N_a \times \Sigma_G \times F_R$$

where N_a = atom density value used in HETC input
F_R = fraction of incident protons that have "real" collisions

$$= \frac{\text{(no. real collisions)}}{\text{(no.real collisions + no.pseudo collisions)}}$$

where these are values printed at end of HETC output.

Then
$$d^2\sigma/dEd\Omega \quad (b/MeV.str) = Y_n(E,\theta)\ \sigma_{in}$$

is to be compared with KfK data.
In Table III the calculated σ_{in} vs. A number are given.

Table III Calculated σ_{in} vs. A number

Mass Number A	σ_{in} (barn)
U-238	1.849
Pb-207	1.683
Ta-181	1.563
In-115	1.183
Nb-93	1.035
Fe-56	0.7486
Al-27	0.4622
C-12	0.2629

NEUTRON SPECTRA COMPARISONS

We show only some examples of the whole comparisons which are made. The complete validation is given in Ref. /3/. Figures 1-4 show comparisons of the calculations and KfK measurements for neutron spectra of uranium at 30°, 90° and 150°, Figures 5-8 for lead, Figures 9-12 for iron and Figures 13-16 for carbon. The basic conclusions we draw from these comparisons are: (a) for all materials there is a good agreement in the evaporation region of the spectrum (few MeV upto 20 MeV) except for the lighter materials as Al and C. The high energy part of the spectrum (> 100 MeV) is underestimated by the calculations, by a factor of 2-3 for small (e.g. 30°) angles, with much worse agreement at the higher angles. This is similar for all target materials.

GAS PRODUCTION CROSS SECTIONS

Also low energy charged particle production from nuclear collisions is very important for predictions related to radiation effects and material selection for high current spallation facilities /4/,/5/. The used nuclear models /2/ are capable of calculating the spatial dependent production of low-energy particles as H, d, t, ^{3}He and ^{4}He. But very little was done to check evaluations against experiments. Together with our evaluation of neutron production measurements of Cierjacks et al. /1/ we got HETC/KFA-1 calculated low energy charged particle cross sections. We compared this data with several sets of measurements which have been made for various target materials for proton beam of about 600 MeV.

As an example in Fig. 17 and 18 the calculated ^{3}He and ^{4}He production cross section vs. A are compared with measured cross sections. The measured data are from several different experiments at, or near, 600 MeV mainly from Ref. /6/. From the limited comparisons shown here it is evident that there are large differences between theoretical evaluations and measurements.

CONCLUSIONS

The major deficiency of the present model is considered to be the underestimate of the high-energy neutrons and protons. We predict the correct neutron production in the evaporation region for elements heavier than iron with larger differences for lighter elements. The present comparisons show an underestimation at high energies (> 100 MeV) by a factor of 2-3 for small angles (e.g. 30°), with much worse agreement at higher angles 90° and 150°. The magnitude of the difference is still questionable because of the energy resolution due to the very short flight pathes (~1 m length). There are model changes which would, we believe, improve the high-energy particle production. But measurements at other energies and with better resolution are needed to provide a complete evaluation.

For that purpose model validation experiments (KFA-LANL(P9)-Collaboration are underway. In the meantime, this problem must be kept in mind in making predictions related to SNQ design.

REFERENCES

/1/ S. Cierjacks, Y. Hino, S.D. Howe, F. Roupp, L. Buth
Differential Neutron Production Cross Section for 590 Protons, Proceedings of the Interna- tional Conference "Nuclear Data for Science and Technology" 6-10 September 1982, Antwerp

/2/ P. Cloth, D. Filges, G. Sterzenbach, T.W. Armstrong, B.L. Colborn
The KFA-Version of the High-Energy Transport Code HETC and the generalized Evaluation Code SIMPEL, KFA-Report, Jül-Spez-196, March 1983

/3/ To be published

/4/ W. Lohmann
Materials Problems in Beam Windows and Structural Components of the SNQ-Target, Proc. 4th Meeting of the International Collaboration on Advanced Neutron Sources (ICANS-IV), Tsukuba, Japan, October 20-24, 1980 (KENS Report II, March, 1981)

/5/ J. Jung
Radiation Effects in Target and Structural Components of a Spallation Neutron Source, Proc. 5th Meeting of the International Collaboration on Advanced Neutron Sources (ICANS-IV) G.S. Bauer and D. Filges (Eds.) Jülich, FRG, June 22-26, 1981 (Jül-Conf-45, Oct. 1981)

/6/ S.T. Kruger, D. Heymann
High-Energy Proton Production of ^3H, ^3He, and ^4He in Light Targets, Phys. Rev. C 7, 2179 (1973)

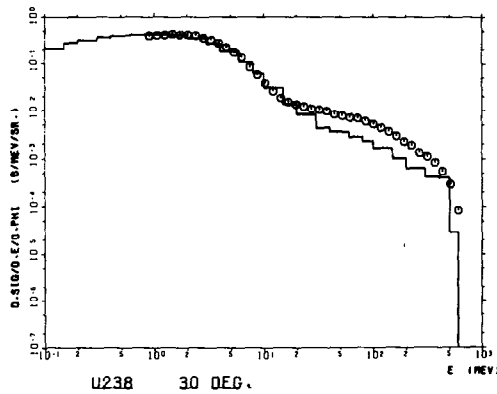

Figure 1 Comparison of calculated and KfK measured neutron cross sections at 30° from a thin uranium target bombarded by 590 MeV protons

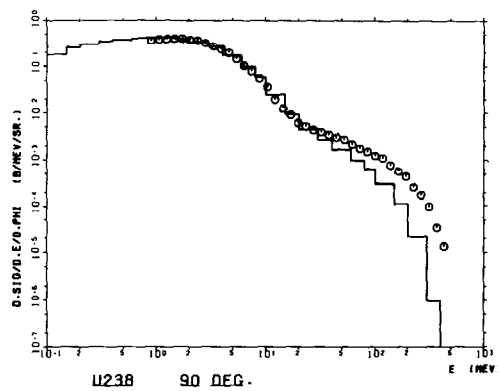

Figure 2 Comparison of calculated and KfK measured neutron cross sections at 90° from a thin uranium target bombarded by 590 MeV protons

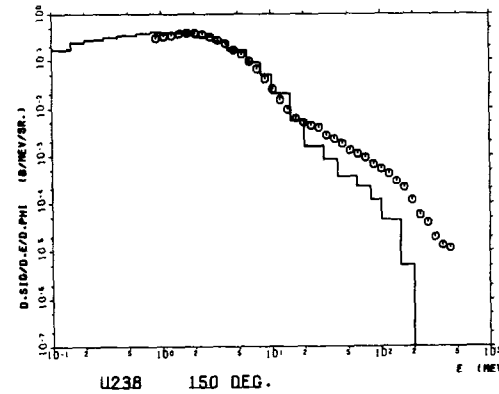

Figure 3 Comparison of calculated and KfK measured neutron cross sections at 150° from a thin uranium target bombarded by 590 MeV protons

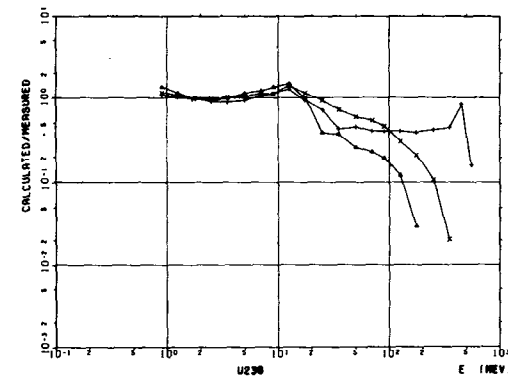

Figure 4 Ratio of calculated to measured neutron cross sections from a thin uranium target bombarded by 590 MeV protons

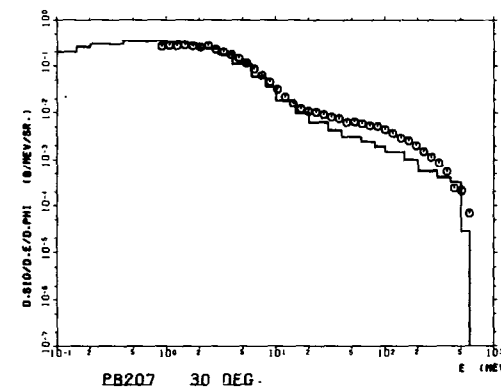

Figure 5 Comparison of calculated and KfK measured neutron cross sections at 30° from a thin lead target bombarded by 590 MeV protons

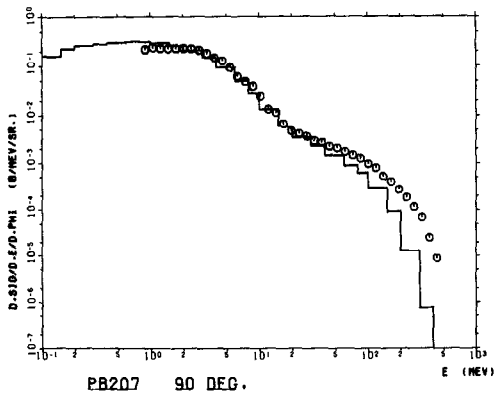

Figure 6 Comparison of calculated and KfK measured neutron cross sections at 90° from a thin lead target bombarded by 590 MeV protons

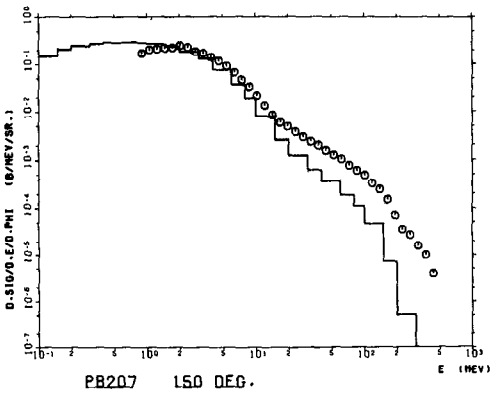

Figure 7 Comparison of calculated and KfK measured neutron cross sections at 150° from a thin lead target bombarded by 590 MeV protons

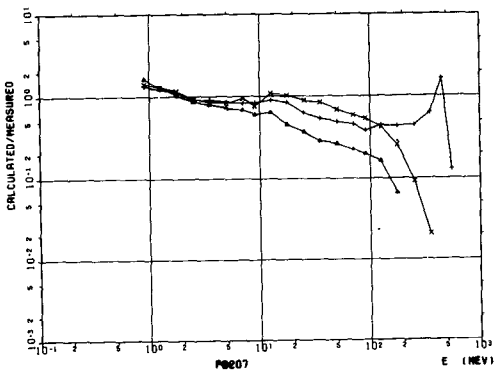

Figure 8 Ratio of calculated to measured neutron cross sections from a thin lead target bombarded by 590 MeV protons

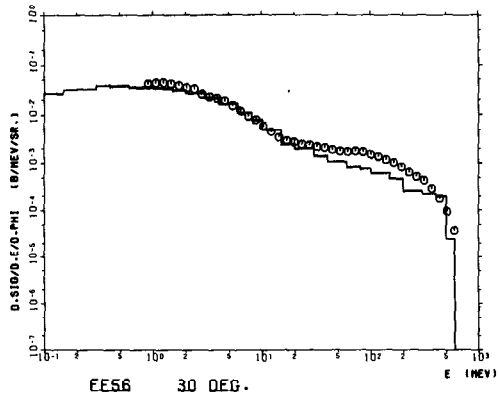

Figure 9 Comparison of calculated and KfK measured neutron cross sections at 30° from a thin iron target bombarded by 590 MeV protons

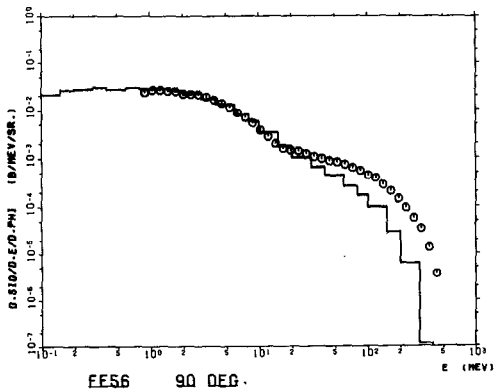

Figure 10 Comparison of calculated and KfK measured neutron cross sections at 90° from a thin iron target bombarded by 590 MeV protons

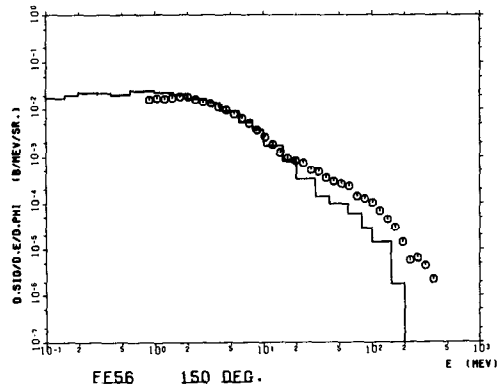

Figure 11 Comparison of calculated and KfK measured neutron cross sections at 150° from a thin iron target bombarded by 590 MeV protons

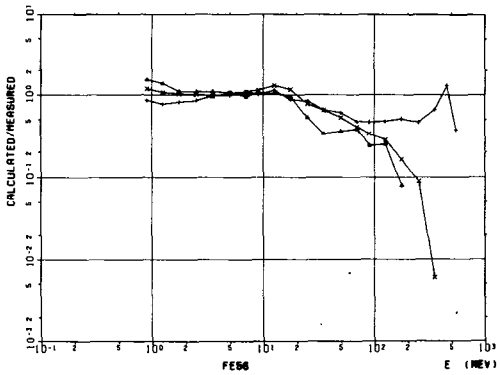

Figure 12 Ratio of calculated to measured neutron cross sections from a thin iron target bombarded by 590 MeV protons

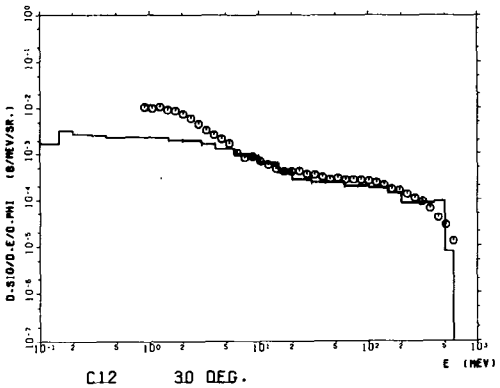

Figure 13 Comparison of calculated and KfK measured neutron cross sections at 30° from a thin carbon target bombarded by 590 MeV protons

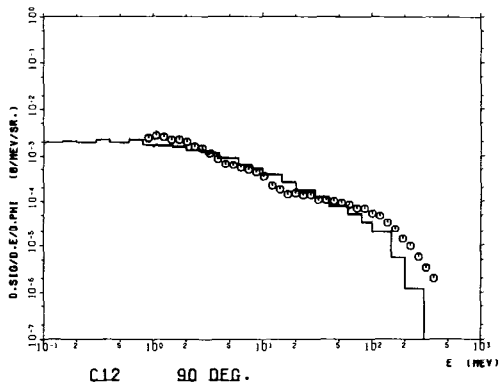

Figure 14 Comparison of calculated and KfK measured neutron cross sections at 90° from a thin carbon target bombarded by 590 MeV protons

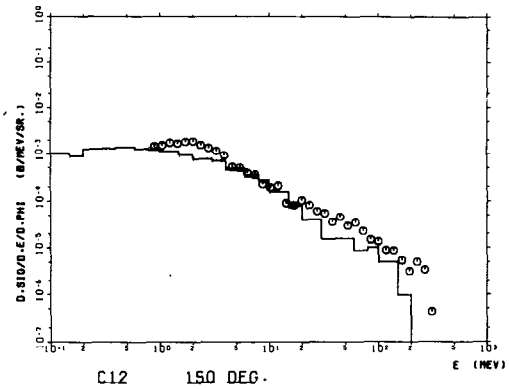

Figure 15 Comparison of calculated and KfK measured neutron cross sections at 150° from a thin carbon target bombarded by 590 MeV protons

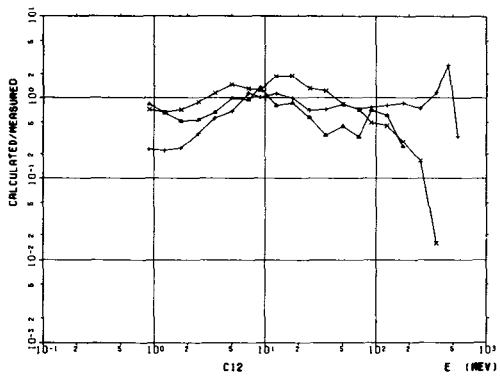

Figure 16 Ratio of calculated to measured neutron cross sections from a thin carbon target bombarded by 590 MeV protons

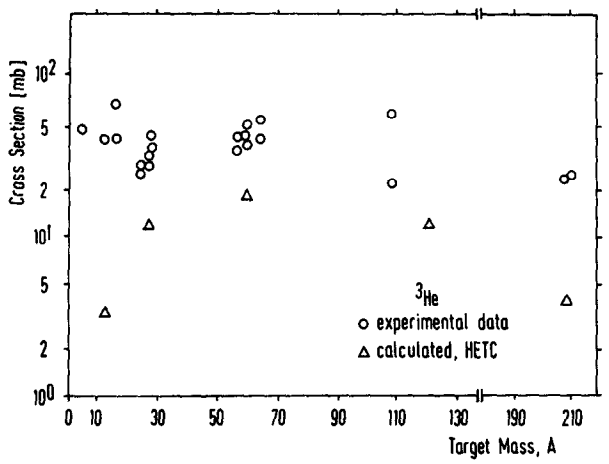

Figure 17 Comparison of HETC calculated cross sections for ^{3}He production with experimental data /6/ for 600 MeV proton bombardment

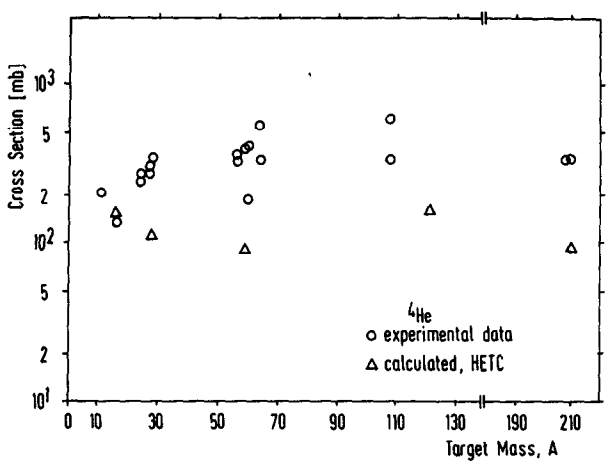

Figure 18 Comparison of HETC calculated cross sections for ^{4}He production with experimental data /6/ for 600 MeV proton bombardment

Proceedings of International Collaboration on Advanced Neutron Sources (ICANS-VII), 1983 September 13-16
Atomic Energy of Canada Limited, Report AECL-8488

SPALLATION NEUTRON SOURCES WITH INTERMEDIATE ENERGY PROTONS

M.A. Lone
Atomic Energy of Canada Limited
Chalk River Nuclear Laboratories
Chalk River, Ontario, K0J 1J0, Canada

Abstract

An assessment is made of the neutron source strength, thermal neutron flux characteristics, and target heat-removal limitations in sources driven by proton beams of intermediate energies. It is shown that a 70 mA, 200 MeV proton accelerator with a Pb-Bi eutectic liquid target would provide an unperturbed peak thermal neutron flux of $\approx 2 \times 10^{15}$ $n.cm^{-2}.s^{-1}$ in a D_2O moderator.

Introduction

The long range goal of development of an Accelerator Breeder (AB) at AECL envisages[1] construction of high current proton accelerators of energies up to 1 GeV. This will be achieved in several steps as outlined by Dr. Schriber in an earlier presentation at this Conference[2]. In particular the second step calls for the development of a high current continuous wave (cw) proton accelerator of intermediate energy, say 100 to 200 MeV. This will provide the front end of a full-demonstration breeder and an Electronuclear Materials Test Facility (EMTF).

My talk is based on a feasibility study[3] of the prospects of the EMTF beam dump as a neutron source for basic research. The scope of this study was to assess the source strength, thermal neutron flux characteristics and target heat-removal limitations assuming various conceptual target-moderator configurations and 100 to 200 MeV proton beam energy.

Neutron Yield Calculations and Measurements

Calculations

We used the CRNL version of the NMTC/MORSE codes for calculation of the neutron yields and thermal neutron flux distributions inside various moderating media. The NMTC code is an earlier version of the currently popular HETC code. These codes have been tested at high energies (E_p > 400 MeV) with the experimental data obtained in several laboratories[4]. The codes are based on theoretical models that are generally considered to be applicable at proton energies above 50 MeV. However, none of the previous studies had tested the codes for proton energies below 400 MeV.

For verification of the theoretical calculations at lower energies we measured total neutron yields and thermal neutron flux distributions in a water moderator from 100 MeV proton bombardment of thick targets of Li, Fe, Cu, Pb and Th. Lithium and lead are important elements for high beam power sources which would require liquid targets whereas iron and copper are important accelerator structure materials. Thorium provided us with an estimate of the neutron yield due to fast fission which was not included in the NMTC calculations.

Measurements

Experimental details of the measurements were described by Dr. Jones at the ICANS-VI Conference[5,6]. Here I will give a brief outline and update of the results. Figure 1 shows a schematic diagram of the water moderator tank with about 70 gold foils placed at various locations for measurement of thermal neutron flux distribution. The insulated water tank, 1.5 m diameter, 1.5 m high was used as a Faraday cup for proton beam current measurement to an accuracy of 1.5%. The total neutron yields were determined from the volume integral of the measured thermal neutron flux distributions and the known absorption cross section of water.

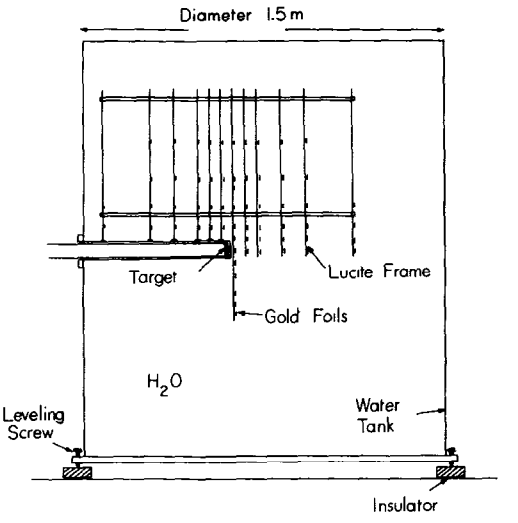

Fig. 1 Schematic setup of the experiment for neutron yield and flux distribution measurements.

Comparison

Table I shows the measured and calculated total neutron yields for various target materials. It is evident that even at this low energy the NMTC code predicts the total neutron yield to an accuracy of about 20% or better. The biggest discrepancy between the measured and calculated yields is for a lithium target. This is not surprising since the evaporation model and the global parameters used in the CRNL version of the NMTC code are optimized for heavier nuclei. It will be interesting to compare the data with the predictions of the KFA version of the HETC code[7] which includes updated input data for nuclear models used in the calculations of evaporation neutrons.

Table 1

Target	Yield Per Proton		
	Experiment	Calculated	Deviation
^{7}Li	0.123	0.160	+ 33%
^{56}Fe	0.115	0.122	+ 6%
Cu	0.145	0.169	+ 17%
Pb	0.343	0.363	+ 6%
Th	0.530	0.449	- 15%

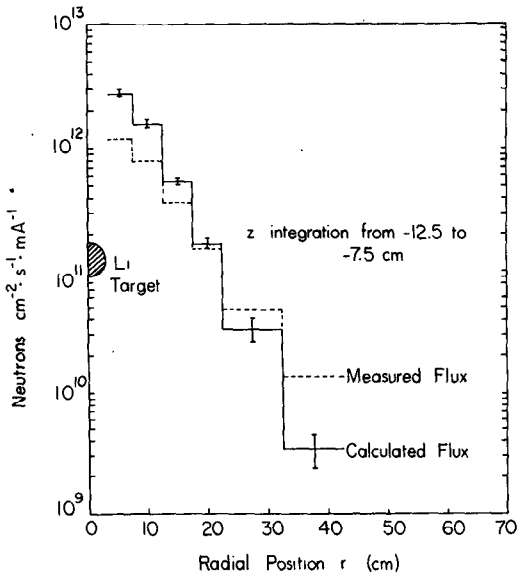

Fig. 2 Comparison between the calculated and measured volume averaged thermal neutron radial flux distributions, inside an H_2O moderator, from ^{7}Li (p,xn) reaction at 100 MeV. The axial interval for averaging is -2.5 cm to +2.5 cm. The error bars show the statistical uncertainties in the Monte Carlo results.

A comparison of the calculated and measured thermal neutron flux distributions for the Li and Pb targets is shown in Figures 2 and 3. The agreement is quite good in case of Pb but not so good for lithium. In case of lithium the calculated peak thermal flux is high by almost a factor of 2.5. Furthermore the calculated fluxes fall off more rapidly than the measured fluxes with radial distance. A better fit to the Li data would require changing the average energy of the calculated source spectrum from 6 MeV to about 16 MeV. This discrepancy emphasizes the inadequacy of the evaporation model with isotropic neutron emission presently incorporated in the NMTC code. Inclusion of the pre-equilibrium neutron emission with an isotropic angular distribution may provide better agreement with the data[8].

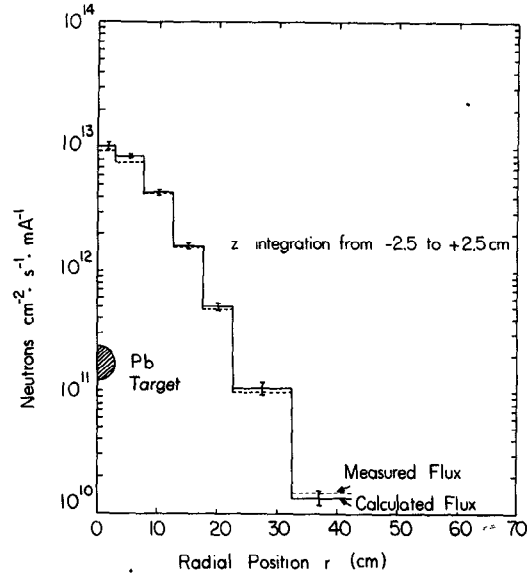

Fig. 3 Comparison of the calculated and measured volume averaged thermal neutron radial flux distributions, inside an H_2O moderator, from Pb(p,xn) reaction at 100 MeV. The axial interval for averaging is -2.5 cm to +2.5 cm. The error bars show the statistical uncertainties in the Monte Carlo results.

Neutron Yield Versus Energy

Figure 4 shows the calculated neutron yield per incident proton for several elements as a function of proton energy from 100 to 400 MeV. The neutron yield increases with atomic number of the target element as well as the proton energy. For practical reasons a high intensity neutron source produced with intermediate energy protons would require a liquid target for transfer of megawatts of heat dissipated in a relatively small volume of the target.

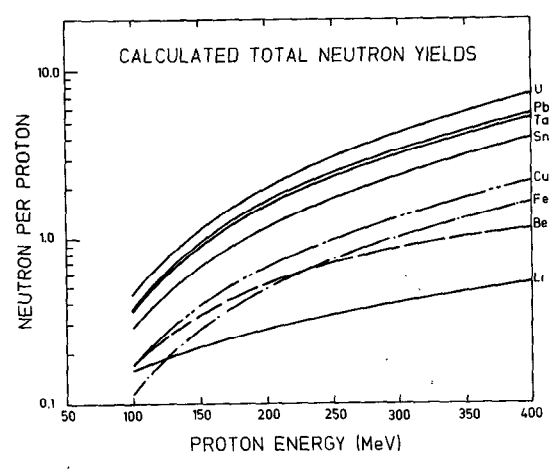

Fig. 4 Calculated neutron yield per incident proton as a function of the proton energy.

Two materials that could be used as liquid targets are lithium and a Pb-Bi eutectic. The neutron yield from lithium is low but the proton range in lithium is considerably larger than in Pb-Bi, see Table II. Thus at lower proton energies much higher beam power may be dissipated in a lithium target than a Pb-Bi target.

Preliminary estimates of the neutron yields and the target heat-dissipation limitations indicated that, with 100 MeV protons, a lithium target would provide the highest possible peak thermal neutron flux whereas, with 200 MeV protons, a Pb-Bi target would be better.

Table II

Element	Melting Point °C	Boiling Point °C	Proton Range 100 MeV cm	200 MeV cm
Li	180.6	1342	17.3	58.2
Pb-Bi (44.5% Pb)	124	1677	1.6	5.1

Target-Moderator Assemblies

Thermalhydraulic considerations of liquid targets of various configurations, e.g. coaxial, jet and falling curtain, indicated that a maximum of 30 MW beam power of 100 MeV protons could be dissipated in a liquid lithium target. Whereas a maximum of 14 MW power of 200 MeV proton beam could be dissipated in a Pb-Bi liquid target. Estimates of target flow rates and temperatures under these conditions are summarized in Table III. In both cases the target flow rates are quite high but practicable.

Detailed calculations of the thermal neutron flux distribution in various moderating media, C, H_2O and D_2O were carried out assuming the idealized geometries of target-moderator assemblies shown in Figure 5. A proton beam of circular cross section 10 cm in diameter, having uniform density within the beam area, was assumed to be incident on the front face of the target.

Table III

Target Temperature and Flow Rates

Beam Energy	100 MeV	200 MeV
Target	Li	Pb-Bi
Power	30 MW	14 MW
Target Inlet Temperature	275°C	275°C
Mean Target Outlet Temp.	375°C	375°C
Target Mass Flow Rate	72 kg/s	952 kg/s
Target Volume Flow Rate	145 ℓ/s	93 ℓ/s

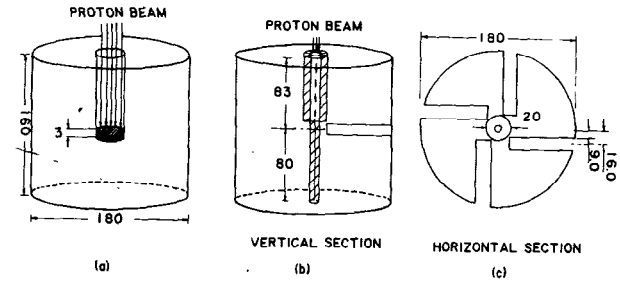

Fig. 5 Schematic drawings of the idealized geometries of target moderator assemblies used in calculations of the moderated neutron flux distributions.

Thermal Neutron FLux Distributions for a 100 MeV, 30 MW Li(p,xn) Source

For a 30 MW beam of 100 MeV protons incident on a lithium disk target the calculated axial thermal neutron flux distributions are shown in Figure 6. The peak values, 6.0, 5.0 and 4.4×10^{14} $n.cm^{-2}.s^{-1}$ occur at distances of approximately 1, 10 and 14 cm from the back face of the lithium target for H_2O, D_2O and graphite respectively. Axial fast neutron flux distributions inside a graphite moderator are shown in Figure 7. The effect of a Be multiplier blanket around the lithium target was investigated but showed little enhancement of the peak thermal flux.

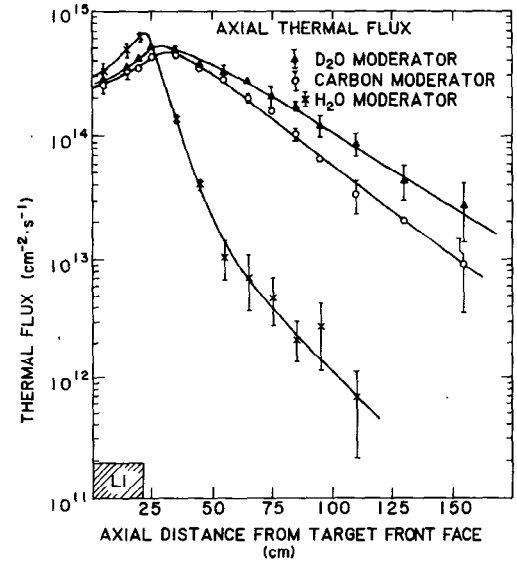

Fig. 6 Axial distribution of the neutron fluxes, inside various moderators, from Li (p,xn) reaction at 100 MeV.

Measurements of the thermal neutron flux from bombardment of a lithium target with a well collimated (1 cm diameter) 100 MeV proton beam and an H_2O moderator gave a peak value which is ≈ 2.5 times lower than the calculated value. From this we estimate that, for the extended proton beam 10 cm in diameter, the calculations overpredict the peak thermal neutron flux by as much as a factor of 2.

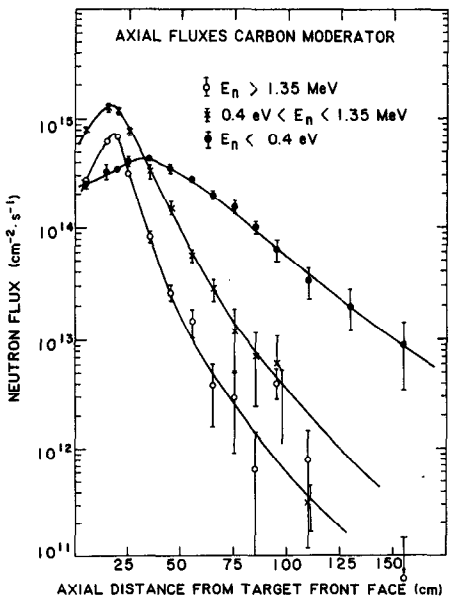

Fig. 7 Fast neutron flux distributions inside a carbon moderator from the ^{7}Li(p,xn) reaction at 100 MeV.

Thus a 30 MW beam power of 100 MeV protons incident on a lithium target would produce a peak thermal flux of only about 3×10^{14} n.cm^{-2}s^{-1} which is already available from our 25 year-old NRU reactor.

Thermal Neutron Flux Distributions for a 200 MeV, 14 MW Pb(p,xn) Source

For higher thermal fluxes the proton energy must be increased. At higher proton energies the increase in neutron yield from lithium is much slower than from Pb or Bi, see Figure 4. For this reason we considered only a Pb-Bi eutectic target with a 200 MeV proton beam of 14 MW power. Two moderators, H_2O and D_2O, were considered. Flux perturbation due to the extended target tube for a liquid target and external neutron beam holes through the moderator was studied by assuming the simple conceptual design shown in Figures 5b and 5c. In addition to the liquid target inlet and outlet tubes, four external neutron beam tubes, each 12 cm ID, were placed as shown in these figures. The location of these tangential tubes was based on the results of unperturbed flux calculations.

For investigation of the perturbed fluxes, parasitic absorption in the target material and in the external neutron beam tube was included in the calculations. The beam tubes were assumed to be made of aluminum tubing of 1 cm wall thickness. The target and its containment tube material was assumed to be Pb. The neutron yield from Bi is comparable to that from Pb but thermal neutron absorption is less. For calculations of fluxes of moderated neutrons the density of the lead target was assumed to be equal to that of the Pb-Bi eutectic.

For the H_2O moderator the axial distribution of the unperturbed neutron fluxes, averaged over a cylindrical slice extending from 5 to 10 cm radius, are shown in Figure 8. The peak unperturbed thermal neutron (E_n < 0.4 eV) flux is ≈ 2×10^{15} n.cm^{-2}.s^{-1} and it occurs very close to the target. The flux falls off very rapidly with distance from the primary source and the region of peak thermal flux is small. Insertion of the external neutron beam tube and the extended target tube in this region perturbs the flux considerably. At the base of the 12 cm ID, 1 cm thick wall Aℓ external beam tube, the thermal neutron flux drops by almost a factor of 3.3. Because of this large perturbation of the flux an H_2O moderator is not suitable for a source with external neutron beam holes.

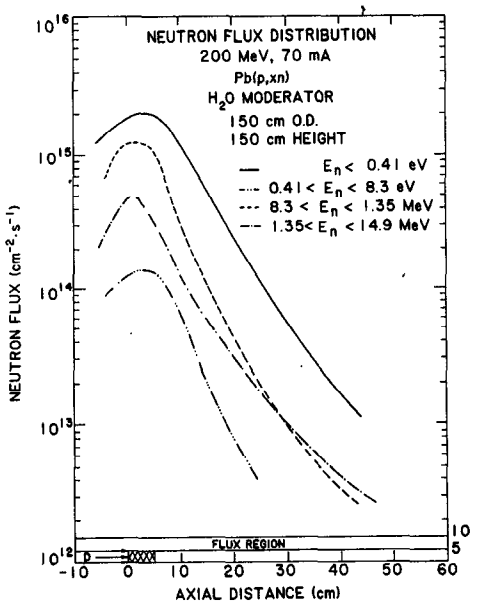

Fig. 8 Axial distributions of neutron fluxes, inside an H_2O moderator, from the Pb(p,xn) reaction at 200 MeV. The fluxes are averaged over a cylindrical slice extending from 5 to 10 cm radius.

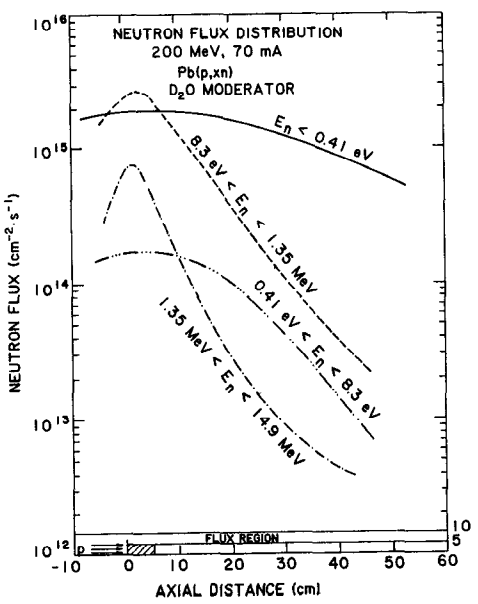

Fig. 9 Axial distributions of neutron fluxes, inside a D_2O moderator, from the Pb(p,xn) reaction at 200 MeV. The fluxes are averaged over a cylindrical slice extending from 5 to 10 cm radius.

Figure 9 shows the axial distribution of the unperturbed neutron fluxes inside a D_2O moderator. Here the peak thermal flux is = 1.9×10^{15} $n.cm^{-2}.s^{-1}$ and falls off gradually with distance from the target. The vertical arrows indicate the location nearest to the target where a tangential external beam tube could be placed.

The distribution, of the perturbed neutron fluxes in the D_2O moderator calculated for a region adjacent to the external beam tube, see Figure 5c, is shown in Figure 10. In this case the thermal neutron flux at the base of the tangential beam tube reduces to $\approx 10^{15}$ $n.cm^{-2}.s^{-1}$.

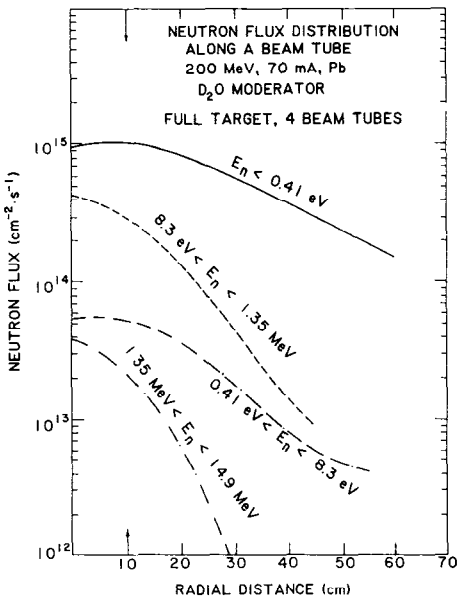

Fig. 10 Neutron flux distributions along a beam tube, see Fig. 7c, for D_2O moderator and Pb(p,xn) reaction at 200 MeV. The arrows indicate the location of the base of the external beam tube.

Conclusions

This preliminary investigation shows that a 70 mA, 200 MeV accelerator with a Pb-Bi eutectic target and a D_2O moderator would provide a peak thermal neutron flux of 10^{15} $n.cm^{-2}.s^{-1}$ at the base of several external tubes with a Cd ratio of ≈ 4.

In this preliminary study we have not investigated the cost effectiveness of the intermediate energy proton induced spallation source reaction for neutron production. However, qualitatively the competitiveness of this reaction can be judged from Figure 11 which shows the neutron yield per incident particle and the target-heat dissipation per available neutron from various source reactions of interest. By comparison, thermal fission reactions yield about 1 available neutron with 200 MeV heat production per fission event. The low energy T(d,n) reaction generates about 2500 MeV per neutron produced. Deuteron induced spallation reactions give about 25% higher neutron yield than do protons at comparable beam power. However, the deuteron beam produces more activation in the accelerator structure. The only reaction that will be very efficient with respect to the heat release is the (t,d) fusion reaction which presently is not technically feasible for very high intensity neutron sources.

Thus if neutron yield and the target heat removal were the only considerations Figure 11 shows clearly the superiority of proton induced spallation reactions, even at intermediate energies (E_p > 100 MeV), for high intensity neutron sources. In addition the γ-ray production will be considerably less for (p,xn) than for (e,xn) reactions or fission. Of course higher proton energies provide higher efficiencies and probably more versatility in the design of a source with special characteristics, such as a pulse-time structure, but probably at the expense of higher background from fast neutrons and high energy γ-rays.

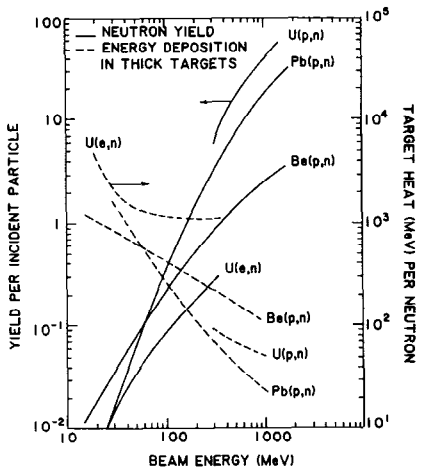

Fig. 11 Comparison of neutron yields and energy disposition in various reactions in targets of thickness equal to the beam penetration.

References

1. G.A. Bartholomew, ICANS-V, Proc. 5th Meeting of Int. Collaboration on advanced Neutron Sources, Jülich 1981, G.S. Bauer and D. Filges eds. Jül-Conf-45 (1981) p. 89.
2. S.O. Schriber, see proceedings of this conference.
3. M.A. Lone, W.N. Selander, B.M. Townes, J. Latouf, E.C. Svensson and G.A. Bartholomew. Atomic Energy of Canada Report AECL-7839 (1983).
4. T.W. Armstrong and D. Filges, ICANS-V, 5th Meeting of Int. Collaboration on Advanced Neutron Sources, Jülich 1981, G.S. Bauer and D. Filges eds. Jül-Conf-45 (1981) 173.
5. R.T. Jones, M.A. Lone, A. Okazaki, B.M. Townes, D.C. Santry, E.D. Earle, J.K.P. Lee, J.M. Robson, R.B. Moore and V. Raut. ICANS-VI, 6th Meeting of Int. Collaboration on Advanced Neutron Sources, Argonne 1982, J. Carpenter ed. ANL-82-80 (1982) p. 583.
6. M.A. Lone, R.T. Jones, A. Okazaki, B.M. Townes, D. Santry, E.D. Earle, J.K.P. Lee, J.M. Robson, R.B. Moore, V. Raut and L. Nikkinen, Nucl. Instr. & Meth. 214 (1983) 339
7. P. Cloth, D. Filges, G. Sterzenbach, T.W. Armstrong and B.L. Colborn. The KFA Version of HETC and the Generalized Evaluation Code SIMPEL KFA report Jül-SPE2-196 (1983).
8. T.W. Armstrong and P. Garvey, private communications (1983).

Proceedings of International Collaboration on Advanced Neutron Sources (ICANS-VII), 1983 September 13-1
Atomic Energy of Canada Limited, Report AECL-8488

HETC/KFA-1, AN UPDATED VERSION OF HETC FOR HIGH-ENERGY SPALLATION PHYSICS CALCULATIONS

T.W. Armstrong*, P. Cloth, B.L. Colborn*, D. Filges, G. Sterzenbach

Institut für Reaktorentwicklung, Kernforschungsanlage Jülich GmbH
Postfach 1913, D-5170 Jülich, Germany
*KFA Consultant, P.O. Box 2807, La Jolla California 92038, USA

ABSTRACT

Several modifications have been made to the high-energy radiation transport code HETC in conjunction with model validation and SNQ target station design calculations being carried out at KFA. The updated features of the new version of the code, designated HETC/KFA-1 are summarized.

1. INTRODUCTION

The High-Energy Transport Code (HETC), Ref. /1/, is being used at KFA for various predictions related to SNQ target station investigations, and basic physics experiments to check the accuracy of the models incorporated in HETC are also being carried out. Several modifications have been made to HETC in conjunction with this work, and others are in progress and planned.

Modifications to the code which have been incorporated and documented to date as a new code version designated HETC/KFA-1 are summarized below in Section 2. The documentation for this version of the transport code, awell as for a general analysis code for transport results called SIMPEL, is contained in Ref. /2/.

In addition, several other modifications to HETC have been implemented, but not yet documented or fully tested; these are summarized in Section 3.

2. CODE MODIFICATIONS INCORPORATED AS HETC/KFA-1

2.1 Updated Nuclear Mass Data

In the evaporation model calculations, atomic masses are needed to determine binding energies for various types of particle emissions. In the standard version of HETC, the evaluated 1964 Atomic Mass Table values are used. These input data have been updated to use the 1977 Atomic Mass Evaluation values of Wapstra and Bos /3/.

Spallation collisions often produce residual nuclei outside of the A and Z range covered by these input mass data (e.g., Figure 1), in which case the Cameron semi-empirical mass formula is used. In computing mass differences, unrealistic values can sometimes be obtained if the table values are used for the starting nuclide and the semi-empirical formula used for the ending nuclide. A change was made to use the mass formula for both nuclides if either one is outside the input table range, which provides a more consistent treatment.

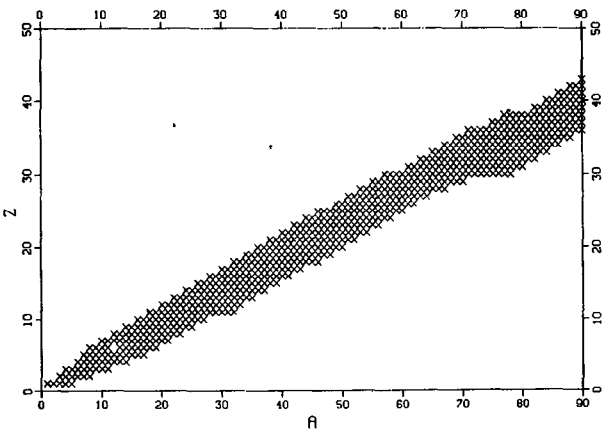

Figure 1 Nuclide A and Z range covered by updated input data for evaporation model. The symbols denote nuclides for which data are available and stored on the input tape. (Only data for A < 90 shown)

2.2 Level Density Option

The level density formulation used in HETC for the evaporation model is $a = (A/B_0)(1 + Y(A-2Z)^2/A^2)$ with $Y = 1.5$, or $a = A/B_0$. The parameter B_0, which has an important influence on neutron production, is set to 8 MeV in the standard version of HETC for all nuclei.

An option has been added to allow B_0 to vary with A. The values used are those compiled by Baba /4/ from experiments on nuclear level spacing (Figure 2).

2.3 Angular Distribution of Evaporation Particles

In the standard version of HETC, emitted evaporation particles are usually assumed isotropic in the laboratory system. Dr. R. Prael of Los Alamos has made the kinematic modifications to take into account the recoil direction of the residual nucleus during evaporation, and these changes have been incorporated into HETC/KFA-1. In this procedure, the evaporation particle direc-

tions are selected from an isotropic center-of-mass distribution, and this angle and the recoil direction are transformed to provide non-isotropic angular distribution in the laboratory system.

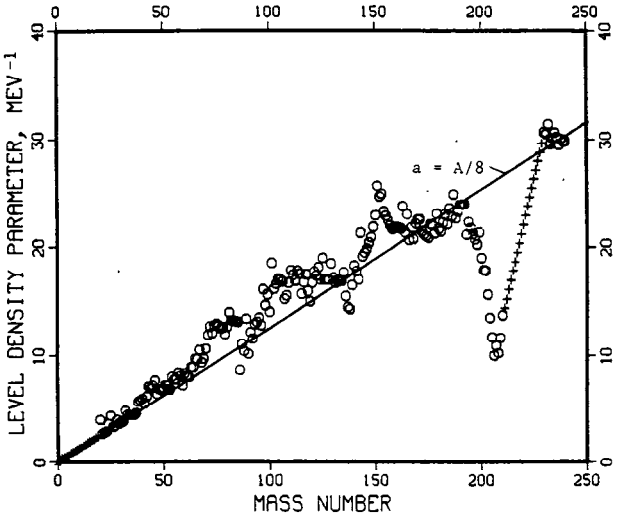

Figure 2 Level density parameters (circle symbols measured data, cross symbol interpolated values) incorporated as a "variable B_0" option in the HETC/KFA-1 code. (The linear dependence of A/8 is usually assumed in the HETC code).

2.4 High-Energy Fission Option

An option for allowing high-energy fission using the Rutherford and Appleton Laboratory (RAL) model written by F. Atchison /5/ has been incorporated into HETC/KFA-1. A series of calculations to check this model against experimental data and the ORNL fission model for both thick and thin targets has been carried out at KFA. Some of these results have been reported at previous ICANS meetings, and all of the comparisons made are included in a recently issued KFA report /6/.

2.5 Low-Mass Heavy Ion Beams

In addition to the standard source particles allowed by HETC (which are p, n, π^+, and μ^+), modifications are incorporated into HETC/KFA-1 to include beam particles with masses up to A = 10. The basic procedure is to represent the projectile ion as a cluster of nucleons, and then treat ion-nucleus non-elastic nuclear collisions as the sum of individual nucleon-nucleus collisions using the standard intranuclear-cascade-evaporation model contained in HETC.

2.6 Miscellaneous

Other updates included in HETC/KFA-1 include range straggling for primary beam particles, different transport energy cutoffs for ionization and nuclear collisions, modifications to the Coulomb scattering treatment, and a procedure for obtaining the spectra of γ-rays from spallation collisions.

3. OTHER UPDATES

The HETC code has also been extended to include elastic scattering and importance sampling, as summarized below. However, these modifications have not as yet been fully tested, so they are not included in the version HETC/KFA-1.

3.1 Elastic Scattering

Updates have been made to allow elastic scattering for neutrons in the energy range from 15 MeV to 20 GeV and protons from 100 MeV to 20 GeV, for target nuclei of arbitrary A.

For elastic cross sections up to the 150 MeV, we have used values from the ORNL HILO cross section library /7/, which are based on optical model calculations. While this library extends to 400 MeV, the values above 150 MeV are too large, as shown for iron, for example, in Figure 3. Thus, in the energy range from 150 MeV to 20 GeV values are taken from the estimates of Wilson and Costner /8/, which are referred to in Figure 3 as the NASA library.

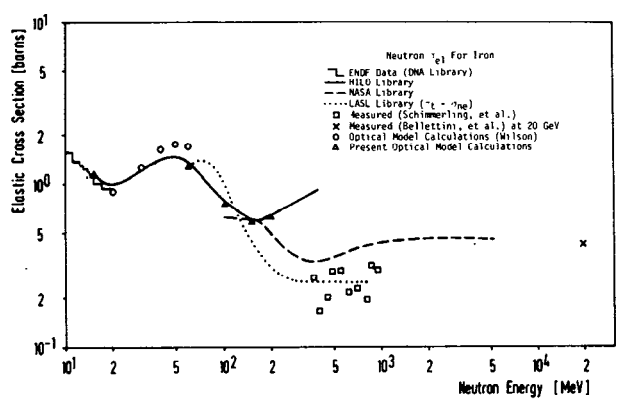

Figure 3 Comparison of neutron elastic cross sections for iron from various sources.

The angular distribution of elastically scattered particles is selected from an approximate optical model expression:

$$f(x) \quad (J_1(x)/x)^2$$

$$\cos\theta = 1-1/2x^2 \; (aA^{1/3} \; (E(E+1878))^{1/2}+1)^{-2}$$

where J_1 is a first kind, first order Bessel function and $a = 7.095 \times 10^{-3}$.

3.2 Importance Sampling

The HETC code has been modified to incorporate the following variance reduction techniques for improved statistical accuracy: (a) collision biasing, where particle splitting and Russian roulette are allowed for cascade particles emerging from collisions, (b) boundary biasing, where splitting and Russian roulette are allowed for particles crossing geometry/media boundaries, and (c) the exponential transform, where path lengths can be biased according to the "importance" of the particle direction. These importance sampling techniques have been programmed in such a way that the degree of biasing can be specified according to various types of criteria that depend on particle parameters, material properties, and target geometry.

4. References

/1/ T.W. Armstrong and K.C. Chandler
HETC - A High-Energy Transport Code,
Nucl. Sci. Engr. 49, 110 (1972)

/2/ P. Cloth, D. Filges, G. Sterzenbach,
T.W. Armstrong and B.L. Colborn
The KFA-Version of the High Energy
Transport Code HETC and the Generalized
Evaluation Code SIMPEL
KFA Report Jül-Spez-196, März 1983

/3/ A.H. Wapstra and K. Bos
The 1977 Atomic Mass Evaluation, Atomic
Data and Nuclear Data Tables 19, 175
(1977)

/4/ H. Baba
A Shell-Model Nuclear Level Density,
Nucl. Phys. A159, 625 (1970)

/5/ F. Atchison
Spallation and Fission in Heavy Metal
Nuclei Under Medium Energy Proton Bombardment, Mtg. on Targetsfor Neutron Beam
Spallation Sources, G. Bauer (Ed.),
KFA Jülich, Germany, 11-12 June 1979,
Jül-Conf-34, January 1980

/6/ T.W. Armstrong, P. Cloth, D. Filges and
R.D. Neef
An Investigation of Fission Models for
High-Energy Radiation Transport Calculations, KFA Report Jül-1859, July 1983

/7/ R.G. Alsmiller,Jr. and J. Barish
Neutron-Proton Multigroup Cross Sections
for Neutron Energies < 400 MeV,
ORNL/TM-7818 (1981)

/8/ J.W. Wilson and C.M. Costner
Nucleon and Heavy-Ion Total and Absorption Cross Sections for Selected Nuclei,
NASA Langley Research Center, NASA-TN
D-8107 (1975)

Proceedings of International Collaboration on Advanced Neutron Sources (ICANS-VII), 1983 September 13-16
Atomic Energy of Canada Limited, Report AECL-8488

CALCULATIONAL METHODS AND HIGH ENERGY CROSS SECTIONS FOR SPALLATION SOURCE SHIELDING

T.W. Armstrong, P. Cloth, D. Filges, H. Schaal

Institut für Reaktorentwicklung
Kernforschungsanlage Jülich
Postfach 1913, D-5170 Jülich 1
Germany

SUMMARY

The features of the calculational methods being used at KFA for SNQ target shield design studies are discussed. The existing high-energy cross section data base is checked against the requirements of these calculations. The two available libraries, HILO and LANL, are intercompared by calculation of neutron fluxes in an iron sphere as a simple benchmark. This benchmark problem was also used to compare codes. A fast running, easy to operate shielding layout and assessment code called CASL is described, which uses approximate, semi-empirical physics treatment.

1 INTRODUCTION

Shielding problems of high proton current spallation neutron sources are unique in terms of calculational requirements because of the combination of a relatively high-energy source, large shielding dimensions, and geometric complexities. Presently there does not exist a computer code system and furthermore only few data suitable for high energy neutron transport calculations are available. There is little experience with the type of calculations needed and the influence of the presently available data bases are not known.

Therefore, we checked the data and computer codes available, whether they are suitable to meet the difficult requirements of this predominately deep penetration problem and proposed a "high-energy neutron shielding benchmark", as neutrons are the main particles in this context. The benchmark allows both comparison of cross-section data libraries and different methods of calculation.

2 CROSS SECTION DATA BASE

The shielding code system suggested here requires high-energy multigroup cross section data for the discrete ordinates transport calculations. Much of the needed cross section data are available, but present data base is not completely compatible with SNQ application requirements because the maximum neutron energy considered is 800 MeV. Also, there are other approximations in the present data base whose accuracy is questionable for the very thick shields of interest for the SNQ.

The approach suggested here is to make ad hoc modifications to the present data to allow "Phase I" calculations to be made, which would include transport calculations to test the importance of present approximations.

2.1 Status of Present High-Energy Transport Cross Section Data Base

A multi-energy group cross section library (called HILO /1/) for coupled neutron/γ-ray transport has recently been developed at ORNL in a format compatible with ANISN and DOT input requirements. Features of this library are summarized in Table I. These data have been obtained by using experimental data at low energies (< 14.9 MeV) and theoretical models at high energies (14.9 - 400 MeV).

Table I

Features of the HILO Library

- Energy Range

  Neutrons: thermal to 400 MeV
  γ rays: 10^{-2} MeV to 14 MeV

- Group Structure

  66 neutron groups
  21 γ-ray groups

- Angular Expansion

  P_5 expansion for E>14.9 MeV
  P_3 expansion for E<14.9 MeV

- Elements Available

  H,B,C,N,O,Na,Mg,Al,Si,
  S,K,Ca,Cr,Fe,Ni,W,Pb

Some work has also been done at Los Alamos /2/ to obtain a high-energy cross section set which extends for neutrons to 800 MeV. These cross sections were obtained in a manner similar to that of the HILO library -- i.e., ENDF data at low energies (<20 MeV) and optical model and intranuclear-cascade-evaporation model calculations for higher energies. The features of the LANL library are given in Table II.

Table II

Features of the LANL Library

- Energy Range

  Neutrons: thermal to 800 MeV

- Group Structure
  41 neutron groups
  (8 groups above 50 MeV)

- Angular Expansion

  P_3 expansion

- Elements Available

  H,C,O,Al,Si,Fe,Mo,W,Pb

It should be noted that the Los Alamos cross section library does not include elastic scattering for nuclides other than H at high energies. This may have implications for

the SNQ bulk shielding calculations in comparing iron vs. cast-iron since cast-iron contains nominally 20 atom per cent C and Si.

2.2 Approximations in Present Data Base

The main restriction in using directly the HILO library is that the maximum neutron energy allowed is 400 MeV, whereas for the SNQ we have neutrons up to the proton beam energy of 1100 MeV.

Other considerations for present applications of the HILO data base include:

1) The high-energy neutron production is based on intra-nuclear-cascade-evaporation model calculations where the spectra were tabulated in rather broad angular intervals(0-30°, 30-60°, 60-90°, and 90-180°) The radiation penetrating deeply in thick shields is mainly high-energy neutrons with peaked angular distributions. Therefore, it is not clear that these few broad angular intervals are adequate for very deep penetration problems.

2) The cross sections represent neutron production by neutron induced collisions. Thus, if neutrons actually produce charged particles (protons or pions) in collisions, and these charged particles produce neutrons, these latter neutrons are not accounted for.

3) The γ-rays produced by low-energy (<14.9 MeV) neutron collisions are included, but γ-ray production by higher-energy neutron collisions is neglected.

4) For the very heavy elements (W and Pb) elastic scattering is neglected because the P_5 order expansion is not adequate to describe the angular distributions.

5) The high-energy neutron cross sections were generated using a version of the intranuclear-cascade-evaporation model that existed in the early 1960's. There have been several improvements to the model (and the input data used) since then. The Los Alamos library was also generated using old versions of the model -- MECC-3 and EVAP-3. There is not much documentation about the Los Alamos library. However the approximations given above are similar also in this library.

2.3 Library Comparison by Benchmark Calculations

Requirements to the Benchmark:

- It is thought of a bulk shielding problem only
- Geometry should be simple that one-dimensional transport codes can run without approximations and results can be compared directly with Monte Carlo.
- Only neutron are considered as they are dominant particles and most radiation transport codes work only on neutral particles.
- Source energy of those neutrons should be sufficiently high and identical in all calculations.

With the above requirements the following modell was defined:

- Iron sphere of 200 cm radius density of the iron: ρ=8 g/cm^3
- no impurities
- a homogeneous and isotropic neutron source is located in the center as a sphere of radius 5 cm. The energy spectrum of that source is a flat distribution from 300 to 400 MeV, comprising exactly the first 4 energy groups of the HILO library and the fifth group of the LANL library, the highest groups that are common to both of the two existing libraries in the high energy region.

The Monte-Carlo-Code considered was the HETC program, and for one-dimensional transpt calculations ANISN. For the calculations here the energy range was taken from 50 to 400 MeV, because onyl high-energy neutrons are of interest to deep penetration and both libraries have group limits at 50 and 400 MeV, respectively.

The iron sphere was radially subdivided into 40 meshes of 5 cm, to perform the following 4 ANISN calculations:

with library	to expansion
HILO	P_0 (HILOP$_0$)
HILO	P_5 (HILOP$_5$)
LANL	P_0 (LANLP$_0$)
LANL	P_3 (LANLP$_3$)

In addition a HETC calculation was made and evaluated with the auxiliary code SIMPEL /3/. SIMPEL produces mesh fluxes for primary and secondary neutrons, the sum of which was compared with the ANISN results.

Results of the Benchmark Calculations

Fig. 1 shows the neutron flux of the source group for ANISN calculations HILOP$_0$ and HILOP$_5$. It is seen, that the flux in the surface mesh (at 200 cm) is higher by orders of magnitude in the HILOP$_5$ than in the HILOP$_0$ calculation. This, however, was to be expected, but leads to the question whether a P_5 expansion of the cross-section is already sufficient to describe transport of high energy neutrons adequately.

Fig. 2 shows the neutron flux of the source group for ANISN calculations LANLP$_0$ and LANLP$_3$. Unlike the results of the HILO calculations the flux in the surface mesh is for LANLP$_3$ only twice that of LANLP$_0$. This somewhat surprising result is due to the fact that there is no elastic scattering cross-section for high energies in the LANL library and on the other hand elastic cross sections in HILO are much too high in this energy region.

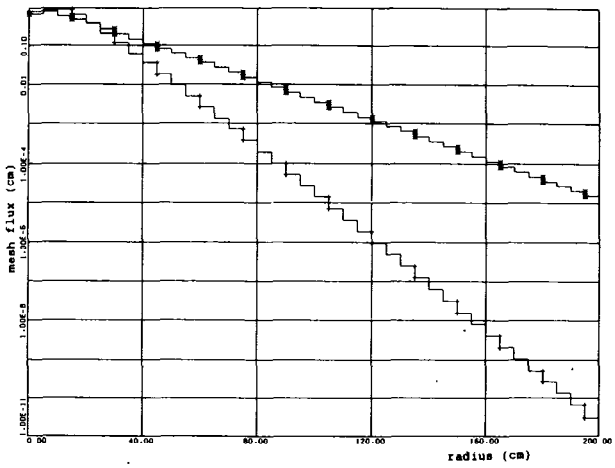

Fig. 1 Neutron Flux (300-400 MeV) per Source Neutron (Integrated over Mesh and Time) + HILOP0 * HILOP5

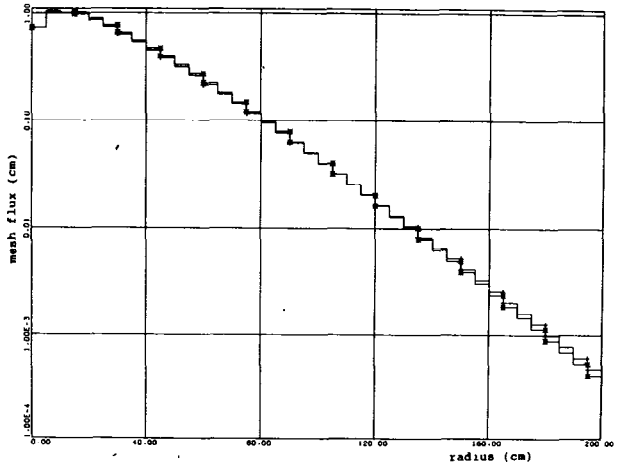

Fig. 3 Neutron Flux (50-400 MeV) per Source Neutron (Integrated over Mesh and Time) + HILOP5 * LANLP3

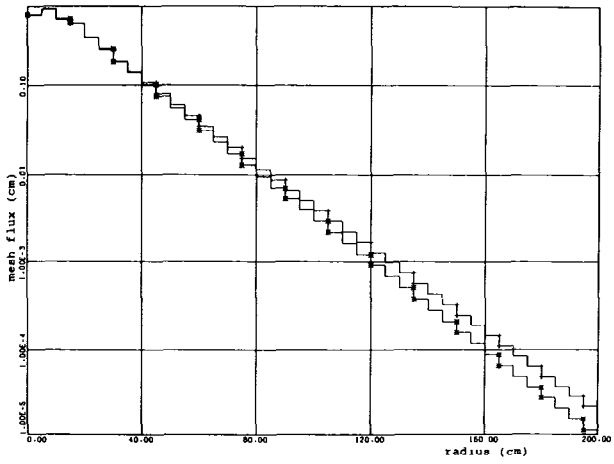

Fig. 2 Neutron Flux (300-400 MeV) per Source Neutron (Integrated over Mesh and Time) * LANLP0 + LANLP5

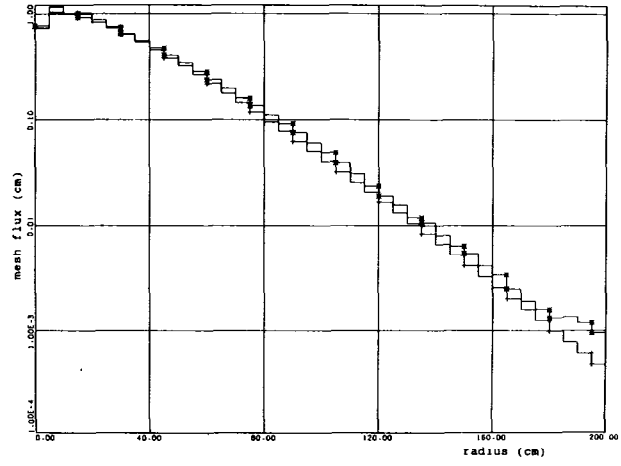

Fig. 4 Neutron Flux (50-400 MeV) per Source Neutron (Integrated over Mesh and Time) * HETC + LANLP3

Because naturally the calculations in the higher P orders give higher fluxes in the surface mesh, the results of these calculations were compared. Fig. 3 shows the flux in the whole energy range from 50 to 400 MeV. The general trend, which is stated here is that using higher P expansion of neutron cross sections leads to higher fluxes in the surface mesh. Thus the question arises whether the current available expansions (P_3 for LANL, P_5 for HILO) are sufficient. To clarify this the ANISN LANLP$_3$ calculation which results in the highest flux was compared to an according HETC-Monte-Carlo calculation.

In general can be stated, that flux values of LANLP$_3$ are lower in the vicinity of the surface than those of the HETC calculation. The discrepancies are, however, with standard deviation of about 30 % marginal in the case of HETC and should therefore not be overemphasized.

How insufficient the representation of the forward peaked cross section data might be, may be judged from Fig. 5 in which the angular distribution of certain LANL data is compared to a HETC calculation.

2.4 Data Base Modifications for Temporary Usage

The high energy cross section library HILO has the advantage of containing γ-cross-sections, but it has the disadvantage that the maximum energy is 400 MeV and that furthermore the elastic scattering seems to be incorrect. The LANL library has the advantage that the maximum energy is 800 MeV, but has the disadvantage that γ-ray-cross-sections are neglected. So we decided to generate a library which combines the advantages of both libraries:

We combined the libraries LANL and HILO in a way, that LANL-data are used for the neutron cross sections in the energy range from 800 MeV to 50 MeV and that HILO-data are

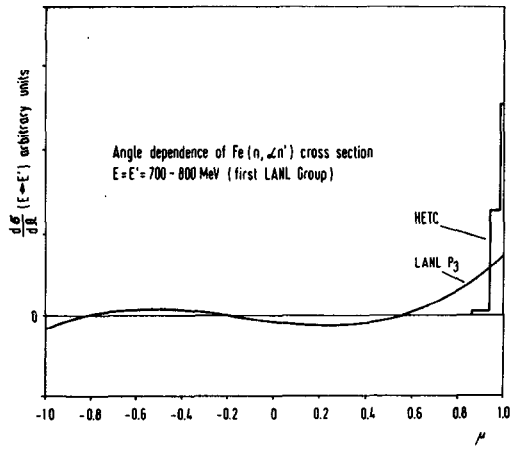

Fig. 5 Comparison of Angle Dependence of LANL P_3 Data with HETC Calculation

used for neutron energies less than 50 MeV and for γ-groups. The new library contains the following eight elements as ANISN-formatted data in Legendre expansion P_3:

H, C, O, Al, Si, Fe, W, Pb

The library consists of 53 neutron groups and 21 γ-groups.

Some provision has to be made for neutrons in the range from 800 MeV (present upper limit) to 1100 MeV (SNQ source energy). One simple method would be to assign all neutrons in this energy range to the midpoint of the energy group (700-800 MeV) presently allowed by the cross section set, but with an increased neutron multiplicity to conserve energy. That is, the statistical weight of a source neutron with energy E>800 MeV would be multiplied by E/750. This is somewhat justified because the neutron total cross sections are approximately constant in this energy range. However, the partial inelasticities (fraction of energy carried away from a collision by secondary particles) varies.

2.5 Data Updates for High-Energy Shielding Codes

We suggest that new cross sections be generated for at least one shielding material (Fe) with the energy range extended to 1100 MeV and with finer angular resolution than the four broad intervals in the present HILO data base. This will allow transport calculations to be made to see the difference in shield attenuation prediction by the present and updated data for the case of an Fe shield. A decision can then be made as to whether new cross sections should be generated for other materials.

One way of obtaining these updated cross sections is to use the same procedure as used in generating the HILO cross section set, which consisted of: (a) calculating differential particle emission spectra and nonelastic cross sections using the Monte Carlo intranuclear-cascade-evaporation model, (b) fitting these histogram data with continuous analytic functions for interpolation and to reduce the influence of statistical fluctuations, and (c) applying these analytic representations to put the data in the multigroup, Legendre expansion format needed by the transport codes. In the HILO library, a 1/E flux weighting factor was used for averaging the cross sections over energy group.

To account for the extreme forward peaking of the new data it is necessary to use very high P order expansion. To give an impression Fig. 6 shows several P approximations of a certain neutron production cross section of protons (the situation for neutrons is very similar). As can be seen, only P_{19} seems to be adequate. This may cause difficulties in using those data by the transport codes.

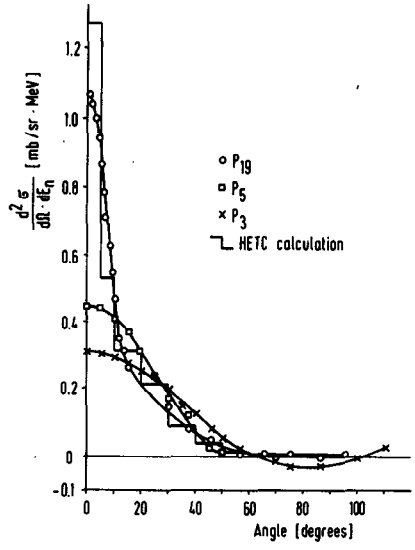

Fig. 6 Legendre Expansion of the Neutron Production Cross Section for Protons on Iron: E_p=1100 MeV, E_n=500-550 MeV

Nuclear elastic scattering at high energies (> 15 MeV) is a mechanism which is often neglected in high-energy radiation transport calculations because the energy loss and angular deflections from such interactions are small. However, there are several situations related to SNQ shielding estimates and heating where elastic scattering effects may be important. For example, small angular changes can effect shield attenuation for very deep penetrations.

Assessment of Elastic Cross Sections

Elastic cross sections for neutrons have been collected from several sources for comparison. For example, Figure 7 compares several sets of data for iron including: (a) Cross sections from the low-energy (< 19.6 MeV) DNA library /4/, which is based on ENDF data. (b) Cross sections from the ORNL high-energy (< 400 MeV) HILO library. (c) Cross sections from NASA compilation for the energy range 100 MeV to 22.5 GeV /5/. (d) The measurents of Schlimmerling et al. /6/ in the 400-1000 MeV range, and the measurements of Bellettini, et al., /7/ at 20 GeV.

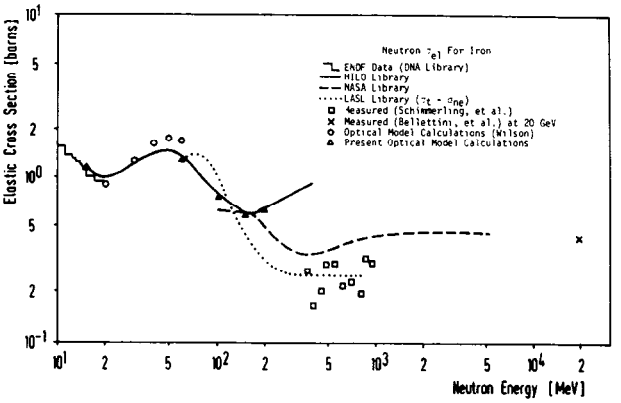

Fig. 7 Elastic Scattering Data

The main conclusion from Fig. 7 is that there are large differences in the data in the 10^2 - 10^3 MeV range. In particular, the HILO values appear incorrect > 150 MeV. (This is also the case for other elements, e.g. the reason for the apparent error in the HILO cross sections at > 150 MeV is probably that the optical model parameters used based on fits to dat < 50 MeV) are not applicable at high-energies.

The A dependence of the HILO elastic scattering cross section at high energies also differs substantially from the NASA values. For example, at 400 MeV, σ_{el} $A^{2/3}$ for the HILO library, whereas σ_{el} $A^{.94}$ for the NASA library. (The NASA values are in good agreement with the measured /7/ dependence of σ_{el} $A^{1.04}$ for energies >10 GeV.)

3 COMPUTER CODES

We have considered different calculational methods for deep penetration problems showing us the following:

The Monte-Carlo code HETC faces difficulties with statistics at depths of 1 m and more. On the other hand this code can treat protons and other charged particles and is capable of complex geometries.

The one-dimensional transport program ANISN can calculate deeply into the shielding if suitable cross-section data is available. The main disadvantage is that it can treat only very simple geometry and no protons.

3.1 HETC/ANISN Coupling

We draw the conclusion that the combined advantages of the two types of codes could be helpful for deep-penetration problems:

Near the source (within the target, the moderators and inner part of shield) calculation is done with HETC as deep into the shield as secondary proton become negligible. In this area a coupling surface is defined at which the angle dependent neutron flux towards the outer surface of the shield is recorded by the auxiliary code SIMPEL. This flux is fed as a surface source into ANISN. Thus, the neutron fluxes within the shield beyond the coupling surface can be calculated in simple geometry (sphere or slab). A "coupled" calculation was performed as a test for the above mentioned benchmark of an iron sphere of 2 m radius. The neutron source was 5 cm volume source in the center with a flat energy distribution between 300 and 400 MeV. A spherical coupling surface was chosen at radius 50 cm. After computing the surface source with HETC/SIMPEL the ANISN calculation was started in spherical geometry with black boundary conditions at the inner side of the coupling sphere.

The LANL library was used in Legendre order P_3. The result of the calculation was compared with an ANISN only calculation starting again with a 5 cm thick volume source in the center of the sphere. The comparison is given in Fig. 8 and shows reasonable agreement.

It is thought of providing coupling also to the 2-D transport code DOT to allow collimator calculations.

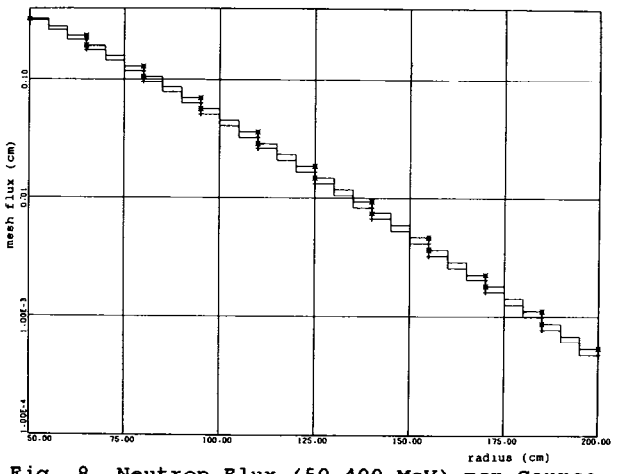

Fig. 8 Neutron Flux (50-400 MeV) per Source Neutron beyond coupling surface (Integrated over Mesh and Time)
* ANISN only + ANISN/HETC Coupling

3.2 The CASL Code

High-energy radiation transport codes (namely, the discrete ordinates codes ANISN and DOT, and the Monte Carlo codes HETC and MORSE) are being applied at KFA to investigate some of the fundamental shielding problems associated with the SNQ. While these codes have the advantage of containing state-of-the-art physics treatments and cross-section data, they require considerable set-up and computing time. It is not practical to run these large transport codes for detailed calculations to address all of the numerous radiation safety questions and engineering-type design problems associated with target station, experimental area, and accelerator shielding.

Therefore, we are writing a simple, fast-running Shielding Layout and Assessment Code (CASL) which has rather general source, material and geometry capabilities but which requires minimal computer and set-up time, and can operate in an interactive mode. While the CASL code uses approximate, semi-empirical physics treatments, it can provide sufficient accuracy for many practical problems and pa-

rameter variation surveys where only approximation estimates are adequate.

The basic calculational approach of the CASL code is to assume a simple, exponential attenuation relation for the shield attenuation of high-energy radiation. The form of this semi-empirical model used here is similar to that used for many years fro accelerator shielding estimates, but with two main differences: (a) the shield attenuation parameters and the neutron production data for proton beams needed for input are generated by detailed radiation transport codes (with options for experimental data input, if available), and (b) the semi-empirical attenuation model is coupled with simple 1-D and general 3-D geometry modules to automate the generation of results for either simple or complicated material/geometry configurations.

Calculational Method of the CASL Code

The form of the attenuation equation used is shown in the Equation, where the notation is as follows:

$$D(\bar{r}) = \frac{\tilde{D}\cdot\dot{S}_n(\bar{\Omega}\cdot\bar{\Omega}_o;E_o,A_t)B(E_o,t)\exp(-t/\lambda(E_o,t))}{\bar{F}_h|\bar{r}-\bar{r}_o|^2}$$

(a) $D(\bar{r})$ is the dose-equivalent rate at location $\bar{r}$ and direction $\bar{\Omega}$ from a proton beam of energy E_o and direction $\bar{\Omega}_o$ bombarding a target material of mass number A_t at location $\bar{r}_o$.

(b) The high-energy neutron flux at material thickness t is $\Phi_h(t)=B\cdot\exp(-t/\lambda)/|\bar{r}-\bar{r}_o|^2$, where B is "buildup factor" and λ is the attenuation length.

(c) The dose rate due only to the high-energy neutrons is then $\Phi_h(t)/\bar{F}_h$, where $\bar{F}_h$ is an average neutron flux-to-dose factor for neutrons >100 MeV.

(d) The dose is determined predominately by the low-energy neutrons whereas the attenuation equation gives only the high-energy dose. Therefore, the dose-ratio factor $\tilde{D}$ (total dose/dose due to neutrons >100 MeV) is applied. (Thus, $\tilde{D}$ depends on the neutron spectra of the particular shield material used, which we obtained from transport code calculations.)

(e) The source term $\dot{S}$ is the rate of high-neutron production, per steradian, in the direction $\bar{\Omega}$ with respect to the beam direction $\bar{\Omega}_o$.

The general capabilities of the CASL code are summarized in Table III. The neutron production data are calculated for thin targets. They can be applied approximately for thick targets by using empirical relations giving the number of collisions in a thick target creating high-energy neutrons; or, more accurately, by using the high-energy neutron leakage for thick targets (e.g., from the SNQ target wheel) calculated by HETC as input.

The parameters Φ_h, λ, B and $\tilde{D}$ are being calculated with ANISN. An advantage of using transport codes for generating shield parameters is that dependence upon shield thickness and source energy (usually neglected in semi-empirical shielding calculations) can be taken into account.

Table III

Capabilities of the CASL Code

- Modes of Operation

  "Layout": 3-D shield requirements for specified dose rate criterion

  "Assesment": dose rates at arbitrary locations for specified simple or 3-D configurations

- Beams/Materials/Geometries Allowed

  proton beams: 100 MeV to 1 GeV
  target materials: arbitrary
  shield materials: those most commonly used

  geometries: simple 1-D or Com-Geom 3-D

- Source Options

  protons on thin targets
  protons on thick targets

  empirical treatment

  use target leakage neutrons from HETC code calculations

4 REFERENCES

/1/ HILO Data Package: "66 Neutron , 21 Gamma-Ray Group Cross Sections for Radiation Transport for Neutron Energies up to 400 MeV", DLC-87, RSIC.

/2/ W. B. Wilson, "Nuclear Data Development and Shield Design for Neutrons Below 60 MeV", LA-7159-T, (1978).

/3/ P. Cloth, D. Filges, G. Sterzenbach, T. W. Armstrong and B. L. Colborn, "The KFA-Version of the High Energy Transport Code HETC and the Generalized Evaluation Code SIMPEL", KFA Report JüL-Spez-196, (1983).

/4/ D. E. Bartine, J. R. Knight, J. V. Pace, and R. W. Roussin, "Production and Testing of the DNA Few-Group Coupled Neutron-Gamma Cross Section Library", ORNL/TM-4840, (1977).

/5/ J. W. Wilson and C. M. Costner, "Nucleon and Heavy-Ion Total and Absorption Cross-Section for selected Nuclei", NASA Langley Research Center, NASA TN D-8107.

/6/ W. Schlimmerling et al., "Neutron-Nucleus Total and Inelastic Cross Sections: 900 to 2600 MeV/c", Phys. Rev. C, 7, 248, (1973).

7/ G. Belletini et al., "Proton-Nuclei Cross Sections at 20 GeV", Nucl. Phys. 79, 609, (1966).

Proceedings of International Collaboration on Advanced Neutron Sources (ICANS-VII), 1983 September 13-16
Atomic Energy of Canada Limited, Report AECL-8488

PROGRESS REPORT ON THE SNS TARGET STATION

A Carne
Rutherford Appleton Laboratory
Chilton, Oxon, UK

1. Introduction

This progress report continues the series given in previous ICANS meetings (1). It should be the last in the design and construction phases and inevitably contains much engineering detail. For the next ICANS meeting we look forward to reporting first operational experiences, the schedule for first neutrons being October 1984. Progress is reported under the five broad headings of Target, Target Assembly, Control System, Bulk Shield and Remote Handling. Additional facilities to the target station are also reported.

2. Target

The dimensions and parameters of the target were given at the ICANS-VI meeting. Since that time prototype production of complete target plates, including two with thermocouple wells, has been successfully completed. Good quality bonding has been achieved in all cases. Accordingly a contract was placed for the production of 2 complete target modules, each consisting of 23 plates, with delivery of the first module in October 1983. Further modules will be ordered as dictated by operational experience. The stress calculations and design report for the target vessel and its components have been completed and certified under the ASME III code, and production is underway for delivery complete by December 1983. A back-up target with tantalum plates will also be built.

3. Target Assembly

(a) Ambient

The reflector vessel has been reduced from twelve units to four in a simplifying re-design. Boron laminate ('BORAL') decouplers will be incorporated within the vessels and utilising its coolant, rather than use a separate cooling system. The material of the vessels will be stainless steel. Production of the vessels and final machining of the beryllium rods are underway, for completion in December 1983. The cadmium decoupler for the target will now be attached to the reflector vessel to obtain contact cooling, which is important when considering target cooling under fault conditions (in thermal isolation the cadmium could melt).

The ambient moderators are in the stage of final design: they will be non-pressure vessels operating at less than 0.7 atm, made of Aluminium-Magnesium (5%) alloy. They will be constructed and tested within the spirit of the British standards for pressure vessels.

(b) Cryogenic

Detailed design of the cold moderators has continued and stressing has been carried out using finite element techniques (NASTRAN). A prototype vessel is being manufactured which will be pressure tested to confirm the computer analysis. Production moderators will use Aluminium-Magnesium alloy, as above, even though this is not a classified material under the ASME III code. The hydrogen moderator, which operates with 25K supercritical para-hydrogen at 15 atm, will be triply-contained to satisfy safety requirements. Figure 1 shows a section of the hydrogen moderator.

Both hydrogen and methane refrigerators have been ordered, delivery of the methane one is due in September, and the complete hydrogen machine is due at the beginning of 1984. A tender exercise is underway for the transfer lines. Test areas for the refrigerators and moderators have been set up within the SNS complex to determine satisfactory performance prior to final installation.

Major components of the water services are on order, including heat exchanges, ion-exchange columns, tank and filters. Service trolleys (part of the movable train for operation-to-maintenance locations) are due for delivery in September.

Major simplifications of the water system have been achieved (in particular in providing the totally independent circuits for the target plates and target pressure vessel) as a result of systems reviews in preparation of safety documents (q.v.).

4. Control System and Safety

The software for the extracted proton beam and target station are on schedule for initial completion by June 1984. Routines have been written for the control of the beam line magnets and the final control program will be started soon. On the target station, the microprocessor control system (MCS) has been extended to drive the dynamic interlock interface controlling the permit state of the SNS proton beam. It now incorporates most of the software fault checks and displays each interlock state on an appropriate 48-channel display board. Some MCS routines have been converted to machine language and the number of data channels increased to allow future extensions and flexibility. Data exchange to the minicomputer (GEC 4070) has been running for several months without faults. The mini-computer control system (MINICS) has two separate master programs for target station control and logging. Control programs include software to display the status of all valves and the status of critical plant parameters from the MCS system. Logging routines include all critical parameters and derived parameters, e.g. effective cooling gaps derived from flow rate and pressure drop. Averaging logging runs will indicate long term performances of the plant.

Development of controls hardware is progressing on schedule, however the production of hardware has been limited by demands for resources elsewhere on the SNS. The program calls for completion of hardware in March 1984, to allow commissioning for first neutrons in October 1984. The target station controls room has been completed.

A major effort has been put into the safety assessment and hazard survey of the target station. Under new regulations, soon to become law in the UK, if a quantity of radioactivity exceeds amounts defined in those regulations, a hazard survey must be written. This has been done, plus a large supportive document ("Safety Assessment of the SNS Target Station", August 1983 (2)), which in turn has a number of detailed supportive papers. In one of these, it has been shown that with beam-off and a catastrophic failure of cooling to the target, the maximum temperature reached under decay heating is less than 540°C, i.e. the uranium will not melt. Notwithstanding this statement, a further paper gives calculations of the dose to RAL staff and to the nearest local population if volatile and gaseous radionuclides were able to escape after a meltdown. Iodines, ^{131}I and ^{133}I, are the most significant radiologically, but the doses received are < 1% ERL* for RAL staff evacuating the experimental hall within 3 hours and for the nearest local population < 10^{-3} ERL over 30 days, The documents are now being examined towards seeking approval to operate the SNS in 1984.

5. Bulk Shield

The six modules of the shielding inserts have been installed. Shielding blocks which fit within the inserts are in manufacture for delivery by December 1983.

The shielding wedges have all been delivered and installed to check alignment, and are seen in position in figure 2. They have now been removed pending delivery of the target void vessel. The target void vessel, a pressure vessel designed under the ASME III, category A code, is due for delivery at the end of September. The bridge to be mounted over the void vessel (and therefore also required to be an "ASME designed" structure) and which supports the shielding above, is due for delivery in mid September. The 20 beam shutters are in manufacture, with delivery to be complete by December 1983. Several part-shutters have been delivered and, as can be seen in figure 3, a whole shutter, weighing some 22 tons, has been assembled for test mounting within the shielding wedges also for ventilation tests. The incoming proton beam window has been designed as a double-walled Inconel vessel with light water cooling, based on the LANL design. Access to this window for repair will be obtained by pulling it into the EPB shielding enclosure, an operation requiring shielding from the induced activity within the void vessel (the γ dose rate at centre of the empty void vessel being 1 Sv/hr).

6. Remote Handling

The foundations of the remote handling cell and shielded services area have been laid, incorporating the rail system for the services trolleys and a double drainage system to take split active liquids, see figure 4.

* ERL = Emergency Reference Level ≡ 50% ALI for occupationally exposed personnel

ALI = Permissible annual limit of intake

The services area construction itself is due for completion at the end of September. This large area 8 (w) x 22 (l) m^2 has walls 7m high and about 1m thick of concrete. This thickness is required to shield against short lived hard γ-emitters (e.g. ^{16}N) from the target primary coolant, the radiation dose rate 1m from the cooling pipes being 1 Sv/hr. The concrete roof will be initially ½m thick, perhaps increased later to 1m according to operating experience.

Construction of the remote handling cell is about to commence, with completion planned for the end of December 1983. Most of the components have been delivered. The main shielding door has been designed and parts are in manufacture. Design, development and testing of the target removal equipment is about to be restarted (after delays due to other priorities), where considerable simplification is now possible following the calculations of thermal behaviour of the target under decay heating. Cooling will be maintained for 24 hours after shut-down, after which no cooling will be provided, even in the temporary storage wells (prudence however requires that provision for cooling be kept).

7. Other Facilities

Components for the irradiation test facility have been on order, with delivery scheduled to match the installation of major target station components. Some studies have started towards proposals for test rigs to be mounted within the access tube, e.g. a furnace for test samples up to a temperature of about 700°C.

The installation of the EPB will allow the provision of an intermediate target (20 mm graphite) some 20m upstream of the main SNS target. The possible secondary beam facilities from this target were described in the last progress report (ICANS-VI). In particular, a pulsed μSR facility of great flexibility was proposed to the Science Board of the SERC in January 1983. However funds were not available at that time for the installation of this facility. Some simplified μSR facility may still be built for R & D work.

In May 1983 an agreement was signed between the RAL (SERC) and KfK, Karlsruhe to build a large neutrino facility on the south side of the SNS experimental hall. Not only does the SNS target generate large quantities of neutrons, at the same time it produces large numbers of pions which emit neutrinos whilst decaying. In particular π^+ at rest produces ν_μ ($E(\nu_\mu)$ = 29.79 MeV) and μ^+ which in turn decays into ν_e and $\bar{\nu}_\mu$ with an energy spectrum with cut-off at about 53 MeV. For a 200 μA incoming proton beam, equal numbers of neutrinos (10^{14} ν/sec) of each kind are produced. This production rate, combined with the low duty cycle ($\sim 10^{-5}$), makes the SNS a uniquely powerful facility.

Over the initial five year life of the facility five major experiments are proposed in the first instance, including elastic-lepton scattering, neutral current excitation of the nucleus and $\nu_e \leftrightarrow \nu_\mu$ oscillations from inverse β-decay in H and C. The count rates are so low that background counts shound not exceed ∿ 1/day from the SNS source and be "negligible" from cosmic sources. Hence massive shielding around the liquid scintillator detectors is necessary. The walls must be 2.2m thick steel and the roof some 3m

thick: total quantity of steel about 5500 tons. The detector itself will weigh between 50 and 300 tons.

Figure 5 shows (roughly) the layout on the experimental floor and the relation to the target station. This figure is of historic interest in that it formed the basis of the agreement, which was supported by the Science Planning Group of the SNS. Figure 6 shows the shielding bunker together with the neutron beam instrument layout in the hall.

Work on building the foundation for the bunker is due to start in October 1983 and should finish May-June 1984. After this the steel shielding will be installed. Careful planning is required to minimise any conflict with the neutron instrument installation. A large support building built against the outside of the south wall of the experimental hall will form part of the facility. Completion of the RAL part is due by about the beginning of 1985 (depending on steel delivery), ready to receive the detectors for experiments to begin. These will be done by staff from KfK with collaboration from UK Universities. The neutrino facility will be an exciting addition to the SNS as a "universal" source.

8. Acknowledgements

It is a pleasure to acknowledge once again the efforts and enthusiasms of the members of the SNS Target and Utilisation Group. The collaboration of members of Neutron Division is acknowledged, also the efforts of EBW Division in developing the design for the neutrino facility.

9. References

1. A Carne, Report on the SNS Target Station: ICANS Reports, in particular ICANS IV and VI

2. "Safety Assessment of the SNS Target Station", Compiled by A Carne and G H Eaton, SNSMC/P6/82, revision 1

10. Figures

1. Section drawing of hydrogen moderator, showing its triple containment.

2. View of target station showing shielding wedges initially positioned.

3. Whole shutter assembly in mounting tests with target station shields.

4. Profiled floor of services area, showing drainage system.

5. Plan of neutrino bunker.

6. Neutrino bunker vis-a-vis neutron instruments in R55.

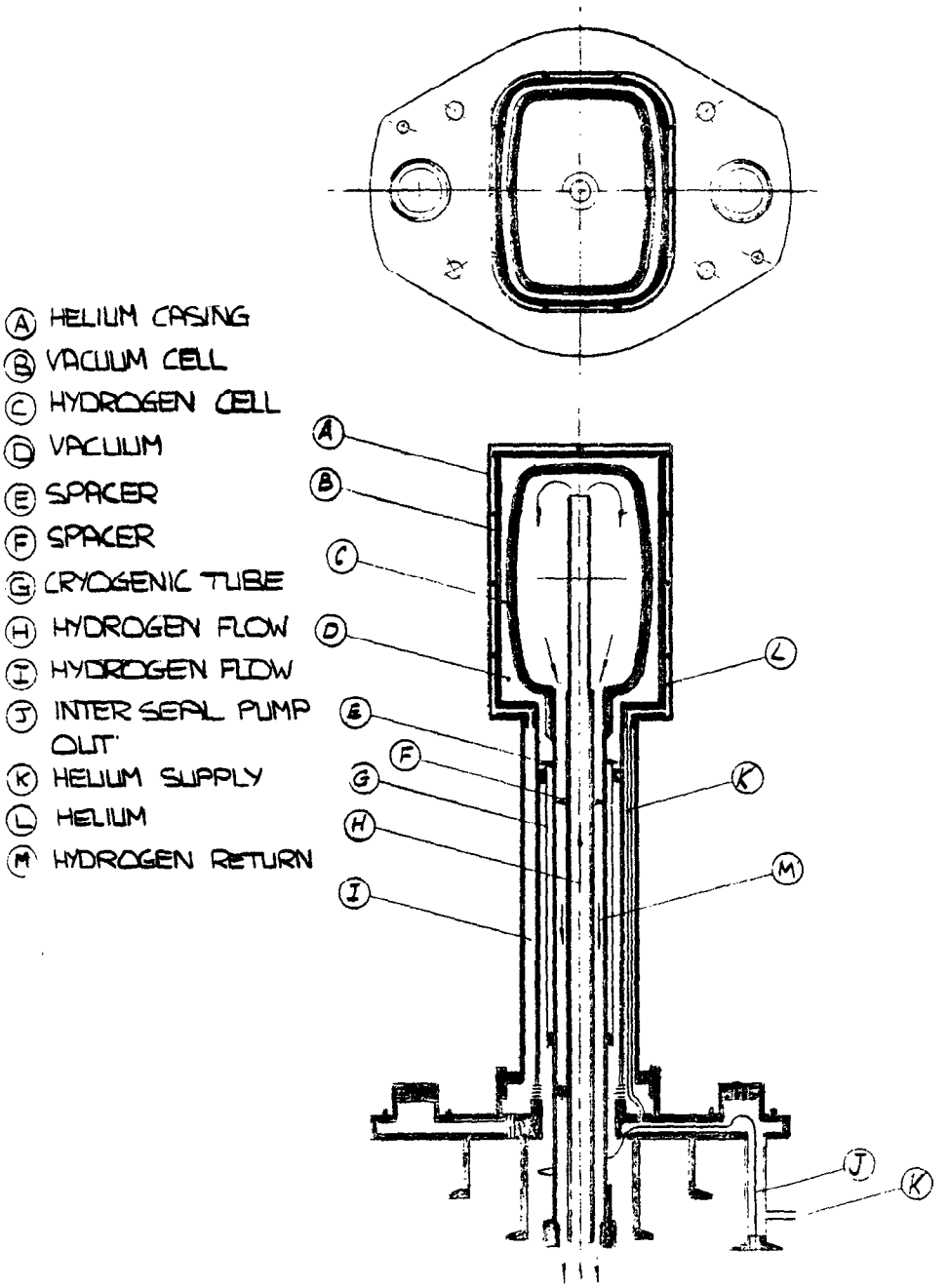

FIGURE: 1 HYDROGEN MODERATOR

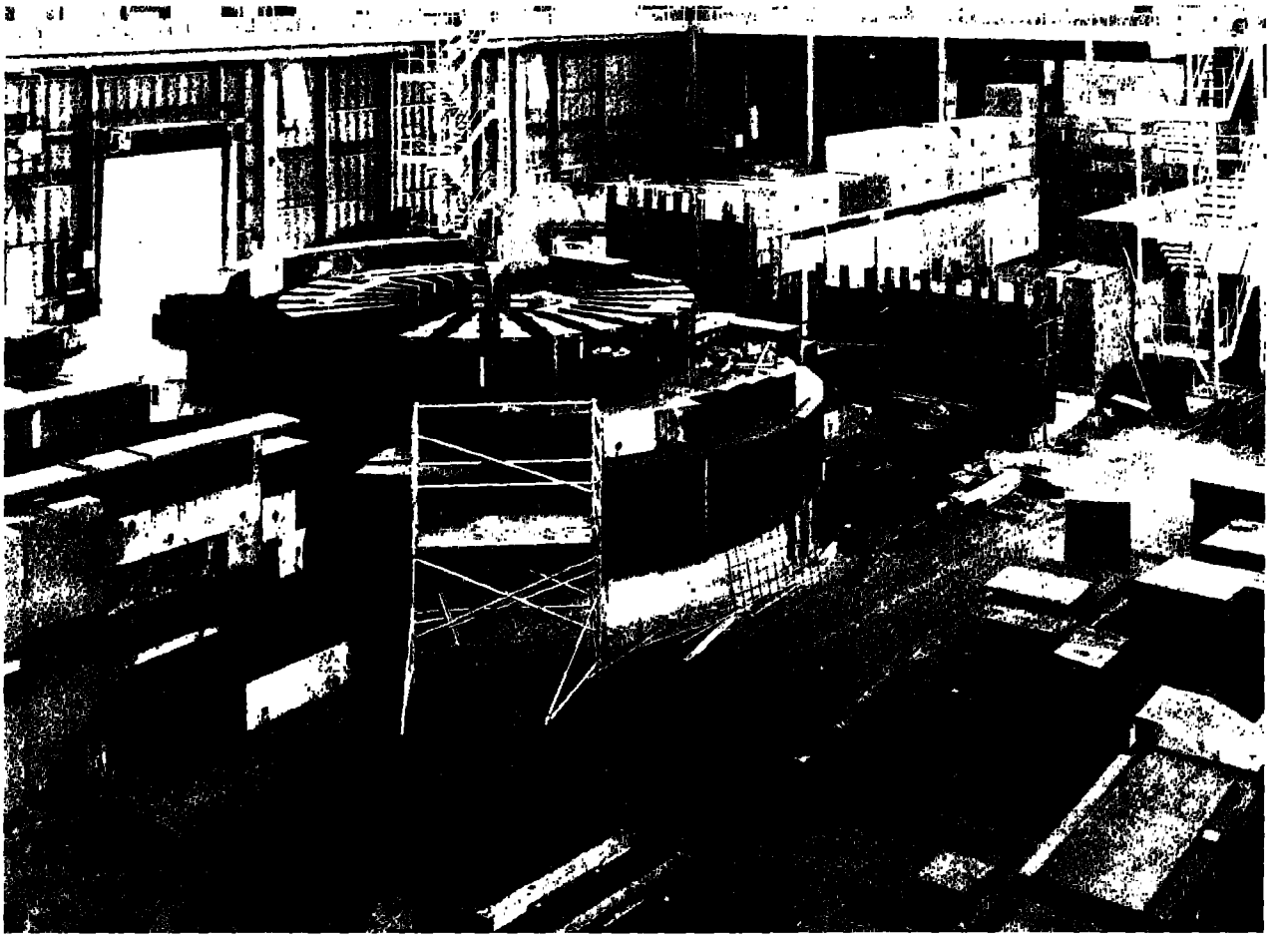

FIGURE 2: View of Target Station Showing Shielding Wedges initially positioned.

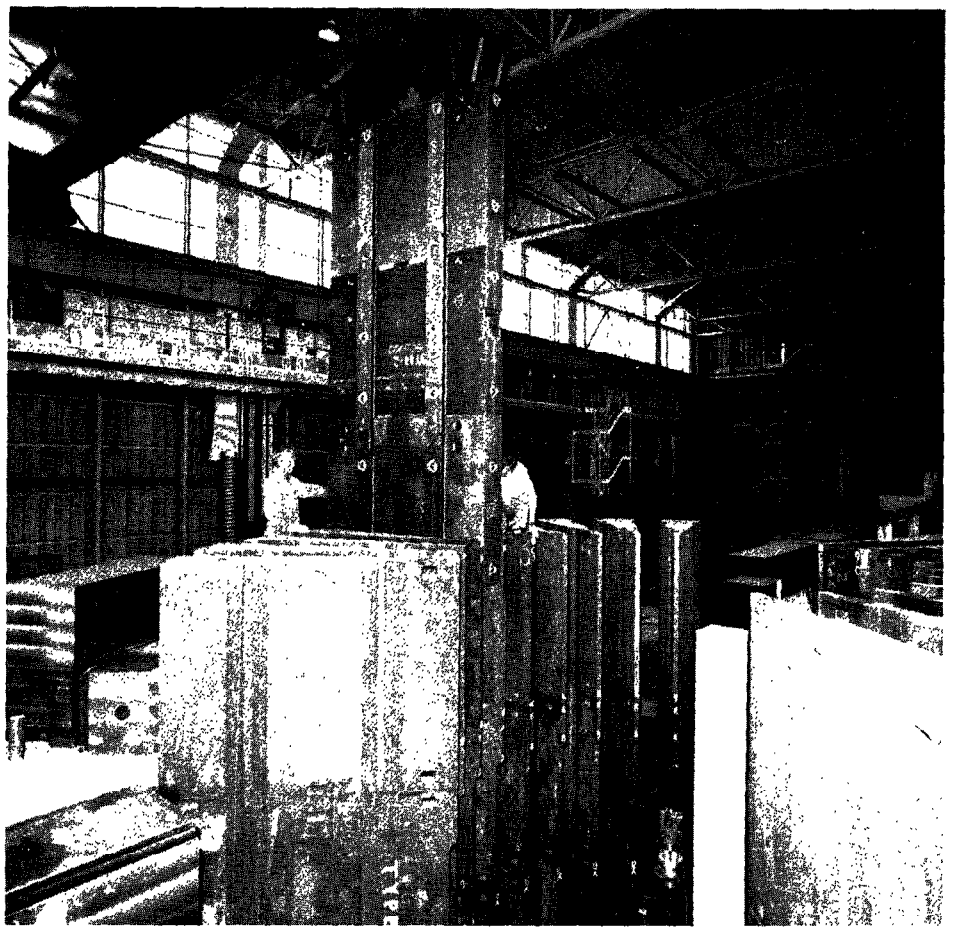

FIGURE 3: Whole Shutter Assembly in Mounting Tests with Target Station Shielding.

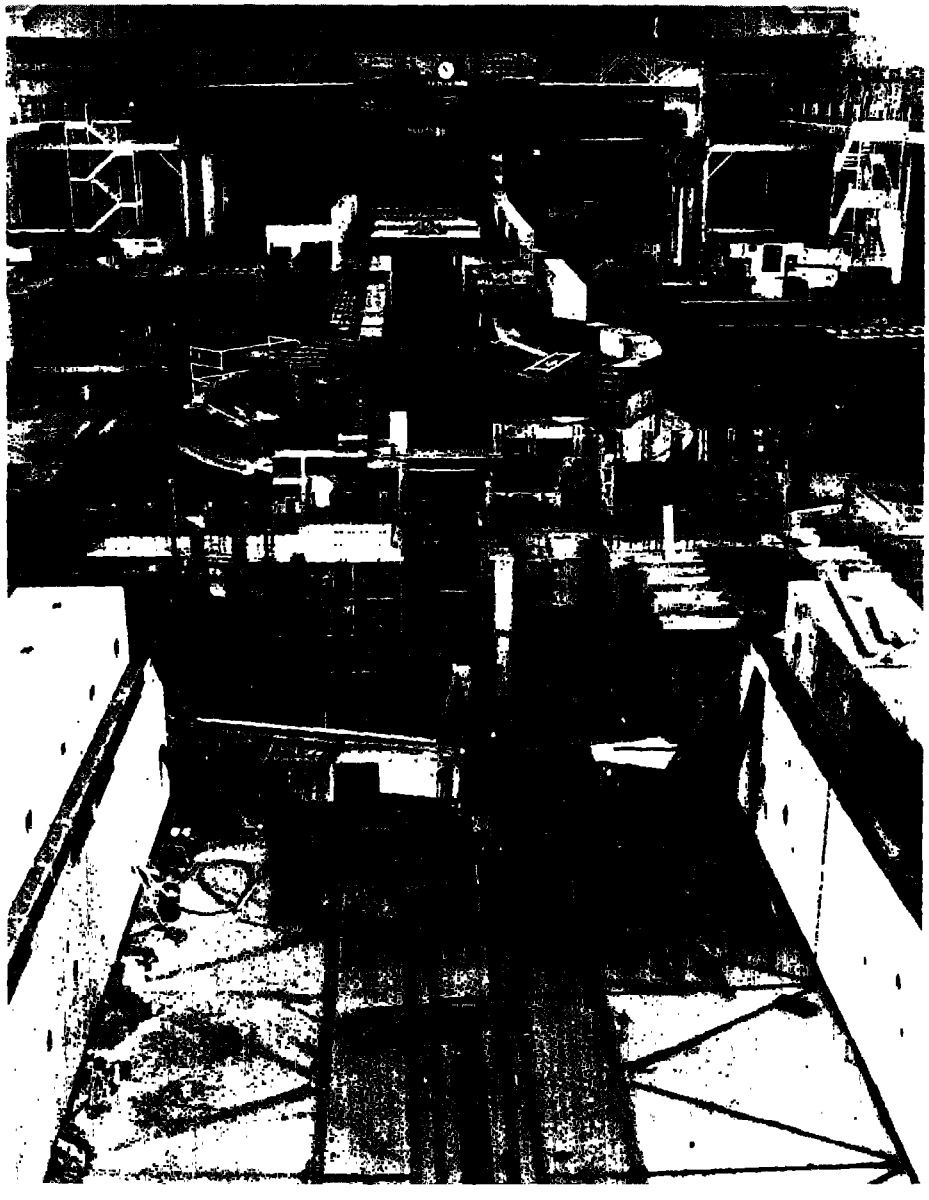

FIGURE 4: Profiled Floor and Services Area Showing Drainage System.

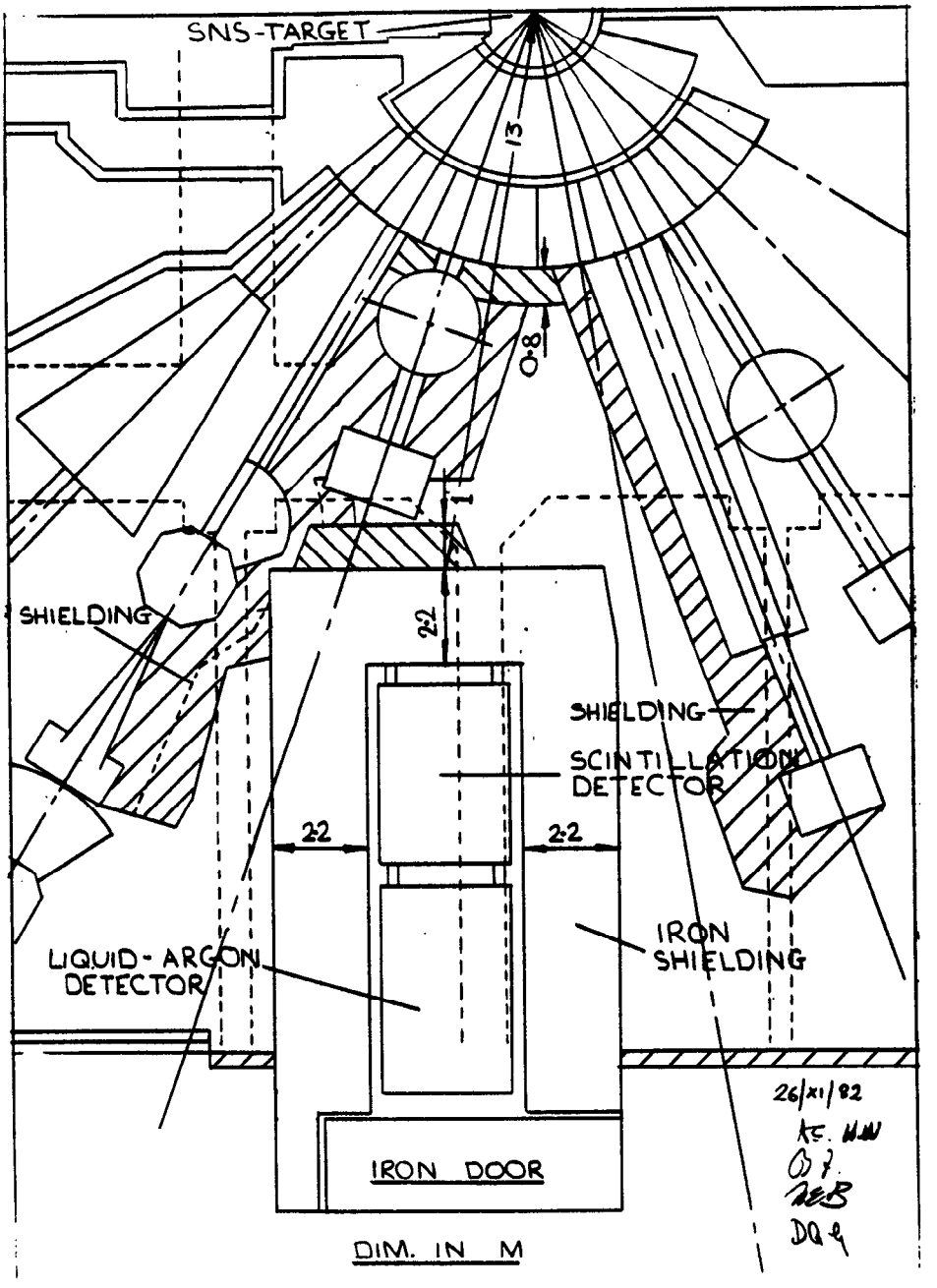

FIG·5 PLAN OF NEUTRINO BUNKER

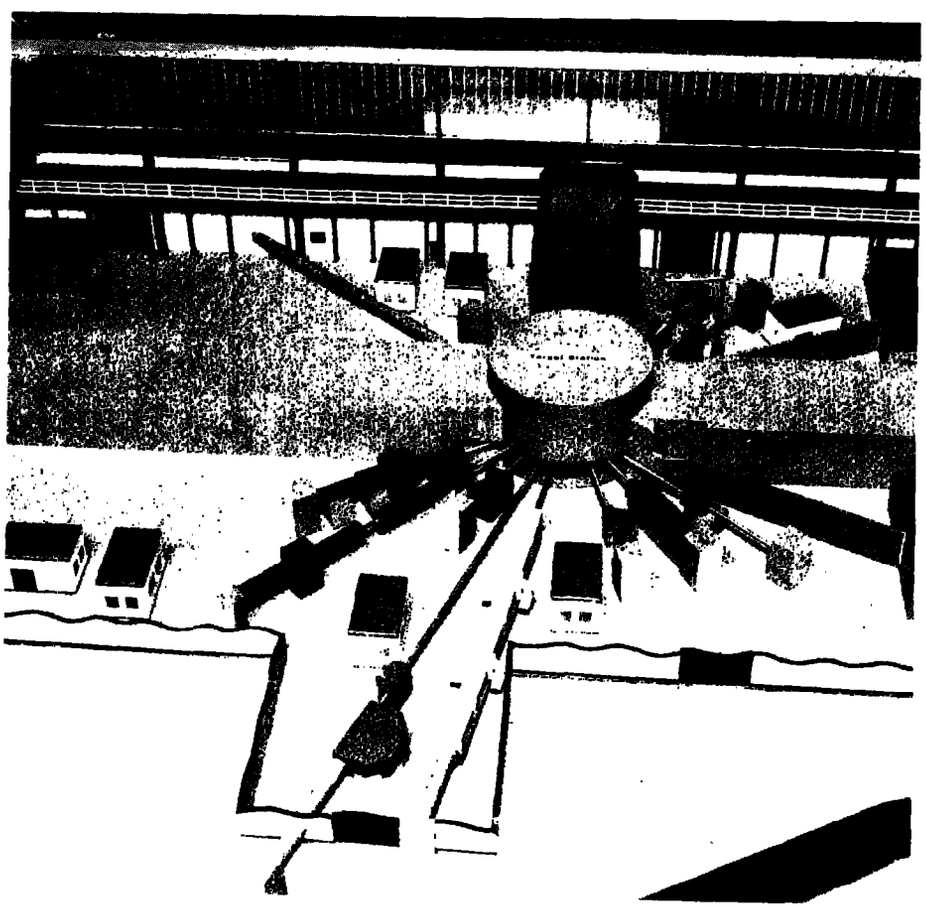

FIGURE 6: Neutrino Bunker Vis-a-vis Neutron Instruments in R55.

Proceedings of International Collaboration on Advanced Neutron Sources (ICANS-VII), 1983 September 13-16
Atomic Energy of Canada Limited, Report AECL-8488

THERMOFLUID DYNAMICS IN LIQUID TARGETS

Y. Takeda
Swiss Institute for Nuclear Research
CH-5234 Villigen, Switzerland

1. INTRODUCTION

The design concept for the SINQ target is to use Lead Bismuth Eutectic (LBE) in the liquid phase in a vertical cylindrical container, with the proton beam entering from the bottom. Natural convection of LBE is to be utilized to transport the deposited energy to a heat exchanger at the top. The thermofluid dynamics of this liquid target is one of the important study subjects for a practical design. A program including theoretical studies and experimental work eventually leading to a full scale test with LBE, is in progress.

The thermofluid behaviour of LBE has been calculated and the effects of several parameters studied. The calculated flow patterns show in many cases a single circulation which contains the majority of the LBE in the target. This is considered to be a desirable feature for the operational target and will be referred to as "total circulation". Several power law relationship between thermofluid-dynamical properties and physical conditions of the target system have been obtained, which are helpful for further applications.

Experimentally, the fluid motion of natural convection of water has been visualised with a small scale apparatus and the development of the circulation of liquid and flow patterns investigated. A threshold Grasshof number to reach "total circulation" has been obtained. A large scale experimental setup is now in operation.

2. CALCULATIONS OF THERMOFLUID BEHAVIOUR

Details of the theoretical model and the calculational method have been given in an earlier report[1]. A series of calculations have been performed in order to see the effects of target height, beam power, beam radius and adiabatic side walls. For the adiabatic side walls two sets of calculations were carried out, one with constant height of target and changing the height of the adiabatic wall, the other with constant height of adiabatic wall and changing the target height.

2.1 Target height

Temperature distributions and flow patterns have been calculated for targets of height from 75 cm to 450 cm. Fig. 1 shows these distributions at the stationary state. For all cases the flow patterns show "total circulation" although their centers are displaced vertically.

The time traces of the maximum temperature are shown in Fig. 2. The development of the temperature distribution during the initial transient was discussed in reference 1. The duration of the transient as a function of height (L) is plotted in Fig. 3 and shows a linear relationship; this is expected since the transient time is proportional to L/U and the characteristic thermal velocity U does not depend on the target height. The maximum temperature rise above the initial temperature (taken as the melting point of LBE) for the stationary states is the same for all four cases and about 25° C.

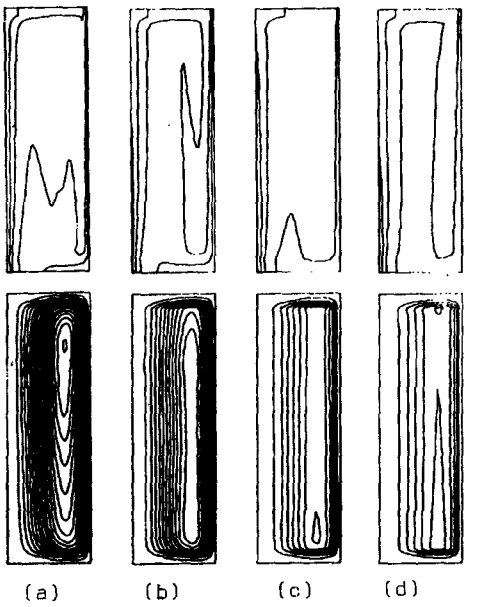

Fig. 1 Distribution of temperature and stream function at stationary state. a) is 75 cm at 25.5 sec, b) 150 cm at 51.0 sec, c) 300 cm at 102.0 sec, and d) 450 cm at 146.8 sec.

Although the development of the flow to "total circulation" during the initial transient is fairly smooth for a target height lower than 300 cm, a multi-cell structure can be seen (Fig. 4) for the 450 cm target. However, this does not persist and is subdued by the stronger "total circulation" once it is fully developed. The temperature distribution is also influenced by this multicell structure, and some distortion of the contour lines can be seen in the upper portion of the target.

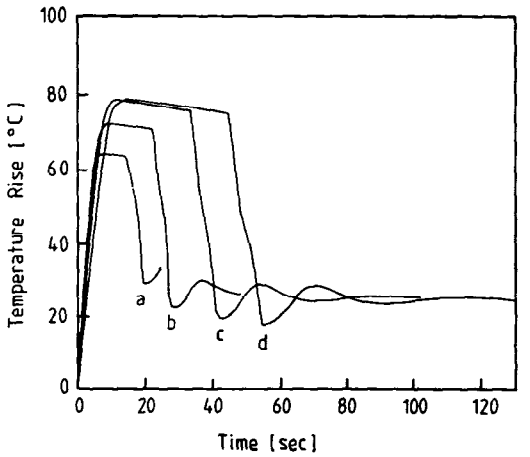

Fig. 2 Time traces of the maximum temperature for target heights; a) 75, b) 150, c) 300 and d) 450 cm.

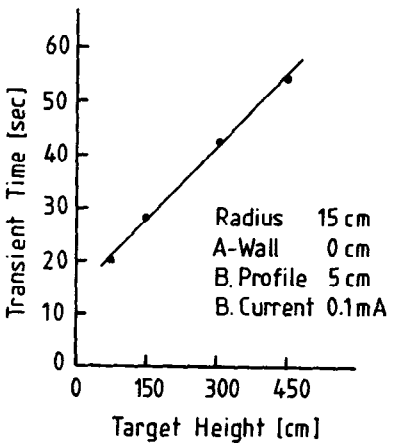

Fig. 3 Transient time versus target height.

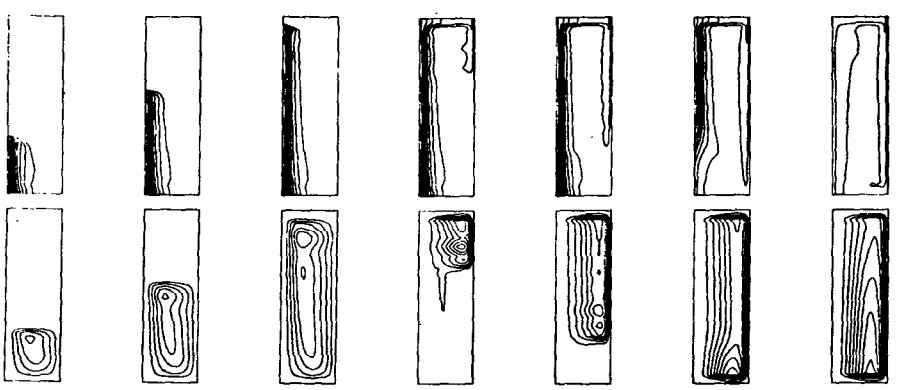

(a) (b) (c) (d) (e) (f) (g)

Fig. 4 Time change of the temperature distribution and stream function distribution for a target height of 450 cm. dT is 0.05 (6.25°C) for all and dΨ is 2 for a)-c) and 10 for d)-g).

2.2 Beam power

To see the effect of beam power, calculations with three different beam currents, 0.1, 0.5 and 1 mA (1 mA ≈ 0.6 MW) have been made. The distributions of temperature and stream function are very similar for the three cases and "total circulation" is obtained.

The maximum temperature rise at the stationary state is plotted as a function of beam current in Fig. 5, and shows a simple power-law relationship. The estimate of the exponent is 0.73, which is within 10 % of the value, 2/3 given by a simple one-dimensional analysis[2].

2.3 Beam profile

Three calculations were performed with beam sizes (values of σ_0 in Eq. 11 of reference 1) of 2.5, 5.0 and 10.0 cm. The center of the circulation shortly after start of heating moves to larger radii as the beam size is increased (Fig. 6), that is, the broader beam generates a rising column with a larger radius about the center line. However, at the stationary state the centers are situated at the same radial position. Fig. 7 shows the variation of axial velocity at mid-center with beam radius.

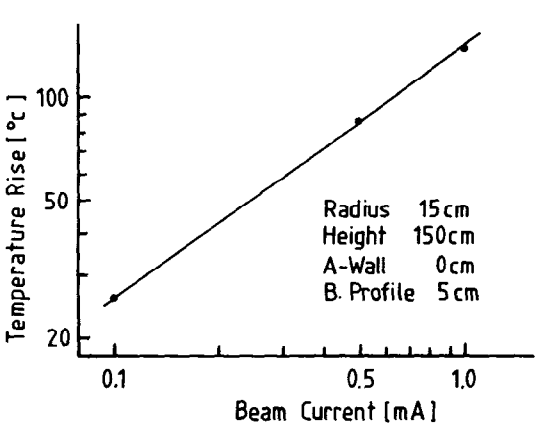

Fig. 5 Power-law relationship for the temperature rise at the stationary state with input beam current.

It shows a fairly good power law relationship to the beam radius R. The estimate of its exponent is -0.6. Simply considered, the convected power is a product of velocity v and temperature rise T and is proportional to the power deposition density q. Since $T \propto q^{2/3}$ (from the previous section) then $v \propto q^{1/3}$ and as $q \propto R^{-2}$ the velocity should be $\propto R^{-2/3}$. The estimate for the exponent is within 10 % of this value, and this relationship is consistent with that for Fig. 5. The temperature-rise at the stationary state as a function of beam profile is shown in Fig. 8. It is lower for the cases with broader beam as expected from the simple analysis ($\propto R^{-4/3}$).

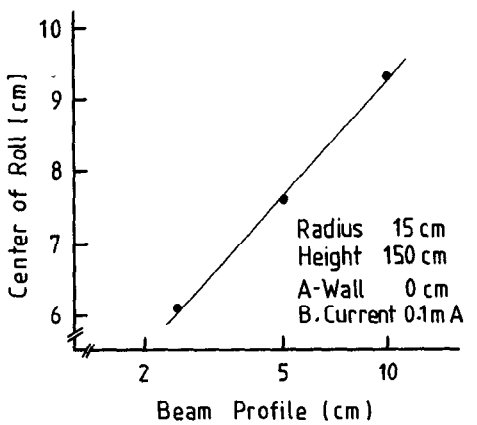

Fig. 6 Positions of the center of circulations at initial stages as a function of beam profile.

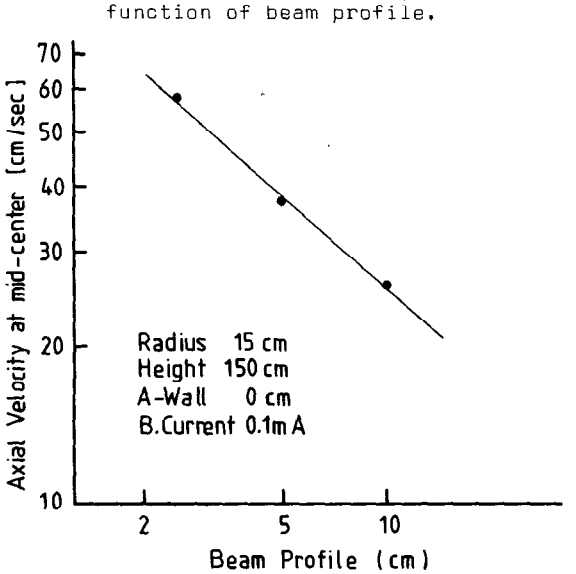

Fig. 7 Axial velocity (v_2) at mid-central position versus beam profile.

2.4 Adiabatic wall with fixed target height

Using a fixed target height of 150 cm, the effects of adiabatic side walls have been studied by calculating systems with their height set to 50, 75 and 100 cm. The adiabatic walls are at the lower end of the target. The calculated flow patterns are very similar to those obtained with a conducting wall, and show "total circulation". The small difference

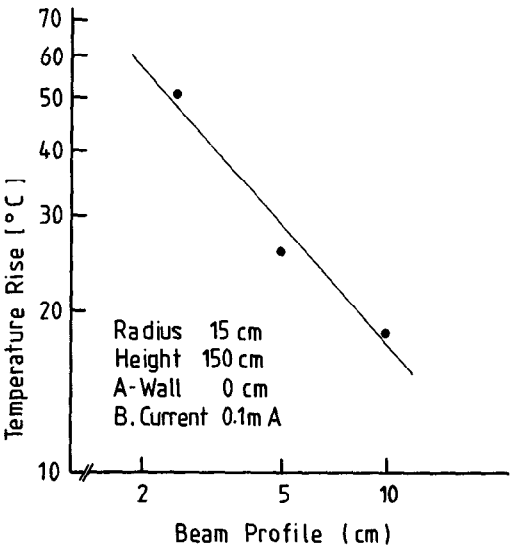

Fig. 8 Temperature rise at the stationary state versus beam profile.

in the velocity distribution is plotted as a function of height in Fig. 9.
With an adiabatic side wall the velocity is increased by about 10 % in the region above the level of the adiabatic wall, but it is only slightly increased elsewhere.

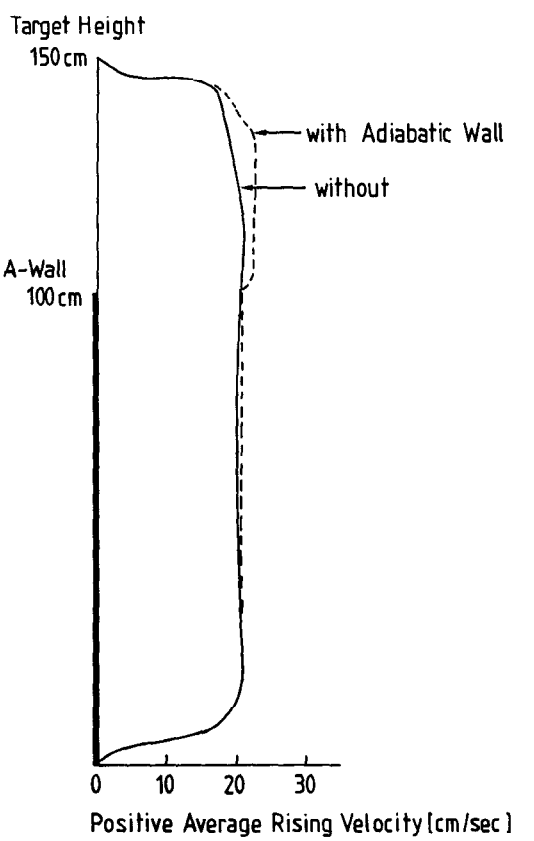

Fig. 9 Comparison of the average positive axial velocity as a function of height for the results with and without adiabatic wall at 51.0 sec.

In the boundary layer near the side wall, there is, as may be expected, a steep temperature gradient toward the conducting surface.

Fig. 10 is the time trace of the maximum temperature. The behaviour during the initial transient is exactly the same for all three cases. This is due to the fact that the temperature of the central portion is not influenced by the conducting wall until "total circulation" is established. Since the smaller cooling area for the higher adiabatic walls results in a higher heat transfer per unit area and hence higher temperature difference, the maximum temperature after the transient naturally becomes higher. For the case of the 100 cm wall the temperature still increases with time.

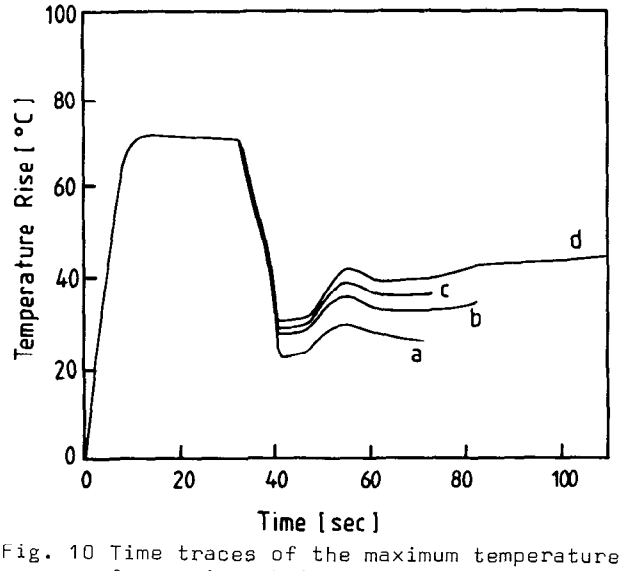

Fig. 10 Time traces of the maximum temperature for various heights of adiabatic side wall. a) is for total conducting wall, b) is 50 cm, c) 75 cm and d) 100 cm.

2.5 Adiabatic side wall with fixed height

Calculations were made for systems with a fixed 100 cm height of adiabatic side wall for five different target heights. The flow patterns show "total circulation" for all cases. However, the temperature distributions become more complicated as the target height is reduced. This is due to the smaller heat transfer area, as discussed in 2.4.

The maximum temperature rise at the stationary state is plotted in Fig. 11 as a function of the target height for cases with and without adiabatic side walls. For a target height larger than 300 cm, the difference between with and without adiabatic wall is only slight.

2.6 Summary

The results of these calculations show that within the parameter value variations studied here, natural convection of target fluid is stable and the temperature distributions are uncomplicated. Power laws for the maximum temperature rise with beam power, beam profile and height of adiabatic walls, are helpful for practical design work.

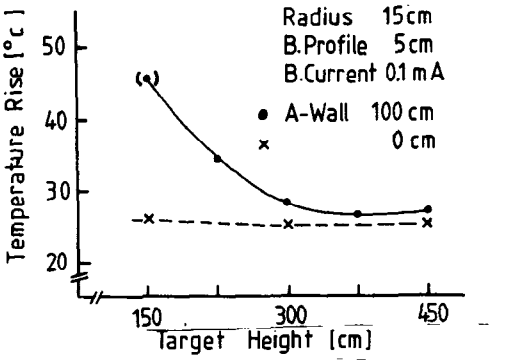

Fig. 11 Temperature rise at the stationary state versus target height with fixed height of adiabatic side wall of 100 cm. The values from the results with total conducting wall are also plotted. As the value for the target height of 150 cm is not at a stationary state, it is plotted in a bracket.

3. EXPERIMENTAL OBSERVATION OF NATURAL CONVECTION IN WATER

As a part of the experimental verification of the calculations, some small scale experiments have been carried out to observe the fluid

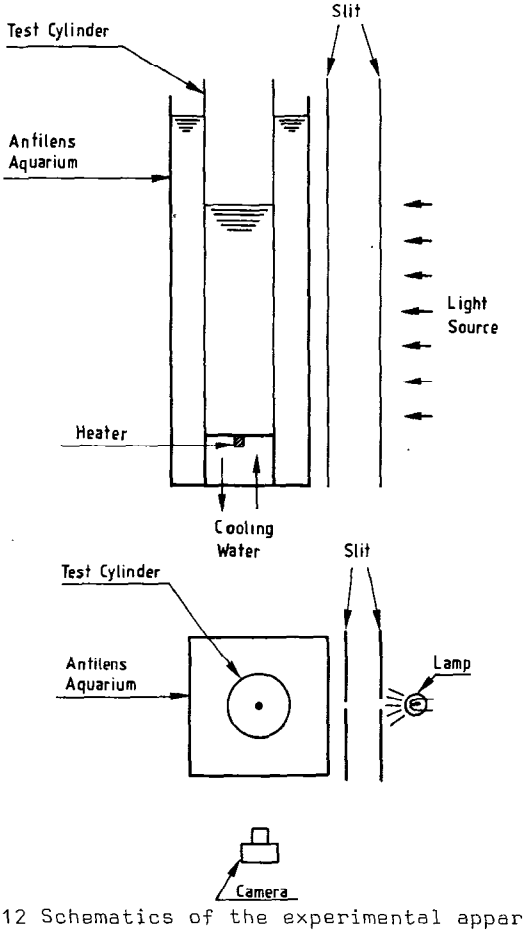

Fig. 12 Schematics of the experimental apparatus arrangement. a) front view, b) top view.

behaviour of natural convection in water. The main interest of this experiment is to study the total fluid motion in a cylinder rather than any local effects like boundary layer flow.

3.1 Apparatus

The apparatus shown in Fig. 12 was used. A glass cylinder of 2.7 cm radius and 55 cm height is set in a square aquarium. The aquarium was used to keep the wall temperature of the cylinder constant and to act as an antilens for taking photographs. The bottom plate is made of Derlin and has a heating area of 9 mm diameter at the center. This plate is water-cooled. The temperature of the heated area was measured by a sheated CA thermocouple at 1.5 mm below the center of the top surface. The wall temperature of the glass cylinder was measured at 10 cm from bottom. The top surface is open and free. The "Aluminium powder method" was used for visualisation of the flow.

3.2 Results

The observed flow motions have been categorised into several patterns, a] partial circulation (only near the heated area), b] "total circulation"(a single roll in a water), c] multi-rolls (vertically several rolls appeared and disappeared) d] swaying core or other three-dimensional motions. The appearance of these flow patterns depends on Gr number and the aspect ratio. For a fixed aspect ratio, only a partial circulation a) is generated at low Gr number, and with increase of Gr, a "total circulation" b] is generated. Photographs of "total circulation" for various water heights are shown in Fig. 13. These stationary state flows could be maintained for several hours. Further increase of Gr leads eventually to flow patterns as in c] or d] Fig. 14 is a map of flow patterns of type a] and b] in a G-γ plane. The definition of Gr is given in the figure, and γ is the aspect ratio defined as L/R. There is a threshold value of Gr for generating "total circulation" which depends on the aspect ratio. As this dependency changes at aspect ratios in the region of 8-10, two straight lines for these threshold values are drawn in the figure. The dependence is larger for smaller aspect ratio (line-1) and vice versa (line-2). Also shown in the figure are two curves derived from the literature. The first is of an empirical critical Gr number in a vertical rectangular box compiled by Ostrach[3], the second, a theoretical critical Gr number in an infinite parallel plate system, derived by Eckert[4].

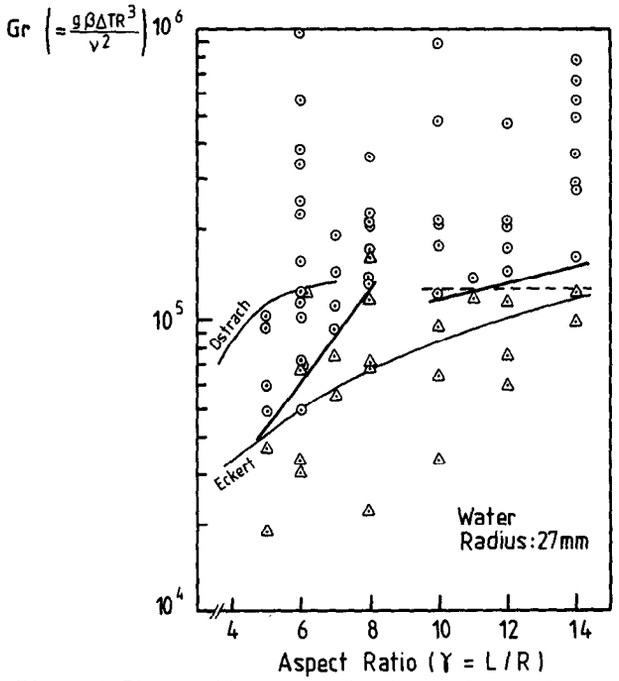

Fig. 14 Flow pattern map in Gr-γ plane. Open circles "total circulation", triangles "partial circulation" (undeveloped flow).

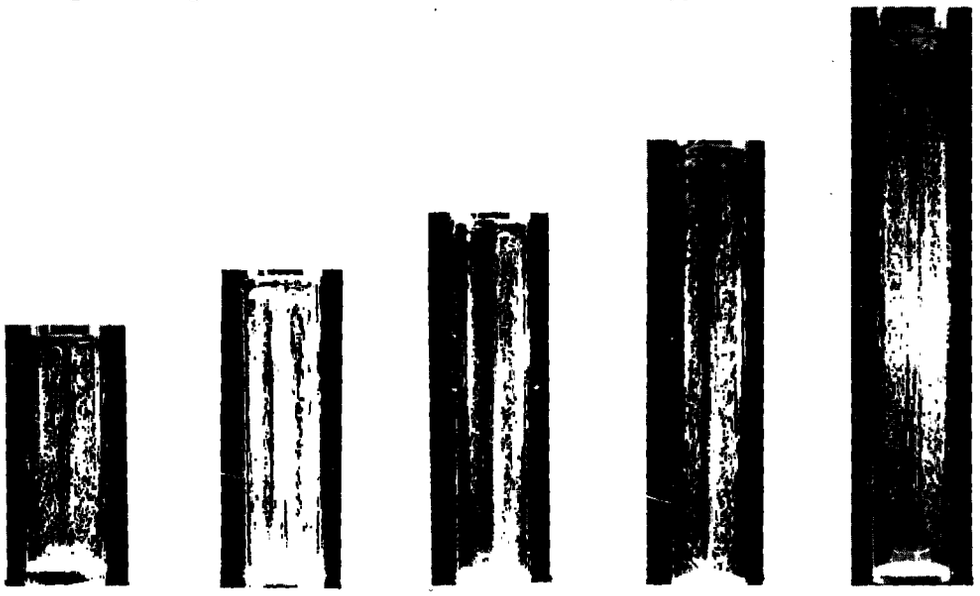

Fig. 13 "Total circulation" for various heights of water.

For both, the temperature difference is applied to two opposite vertical side walls. The gradient of line-1 is close to that of the "Ostrach line" and of line-2 close to that of the "Eckert line". This implies that for an aspect ratio smaller than 8 the effect of the top and bottom surface is large, and for larger aspect ratio than 10 the problem might be treated as a system of infinite height. The dashed line is a simple average of the values between 10 and 14, and agrees well with the saturated value of the "Ostrach curve".

4. EXPERIMENTAL TEST RIG - "NACOSPANS"

To allow the study of systems of the proposed size for the SINQ target, a large scale test rig (again using water) has been built.This is shown in Fig. 15. The principle of this rig is similar to that for the small scale apparatus used for the flow visualisation. A glass cylinder of 20 cm diameter and 250 cm height is set in a square aquarium of 45 cm side and 300 cm height. A 40 cm long heating rod is inserted from the bottom which has a distributed heat generation decreasing exponentially with a relaxation length of 30 cm. This gives a first approximation to the expected beam heating.

The main purpose of this test rig is to measure temperature distributions. A total of 70 thermocouples are installed: on the heater surface, cylinder surface, bottom plate and inside the water. A glass tube of 16.2 cm diameter and 200 cm length is also available, to be used for experiments including a guide tube.

Fig. 16 shows photographs of a general view of the test rig together with a part of the data taking system. The test rig is now in operation and experiments are in progress.

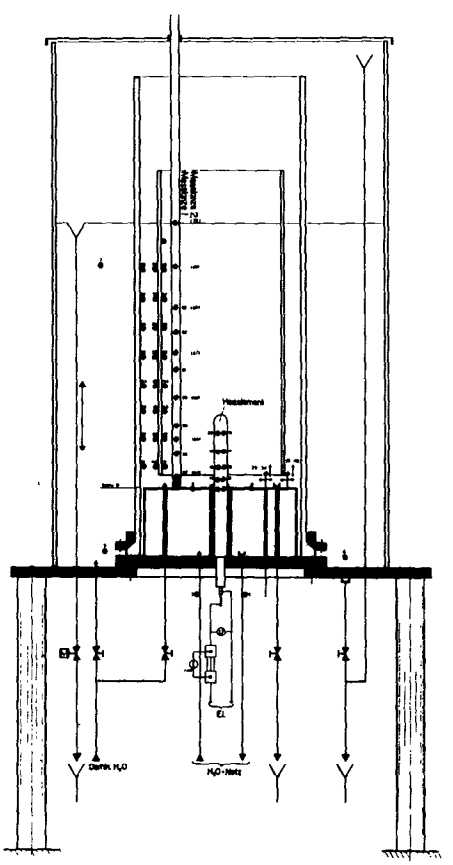

Fig. 15 Schematics of the large scale test rig (NACOSPANS).

Fig. 16 Photograph of general view of the apparatus, NACOSPANS.

REFERENCES

1. Y. Takeda, Proceedings ICANS-VI, ANL (1982)
2. C. Tschalär, Proceedings ICANS-V, Jülich
3. S. Ostrach, Lecture note at Haifa Univ., Israel, 1978
4. E.R.G. Eckert, Int.J.Heat Mass Transfer, Vol. 2 (1961) 106

Session G

Moderators

Chairman - G. Manning

Proceedings of International Collaboration on Advanced Neutron Sources (ICANS-VII), 1983 September 13-16
Atomic Energy of Canada Limited, Report AECL-8488

GROOVED COLD MODERATOR AT KENS

Y. Ishikawa
Physics Department, Tohoku University, Sendai, 980 Japan

S. Ikeda, N. Watanabe and K. Kondo
National Laboratory for High Energy Physics, Ibaraki, 305 Japan

K. Inoue, Y. Kiyanagi and H. Iwasa
Department of Nuclear Engineering, Hokkaido University, Sappro, 060 Japan

K. Tsuchihashi
Japan Atomic Energy Research Institute, Tōkai, 319-11 Japan

Summary

A grooved cold moderator was installed at the KENS target station which increased the cold neutron intensity by 1.4 compared with the flat one which had been operative without any trouble for more than two years and a half. The paper discusses the results of the mock-up experiment as well as a simulation calculation performed to find optimal parameters and reports the final design of the moderator. By employing the same refrigerator (PGH-105), the moderator could be cooled down to 20.5 K under the operation of maximum proton current. The neutron energy and time spectra from the grooved moderator as well as the heat deposit in the moderator by nuclear radiation were measured to compare with the results obtained for the flat one. A recent chemical analysis of radiation decomposition of solid methane in the old flat moderator suggests that the decomposition is about three times faster than the previous case reported in ICANS-IV.

Introduction

The KENS first cold moderator made by solid methane with a dimension of 5 x 12 x 15 cm^3 (flat moderator)[1),2)] had been operative without any trouble for more than two years and a half, and had proved a satisfactory performance for its high coupling efficiency and effective cooling ability. Many experiments with the KENS cold neutron source have also demonstrated that the spallation neutron source has a good potential for cold neutron scattering works.

With an increase of population in this research field, however, the requirements for the machine time and for increasing the cold neutron intensity became much strong, which made us investigate the possibility of replacing the old moderator by a grooved one to improve the situation. A promising aspect of the grooved moderator was discussed by Bauer[3)] and Carpenter[4)] in ICANS-IV (KEK) and it attracted the attention of many neutron people, because the moderator was shown to improve substantially the intensity of the slow neutrons. Many mock-up experiments reported in ICANS-IV - VI have shown that the improvement by the grooved moderator would be a factor of 1.2, if the moderator is embeded in a good reflector and the comparison is made for the moderator with an equal volume[3)-9)]. The gain factor depends strongly on the condition of the reflector[10)]. Recent mock-up experiments using Hokkaido University LINAC as well as a simulation calculation have suggested that the grooved moderator with optimal parameters would increase the present cold neutron intensity at KENS by about 50 %. We therefore decided to replace the flat moderator by the grooved one and the replacement was completed at the end of March 1983. The paper discusses first the results of the simulation calculation and mock-up test, and describes the actual design and performance of the new moderator. Note that the replacement is the first step of the KENS-I' project.

Simulation calculation

A simulation calculation was made for a simple model system to find the optimal parameters. The model used for the calculation was of polyethylene at ambient temperature without reflector. The calculation was made by using a two dimensional SN transport code TWOTRAN-II[11)]. Then the geometries of grooved and flat moderators under consideration are the infinitely long columns, the sections of which are shown in Fig. 1, both having the same volume. The nine group neutron cross sections were calculated by the SRAC code[12)]

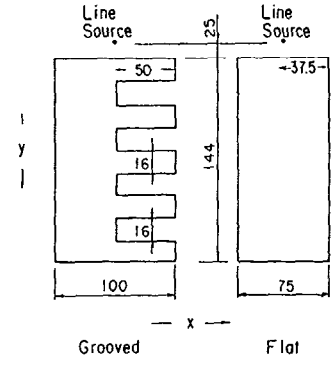

Fig. 1 Two-Dimensional Model for Reference Moderators

As a demonstration shown in Fig. 2 are the spatial distributions along y-direction of the beam currents of the eighth energy group (0.04 ∿ 0.01 eV) from the grooved and the flat moderators. Both curves are normalized by the unit line source. We can see the sharp shoots of beam currents appearing from the bottom of grooves. The results are in good agreement with those obtained in a previous test experiment[9)].

The mechanism of the increase of neutron beam currents from the grooved surface is discussed in detail in the original paper[13)]. Here we refer to the ratio of the first flight collision in the grooved moderator to that in the flat one with the same volume, G/F = 1.15 obtained by this simulation calculation. This ratio, η = G/F is important for comparing the heat deposit in two moderators.

The parameter survey was performed for position of target, overall dimension of moderator (thickness and height) and geometry of grooves (depth of groove, pitch of groove-fin and ratio of groove width to fin's). The results for the important parameters are summarized below.

1) The position of target in the x direction (cf. Fig. 1) has small influence on the neutron gain.

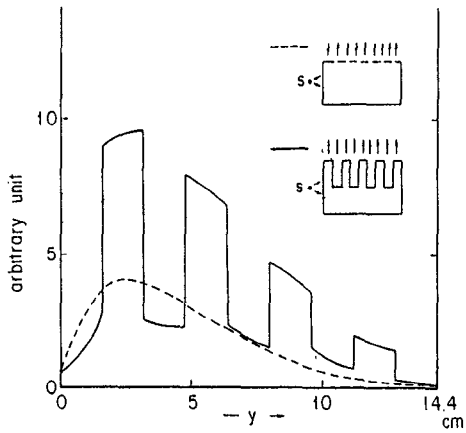

Fig. 2 Y-Dependence of Beam Currents (8th Group) from the Reference Moderators

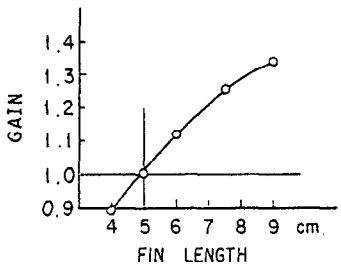

Fig. 3 Effect of Fin Length on Beam Current

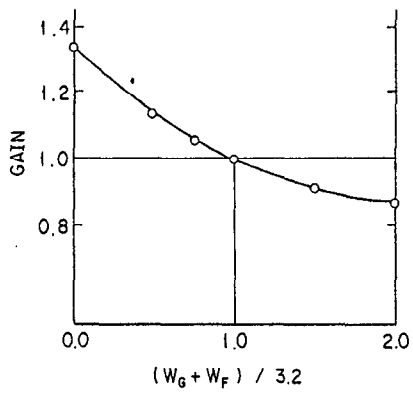

Fig. 4 Effect of Groove Pitch on Beam Current

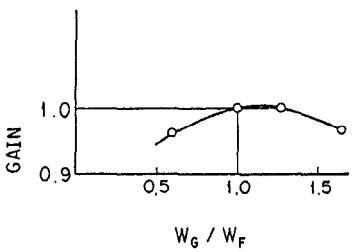

Fig. 5 Effect of Ratio of Groove Width to Fin Width on Beam Current

2) The extension of the thickness of the moderator in the backward direction beyond 5 cm increases the intensity by 10 % for 1 cm extension.
3) The extension of the height beyond 14 cm does not effect the neutron gain as is found in Fig. 2.
4) The extension of the fin length has a significant effect on the gain (12 % gain/cm), which is illustrated in Fig. 3. We can find there is still 6 % of gain per cm beyond 3 cm extension.
5) The effect of pitch, the sum of groove and fin widths, was surveyed by changing the pitch upon keeping both widths equal and total height unchanged. The result shown in Fig. 4 indicates that the more narrow pitch yields the more gain.
6) The ratio of groove width to fin's was surveyed by changing the ratio upon keeping the pitch 3.2 cm. As shown in Fig. 5, it seems that the optimum ratio is between 1.0 and 1.25.

Mock-up experiments

The mock-up test experiments for surveying the design parameters were carried out at the Hokkaido University LINAC neutron source by employing the polyethylene moderator at ambient temperature which was embeded inside a graphite reflector with a similar shape to the upper part of the KENS reflector. The energy spectra of neutrons from a 15 x 15 x 5 cm^3 flat moderator and a 15 x 15 x 10 cm^3 grooved one with 5 cm depth grooves are compared in Fig. 6, which shows that the intensity gain by the grooved moderator is about 1.4 at the peak of energy spectrum and it becomes higher for longer wave lengths. If referred to the flat moderator with the same volume, the intensity gain is anticipated to be 1.3 at the spectrum peak. For the parameter survey, the effect of depth of grooves was examined under the condition of the constant volume.

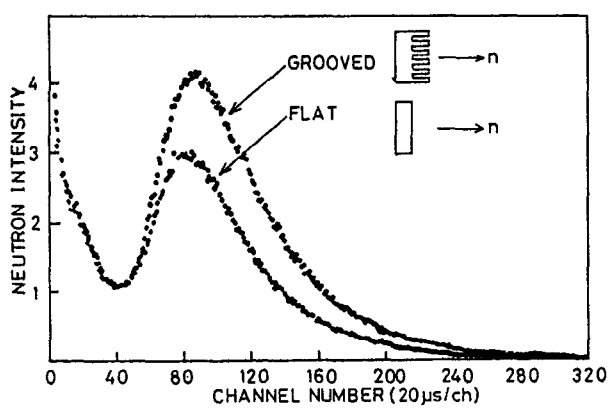

Fig. 6 Time-of-flight Spectra from Grooved and Flat Moderators

The total moderator thickness was limited to be 10 cm because of spatial allowance in the KENS Be reflector. The results are displayed in Fig. 7, which suggests that the maximum intensity is obtained for the maximum fin's length of 5 cm. The result agrees satisfactorily with the simulation calculation. In Fig. 8 are also shown the neutron intensities from the grooved moderators with various height of the lowest fins. The neutron intensity was found not so sensitive to this height in a range of 10 ∿ 20 mm.

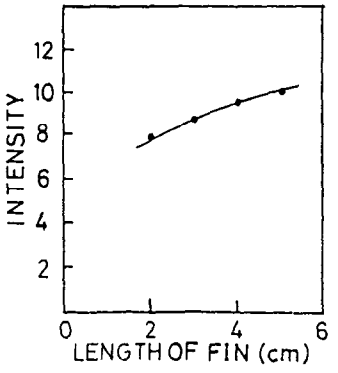

Fig. 7 Effect of Length of Fins

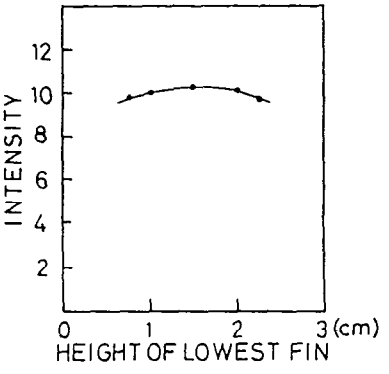

Fig. 8 Effect of Height of the Lowest Fin

Design and fabrication of KENS grooved cold moderator

Figure 9 is the side view of the grooved moderator we finally fabricated with its photograph. The overall dimension of the new moderator, the ratio of grooved width to fin's (1.28), number of fins, depth of grooves and height of the lowest fin are determined based on the results of mock-up test experiment and simulation calculations described in previous two sections. The methane container is made by pure Aℓ, the wall of fins is only 2 mm thick, while other parts of the container have the thickness of either 4 or 5 mm. The container is cooled by the same method as the previous one with some improvement. The total volume of methane is 1,544 cc which is an increase of 70 % of volume compared with the previous one. The reservoir tank for methane gas was also replaced to a new bigger one (0.8 m^3) corresponding to the volume change of the container. Several small pieces of Be reflector were also fabricated to fill up the vacancy between the new moderator cryostat and the main unchanged Be reflector.

Performance of the new moderator

The energy spectra at the exit of the neutron guide tube from the new grooved and old flat moderators were measured by the neutron scattering from a standard vanadium sample. Their intensities were normalized by measuring epithermal neutron current from an ambient temperature moderator located at the opposite side of the target. An appreciable change was found in the energy spectra as seen in Fig. 10. The ratio of the intensity of cold neutrons from the grooved moderator I_g to that from flat one I_f was found to be wave length dependent. The ratio is 1.4 ∿ 1.5 in the wave length range 5 ∿ 8 A which is important for the spectrometers with neutron guide tubes (SAN, TOP and LAM-80), while the value is only 1.2 at the Maxwellian peak of the cold spectrum (λ = 4 A). (Note that the energy spectra shown in Fig. 10 are modified by the transmittance of the neutron guide tube and are different from the real one.) The values are less than those anticipated from the mock-up tests, presumably due to the better reflector system for KENS.

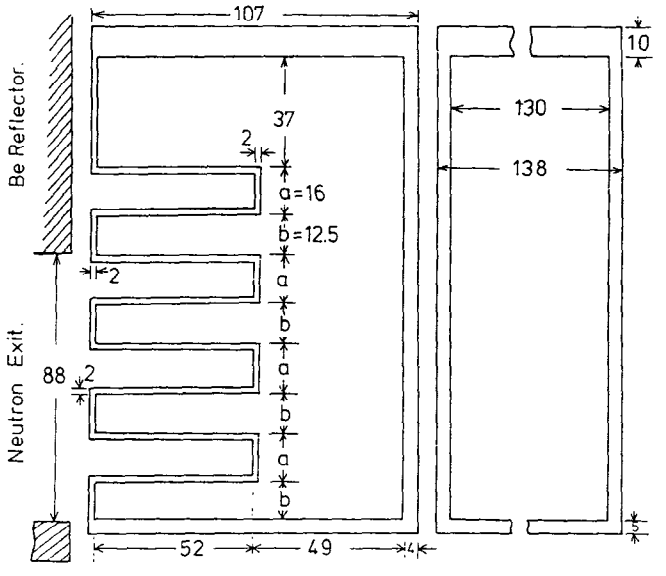

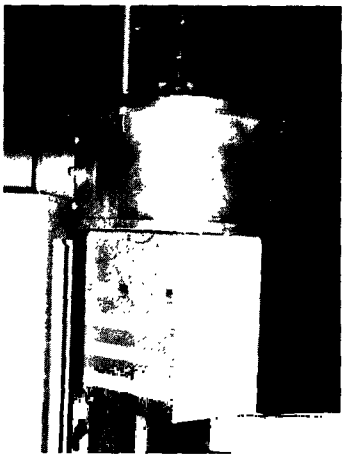

Fig. 9 The Side View of Grooved Moderator and its Photograph

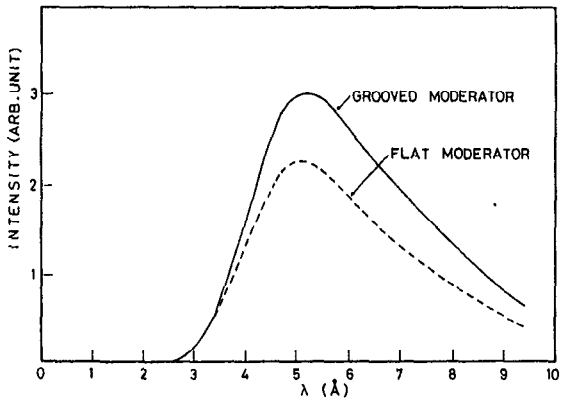

Fig. 10 Energy Spectra of Grooved and Flat Moderators

The time spectra of cold neutrons were measured by back scattering from a mica single crystal and are displayed in Fig. 11. The spectra have a time-structure in the rising part, which becomes substantial for longer wave lengths. However, it is confirmed that the structure gives no serious problem to the profile analysis for the quasi-elastic spectrometer LAM-40 which utilizes 4 A neutrons. This was turned out to be also the case for the high resolution quasi-elastic spectrometer LAM-80 even if it employs the neutrons of 6.6 A.

The result of cooling performance with and without proton beams are displayed in Fig. 12. Without the proton beams, the methane could be cooled down to 16.8 K, the lowest temperature that our refrigerator (PGH 105) can attain. The temperature of methane was found to rise up to 20 K by full proton currents 1.5 μA). The result in Fig. 12 was obtained with the proton currents of 1.0 μA to get an accurate temperature rise. The amount of heat q deposited in the moderator by nuclear radiation could be estimated from the temperature rising curve in Fig. 12 as was done in the previous paper[2]. The temperature rise ΔT(t) is given by

$$\Delta T(t) = g(1 - e^{-ht}) ,$$

with g = q/K and h = K/C, K and C being thermal conductance and heat capacity of the moderator respectively. By employing the parameters g and h determined from Fig. 12, q was estimated to be q = ghC = 4.9 watt.

The total heat deposit thus estimated is almost four times larger than that in the old moderator as is compared in Table 1. If the total deposit is normalized by the proton current, the total volume of the moderator and the ratio of the first flight collision rate η = G/F = 1.15 obtained by calculation, the normalized heat deposit becomes 1.9 times larger than the flat case (Feb. 1983). It is not clear whether such a discrepancy is due to the real change of situations or is simply due to the accuracy of the approximate calculation for q. Note that the normalized heat deposit estimated for the flat moderator at the end of its use (Feb. 1983) is 1.3 times higher than that measured at the beginning (Jul. 1980).

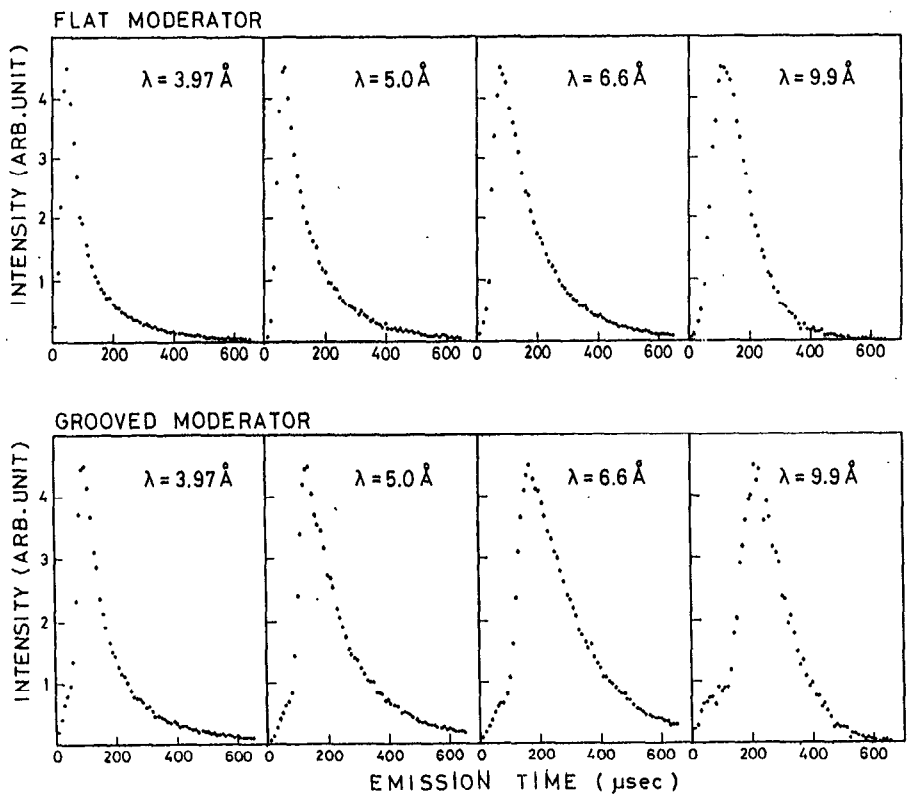

Fig. 11 Time Spectra of Grooved and Flat Moderators

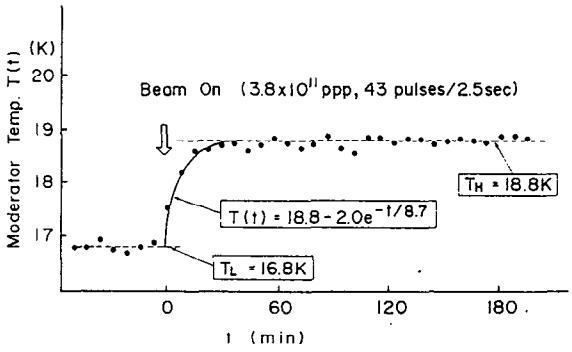

Fig. 12 Temperature Rise of Grooved Moderator by Nuclear Radiation

Table 1 Heat Deposit in Cold Moderators by Nuclear Radiation

	Flat Moderator (Jul. 1980)	Flat Moderator (Feb. 1983)	Grooved Moderator (Jul. 1983)
Proton Intensity (current I, μA)	7.3×10^{12} protons/sec (1.2)	8.0×10^{12} protons/sec (1.3)	6.5×10^{12} protons/sec (1.0)
Volume V (cm^3)	900	900	1,544
Bottom Area S (cm^2)	60	60	131
Temperature Rise (K)	1.0	1.4	2.0
Thermal Conductance K(J/K·sec)	1.08	1.09	2.46
Total Heat Deposit q(W)	1.2	1.7	4.9
Normalized Heat Deposit (= q/VηI) ($mW/cm^3 \cdot \mu A$)	1.11	1.44	2.75

Radiation decomposition of solid methane

The chemical analysis of radiation decomposition products in the exhausted gas was carried out for the methane gas used for the flat moderator. The analysis for the grooved moderator is in progress. The sample gases A and B to be assayed were taken from the reservoir tank, and the total number of 500 MeV protons on the W target were 2.74×10^{18} for the sample A and 1.35×10^{18} for the sample B, respectively. The chemical analysis was performed by gaschromatography. The concentrations of individual products (listed in Table 2) were calculated from the peak area in the gas-chromatograms and sensitivity of each gas to the detector. The results were listed in Table 2, together with the total number of protons for each sample. The results obtained in an earlier measurement are also listed for reference. As far as the present results are concerned, a linear relation holds between the H_2 product and the total number of protons on the W target. However, the H_2 production rate is three times larger in the recent measurement than the previous one. At present we have no explanation for the discrepancy, but we suspect that the recent increase of production rate would be related with the increase of the heat deposit. Further investigation is required before we get a confirmative conclusion.

Table 2 Product Yields Due to the Radiation Decomposition of Solid CH_4 Moderator

	H_2 (%)	CH_4 (%)	C_2H_6 (%)	C_2H_4 (%)	Other (%)	H_2 Production Rate (%/10^{18} protons)
Sample A (Feb. '83)	0.81	98.8	0.15	0.2	0.1	0.30
Sample B (Mar. '83)	0.35	99.5	0.1	<0.1	<0.1	0.26
Sample C (Jul. '80)	0.15	~100	0.03	0.06	0.03	0.11

Irradiation condition

	Proton Current (μA)	Irradiation Time (hours)	Total Protons (x 10^{18})
Sample A	1.40	87.0	2.74
Sample B	1.47	40.9	1.35
Sample C	1.2	52.7	1.42

It should be noted that the replacement gave us an opportunity for examining the inside of the old cold moderator container to find the deposits created during the 2.5 years operation. This would give us an important information on the decomposition process of solid methane by spallation neutrons. This examination will be carried out as soon as the radiation level of the cold moderator container reduces to the accessible one.

Conclusion

The KENS grooved cold moderator has also been operative since April 1983 with a satisfactory performance. The change of the time spectra has practically no influence on the present spectrometers. The increase of the cold neutron intensity from the guide tubes by 40 ~ 50 % is quite invaluable. The total cost for realization of this increase is about ¥16.5 x 10^6 including the expenses for the mock-up tests and for the modification of the Be reflector.

We should also remark that the increase of 40 % of the cold neutrons by the new grooved moderator is partly due to the increase of the moderator volume. Therefore, our result obtained with a real good reflector target system gives an experimental support to the expectation that the net gain by grooving is of order of 1.2 in case of the good reflecting system and the gain is significant only in a long wave region.

The authors would like to thank KEK-BSF staffs and KENS group's members for installation of the moderator. Their thanks are also due to Osaka-Oxygen Industries Ltd., for fabrication of the moderator chamber.

References

1) Y. Ishikawa and S. Ikeda, Cold Neutron Source, Mock-up Experiment and Final Design, KENS Report-I, KEK Internal (1980) 19.
2) S. Ikeda, Y. Ishikawa and K. Inoue, KENS Cold Neutron Source, Proc. ICANS-IV (KEK) (1981) 200.
3) G. S. Bauer, Layout of the Target Station for the German High Power Spallation Neutron Source Project, Proc. ICANS-IV (KEK) (1981) 154.

4) J. M. Carpenter, Summary of Results from the ZING-P' Pulsed Neutron Source, Proc. ICANS-IV (KEK) (1981) 105.
5) G. S. Bauer, Summary of Discussion on Moderator with Grooved Surface, Proc. ICANS-IV (KEK) (1981) 423.
6) G. S. Bauer, H. M. Conrad, H. Spitzer, K. Friedrich and G. Milleret, Measurement of the Time Structure and Thermal Neutron Spectra for Various Target-Moderator-Reflector Configurations for a Spallation Neutron Source, Proc. ICANS-V (Jülich) (1982) 475.
7) G. S. Bauer, J. P. Delahaye, H. Spitzer, A. D. Taylor and K. Werner, Relative Intensities and Time Structure of Thermal Neutron Leakage from Various Moderator-Decoupler Systems for a Spallation Neutron Source, Proc. ICANS-V (Jülich) (1982) 417.
8) G. S. Bauer, W. E. Fischer, F. Gompf, M. Küchle, W. Reichardt and H. Spitzer, Thermal Neutron Leakage and Time Structure Measurement for Various Target-Moderator-Reflector Configurations for a Spallation Neutron Source, Proc. ICANS-V (Jülich) (1982) 445.
9) K. Inoue, Y. Kiyanagi, H. Iwasa, N. Watanabe, S. Ikeda, J. M. Carpenter and Y. Ishikawa, Grooved Cold Moderator Tests, Proc. ICANS-VI (Argonne) (1982) 391.
10) G. S. Bauer, Summary of the Discussion on the Gain in Thermal Neutron Flux by Using Grooved Hydrogeneous Moderators, Proc. ICANS-VI, (Argonne) (1983) 497.
11) K. D. Lathrop and F. W. Brinkley, An Interfaced, Exportable Version of the TWOTRAN Code for Two-Dimensional Transport, Los Alamos Scientific Laboratory Report LA-4432-MS, July (1973).
12) K. Tsuchihashi, et al., SRAC, JAERI Thermal Reactor Standard Code System for Reactor Design and Analysis, JAERI-1285, January (1983).
13) K. Tsuchihashi, Neutronics Study of Grooved Moderator and Parameter Survey, Proc. Future Project of BSF-II, KEK (1983), in press.

Proceedings of International Collaboration on Advanced Neutron Sources (ICANS-VII), 1983 September 13-16
Atomic Energy of Canada Limited, Report AECL-8488

MEASUREMENT AND FITTING OF SPECTRUM AND PULSE SHAPES OF A LIQUID METHANE MODERATOR AT IPNS

J. M. Carpenter

Argonne National Laboratory
Argonne, Illinois 60439

R. A. Robinson

Los Alamos National Laboratory
Los Alamos, New Mexico 87545

and

A. D. Taylor
Los Alamos National Laboratory
Los Alamos, New Mexico 87545
and
Rutherford Appleton Laboratory
Oxfordshire, England

Abstract

We have measured the absolute intensity, and the energy spectrum, and the pulse shapes as function of neutron energy for the IPNS liquid CH_4 "F" moderator, at 108 K. We have fitted the spectrum, corrected for attenuation by aluminum in the beam, using a new cut-off function and fitted the pulse shapes to a new function which is the sum of two decaying exponentials, convoluted with a gaussian, and determined the wavelength variation of the parameters. We present here the results of a preliminary analysis.

Introduction

Information on the spectrum, the absolute intensity and pulse shapes as function of energy, for pulsed source moderators is essential for the design of neutron spectrometers and for the analysis of measurements. Liquid methane, CH_4 is of special interest because of its high proton density, its excellent thermalization properties, and its good heat removal capacity in flowing systems. During the time that the cryogenic moderator-reflector system was operating at IPNS, we measured the neutronic properties of the liquid methane "F" moderator. Table I gives the parameters of the "F" moderator. Figure 1 shows the cryogenic moderator-reflector system.

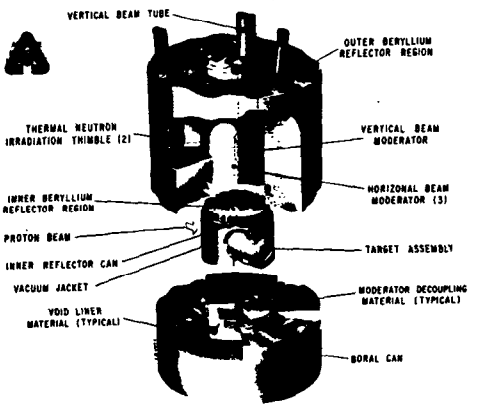

Fig. 1 The IPNS cryogenic moderator-reflector system. The liquid-methane "F" moderator is at the bottom, viewed from both sides. The text gives the physical parameters of the moderator.

Table 1

Dimensions:	10.2 x 10.2 x 5.1 cm^3
Heterogeneous poisoning:	none
Decoupler:	1 x 10^{20} Gd/cm^2
Void liner:	4 x 10^{21} $^{10}B/cm^2$
Reflector:	30 cm ϕ Be @ 100 K, 60 cm ϕ Be ambient
Aluminum in beam path:	1.11 cm $\sim$ 100K, .52 cm ambient
Temperature:	108 K

We used the resonance activation of a .0127-mm gold foil[1] to determine the absolute epithermal beam current, with the result,

$$I_{epi} = EI(E)_{1eV} = 2.91 \times 10^{10} \text{ n/sr.-}\mu\text{A-s}$$

for 451 MeV protons on the depleted-uranium target. This compares quite favorably with the result calculated by our HETC-VIM monte-carlo simulations[2]

$$I_{epi} = 2.57 \times 10^{10} \text{ n/sr. - } \mu\text{A - s}$$

(scaled from 2.95 x 10^{10} at the conditions of the calculation, 500 MeV, to 451 MeV according to the relative neutron yield, $Y(E) \propto (E_{Gev}^{-.12})$.[3]

A thin BF_3 "pancake" beam monitor detector placed 13.69 m from the moderator surface provided the wavelength distribution of the neutrons. We fitted a function of the form

$$C(\lambda) = \eta(\lambda) \left[a_1 \frac{\lambda_T^4}{\lambda^5} \exp-(\lambda_T^2/\lambda^2) + a_2 \, \Delta(\lambda) \, \lambda^{2\alpha-1} \right] T(\lambda)$$

to the counting rate per unit wavelength. Here, we took the efficiency $\eta(\lambda) \propto \lambda$, a_1 represents the magnitude of the maxwellian term, λ_T is the characteristic maxwellian wavelength, a_2 is the magnitude of the slowing down term, $\Delta(\lambda)$ is the "joining function" which we took to have the novel form devised by Taylor[4]

$$\Delta(\lambda) = [1 + \exp(a_3 \lambda - a_4)]^{-1},$$

α is the leakage exponent, and $T(\lambda)$ a tranmission correction for the structural aluminum in the beam. We find Taylor's joining function to be superior to any of those suggested (for other purposes) by Wescott.

The transmission correction $T(\lambda)$ was taken to be of the form

$$T(\lambda) = \exp(-n\,\sigma_T(\lambda))$$

$$\sigma_I(\lambda) = \begin{cases} \sigma_{\ell o}(\lambda/\lambda_{co}); & \lambda > \lambda_{co} \\ \sigma_{Bragg}(\lambda) + \sigma_{inel}(\lambda); & \lambda_{co} < \lambda < .95\ \text{Å} \\ \sigma_o = 1.49\ \text{b} & \lambda > .95\ \text{Å} \end{cases}$$

The low energy cross section, $\sigma_{lo} = .77$ b which represents sub-Bragg inelastic scattering, was taken from the "Barn book" for $\lambda > \lambda_{co} = 4.67$ Å. The structured part of the cross section was modeled[5] assuming perfect polycrystalline FCC aluminum with Debye-Waller factors taken for 300K and a Debye spectrum with $\Theta_D = 36.92$ meV,

$$\sigma_{Bragg}(\lambda) = (\sigma_o/V_o)\,\frac{\lambda^2}{4}\sum_{\tau<2k}\frac{Z(\tau)}{\tau}e^{-2W(\tau)}$$

where $k = 2\pi/\lambda$, τ are the reciprocal lattice vectors $\tau = 2\pi/d$, and $Z(\tau)$ are the reciprocal lattice weighting factors and V_o the unit cell volume. The inelastic term was modeled assuming

$$\sigma_{inel}(\lambda) = \sigma_o\,(1 - e^{-2W(2k)});$$

(we recognize that this approximation is not correct). The resulting fitted parameters (a_1 and a_2 are unnormalized as tabulated below) were

$a_1 = 7.61$
$a_2 = 2.34$
$T = 11.1$ meV ($\lambda_T = 2.71$ Å)
$\alpha = .06$
$a_3 = 5.95$ Å^{-1}, $a_4 = 6.65$

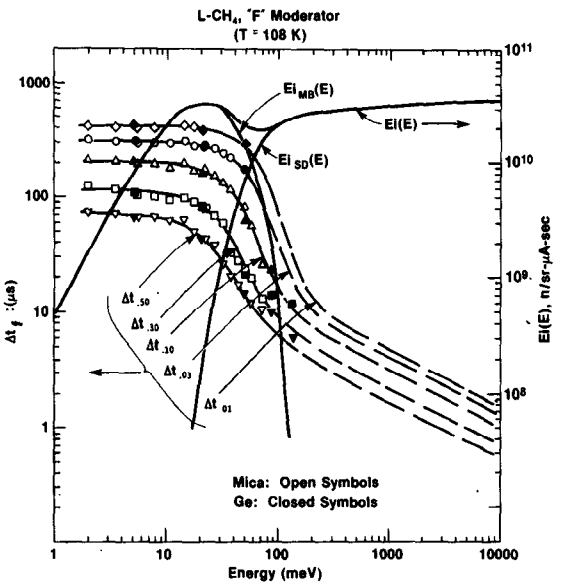

Fig. 2 Pulse widths at fraction f of maximum Δt_f, and the absolute beam current per unit lethargy, Ei(E), for the L-CH_4 "F" moderator. The current is for 451 MeV protons on the depleted-uranium target. The extrapolation of pulse widths to higher energies is according to the high-energy limiting values for an infinite medium of liquid methane.

Figure 2 shows the fitted spectrum, plotted as the beam current per unit lethargy, Ei(E) normalized to the measured epithermal beam intensity at 1 eV. The corrected spectrum was not free of Bragg-edge structure, even though we adjusted the aluminum thickness in attempts to produce a smoother spectrum. We believe this indicates a preferred orientation in the grain structure of the aluminum.

Using roughly 2.5 x 2.5 cm^2 crystals of mica (d = 9.94 Å) and Ge(110) (d = 2.00 Å) and one detector of the SEPD at $2\theta = 152.3°$, we measured the shape of the neutron pulses at wavelengths $n\lambda = 2d \sin\theta$ for the first six orders of reflection from Germanium, and for the third through twenty-third orders of reflection from artificial mica. The total flight path length from moderator to detector was approximately 15.5 m. (The distance was not well-enough known to enable independent determination of emission time delays.) Figure 3 shows the peaks measured for three typical wavelengths. The data have not been corrected for resolution of the instrument.

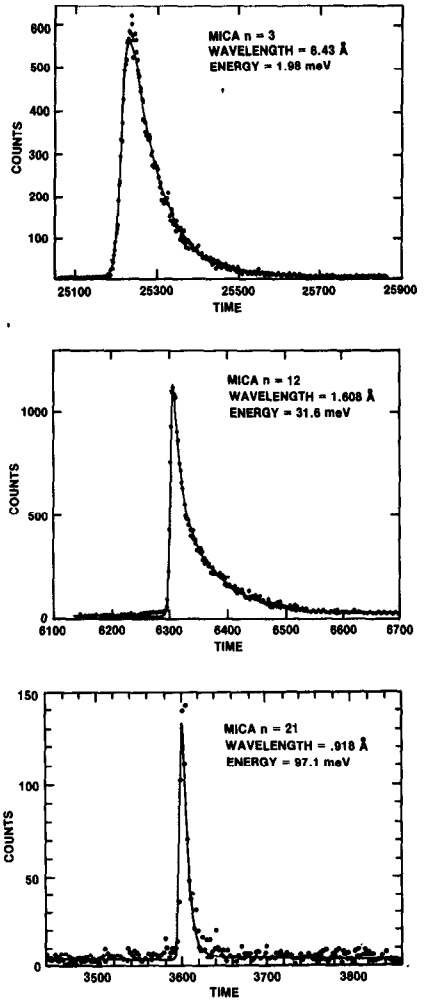

Fig. 3 Pulse shapes for three wavelengths, measured with a mica crystal. Times are in microseconds.

We chose to fit a function which is the sum of two decaying exponential functions, convoluted with the same gaussian. Although there are excellent theoretical grounds for fitting a sum of chi-square distribution functions to the data (at shortest wavelengths, the shape is expected to be of the form $(t-t_o)^2 \exp-a(t-to)^2$; Coceva[6] has recently fitted Monte Carlo simulations of the ORELA target response to such a function), the purpose of our fitting is to provide functions useful in Rietveld profile analysis. Existing Rietveld codes use a function which is the sum of a rising exponential, joined continuously to a falling exponential, convoluted with a gaussian. This function is non-physical (neutrons emerge before the source pulse) but provides a reasonably good fit to room-temperature polyethylene moderator pulse shapes. We found that such a function cannot adequately describe our L-CH_4 data. Use of the chosen function would require only minor modifications of the pulse shape description in existing Rietveld codes, since the pulse shape function is of mathematically similar form to that in current use.

The fitted function tends to undershoot the peaks at longest wavelengths, but is otherwise an excellent fit for the entire range of times and wavelengths.

We did not presuppose the wavelength variation of the fitted parameters except that of the longest-lived exponential, which we assumed constant, as is theoretically defensible. Figures 4, 5, and 6 give the wavelength variation of the long-lived (β_1) and short-lived (β_2) exponentials, the ratio of their amplitudes, and the gaussian standard deviation. The solid lines on Fig. 3 represent the fitted function. Resolution broadening appears as a contribution to σ, which is proportional to wavelength.

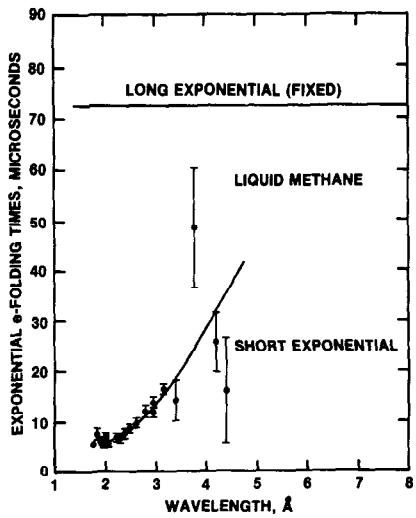

Fig. 4 Wavelength variation of the exponential-decay factors for the pulse-shape function. The value of β_1 was determined from the long-time part of the lowest-energy peaks, and held fixed in fitting the remaining parameters. The curve is a "best guess" at the smooth variation of $1/\beta_2$.

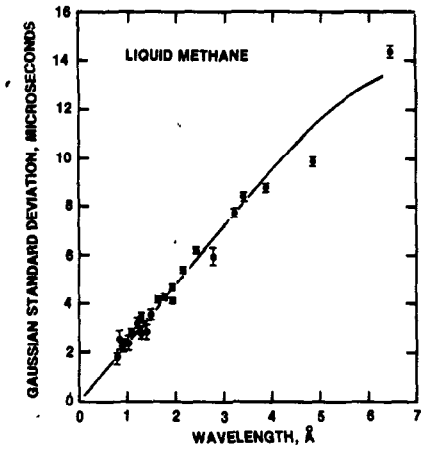

Fig. 5 Wavelength variation of the standard deviation of σ the gaussian function. The curve is a "best guess" at the smooth variation of $\sigma(\lambda)$.

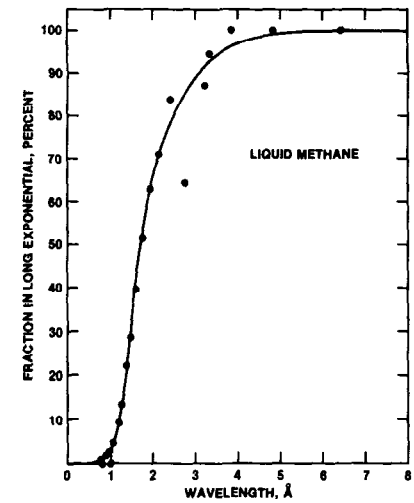

Fig. 6 Wavelength variation of the fraction of the total intensity in the slow exponential. The curve is a "best guess" at the smooth variation of the fraction.

Figure 2 shows also the pulse full-widths Δt_f at fraction f of maximum, uncorrected for resolution, which we estimate to be a small effect.

We have compared our measurements to TIMOC calculations of Picton, et al.[7] on a 90 K CH_4 moderator of the same dimensions as ours. The calculated pulse widths Δt_f are significantly smaller than our measurements, but the long-time decay at low energy agrees quite well; the calculation giving 77 μs e-folding time, and the data 72 μs.

Conclusion

We have measured the spectrum and pulse shapes as function of wavelength for a 108 K Liquid CH_4 moderator, and developed simple mathematical functions which provide satisfactory fits to the data.

References

1. T. G. Worlton and J. M. Carpenter, Internal Note (unpublished) 1979.
2. H. H. Hubeney to J. M. Carpenter, ANL memorandum, February 16, 1981.
3. J. M. Carpenter, Nucl. Inst. & Meth. 145, 91 (1977).
4. G. J. Russell, M. M. Meier, H. Robinson and A. D. Taylor, ICANS-V Proceedings of the Fifth Meeting of the International Collaboration on Advanced Neutron Sources, Jül-Conf-45, 389 (1981)
5. W. Marshall and S. W. Lovesey, "Theory of Thermal Neutron Scattering, Oxford, 1971, p. 101.
6. C. Coceva, R. Simonini and D. K. Olsen, Nucl. Inst. & Meth. 211, 459 (1983).
7. D. J. Picton, D. K. Ross and A. D. Taylor, "The Use of the Monte Carlo Code TIMOC in the Prediction of Neutron Time Distributions in Pulsed Moderators." To appear in J. Physics D (1983).

Proceedings of International Collaboration on Advanced Neutron Sources (ICANS-VII), 1983 September 13-16
Atomic Energy of Canada Limited, Report AECL-8488

THE INFLUENCE OF TARGET AND REFLECTOR COOLANT ON THE THERMAL NEUTRON LEAKAGE FLUX FROM AN SNQ-TYPE MODERATOR

G.S.Bauer, H.Conrad, K.Grünhagen, G.Milleret* and H.Spitzer
Projekt Spallations-Neutronenquelle
KFA Jülich, D-5170 Jülich, FRG
*Laboratoire National SATURNE,
Saclay, France

Summary

Light and heavy water as a cooling fluid have been compared experimentally for both the target and the reflector in the SNQ mock-up with respect to their effect on thermal neutron leakage from the SNQ-moderator. The cumulative gain (i.e. both target and reflector cooled with heavy water) in thermal neutron leakage flux was found to be less than 12 %. This figure does not appear to justify the effort of using heavy water as a cooling medium for the SNQ target station.

Introductory Remarks

Fluids are ubiquitous in the target-moderator-reflector assemblies of spallation neutron sources. Since we are dealing with very high radiation fields atomic or light molecular fluids with low absorption cross section are to be preferred. Light water seems to be a good choice in this respect, especially since it is easy to handle and cheap. On the other hand, its outstanding moderation properties might make it undesirable to have water in the target to avoid premature neutron moderation and resulting increased absorption of the neutrons. The situation is particularly critical, if a thermal neutron decoupler is used around the moderator, whence it was concludet that the SNS-target should have D_2O cooling. D_2O is less strongly moderating and shows virtually no neutron absorption. Were it not for the increased cost of a D_2O cooling system (tritium handling etc.), this would certainly be the best choice. In order to obtain a quantitative basis for this decision, we performed measurements with both H_2O and D_2O as target and reflector coolant of the SNQ target station mock-up at Saclay, France. Although no decoupler will be used around the SNQ-moderator, the interest in these measurements was triggered by an indirect conclusion drawn from earlier measurements that polyethylene, used to simulate the reflector coolant seemed to have a negative effect on the thermal neutron leakage from the moderator.

Experimental Details

The experimental set-up is shown in a series of sectional views in figure 1. The targets were contained in a 30 ton lead shielding part of which could be rolled back for access. A 60x60x40 cm^3 graphite block under the target was used to simulate a large moderator (D_2O-tank) and the moderator-reflector assembly under investigation was placed on top of the target. The targets used were the sandwich-type lead slab targets of our former investigations[1] and, for the first time, a realistic simulation of the proposed SNQ rod-type lead slab target. In contrast to the sandwich-type target, where the coolant was simulated by polyethylene sheets resulting in an average "dilution" to 90 % by volume for the heavy metal (including aluminum sheets simulating the heavy metal canning), the rod-type target shown in figure 2 had the same composition as the SNQ target wheel (76 % heavy metal, 16 % coolant, 8 % canning aluminium). The integrated moderator-reflector assembly shown in figure 3 contained separating walls between the moderator volume and the reflector part in order to be able to employ H_2O as moderating fluid and D_2O as reflector coolant independently.

The applied proton currents were of the order of 1nA and 1.1 GeV kinetic energy. The proton beam cross section, monitored by several wire chambers in front of the target, was of approximately circular shape of

about 3 cm half height diameter. The absolute proton calibration and the therefrom deduced absolute neutron leakage fluxes have been obtained as described in a previous paper.[2]

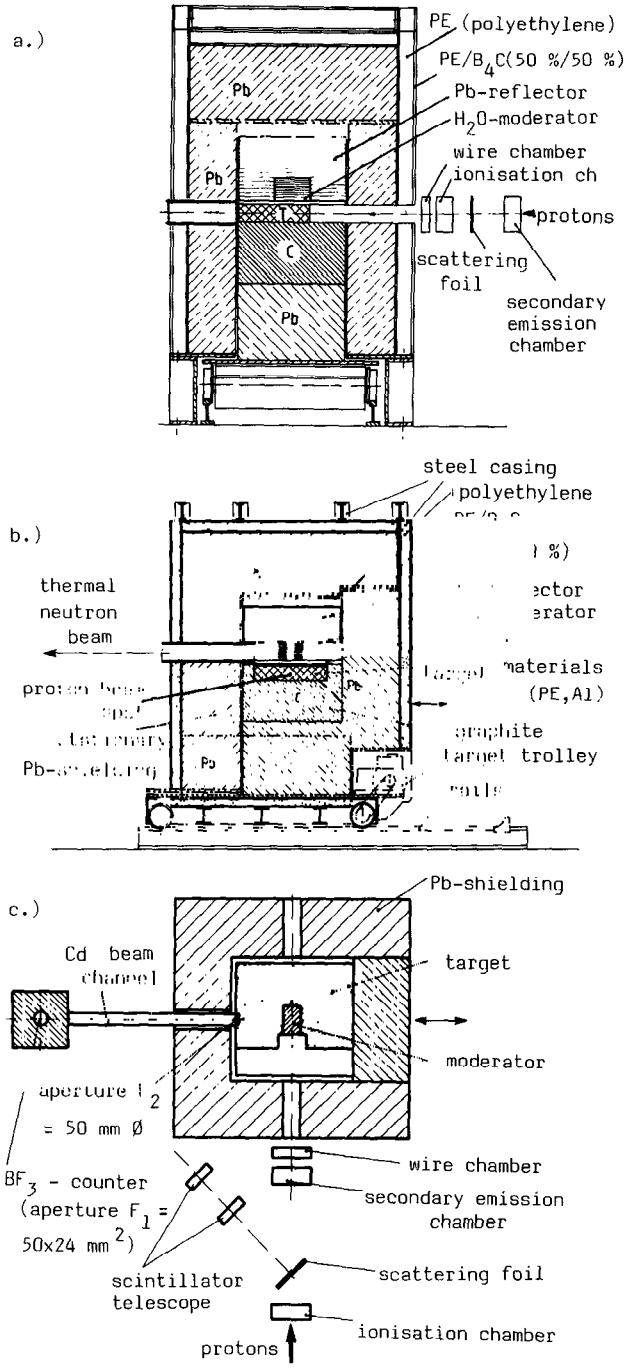

Figure 1. The SNQ target station mock-up

a.) vertical section parallel to proton beam

b.) vertical section perpendicular to proton beam

c.) schematic horizontal section

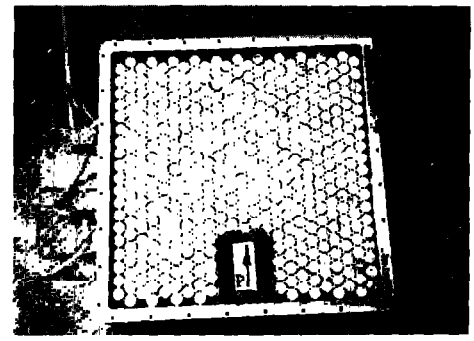

Figure 2. SNQ rod-type model target
rod diameter: 23 mm, rod height: 100 mm
separation between rod centers: 25 mm,
aluminium canning simulated by 5 mm
diameter rods in each triangular space
between rods.

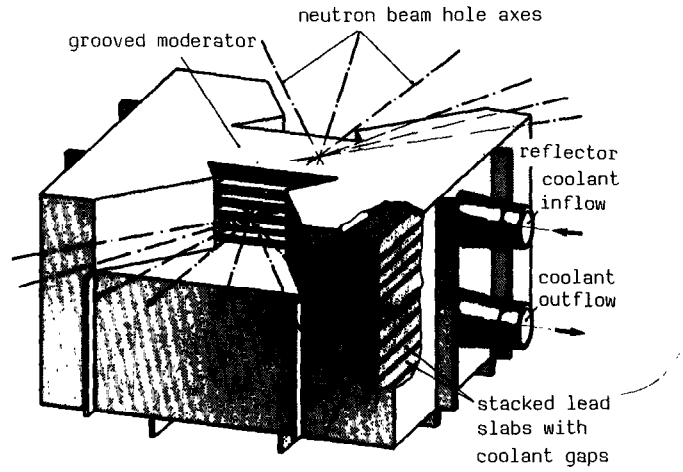

Figure 3. SNQ moderator-reflector arrangement

Results and Discussion

All together 12 combinations of targets, target-coolants and reflector-coolants have been measured including for comparison air in the coolant gaps of both target and reflector. Also including again the sandwich-type target extensively employed in earlier investigations should both confirm the reproducibility of our results and serve as a direct comparison of the two targets. The results of all measurements are compiled in Table 1.

meas. #	target	target coolant	reflector (vol.%)	reflector coolant	thermal neutron leakage flux ϕ_{th} [10^{14}n cm^{-2} s^{-1}]
1	Pb (sandw.)	polyeth.	-	-	4.42
2	"	"	Pb (90%)	air (10%)	5.48
3	"	"	"	H_2O "	5.35
4	"	"	"	D_2O "	5.75
5	Pb (rods)	air	-	-	3.49
6	Pb (rods)	D_2O	-	-	4.24
7	"	"	Pb (90%)	air (10%)	5.18
8	"	"	"	H_2O "	5.10
9	Pb (rods)	H_2O	-	-	4.02
10	"	"	Pb (90%)	air (10%)	4.80
11	"	"	"	H_2O "	4.91
12	Pb (rods)	H_2O (void)	Pb (90%)	H_2O (10%)	5.15

Table 1: Comparison of measured thermal neutron leakage fluxes for various target, reflector and coolant combinations. The flux values are scaled to 5 mA proton current. Measurement # 12 differs from # 11 with respect to displaced coolant water ("void") at the entrance (front gap of the rod assembly of Fig. 2) of the beam.

Effect of reflector coolant

For both targets we started with (using a polyethylene moderator of the same shape as the H_2O moderator) measurements with a void at the reflector position inside the shielding. The increase in neutron leakage flux measured with the reflector filling the void, once again demonstrates the advantage of a tight target-moderator-reflector-shielding arrangement. Using light water instead of air as a coolant does not significantly alter the measured fluxes, as can be seen by comparing the results of measurement # 2 and # 3, # 7 and # 8 as well as # 10 and # 11 of Table 1. From this consistent set of results an important gain in thermal leakage flux using D_2O as reflector coolant could no longer be expected. As a matter of fact the measurement # 4 (D_2O reflector coolant) exhibited only a 7.5 % flux increase as compared to H_2O coolant (# 3).

Effect of target coolant

The SNQ target wheel will contain about 16 % (by volume) of coolant in the reaction zone. Especially for the case of protons on lead when the range is rather long, this will lower the absolute neutron flux due to stronger heavy metal dilution. Apart from this one would expect that using D_2O as coolant results in a flux gain by at least the same factor as obtained for the reflector cooled with D_2O. The reason for this expectation is the particular geometry of the SNQ-target-moderator configuration: Absorption of neutrons thermalized in the large D_2O-moderator (simulated in this experiment by a graphite block, compare fig. 1) will be much stronger in a H_2O-cooled target thus preventing them from reaching the H_2O-moderator on the other face of the target, where they could contribute to the measured leakage flux. Somewhat surprisingly, the measured flux gain amounted to only about 4 % (meas. # 8 and # 11), which might as well be within the experimental uncertainty. These results indicate that, for the particular geometry of the SNQ target-moderator geometry, moderation in the target plays no significant role and also cross talk between both moderators is not very important, not even for the low absorption material lead-D_2O. The fact that the extra dilution in going from the sandwich type target (90 % heavy metal) to the rod target (76 % heavy metal) results in only 4 % flux reduction (measurements # 3 and # 12) might be due to spallation processes in the oxygen of the coolant.

Conclusion

Gain factors of 1.08 for a D_2O-cooled reflector and 1.04 for a D_2O-cooled (rod-type) target, which might combine to a total gain factor of 1.12 certainly do not justify the complications implied by using D_2O as target and reflector coolants for the SNQ-project. At the same time we were able to show that a hexagonal packing of targets rods, necessarily resulting in a stronger dilution of the target than the sandwich target we used for earlier experiments, does virtually not lower the thermal neutron leakage flux. The measurements thus have essentially confirmed the H_2O-cooled concept selected for the SNQ target station DIANE.

References

1. Bauer, G.S.; Fischer, W.E.; Gompf, F.; Küchle, M.;
Reichardt, W. and Spitzer, H.
ICANS-V (1981), p. 445-474, Jül-Conf-45

2. Bauer, G.S.; Conrad, H.M.; Grünhagen, K.;
Spitzer, H. and Milleret, G.
ICANS-VI (1982), p. 619-627, ANL-82-80

Session H

Shielding and Remote Handling

Chairman - G.H. Lander

Proceedings of International Collaboration on Advanced Neutron Sources (ICANS-VII), 1983 September 13-16
Atomic Energy of Canada Limited, Report AECL-8488

RADIATION-RESISTANT BEAMLINE COMPONENTS AT LAMPF*

R.J. Macek, D.L. Grisham, J.E. Lambert, R. Werbeck
Los Alamos National Laboratory, Los Alamos, NM 87545

Summary

A variety of highly radiation-resistant beamline components have been successfully developed at LAMPF primarily for use in the target cells and beam stop area of the intense proton beamline. Design features and operating experience are reviewed for magnets, instrumentation, targets, vacuum seals, vacuum windows, collimators, and beam stops.

Introduction

Beamline components for the target cells and beam stop area of the 1 mA, 800 MeV main proton beam at LAMPF are exposed to very intense radiation fields. The requirements for reliable operation in this environment are formidable. The components must be highly resistant to radiation damage, be able to dissipate large beam-induced heat loads, be remotely serviceable, and be highly reliable. The development of components meeting these requirements has been a long-term challenge for the experimental areas staff.

In practice, radiation hardening has meant the exclusion of plastics and other organic materials from use in these components. Less familiar, substitute materials, such as ceramics, mica, mineral-insulated cable, etc., while very radiation resistant, have other properties which are not always desirable and have lead to modes of failure other than from radiation damage. For example, ceramics are highly radiation-resistant electrical insulators, but they are often porous or hygroscopic and lose their insulating properties in the presence of moisture. In addition, they are brittle and easily fractured during some handling operations.

The remote handling and servicing of highly radioactive components is a major, if not dominant, design consideration. As a first criterion, extraordinary reliability is desirable so that less frequent remote servicing is needed. Secondly, the procedures of remote handling in the confined space of a target cell are restrictive and time-consuming. Simplicity of design, of operation, and of installation cannot be over-emphasized.

Magnets

Three different types of mineral insulation have been used successfully at LAMPF to construct radiation-hardened magnets: 1) An inorganic, castable cement,[1] 2) Arc-sprayed alumina,[2] and 3) Mineral-insulated cable from Pyrotenax of Canada, Ltd.[3] The mineral-insulated quadrupole magnets of the drift-tube linac have had a very successful operating history for more than 10 years. They are insulated with a castable cement consisting of a calcium aluminate binder with 60-mesh aluminum oxide filler. It was developed at Los Alamos primarily to withstand the 1500° Fahrenheit temperatures encountered during the H_2 brazing furnace cycle used in the fabrication of the drift-tube bodies. This cement is hygroscopic and can pick up moisture from the air. However, for the drift-tube application, this is not a problem since the magnets operate in a soft vacuum of about 50×10^{-3} Torr.

Coils for magnets close to the meson production targets in the experimental area target cells are most commonly radiation hardened through the use of the mineral-insulated Pyrotenax cable. This cable consists of a water-cooled inner conductor, a layer of powdered MgO insulation, plus an outer copper sheath to contain the MgO. This insulating material is hygroscopic and will develop low electrical resistance when exposed to air for a period of time. Therefore, the ends of the cable are terminated with ceramic seals to keep out air and moisture and to insulate the sheath from the inner conductor. Ceramic water-carrying insulators with brazed-on metal ends are used to connect the water circuits of the conductors to the water piping.

Over 60 mineral-insulated magnets of this design have given generally satisfactory service at LAMPF since 1972.[4] Radiation damage has not been a major problem. Most failures have other causes which are usually related to water problems. One ceramic insulator failed by electrolytic corrosion in the early years of operation during a period when the water conductivity was not kept below 10^{-6} mho/cm, but rose to 10^{-4} mho/cm. High-pressure water leaks in the magnet or in nearby water-cooled components have caused several failures, such as ground faults and interrupted thermal interlock strings. A thoroughly wet magnet suffers from electrolytic corrosion of thermal switches and interlock wiring. Corroded copper wiring becomes brittle and breaks easily.

Overheating of the target cell triplets (TCT) has occurred in recent years. Some of these magnets operate at 10-15% above design current and normally run close to a thermal trip point. A layer of CuO builds up in the water passages and apparently reduces the heat transfer from conductor to the cooling water sufficiently to raise the conductor temperature several degrees. Backflushing the magnets for several hours with a weak (4%) solution of phosphoric acid removes CuO and will restore the magnet to an operable condition. Backflushing is now a standard preventive maintenance procedure applied once or twice per year during down times and has essentially eliminated overheating problems.

The TCT's are shielded from scattered beam by water-cooled collimators. Even with this protection, the magnets become too radioactive for hands-on maintenance after any significant use at present intensities. Two TCT's suffering from ground faults and water leaks were removed this past year, but have not been repaired or disassembled for diagnosis because of the residual radioactivity. Radiation levels of several hundred R/hr are encountered which prevents hands-on work.

Operating experience to date has motivated several detailed improvements, some of which can be seen in the photograph of an improved TCT shown in figure 1. The water and electrical connections have been moved to the top of the triplet assembly where they can be more readily serviced with a remotely operated manipulator. The number of water insulators has been reduced by a factor of two while, at the same time, reducing the overall impedance to water flow. Thermal switches are mounted on the cable sheath instead of on the electrical conductor as before. Thermal protection is not compromised since the temperature drop from conductor to sheath is only a few degrees Fahrenheit. Electrolytic corrosion of wet thermal switches and interlock wiring is reduced by having the switches on the sheath at ground potential and using 6 volt ac instead of 24 volt dc excitation.

It is worth noting that the electrical impedance as a function of frequency for a magnet wound with the Pyrotenax cable is much different than that for the same magnet equipped with conventional epoxy-potted

*Work supported by the US Department of Energy.

coils.[5] This behavior can be explained by realizing that the mineral-insulated (MI) magnet can be pictured as a transformer whose secondary (the outer sheath) is a shorted turn. Measurements of LAMPF magnets show that below 500 Hz, the impedance is mainly resistive and at 60 and 360 Hz, it is an order of magnitude lower than the impedance of the same magnet equipped with conventional coils. As a result, the ripple current, for the same ripple voltage, is an order of magnitude larger for the MI magnet. Fortunately, the ripple flux is about the same in both.

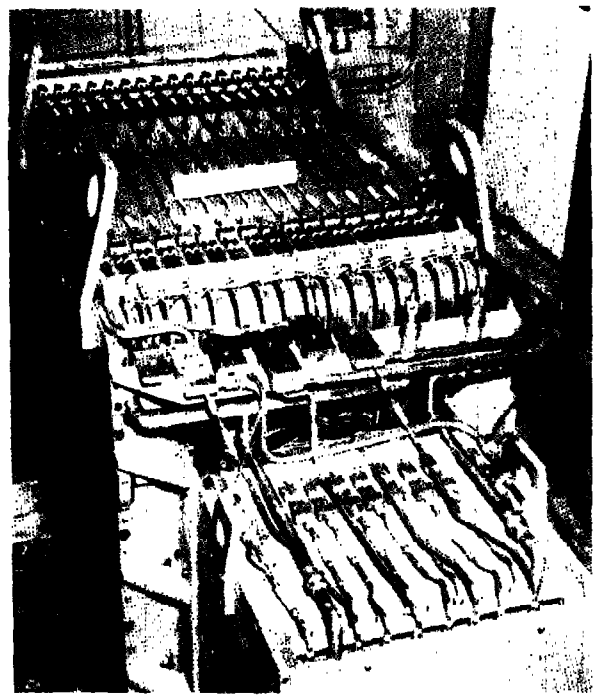

Figure 1. Improved target cell triplet.

Instrumentation

Several radiation-resistant instruments have been developed for beam diagnostics and beamline protection. For this paper we have chosen to discuss three of the most important devices, i.e., the harp profile monitors,[6] toroid current monitors,[7] and the secondary emission guard rings.[8]

Harps

These are secondary emission grids which sample the beam profile and are used to estimate beam centroid and spot size. The harps used in the experimental areas are not movable; they are always in the beam. This approach has the advantage that no radiation-hardened, moving mechanisms are required. However, it does require a thin, low Z filament that can survive the full intensity beam and produce negligible beam scattering. The filaments are radiation cooled and must operate below the temperature where thermionic emission becomes important.

Harps presently in use consist of two orthogonal planes of signal wires and three planes of clearing field wires at a potential of 57 volts. The signal wires are attached to alumina ceramic substrates via silver-based printed circuit inks. The ceramic boards and clearing field planes are mounted on a central stainless steel frame which hangs from a vacuum-sealing lid that contains an electrical feedthrough for each signal wire. A pair of ceramic p.c. edge connectors are mounted on the atmospheric side of the lid. A photograph of the harp assembly is shown in figure 2.

Both carbon and silicon carbide filaments are used for the wires that span the beamline aperture. Carbon filaments are easily pre-stressed and soldered to the printed circuit lands, but suffer from low strength since the maximum diameter commercially available is 0.05 mm. We are presently using 0.1-mm diameter silicon carbide filaments with a tensile strength of about 4×10^5 psi for the large harps. This wire is mounted by crimping a copper adapter to each end of the wire and using spring to maintain $1\text{-}2 \times 10^5$ dynes of tension. The springs were found to be necessary because the SiC elongates by about 1% when exposed to proton fluences of about 10^{20} cm^{-2}.

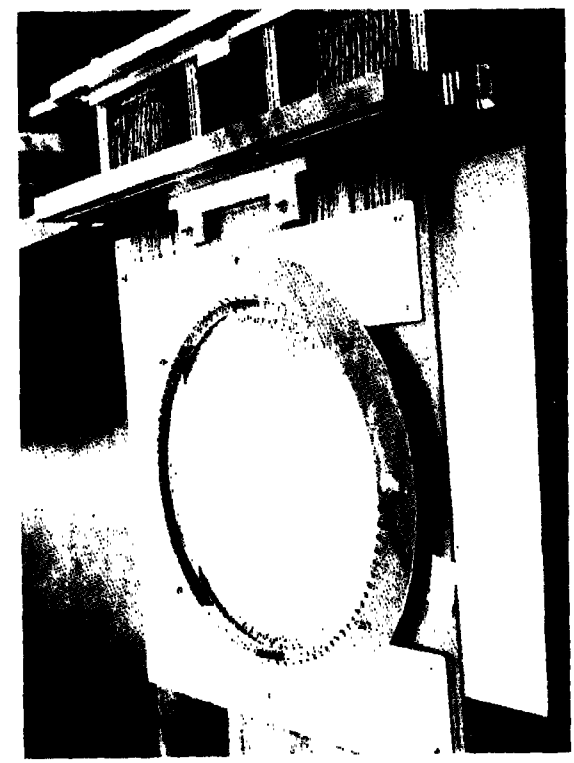

Figure 2. Harp assembly (33-cm inner diameter).

The harps are shielded from scattered beam, from secondary particle fluxes, and from errant beams by appropriately located collimators. They limit the thermal load to the massive outer parts of the harp and limit the flux of particles which can produce spurious signals by secondary emission from the relatively large area printed lands on the ceramic cards.

The harps perform as required for beams from 1 microamp to 1200 microamp average proton currents. Most difficulties are associated with thermal loads, gas flow forces, poor vacuum, water leaks, and mechanical connections. The ceramic insulated electrical feedthrough performs well when dry, but is prone to exhibit unacceptably low leakage resistance when damp. The reliability of ceramic edge connectors has been a continuing source of difficulty. Shrinkage during fabrication is difficult to control and breakage is a problem. They are also susceptible to the same moisture problems affecting the ceramic feedthroughs.

The signal cables that connect to the harp are either RG-174 or mineral-insulated coaxial cable. The MI bundle is very difficult to bend or flex and the cable itself is less reliable because of the difficulty

of producing and maintaining a good hermetic seal at each end. Our experience to date indicates that the RG-174 is usable, with care, for a few years at two-thirds of the harp locations even though the insulation becomes brittle and develops cracks. We use the RG-174 cable whenever it is at all possible because the increased reliability and ease of installation outweigh the concern for long life, at least for the present.

Current Monitors

Radiation resistant toroids configured as beam current transformers are the principal current monitors for both beam diagnostic and beamline protection purposes. They are key elements of the beamline protection system where they function as transmission monitors. For this application, the current monitor signals are processed electronically to give an accurate determination of transmission or loss between two monitoring locations.

Construction of the latest version of the toroids is shown in figure 3. The toroid core is wound of mu-metal tape insulated with a thin coating of MgO. The core is enclosed in an anodized aluminum casing packed with MgO. The anodized aluminum enclosure is fabricated with an insulated circumferential break which prevents the transformer from having, in effect, a shorted secondary turn. The actual secondary is wound on the ceramic spacer ring which is slotted to immobilize the windings. Finally, the wound core assembly is placed in a steel container, filled with an inorganic potting material known by the commercial name of Saureisen, and then baked and evacuated. The steel container also has a circumferential break to prevent a shorted secondary turn.

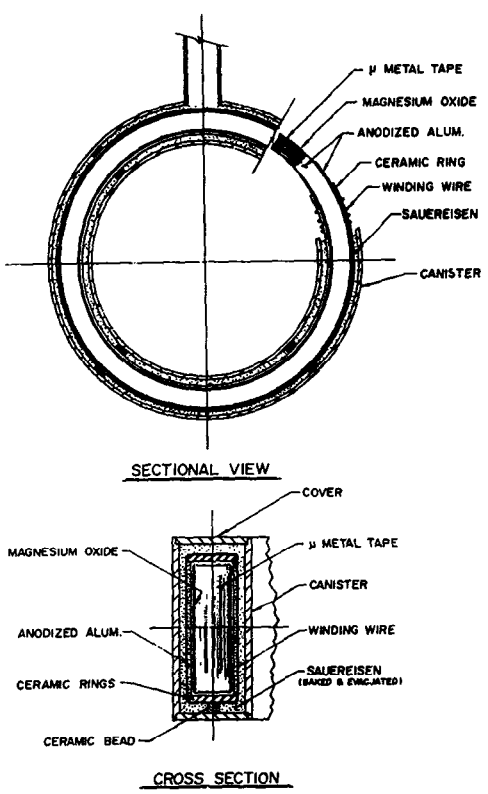

Figure 3. Toroid current monitor assembly.

Collimators are also used to shield the toroids from scattered beam, secondary particle fluxes, and errant beams. This is necessary to limit the thermal load on the toroid and to suppress spurious signals induced by charged particles striking the toroid.

Since the toroid is constructed from purely inorganic materials, it is very resistant to radiation damage to its mechanical structure. However, it is susceptible to a more subtle degradation of its electrical performance. The initial permeability, hence inductance, drops as a function of integrated radiation dose.[9] The toroids at the beam stop are the most affected. A plot of inductance of a beam stop toroid as a function of total integrated beam current is shown in figure 4. This toroid has suffered a drop in inductance by a factor of 25 in less than 6 months of operation. The current monitor electronics system has been improved to the point where it can just handle a change of this magnitude without serious error. The neutron fluence at the toroid for this same period of time has been estimated at about $2\times10^{+17}$ n/cm^2 (neutrons below 20 MeV) from Monte Carlo simulation using the nucleon-meson cascade code, HETC, and the neutron transport code, MCNP.[10]

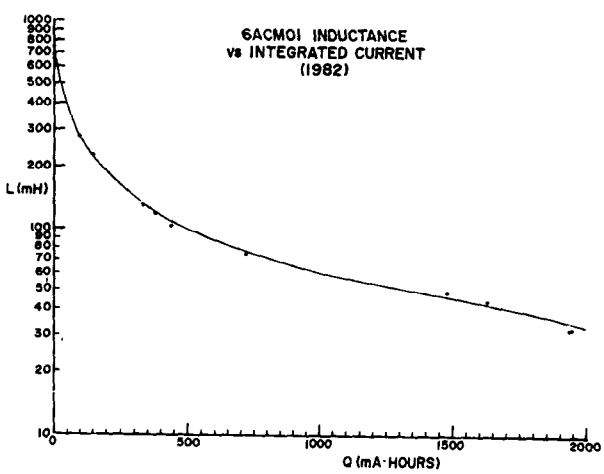

Figure 4. Toroid inductance degradation.

Secondary Emission Guard Rings

These are fast, radiation-hardened beam spill monitors that are placed in the vacuum envelope in front of collimators in the target cells and near the beam stop. They are used both for protection and diagnostic purposes. The detector shown in figure 5 consists of two signal planes each divided into quadrants and three high voltage planes surrounded by an isolated ground casing. The spacers between planes are ceramic insulators. The vacuum feedthrough is a Gulton Durock Hermetic TI-12-10 connector with a radiation hard (about 10^{15} rads) silico-ceramic insulation. Nickel wire, sleeved with alumina beads, is used to make connections that are spot welded rather than soldered.

Except for failures due to water damage, the operating experience with the guard ring system has been quite satisfactory. The devices are radiation hard, have a fast response time, low false alarm rate, good sensitivity (<100 nA) for protection, and even better for diagnostic uses. They are very specific in the sense that they directly measure beam spill in a geometrically well-defined region. Water leaks in the target cell short out the connectors and fiberglass-insulated cables. Electrolytic corrosion of

wet conductors under the influence of the clearing field potential leads to permanent damage.

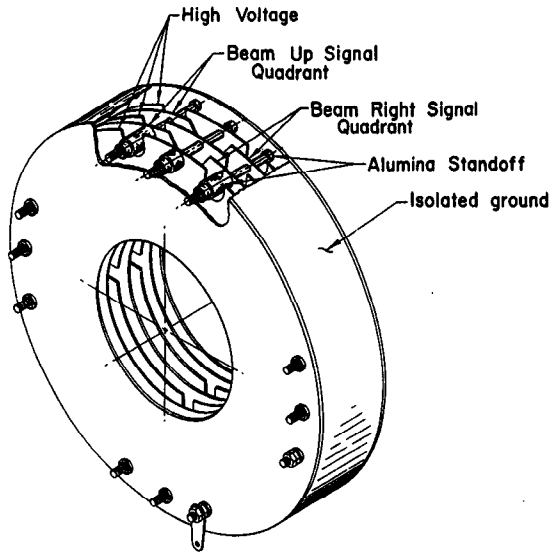

Figure 5. Guard ring detector assembly.

Targets[11,12,13]

Two types of pion production targets are used in the main proton beamline at LAMPF. The first two target cells use rotating wheels of normal graphite (ATJ) with a density of 1.73 gm/cm^3. They are 3 cm and 6 cm in length, respectively. As shown in figure 6, the machined wheel is mounted on a spindle and rotated by a roller chain which is driven from outside the shielding. The wheels rotate at approximately 1 revolution per second to prevent two consecutive beam pulses from hitting the same spot and to rotate the hot spot to a cooler area. Since all cooling is radiative, the wheel operates at a high temperature. Calculations indicate that the maximum temperature at 1 mA is approximately 1900°K, but varies only 10-20°K per revolution.

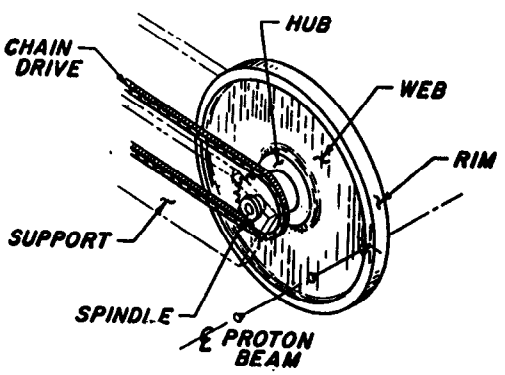

Figure 6. Radiation-cooled rotating graphite target.

The primary problems with with wheels have been with bearing wear or seizure with a lessr problem of chain stretch and wear during continued rotation under the severe conditions of high radiation fields, high temperature, and being in a vacuum. The radiation level has not been measured, but the use of melt wires in the spindle indicates that the bearing temperatures exceed 900K at approximately 700 μA beam current. The bearings have progressed from standard commercial stainless steel ball bearings to special high temperature stainless ball bearings, then special high temperature graphite sleeve bearings, finally to the present powder metallurgy molybdenum sleeve bearings impregnated with molybdenum disulfide. Table I gives the estimated running times for the various bearings at a beam current of 1 mA.

Table I

Bearing	Estimated running time months
standard SS	.0001
special SS	.01
graphite	2-3
molybdenum	9-12

The remaining target is a water-cooled pyrographite target at a density of 2.2 gm/cm^3. As shown in figure 7, it consists of pyrographite plates brazed to five copper cooling tubes which, in turn, combine in common inlet and outlet manifolds. The critical technique of the brazing of the pyrographite to the cooling tubes is the key to the success of this target, and has now become routine.

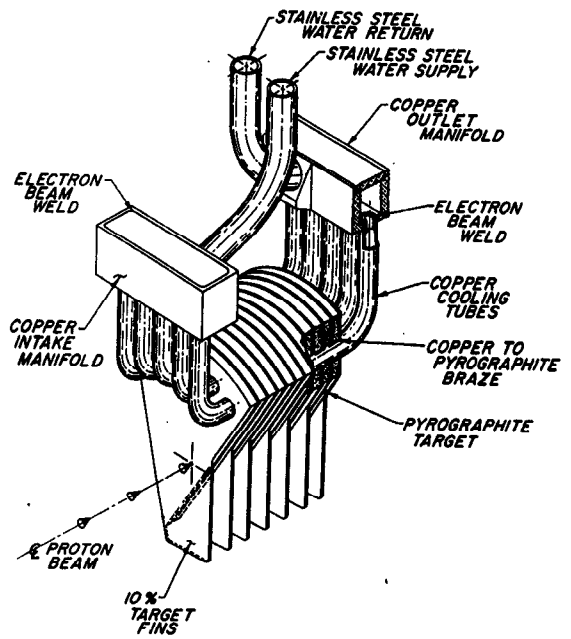

Figure 7. Water-cooled pryographite target.

The difficulties with this target have been caused by the swelling of the pyrographite due to radiation damage and accentuated by having a stationary target. The condition can be helped by occasionally moving the beam spot, but is only partially successful since the swelling extends beyond the actual beam spot. The estimated life of this design at a beam current of 1 mA is about 6 months.

Vacuum Seals

Figure 8 is an isometric sketch of a typical radiation-hardened vacuum joint used in the LAMPF main beamline. The seal consists of a stiff annulor body with integral sealing lips. The seal is machined from heat-treated AISI-4340 steel, and plated with a soft metal, such as lead, silver or gold, depending upon the operating temperature of the particular joint. Compression of the sealing lips is controlled by the thickness of the seal body. When compressed, the seal

lips are not stressed beyond the elastic limit, thereby retaining relatively constant sealing forces during thermal cycling of the joint. Elastic metal seals of this type require relatively low sealing forces (~100 newton/cm), while other metal seals which require crushing beyond the elastic limit require sealing forces up to 5000 newton/cm.

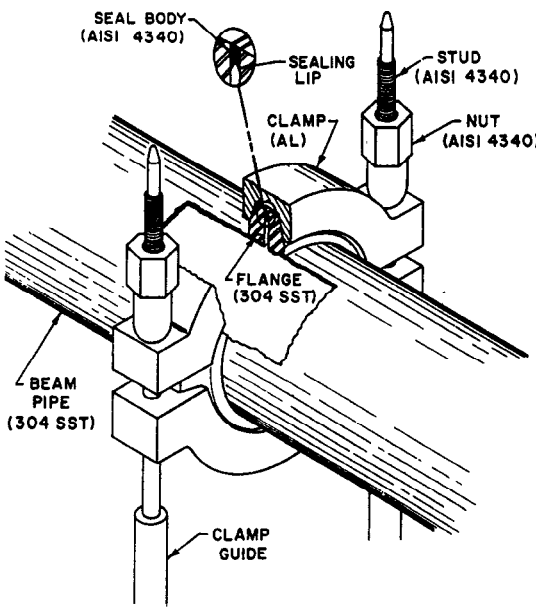

Figure 8. Radiation-hardened vacuum joint.

Crush-type metal seals are also not satisfactory for joints subject to thermal cycling as they do not have sufficient elasticity to accommodate even small dimensional changes in the joint. Other disadvantages include the requirement for larger, more complicated clamping devices which are not suited for remote handling.

Operating experience at LAMPF has shown that simple two-piece clamps as illustrated in figure 9 provide adequate sealing forces for flanges up to 60-cm diameter. The simplicity of this design is well suited to remote handling. The studs and nuts used in this design are made from heat-treated high alloy steel to minimize possible thread damage during remote assembly operations. The clamping angle of 20° (40° included) represents the best compromise between mechanical advantages and ease of removal. Prior to assembly of a joint, all threads and clamping surfaces are lubricated with dry molybdenum disulfide. Organic lubricants should be avoided, as the residue from decomposition may create problems in later disassembly of the joint. The use of any organic materials in joints subject to high radiation would not be worthwhile due to short useful service life.

Beamline Window[14]

At the end of Line A, a window is required since isotope production stringers as well as the beam stop are not under vacuum. During the first few months of operation, an air-cooled foil window was used. Although the allowable power level could have been increased by using helium as a coolant, it was decided to convert to a water-cooled window in late 1976. After the water flow for the first window failed due to a manufacturing defect, the design shown in figure 10 was placed in operation and has been in continuous service since. Another new window of this design was just recently installed. It consists of two stepped flat plates that are cooled by water flowing transversely at high velocity between the plates. The inherent disadvantage of this design is the high stress due to internal water pressure. The hardened Inconel window has allowable strengths sufficient for this application, but manufacturing tolerances, surface finishes, and elimination of stress risers become very critical. Table II gives the maximum stresses for two conditions and the yield stress of Inconel 718 for comparison.

Table II

Condition	Stress/strength-MPa
water pressure only	895
water + 1.05 mA	1020
yield strength	1100

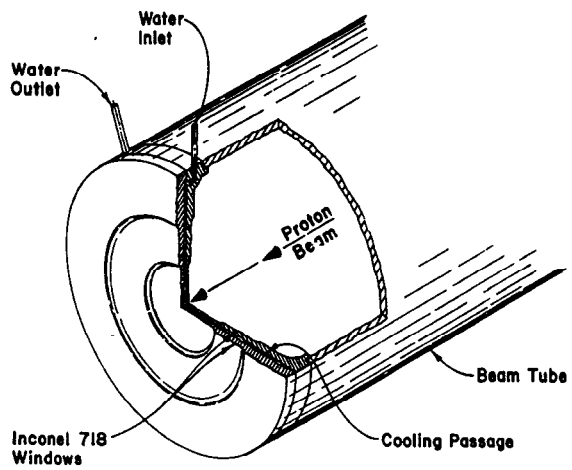

Figure 9. Water-cooled beamline window.

To reduce the high stresses, a new design was developed and is now in the fabrication stage. It consists of a pair of spherical windows with water flowing between them. The main advantage is that the total stress is reduced to ~240 MPa for the same beam conditions. Further cold testing will take place soon and it is expected that the spherical window will be installed in the spring of 1984.

Beam Stop[14]

The original (and the present) beam stop design for the high intensity primary beam at LAMPF is shown in figure 10. It consists of a stainless steel shell with an Inconel 718 stepped flat plate window with 29 OHFC copper plates of varying thickness as the stopping material. The plates, as well as the window, are cooled by high velocity water flowing transversely between the plates. The copper plate thickness was determined by its heat deposition so as to limit the maximum temperature in the copper. The copper plates are plated electroless nickel followed by a flash of gold to reduce the corrosion of the copper accelerated by the decomposition of the water as it passes through the beam.

The first beam stop operated from early 1976 to late 1980 at which time it was replaced by the present one. The first beam stop received ~4.7×10^6 μA-h without obvious damage or functional degredation. A detailed post mortem examination of the copper plates will be completed in the next few months. At that point we will better understand the actual damage, possibly can infer the cause, and, hopefully, can determine future improvements. The present stop is scheduled to be replaced next year at which point it

will have received more protons than the original. This will give us another chance to assess our design.

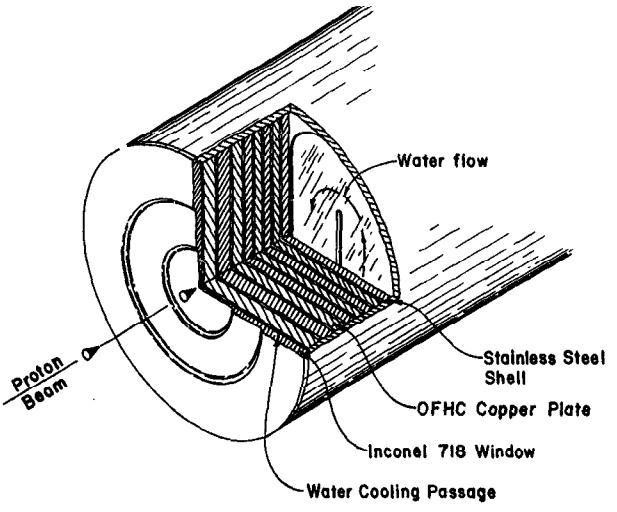

Figure 10. Water-cooled beam stop.

Collimators[14]

Because of the high beam current and subsequently high heat depositions in the components around the pion production target, water-cooled collimators have been placed between the target and such components. An illustration of this arrangement is shown in Reference 10.

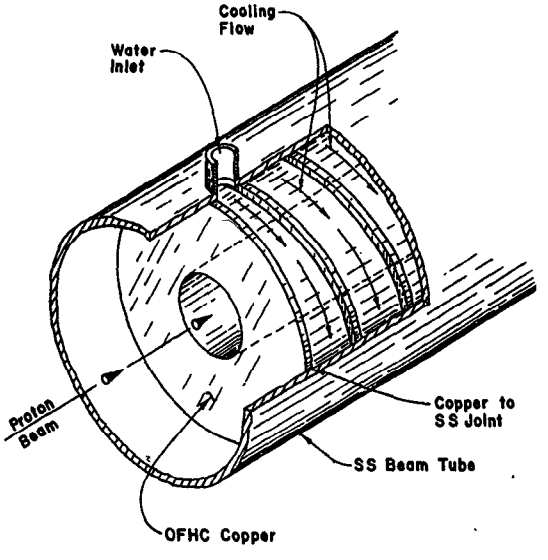

Figure 11. Water-cooled collimator.

Some of the original collimators were made of tungsten brazed inside a stainless steel tube that had cooling water tubing brazed to the outside. These are primarily placed to reduce backscattering from the target to upstream diagnostic instrumentation and are not suitable for areas of high heat deposition.

The collimators for high heat deposition areas consist of an OHFC copper cylinder directly water cooled on the outside and welded to the inside of a stainless steel tube as shown in figure 12. The secret to the success of this design is the copper to stainless steel joint which is the barrier between the cooling water system (2.07 MPa) and the beamline vacuum. The joint is made with a tungsten inert gas welding torch using RTSN brazing material as a filler. Although the technique is critical, trained welders can learn it in a few hours.

A number of collimators of this design have been in service since early 1976 with no leaks across the joints. The new collimators recently installed in the new A-2 target cell are of the identical design and just differ in size and flow passage arrangement. The collimators for the upcoming A-1 target cell rebuild will, again, be of the same design.

Acknowledgments

Space does not permit individual acknowledgment of all of the many colleagues who have contributed over the years to the work reported here. However, we wish to make special mention of the leading contributions by A. Harvey and E.D. Bush, Jr., to magnet development and by Earl Hoffman, David Lee, and Calvin Hansen to the instrumentation progress reported here.

References

1. E.D. Bush, Jr., "Fabrication of 201.25-Mhz Drift-tube Linac Quadrupole Magnets," Los Alamos Scientific Laboratory report LA-4276 (1970).
2. E.D. Bush, Jr., and R.L. Rohrer, "Construction of Alumina-Insulated Bending Magnets for LAMPF," Proceedings of the 1972 Proton Linear Accelerator Conference, Los Alamos, LA-5115, pp. 318-325, 1972.
3. A. Harvey, "Radiation-Hardened Magnets Using Mineral-Insulated Conductors," Proceedings of the 4th International Conference on Magnet Technology, CONF-720908, MT-4, p. 456, 1972.
4. A. Harvey, "Experience with the LAMPF Mineral-Insulated Magnets," Proceedings of the 6th International Conference on Magnet Technology, MT-6, 1977.
5. E.J. Schneider, "Ripple Current and Flux in Mineral-Insulated Magnets," Proceedings of the 1972 Proton Linear Accelerator Conference, Los Alamos, LA-5115, pp. 403-406, 1972.
6. E.W. Hoffman et al., "High Intensity Beam Profile Monitors for the LAMPF Primary Beam Lines," IEEE Trans. Nuc. Sci., NS-26, No. 3, pp. 3420-3422, June 1979.
7. P.J. Tallerico, "LAMPF Experimental-Area Beam Current Monitors," J. Vac. Sci. Tech., Vol 12, No. 6, pp. 1200-1202, 1975.
8. R.J. Macek et al., "LAMPF Primary Beam Line Protection System," IEEE Trans. Nuc. Sci., NS-26, No. 3, pp. 4137-4139, June 1979.
9. R.S. Sery and D.I. Gordon, "Nuclear Irradiation Effects on Ferromagnetic Core Materials," Solid State Physics in Electronics and Telecommunications, (Academic, London, 1960) Vol 4, pp. 824-858.
10. L. Agnew et al., "Design Features and Performance of the LAMPF High Intensity Area," Proceedings of this Conference.
11. L. Agnew et al., "Graphite Targets for Use in High Intensity Beams at LAMPF," IEEE Trans. Nuc. Sci., NS-26, No. 3, pp. 4143-4145 (1979).
12. R.D. Brown and D.L. Grisham, "Design and Operation of Water- Cooled Pyrolytic Graphite Targets at LAMPF," IEEE Trans. Nuc. Sci., NS-28, No.3, pp. 2940-2942 (1981).
13. R.D. Brown and D.L. Grisham, "Graphite Targets at LAMPF," IEEE Trans. Nuc. Sci., NS-30, pp. 2801-2803 (1983).
14. D.L. Grisham and J.E. Lambert, "Water-Cooled Beamline Components at LAMPF," IEEE Trans. Nuc. Sci., No. 3, pp. 2850-2852 (1981).

Proceedings of International Collaboration on Advanced Neutron Sources (ICANS-VII), 1983 September 13-16
Atomic Energy of Canada Limited, Report AECL-8488

REMOTE HANDLING AT LAMPF*

D. L. Grisham and J. E. Lambert
Los Alamos National Laboratory
P. O. Box 1663, MS H840
Los Alamos, NM 87545

Introduction

Experimental area "A" at the Clinton P. Anderson Meson Physics Facility (LAMPF) encompasses a large area. Presently there are four experimental target cells along the main proton beam line that have become highly radioactive, thus dictating that all maintenance be performed remotely. Figure 1 is a layout of experimental area "A."

The Monitor remote handling system was developed[1,2] to perform in situ maintenance at any location within area "A." Due to the complexity of experimental systems and confined space, conventional remote handling methods based upon "hot cell" and/or "hot bay" concepts are not workable. Contrary to conventional remote handling which require special tooling for each specifically planned operation, the Monitor concept is aimed at providing a totally flexible system capable of remotely performing general mechanical and electrical maintenance operations using standard tools.

The Monitor System

A Monitor system consists of a pair of slave manipulators mounted on the boom of a portable hydraulic crane positioned at the work location. Figure 2 is a view of the slave unit.

Operations are conducted from a master control station, installed in a trailer, positioned at a safe distance from the radioactive work area. Viewing is accomplished only by closed circuit television. Figure 3 is a view inside the master control station.

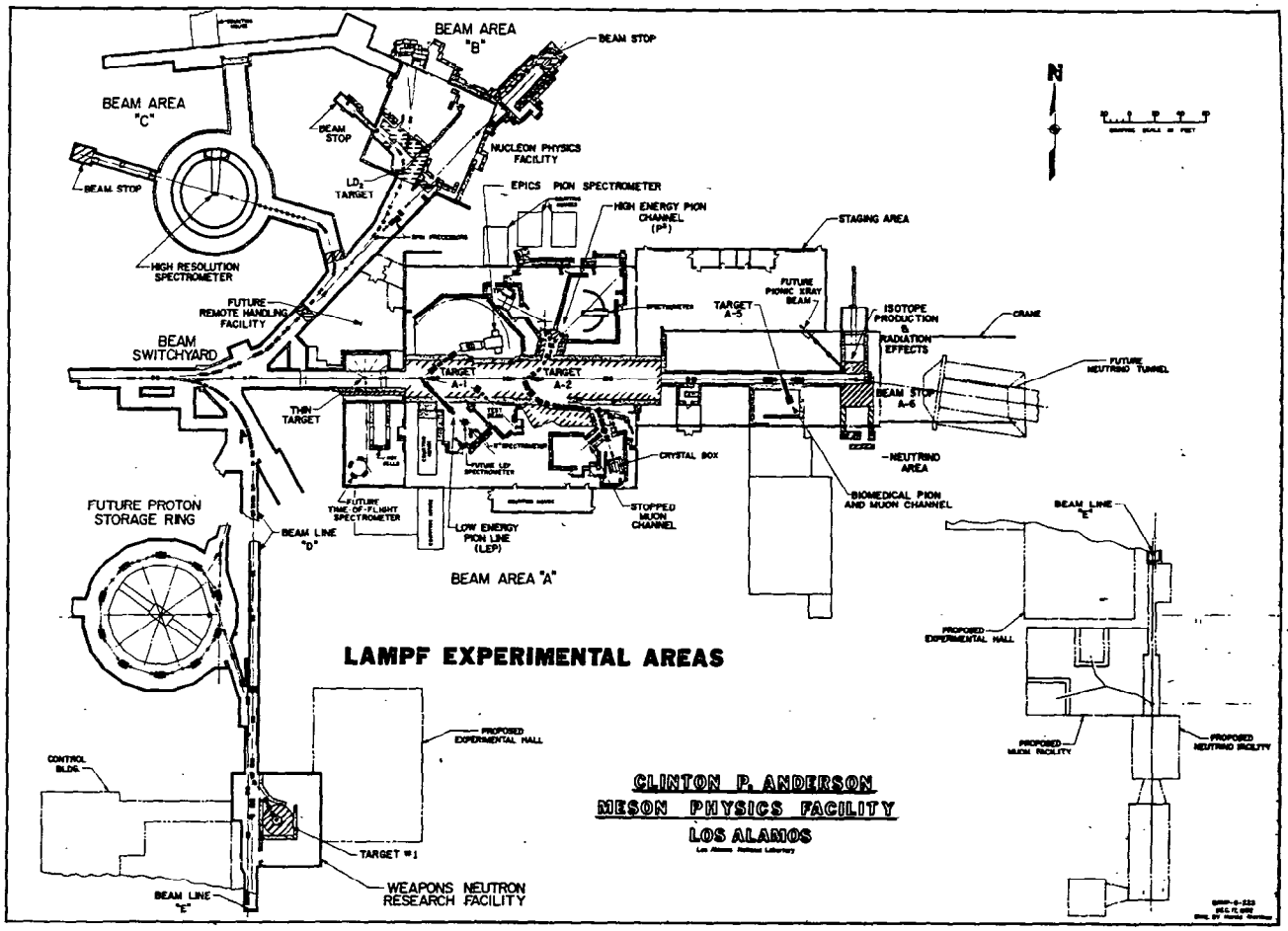

Fig. 1. Area A

*Work supported by the US Department of Energy.

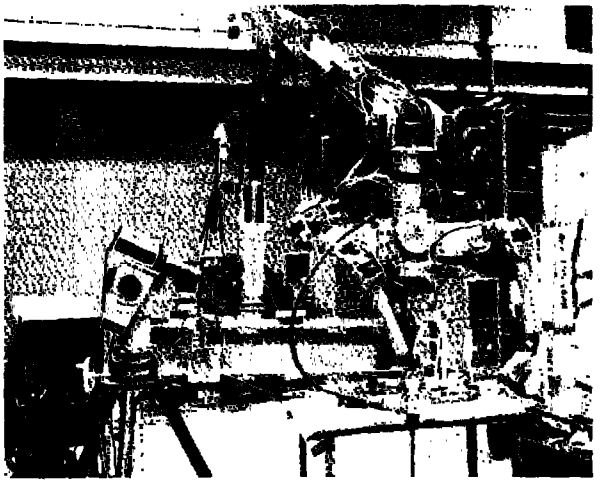

Fig. 2. Monitor Slave Unit

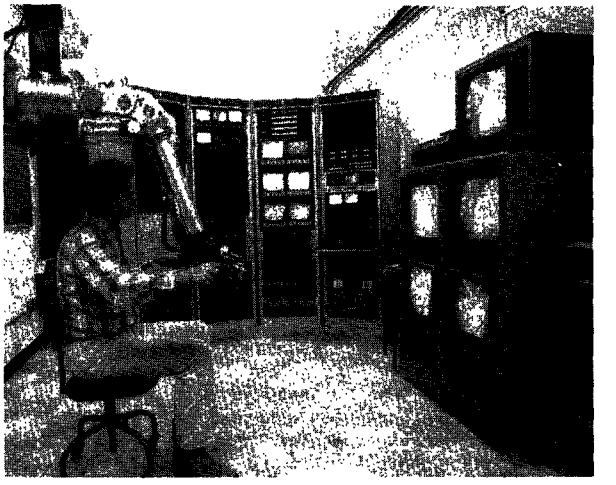

Fig. 3. Monitor Control Room

The Monitor operating crew consists of:

1. The manipulator operator (seated as shown) performs the actual work using master/slave manipulator and various tools as required for the job.

2. The crane operator (not shown) operates remote controls for the hydraulic crane from the console in the right rear, to maintain proper working position for the slave manipulators.

3. The camera operator (not shown) operates the pan, tilt and zoom functions for the television cameras from the center rear console to provide optimum viewing for the manipulator operator. As many as six cameras may be in use at one time.

The prototype Monitor system was first used in 1976 to replace an air cooled beam window in the beam stop area with a newer water cooled version to allow higher beam current. The prototype Monitor used a hydraulic servomanipulator (without force reflection) and an electric manipulator (PAR model 3000.) The operating end of the slave unit is shown in Fig. 4. The master control station consisted of a pair of panel racks and "stick" master located in the experimental hall. This system is shown in Fig. 5.

Since 1976, many ongoing major improvements were made to keep pace with increasing radiation levels and continually increasing complexity of tasks to be performed. The most significant single improvement was the addition of bilateral force reflecting servomanipulators (mfg. to LAMPF specifications by Teleoperator Systems, Inc., Batavia, NY.) Other important improvements were climate controlled trailers for master stations, better control systems, and improved control and viewing console layout.

At the present time, two systems (Monitor I and Monitor II) are fully operational. A third system (Monitor III) is now under construction.

Monitor I and Monitor II were designed to operate primarily within experimental area "A" as they depended upon overhead radio-controlled cranes for mobility and require electrical power from the facility.

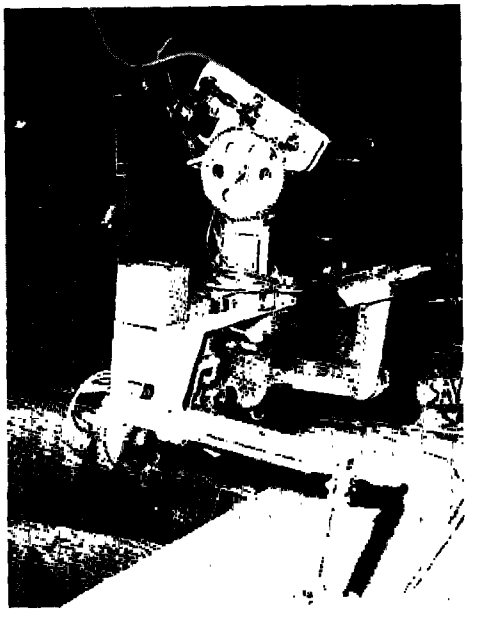

Fig. 4. 1976 Monitor Slave Unit

Fig. 5. 1976 Monitor Controls

Monitor III will be a totally portable system, with its' own power generator, capable of operating at any location accessible by truck.

Monitors I and II have served well in maintaining existing experimental equipment within area "A"; however, Monitor III will be needed to accomplish planned major rebuilding of target cells A1 and A6, particularly from the standpoint of removal and disposal of radioactive structural components. Figure 6 is a sketch of the Monitor III system. In addition to maintenance and construction, Monitor III will be used in transport and disposal of radioactive materials removed from the facility.

Major Accomplishments

Since 1976, the Monitor system has developed and expanded to keep pace with maintenance requirements and improvements to experimental area "A." The original Monitor system was limited to performing relatively simple tasks, while the present systems have evolved to the point where it is possible to remotely perform tasks previously possible only by direct "hands on" methods. Some of the more complex tasks now performed by Monitor or a routine basis include "in place" fabrication of piping systems, soldering, brazing and grinding.

The most significant accomplishment to date for Monitor was the total rebuilding of LAMPF target cell A2. This involved the replacement of the target chamber, upstream collimator, three large magnets, profile monitor, and a myriad of piping and electrical systems. Weights of the components replaced ranged from a few kilograms to 25 metric tons. Since most of the components replaced were newly designed, the existing piping and electrical systems had to be totally replaced to suit the geometry of the new components. The new target chamber had to perfectly match four existing vacuum flanges from the main beam line, two secondary beam lines and target insertion port. This was accomplished by positioning an alignment fixture with adjustable flanges in the target cell and mating the flanges to the existing ports.

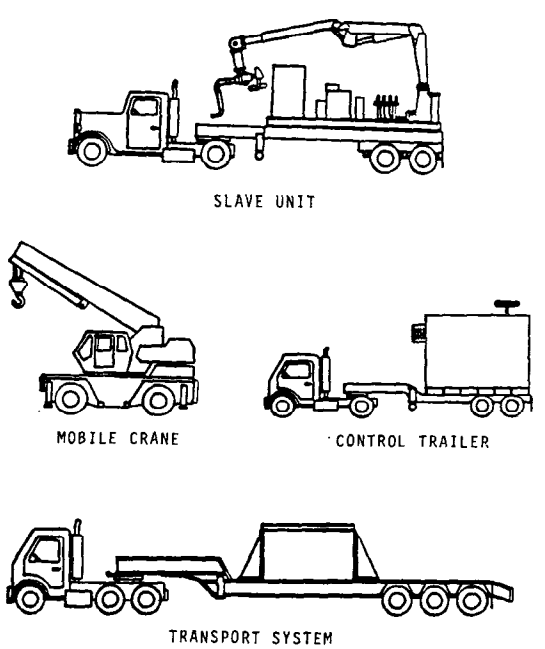

Fig. 6. Monitor III

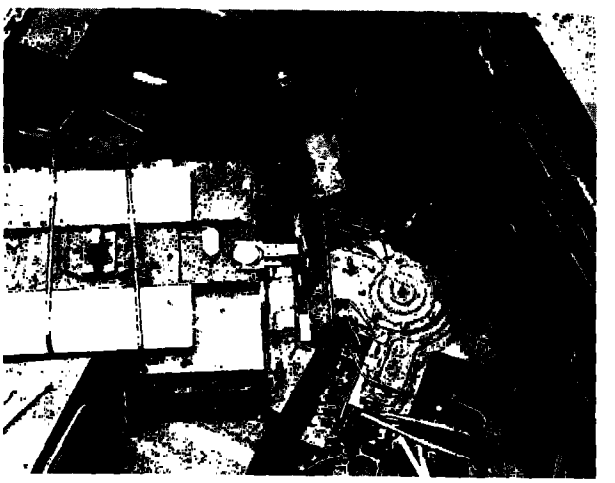

Fig. 7. Target Cell A-2, 1976

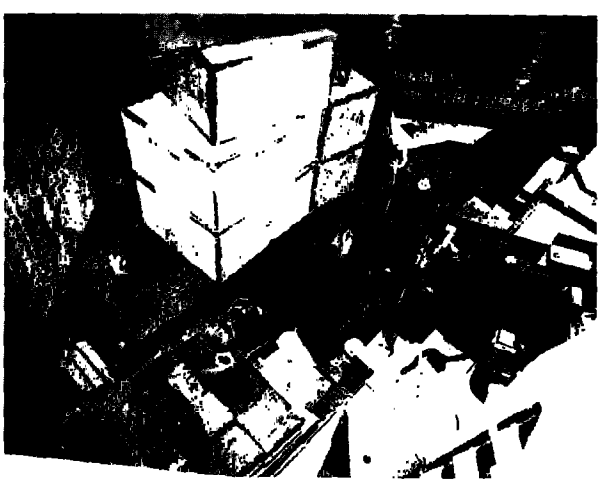

Fig. 8. Target Cell A-2 with all Components Removed

After the adjustable flanges were mated, they were remotely tack welded to preserve alignment during removal from the cell. The fixture was then removed, decontaminated, and placed on a large metal table. An external jig was then adjusted to match the flanges on the alignment fixture, then the jig was used for construction of the new target chamber. Figure 7 is a partial view of target cell A as built in 1976. Figure 8 is a view of the same cell with all the components removed. Figure 9 is the new target chamber just before installation. Figure 10 is a view of the partially reconstructed target cell.

Conclusions

The Monitor system has been totally successful in maintaining LAMPF experimental area "A." In addition to performing planned improvements to the facility during scheduled down times, it has performed emergency repairs with minimal loss of operating time. The useful work output of the Monitor systems has risen by a factor of four since 1976, with a less than 20% increase in operating personnel.

In its present state of development the system is capable of performing any foreseen task; however, in order to satisfactorily meet the future programmatic needs to LAMPF, operating efficiency must continue to improve at the same rate or greater, than experienced between 1976 and 1983.

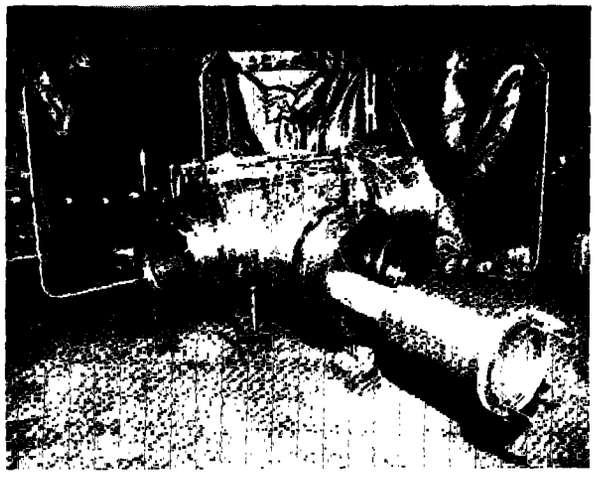

Fig. 9. New A-2 Target Box

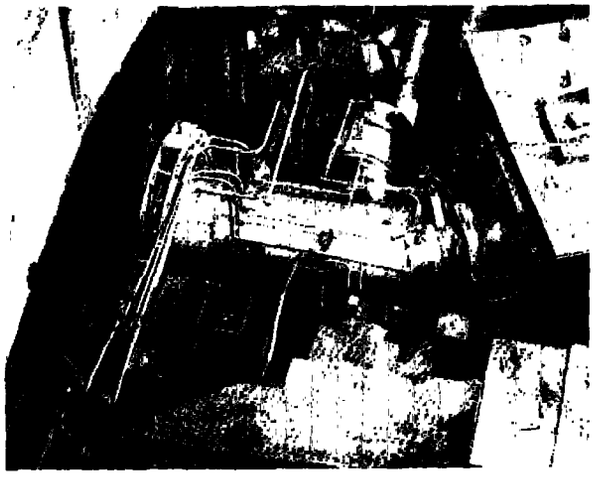

Fig. 10. Target Cell A-2, 90% Complete 1983

References

1. J. E. Lambert and D. L. Grisham, "History of Remote Handling at LAMPF", Proceedings of the 30th Conference on Remote Systems Technology, American Nuclear Society.

2. D. L. Grisham and J. L. Lambert, "Monitor 1983", Proceedings of 1983 Particle Accelerator Conference Volume NS-30, Number 4, p 2267.

Proceedings of International Collaboration on Advanced Neutron Sources (ICANS-VII), 1983 September 13-16
Atomic Energy of Canada Limited, Report AECL-8488

Operational, Handling and Safety Aspects of the SNQ Target Station

H. Buttgereit*, H. Stechemesser**, G. Thamm*, J. Wolters***
* Kernforschungsanlage Jülich, D-5170 Jülich, FRG
* SNQ-Projekt
** KFA-Jülich, Zentralabteilung Allgemeine Technologie
*** KFA-Jülich, Institut für Nukleare Sicherheitsforschung

Summary

Although SNQ accelerator and parts of the target station will be constructed in two stages, the main operation, handling and safety procedures based on the requirements to operate the uranium target in stage II (1100 MeV, 5 mA) should be applied to the target station very similary and nearly uniformly in the two stages. A general view on operation, handling and safety aspects is presented and illustrated by a few selected examples as

- start up and shut down procedures,
- handling of the target wheel in the case of replacement,
- decay heat removal

each under normal and irregular conditions. In the case of failures in the decay heat removal system proof is given for the uranium target of stage II that more than about 7 hours - under pessimistic assumptions - are left to restart the forced cooling, before the cladding (Al) melting temperature is reached. From the more detailed safety analysis currently under investigation it is expected that an emergency cooling system for decay heat removal even in the afore mentioned case is most probably not needed.

1. Introduction

In /1/ it was explained how the target station for the two stages (stage I 350 MeV, stage II 1100 MeV, both 5 mA) will be constructed. It was pointed out, that depending on the tested target materials lead, tungsten and uranium in the first stage the target wheel design can be simplified by omitting tie rods, because of lesser depth of the target material. Additionally for optimum coupling of the lower H_2O-moderator at stage I a somewhat reduced target wheel diameter (a few centimetres) is required. Furthermore a two stage concept for cooling (including shut-down cooling) secures heat removal from the target during operation and shut-down. The cooling system of stage I can also be used for cooling a lead or tungsten target in stage II. Regardless of the mentioned deviations in design the main operation and handling procedures as well as the necessary safety installations for the SNQ target station are uniform during both stages and are designed with respect to the operation of the uranium target of stage II. For the operation of the SNQ-target station with non-uranium targets during stage I significantly lower requirements compared with the final uranium installation are to be expected. Therefore this gives a convenient opportunity to test all installations for operation, handling and safety and to carry out modifications where needed.

2. Operation

2.1 Operation-cycles

The design of the accelerator and target station of SNQ provides for the possibility to run the target station similar to a research reactor. It is anticipated to operate the plant for 9 cycles a year, each of 5 weeks duration. There will be up to 30 days of operation per cycle, with 5 days shut-down time. It is aimed at reaching a

total operation time of 6000 hours per year. Additionally there will be one longer shut-down time of the duration of one operation cycle for maintenance, repair and rearrangement work (on experiments too) but mainly for repetition of plant component testing due to licencing requests, which have to be carried out during plant shut-down and which usually take a longer time for preparation. For these reasons there will be a planned operation schedule for about 350 days each year. The remaining time, if needed, will be used in a rather flexible way for special activities, which will either be carried out when the plant is in operation (perhaps at part-load) or during shut-down.

2.2 Start-up, shut-down and normal operation of the target station

The following essential conditions for operation of the target station - shooting with protons at the target - have to be provided for

1. Target wheel in rotation at nominal speed.
2. Target cooling (nominal flow) in operation.
3. Moderator cooling (H_2O and D_2O) on
4. Shield cooling (target block and trolley) on.
5. Shut down cooling and possibly cavern flooding system prepared for start.

Interlocks prohibit, if one of the conditions is missing, the aiming of the proton beam at the target. For this reason the relevant data of each of the conditions are controlled partially in a multiple way (redundant and diverse). For instance, for the first one (target wheel in rotation) the following data are measured:

- rotation speed by two inductive systems
- pressure and flow in both the drive and bearing circuit with additional control of the pumps power consumption.

The target station is started-up by stepwise starting the KLA-H_2O-moderator system.[1.)] At first the part of the circuit for the axial and radial bearings of the target wheel is started. Only when the nominal values of pressure (60 bars radial, 30 bars axial) and flow (4,5 m³/h) are reached in this circuit, the control of the turbine circuit is unlocked for start-up. This circuit sets the target wheel in motion. The circuit is operated at a pressure of 37 bars and a mass flow of maximum 126 m³/h until close to the nominal rotation speed of the wheel (0,5 rotations per second ± 5%). By automatic control the mass flow in the turbine loop will be controlled for reaching and thereafter keeping constant nominal rotation speed. Only then the target cooling loop will be switched on and the cooling flow through the target will be set at 250 m³/h during stage I respectively at 500 m³/h during stage II including the part mass flow of the turbine and bearing circuits. After the start-up of the circuits for the H_2O-and D_2O-moderator as well as for the shielding the central interlock will be unlocked when reaching nominal mass flow in these circuits, so that the proton beam can then be aimed at the target.

During operation all relevant data of the cooling and supply circuits as well as target rotation are automatically monitored. If the speed of the target wheel or mass flow of the target cooling decreases below the fixed limits (about -20%), the proton beam will be stopped by automatic control within a second. In this case injection and high frequency of the accelerator are switched off. Accordingly, a decrease of the values in the moderator circuits (about -30%) sets off automatic warning in the control room, where switch-off of the proton beam can be carried out manually.

Additionally the SNQ-plant is equipped with a fast shut-down system, that automatically switches off the proton beam in less than 10 ms taking into account the total

1.) KLA: Kühlung-cooling, Lagerung-bearing Antrieb-drive (table 5 /1/)

response time. For the target station only the condition "unpermissible high beam losses of the bending magnet" triggers the fast switch. (see Fig. 2 /1/)
As an example in chapter 4 for the cases
- loss of target cooling and
- decrease of target speed
proof is given, that a switch-off of the proton beam in the order of a second is sufficient to limit temperature increases in the materials (target pin) and other structural materials of the wheel to a level, that destruction (melting) can be excluded. If automatic switch-off occurs due to a decrease of the speed of the wheel, the main pumps of the target cooling circuit remain in operation for about 15 minutes before the shut-down pump takes over the water circulation for decay heat removal. However, if loss of target cooling has caused the switch-off, then automatically the shut-down circuit takes over the after-heat removal at once.

3. Handling Concept of SNQ Target Station

3.1 Remotely handled Components

The material tests at present in progress already indicate, that for the components under the highest load in the radiation field of the target station (for instance, beam hole windows, D_2O Moderator tank bottom...) rather long life times (several years) are permissable /2/. This will in future be confirmed in part through extensive irradiation tests in high-capacity accellerators. The design basis at present still is exchangeability of important components - listed up below - of the target station. Additionally the stepwise realisation of the SNQ requires the use of different target wheels (at least lead and/or tungsten and uranium in the first and second stage). For this in the conceptual design exchangeability has to be considered in any case.
The components to be exchanged and therefore remotely to be handled can be classified into three categories:

1. target wheel
   KLA-unit
   H_2O-moderator
   cooled shielding (removable)
2. bending magnet
   neutron beam stop
   connections of the target trolley
   end plate
   pipes/valves of proton beam line
3. D_2O-moderator
   cold source
   beam hole rotating shutter (or parts of it)
   beam hole windows
   (For position and size of these components see fig. 1 and 2 /1/)

The components of categorie 1, especially the target wheel, are of greatest importance for the design of the handling concept of the target station. Therefore, as described in /1/ and the following chapter, they are placed on the target trolley, which can be moved into the operating position in a cavern in the centre of the shielding block of the target station. The IWR[1.)] service cell, immediately connected to the target block therefore serves the purpose of remote handling of the target trolley with the components positioned on it.

The components of categorie 2, aside from faults of their own, only have to be handled, if the target trolley is to be brought into the IWR cell. That means, that the frequency of handling those components is not determined from their design but from the components of the target trolley.

For the components of category 3 like for parts of modern high-flux reactors exchangeability must be provided for in the design. These components are either disassembled or complete size to be replacable by means of shielding containers. If such replacement is necessary, it is advan-

[1)] IWR (Inspektion-inspection, Wartung-maintenance, Reparatur-repair)

tageous, that the components can be transported into the IWR-cell in a short distance and be inspected, overhauled and even to a certain extent be repaired. In this case the for other reasons necessary IWR cell is rather usefull. However, in principle transportation of these components in the above mentioned shielding containers to other Hot Laboratories outside SNQ is conceivable. The design of the IWR-cell takes into consideration size and weight of all components to be handled in it. From the level of radioactivity and surface doserate the uranium target wheel of stage II is the deciding component.
It is antipated to handle the uranium target wheel of stage II first 5 days after shut-down of the SNQ-target station. At this time the decay heat is about 18 KW, the activity about 3 M curies.
Activity inventory and after heat of the other materials (lead/tungsten) are significantly lower, so that handling can already be started one day after shut-down of the target station. The uranium target of stage I can also be handled at this earlier date. In this case the expected activity inventory is lesser than 3 M curies and after-heat below 7 kW. The afore mentioned waiting times will be maintained under all circumstances during the later operation of the SNQ plant. From this follows, that only the targets of stage I and the non-uranium targets of stage II can be handled within the normal shut-down period of each cycle. For the exchange of a uranium target stage II including the waiting time (5 days) a minimum of 7 to 8 days will be needed, a lenght of time that requires special planning (depending on requirements) respectively will have to be planned within the annual long-term plant shut-down.

3.2 IWR Cave Line

Formerly the Hot Cells necessary for remote handling of target block components were referred to as IWR cell (see /1/ and 3.1). However, because of its actual design as a subdivided line of caves it is now called IWR-cave line.
For the purpose of handling the above mentioned highly activated components the IWR-cave line connected to the target block by the cavern ante-room was designed. (see Fig. 2 /1/). In this cave line all necessary handling can be carried out with the appropriate equipment installed in there. Because of handling reasons and operation sequences the design is a rather narrow cave line of 5 m width with a total lenght of 30 m excluding the ante-room. It is subdivided by shielding doors into three caves

- assembling/disassembling cave adjacent to the cavern ante-room
- workshop cave
- entrance cave

The cave line is separated from the ante-room by another shielding door and from the hall in which it is located by an airtight shielding door. The cave line over its total lenght has shielding windows and extended reach masterslave manipulators on either side. Inside a power manipulator and crane are moved on rails with the crane moving in the higher position close to the cave ceiling. (see Fig. 1) Alternatively the working arm of the power manipulator can be replaced by a telemanipulator.
In order to be able to move the afore mentioned (3.1) components about into the wanted positions a railtrack is installed over the total lenght of the cave line floor and extended through the cavern ante-room to the entrance of the cavern in the target block. Shielding gate locks and shielding plugs on the cave line roof provide for travel of radioactive or heavy components into and out of the cave line. Additionally the entrance cave can be used for the same purpose - especially for new components or materials and waste removal in shielded containers.
For shipment of small-size tools or spares in and out of the caves glove boxes with shielding gates or one-way sluices are provided for. Under floor, with entrance from the workshop cave, a dry storage

bunker for active materials and components and a wet storage bunker for a uranium target are availlable.

FIG. 1: EQUIPMENT FOR HANDLING IN IWR-CAVE-LINE (VERTICAL VIEW)

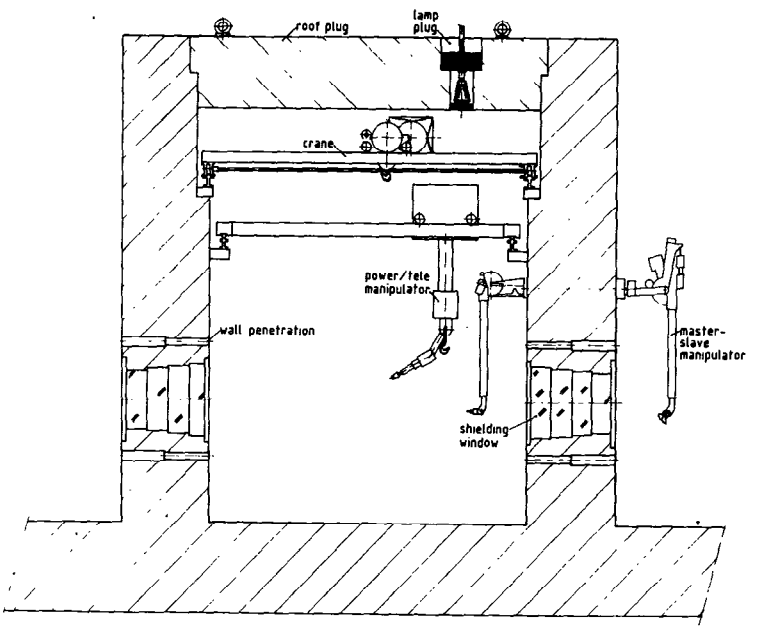

Several wall penetrations in various positions around the shielding windows supply electricity, gases, water and air to the caves or can be equipped with viewing devices.

Special handling equipment is only transported into the caves when needed.

All walls of the caves have a painted stainless steel liner in order to facilitate decontamination of the caves.

In the cave floor drains are placed.

3.3 Handling of the Target Wheel

The target wheel with its drive is fixed on a trolley. When inspection, repair or exchange is required or necessary the trolley will be moved into the assembly cave where the actual handling takes place. Before it is possible to actually remove the target wheel with the trolley from its working position in the target block cavern it is necessary to carry out a number of operations prior to this in the following sequence:

Handling under normal conditions

Special equipment for remote handling in the cavern ante-room comprising crane, telemanipulator, robot plus auxilliary tools, (Fig. 2) viewing equipment and trolley drive are inserted into the IWR caves and moved into their working positions in the ante-room. In combined or successive operations of the handling equipment in a suitable order of steps all connections and fixings are removed and beam stop, bending magnet as well as all other, disassembled parts are brought to a parking position in the front end (workshop

FIG. 2: VERTICAL VIEW OF CAVERN ANTE ROOM

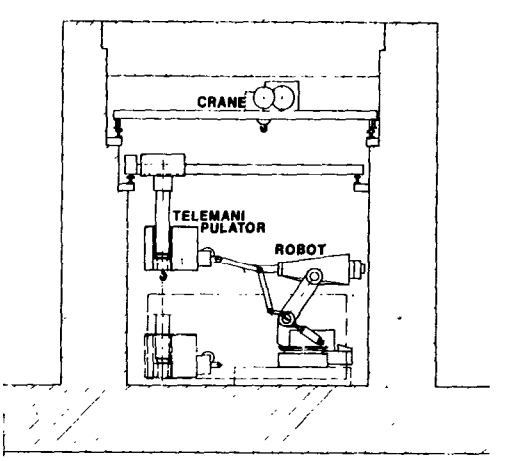

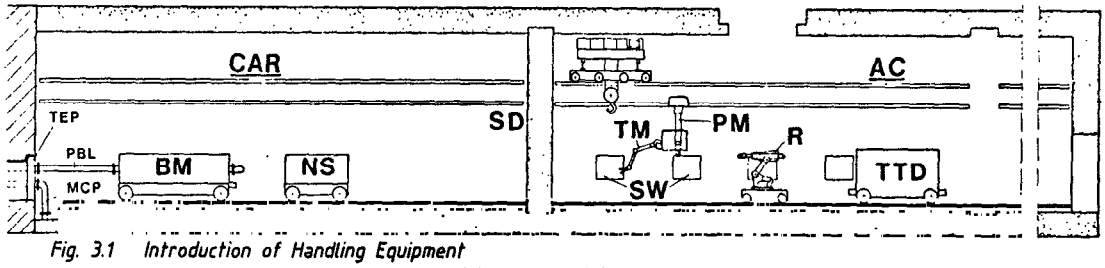

Fig. 3.1 Introduction of Handling Equipment

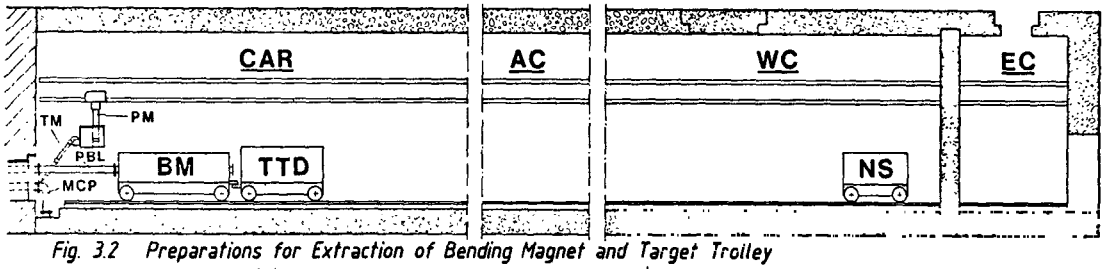

Fig. 3.2 Preparations for Extraction of Bending Magnet and Target Trolley

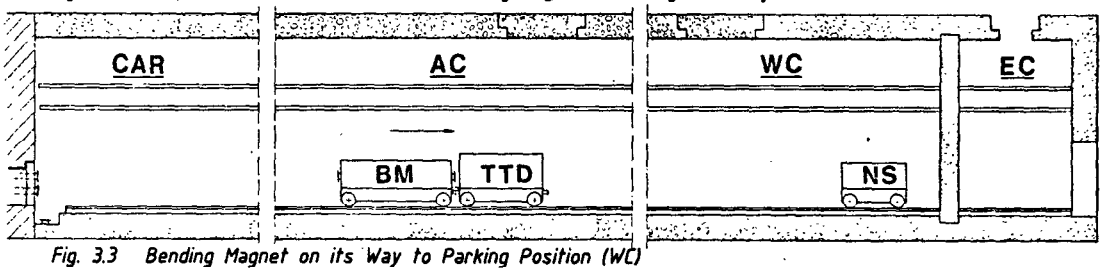

Fig. 3.3 Bending Magnet on its Way to Parking Position (WC)

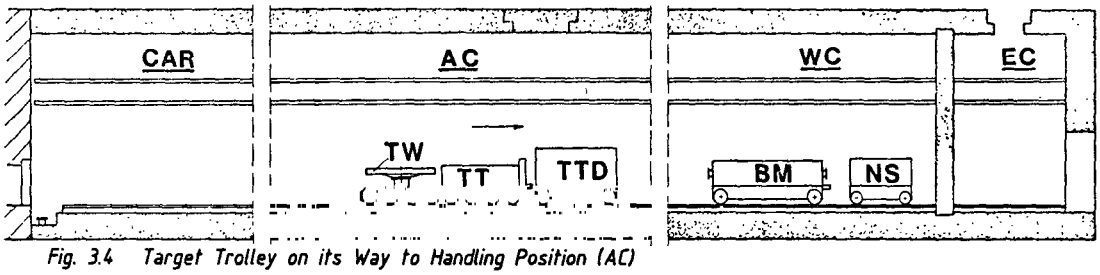

Fig. 3.4 Target Trolley on its Way to Handling Position (AC)

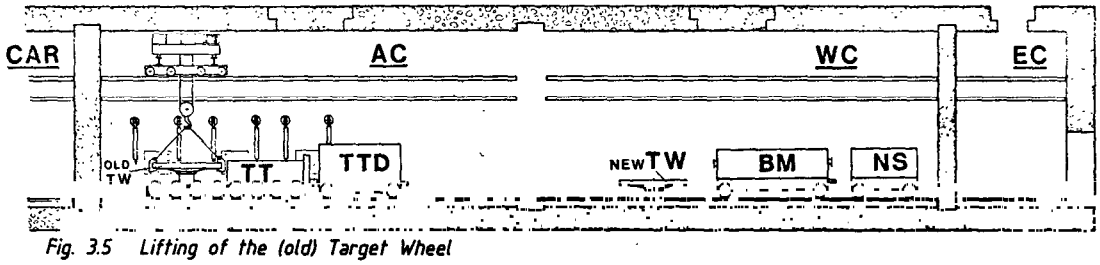

Fig. 3.5 Lifting of the (old) Target Wheel

AC	ASSEMBLING CAVE	SD	SHIELDING DOOR
BM	BENDING MAGNET	SW	SHIELDING WINDOW
CAR	CAVERN ANTE ROOM	TEP	TROLLEY END PLATE
EC	ENTRANCE CAVE	TM	TELEMANIPULATOR
MCP	MAIN COOLING PIPE	TT	TARGET TROLLEY
NS	NEUTRON STOP	TTD	TARGET TROLLEY DRIVE
PBL	PROTON BEAM LINE	TW	TARGET WHEEL
PM	POWER MANIPULATOR	WC	WORKSHOP CAVE
R	ROBOT		

or entrance cave) of the cave line. Finally, again using the above handling equipment, the vacuum seal between trolley end-plate and cavern is removed and removable pieces of the rail track are fixed to brigde the gap between rail track and cavern. Having taken the trolley by means of the drive connected to it into the

handling position in the assembly cave the remote handling operations are then carried out in the usual well known ways. If work on the target wheel is finished, all operations for relocation of the target wheel into its working position follow the same pattern of steps in reverse order. A spent target wheel will be disconnected and removed from its drive, fixed into a rack in upright position and stowed away into the wet storage bunker for later examination and/or disposal. Fig. 3 shows the above mentioned handling sequences.

Handling under faulted conditions

The afore handling procedures describe handling under normal conditions. However, if faulted conditions occur, provisions have been made in the following manner. The worst of thinkable faulted conditions is, if, after having disconnected the cooling water pipes from the trolley end plate, the trolley for whatever reason cannot be pulled out of the cavern. In this case a small size flexible water pipe will be connected to the flange of the target cooling pipe providing for the removal of the target after-heat (see also 4.3) and then one can start other appropriate actions, for instance in the case of drive failure the introduction of a 50 ton-winch and drawing trolley and drive by force into the IWR-cave line and only then doing whatever repair is needed by means of the equipment available in the cave-line. A less grave case is, that the trolley is stopped before reaching the handling position in the assembly cave. In this case some cooling is available already from the normal cave ventilation (a total amount of air flow of about 40.000 m^3/h). By means of a movable fan a significant portion of this air flow can be directed onto the target surface.

Thus having secured cooling for the target wheel the following procedures are carried out as explained before.

4. Safety aspects of the SNQ Target station

In stage II of SNQ the uranium target reaches a radioactivity level of 3.10^7Ci, mainly fission products from high energy and fast fission of uranium /3/. The radioactivity generates a decay-heat of half the magnitude of a fission reactor with the same time dependency. Save enclosure is provided for by several barriers in sequence and a reliable after-heat removal like in nuclear reactors. As a longer interruption of target wheel cooling is tolerable from the safety point of view, after heat removal is easier compared with research reactors.

4.1 Multiple enclosure of radiactivity

The arrangement of the activity barriers is shown in principle in fig. 4. The barriers are

- the metallic cladding of the target pins
- the primary circuit and
- the target wheel cavern, the IWR-cave line, the proton beam line and the room for auxilliary plant installations.

During normal operation the cavern is under vacuum maintained by a vacuum system. The vacuum system is equipped with retention units like condenser, filters for air-borne particles and silicagel dryers in order to retain over 99 % of aerosols and water, stemming from leakages of the sliding seal of the target wheel. If necessary, the vacuum system can be shut-off and closed. The cavern is connected to the accelerator by the proton beam line. If the vacuum in the cavern breaks down, this connection is closed by valves.

The IWR-cave line and the room for auxilliary systems, in which the primary loop is housed, are kept under underpressure by ventilation systems during normal operation. If needed, the exchaust channels can be closed. In addition, target block and IWR-cave line are situated in a hall, which is ventilated by a ventilation system too, and is also kept under a little underpressure compared with the atmospheric pressure out-

side. Thus it has been secured, that no radioactivity is uncontrolled released into the environment.

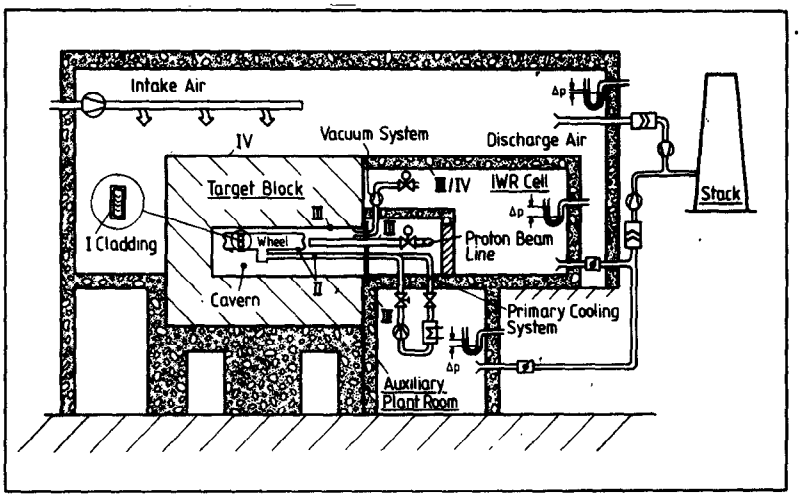

FIG. 4: ARRANGEMENT OF THE ACTIVITY BARRIERS OF SNQ TARGET STATION (SCHEMATIC)

4.2 Decay-heat removal

Generally, decay-heat is removed by the primary and secondary circuits (fig. 5) The turbine loop is not needed for this purpose, and is therefore switched off. After shut-down one of the two shut-down pumps fed by emergency diesels in the case of power failure takes over the circulation of cooling water in the primary loop. The decay-heat is transmitted into the environment by the secondary circuit. The cooling tower ventilators are not needed for this and are therefore switched off. The secondary cooling water is circulated by one of the main pumps. Mostlikely no emergency power supply is required for the secondary pumps, as an interruption of cooling of the secondary loop is tolerable for more than one day. (see fig. 6)

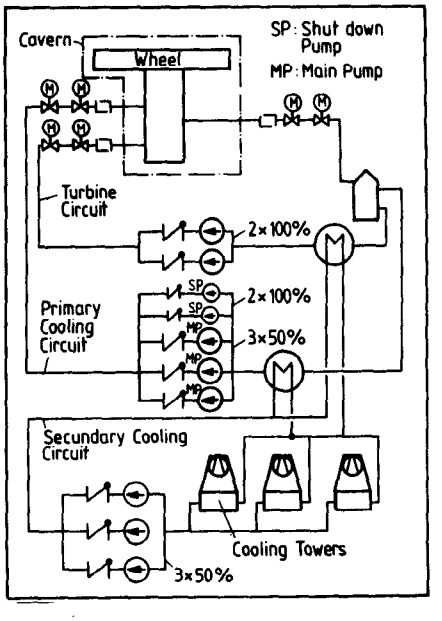

FIG. 5: PRIMARY AND SECONDARY COOLING SYSTEMS OF SNQ TARGET STATION (SCHEMATIC)

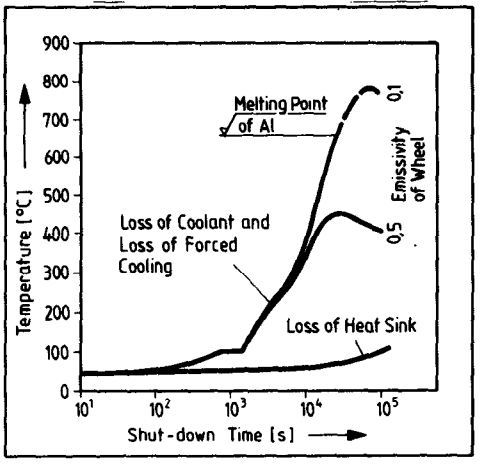

FIG. 6: TIME DEPENDENT MEAN TEMPERATURE OF THE URANIUM TARGET PINS FOR VARIOUS ACCIDENTS

4.3 Decay-heat removal failures

The loss of heat sink in continued operation of primary circulation only leads to a very slow temperature increase in the primary circuit as the lower curve of fig. 6. shows.

For an assumed volume of 20 m³ of the primary circuit it takes more than one day to heat the water up to the saturation temperature. This time should be sufficient to put secondary circuit back into operation after failure.

In the case of loss of forced cooling the decay-heat is stored in the target wheel and transfered via wheel surface to the cavern and its structure. The expected temperature increase is shown by the upper curve of fig. 6. At first the temperatures raise monotonously up to the saturation temperature. The stagnation of the temperature curve is due to the evaporation of the cooling water trapped between the target pins. The steam is forced into the cooling circuit. After complete evaporation the target pins and the wheel continue to heat up, until the generated heat is transfered from its surface into the cavern and its structures by radiation. With unprepared surfaces of the chosen materials

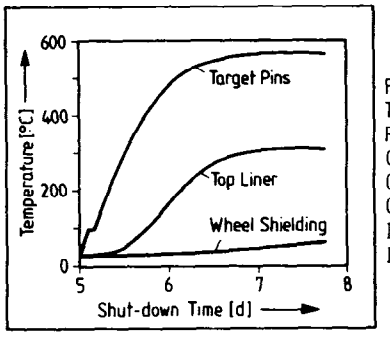

FIG. 7: TIME DEPENDENT TEMPERATURE OF VARIOUS COMPONENTS IN THE CAVERN IN THE CASE OF LOSS OF COOLING DURING HANDLING 5 DAYS AFTER SHUT-DOWN

the temperature maximum exceeds the melting temperature of aluminium, which is the chosen material for the wheel and for the canning of the pins. The melting temperature would be reached after about 7 hours at the earliest leaving plenty of time for restarting the forced cooling. Reaching the melting temperature can be excluded, if the emissivity of the heat exchanging surfaces can be improved to 0,5 respectively 0,6. This can be achieved for the target wheel by anodizing the surface.

Loss of coolant accidents are to be separated into two categories, whether a rupture of the primary circuit occurs inside or outside of the cavern. In the first case the cavern will be flooded, the cooling circuit however is not interrupted by this, so that decay-heat removal is still secured. In the second case a temperature increase occurs similar to the loss of forced cooling as the target wheel remains filled with water too. Whether in this case emergency cooling must be provided for lastly depends upon whether or not the temperature maximum remains below the melting temperature without emergency cooling. One of the suitable measures for emergency cooling would be flooding of the cavern and heat transfer via the cavern liner to the target block. The loss of cooling during handling of the target wheel does not present a problem as 5 days after shut-down handling will be started at the earliest and then a temperature of 600° C cannot be exeeded. (fig.7).

4.4 Decrease of target wheel speed.

If the target wheel speed decreases below the fixed limit (0,5 s^{-1} - 20 %) the proton beam will be stopped automatically by the normal shut down system within a second. Since even in the case of a pressure loss in the turbine and bearing circuit several seconds are needed for slowing down the wheel the shut down time of about one second is sufficient to prevent temperature rises in the target pins which might lead to destruction by melting of the (Al) cladding material. At a speed of 0,4 s^{-1} only a small part of the area (4 cm Ø see /1/) at the wheel circumference will be hit by two proton pulses and heated up to about 280°C.

References:

/1/ H. Stechemesser et al (1983)
"Target Designs for Stepwise Development of SNQ",
Proc. ICANS-VII, this volume

/2/ Lohmann, W. and Krautwasser, P. (1983)
"Progress in Materials Investigation for the SNQ-Target"
Proc. ICANS-VII, this volume

/3/ T.W. Armstrong et al
"Theoretical Target Physics Studies for the SNQ Spallation Neutron Source"
Jül-Spez-120, July 1981.

Session I

Concepts, Materials and Performance

Chairman - G. Bauer

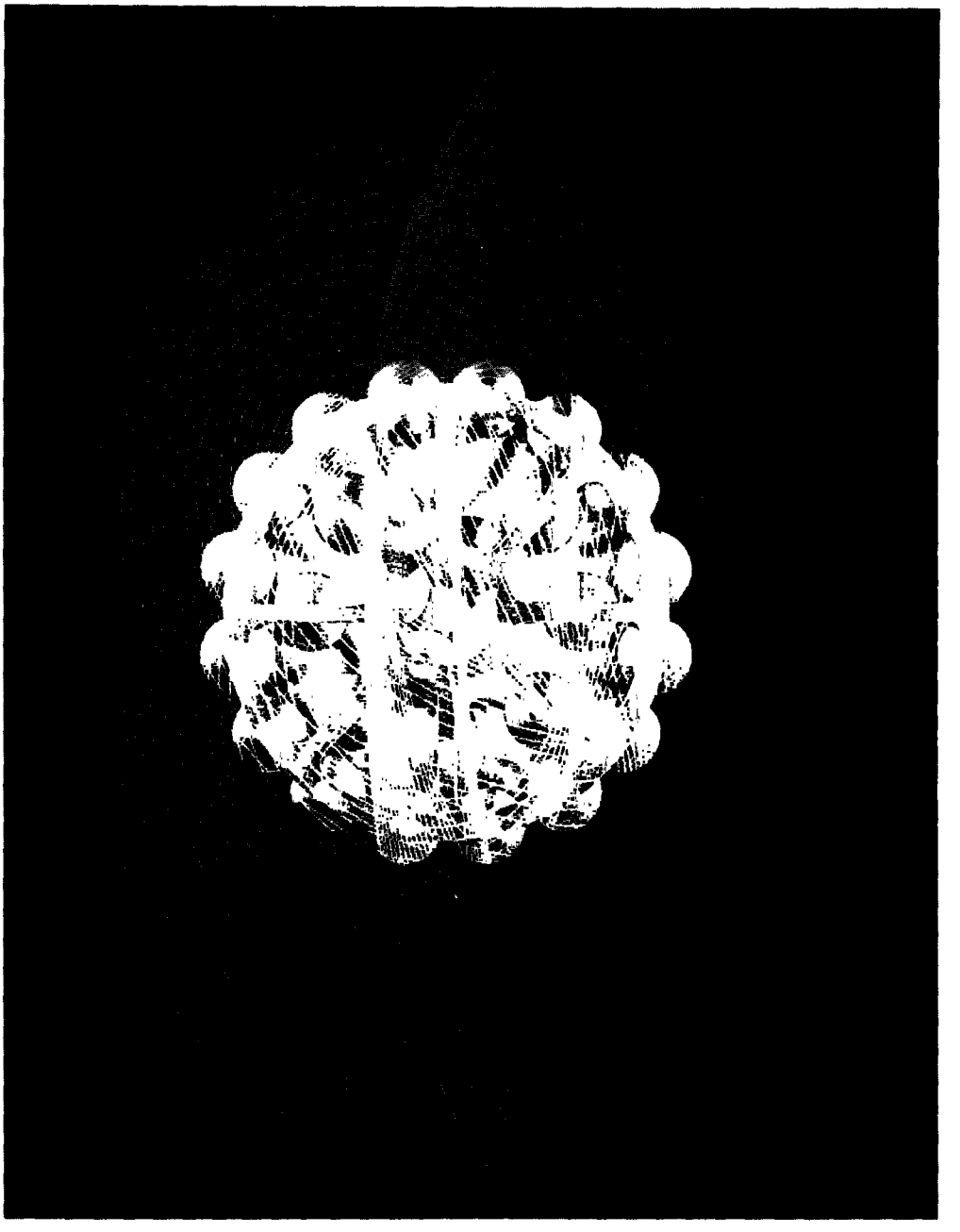

Proceedings of International Collaboration on Advanced Neutron Sources (ICANS-VII), 1983 September 13-16
Atomic Energy of Canada Limited, Report AECL-8488

BEAM TUBE CONCEPT FOR SINQ

F. Atchison
Swiss Institute for Nuclear Research
CH-5234 Villigen, Switzerland

1. INTRODUCTION

One of the design goals for SINQ is to achieve working conditions in the neutron experimental hall comparable with those found at reactors. Implicit in this aim is the requirement to have a very low fast and high-energy neutron flux at the sample, both from the point of view of radiological protection and experiment backgrounds.

Diagrams of proposed layouts for SINQ may be seen in Figs. 11 and 12 of ref. 1. Both beam-tubes and guides are included. Currently there is discussion within the project group, of the wavelength range which might be better (or as well) handled with guides and examination of the possibility of using them to replace some beam-tubes. In principle guides will not be subject to the background problems of beam-tubes.

The 'thermal' flux at the sample will be determined finally by the losses from meeting background conditions. The performance of the beam-tubes will depend on careful design. This work will mainly be carried out by the monochromator designers, with the 'neutron calculators' supplying necessary information on fluxes and attempting to calculate backgrounds; these calculations are difficult.

In view of these difficulties, as much freedom as possible has to be given to the designer: By decoupling the beam-tubes from the target station infrastructure: By avoiding having them on a critical path in the design and/or construction programme: By allowing sufficient flexibility that modifications may be carried out as operational experience is gained.

The above paragraphs present a 'mechanical' concept. The aim of the rest of this paper is to try and set out the problems from the high-energy neutrons and examine what needs to be calculated. That is, to consider the important question of a concept for the calculations. Because of its obvious advantages, some work has been done on trying to speed up the high-energy Monte-Carlo neutronics calculations; this work is incomplete, but presented in the hope it might provide useful ideas for other groups.

2. BEAM TUBES

2.1 General

The beam-tube is taken to include the whole region between the beam-tube tip in the moderator tank and the neutron port at the sample. It therefore includes collimators, tube liners, filters and monochromators. This is shown schematically in Fig. 1.

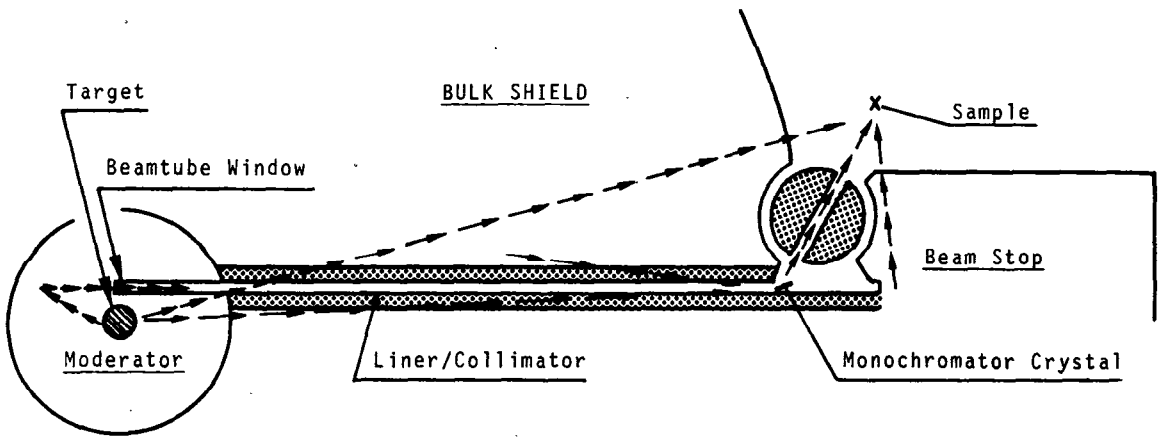

Fig. 1 Schematic layout for a beam-tube system. The arrowed lines →→→→ illustrate the principal sources of background caused by high energy neutrons.

The problem is to reduce the flux of unwanted neutrons to acceptable levels whilst also minimising the loss of wanted neutrons. At present it is not known what an 'acceptable level for background' means, but it is hoped to obtain some quantification by experiment at the "NE 1"neutron beam here at SIN.

The principle cause of neutron flux loss will be distance but other contributions might come from having to use beam-tip radii away from the thermal flux maximum in the moderator, double-monochromators and filters.

2.2 Backgrounds

Monochromator and instrument designers have come to terms with the fast neutrons present in reactors. SINQ will have these also, but the principle new problems stem from neutrons above 2 MeV and extending close to that of the primary proton energy (590 MeV).

The background at the sample from this 'new' problem area will mainly arise from:

1. The scattering of high-energy neutrons by the monochromator crystal.
2. Direct background through the shield and from the beam-stop.

The neutrons causing these may be considered to come from four sources:

(i) High-energy neutrons scattered by the D_2O into the beam-tube.

(ii) Secondaries from interactions in the beam-tube window.

(iii) Direct transmission through the shield and including reduced shield efficiency from voids created by the beam-tube and other equipment.

(iv) Leakage from the shield.

A schematic illustration of these background sources is included in Fig. 1.

2.3 High energy neutron scattering by a monochromator crystal

As the scattering of high-energy particles by the monochromator is probably going to be the main cause of background, a first estimate of the extent of the problem has been made using the deliberately pessimistic case of a 1 cm thick copper crystal.

Cierjacks et al.[2] have measured the high-energy neutron spectrum from a beam tube in a H_2O moderator. This measurement should include contributions from all four sources mentioned in subsection 2.2. In absolute flux terms, it is believed these results are pessimistic compared to the situation we will have in SINQ[3].

The calculation has used MECC (see section 3.2) to estimate inclusive differential cross-sections averaged over the measured spectrum and includes the effective thickness change as the crystal is tuned. The results are shown in Fig. 2.

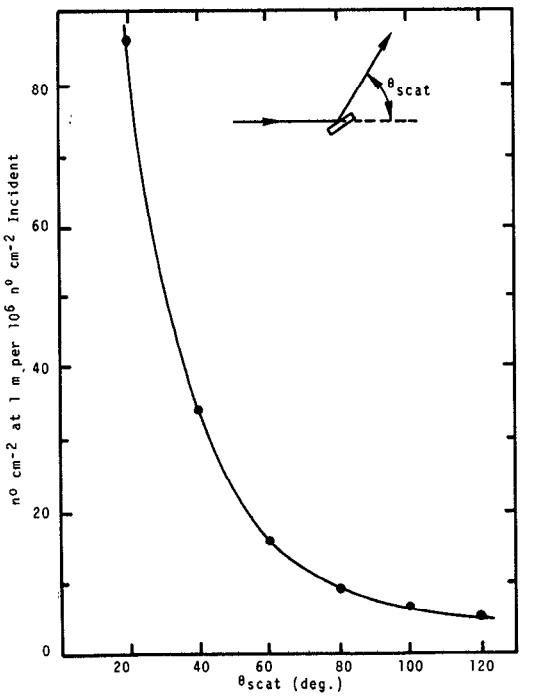

Fig. 2 Scattering by copper averaged over the HE neutron spectrum measured by Cierjacks et al.[2].

3. BEAM TUBE CALCULATIONS

3.1 General

The type of system to be calculated has been shown in Fig. 1 and the sources of background in section 2.2.

For radiation protection purposes there needs to be about 4 m of iron and 1 m of concrete between the moderator tank outer wall and the neutron hall. The calculations will need to quantify the spectra deep inside this shield, including asymmetries and inhomogeneities. The major problem in carrying out calculations is choice of method. No single method seems, at present, capable of doing this job.

The HETC package[4] is the major tool for detailed high-energy transport studies. It suffers from the major drawback of slow calculation speed, but can tackle the anisotropy and inhomogeneity of the problem; that is we can set the problem up but probably do not have enough time to actually complete the calculation. Similar remarks apply to Monte-Carlo neutronics codes, e.g. Morse[5], O5R[6] etc.

Deterministic methods are well developed for 2-D calculations and are being used for the SINQ bulk shield calculations[7]. Their use for beam-tube problems was reviewed by Armstrong et al.[8] at ICANS-VI. Extensions to 3-D are available, Takeuchi[9], and a test case based on the Cierjacks measurement (see section 2.3) is being sent to Dr. K. Takeuchi for comments and (hopefully) calculation.

Examination is being made of ways to speed up Monte-Carlo for the high-energy neutrons to enable some first estimates for their effect to be obtained. In the next few sub-sections these will be described and some results presented.

3.2 HET

The principle component of HET is a subroutine version of the Medium Energy Cascade code of Bertini[10]. This uses Monte-Carlo to compute the interaction of medium-energy particles with nuclei. In HET it operates at two levels; to calculate the interaction cross-section from the 'geometric' cross-section; to sample an outcome of an interaction. The Bertini code has been isolated from HET to allow direct calculation of interaction cross-sections. This will be referred to as MECC.

There is an 'outer loop' Monte-Carlo to follow the propagation of the particle cascade through the material which also takes account of other relevant physical processes. The remainder of HET contains geometry, bookkeeping and (user written) source description routines.

The 'slowness' of HET comes from the need to calculate each interaction.

3.3 Acceleration of the calculation

Calculations for beam-tubes will be made mainly to obtain particle fluxes. These depend on the geometry of the cascades, source particle distribution and calculated system. The geometry of the cascade only depends on the type and energy of the initiating particle and the material through which it is propagated.

A major increase of speed is obtained if calculations makes more use of the information in the cascades. This is most easily demonstrated with an example.

3.4 Calculation of a large iron sphere

The problem is to calculate the dose due to escape particles from various radii iron spheres with a 300 to 400 MeV neutron source at the middle. A full description of the calculation may be found in reference 11.

Escape particles are the result of the truncation of an infinite region particle cascade by the size of the system. The cascades will be initiated by the primary particles at various depths in the shield with the usual exponential probability.

HET was used to generate a set of 2000 infinite-extent-medium cascades. These were then subjected to a straightforward geometric transform to bring their starting point (the first interaction) to various depths in the shield (i.e. first collision biasing) and then analysed to enable the escapes (cascade track segments which cross the outer boundary) to be picked out. The total escapes are calculated by summation of the appropriately weighted contributions of all bias shells, but using the same set of cascades.

The calculation was made for radii up to 5 m. A plot of the calculated dose from escapes as a function of sphere radius is shown in Fig. 3 and the escape-neutron spectra for various thicknesses in Fig. 4.

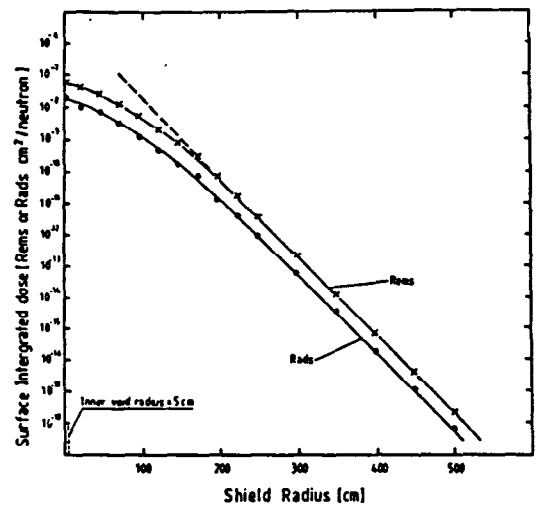

Fig. 3 Calculated surface integrated dose and dose-equivalent for various radii iron shields and source neutrons of energy 300 to 400 MeV.

In effect, the method makes the assumption that the 2000 cascades give a proper description of all that are possible. Further cases, for different neutron energies and also with concrete have been calculated. The shielding effect as represented by the large depth 'absorption' length were in reasonable agreement with typical values used in 'hand estimation' of shields.

3.5 Extension to beam-tube fluxes

The method of section 3.4 is at present limited to single media, mainly because no satisfactory storage system has yet been devised by us for the extra cascades for more than one medium.

A straightforward extension has been made to include the effect of voids. This is simply a matter of extending the length of cascade segments which cross a void. At present this has only been used for a test calculation of the effect of voids on surface escapes. It

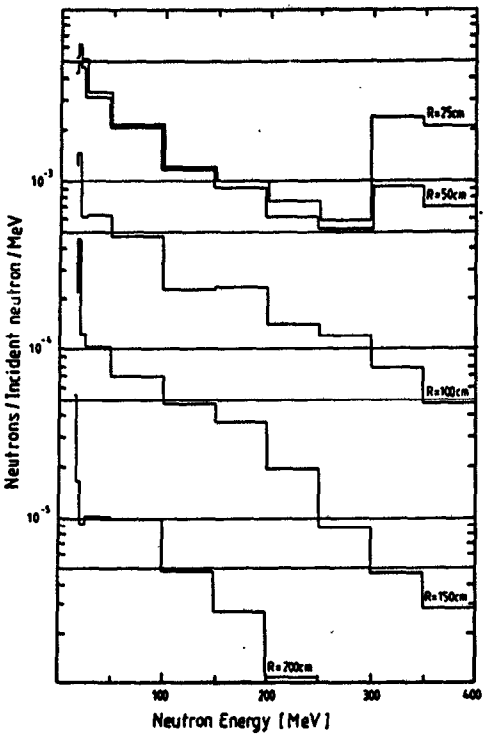

Fig. 4 Escape-neutron spectra for shields of thickness from 25 to 200 cm.

can also be used to allow estimates of the HE contribution from shield leakage into the beam-tube, but not in a straightforward manner for seeing the effect of different liner materials.

No suitable results are available for presentation.

3.6 High energy scattering by D_2O

The methods used for the bulk shield estimate in section 3.4 have been taken a stage further to estimate the HE neutron flux scattered by the D_2O into the beam-tube (see Fig. 1).

The distribution (in position, angle and energy) of HE particle escapes from the target can be calculated directly with HET. The probability of scattering into the beam tube should be rather small. For design purposes a survey of how this component varies with beam tube tip radius is required.

The set of sample cascades (in D_2O this time) contains full information about the geometry of the cascade. A cascade segment can be used to compute the geometric transform which puts it along a beam-tube (a 2-D representation of this is shown in Fig. 5). The transform is then applied to the whole cascade, and if the transformed cascade-initiating particle's trajectory intersects the target at a point where it could have been produced (correct production angle and energy), the cascade then represents a contributing event.

As we 'know' the D_2O interaction cross-section (from the MECC code - modified to treat D collisions), both the initiating trajectory and the track-segment entering the beam-tube can be extended (or contracted) with a probability correction according to the usual exponential law. It should also be noted that the cascade transform is 'free' in the rotation about the cascade segment.

Full exploitation of the cascade information is made: The branches of the cascade following a track segment also represent a cascade but initiated by a particle of type and energy on this track segment.

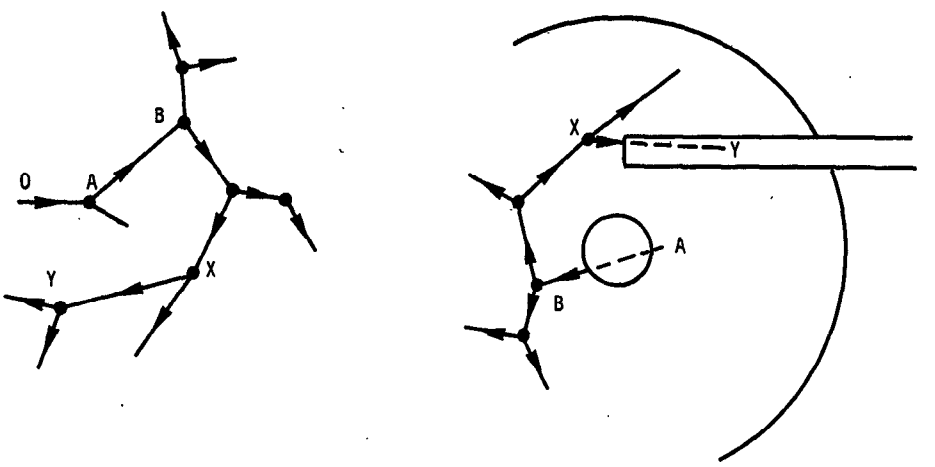

(a) Sample cascade (b) Transformed into moderator

Fig. 5 Two-dimensional representation of cascade selection for D_2O scattering calculation. (a) Cascade is initiated at A by particle starting from O. The track segment X-Y is used to construct the transform which puts this along the beam-tube (b). The segment A-B intersects the target.

First results are presented in Fig. 6 and show the relative HE neutron scattered flux in a beam-tube as a function of position. For reference the thermal flux variation is also shown. So far the calculation has not been absolutely normalised.

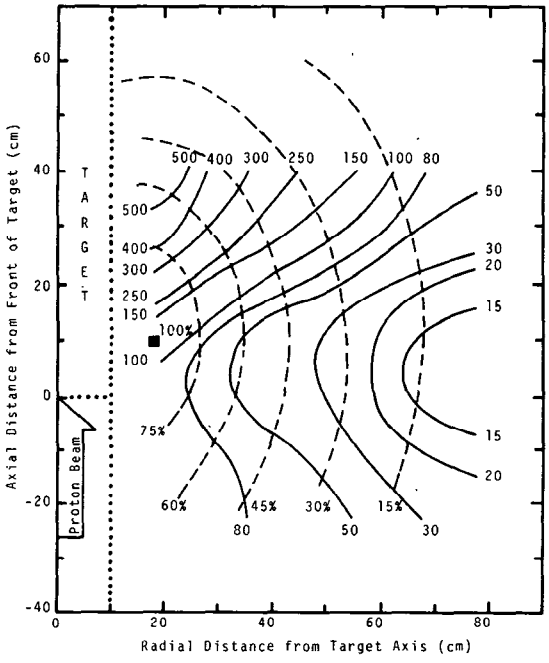

Fig. 6 Contours for the relative intensity for high-energy neutron scatters by D_2O into a tangential beam-tube. For comparison, the thermal flux distribution is also shown (- - -).

4. CONCLUSIONS AND DISCUSSION

There are many parameters available which are more or less effective in background reduction; beam-tube tip position in the moderator; size of the beam-tube; the material and dimensions of the beam-tube liner and collimators; layout geometry, materials etc. of the monochromator.

First estimates for the scattering of high energy neutrons by a monochromator crystal (section 2.3) show reduction factors of the order of 10^{-4} to 10^{-6} or better. Without knowing what incident flux or background level is tolerable it is not possible to judge if this is sufficient. Increased reduction may be obtained by choosing a thinner or possibly double monochromator. The incident HE flux will be minimised by correct choice of dimensions and material for the beam-tube liner and by variation of the beam-tube position in the moderator (section 3.6). Most of these measures will also entail loss of thermal flux.

The speeding up of Monte-Carlo calculations for high energy neutron fluxes has been successful for systems of one material whilst retaining the ability to handle complex geometries. It is also possible to treat voids. The calculation presented in section 3.4 required 1 hour to generate the cascades and an average of about 20 minutes for each of the radii. No one-step calculation has been attempted for comparison.

The application of Monte-Carlo effectively to the problems of the beam-tubes only looks feasible by reorganisation of the way the calculations are carried out. It does not seem possible to use HET as a 'complete package'. It still remains to be seen if some acceleration of the low-energy neutronics Monte-Carlo can also be made.

REFERENCES

1. F. Atchison, W.E. Fischer, SINQ status report. These proceedings
2. S. Cierjaks et al., Proceedings of ICANS V, JuL-Conf-45, 215 (1981)
3. A. Furrer (editor), Bericht der Diskussionstagung über Neutronstreuung. IRT report AF-SSP-123, 35 (1983)
4. Radiation Shielding Information Service code package CCC-178, HETC
5. M.B. Emmett, ORNL-4972 (1975)
6. R.R. Coveyou et al., ORNL-3622 (1965)
7. V. Herrnberger, Private communication (1983)
8. T. Armstrong, P. Cloth, D. Filges, Proceedings of ICANS VI, ANL 82-80, 504 (1982)
9. K. Takeuchi, Y. Kanai, presented at 6th International Conference on Radiation Shielding, Tokyo, May 1983
10. H.W. Bertini, Phys. Rev. 188, 1711 (1969)
11. SIN Studien, TM-37-19 (1982)

Proceedings of International Collaboration on Advanced Neutron Sources (ICANS-VII), 1983 September 13-16
Atomic Energy of Canada Limited, Report AECL-8488

NEW DIRECTIONS IN NEUTRON DIFFRACTION

P.A. Egelstaff
Physics Department
University of Guelph
Guelph, Ontario N1G 2W1

Abstract

The possibility of greatly improving or extending existing types of research and of opening quite new fields of research occur when new intense neutron sources are produced. Two examples will be given in the field of neutron diffraction from isotropic materials. These examples have been chosen both because of their scientific interest and because they illustrate the continuing need to stretch the capabilities of present accelerator and target designs.

Introduction

The advent of a new neutron source usually allows the users to open up new areas of study not accessible previously (e.g. the new developments at the Institut Laue Langevin), and the new generation of pulsed sources is expected to provide such opportunities. Some possible examples have been given in previous talks, but these have involved mainly a modest extrapolation of existing work. In this paper I will consider some more extreme possibilities.

Papers about neutrons have been published for some 50 years, and almost every conceivable speculation concerning their uses has been made. The versatility and utility of neutrons in the study of condensed matter is fully understood, but many of the experiments have fallen far short of the ideal neutron experiment envisaged in the speculations. Most experimentalists do what is possible as a first approximation to what is needed! Consequently from the ideal point of view we can categorise most results as coming from "bad experiments". The advent of a new source not only allows much needed improvements to be made, but also allows radical changes in experiments and some new directions to be opened. To discover which of these opportunities might become possible, we have to fit the properties of the new source to the speculations of the past. In the following discussion I shall present two examples of this fit.

High Energy Neutron Diffraction

Neutron diffraction experiments on liquids and glasses are usually carried out with wavelengths of about 1 A ($\sim$ 80 meV) largely because the intensity is high at this wavelength and results are not too bad. But it is well known that ideally the results would be improved if the energy were higher. Energies of $\sim$.3 eV have been used for some work and somewhat higher proposed: but what energy (E) is really needed? I will consider three arguments related to this question.

The first concerns the structure of liquids, non-crystalline biological materials and chemical solutions all of which may contain H or D. Because hydrogen has a mass almost the same as the neutron there is a significant neutron energy change (ΔE) on scattering. A correct diffraction experiment requires $\Delta E \ll E$, and since this is not achieved the observed data are corrected to make them correspond to this limit. This correction is accomplished by ad hoc models and usually amounts to many times the quantity being sought (namely the interference term in the cross section). The relative size of the correction at any given value of the momentum transfer ($\hbar q$) can be reduced by using a higher energy, because the given momentum transfer now corresponds to a lower angle of scatter. At high energies the principal effect is recoil and it is easy to show that a 1% correction to the cross section occurs at an angle (θ) of 8°. One might say that reasonable results occur when the correction is the same magnitude as the signal. Since the interference term may be $\sim$1% of the self term at 10 A^{-1}, this means $q \sim 10\ A^{-1}$ must occur for $\theta \sim 8^o$, or $E \sim 100$ eV.

The second example concerns the measurement of the pair correlation functions, g(r), for materials in which the nearest neighbour peak is very sharp (and may be separated from the remainder of g(r) and also have some structure). This probably occurs for a number of metallic glasses and simple molecules. If we ask for a resolution in r space of $\sim$.05 A we need data to $q \sim 100\ A^{-1}$, and for a peak in g(r) at $r = d \sim 1$ A the intensity (i.e. (Sin qd)/qd) in the diffraction pattern will have fallen to 1% at 100 A^{-1} compared to its value at $q \to 0$. Thus for this case it is useful to take data to 100 A^{-1}. It is still necessary to keep recoil corrections small but since the elements involved in many such samples are heavier than H, angles up to $\sim 25^o$ may be accepted and then E is $\sim$ 100 eV.

The final point concerns the general interpretation of the experimental condition $\Delta E \ll E$. Recoil of heavy elements at large angles will transfer several eV for $E \sim 100$ eV. Since this should be enough to break chemical bonds it is sufficient, and suggests that $\sim$ 100 eV is a maximum requirement. More generally the energy transferred in neutron scattering can induce chemical reactions in the sample, for example we can knock a proton from one water molecule to another:

$$2H_2O \rightarrow H_3O^+ + OH^-$$

which requires about 3 eV. Since this is a light element sufficient recoil energy will be found at a low angle and an unusual shape will be seen in the cross section in the region where normal diffraction effects are seen also. Thus for samples in which chemical reactions might occur we need $E \gg 3$ eV to avoid this type of distortion: that is $E \sim 50$ to 100 eV. But if a "diffraction" pattern was recorded for $E \sim 3$ eV, it would differ significantly from that observed for $E \sim 100$ eV and the difference might be used to determine some properties of the chemical reaction. This opens up a new field of study ultimately leading to different experiments which determine $S(q,\omega)$ for the chemical reaction.

To perform neutron diffraction experiments of this kind requires an intense source for $50 < E < 150$ eV, and pulsed spallation sources may meet this need. Because these neutrons are travelling at $\sim$ 7 μsec/m, short pulses $\sim$ 0.2 μsec are needed but the repetition rate may (if desired) be up to several kilohertz. In addition new instruments would be needed: Dr. K. Suzuki (Tohoku University) and I have designed one for a source similar to the S.N.S. and it is shown in figure 1. Since it is desirable to avoid contamination with lower energy neutrons we propose using a broad capture resonance in the detector. At present the most suitable appears to be cobalt at 132 eV, although the energy is perhaps twice as high as we

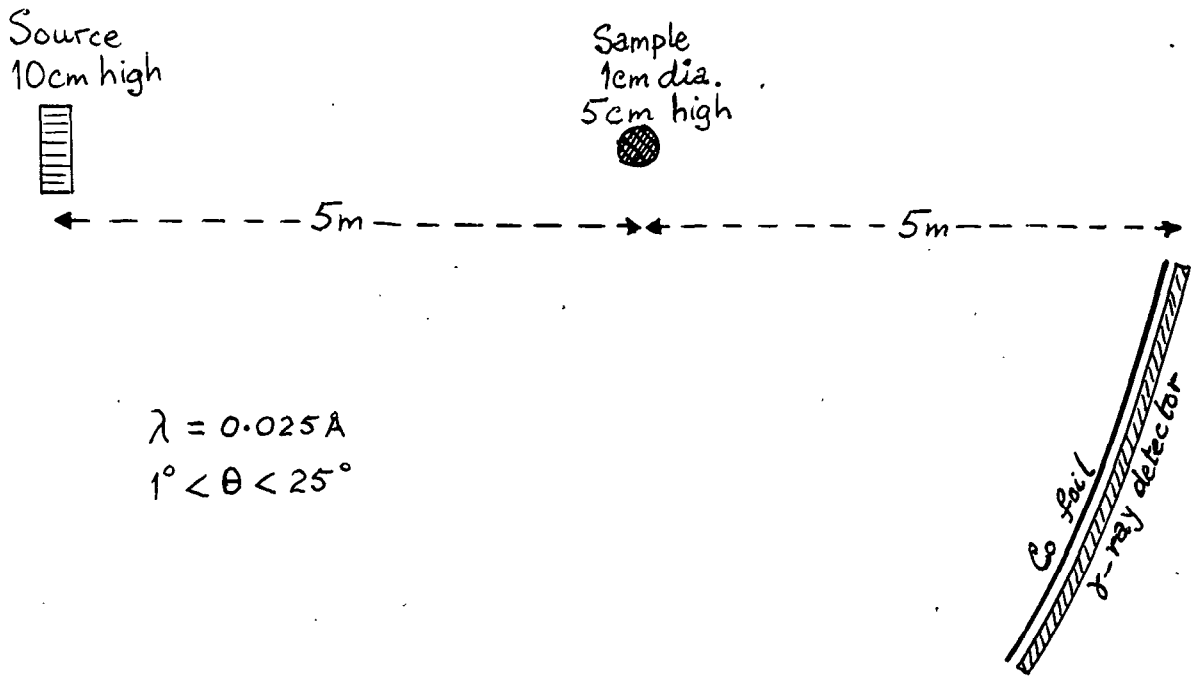

Figure 1. Single Energy Neutron Diffractometer for Amorphous Investigations (SENDAI): an instrument using T-o-F to select an energy in the neighbourhood of 100 eV, and which allows a high quality conventional fixed energy variable angle diffraction pattern to be measured out to $\sim$100 A^{-1}.

would like and there is a significant amount of scattering in this resonance. At the 100 barn level the width is 132±25 eV, and so a 1 mm thickness is appropriate (60 time channels of 0.2 μsec and a path of 10 m will cover 132±25 eV). Capture γ-rays would be detected by a position sensitive detector of large size (2 m long by 0.2 m high and 5 mm position resolution). Each time channel of 0.2 μsec would correspond to a well defined energy (such that $\Delta q \sim .5\ A^{-1}$ at 100 A^{-1}), and thus each time channel would give a structure factor of the convential kind with fixed energy and variable angle. For this reason it's called the Single Energy Neutron Diffractometer for Amorphous Investigations (SENDAI). After data reduction the 60 sets would be averaged, and added to data for $q < 4\ A^{-1}$ obtained at low angles in the present day type of diffractometer. Some other details are given in the figure. Assuming that the detector can be made 10% efficient, we estimate that $\sim 10^5$ counts for each of 400 angular positions would be obtained in 24 hours operation at the S.N.S. This study was done to demonstrate the feasibility of diffraction work using E $\sim$ 100 eV, although pilot experiments with energies of 20-60 eV and conventional detectors giving lower rates may offer a better starting point. Also this would allow complementary issues, such as whether resonances can be exploited for anomalous dispersion experiments, to be explored.

Single Pulse Diffraction

The use of pulsed sources to study transient behaviour has been discussed frequently and some experiments have been undertaken in a number of laboratories. I will call these experiments "weak transient" studies since the sample is not damaged significantly by the transient and it may be exercised over a very large number of cycles. However, "strong transient" work is perhaps of greater interest, since in such experiments a single transient damages or destroys the sample which is taken to the experimental limit of pressure, temperature etc. Examples are provided by the impact of projectiles, intense shock waves, implosions etc. or by giant laser pulses, large electrical discharges etc. It is desired to study the state of matter as the transient progresses through the sample and up to the point at which the sample is severely damaged. In such experiments some data must be taken with a single neutron pulse, although one can imagine samples being recharged at the rate of several per minute down to $\sim$ 1/day. In any event the whole experiment (both time and position behaviour through the transient) might have to be completed with 10-100 samples. One might also argue that the proton target could be changed after 100 pulses.

Paper studies of accelerators giving intense pulses have been made at Triumf in connection with the Kaon factory proposal. TRINS 2B (Triumf Intense Neutron Source 2B) for example would deliver a 3 GeV proton beam with $\sim 10^{15}$ p.p.p. at 0.5 Hz. A better solution would be $\sim 10^{16}$ at 0.1 Hz, as calculations (using existing general purpose diffractometers as a base) suggest 10^{15} p.p.p. is the lower limit for such experiments. At this limit single pulse data (with modest statistical errors) could be taken on a relatively large sample (20 cm^2 beam area) of a simple crystalline material which would give a set of strong

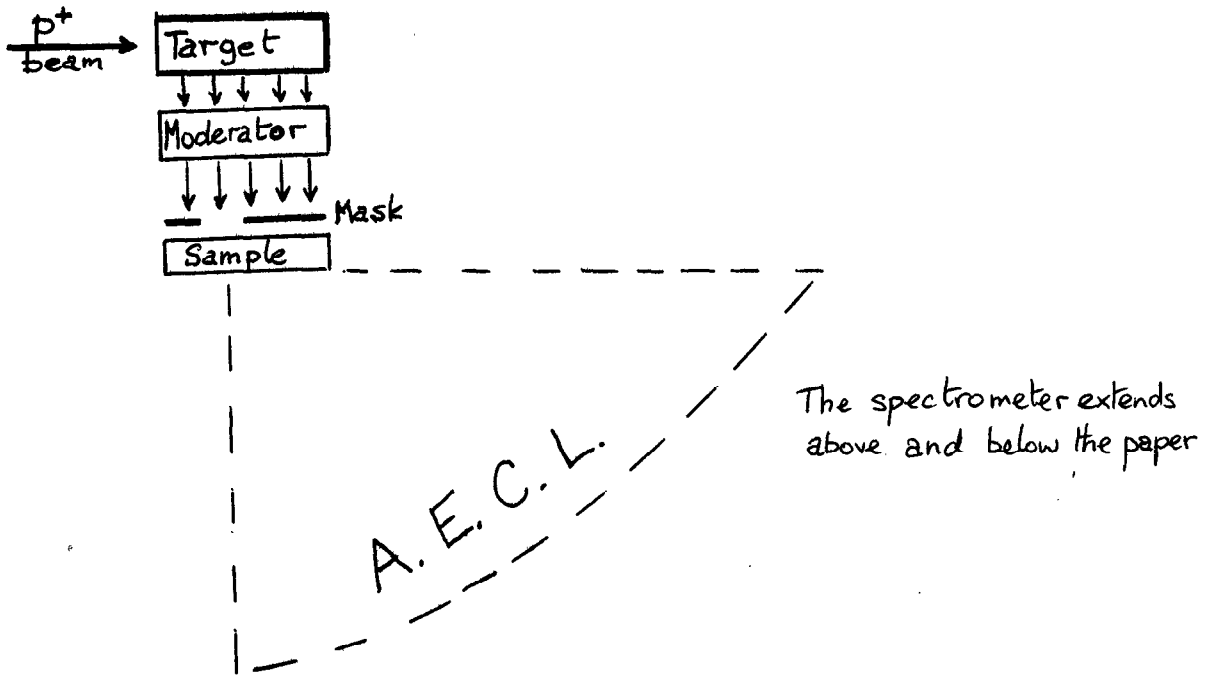

Figure 2. Angles and Energies Collected without Limit (AECL) Spectrometer used to measure the diffraction pattern of a point on a polycrystalline sample, which is being destroyed in a strong transient phased in time with the proton pulse.

Bragg reflections. The alteration in these reflections would be studied as the transient proceeds.

In the first method (figure 2) the sample is placed close to the moderator so that a pulsed white spectrum of neutrons passes through it at a given (time) phase relationship to the transient. With subsequent samples the phase could be altered. To obtain adequate statistics all wavelengths and angles of scatter should be collected and the data reduced to a single intensity vs. momentum transfer curve. Moreover fast electronics and detectors would be needed to handle the high peak counting rates (which are made manageable by the spread in time of the neutron pulse over the flight path). A new Angles and Energies Collected without Limit (AECL) spectrometer should be designed for this purpose. Initial calculations suggest this instrument is technically feasible, although the problem of making fast enough 'neutron only' detectors is difficult. If sufficient intensity is available the sample would be masked so that a pre-chosen region of it is irradiated and the masks moved for subsequent samples.

The above method has two disadvantages, the background will be high with the sample so close to the moderator, and many different samples are required to obtain phase shifted data. A simple way to overcome these disadvantages is to place the sample several metres from the source so that collimators may reduce the background and the spreading in time of the different wavelengths may be used to stobe a single sample. A number of diffraction patterns, one for each wavelength, is obtained to give the change in structure with time. Unfortunately this requires higher intensity, perhaps $\sim 10^{17}$ p.p.p, at which stage the performance of the proton target may be a limiting factor.

Conclusion

The advent of a new generation of spallation sources will allow new ground to be broken in the field of neutron diffraction. Two examples were considered in this paper, but others are to be expected. In the first example an intense average output was required and the pulse repetition frequency could be relatively high (kHz). In the second example intense single pulses were required at a very low repetition rate. From the point of view of the accelerator designer or target designer this look into the crystal ball has presented two opposite limits and both of them need to be explored.

Proceedings of International Collaboration on Advanced Neutron Sources (ICANS-VII), 1983 September 13-16
Atomic Energy of Canada Limited, Report AECL-8488

Irradiation Effects in Candidate Materials for the SNQ-Target Station

W. Lohmann
Institut für Festkörperforschung (IFF-SNQ)
KFA Jülich, D-5170 Jülich, FRG

Abstract

Based on calculations of the expected kind and amount of radiation damage for heavily loaded SNQ-target wheel components, an irradiation program for promising candidate materials is presented. It includes simulation experiments, neutron irradiations and various proton irradiation experiments. Typical examples are discussed in detail with the emphasis on medium energy - high current proton irradiation experiments to be performed at the LAMPF-accelerator.

1. Introduction and calculated radiation damage

In order to achieve a reliable operation of the SNQ-target wheel during its 12.000 h lifetime, a sufficient stability of the used materials against radiation damage effects is needed. Fig. 1 shows the most heavily loaded components from irradiations point of view.

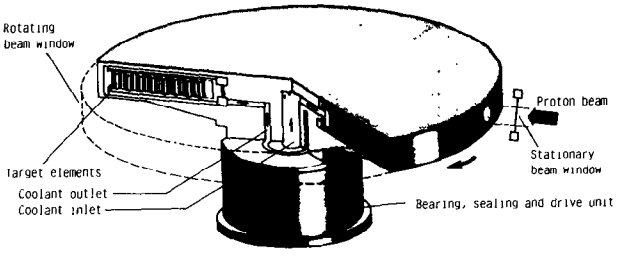

Fig. 1 SNQ-target wheel components exposed to intensive proton and neutron irradiation.

The amount of the expected radiation damage has been calculated by usual methods (Lohmann, 1981) in terms of displacement damage rates and He-/H-production rates for a variety of materials. The underlying assumptions are:

- proton beam energy 1100 MeV, time-averaged beam current 5 mA, characterizing the worst case,
- applicability of known 800 MeV-proton damage parameters to the 1100 MeV case,
- possibility of the evaluation of unknown proton damage parameters by linear extrapolation from the known data base,
- neglectability of neutron damage contributions for the stationary proton beam window (Coulter, 1977).

Results from these and other considerations are compiled in Tab. 1, indicating the supposed problem areas, too.

Component	Material	$\dot{S}$ (dpa/day)	P_{He} (appm/day)	P_H (appm/day)	Main problem(s) under irradiation
Stationary beam window	SAP	0 2	60	260	He-embrittlement, high-cycle fatigue
	HM-based metallic glasses	1.9	170	1190	He/H-effects, thermal stability, high-cycle fatigue
Rotating beam window and target element cladding	AlMgSi, AlMg	0 01	0.6	1 6	fatigue, swelling, creep He-embrittlement
	Zry-2	0.02	0 7	4 5	H-effects, creep, fatigue, swelling, He-embrittlement
Target material	Pb	~ 0 02	~ 0.9	~ 7 8	gas production, swelling
	W	0.02	0.9	7 8	DBTT, He-embrittlement, fatigue
	U^{238}	0.3	0 7	6 1	dimensional stability, fatigue, anisotropic growth, He-effects
Slide ring sealing	SiC, WC, C	n- fluences up to 10^{20} n/cm^2 (> 0 1 MeV)			dimensional stability, friction coefficient
Coolant	H_2O	P_{H_2} = 110 g / h			radiolysis effects, enhanced corrosion

Tab. 1 Calculated radiation damage for various SNQ-target wheel components and expected main materials problems.

Inspection of Tab. 1 reveals the highest damage rates - exceeding even those of fusion reactor devices by

orders of magnitude - for the stationary proton beam window. This component is hence considered as a desirable, but not imperatively needed part for the SNQ-target station. Promising materials are SAP (sintered aluminium product, Al-matrix + 7 % Al_2O_3), offering sufficient strength up to 400°C and the ability of accomodating high amounts of both He and H without drastic degradation of its mechanical properties (Krautwasser, 1983), and metallic glasses with high thermal stability like $Nb_{40}Ni_{60}$ being insensitive at least to displacement damage intrinsically (Lohmann, 1982).

Much lower damage rates can be seen for all rotating components, demonstrating thus the advantages of the rotating target wheel concept. Useful materials for the rotating proton beam window, the target wheel structure and the target element cladding are Al-alloys and - if needed from temperature conditions - Zircaloy-2. The choice of the target material itself is mainly determined by neutron yield considerations leading therefore to either Pb or W for non-fissile materials or to depleted U (Krautwasser, 1983) including fast fission contributions to the total neutron yield.

The concern in the case of the slide ring materials is the applicability of conventional (WC, C) and improved (SiC, C) combinations under SNQ-conditions (temperature, n-fluence).

As the proton beam penetrates the cooling water, the effects of water radiolysis possibly leading to enhanced corrosion of structural components have to be investigated, too, together with the development of suitable water conditioning techniques.

In general, a strong necessity for extensive irradiation tests is felt for all materials and components discussed above.

2. SNQ materials irradiation program

The basic idea of the SNQ materials irradiation program is to match both with the expected irradiation effects (cf. Tab. 1) and with the availability of existing irradiation facilities. A staged proceeding has therefore been chosen, summarized in Tab. 2.

This program includes a variety of experiments of different kinds ranging from small-scale simulation tests using KFA-facilities over more complex fast neutron and spallation neutron irradiations to experimental conditions under 800 MeV-p-irradiation being close to the real SNQ operating conditions; the latter investigations are hence basically considered as a proof test of certain SNQ-components up to a complete target wheel. A special advantage of this procedure should be mentioned: each program stage introduces more complicated irradiation and thermomechanical loading conditions, offering thus the possibility to proceed from simple irradiation effects (e.g. He- or p-effects only) to the complex SNQ-environment ultimetely.
In order to illustrate the SNQ materials irradiation program, some typical examples and experiments will be discussed below.

Irradiation type	Location	Purpose	Experiment type	Status
28 MeV - α	KFA-IFF (cyclotron)	Simulation of He-effects by α-implantation	- Post-irradiation test - in situ-thermal fatigue (designed)	- Current experiments for Al, SAP, metallic glasses - Planned for 1984
24 MeV - p	KFA-IFF (cyclotron)	Simulation of water radiolysis	in situ-tests on a closed water system	Planned for 1984
Fast n	Reactors: KFA-2FR, HFR Petten	- Basic data for n-irradiated materials and components - compatibility of p- and n-damage data	Post-irradiation test	Planned after fall, 1983 for SiC, WC, C and W, U
Spallation n, mixed n/p-spectrum	LAMPF beam stop area	Proof test under realistic conditions	Post-irradiation test (SNQ-0, SNQ-SM-1/2)	Current experiments for Al and SiC/C
800 MeV - p	LAMPF beam stop area	- p-irradiation effects in SNQ candidate materials	- Post-irradiation test (SNQ-Ia/b) - in situ-thermal fatigue (SNQ-II)	Approved experiments for 1984 (Al, SAP, metallic glasses
		- Water radiolysis effects	in situ-measurement and conditioning	To be attached at SNQ-Ia
		- Proof test of a complete small target wheel under realistic conditions	in situ- and post-irradiation test (TRLA)	Proposed for 1985

Tab. 2 Survey over the SNQ materials irradiations program.

3. Examples of experiments from the SNQ materials irradiations program

3.1 Neutron irradiation experiments on W

W is one of the non-fissile target material candidates for SNQ. Whereas no major problems are seen concerning thermomechanical load and irradiation effects like swelling or change of mechanical properties (Bauer, 1981), at least one special irradiation effect remains to be investigated: the irradiation-induced shift of the ductile-to-brittle-transition-temperature (DBTT) as depicted in Fig. 2.

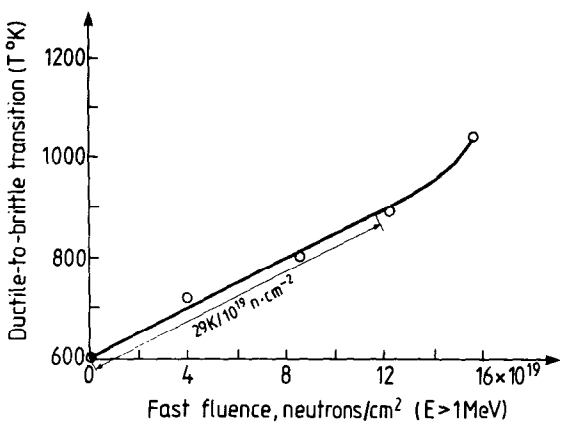

Fig. 2 Ductile-to-brittle transition of polycrystalline, recrystallized W as a function of the fast neutron fluence (Younger, 1970). The results are based on postexposure tests on samples preirradiated at about 395 K.

A distinct materials deterioration must be expected, if the DBTT is higher than or similar to the SNQ operating temperature, leading thus to either operation within the brittle range or - even worse - to a periodical thermal cycling over the DBTT during each wheel revolution.

The ongoing experiments are intended to generate data on the DBTT-increase rate and on mechanical properties of irradiated material. They include fast neutron preirradiations at SNQ-typical temperatures and fluences (350-400°C, $< 1 \times 10^{21}$ n/cm^2, E > 1 MeV) and corresponding post-irradiation tests. The materials to be investigated are pure W, W-10Re and W-26Re (both with an intrinsically low DBTT) and the sintered alloy Densimet 18. Promising materials from this screening experiments will be selected for more specific irradiation tests like TRLA (cf. Tab. 2).

3.2 Proton irradiation experiments

All proton irradiation experiments will be performed at the LAMPF-beam stop area, where a 800 MeV/$\leq$ 1 mA proton beam is available.

3.2.1 Static irradiation experiments

A set of suitable irradiation capsules (SNQ-Ia, -Ib) has been developped and is schematically shown in Fig. 3.

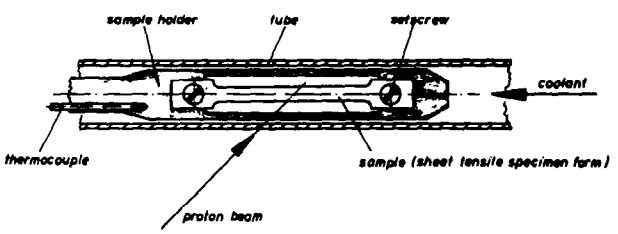

Fig. 3 Schematic sketch of the SNQ-Ia-, -Ib-experiments for static proton irradiations.

Capsule SNQ-Ia has an Al-structure and is dedicated to the irradiation of Al-alloys (cf. Tab. 1) at about 100°C to SNQ-relevant fluences. As can be seen in Fig. 4, it consists of 9 sample tubes at 4 different beam positions, providing thus also information on the dose dependence. Each sample tube contains a stack of 8 sheet tensile specimens, which are surface cooled by water.

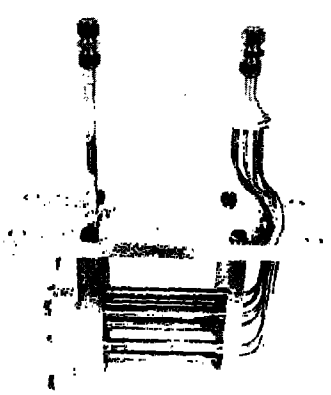

Fig. 4 Capsule SNQ-Ia for static proton irradiation experiments at temperatures up to 150°C.

Capsule SNQ-Ib has a stainless steel structure and will hence be used for irradiations at elevated temperatures (up to 500°C) on beam window candidate materials (cf. Tab. 1) like SAP or metallic glasses ($Nb_{40}Ni_{60}$) and also on promising W-alloys (cf. 3.1). The general de-

sign (Fig. 5) is similar to SNQ-Ia with the exceptions of only 3 sample tubes and a He-gas surface cooling of the samples.

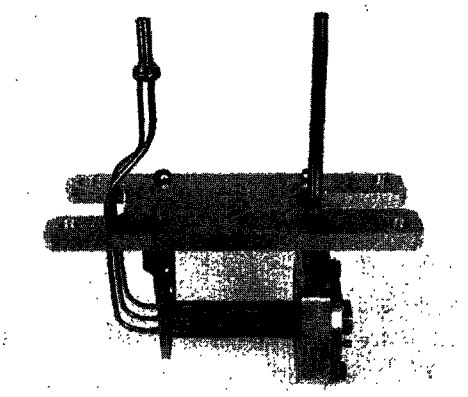

Fig. 5 Capsule SNQ-Ib for static proton irradiation experiments at elevated temperatures ($\leq$ 500°C).

The envisaged data analysis for these experiments will be described under 3.2.3.

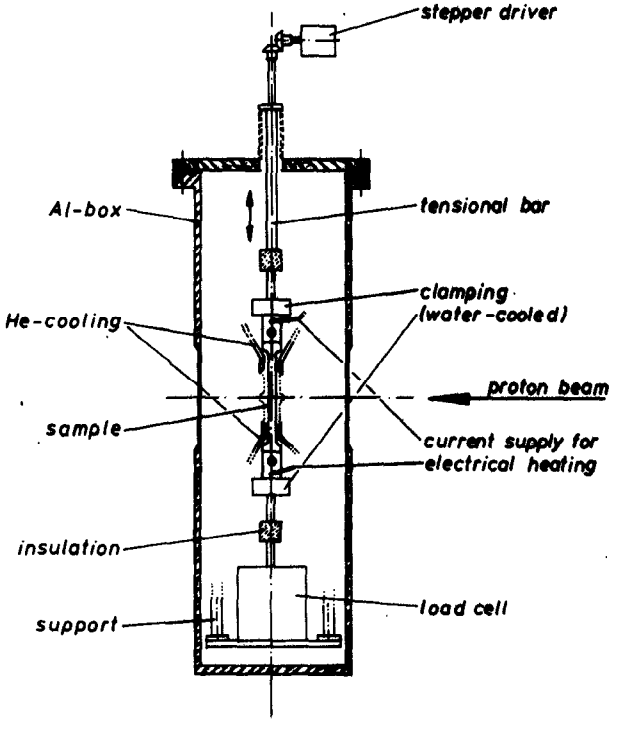

Fig. 6 Schematic sketch of the in situ-thermal fatigue experiment SNQ-II.

3.2.2 In situ-thermal fatigue experiment

In situ-thermal fatigue tests are of special importance because of observed synergistic effects of mechanical stress and irradiation (Sommer, 1983). This holds for all rotating parts of the target wheel, which are periodically hit by the proton beam (cf. Fig. 1). An apparatus for corresponding investigations without irradiation is operating at KFA, from which the design for the capsule SNQ-II has been derived. Fig. 6 shows the basic layout of SNQ-II.

The sample - again with sheet tensile geometry - is mechanically prestressed in tension and periodically heated up by a pulsed dc-current through its gauge length. Variation of both the mechanical prestress via the movable upper clamp and the electrical heating power input allows the determination of the materials thermal fatigue characteristic under mean stress-control. In order to get a rapid cooling-down after each heating pulse, the specimen is intensively cooled by He-gas on its surface and by edge-cooling in the water-cooled clamps. Sample temperature measurement is achieved mainly be resistance measurement of the gauge length. Materials to be investigated are primarily Al-alloys (cf. Tab. 1) close to SNQ-conditions, i.e. at a mean temperature of about 100°C and a ΔT of 24°C per heating pulse. Capsule SNQ-II allows the simultaneous operation of two specimens with independently variable parameters.

3.2.3 Data analysis for the foil specimen experiments

There will be a joint data analysis for the specimens of SNQ-I and SNQ-II. A preliminary compilation of the planned post-irradiation investigations is given in Tab. 3.

Analysis	Al-alloys	SAP W-alloys	Metallic glasses
Yield Stress	x	x	x
Flow Stress	x	x	x
Uniform and fracture strain	x	x	x
Ultimate tensile stress	x	x	x
Fracture characterization by scanning electron microscopy	x	x	x
Metallography	x	x	x
Microhardness	x	x	x
Microstructure characterization by transmission electron microscopy	x	x	x
Thermal fatigue (in-situ at SNQ-II)	x	-	-
Chemical analysis	x	x	x
Thermal conductivity	x	x	x
Crystallization temperature by differential thermal analysis	-	-	x

Tab. 3 Data analysis for the experiments SNQ-I and SNQ-II.

3.2.4 Test wheel experiment TRLA

In order to match the SNQ operating conditions as best as possible, a proof test of a complete small SNQ-target wheel TRLA (Testrad Los Alamos) is indicated as the ultimate goal of the irradiation experiments. The possible TRLA-design is shown in Fig. 7.

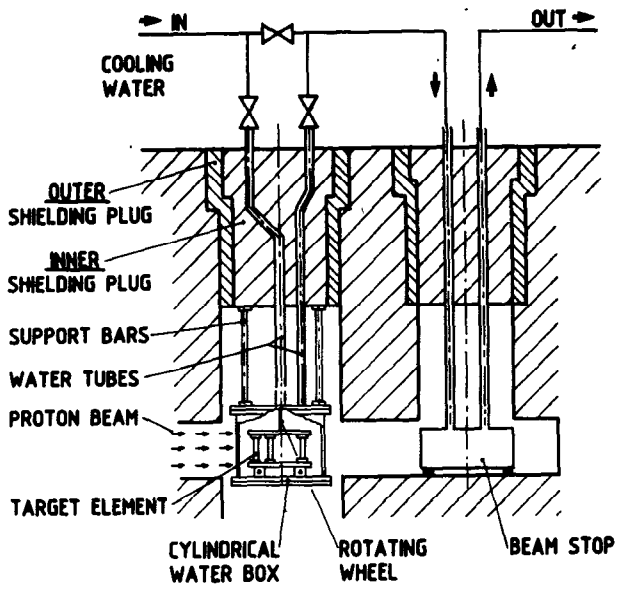

Fig. 7 Schematic sketch of the proposed test wheel experiment TRLA.

TRLA consists basiçally of a rotating target element structure within a cylindrical water-cooled box suspending from a shielding plug. Being mainly a materials test experiment, a total of 180 test pins will be inserted, subdived into Pb-, W- and U-sectors. Each sector contains different combinations of the target material alloy, the cladding material alloy and - if needed - an intermediate bonding layer. Provisions will be made to withdraw single target elements for inspection purposes. Essential engineering aspects like the test of the slide ring sealing and the driving water turbine as well as temperature measurements within certain target elements will also be covered by TRLA.

To guarantee a safe operation without major impact on the LAMPF operation in general, the TRLA experiment is located in front of the usual beam stop, offering thus the possibility to pull the whole experiment out of the proton beam area in case of a failure without a need for a shut-down of the accelerator, because there is a series connection of the cooling systems for both TRLA and the beam stop.

4. References

Bauer, G.S.; Lohmann, W. and Stelzer, F.
"Some Remarks Concerning the Use of a Rotating W-Target in a High-Power Spallation Neutron Source"
Proc. ICANS-V (1981), Jül-Conf-45, pp. 591-610

Coulter, C.A.; Parkin, D.M. and Green, W.V.
"Calculation of Radiation Damage Effects of 800 MeV Protons in a Thin Copper Target"
J. Nucl. Mat. 67 (1977), 140-154

Krautwasser, P. and Lohmann, W.
"Progress of the Materials Investigations for the SNQ-Target"
Proc. ICANS-VII (1983), this volume

Lohmann, W.
"Realisierungsstudie zur Spallations-Neutronenquelle"
Teil II, Kap. A 2.7 (1981)

Lohmann, W. and Kesternich, W.
"On the Possibility of Using Amorphous Metals in High Radiation Environments"
Proc. 11th Conference on Effects of Radiation on Materials, ASTM-STP 782 (1982), 779-798

Sommer, W.F.; Phillips, D.S.; Green, W.V.; Hobbs, L.W. and Wert, C.A.
"Proton Irradiation Damage in Cyclically Stressed Aluminum"
J. Nucl. Mat. 144 (1983), 267-276

Younger, C.L. and Wrights, G.N.
"Effect of Reactor Irradiation on Ductile-Brittle Transition and Stress-Strain Behavior of Tungsten"
NASA-TN-D-5991 (1970)

Proceedings of International Collaboration on Advanced Neutron Sources (ICANS-VII), 1983 September 13-16
Atomic Energy of Canada Limited, Report AECL-8488

DESIGN FEATURES AND PERFORMANCE OF THE LAMPF HIGH INTENSITY BEAM AREA*

L. Agnew, D. Grisham, R. J. Macek, W. F. Sommer, and R. D. Werbeck
Los Alamos National Laboratory
Los Alamos, New Mexico 87545

Summary

LAMPF is a multi-purpose high-intensity "meson factory" capable of producing a 1 mA beam of 800 MeV protons. The three target cells and the beam stop facilities in the high intensity area have many special design features that are required for operation in the presence of high heat loads and intense radiation fields where accessibility is extremely limited. Reliable targets, beam windows, beam stops, beam transport and diagnostic components, vacuum enclosures, and auxiliary systems have been developed. Sophisticated remote-handling systems are employed for maintenance. Complex protection systems have been developed to guard against damage caused by errant beam. Beam availability approaching 90% has been achieved at currents of 600-700 μA. A new facility for direct proton and neutron radiation effects studies will be installed in 1985. The new facility will provide an integrated spallation neutron flux of up to 5×10^{17} $m^{-2}s^{-1}$ and will enable proton irradiation studies in the primary beam.

Overall Design Features

LAMPF is an 800 MeV proton linac capable of simultaneously accelerating H^- ions to energies in the 200-800 MeV range. An overview of LAMPF was presented at the 1981 ICANS meeting in a paper entitled "Operating Experience with the Meson Factories," by R. J. Macek.[1] The principal design goal for LAMPF was to provide high-intensity (up to 1000 μA) proton beams for "meson factory" use for a number of non-interfering secondary beams of pions and muons, while also providing low-intensity variable-energy polarized and unpolarized primary beams, and additionally providing high-peak-intensity 800 MeV proton beams for a pulsed neutron facility at the Weapons Neutron Research (WNR) area.[2] Starting in 1985, LAMPF will also provide up to 100 μA of H^- beam for injection into the 800 MeV Proton Storage Ring (PSR) now under construction.[2]

A layout drawing of the LAMPF experimental areas is given in Fig. 1. Low intensity beam from the accelerator is bent 45° to the left at the switchyard to serve the needs of experiments that utilize variable energy protons and neutrons at three target stations. High-peak-current beam is bent 90° to the right at the switchyard for delivery to the WNR and the PSR areas. The high-intensity main beam, currently operating at about 700 μA average current with a macroscopic duty factor of six percent, is transported through the switchyard to Beam Area A where it passes successively through three graphite production targets that serve six pion and muon beams. After passing through the three targets, the residual beam (reduced to about 745 MeV in energy and to about 2/3 of the incident current) is transported to the beam stop area for isotope production,[3] neutron and proton irradiation studies, and neutrino experiments.

The use of sequential targets mandates several design characteristics. Transport elements must be scaled to handle beams of large phase space. Quadrupole focusing elements must be placed as close as possible downstream of the targets to conserve useful beam. Collimators capable of accepting high power levels are needed to shield transport elements, diagnostic devices, and vacuum joints from intense heat loads.

Operation at very high intensity requires accurate knowledge of beam optics, precision in beam tuning, and the utilization of special radiation-hardened diagnostic devices (see "Radiation Resistant Beam Components at LAMPF," presented by R. J. Macek at this conference).[4] Fail-safe, fast-acting, redundant protection systems against faulty beam control must be provided, as a missteered high-intensity beam could cause severe component damage in times of the order of a second.

Target and beam stop areas must be heavily shielded, and, of course, become highly activated. Residual gamma ray levels up to 10^5 R/h have been observed at LAMPF. Maintenance and replacement of targets and beam line components must be done by remote handling methods in order to avoid unacceptable radiation doses to personnel. At LAMPF, the "Monitor" system of special components, tools, and mobile manipulators is used for remote maintenance. Key elements of this system include highly maneuverable and flexible manipulators mounted on a remotely controlled hydraulic boom, remote-control television viewing systems, and remote crane controls. See another paper presented at this conference for more details: "Remote Handling at LAMPF," by D. Grisham and J. Lambert.[5]

Auxiliary systems require special attention at a high-intensity facility. Water-cooling systems must be designed for high levels of activation, including the generation of large quantities of tritium and ^7Be. Maintaining high-purity low-conductivity water systems is particularly difficult in high radiation areas. Vacuum systems cannot be exhausted into personnel areas or experimental caves. Air activation (e.g., the production of ^{10}C, ^{11}C, ^{13}N, ^{16}N, ^{15}O, and ^{41}Ar) will occur where main beams or scattered beams pass through air. Waste products and trash from beam areas pose a hazard to personnel and precautions must be taken to protect the local environment.

Target Cell Features

LAMPF's intense beams place extreme operational requirements on pion-production targets, target cell components, and shielding. Targets and nearby components must operate at high temperatures in a vacuum and in intense radiation fields. During routine operation, the beam power is more than 500 kW, and nearly 1 MW of power was delivered during a recent 1200 μA test run. This power is distributed between three target cells and the beam stop area, with the latter absorbing about 2/3 of the total. Target cell enclosures and components are water cooled, as are the vacuum window and the beam stop. Materials of choice include stainless steel for enclosures and Inconel 718 for beam windows, with OFHC copper being used for collimators and the beam-absorbing plates of the beam stop. A drawing of the LAMPF beam stop design is shown in Fig. 2. No failures have been experienced with this design. Target box enclosures now employ a double-wall design with highly effective cooling provided by carefully directed water circulation between the two jackets. Regions of highest heat load have copper inserts that are welded directly to stainless steel. Fig. 3 shows the newest LAMPF target box, with collimated channels for two secondary beams (P^3 and SMC) and a radiatively-cooled rotating wheel target.

*Work supported by the US Department of Energy.

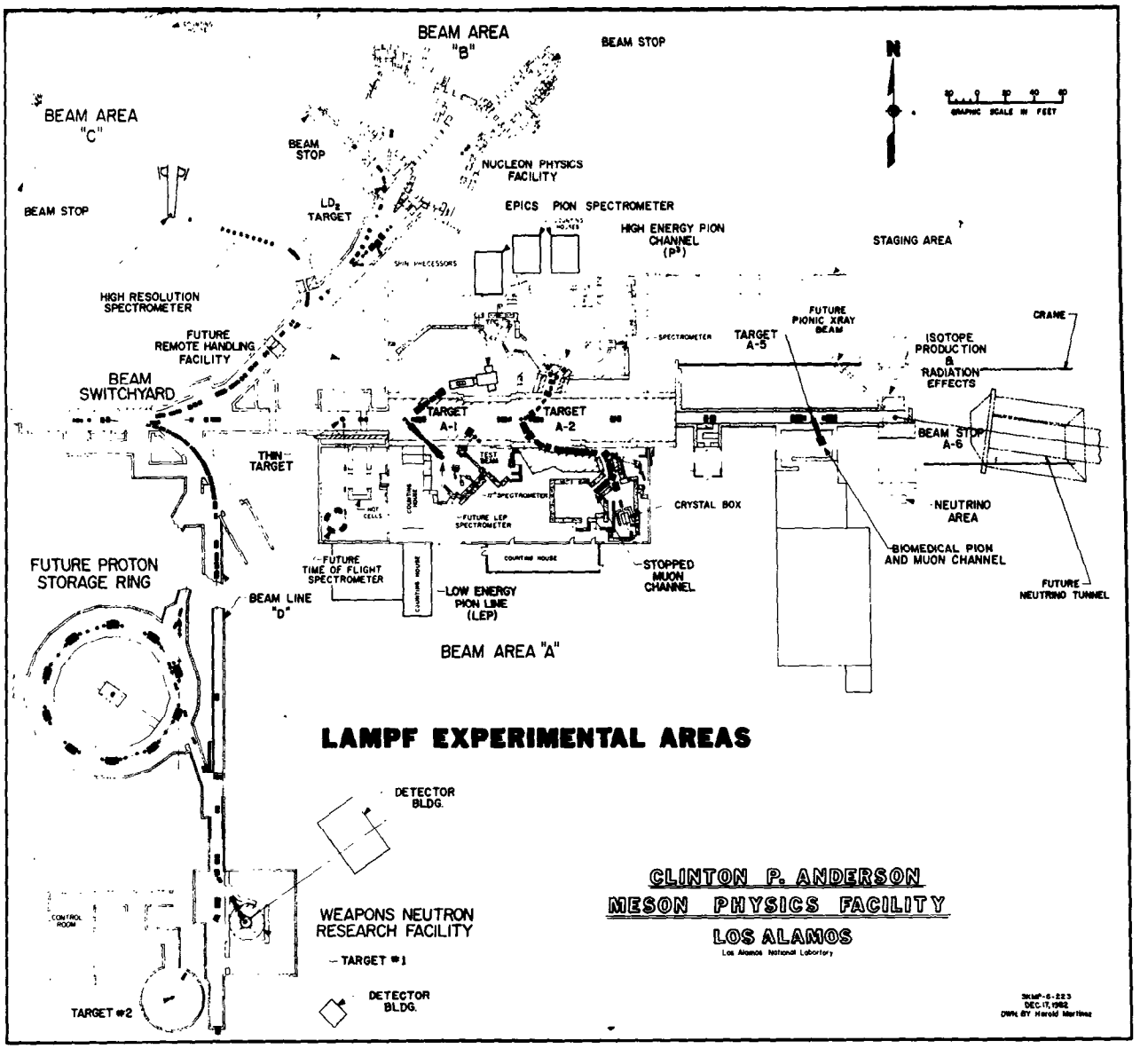

Fig. 1. LAMPF Experimental Areas

Vacuum enclosures and collimators are subjected to heat-cycling to temperatures in the 300 C range, while temperatures of about 500 C have been observed on the main beam window. All-metal vacuum seals are located away from the high heating rates and are shielded for minimal thermal cycling. Water-cooled target boxes and beam line components at LAMPF are more fully described elswhere in these Proceedings[4] and in two previous publications.[6,7] Fabrication techniques are continually developed to increase operational reliability and lifetime, and schemes to ease installation, alignment, and removal by remote handling are steadily improved.

Graphite targets of two different types are used for pion production at LAMPF. At two target cells, rotating-wheel radiation-cooled polycrystalline graphite targets are used, while a water-cooled pyrolytic graphite target is used at the third target station. Both of these basic target designs have been successfully developed to the point of high reliability. The principal design concern for the rotating target has been with the bearings. Satisfactory performance is now obtained from bearings using a proprietary powder metallurgy product containing MoS_2. The principal concern for the stationary pyrolytic graphic target has been deterioration of strength and conductivity, accompanied by material swelling. This occurs in the small beam-spot area where thermal stresses and radiation damage are extreme. Target development at LAMPF and detailed descriptions of the target assemblies are given elsewhere in these Proceedings[4] and in three previous publications.[8-10]

Magnets and beam diagnostic instrumentation must be able to survive the extreme radiation and heat conditions in the target cells. These devices are described elsewhere in these Proceedings.[4]

Massive shielding and high activation levels combine to limit very severely the opportunity to carry out routine trouble-shooting efforts. Electrical faults, vacuum leaks, cooling water leaks, etc., can and do occur deep within the shielding. Beam components are generally inaccessible quickly, and are always unapproachable. This necessitates the adoption of special techniques for diagnosing hardware problems. These include the use of redundant interlock systems,

special cabling, and the employment of numerous prepositioned tubes that penetrate the shielding to enable helium leak checking.

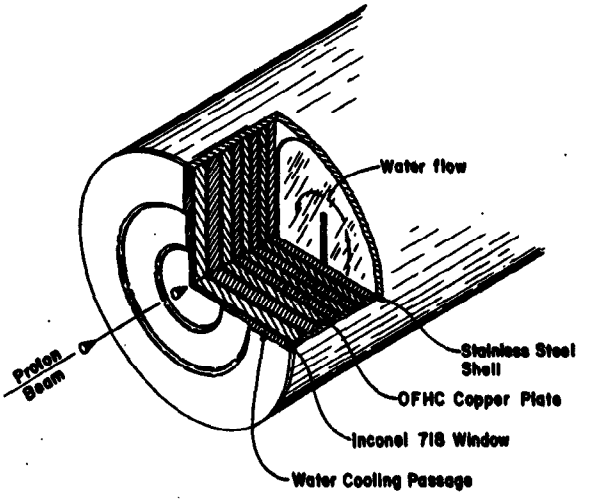

Fig. 2. LAMPF Beam Stop

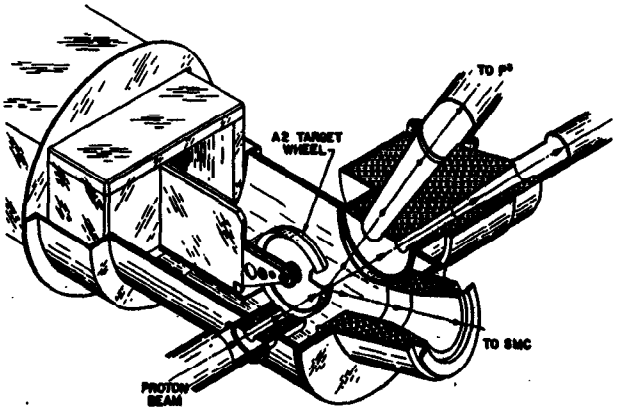

Fig. 3. A-2 Target Chamber

Beam Diagnostics and Protection Systems

A comprehensive system of beam diagnostics and beamline protection devices and instrumentation is in place for the high intensity primary beamline. In a paper of this length, only selected points can be mentioned. Additional information is presented in two other papers at this conference,[4,5] and in prior documentation in the literature.[11,12]

In general, beam diagnostic instrumentation is used to obtain data, such as beam position, spot sizes and losses, which are useful for tuning and monitoring important beam parameters. The emphasis here is on accuracy, large dynamic range (0.1-1000 μA), completeness and flexibility. Computerized data acquisition, processing, logging, and display in the central control room are necessary features for effective control of the beam.

Protection devices and instrumentation, while often useful for diagnostic purposes, have as their main function the prevention of physical damage to beamline components from errant, high-powered beams. Fast, automatic response, redundancy, fail-safe, highly reliable operation, and credibility with operations personnel are important criteria for the protection system. Personnel protection is a related, but separate, issue not discussed here. In the meson area beyond the switchyard, components of both systems must be long-lived, radiation resistant, and remotely serviceable.

Beam profiles are obtained by sampling secondary emission signals from wire scanners or wire grids known as harps. Wire scanners are used in areas of hands-on maintenance, such as the beam switchyard, while radiation-hardened harps are in place in the primary beamline of the meson area. A schematic layout of the A-2 Target Cell is shown in Fig. 4.

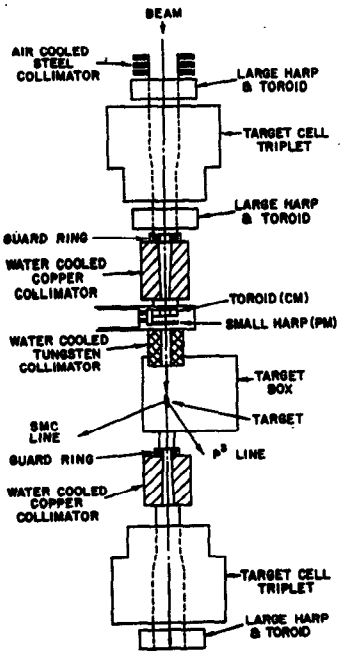

Fig. 4. Layout of the A-2 Target Cell

Harps are located at the entrance and exit of the target cell and at two interior points. The spot sizes obtained at these four locations are sufficient, in principle, for a complete determination of the beam envelope parameters including extrapolation to the production target. In practice, the uncertainties in the profile measurements and the magnet transport parameters combine to produce larger-than-desired, but still acceptable, uncertainties in the spot size estimate at the target. A profile measurement closer to the target would be desirable for greater accuracy; however, the difficulties of retrofitting and of operating close to the target are likely to prohibit any improvements in the near future.

Beam currents are accurately (~1 μA) measured with toroids configured as beam current transformers. Beam halos or spills are sensed in the secondary emission guard rings located in front of collimators. In the lower-spill areas, such as the beam switchyard, beam spills are detected by scintillator detectors.

The beamline protection system is composed of a number of fixed-aperture collimators for passive protection of components, plus hardwired instrumentation which detects unacceptable operating conditions and either shuts down the beam completely or automatically limits the current to acceptable levels. Typical locations for collimators are also shown in Fig. 4. Collimators are the limiting apertures of the beamline; they serve to shield components from excessive beam-induced heat loads and to reduce or limit spurious radiation-induced signals on instrumentation.

Anomalous overall beam losses which exceed preset tolerances are sensed by a hardwired transmission monitor based on beam current-sensing toroids. Beam spills are directly detected at specific locations by the system of secondary emission guard rings and scintillation detectors mentioned earlier. All of these instruments limit the average current through the so-called "fast protect" system. In this manner, the current is limited to a safe level, but enough beam is available for tuning or trouble-shooting.

Temperature sensors are radiation-hardened thermocouples or thermal switches. Beam is automatically interrupted when excessive temperatures are sensed at critical locations, such as a vacuum flange or the vacuum window at the end of the beamline. Poor vacuum interferes with proper functioning of harps, guard rings, and current monitors. Poor vacuum results in more rapid oxidation of targets and is often a precursor of greater difficulties. For these reasons, beam is also interrupted when the primary beamline vacuum exceeds 10^{-2} Torr.

Sensor data and status information from the protection system are acquired by the central control computer for logging and monitoring purposes; however, we do not rely on computer processing for the decision to interrupt beam. Dedicated analog electronics and hardwired logic elements process signals and automatically interrupt the beam when pre-established conditions are detected. Operating experience for several years has shown this to be an effective system. If has prevented major damage from the effects of high-powered errant beams.

Operating Experience

LAMPF has been operating at high intensity for more than five years, with average currents gradually climbing from 300 μA in early 1978 to periods of 700 μA operation in late 1982. A high intensity beam test was carried out successfully at 1200 μA in February 1983. Beam availability has been close to 90% during recent production runs. The yearly operating time, which is sharply dependent upon budgetary strength as well as major maintenance needs, will fall off to well below 3000 h of high-intensity research in 1983 after several years in the 3400 h range. In a typical year about 60 nuclear science experiments are carried out by about 450 scientists, most of whom are members of university research teams. The experimental areas can serve 10 to 12 simultaneous experiments, exclusive of pulsed neutron experiments at the WNR facility. The record of LAMPF's high intensity operation to date is presented in Fig. 5.

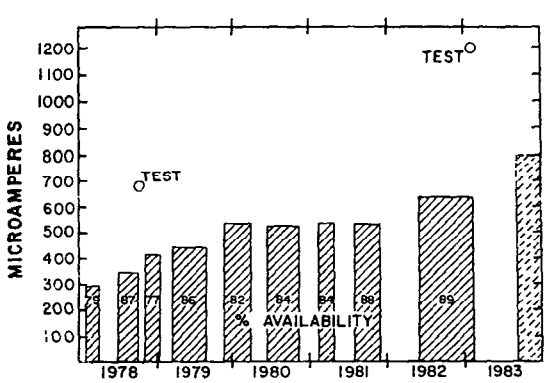

Fig. 5. LAMPF High Intensity Operation

After reaching production currents of 500 μA several years ago, LAMPF's management chose to emphasize high reliability and research output instead of increased intensity. Target cell and beam stop components that were marginal are being replaced or upgraded as beam schedules and resources permit. The normal production current for the near future is expected to be 700 to 900 μA.

Through the development of increasingly advanced remote handling techniques, and through the practice of good staff discipline, it has been possible to hold radiation exposures to maintenance personnel to limits that have not increased during the past six years--a period when hardware activation has increased an order of magnitude.

LAMPF's basic schedule has been changed to a format of long running periods (~6 months) alternating with long shutdowns during the 1982-1985 period. Such a schedule allows lengthy major improvements to be carried out, and also results in some economy of operation through the reduction of tune-up and checkout periods. In a major facility upgrade that required a full remote handling approach, LAMPF's A-2 target cell was completely rebuilt during the 1983 long shutdown. This will be followed by the replacement of the A-1 target cell in 1984 and a major revision of the beam stop facility in 1985.

Neutron Facilities at LAMPF

Although a major research program utilizing spallation neutrons is based at the Weapons Neutron Research Facility (WNR), described elsewhere in these proceedings,[2] there exists at LAMPF additional opportunity for realizing a spallation neutron flux. At present, at the beam stop area (Target Station A-6), it is possible to emplace samples in a neutron flux of $\sim 1 \times 10^{17}\ m^{-2}s^{-1}$.[13] Line of sight apertures are available at 5° and 135° relative to the direct proton beam. Neutrons, as well as protons, pions, and other secondaries, are generated as the incident proton beam (~745 MeV at 500-700 μA) interacts with isotope production targets and finally with the beam stop. These facilities have been used for a limited number of radiation damage/effects studies, as well as for neutron flux and spectrum measurements.

Now, a major upgrade of the beam stop area is in progress. This effort has practical application for LAMPF: improved environment for beamline diagnostics, improved shielding, the elimination of cracks to capture activated gas, remote handling and shielded transport of radioactive material, and rapid repair/replacement of components or experimental hardware.

A new facility for both direct proton and neutron radiation effects studies, improved facility for high-speed ("rabbit") and ultra-high-speed ("gas-jet") isotope identification, and access for additional experiment initiatives in nuclear and solid state physics, will be provided at the upgraded beamstop area.

All penetrations into the new target chamber are vertical shield plugs that support individual experiments or beam line components. A basic design criterion is that all services, including cooling water and controls needed for equipment and experiment, be carried with the shielded insertion plug for the component that they service. All connections will be made at the top of the shield plug. The line-of-sight capability has been retained.

The new design is shown in schematic form in Fig. 6. Handling and subsequent transport of radioactive material is accomplished by employing a remotely-operated bottom-entry shielded cask, shown schematically in Fig. 7.

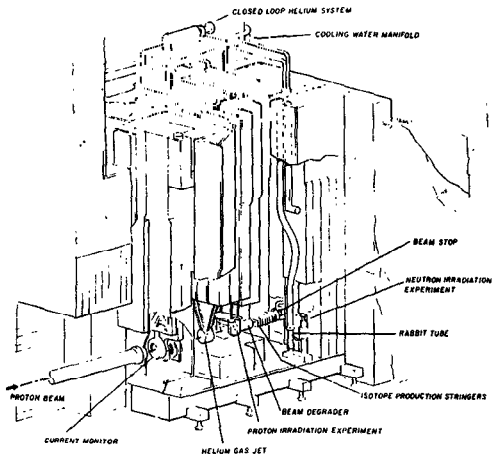

Fig. 6. Schematic layout of the new LAMPF Target Station A-6.

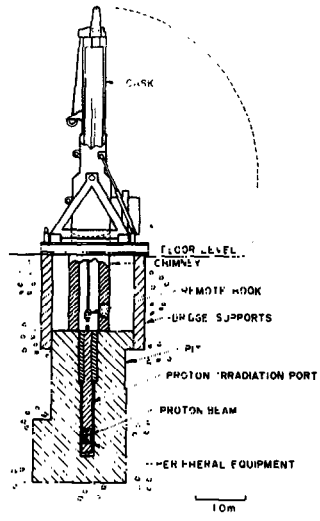

Fig. 7. Schematic showing the removal of a shield plug and experiment. Note the scale.

As an aid in the design of this facility, Monte Carlo calculations (2) using the Monte Carlo Code for the Transport of Neutrons and Protons (MCNP) and the High Energy Transport Code (HETC) were done to give an estimate of the expected neutron and secondary particle flux and spectrum at all locations in this facility. These results were used to design the placement of water-cooled shielding.

Fig. 8 shows an example of the results of the calculation. This histogram predicts the neutron flux and spectrum adjacent the second isotope production target. This location was found to have the maximum neutron flux in the facility, according to the calculation. Here, with LAMPF at 1000 μA, the integrated neutron flux was calculated to be $\sim 5 \times 10^{17}\ m^{-2}\ s^{-1}$.[14] Notice that substantial numbers of high energy (>20 MeV) neutrons will be available. Twelve independent penetrations into this neutron area will be available.

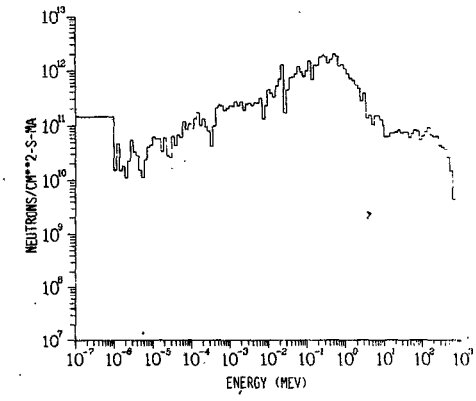

Fig. 8. Neutron flux and spectrum near the second Isotope Production Stringer calculated with MCNP and HETC.

Plans call for the completion of this facility in spring 1985. Several experiments have been identified, including a systematic study of materials intended for the German spallation neutron source (SNQ) target wheel.

References

1. R. J. Macek, "Operating Experience with the Meson Factories," invited talk at the ICANS V, Workshop on High-Intensity Accelerators and Compressor Rings, Karlsruhe, (June 25-26, 1981).

2. C. D. Bowman, "Status Report on WNR/PSR," presented at the opening session of this conference.

3. H. A. O'Brien, A. E. Ogard, and P. M. Grant, "The LASL Medical Radioisotope Research Program: An Overview of LAMPF and the Isotope Production Facility," Medical Cyclotrons in Nuclear Medicine, pp 16-22, Published as part of the series on Progress in Nuclear Medicine by S. Krager, Basel, (1978).

4. R. J. Macek, D. L. Grisham, and R. D Werbeck, "Radiation Resistant Beam Components at LAMPF," Proceedings of this Conference.

5. D. L. Grisham and J. E. Lambert, "Remote Handling at LAMPF," Proceedings of this Conference.

6. D. L. Grisham and J. E. Lambert, "Water-Cooled Target Box Design at LAMPF," IEEE Transactions on Nuclear Science, Vol. NS-30, No. 4, (August 1983).

7. D. L. Grisham and J. E. Lambert, "Water-Cooled Beam Line Components at LAMPF," IEEE Transactions on Nuclear Science, Vol. NS-28, No. 3, (June 1981).

8. R. D. Brown and D. L. Grisham, "Graphite Targets at LAMPF," IEEE Transactions on Nuclear Science, Vol. NS-30, No. 4, (August 1983).

9. R. D. Brown and D. L. Grisham, "Design and Operation Water-Cooled Pyrolytic Graphite Targets at LAMPF," IEEE Transactions on Nuclear Science, Vol. NS-28, No. 3, (June 1981).

10. L. Agnew, T. S. Baldwin, D. L. Grisham, R. C. Holmberg, J. E. Lambert, L. O. Lindquist, R. D. Reiswig, and L. L. Thorn, IEEE Transactions on Nuclear Science, Vol. NS-26, 4143-4145 (June 1979).

11. E. W. Hoffman, et al., "High Intensity Beam Profile Monitor for the LAMPF Primary Beam Lines," IEEE Transactions on Nuclear Science, Vol. NS-26, No. 3, pp 3420-2, (1979).

12. R. J. Macek, et al., "LAMPF Primary Beam Line Protection System," IEEE Transactions on Nuclear Science, Vol. NS-26, No. 3 pp 4137-9, (1979).

13. D. W. Barr and S. S. Gilmore, "Neutron Dosimetry at LAMPF Radiation Effects Facility," Los Alamos National Laboratory internal memorandum, (1979).

14. D. R. Davidson, W. F. Sommer, J. N. Bradbury, R. E. Prael, and R. C. Little, "Characterization of the LAMPF Beamstop Area Radiation Environment," Los Alamos National Laboratory report, LA-UR-83-33 (1983). Submitted to Third Topical Meeting on Fusion Materials, Albuquerque, NM, (September 1983).

Proceedings of International Collaboration on Advanced Neutron Sources (ICANS-VII), 1983 September 13-16
Atomic Energy of Canada Limited, Report AECL-8488

OPERATING EXPERIENCE WITH THE IPNS NEUTRON GENERATING SYSTEM

A. W. Schulke, D. E. Bohringer, B. S. Brown, J. M. Carpenter

Argonne National Laboratory
Argonne, Illinois 60439

Summary

The Intense Pulsed Neutron Source (IPNS) has operated since May, 1981, using two Zircaloy-2 clad uranium targets, their light-water cooling systems and various moderator-reflector systems. IPNS has two independent facilities, the Neutron Scattering Facility (NSF) and the Radiation Effects Facility (REF). This paper describes these IPNS facilities, the Neutron Scattering Moderators, and operational experiences with the systems.

Description of Neutron Generating Systems

The proton acceleration process begins with production of H^- ions in the ion source; these are accelerated to 750 KeV in the Cockroft-Walton preaccelerator and further accelerated to 50 MeV in the linear accelerator. At injection into the rapid cycling synchrotron, two electrons are stripped off in a thin polymer foil and the resulting proton is accelerated to an energy of 400-500 MeV. All of the protons are extracted in a single revolution so that very short (100 nano-seconds) pulses of protons are delivered to the uranium targets. This process is repeated 30 times per second. The proton beam passes through an aluminum vacuum window at the end of the proton transport line into the IPNS neutron generating system. A switching magnet just before the vacuum window diverts the proton beam 5° either to the right or to the left into the chosen uranium target. Between the switching magnet and the targets is a proton beam gate to guarantee exclusion of proton beam from the non-operating target in case of switching magnet failure. Also in front of each target is a proton beam diagnostic well containing instruments (PAS/SWIC) designed to assure that the proton beam characteristics (position and size) are proper before impinging on the targets.

The IPNS Zircaloy-2 clad uranium targets have been in use in both the neutron scattering facility (NSF) and radiation effects facility (REF) since startup (1981). The depleted uranium targets consist of eight 25 mm-thick, 100 mm-diameter uranium alloy disks, clad with 0.5 mm Zircaloy-2, (1.5 mm on circumference) cooled by demineralized water flowing in 1 mm channels between the disks. Disks 1, 3, 5, and 7 contain small, steel-sheathed thermocouples in zircaloy wells at their centers.

The thermocouples in disks 1 and 3 provide diagnostic information. The disks are housed in a 304 stainless steel vessel. The two targets are identical except for a 90° rotation about an axis parallel to the proton beam.

Demineralized water for target cooling is provided by two separate, but identical, closed-loop water systems that transfer target heat to a secondary water cooling system. Each system has a primary pump, heat exchanger, a helium-gas covered surge tank equipped with a hydrogen recombiner, storage tank, ion exchange column, filters, piping and associated valves, as well as necessary control and diagnostic instrumentation. The systems are sealed inside a 6 ft^3 aluminum box. A Geiger counter mounted near the ion exchanger, monitors gross gamma activity primarily due to positron-annihilation and nitrogen 16 gamma rays. In case of target clad failure, the level of accumulated fission products in the target coolant ion exchanger and surge tank cover gas is an indication of the target cladding integrity.

The cover gas from the surge tank is also circulated outside the biological shield to a NaI gamma ray detector and then returned to the surge tank. The circuit provides a 180 minute holdup time which allows decay of the intense short-lived gaseous activity (^{13}N, ^{11}C, etc.) generated by the reaction of protons and neutrons with the cooling water and dissolved gases. The 250 KeV gamma rays associated with the decay of ^{135}Xenon are then measured, whose presence in the gas above the surge tank has been determined to be the most sensitive on-line indication of fission products leaking from the target. The fission yield of ^{135}Xenon is high; the specific activity is high; and xenon, as a gas, moves readily through very small openings in the target clading. The fission product monitor is backed up by grab samples from an on-line gas sampling station. The cover gas in the surge tank exhausts through a holdup device, a HEPA (High Efficiency Particulate Air) filter, the neutron facility ventilation exhaust blower and then exits to the exhaust stack. A stack monitor is located in the exhaust gas stream to monitor the effluent.

The neutron generating facilities and target support systems are surrounded by a biological shield which provides structural support, shielding, and physical protection against damage from external forces. The biological shield consists of an inner steel shield (1100 tons) immediately surrounding the neutron generating system components and an outer concrete shield (50 tons). The steel shield is enclosed in an atmospheric control tank which functions as the boundary of the shield atmosphere control system, which is operated at slight vacuum. The shield is designed to limit radiation dose rate at any accessible location in the experimental area from all radioactive sources within the shield during normal operation to 0.5 mrem/hr. The shielding also keeps the background levels at the neutron scattering instruments to a minimum.

Neutron Scattering Facility (NSF)

In the neutron scattering facility, the fast neutrons produced by fission and spallation reactions in the target are thermalized by moderators (with a high hydrogen density) located above and below the target. We have used two types of moderators. One type consists of four, ambient-temperature polyethylene moderators with an inner graphite reflector. The second consists of four 100 K circulating liquid CH_4 moderators with an inner 100 K beryllium reflector. These moderators are surrounded by an outer, 300 K beryllium reflector. Twelve horizontal neutron beam tubes and one vertical neutron beam tube view selected faces of the moderators to provide neutron beams to instruments. Each horizontal beam tube contains a 36" thick steel beam gate. Two vertical holes (VT3 and VT4) and two horizontal holes (F-6 and H-2) may be used for sample irradiations. A polyethylene insert has been added to one of the vertical holes to enhance the neutron flux and has resulted in an increase in the thermal neutron flux by a factor of two.

Radiation Effects Facility (REF)

In the radiation effects facility, the neutrons emitted from the target pass into high density reflector materials (lead) which maximizes the fast neutron flux within irradiation holes, two vertical (VT1 and VT2) and one horizontal. Thimbles are provided to permit samples to be inserted and removed. Two vertical tubes are equipped for irradiation of samples at controlled temperatures between 4 K and 600 K; the horizontal tube operates only at ambient temperature.

Control and Monitoring Systems

The control system for IPNS consists of 1) a mini-computer for processing information, 2) a hardwired data input/output system for gathering information providing for control and proton beam shutdown and 3) a Cathode Ray Tube display and keyboard. The computer also fills a backup role to the separate hardwired proton beam shutdown system by providing alarms and a software proton beam shutdown.

Moderators

The moderator-reflector assembly used during the first year was of room temperature polyethylene with graphite reflector. This was installed to allow modification of the beryllium-reflector L-CH_4-L-H_2 system, which we discovered would not function as designed.

After 15 months operation, the polyethylene moderators and graphite reflector assembly was removed from the NSF during the August, 1982 shutdown. The polyethylene-graphite assembly had three ambient-temperature poly moderators, with inner graphite reflector and outer beryllium reflector, and cadmium decoupling and void liners throughout. This assembly did not provide a vertical beam moderator. Upon removal of this assembly, the radioactivity levels were found to be 40 mr/h to 120 mr/h on the two steel shield plugs above the reflector and 200 mr/h at 5 cm for the graphite-poly assembly. These parts were bagged and stored in shielded containers. The removal procedure was relatively easy with the only surprise being loose rust contamination around the top area of the moderator well. Activity levels ranged up to 2 x 10^3 dis cm^2/min $\beta\gamma$ with no detectable α contamination. These areas were wiped down (wet) and covered with anti-rust paint to reduce the spread of activity. It was thought that the areas where the rust was found were in a helium atmosphere. We investigated the operation and integrity of the helium system. The system was found intact and the helium flow increased. Our best guess for the cause of the rust was that the two concrete and lead shot filled, steel cased shield plugs were not dried long enough to rid the concrete of its moisture and the moderator housing was not sealed properly so as to let air leakage in via the neutron facility ventilation system.

The liquid methane moderators and inner beryllium reflector assembly were checked, tested and cycled three times using its refrigeration equipment before it was installed in the NSF facility. In process of testing, we found that the "L-H_2" systems could not operate at 20 K while the "L-CH_4" systems operate at 100 K. We decided to forgo use of 20 K L-H_2 moderators, and to operate all four moderators with 100 K L-CH_4. All tests then indicated that reliable operation could be expected. The proton beam was put on the NSF target from 29 September to 4 October 1982 (total of 2.17 x 10^{19} proton pulses) with a proton energy of 400 MeV. After two days of beam on target the flow to "H" moderator showed degradation, by the fourth day the flow was blocked. Various attempts to restore flow were tried including cycling the throttle valve (thought to have frozen due to moisture), changing liquid nitrogen flow to the heat exchanger, and bypassing part of the methane flow. All attempts were to no avail. The facility was shutdown and the moderator systems were warmed up. The methane gases were circulated, gas samples were taken and the methane gas was changed. The original methane charge was Grade 4.2: methane (CH_4) 99.992%, nitrogen (N_2) 20 ppm, oxygen (O_2) 4 ppm and ethane (C_2H_6) 12 ppm. The new charge was Grade 4 99.95% methane (CH_4) and would not result in a significant change in impurity levels.

After another attempt at operating the system we decided the problem was the plugging of the 15 micron filters which were located in the weld-sealed, evacuated heat exchanger box. These filters were removed and replaced by 90 micron filters. The new filters were relocated in an accessible part of the system and fitted with easily removed slip couplings. Proton beam was again delivered to the system and flows to the 4 liquid methane moderators at 100 K were much improved. Prior to this run, we also changed the 90 micron filters to assure ourselves that we had cleaned the foreign residue from the system (see picture). Samples of the methane gas were also taken again.

This photo is a magnification (70X) focusing on large particles in the upper right quadrant. Light colored regions indicate a non-conductive material.

From 7 December to 21 December the system ran with proton beam on target; the 4 methane moderator systems ran with no problems. A significant increase in the neutron flux was seen (factor of about 8 at 5Å). Experiments that were run at this time indicated that the larger moderator, (thicker in the direction of the neutron beam) resulted in an increase in time width of the pulse that degraded the resolution in the powder diffractometers. This led to the decision that the moderators would be reworked. During the last operating cycle on the methane system, we erected a vacuum line to test the solubility of various boron compounds in cryogenic moderator fluids to seek an easy fix to the degraded resolution problem on the powder instruments. No practical solution was found. Methane gas samples were taken after the run.

Table 1 - Summary of Mass Spectrometer Measurements on Irradiated CH_4

Irradiation Conditions	Moderator	Mole % CH_4	Mole % H_2	Mole % C_2H_6	Mole % C_3H_8	Mole % C_4H_{10}	Mole % Other Hydrocarbons (C_n,n>4)	Mole % H_2O
After 2.2 x 10^{19} protons on target	H	99.6	-	0.3	0.1	-	<.02	<.05
	F	98.8	-	0.9	0.2	-	.08	.02
	C	99.6	-	0.3	0.1	-	<.02	<.03
	V	99.3	-	0.5	0.2	-	<.02	≤.03
After 5.2 x 10^{18} protons on target	H	99.2	<.06	0.4	0.2	0.1	-	<.03
	F	99.7	<.06	0.2	0.08	0.02	-	<.03
	C	99.1	<.06	0.5	0.3	0.1	-	<.03
	V	99.3	<.06	0.5	0.1	0.02	-	<.03
After add'l 4.6 x 10^{19} protons	F	99.8	-	0.2	0.03	0.003	-	<.03
	V	99.8	-	0.2	0.01	0.002	-	<.03
After add'l 4.8 x 10^{19} protons	H	98.0	1.5	0.4	0.06	-	≤0.02	-
	F	97.9	1.5	0.5	0.06	-	0.02	-
	C	99.1	0.7	0.2	≤0.02	-	<0.03	-
	V	98.4	1.2	0.3	0.04	-	0.04	-

Prior to changing of the in-line filters, there was a concern that flow problems were due to possible heavy hydrocarbon buildup, but the gas samples taken at various times proved that this buildup was minimal. The mass spectrometer analysis of the methane prior to irradiation was CH_4 99.9, $H_2O \leq .02$, $N_2 + CO < .01$, O_2 .005, Ar < .005, $CO_2 < .005$, H_2 0.0, C_2H_6 0.0, C_3H_8 0.0, C_4H_{10} 0.0, other hydrocarbons ≤ .05. These numbers are in mole percent. The results of the analysis after irradiation are given in Table 1. ANL's chemical analytical lab ran tests on the used filters and recommended a cleaning agent for cleaning hydrocarbon buildup if needed. The most effective solvent for cleaning seems to be tetrahydro-furan.

One other minor problem was the activity level of ^{11}Carbon that built up in the heat exchangers during operation. Activity levels up to 250 mr/hr βγ were measured. If this system would operate continuously, shielding would need to be added around the heat exchangers.

The polyethylene graphite beryllium moderator assembly was modified to provide a vertical moderator (LN_2 cooled polyethylene) for the ultracold neutron experiment. Also, new polyethylene moderators replaced the ones inserted August 1981. This system has been in operation since February 1983 till August 1983.

During this summer shutdown, August-September 1983, we are building a new graphite/polyethylene reflector moderator system. The new system will have an L-N_2-cooled polyethylene moderator in the "C" position. This should provide a higher intensity of long wave neutrons to the SAD, ^{3}He and polarized neutron instruments.

The removal of the methane/beryllium moderator from the NSF went well; levels of radiation were 2.1 R/h at 5 cm βγ. A portable hyperpure germanium detector and 8 K multichannel analyzer were used to identify predominent radioactive nuclides. Using the observed relative intensities and known values for exposure rate per unit activity and gamma's per desintegrations, the relative contribution of the observed nuclides was calculated. Using the respective values for half-life, the time dependence of the radiation field was estimated for several points in time up to one year. The exposure rate is expected to decrease by ∿ 18% the first month and ∿ 6 % for the first year. Monthly readings taken by the radiation safety people on the moderator has shown these calculations to be fairly accurate. The moderator as of August 1983 reads ∿ 565 mr/h βγ. At this time we have not decided whether or not to rework the moderator seen by the powder diffractometers.

Primary Water Cleanup Ion Exchange System and Water and Gas Sampling Program

Each of the two target cooling systems has a prefilter made up of three (3 micron) cartridges. Approximately 25% of the total system flow (50 gpm) goes through this filter housing with the remaining flow through a bypass line around the filter.

Down stream from the pre-filter is a motorized valve which is set to divert some of the water (1-10 gpm) thru a mixed resin bed. The resin column contains ∿ 1.9 cubic feet of Illinois Water Treatment #NR-6 (HOH) resin. Part of the total flow is also diverted to a water quality-sample station with an on-line conductivity instrument then returned to the main flow stream. Water samples for checking Ph and radioactivity can also be taken at this station. All primary flow then passes through an after-filter made up of three (3 micron) sintered stainless steel cartridges. This after-filter's primary function is to stop any resin that might escape from the ion exchange which could possibly plug the target flow channels. The resin in the ion exchangers has been in the system since startup of IPNS. These resins have kept the deionized water used in the primary system at a conductivity level below .1 μmho's and a Ph of ∿ 6.8.

Since we are concerned with the U target and the possibility of a target clad failure, we decided to periodically remove a sample of resin from the ion exchanges so it could be analyzed for uranium content. The methods used are (EDXRF) x-ray fluorescence and gamma-ray analyses. The fluorescence method is the most sensitive. A sample of factory-fresh resin showed 20 nanograms/gram uranium by x-ray fluorescence and none detected by gamma-ray analysis. Samples of

the system resins ranged from 22 to 53 nanograms/gram over a two year period. Gamma-ray analyses showed various isotopes that one might expect ^{7}Be, ^{46}Sc, ^{51}Mn, ^{57}Co, ^{58}Cu, and ^{88}Y, but no detectable fission products. We feel this is a good operational diagnostic tool.

The primary water samples that are taken periodically are analyzed for radioactive nuclides dissolved or suspended in the water. After several hours decay, the most significant activity in the water is ^{7}Be, and ^{3}H. Other nuclides in much lesser amounts are detected but the purpose of these analyses are for evidence of target clad failure. These analyses have also given no evidence of target clad failure. Lead shielding was added around the ion exchangers and dense concrete shielding put on top of the primary water coolant boxes to reduce the high gamma-levels produced primarily from ^{7}Be from the water (i.e., spallation product).

The gas sampling program has also been conducted since startup of IPNS. Gas samples from the primary coolant cover gas are taken periodically during operation. The samples are analyzed for radioactive gases and act as a backup to the automatic fission product monitor. These samples are also analyzed for any possible hydrogen buildup in the cover gas. The analysis of the grab samples has shown presence of ^{76}Kr, ^{77}Kr, ^{79}Kr and ^{41}Kr. The samples are analyzed after the very short half-life nuclides such as ^{13}N, ^{16}N, ^{15}O, and ^{11}C are allowed to decay. No other gaseous nuclides have been detected. Typical concentrations of ^{77}Kr are $5 \times 10^{-5}\mu Ci/ml$ and ^{41}Ar $1 \times 10^{-4}\mu Ci/ml$.

A mass spectrometer determines H_2 concentration. The H_2 concentration is typically less than 0.5%. The experience with hydrogen buildup that we encountered with the Zing-P' cooling system has not occurred with the IPNS cooling systems. Possible causes for elimination of the hydrogen buildup are the HOH resins that we now use, the better gaseous mixing device installed in the surge tank, the addition of pre-heating the palladium-coated aluminum oxide pellets in the recombiner, and the Zircaloy-2 clad of the uranium. Therefore it remains a mystery why we found the excess hydrogen at Zing-P' and essentially none at IPNS.

Uranium Targets

The uranium targets have functioned trouble free. Two situations have occurred that are worth mentioning. During the early testing of the cold methane moderators the coolant flow to the NSF target was shutdown for the night. A casual check of target temperatures indicated that they were very close to freezing. This happened because a thermal short developed between the 100 K surfaces in the moderator-reflector assembly and the outer surface on which the target housing rests. The moderator systems were shutdown for the night and allowed to warm up. We then visually inspected the target to assure it was not damaged and took photographs of the target. Target flow was reestablished and various target system parameters were checked. One should make sure that standard operating procedures are established when the target coolant systems are operating and the cold moderators are operating. An option is to install an interlock between the two systems.

The second operating experience that occurred recently (within the last few months) was that two thermocouple readouts to each of the targets opened. We investigated this during our present shutdown and discovered corrosion at the thermocouple connection. These connectors were cleaned and the readouts returned to normal. We hope to prevent reoccurrences of this problem by adding an interlocking neoprene boot around the connector, and also bagging the connector in an inert atmosphere. The junctions themselves, within the target disks, were not involved nor affected.

Proton Beam Diagnostic Systems

The purpose of this system is to provide safe beamline operation and to prevent "hot spots" on the targets. The beamline performance is assessed by a position and size (PAS) monitor (ionization monitor) and a segmented wire ionization chamber (SWIC). The PAS produces proton beam shutdown signals for beam too small, too large or off axis. The SWIC produces a separate signal to obtain two profiles from which are obtained the beam size and position in the horizontal and vertical planes. Each target is equipped with a PAS and SWIC in the diagnostic well.

These monitors have been very reliable but as mentioned in previous sections of this paper, corrosion in these wells had been a problem. These wells are made of steel and have a helium supply system. The helium supply was inadequate, so an additional helium line was added to directly blow inert gas on the diagnostic monitors. The steel shield plug was sprayed with molykote molybdenum disulfide compound to decrease rust and other corrosion buildup.

The point to be made here is that during construction stages the steel should be coated with some anti-corrosion agent, painted or even electro-plated. This would make life much easier for operations personnel who have to maintain equipment located in these environments.

Stack Monitoring System

The IPNS stack monitor system serves three purposes. Primarily, it provides real time information on the radioactivity being released up the stack along with alarm capability to alert operating personnel to a problem. Second, it provides record documentation to support required reports of the total quantity of radio-nuclides released to the environment in the gaseous effluent from the IPNS. Third, this system provides a measure of backup monitoring and alarm capability for the target coolant and the ion exchange resin monitoring systems to trigger an alarm in the event of a major release of radioactive nuclides through these systems.

The IPNS stack monitor is composed of a set of radiation detectors on a sampling line designed to quantitatively measure the radioactive gases and particulates in the stack effluent of the IPNS. The system includes the air pumps, flow control, signal processors, data readouts, power supplies and piping, and electrical interconnection between components. The air pump pulls a continuous sample from the stack effluent stream, downstream of the HEPA filters, and passes it sequentially through a particulate filter, an activated charcoal gas adsorbent, and a noble gas counting chamber before returning the sample flow to the stack. The sample flow rate is controlled to be isokenetic with the flow of the effluent stream. The materials collected on the particulate filter are counted for β activity with a plastic β scintillator (50 mm diameter x 4 mm thick)/photo tube assembly. The activated charcoal adsorber is continuously counted for γ activity with a NaI(Tl) (50 mm x 50 mm) scintillation detector. The ~ 300 cm^3 noble gas chamber is continuously counted for β activity with a similar plastic β scintillator. All three detector channels are provided with background compensation to

reduce the effects due to changes in the ambient γ ray background. Each detector is shielded by a minimum of 5 cm of lead in the form of fine shot contained in a welded steel box.

The output data from each counting channel is sent to the IPNS central control CAMAC system, at one minute intervals. The display readout is provided in the IPNS main control room either on operator command or whenever one or more alarm points are exceeded.

The readout is printed at the terminal once each hour when all operating conditions are within normal range. Under abnormal conditions, e.g., an alarm point exceeded, the channel data is printed once each minute. The format for the channel data printout is digital and graphic in form with time of day and six channels of data being printed and the data graphed on the same line of print

The stack monitor is a good diagnostic tool for operations personnel. After background and running limits are set, operations personnel can also be alerted to changes various experimenters make on the instruments, i.e., off gassing from pumps, warming up and pumping out of cryostats etc. The stack monitor can also act as a backup to the fission product monitor.

Conclusions

The Neutron Generating Systems have operated without serious trouble since the startup of IPNS. The original cold moderator system as designed would need extensive changes, especially to the liquid hydrogen moderator hardware. The available sub-cooling was also marginal for the liquid methane moderators. Therefore, with the prospect of an increased heating load from an enriched uranium target, a new cold moderator system will be designed and built.

LIST OF ATTENDEES

	Name	Affiliation
1.	T.W. Armstrong	SAI
2.	F. Atchison	SIN
3.	R. Baartman	TRIUMF
4.	G.A. Bartholomew	CRNL retired
5.	G.S. Bauer	KfA
6.	E.W. Blackmore	TRIUMF
7.	D. Bohringer	ANL
8.	C.D. Bowman	LANL
9.	H. Brockmann	KfA
10.	W.J.L. Buyers	CRNL
11.	A. Carne	RAL
12.	J.M. Carpenter	ANL
13.	K.C.D. Chan	CRNL
14.	R. Chiba	Tokyo Ins Tech
15.	B.G. Chidley	CRNL
16.	P. Cloth	KfA
17.	P. Clout	LANL
18.	W.G. Cross	CRNL
19.	B. Diplock	RAL
20.	G. Dolling	CRNL
21.	T. Dombeck	LANL
22.	P.A. Egelstaff	Guelph
23.	D. Filges	KfA
24.	W.E. Fischer	SIN
25.	J.S. Gilmore	LANL
26.	P. Grand	BNL
27.	D.L. Grisham	LANL
28.	R.A. Hardekopf	LANL
29.	E.A. Heighway	CRNL
30.	T.M. Holden	CRNL
31.	H. Ing	CRNL
32.	A. Jason	LANL
33.	R.T. Jones	CRNL
34.	V. Kempson	RAL
35.	T.K. Khoe	ANL
36.	M. Kimura	Sendai
37.	M.A. Kirk	ANL
38.	R.L. Kustom	ANL
39.	J.E. Lambert	LANL
40.	G.H. Lander	ANL
41.	G.P. Lawrence	LANL
42.	W. Lohmann	KfA
43.	M.A. Lone	CRNL
44.	J. McKeown	CRNL
45.	G.E. McMichael	CRNL
46.	R.J. Macek	LANL
47.	G. Manning	RAL
48.	M. Meier	LANL
49.	J. Norem	ANL
50.	J.H. Ormrod	CRNL
51.	C.W. Potts	ANL
52.	A. Rauchas	ANL
53.	J.A.L. Robertson	AECL-HO
54.	H. Robinson	LANL
55.	G.J. Russell	LANL
56.	H. Sasaki	KEK
57.	J. Schelten	KfA
58.	S.O. Schriber	CRNL
59.	M.R. Shubaly	CRNL
60.	R.N. Sinclair	Harwell
61.	H. Stechemesser	KfA
62.	G. Stirling	RAL
63.	H. Takahashi	BNL
64.	Y. Takeda	SIN
65.	G. Thamm	KfA
66.	I.M. Thorson	TRIUMF
67.	Y. Uemura	BNL
68.	R. Woods	LANL

AUTHOR INDEX

A

Agnew, L. 279
Amian, W. 62
Armstrong, T.W. 194, 205
Atchison, F. 23, 266

B

Bauer, G.S. 1, 240
Blaby, R.E. 31
Blackmore, E.W 55
Bowman, C.D. 8
Brandeberry, F. 140
Brockmann, H. 105
Brumwell, F.R. 144
Burgerjon, H. 31
Buttzereit, H. 256

C

Carne, A 100, 214
Carpenter, J.M. 40, 236
Chan, K.C.D. 166
Chidley, B.G. 162
Cloth, P. 78, 194, 205
Clout, P. 128
Colborn, B.L. 205
Conrad, H. 240

D

Dombeck, T. 175

E

Egelstaff, P.A. 271

F

Filges, D. 78, 194, 205
Fischer, W.E. 23

G

Gilmore, J.S. 68
Grisham, D.L. 246, 252, 279
Grünhagen, K. 240

H

Hardekopf, R.A. 134
Herrnberger, V. 122
Hodges, T.A. 31

I

Ikeda, S. 230
Inoue, K. 230
Ishikawa, Y. 230
Iwasa, H. 230

J

K

Khoe, T.K. 40, 46
Kimura, M. 90
Kirk, M.A. 185
Kiyanagi, Y. 230
Kondo, K. 230
Krautwasser, P. 84
Kustom, R.L. 40, 46

L

Lambert, J.E. 246, 252
Lander, G.H. 40
Lohmann, W. 84, 274
Lone, M.A. 200

M

McKeown, J. 166
McMichael, G.E. 162
Macek, R.J. 246, 279
Manning, G. 34
Milleret, G. 240

N

Neef, R.D. 78
Narem, J. 140

O

Ostrowski, G. 157

P

Peek, N.F. 62
Pelizzari, C. 157
Pepin, M. 118
Potts, C.W. 144
Prael, R.E. 68

Q

R

Rauchas, A. 157
Robinson, H. 68
Robinson, R.A. 236
Russell, G.J. 68

S

Sasaki, H. 14, 50
Schaal, H. 78
Schelten, J. 148
Scherer, W. 105
Shaddon, D.J. 62
Shubaly, M.R. 162
Sinclair, R.N. 172
Sommer, W.F. 279
Spitzer, H. 240
Stechemesser, H. 109, 256
Sterzenbach, G. 62, 205
Stiller, P. 122
Stipp, V.F. 144

T

Takeda, Y. 223
Taylor, A.D. 236
Thamm, G. 109, 256
Thorson, I.M. 31
Tsuchihashi, K. 230

U

V

Volk, G. 157

W

Watanabe, N. 230
Werbeck, R.D. 246, 279
Wolters, J. 256

X

Y

Z

Zettler, C. 148

ISSN 0067-0367

To identify individual documents in the series we have assigned an AECL- number to each.

Please refer to the AECL- number when requesting additional copies of this document

from

Scientific Document Distribution Office
Atomic Energy of Canada Limited
Chalk River, Ontario, Canada
K0J 1J0

Price $11.00 per copy

ISSN 0067-0367

Pour identifier les rapports individuels faisant partie de cette série nous avons assigné un numéro AECL- à chacun.

Veuillez faire mention du numéro AECL- si vous demandez d'autres exemplaires de ce rapport

au

Service de Distribution des Documents Office
L'Energie Atomique du Canada Limitée
Chalk River, Ontario, Canada
K0J 1J0

Prix $11.00 par exemplaire

©ATOMIC ENERGY OF CANADA LIMITED, 1984

3003-84